Optimization of an X-ray diffraction imaging system for medical and security applications

Fanny Marticke

To cite this version:

Fanny Marticke. Optimization of an X-ray diffraction imaging system for medical and security applications. Signal and Image processing. Université Grenoble Alpes, 2016. English. NNT : 2016GREAT055 . tel-01381173v2

HAL Id: tel-01381173

https://theses.hal.science/tel-01381173v2

Submitted on 28 Nov 2016

Communauté
UNIVERSITÉ Grenoble Alpes

THÈSE

Pour obtenir le grade de

DOCTEUR DE LA COMMUNAUTÉ UNIVERSITÉ GRENOBLE ALPES

Spécialité : **Signal, Image, Parole, Télécoms**

Arrêté ministériel : 7 août 2006

Présentée par

Fanny MARTICKE

Thèse dirigée par **Caroline PAULUS**
Guillaume MONTEMONT
Olivier MICHEL
Jérôme I. MARS

préparée au sein du **Laboratoire détecteurs (CEA/LETI)**
dans **l'École Doctorale : Electronique Electrotechnique Automatique et Traitement du Signal**

Optimization of an X-ray diffraction imaging system for medical and security applications

Thèse soutenue publiquement le **19 juillet 2016**,
devant le jury composé de :

Dr. Alberto BRAVIN
University of Milano-Bicocca, Rapporteur
Prof. David BRIE
Université de Lorraine-Cran, Rapporteur
Prof. Alice CAPLIER
Institut polytechnique de Grenoble, Présidente
Dr. Philippe DUVAUCHELLE
INSA Lyon, Examinateur
Dr. Jens-Peter SCHLOMKA
Morpho Detection Germany GmbH, Examinateur
Prof. Jérôme I. MARS
Institut polytechnique de Grenoble, Directeur de thèse
Prof. Olivier MICHEL
Institut polytechnique de Grenoble, Co-directeur (invité)
Dr. Caroline PAULUS
CEA, LETI, Grenoble, Co-encadrante (invitée)
Dr. Guillaume MONTEMONT
CEA, LETI, Grenoble, Co-encadrant (invité)

Communauté
UNIVERSITÉ Grenoble Alpes

THÈSE

Pour obtenir le grade de

DOCTEUR DE LA COMMUNAUTÉ UNIVERSITÉ GRENOBLE ALPES

Spécialité : **Signal, Image, Parole, Télécoms**

Arrêté ministériel : 7 août 2006

Présentée par

Fanny MARTICKE

Thèse dirigée par **Caroline PAULUS**
Guillaume MONTEMONT
Olivier MICHEL
Jérôme I. MARS

préparée au sein du **Laboratoire détecteurs (CEA/LETI)**
dans **l'École Doctorale : Electronique Electrotechnique Automatique et Traitement du Signal**

Optimization of an X-ray diffraction imaging system for medical and security applications

Thèse soutenue publiquement le **19 juillet 2016**,
devant le jury composé de :

Dr. Alberto BRAVIN
University of Milano-Bicocca, Rapporteur
Prof. David BRIE
Université de Lorraine-Cran, Rapporteur
Prof. Alice CAPLIER
Institut polytechnique de Grenoble, Présidente
Dr. Philippe DUVAUCHELLE
INSA Lyon, Examinateur
Dr. Jens-Peter SCHLOMKA
Morpho Detection Germany GmbH, Examinateur
Prof. Jérôme I. MARS
Institut polytechnique de Grenoble, Directeur de thèse
Prof. Olivier MICHEL
Institut polytechnique de Grenoble, Co-directeur (invité)
Dr. Caroline PAULUS
CEA, LETI, Grenoble, Co-encadrante (invitée)
Dr. Guillaume MONTEMONT
CEA, LETI, Grenoble, Co-encadrant (invité)

Acknowledgement

Even though this part of my thesis manuscript is placed at the beginning, it was written at last. In fact, I find it more difficult to write the acknowledgments than a thesis work. This is because, I would like to avoid the standard expressions which can be found in any acknowledgement in a PhD work. I would like it to be something special for all the people who helped me and supported me during these three years. Even though my manuscript is entirely in English, I will write the acknowledgements in different languages to be sure that the person concerned understands each of my words and also to be more natural.

First of all, I would like to thank Prof. Alice Caplier, Dr. Philippe Duvauchelle and Dr. Jens-Peter Schlomka who were respectively the president and the two examinators of my thesis jury. Thank you for your interest in my work and your interesting questions and comments during my thesis defense. I would also like to thank Dr. Alberto Bravin and Prof. David Brie for having accepted the role of rapporteurs asking some additional work. Thank you also for the interesting discussions during my thesis defense especially concerning possible future work.

Ensuite, je tiens à remercier mes encadrants de thèse. J'ai eu la chance mais aussi la difficulté d'avoir été encadrée par quatre personnes, deux du côté CEA Caroline Paulus et Guillaume Montémont et deux du côté Gipsa-Lab Jérôme Mars et Olivier Michel. C'était une chance car vous avez tous des compétences et des qualités différentes dont j'ai pu profiter tout au long de ma thèse. Cependant, c'était aussi difficile car il fallait prendre en compte quatre emplois du temps différents pour planifier des réunions et car vous n'aviez pas toujours des avis qui convergeaient.
Merci beaucoup, Caroline, pour ton accompagnement tout au long de ma thèse et pour toute ta "pénibilité" dans les corrections de mes documents et ton soutien organisateur et moral notamment vers la fin de ma thèse.
Guillaume, je te remercie pour tout le temps que tu as passé afin de m'aider à aller jusqu'au bout des choses, pour tout ce que tu m'as appris et pour ces discussions techniques fructueuses pas toujours facile pour moi et parfois frustrantes.
J'ai été contente de t'avoir comme directeur de thèse, Jérôme. Je te remercie pour ta forte présence, ton insistance sur l'aspect publication, et surtout, pour ton fort engagement dans la correction de mon manuscrit et de ma présentation de soutenance.
Olivier, merci pour ton regard critique sur mon travail. Les discussions techniques que nous avons eues et ton engagement pour la correction de la soumission au Gretsi m'ont énormément aidée.

Le début de ma thèse était pour moi un peu comme rentrer à la maison. Je connaissais déjà tout le monde du LDET de mon poste de CDD qui a précédé ma thèse. C'est aussi en partie

à cause de cela que j'ai choisi ce sujet de thèse plutôt qu'un autre. J'ai apprécié l'accueil chaleureux et la bonne ambiance dans ce laboratoire. Merci beaucoup à toute l'équipe du LDET pour tous ces moments que l'on a pu partager lors du repas de midi, d'une pause café, d'un goûter d'anniversaire, d'une petite discussion dans le couloir ou d'un petit cours de Zumba.
Je remercie en particulier le chef du LDET, Loïck Verger, de m'avoir accepté dans son laboratoire et d'avoir assuré les conditions pour le bon déroulement de ma thèse. Merci aussi pour ta compréhension et ton soutien quand je t'ai annoncé le changement de planning de ma thèse lié a l'arrivée de notre petit franco-allemand.

Au cours de ces trois années de thèse, j'ai partagé beaucoup de bon moments avec les autres thésards du LDET. Vous êtes devenus plus que des collègues de travail. Camille, j'étais contente de te retrouver au LDET et de mieux te connaître que pendant notre temps à Phelma. Merci à mes deux collègues de bureau Alexandra et Mélanie. J'ai pu partager tous mes soucis mais aussi toute ma joie avec vous. Anne, j'ai été très contente que tu aies été en bas avec les thésards pendant ton stage et que j'aie pu faire ta connaissance. Amr, Damien, Artur et Yoann, j'ai aussi été très contente que nos chemins se soient croisés. Je vous remercie pour tous ces bons moments (pauses café, soirées, fêtes d'anniversaire) que l'on passé ensemble, votre soutien dans les moments un peu critiques de ma thèse et votre amitié. Merci aussi pour votre intérêt que vous avez porté à ma grossesse et ma vie de maman.

Je tiens aussi à remercier mes amis qui étaient tous loin pendant ma thèse mais qui m'ont soutenu à leur manière. Laureline et Katia, on s'est connu ici à Grenoble et je suis la seule qui suis restée. Merci d'avoir écouté mes inquiétudes et partagé ma joie sur skype ou au téléphone. Jeanne und Sophia, Ihr seid die beiden Freundinnen, die mir noch vom FG geblieben sind. Auch Eure Freundschaft (Telefonate, Skype und Besuche) hat mir geholfen, die Doktorarbeit zu meistern. Besonders habe ich mich gefreut, dass Du, liebe Jeanne, extra zu meiner Doktorarbeitsverteidigung angereist bist.

Mes remerciements seraient incomplets sans remercier ma famille. Je tiens à remercier ma belle-mère sans qui les quatre derniers mois de ma thèse se seraient certainement moins bien passés. Merci pour ton aide avec Elouann et aussi de nous avoir préparé à manger de temps en temps. Un grand merci aussi à toi, Jonathan, pour ton soutien, ta compréhension, ton aide (sans toi, notre appartement aurait été un véritable chaos) et ta présence auprès d'Elouann. Elouann, mein kleiner Sonnenschein, Du hast mir das Ende der Doktorarbeit nicht unbedingt leichter gemacht, da Du anscheinend der Meinung warst, dass Schlafen komplett überbewertet wird. Allerdings hat mich ein Lächeln von Dir am Morgen die schlaflose Nacht sofort vergessen lassen. Durch Dich habe ich auch vieles relativiert und war am Ende der Doktorarbeit vielleicht weniger gestresst als ich es ohne Dich gewesen wäre. Ich möchte mich auch sehr bei meinen Großeltern bedanken, die mich mein ganzes Leben lang begleitet haben und mich während meines Studiums und der Doktorarbeit sowohl moralisch als auch finanziell viel unterstützt haben. Ein besonderer Dank gilt auch meinen Eltern, die mich immer in meinen Vorhaben (Austauschjahr, Schulwechsel, Auslandsstudium, Doktorarbeit) bestärkt haben. Mutti, jetzt, wo ich selber Mutter bin, ist mir klar geworden, wie schwierig es sein muss, sein Kind seine eigenen Wege (vor allem wenn sie weit weg von zu Hause führen) gehen zu lassen. Darum bin ich Dir umso dankbarer, dass Du mir das alles ermöglicht hast, mir bei meinen zahlreichen Umzügen zur Seite standest und immer da warst, wenn ich Dich gebraucht habe.

"*Why does this magnificent applied science which saves work and makes life easier bring us so little happiness? ... The simple answer runs: Because we have not yet learned to make sensible use of it.*"

Albert Einstein

Abstract

X-ray diffraction imaging is a powerful noninvasive technique to identify or characterize different materials. Compared to traditional techniques using X-ray transmission, it allows to extract more material characteristic information, such as the Bragg peak positions for crystalline materials as well as the molecular form factor for amorphous materials. The potential of this technique has been recognized by many researchers and numerous applications such as luggage inspection, nondestructive testing, drug detection and biological tissue characterization have been proposed. The method of energy dispersive X-ray diffraction (EDXRD) is particularly suited for this type of applications as it allows the use of a conventional X-ray tube, the acquisition of the whole spectrum at the same time and parallelized architectures to inspect an entire object in a reasonable time. The purpose of the present work is to optimize the whole material characterization chain. Optimization comprises two aspects: optimization of the acquisition system and of data processing. The last one concerns especially the correction of diffraction pattern degraded by acquisition process. Reconstruction methods are proposed and validated on simulated and experimental spectra. System optimization is realized using figures of merit such as detective quantum efficiency (DQE), contrast to noise ratio (CNR) and receiver operating characteristic (ROC) curves. The first chosen application is XRD-based breast imaging which aims to distinguish cancerous tissues from healthy tissues. Two non-multiplexed collimation configurations combining EDXRD and ADXRD are proposed after optimization procedure. A simulation study of the whole system and a breast phantom was realized to determine the required dose to detect a 4 mm carcinoma nodule. The second application concerns detection of illicit materials during security check. The possible benefit of a multiplexed collimation system was examined.

Résumé

L'imagerie basée sur la diffraction des rayons X est une technique non-invasive puissante pour l'identification et caractérisation de matériaux différents. Comparée aux techniques traditionnelles utilisant la transmission des rayons X, elle permet d'extraire des informations beaucoup plus caractéristiques pour le matériau inspecté, comme les positions des pics de Bragg pour des matériaux cristallins et le facteur de forme moléculaire pour les matériaux amorphes. Le potentiel de cette méthode a été reconnu par de nombreuses équipes de recherche et de nombreuses applications comme l'inspection de bagage, le contrôle non-destructif, la détection de drogue et la caractérisation de tissus biologiques ont été proposées. La méthode par dispersion d'énergie (EDXRD) est particulièrement adaptée à ce type d'application car elle permet l'utilisation d'un tube à rayons X conventionnel, l'acquisition du spectre entier en une fois et des architectures parallélisées pour l'inspection d'un objet entier en un temps raisonnable. L'objectif de ce travail est d'optimiser toute la chaîne de caractérisation. L'optimisation comprend deux aspects : l'optimisation du système d'acquisition et du traitement des données. La dernière concerne particulièrement la correction des spectres de diffraction dégradés par le processus d'acquisition. Des méthodes de reconstruction sont proposées et validées sur des spectres simulés et expérimentaux. L'optimisation du système est réalisée en utilisant des facteurs de mérite comme l'efficacité quantique de détection (DQE), le rapport contraste sur bruit (CNR) et les courbes de caractéristiques opérationnelles de réception (ROC). La première application choisie, c'est l'imagerie du sein basée sur la diffraction qui a pour but de distinguer des tissus cancéreux des tissus sains. Deux configurations de collimation sans multiplexage combinant EDXRD et ADXRD sont proposées suite au processus d'optimisation. Une étude de simulation du syst ème entier et d'un fantôme de sein a été réalisée afin de déterminer la dose requise pour la détection d'un petit carcinome de 4 mm. La deuxième application concerne la détection de matériaux illicites pendant le contrôle de sécurité. L'intérêt possible d'un système de collimation multiplexé a été étudié.

Contents

Acronymes

ADXRD = Angular Dispersive X-ray Diffraction
AUC = Area under the Curve
CACSSI = Coded Aperture Coherent Scatter Spectral Imaging
CAXSI = Coded Aperture X-ray Scatter Imaging
CCD = Charge-Coupled Device
CNR = Contrast to Noise Ratio
CT = Computed Tomography
DQE = Detective Quantum Efficiency
EDXRD = Energy Dispersive X-ray Diffraction
FCT = Focal Construct Technology
FOM = Figure of Merit
FN = False Negative
FP = False Positive
FWHM = Full width at half maximum
HME = Home-Made Explosive
HPGe = High Purity Germanium
IAM = Independent Atom Model
KL = Kullback-Leibler
MC = Monte-Carlo
MFXS = Multi-Focus X-ray Source
MIF = Molecular Interference Function
MLEM = Maximum Likelihood Expectation Maximization
MTF = Modulation Transfer Function
MVA = MultiVariate Analysis
PSF = Point Spread Function
ROC = Receiver Operating Characteristic
SAXS = Small Angle Scattering
SNR = Signal to Noise Ratio
SVD = Singular Value Decomposition
SVM = Support Vector Machines
TN = True Negative
TP = True Positive
WAXS = Wide Angle Scattering
XRD = X-ray Diffraction
XRF = X-ray Fluorescence
Z = Atomic Number

List of symbols

Symbol	**Description**	**Units**
$d\sigma/d\Omega$	Differential cross section	m^2
f	Atomic form factor	electrons
$\vec{k}$	Wavevector	nm^{-1}
d_{hkl}	Spacing between the atomic planes of a crystal	nm
χ	Momentum transfer	nm^{-1}
Z	Atomic number	
E_i	Incident photon energy	keV
A	Detected amplitude	keV
Θ	Nominal scattering angle	degrees
θ	Effective scattering angle	degrees
hc	Product of Planck constant and velocity of light	$keV \cdot nm^{-1}$
$\mathbf{F}$	Diffraction signature	$cm^{-1} \cdot sr^{-1}$
$\mathcal{R}$	Global system response matrix	$photons \cdot cm \cdot sr$
R_d	Detector response matrix	
S_{inc}	Incident X-ray spectrum	$photons \cdot sr^{-1}$
At	Attenuation	
R_c	Collimation response matrix	$cm \cdot sr^2$
$\mathbf{m}$	Observed diffraction measurement	photons
$\boldsymbol{\mathcal{M}}$	Expected diffraction measurement	photons
L	Log-likelihood function	
I	Fisher information matrix	
$E\left[\,\right]$	Mathematical expectation	
$\Gamma_{\mathcal{R}}$	Local autocorrelation of $\mathcal{R}$	
$\mathscr{F}\left\{\,\right\}$	Fourier transform	
$\mathscr{I}$	Fourier transform of Fisher information matrix	
$D_{KL}\left(\,\|\,\right)$	Kullback-Leibler divergence	
$D\left(\,\|\,\right)$	Generalized Kullback-Leibler divergence	
$\Lambda\left(\mathbf{x}\right)$	Likelihood ratio	
$\lambda\left(\mathbf{x}\right)$	Logarithm of the likelihood ratio	
E_{rel}	Relative error	

Introduction

X-ray diffraction (XRD) has historically been used in crystallography to examine the structure of crystalline materials, the inter-atomic and inter-molecular distances determining the presence of sharp peaks characteristic of each material and due to crystals' long-range order. In the last years, it has been shown that non-crystalline materials presenting a certain short-range order, such as liquids and amorphous materials, also rise to material characteristic X-ray diffraction patterns featuring one or more broad peaks. Hence, the possibility to use X-ray diffraction to differentiate materials in cases, where other techniques only yield little contrast, e.g. X-ray transmission imaging for low atomic number elements, was discovered.

A number of authors have investigated the potential of X-ray diffraction based material classification in different fields of application. Numerous studies concentrated on the detection of explosives in baggage ([Harding, 2004], [Harding, 2009], [Jupp *et al.*, 2000], [Madden *et al.*, 2008], [Speller, 2001], [Zentai, 2008]). Harding *et al* developed different generations of imaging systems for luggage control at the airport ([Harding, 2009], [Harding *et al.*, 2009]) and their system will soon be used at different airports. As explosives can be polycrystalline materials or liquids, liquid identification using X-ray diffraction was investigated as well ([Harding and Delfs, 2007], [Harding *et al.*, 2010a], [Qu *et al.*, 2010], [Zhong *et al.*, 2010]) and it was shown that XRD is also a promising technique to classify liquids. Other applications such as drug detection in parcels ([Cook *et al.*, 2009b], [Koutalonis *et al.*, 2009], [Pani *et al.*, 2009]) and nondestructive testing [Garrity *et al.*, 2010] have also been proposed.

In addition to material classification X-ray diffraction has also the potential to separate different biological soft tissues, which present an amorphous structure. Several studies have been carried out to get to know, which tissue types could be distinguished by XRD technique. It was shown that XRD is suitable to classify different breast tissues and especially to separate healthy tissue from cancerous tissue ([Evans *et al.*, 1991], [Kidane *et al.*, 1999], [Pani *et al.*, 2010]).

X-ray diffraction pattern can be obtained in two ways: by angular dispersive X-ray diffraction (ADXRD) or energy dispersive X-ray diffraction (EDXRD). The first one requires a monochromatic incident X-ray spectrum, whereas the latter one can be realized using a conventional polychromatic X-ray tube associated to a spectroscopic detector. Furthermore, it allows acquisition of the whole spectrum at the same time and parallelized architectures to inspect entire objects in a reasonable time. Thus, acquisition systems proposed in this study are based on EDXRD using a semi-conductor energy resolving detector, e.g. cadmium telluride (CdTe and CdZnTe), which present the advantage to work at room temperature, still providing a sufficient energy resolution.

The purpose of this work is to propose an optimized material characterization chain for one or two applications. The application on which the work will be focused on are: XRD-based breast imaging and security screening of hand baggage at the airport. For breast cancer detection there is no existing clinical XRD-system. The present work intends to propose an adapted system architecture, which is sufficiently sensitive to detect small tumors in a reasonable scan time and by delivering an acceptable dose. For security screening, there are already existing EDXRD system. However, they only use one scattering angle, which limits the system sensitivity. Here, the combination of EDXRD and ADXRD is suggested in order to improve sensitivity. To further increase system sensitivity limited multiplexing will be considered as well.

Optimization is necessary on two aspects: optimization of the acquisition system and optimization of data processing. In fact, EDXRD spectra quality is deteriorated by system geometry, various interactions of radiation with matter and finite energy resolution. In order to restore the characteristic signature of the material, regardless of the disturbing instrumental factors, one part of this work consisted in the study of reconstruction methods suitable for the different types of diffraction signatures. Optimization of the acquisition system depends on the application because each application implies different constraints.

Different tools to characterize an XRD system are used to compare performance of different system geometries. First of all, purely geometrically considerations with detective quantum efficiency (DQE) allowed to propose two optimized configurations. The figures of merit such as contrast to noise ratio and receiver operating characteristic (ROC) curves are used to assess material separability and the associated required photon number, determining required radiation dose and scan time.

This dissertation is composed of five chapters.

The first chapter summarizes the physical principles involved in X-ray diffraction. Moreover, the state of the art of tissue characterization and the detection of illicit materials using X-ray diffraction is presented. At first, the different types of fundamental interactions between radiation and matter are introduced. Afterwards diffraction is explained in detail, and a description of physics of spectroscopic detectors used for EDXRD imaging technique is given. In the second part of the first chapter, the state of the art of tissue characterization using X-ray diffraction is presented. First, studies concerning diffraction signatures of any biological tissue are described to then focus on breast tissue classification. This is the mostly considered medical application of XRD. The different propositions of XRD imaging systems and the association of XRD to other imaging techniques are also explained in this bibliographic review. The last part of the chapter is dedicated to the state of the art of the characterization of illicit materials. Typical measured XRD spectra of illicit materials such as explosives and drugs are shown. Then different proposed and existing ADXRD and EDXRD systems to detect explosives and the associated classification methods are presented. XRD-based drug detection with different systems and signal processing methods is discussed subsequently as well as liquid detection. Finally, the system approach considered in this work is explained.

To optimize an acquisition system, it is necessary to be able to characterize and to compare the performances of different systems. Therefore, it is first of all required to be able to model an XRD system. Then, performances can be assessed by the use of figures of merit. Chapter II introduces a model of an energy dispersive X-ray diffraction system taking into account the different sources of degradation of acquired data. In addition, to the conventional mono-angle EDXRD system, a model for multi-angle EDXRD is presented. Then, the different figures of merit employed in this thesis are explained in detail. First, detective quantum efficiency (DQE), a figure of merit independent from the inspected object and permitting to access to system sensitivity and resolution, is introduced. After its general definition, its adaption to EDXRD-imaging and its link to Fisher information are presented. Material separability of the system can be quantified using contrast to noise ratio (CNR) calculations and receiver operating characteristic (ROC) curves. Both of them are defined and explained, and then, a new method of analytical ROC curve calculations is introduced. The last part of the second chapter, presents DQE calculation results of a basic EDXRD system. In particular, the performance of a mono- and a multi-angle system are compared, and the influence of different geometrical parameters on system performance is studied.

EDXRD spectrum quality suffers from deterioration due to different parts of the acquisition system. Chapter III is dedicated to the reconstruction of X-ray diffraction spectra in order to remove blurring due to the acquisition system and to restore material proper information. Different possible reconstruction techniques are briefly discussed. The reconstruction method chosen for the present work is a maximum likelihood expectation maximization (MLEM) algorithm, which uses the model of EDXRD systems introduced in the chapter II. MLEM reconstruction method is tested on simulated and experimental EDXRD data. Crystalline XRD signatures are well reconstructed and multi-angle reconstruction was validated on these data. However, reconstructed amorphous XRD pattern are not satisfying. They present lots of oscillations, especially if the data are acquired experimentally. Hence, different regularization methods such as the use of a base and of a resolution kernel are introduced and tested on the same data.

Chapter IV is dedicated to the application of XRD to resolve unclear outcome of a conventional mammography. The idea is to reduce the number of invasive breast biopsies by the use of a non-invasive XRD-based breast tissue characterization. After an introduction concerning the different types of breast tissues and the definition of the case to be separated, the system constraints for optimization process are fixed. The most important element to optimize is the secondary collimation system. Hence, an analytical method to calculate the detective quantum efficiency of a collimation system without multiplexing is proposed. After a study of the impact of different system parameters on resolution and sensitivity, two optimized system configurations are determined: a monofocal and a multifocal secondary collimation system. The last part of this chapter presents a simulation study of the complete XRD system associated to a breast phantom. Both collimation systems are compared in terms of tissue separation power, and the impact of the incident spectrum, breast density and tumor position on the required dose delivery are studied. Reconstruction techniques were applied to spectra simulated for the multifocal collimation to reconstruct a phantom slice. Finally, a small study of the use of multiplexing in this application is presented.

Reflections on an alternative XRD system with higher sensitivity than existing systems for security screening of hand luggage are presented in chapter V. The idea is to propose a multi-angle EDXRD system, i.e. a combination of EDXRD and ADXRD, which is slightly multiplexed. After the presentation of the kind of materials and their associated spectra to be detected and the introduction of system constraints for this application, an analytical DQE calculation method for a collimation system with limited multiplexing is proposed. The influence of the different system parameters for a given multiplexing level is studied. In the last part of this chapter systems with different multiplexing levels are compared and the improvement of sensitivity distribution by changing the distribution of focal distances or the repartition of detector area is evaluated.

Finally, the results of this work will be shortly summarized and prospects for further work will be laid out.

Chapter I

Physical principles and state of the art of the material characterization using X-ray diffraction

This first chapter is dedicated to the explanation of the phenomenon of X-ray diffraction and the state of the art in different fields of application. First of all the different types of interaction of X-rays in matter are summarized. Afterwards, physics of diffraction and different X-ray diffraction measuring methods are explained. As this work is based on the use of spectroscopic detectors, the physical principles of this kind of detectors as well as some techniques to enhance the resolution are also presented in the first part of this chapter. The second part is dedicated to the state of the art of material characterization with X-ray diffraction technique. It focuses on two applications: characterization of biological tissues and characterization of illicit materials. Finally, the approach of X-ray diffraction system chosen for this work will be presented.

I.1 Physical principles of X-ray diffraction

I.1.1 Interaction of radiation and matter

When X-ray radiation encounters matter, a part of this radiation will interact with the matter to be crossed. Interactions of X-ray photons with matter can be categorized in four basic interactions (Fig. I.1 and Fig. I.2): photoelectric absorption, Rayleigh scattering, Compton scattering and pair production [Leo, 1994].

I.1.1.1 Photoelectric absorption

Photoelectric absorption corresponds to the interaction of the incident X-ray photon with an inner shell electron of the interacting matter, where all of the incident photon energy is transferred to the electron (see figure I.1 label B). In fact, it is the manifestation of "particle characteristics" of photons which are inherent to the particle-wave duality of quantum mechanics. During photoelectric interaction, a photon, having an energy higher or equal to the binding energy of the inner shell electron, is absorbed and the electron is ejected from its shell (most often the K-shell, which is the most inner shell of an atom). The ejected electron is called a photoelectron. Its kinetic energy corresponds to the difference between its binding energy and the photon energy. As a result, an ionized atom and a free electron are obtained. Further ionizations may occur through interaction of the free photoelectron with orbital electrons. The structure of the ionized atom is unstable because of the hole in the inner shell. Hence, electrons from higher orbitals fill the hole, and the energy corresponding to the difference of the two orbitals is released in the form of a photon. This radiation is known as fluorescence. It is characteristic of the atoms present in the irradiated matter.

I.1.1.2 Rayleigh scattering

The interaction of a photon with an electron of the crossed matter can also take place without loss of energy (see figure I.1 label C). In this case, the incident photon interacts with and excites the total atom, as opposed to individual electrons as in Compton scattering or the photoelectric effect. The electric field of the incident photon's electromagnetic wave expends energy, causing a deformation of the atom's electron cloud. The positively charged nucleus and the moving electron cloud form an oscillating electric dipole, which emits radiation at the same wavelength as the incident photon but in a slightly different direction. This is a wavelike kind of interaction is referred to as Rayleigh scattering or coherent or elastic scattering. All the atoms of matter form an entity of coherent X-ray sources whose radiation might interfere. As distances between atoms in matter are of the same magnitude as the wavelength of X-rays, diffraction might be observed. This is the phenomenon used in the present work and it will be presented in more detail in the following section.

I.1.1.3 Compton scattering

Compton scattering, also known as inelastic or incoherent scattering, occurs when the incident X-ray photon is deflected from its original path by an interaction with an outer shell electron (see figure I.1 label D). The electron is ejected from its orbital position and the X-ray photon loses energy and changes direction. As this kind of interaction cannot be explained by wave characteristics of light, it was seen as a further proof of "particle" characteristics of light. As with all types of interactions, both energy and momentum must be conserved. The energy shift depends on the scattering angle and not on the nature of the scattering medium. Since the scattered X-ray photon has less energy, it has a longer wavelength.

I.1.1.4 Pair production

Pair production is the materialization of one photon into an electron and a positron, requiring photon energy at least twice as great as the rest mass energy of an electron, i.e. 2×0.511 MeV (see figure I.2). The electron-positron pair is emitted in the forward direction in relation to the direction of the incident photon beam. After the loss of its kinetic energy, the positron will recombine with any available electron and produce annihilation radiation, i.e. generation of two oppositely directed 511-keV photons.

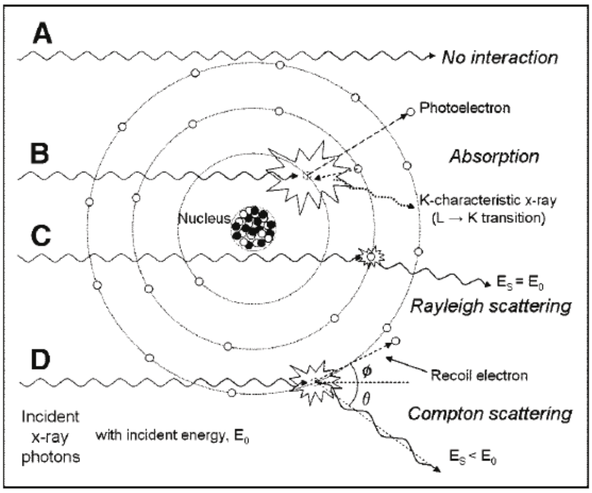

Figure I.1: Schematic summary of X-ray interactions with matter relevant in medical imaging. A: No interaction with crossed matter; B: Photoelectric absorption (called absorption in the diagram); C: Rayleigh scattering; D: Compton scattering (Image taken from [Seibert and Boone, 2005].)

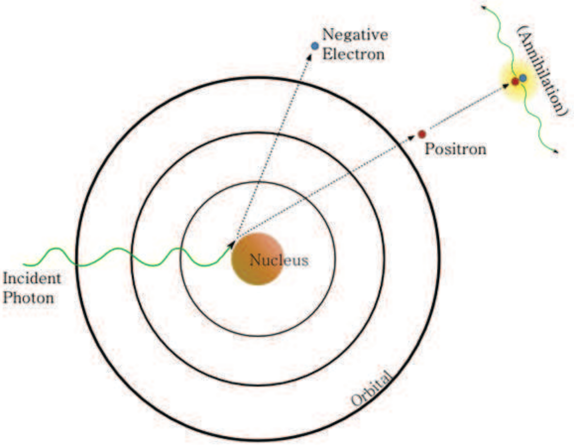

Figure I.2: Schematic representation of pair production. (Image taken from [Pease *et al.*, 2013].

After this short introduction on physical principles of interactions, we present the relationship between atomic weight and energy.

I.1.1.5 Dependency on energy and the atomic weight

The probability of the different interactions depends, among other things, on the energy and atomic number of the material crossed by the photon beam. As seen in Figure I.3, the photoelectric effect is predominant at low energy ($E^{-\frac{7}{2}}$ dependence) and for high Z materials (Z^4 to Z^5 dependence), whereas pair production is predominant at high energy ($\ln(E)$ dependence) and in high Z materials (Z^2 dependence). Compton scattering predominates at medium energy and increases with the atomic number Z (Z dependence).

In the range of energy used in the present work (some keV to 200 keV) and the kind of material (low Z), photoelectric effect, coherent and incoherent scattering are predominant.

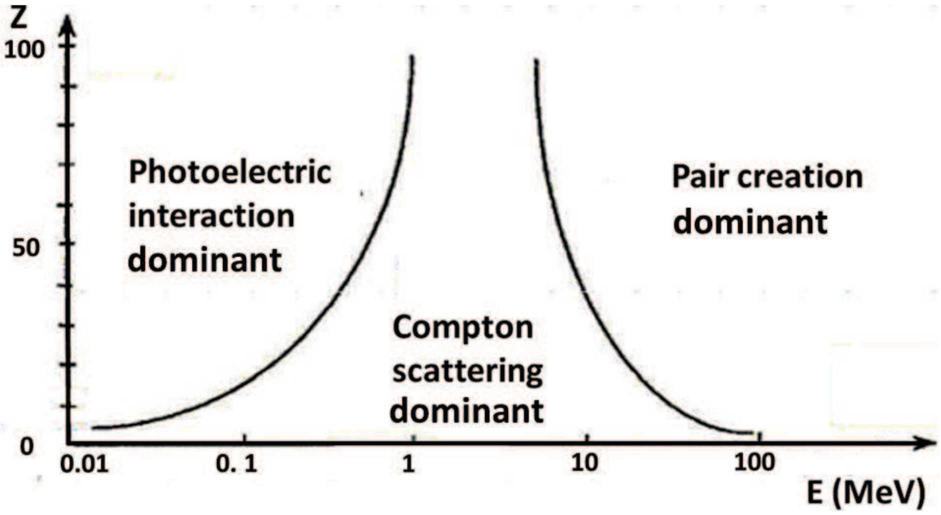

Figure I.3: Predominance of the different interaction possibilities of photons with matter (source: personal lecture by J.F. Adam)

I.1.2 Diffraction: interference of waves

Diffraction is a phenomenon which is due to interference of X-rays. Interference occurs, when X-rays interact in matter without loss of energy, i.e. in the case of Rayleigh scattering. All of the atoms form an entity of coherent X-ray sources whose radiation might interfere. Whether interference is constructive or destructive depends on the relative phase of the waves and thus, on the atomic arrangement of the interacting matter. This arrangement is different for each material. The following section will first explain in general how X-rays are coherently scattered by a free electron, an electron bound to a free atom as well as a set of atoms, and the associated possibilities of interference. Afterwards, the structure of the two existing types of matter, crystalline and amorphous matter, will be described and how their structure impacts on diffraction pattern. Finally, the different ways of measuring X-ray diffraction data are presented.

I.1.2.1 Coherent scattering

Coherent scattering or Rayleigh scattering is the interaction type, which give rise to X-ray diffraction. The electric field $\vec{E}$ of an incident photon wave induces vibrations to the electric charges in the irradiated matter. Following electromagnetic laws, these charges will emit electromagnetic waves at the same frequency as the incident wave but with a phase shifted by π and in another direction. Here, only waves emitted by vibrating electrons will be considered as their amplitudes are much higher than the ones emitted by protons, due to their lower mass. We discuss different types of interaction.

I.1.2.1.1 Scattering by a free electron

Let an electron e be subjected to a photon wave with electric field amplitude $\vec{E} = \vec{E}_0 e^{j\omega t}$.

Then the force acting on the electron is equal to $\vec{f} = e\vec{E}$ and following Newton's second law, the acceleration $\vec{\gamma}$ of the electron is given by:

$$\vec{\gamma} = \frac{-e}{m_e}\vec{E}_0 e^{j\omega t} \tag{I.1.1}$$

The electric field emitted by the accelerated electron at a distance r at the moment t is equal to:

$$\vec{E}\left(r,t\right) = \frac{-\mu_0}{4\pi}\frac{-e}{r}\vec{\gamma}_\perp\left(t - \frac{r}{c}\right) \tag{I.1.2}$$

where $\mu_0 = 4\pi \cdot 10^{-7} NA^{-2}$ corresponds to the permeability of free space, c to the speed of light and $\vec{\gamma}_\perp$ to the acceleration perpendicular to direction $\vec{r}$.

By replacing $\vec{\gamma}$ by its expression, by using the relation $\omega = 2\pi\frac{c}{\lambda}$, where λ is the incident wave length, and by defining the wave number k as $\frac{1}{\lambda}$, equation I.1.2 becomes:

$$\vec{E}\left(r,t\right) = -\frac{\mu_0}{4\pi}\frac{e^2}{m_e}\frac{1}{r}\vec{E}_{0\perp}e^{j(\omega t - 2\pi k r)} \tag{I.1.3}$$

It can be noticed that the quantity $\frac{\mu_0}{4\pi}\frac{e^2}{m_e} = 2.818 \cdot 10^{-13} m$ is known as the classical electron radius r_e. The squared module of $\vec{E}_{0\perp}$ is given by the following expression:

$$E_{0\perp}^2 = \left(\frac{1 + \cos^2\theta}{2}\right)E_0^2 \tag{I.1.4}$$

where θ corresponds to the angle between the direction of the incident photon and the direction of the scattered photon. $\left(\frac{1+\cos^2\theta}{2}\right)$ is called the polarization factor of the incident wave.
The differential cross section, which describes the likelihood of radiation being scattered by a free electron, is given by [Miller, 2014]

$$\frac{d\sigma_{Th}}{d\Omega} = r_e^2\frac{1 + \cos^2\theta}{2} \tag{I.1.5}$$

It is also called Thomson scattering because the Physicist J.J. Thomson was the first to explain this phenomenon.

I.1.2.1.2 Scattering by a free atom

A photon undergoing elastic scattering by a free atom will interact with bounded electrons and each of them will emit radiation of the same wavelength. Since they form an ensemble of coherent sources, their radiation can interfere.
In order to describe the electric field $\vec{E}$ generated by the accelerated electrons of the atom at a distance r from the scattering charge volume[1] the incident excitation field $\vec{E}_0 e^{j\omega t}$ and the

---

[1] It corresponds to the volume attributed to the scattering atom.

charge $-e$ of equation have to be replaced by $\vec{E}_0 e^{j\left(\omega t - 2\pi \vec{k}\cdot\vec{m}\right)}$ and $-e\rho_{atom}\left(\vec{m}\right)dV$ respectively. The first term takes into account the phase difference between waves interacting with electrons located at the points O and M as can be seen in figure I.4. In the second term $\rho_{atom}\left(\vec{m}\right)$ is the probability of the presence of an elementary charge at M and hence, this term corresponds to the charge amount contained in an elementary volume dV. The electric field is then given by:

$$\vec{E}\left(\vec{R}, r, t\right) = -\frac{r_e}{r}\vec{E}_{0\perp} e^{j(\omega t - 2\pi k r)} \int_{space} \rho_{atom}\left(\vec{m}\right) e^{2j\pi \vec{R}\cdot\vec{m}} dV \tag{I.1.6}$$

where $\vec{R} = \Delta\vec{k} = \vec{k} - \vec{k}^{'}$ is called the scattering vector and corresponds to the difference between the incident wavevector $\vec{k}$ and the scattered wavevector $k^{'}$. The integral known as the atomic form factor or scattering factor f is given by:

$$f\left(\vec{R}\right) = \int_{space} \rho_{atom}\left(\vec{m}\right) e^{2j\pi \vec{R}\cdot\vec{m}} dV \tag{I.1.7}$$

This factor corresponds to the Fourier transform of the electron charge density. It is a measure of the scattering amplitude of a wave by an isolated atom and takes into account the interference between the radiation of electrons being part of the same atom. In general, atoms are considered as spherical and therefore f depends simply on $R = 2\frac{\sin\frac{\theta}{2}}{\lambda}$ and not on $\vec{R}$. In the following, we will consider the variable $\chi = \frac{\sin(\theta/2)}{\lambda}$, which is referred to as momentum transfer[2]. Furthermore, f is directly proportional to the number of electrons Z in the scattering atom. Hence, f is a function of the momentum transfer χ and the atomic number Z. Its values have been tabulated by [Hubbell and Veigele, 1975] for Z from 1 to 100. For zero momentum transfer, $f\left(\chi, Z\right)$ is equal to Z and its lowest value is 0 at high χ. Figure I.5 shows some atomic form factors as a function of Z and the momentum transfer.

The differential cross section for scattering by a free atom, also called Rayleigh cross section, accounts for intra-atomic interference, and is given by:

$$\frac{d\sigma_{Ray}}{d\Omega} = \frac{d\sigma_{Th}}{d\Omega} f^2\left(\chi, Z\right) \tag{I.1.8}$$

I.1.2.1.3 Scattering by a set of atoms

When X-rays undergo elastic scattering by a set of atoms, the scattered waves by each atom can interfere with each other. To express the differential cross section for scattering by a set of atoms, the number of atoms in the inspected volume and the previously mentioned inter-atomic interference phenomenon have to be accounted for:

$$\frac{d\sigma}{d\Omega} = \frac{d\sigma_{Th}}{d\Omega} \sum_{i=1}^{N_{atom}} f^2\left(\chi, Z_i\right) n_i V s_i\left(\chi\right) \tag{I.1.9}$$

---

[2] In most articles this physical quantity is called momentum transfer. However, χ is only proportional to the modulus of the momentum transfer q and the precise relationship depends on the system of units used [Harding and Schreiber, 1999].

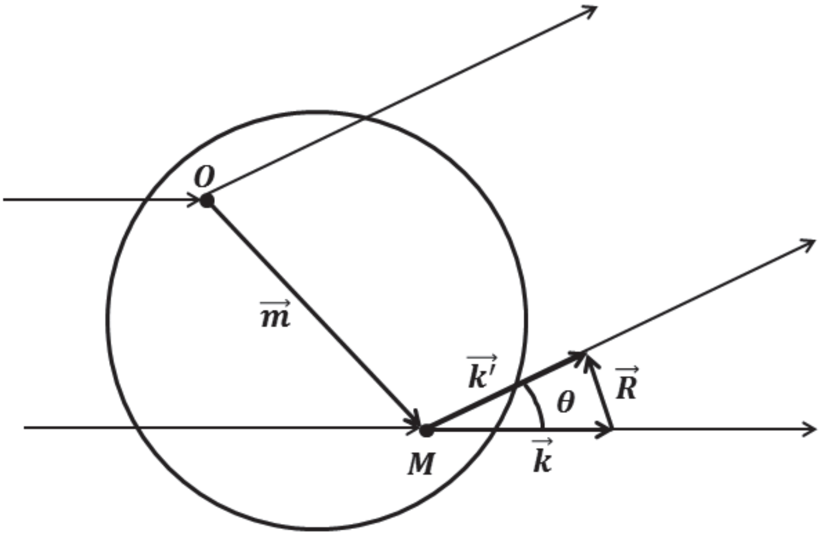

Figure I.4: Illustration of the different vectors used to describe scattering by a free atom.

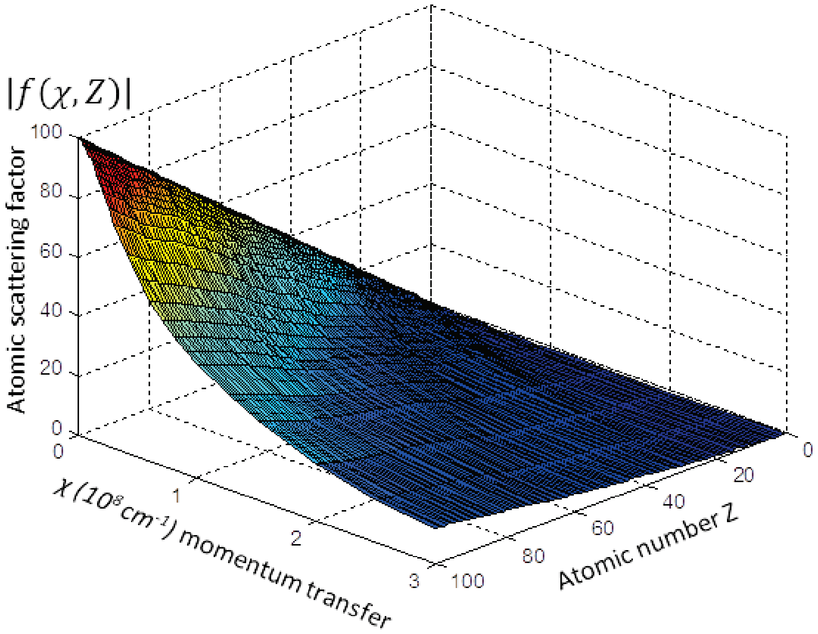

Figure I.5: Modulus of the atomic scattering factor $|f(\chi, Z)|$ as a function of momentum transfer χ and atomic number Z. Elastic scattering is higher at low χ values [Ghammraoui, 2012].

where N_{atom} is the number of different atoms present in the inspected volume V, n_i the number of atom i per unit of volume and s_i is a function taking into account inter-atomic interference. Its aspect is dependent on the structure of the inspected matter. In the following, the two principal types of matter and the associated function s will be presented.

I.1.2.2 Scattering by crystalline matter

The first kind of matter and its associated diffraction properties, that will be presented, is crystalline, e.g. salt and TNT or crystallized proteins. Its structure is ordered in short and long range.

I.1.2.2.1 Crystalline matter

Crystals or crystalline solids are a class of solids that present a regular or nearly regular crystalline structure. This means that their constituent atoms, molecules or ions are arranged in an ordered pattern extending in all three spatial dimensions. A huge part of solid materials, such as salts, metals, minerals, semiconductors, as well as various inorganic, organic and biological molecules, can form crystals.

I.1.2.2.1.1 Crystal structure

A crystal structure can be described as an infinitely repeating of three-dimensional patterns. Any periodic pattern can be described by placing lattice points at equivalent positions within each unit of the pattern. The unit is called motif. In order to recover the pattern, the motif has to be added at each lattice point. An illustration of this principle can be seen in figure I.6.

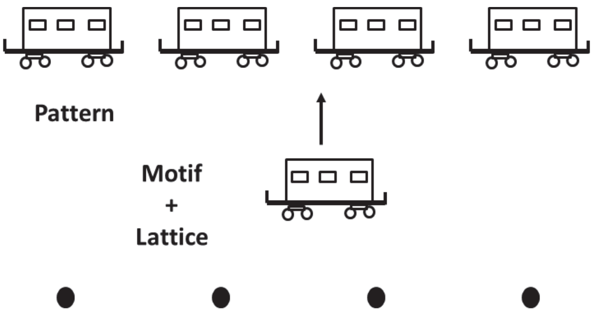

Figure I.6: Illustration of the difference between pattern, motif and lattice. The motif corresponds to one train coach, the lattice corresponds to regularly spaced points in space. By placing a coach at each point, the pattern is obtained. In fact, the pattern is obtained by convolution of the motif by the lattice (considered as a Dirac distribution).

In crystal, the motif consists of atoms or groups of atoms. By replacing each group of atoms by a representative point, which is not necessarily associated with the position of atoms, the crystal lattice is obtained. The crystal lattice can be sub-divided in small entities known as unit cells. A unit cell is the smallest portion of the lattice presenting the same symmetry as the crystal lattice itself. The differences between motif, lattice and unit cell are illustrated in figure I.7.

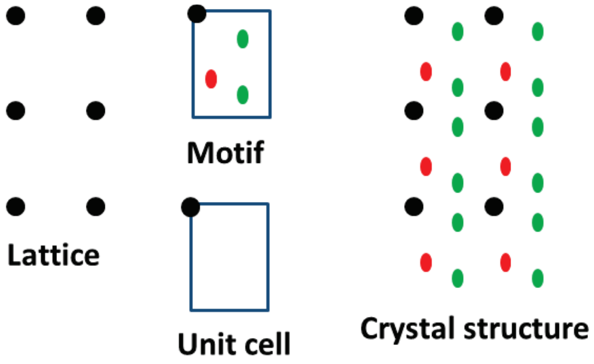

Figure I.7: Difference between motif, lattice, unit cell and crystal structure.

I.1.2.2.1.2 Lattice parameter

The lengths of the edges of a unit cell and the angles between them are called the lattice parameters (Fig.I.8). In the most complex case, the triclinic lattice, it is described by six parameters: three lengths a, b and c and three angles α, β and γ. In the orthorhombic case, there are three parameters a, b and c ($\alpha = \beta = \gamma = 90°$ and in hexagonal case only two a and c ($a = b$, $\alpha = \beta = 90°$, $\gamma = 120°$). The simplest lattice is the cubic one since there is only one parameter a ($a = b = c$, $\alpha = \beta = \gamma$).

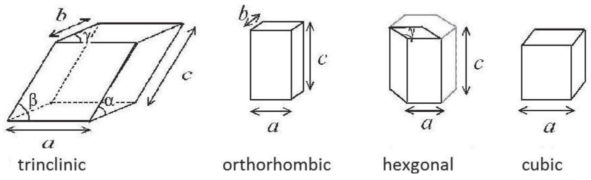

Figure I.8: Parameters of four classical unit cells.

I.1.2.2.1.3 Planes and Miller indices

Crystallographic planes, often called atomic planes, are geometric planes linking nodes (Fig. I.9). These planes play a very important role in X-ray diffraction and are described by a three-value Miller index notation (hkl). Miller indices indicate the orientation of the normal vector of the atomic plane in the basis formed by the sides of the unit cell. It is important to know, that this basis is neither necessarily orthogonal nor normed except for cubic lattice. Thus, an atomic plane is characterized by the coordinates of its normal vector. As in most crystal lattices the basis is not orthogonal, the angle between the atomic plane and the normal vector is mostly not 90°. Due to the translation symmetry of a crystal there is an infinity of parallel planes labeled by the same Miller indices and separated by a distances denoted d_{hkl}. The higher the indices are the closer the planes, i.e. the smaller the distance d_{hkl}.

In some crystal structures nodes can be found in the center of a unit cell or on one of its sides and it is possible to define additional planes, which have higher Miller indices (Fig. I.10).

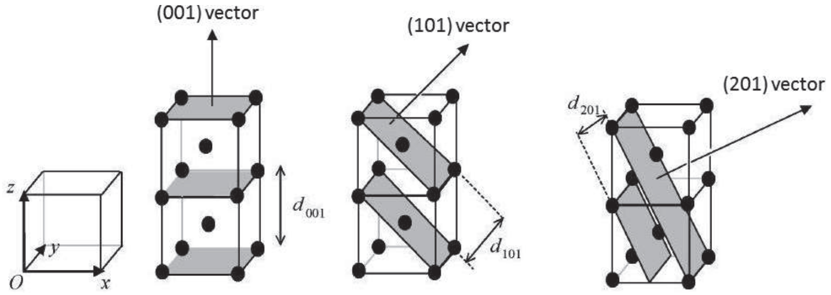

Figure I.9: Atomic planes, normal vectors and interplanar distances.

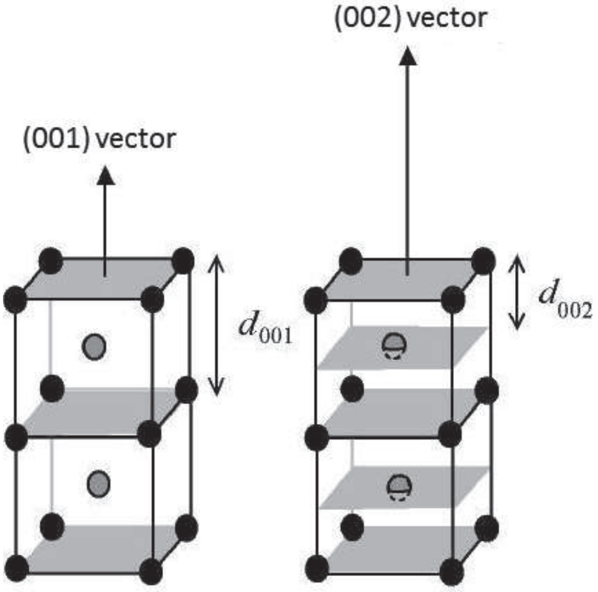

Figure I.10: Example of an additional plane in a cubic crystal lattice.

I.1.2.2.1.4 Single crystal and polycrystal

Polycrystals are solid materials composed of many small microscopic crystals, known as crystallites or grains, of various sizes and orientations. On the contrary, a single crystal is composed of only one unique crystal, which is continuous and unbroken to the edges of the sample. Most of metals and ceramics are polycrystalline. An important example of single crystals is single crystal silicon, which is use in the fabrication of semiconductors. Figure I.11 illustrates the difference between these two types of crystals.

I.1.2.2.2 Scattering by a set of atoms in a crystalline structure

When X-rays undergo elastic scattering in a crystal lattice, the scattered waves of each atomic plane can interfere with each other. If the interfering waves are in phase in a given direction, the waves will add (constructive interference) and a maximum of wave amplitude can be measured in this direction. This phenomenon is called diffraction and will only occur if the spacing between the atomic planes is comparable in size to the incident wavelength, which is

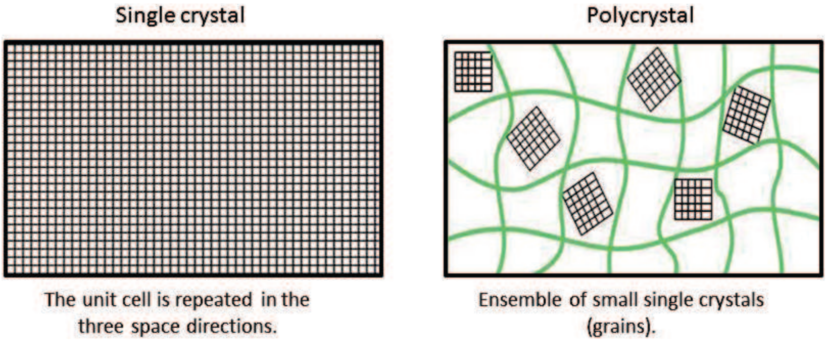

Figure I.11: Difference between single crystals and polycrystals.

the case for X-rays.
The conditions for diffraction can be expressed by the Laue equations. Let us consider a crystal lattice whose nodes are occupied by atoms and an incident wave (X-rays in this case) with an incoming direction given by the wavevector $\vec{k}$ and wavelength λ. The incident beam will interact with the electrons of each atom, which will emit a second wave of wavevector $\vec{k'}$ (Fig. I.12.a) of the same norm as $\vec{k}$ but with different direction. Let $\Delta\vec{k} = \vec{k} - \vec{k'}$ be the scattering vector and $\vec{a}$, $\vec{b}$ and $\vec{c}$ the primitive vectors of the crystal lattice, then the Laue equations are as follows:

$$\vec{a} \cdot \vec{\Delta k} = 2\pi h \qquad \vec{b} \cdot \vec{\Delta k} = 2\pi k \qquad \vec{c} \cdot \vec{\Delta k} = 2\pi l \tag{I.1.10}$$

where h, k, and l are integers and:

$$\|\vec{k}\| = \|\vec{k'}\| = \frac{2\pi}{\lambda}$$

The Laue equations can be decomposed into two conditions [Cullity, 1956]:

1. The interfering waves must be in phase. This condition is given by Bragg's law (Fig. I.12.a)
$$2d_{hkl} \sin\left(\frac{\theta}{2}\right) = n\lambda \tag{I.1.11}$$
where d_{hkl} is the spacing between the atomic planes of Miller indices h, k and l and n an integer.

2. The crystal must be correctly oriented to the incident wave: The normal vector to the atomic planes must be parallel to the scattering vector $\Delta\vec{k}$ (Fig. I.12.b, Fig. I.13).

Figure I.13 illustrates the second condition. In the first case, the atomic planes are correctly oriented and Laue's conditions are satisfied whereas in the second one, it is not. The condition of correct orientation is very difficult to be satisfied in single crystals because there is only one possible orientation. In polycristalline materials Laue equations will be always satisfied because of the numerous small crystallites with different orientations. Hence, every crystalline material used in this work will be polycrystalline.

Figure I.12: a: Illustration of the Bragg law (left). b: Parallel atomic planes with different spacing and orientation can be defined in a same crystalline lattice (right).

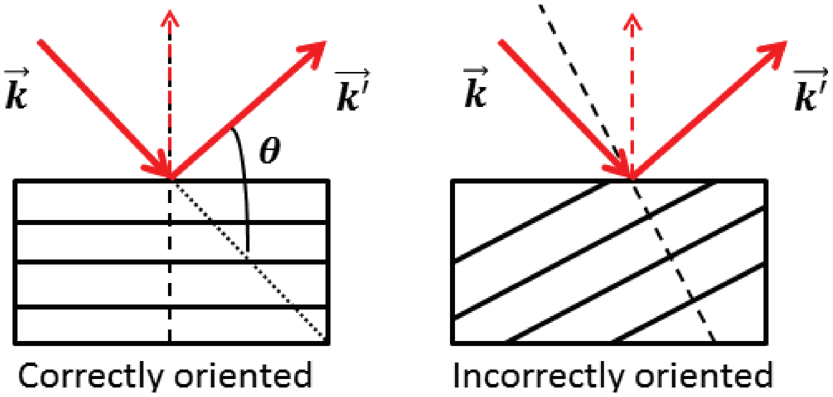

Figure I.13: Example of a correctly oriented crystal for diffraction of the considered atomic plane (left) and an incorrectly oriented crystal (right).

I.1.2.2.2.1 Structure factor and scattered intensity

In the case of crystalline matter, the function s from equation I.1.9 accounts for the periodicity of the crystal structure and discrete interference conditions. In fact, it corresponds to a Dirac comb. Hence, the so called structure factor can be expressed as:

$$F\left(\vec{R},\vec{x}_i\right)=\left[\sum_{i=1}^{N_{atom}} f_i e^{2j\pi\vec{R}\cdot\vec{x}_i}\right]\cdot\left[\frac{1}{v}\sum_{\vec{T^*}}\delta\left(\vec{R}-\vec{T^*}\right)\right] \tag{I.1.12}$$

where N_{atom} corresponds to the number of atoms in the unit cell, f_i the atomic form factor of atom i (see section I.1.2.1), $\vec{R}$ the scattering vector, $\vec{x}_i$ the position vector of atom i within the fixed axis system, v the volume of a unit cell and $\vec{T^*}$ all possible scattering vectors. In fact, the structure factor is the convolution product of the electron density within the crystal and a Dirac comb. F is non zero if, and only if, the Laue conditions are satisfied. Hence, it can be simplified to:

$$F_{hkl}=\sum_{i=1}^{N} f_i\cdot\exp\left(2j\pi\left(x_i h+y_i k+z_i l\right)\right) \tag{I.1.13}$$

where (x_i, y_i, z_i) are the coordinates of atom i within the fixed axis system.

The scattered relative intensity I_{hkl} is equal to the area under the measured diffraction peak and corresponds to the energy diffracted by the atomic plane (hkl). Its magnitude is proportional to the square of structure factor F_{hkl}. It also depends on:

1. the polarization factor $P(\theta) = \left(1 + \cos^2\theta\right)/2$ of the incident beam
2. the Lorentz factor $L(\theta)$, which depends on θ and the system geometry [Lauriat, 2003], [Cullity, 1956].

$$I_{hkl} \propto F_{hkl}^2 P(\theta)\, L(\theta) \tag{I.1.14}$$

The relative intensities of most crystals are known and tabulated. Figure I.14 shows an example of structure factors of salt and TNT.

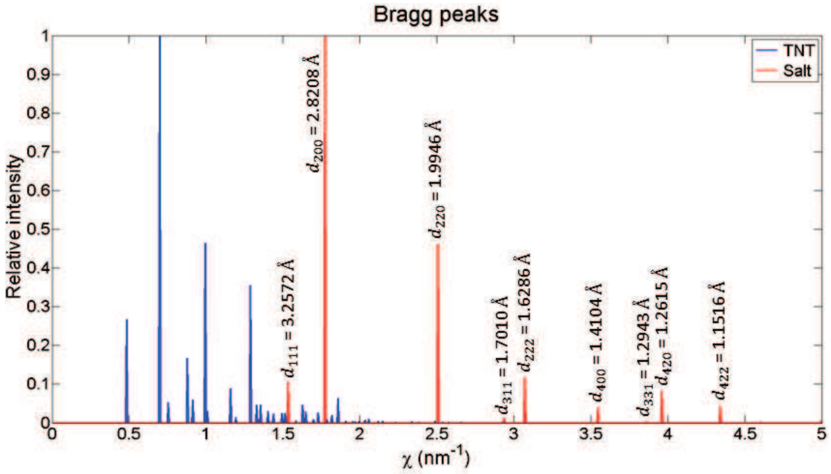

Figure I.14: Example of Bragg peaks from salt (red) and TNT (blue). For salt, the d_{hkl} values corresponding to the different peaks are given (data taken from RRUFF Project website). Diffraction intensity of d_{331} is only about 1 % of the main peak. That is why it is not visible on the figure.

The peak positions are proportional to the inverse of the different atomic plane distances d_{hkl}, present in the crystal. They are called Bragg peaks because they satisfy Bragg's law. In fact, here:

$$\chi = \frac{1}{2d_{hkl}} \tag{I.1.15}$$

TNT has more Bragg peaks than salt, which reflects the fact that TNT crystal structure is more complex than salt crystal structure.

I.1.2.3 Scattering by amorphous matter

The second kind of matter is amorphous matter, which does not present a long range order, such as liquids and biological tissues.

I.1.2.3.1 Amorphous matter

In opposition to crystalline materials where the atoms or atom groups are disposed regularly on a three-dimensional lattice, amorphous materials are characterized by atoms disposed irregularly without long-range order (Fig. I.15). However, some amorphous materials present a short-range order (several atomic diameters, 10^{-10} m, up to several nm.), which might be observed by X-ray diffraction. The class of amorphous materials includes liquids, glasses, numerous polymers as well as some inorganic components.

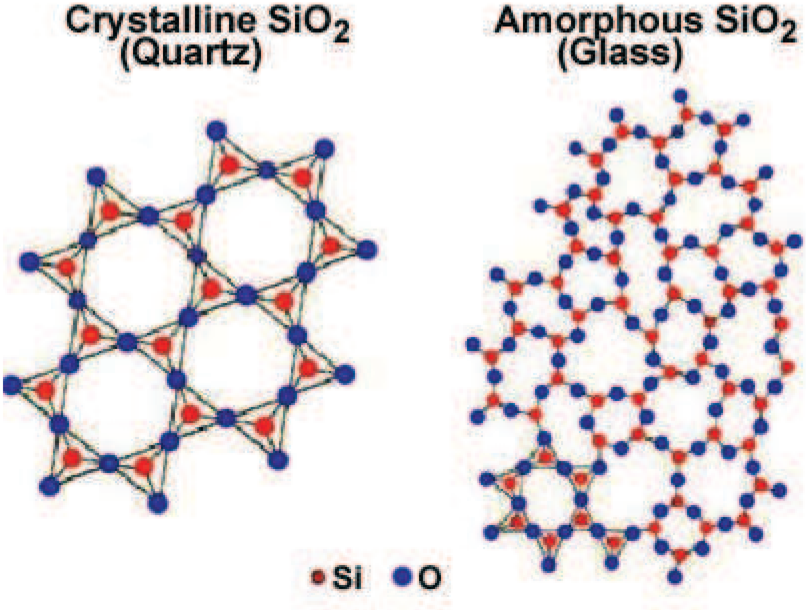

Figure I.15: Difference between crystalline and amorphous structure [Iowa, 2014].

I.1.2.3.2 Scattering by a set of atoms in an amorphous structure

For coherent scattering of amorphous materials, two different models can be found in literature [Peplow and Verghese, 1998], [Harding and Delfs, 2007]:

- The first model is the independent atom model (IAM). This model does not consider interference between waves scattered by different atoms, i.e. s from equation I.1.9 is not taken into account. In fact, it corresponds to a gas of independent atoms. The cross section is given by:
$$\frac{d\sigma}{d\Omega} = \frac{d\sigma_{Th}}{d\Omega} F_{IAM}^{2}\left(\chi\right) \tag{I.1.16}$$
with $F_{IAM}^{2}\left(\chi\right) = \sum_{i=1}^{N} n_i f_i^2\left(\chi, Z_i\right)$, N the number of atoms in one molecule, n_i the number of atom i in one molecule and f_i the atomic form factor of atom i (Sec. I.1.2.1).
- The second model incorporates the fact that numerous amorphous materials present a short-range order, i.e. a regular arrangement of atoms over a distance of some

nanometers. This kind of order is determined by strong chemical bonds such as covalent and ionic bonds. It allow intra- and inter-molecular (E.g.: hydrogen bond and van der Waals) interference. Here, the cross section is expressed by:

$$\frac{d\sigma}{d\Omega} = \frac{d\sigma_{Th}}{d\Omega} F_{MOL}^2 (\chi) \tag{I.1.17}$$

F_{MOL}^2 is known as molecular form factor and determined experimentally. It can be separated in two factors [Narten and Levy, 1971]

$$F_{MOL}^2 (\chi) = F_{IAM}^2 (\chi) \, s (\chi) \tag{I.1.18}$$

where $s(\chi)$ is the molecular interference function (MIF), which describes the modification to the atomic scattering cross section induced by intra- and inter-molecular interference effects. This function is generally oscillating around 1 and converges to 1 for $\chi \to \infty$ [Harding *et al.*, 2010a], [Cozzini *et al.*, 2010]. Thus, for high χ ($\chi > 3$ nm^{-1}) values amorphous scattering properties converge to scattering of independent atoms (IAM). $s(\chi)$ is linked to the radial distribution function $g(r)$ corresponding to the probability to find a molecule at a distance r. This probability is not known but it can be modeled, e.g. "the hard sphere model" [Harding *et al.*, 2010a], where the molecules are considered as impenetrable spheres that cannot overlap in space. Hence, distances r smaller than the sphere's radius are forbidden. In fact, s and g form a Fourier pair and knowing one of them allows to determine the other one. Figure I.16 shows an example of a molecular interference function calculated for a hypothetical hard-sphere fluid having unit particle radius.

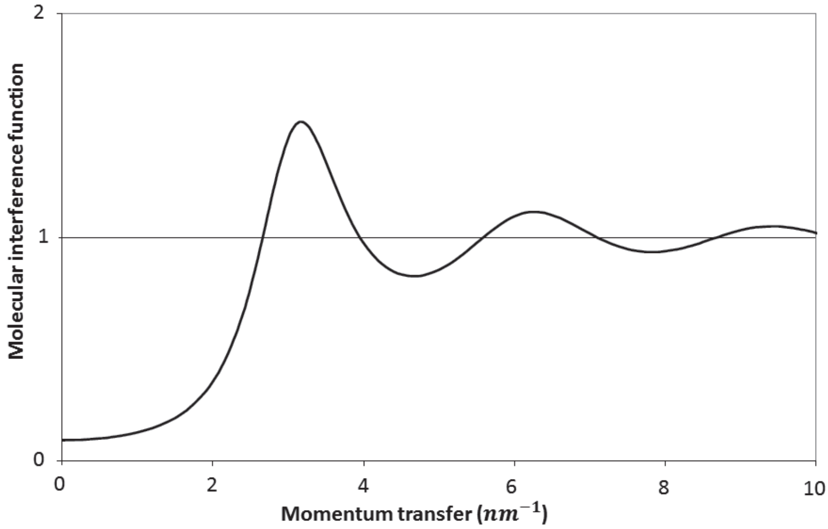

Figure I.16: Molecular interference function derived from Percus-Yevick equation for a hard-sphere fluid with packing fraction 0.3 [Harding *et al.*, 2010a].

Figure I.17 represents a comparison between the two models of elastic scattering of X-rays in amorphous matter for acetone and hydrogen peroxide. It can be seen that by accounting for intra- and inter-molecular interference, the scattering pattern present one or more maxima. These maxima reflect the fact, that even in amorphous structures, there are preponderant distances. The inverse of the momentum transfer value at maximum position corresponds to the most probable distance between molecules in the considered amorphous matter.

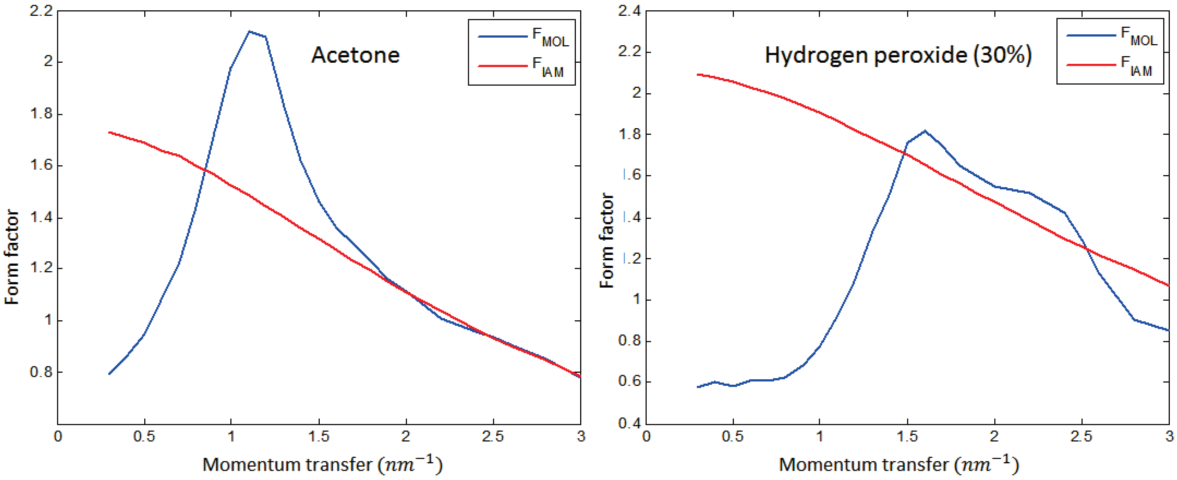

Figure I.17: F_{MOL} (molecular model) and F_{IAM} (independent atom model) for acetone and hydrogen peroxide (30%) [Cozzini *et al.*, 2010].

There is no database for molecular form factors. However, some research teams ([Peplow and Verghese, 1998], [Cozzini *et al.*, 2010], [Tartari *et al.*, 2002], [Kidane *et al.*, 1999], [Chaparian *et al.*, 2009], [King and Johns, 2002], [Poletti *et al.*, 2004]) have measured molecular form factors for several materials (water, kapton, acetone, plexiglas) and tissues (fat, kidney, heart, breast tissue,...). Figure I.18 shows examples of measured form factors. The more the molecule is complex, the more the principal broad peak is at lower χ-values, i.e. the distances between molecules are higher.

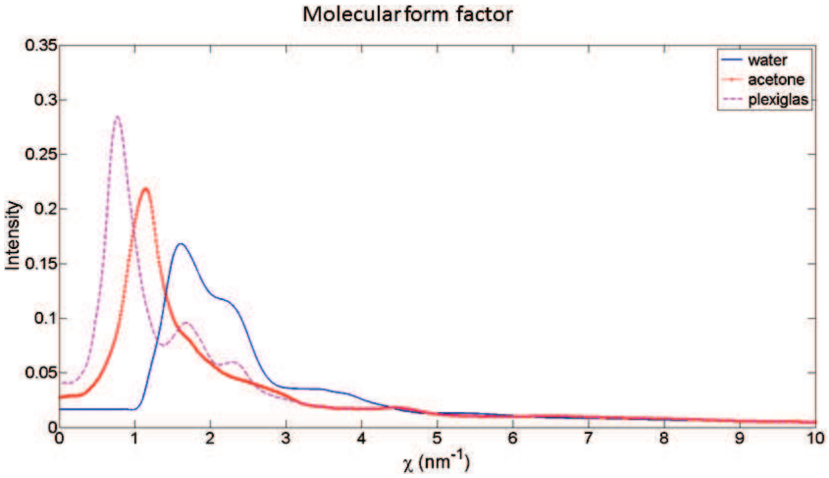

Figure I.18: Molecular form factors of water, acetone and plexiglas ([Peplow and Verghese, 1998]).

I.1.2.4 X-ray diffraction measuring

In X-ray diffraction, the momentum transfer χ is used to characterize materials, where χ is given by:

$$\chi = \frac{E}{hc} \sin\left(\frac{\theta}{2}\right) \tag{I.1.19}$$

with $E = hc/\lambda$, h the Planck constant and c the velocity of light.
Therefore, X-ray diffraction may be measured in two ways: 1. angular dispersion and 2. energy dispersion, as we will see below.

I.1.2.4.1 Angular dispersive X-ray diffraction

Angular dispersive X-ray diffraction (ADXRD) uses a monochromatic (photons of only one wavelength, i.e. one energy) incident X-ray beam and measures the scattering intensity as a function of the scattering angle (Fig. I.19). This technique is the conventional way to measure and is generally used in crystallography [Ladd and Palmer, 2013]. It provides a very high diffraction peak resolution. However, it is difficult to obtain a high intensity monochromatic beam. Synchrotron light sources are often used. The detector does not need to be energy resolving but if the spectrum is to be acquired at once, a good spatial resolution will be required.

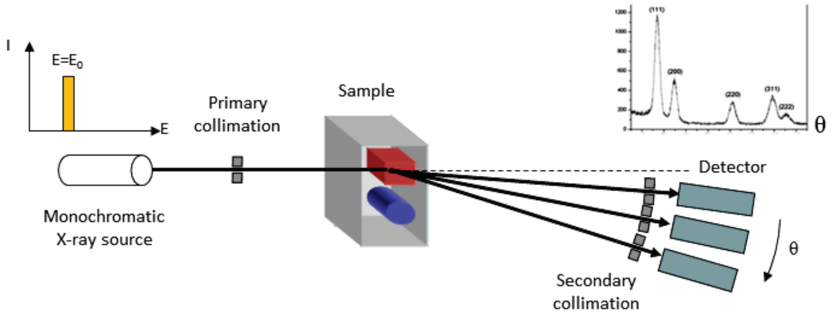

Figure I.19: Schematic view of an angular dispersive X-ray diffraction (ADXRD) system: Constant energy E (monochromatic source) and different diffraction angles θ.

I.1.2.4.2 Energy dispersive X-ray diffraction

Energy dispersive X-ray diffraction (EDXRD) uses a polychromatic X-ray source and measures the diffraction pattern at a fixed scatter angle as a function of incident photon energy (Fig. I.20). This technique requires an energy-resolving detector such as high purity germanium (HPGe) or CdTe [Verger *et al.*, 2007] detector. In this case, it is possible to use a conventional X-ray tube with no need to filter to obtain a monochromatic beam. High spatial resolution of the detector is not necessary to acquire one spectrum.
At equivalent detector area EDXRD systems are faster than ADXRD systems. However they have a limited energy resolution due to combined effects of angular resolution of the collimation and energy resolution of the detector.

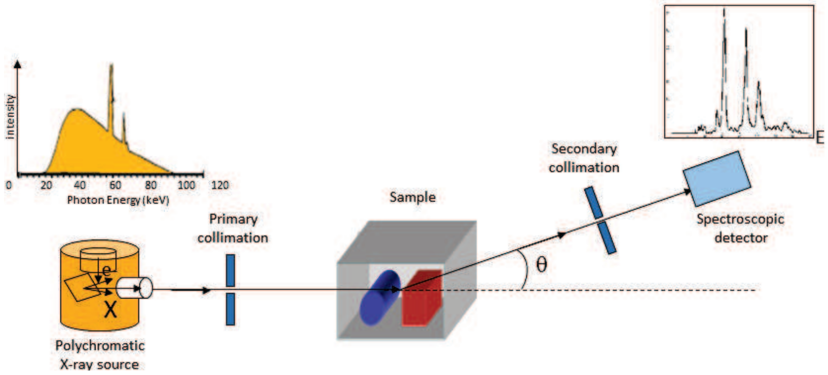

Figure I.20: Schematic view of an energy dispersive X-ray diffraction (EDXRD) system: Constant diffraction angle θ and different energies.

After this presentation of the physics of diffraction phenomena, the physics of spectroscopic detectors will be described.

I.1.3 Physics of spectroscopic detectors

This work is focused on the measuring of diffraction pattern as a function of incident photon energy, which requires a spectroscopic detector. The following paragraph will explain the operating mode of semiconductor spectroscopic detectors and especially $CdTe$ and $CdZnTe$ detectors, which can operate at room-temperature.

I.1.3.1 Interaction of X-rays in semiconductor materials

Owing to their good energy resolution, semiconductor detectors have replaced scintillation and gas detectors in some applications. Semiconductors have different densities, which allows to chose the suitable semiconductor material for a given energy range. Here, we ar interested in semiconductors, whose density permits the detection of gamma and X-rays (100 eV to several 100 keV) with good efficiency. The incident photons interact principally by photoelectric effect or Compton scattering, which generate a number of electron-hole pairs (free charges) proportional to the deposited energy. These free charges move in the material by the effect of an electric field which is applied by the electrodes of the detector, and induce a signal of charge variation at the electrodes (Fig. I.21). This signal is exploited by an adapted electronic system.

This direct conversion between incident photons and free charge creation presents two advantages:

- The free charges that are created at the place of interaction are drained by the electric field without loss of the spatial information. Thus, it is possible to use thick detectors without loss of spatial resolution. In the case of scintillators, there is a trade-off to be made between detection efficiency and resolution: thick scintillator with high detection efficiency and low spatial resolution, or thin scintillator with low detection efficiency and high spatial resolution.

- The quantity of created charges by one interaction is much higher (about twenty times) than in a detector based on scintillation. Hence, quantum noise is reduced.

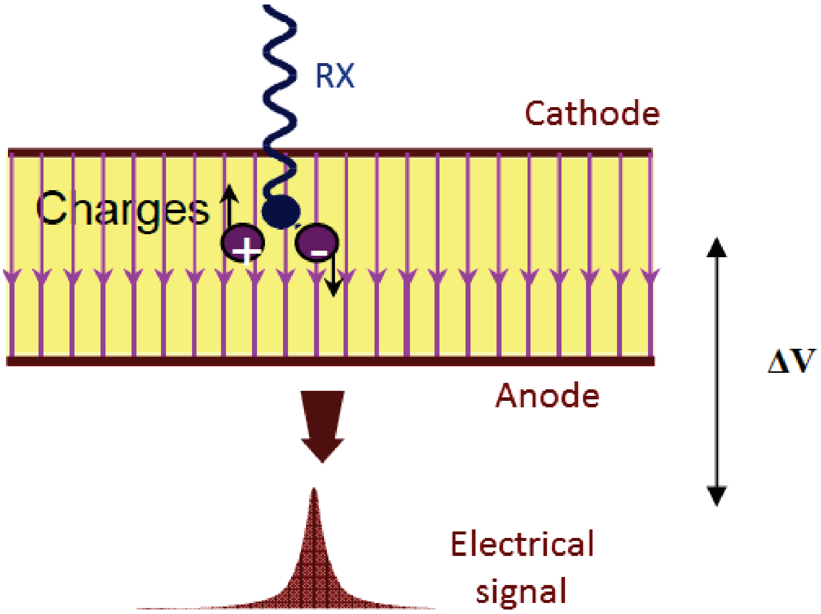

Figure I.21: Direct conversion of X-ray radiation in semi-conductor detectors.

I.1.3.2 Selection criteria for semiconductor materials

Semiconductors do not have all the same characteristics. Thus, all semiconductor materials are not suitable for X-ray diffraction imaging. The properties of the established semiconductor materials have been compared before [Verger *et al.*, 2004]. This paragraph will present the selection criteria as well as the results of the comparison.

To be a good candidate for X-ray diffraction imaging, the semiconductor material should offer a good photon stopping power and good spectroscopic performances. High volumetric mass density ρ and high atomic number Z confer good photon stopping power to the material. However, it should be noticed that the stopping power depends on the energy range and hence, the stopping power criteria is more or less easily achieved depending on the chosen energy range. In addition to stopping power and spectroscopic performances, several other criteria have to be considered to assure good detection efficiency, as:

- low energy required to create electron-hole pairs to generate a high number of free charges
- high electrical resistivity assuring a low level of noise due to dark current fluctuations. Electrical resistivity depends on electrical mobility, the width of forbidden bands, material impurities, crystallographic defects and the temperature.

- a product $\mu\tau$ as high as possible, where μ corresponds to the charge mobility and τ the mean free time. Indeed, the more charges are mobile and the higher their mean free time, the better are the charge collection properties of the material

- a good crystal quality. This means that the crystal growth of the material has to be well known and as homogeneous as possible.

The afore mentioned study of semiconductor performances compares the performances of germanium (Ge), silicon (Si), $CdTe$, $CdZnTe$ and HgI_2, which are the most commonly used semiconductor materials for detection. It has been shown that materials belonging to the family of cadmium telluride ($CdTe$ and $CdZnTe$) present a good compromise between efficiency, energy resolution and other properties in the considered energy range (20 to 200 keV). Thanks to their high resistivity they can be used at room temperature. Their crystal quality and their charge transport properties have been significantly improved during the last years. However, they remain lower than for HPGe. Correction techniques were developed to maintain a good detection efficiency.

I.1.3.3 Pixelated monolithic detectors

In order to induce the migration of free charges created during interaction of X-rays and the detector, electrodes are deposited on each surface of the detector. The materials that are usually used to establish these contacts are gold, platinum and indium. Depending on how the anode electrode is structured, two types of detectors can be distinguished: planar detectors and pixelated monolithic detectors. Today, the latter ones are the most commonly used detectors. Therefore, in the following only this type of detectors will be considered.
Pixelated monolithic detectors have a segmented anode and an un-segmented cathode (Fig. I.22). Hence, one detector pixel is defined as the area between one anode electrode and the cathode. This separation allows to process each electrode separately and it is possible to localize the interaction with pixel precision. As the achievable pixel size is very small (< mm) nowadays, pixelated monolithic detectors have a very high intrinsic spatial resolution. High surface areas can be obtained by juxtaposing some of these detectors (typically 20×20×5 mm).

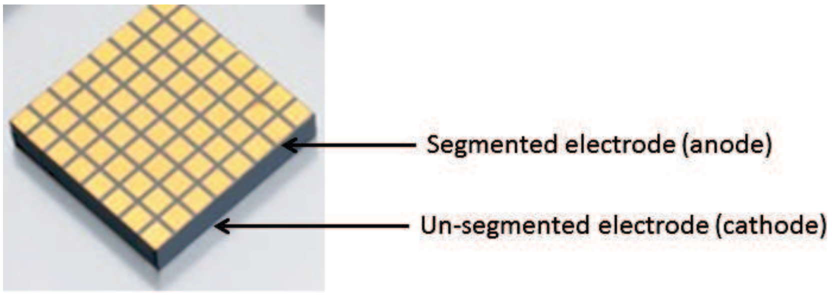

Figure I.22: Picture of a pixelated monolithic detector (20×20×5 mm and 2.5 mm pixel size): in contrast to planar detectors, the anode is segmented.

I.1.3.4 Enhancing intrinsic resolution of the detector by interaction depth effect correction

$CdTe$ and even more $CdZnTe$ suffer from poor hole mobility due to hole trapping during migration. This trapping is essentially caused by the numerous crystallographic defects of $CdTe$. Consequently, the measured signal amplitude depends on photon interaction depth in the detector. This is reflected by an enlargement of the detected energy spectrum and in particular, a low-energy tail. However, the depth of interaction can be determined for each photon and it is possible to correct this effect.

Correction of interaction depth effect can be done by using the cathodic signal or the signal of adjacent anodes, or by measuring the rise time of the anodic signal. The time of signal induction is calculated for each interaction. If the electrical field in the detector is homogeneous, the rise time will be proportional to the interaction depth (Fig. I.23).

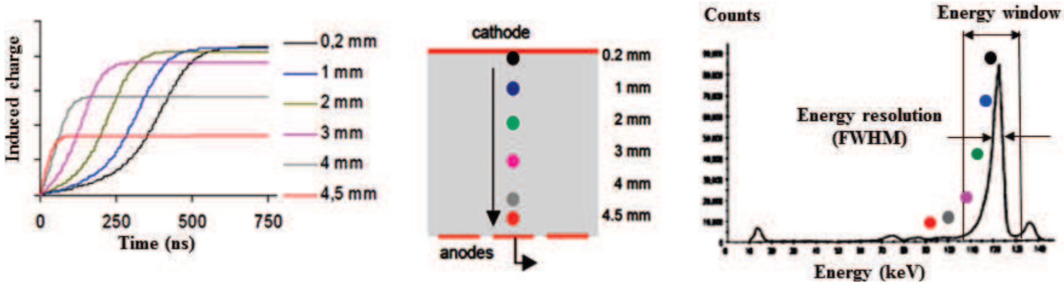

Figure I.23: Induced charge depending on photon's interaction depth in the detector and the consequential detected energy spectrum by a monolithic detector [Ghammraoui, 2012].

The correction is realized by using a biparametric spectrum (Fig. I.24). This spectrum represents an information proportional to interaction depth (in general, the transit time of electrons) on the ordinate axis, and an information proportional to incident photon energy (in general, the signal amplitude measured at the anode) on the abscissa axis. Knowing maximum measured and incident energies for each rising time, this biparametric spectrum can be corrected by homothety of the energy axis depending on the time. Energy resolution is significantly improved as well as detection efficiency in a lesser extent. Figure I.24 shows an example of such a correction. The rising time and the measured charge were determined for a ^{57}Co source. This source emits photons at two different energies (122 keV and 136 keV) and measured charge should be the same for photons of the same energy. However, as can be seen in figure I.24.a, measured charge depends on the rising time, and hence, on interaction depth. As the energies of incident photons are known, this effect can be corrected (Fig. I.24.b).

I.1.3.5 Enhancing spatial resolution of the detector by sub-pixel positioning

Spatial resolution of a pixelated detector is usually limited by its pixel size. However, techniques have been developed that allow to locate photon interaction position on the detector with a higher precision than pixel size [Lux, 2012]. This technique consists in virtually dividing a physical pixel in smaller entities called sub-pixels. It allows to obtain a smaller pixel size without multiplying the number of reading channels. An increase of reading channels implies more electronic noise. Figure I.25 illustrates this principle.

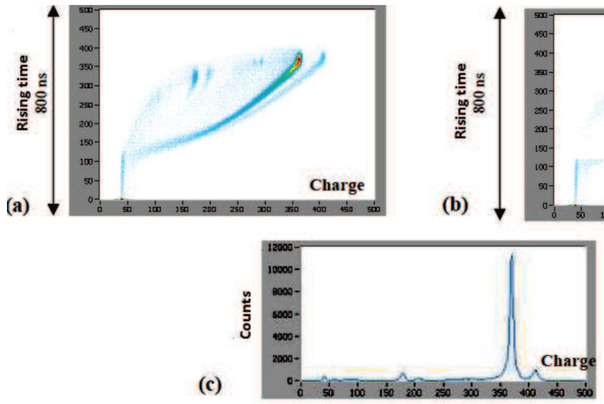

Figure I.24: Illustration of biparametric spectrum correction of a ^{57}Co spectrum (122 keV and 136 keV) using electron transit time for a planar $CdZnTe$ detector: a) raw biparametric spectrum (due to different interaction depths, measured charge is not the same for photons of the same energy), b) corrected biparametric spectrum and c) corrected energy spectrum (projection of the biparametric spectrum on charge axis).

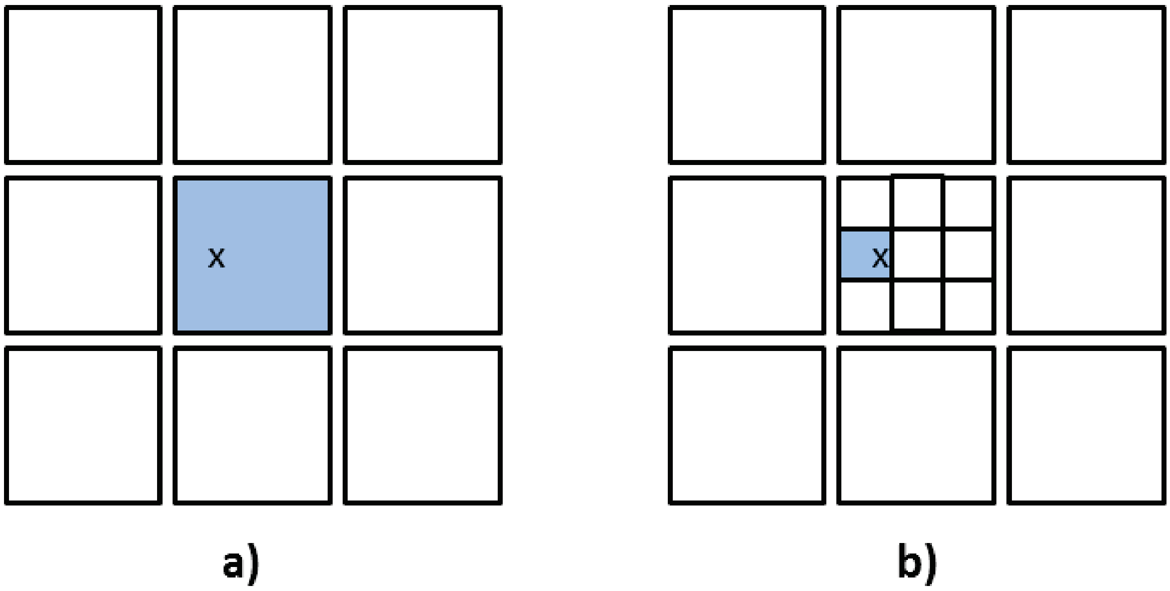

Figure I.25: Illustration of sub-pixel positioning principle: A photon interacts with the central pixel of a 3×3 detector. a) Without sub-pixel positioning the position of the photon is given by the central pixel. b) With a 3×3 sub-pixel positioning its position is given by the virtual subpixel.

There are a multitude of possible methods to process the signal on neighboring pixels to virtually subdivide the pixels of a detector. Two categories can be differentiated: localization by the barycentre technique and maximum likelihood. Localization by the barycentre technique consists of the determination of the barycentre of the detected charge. It allows to reduce the measurements to one adimensional quantity. Sub-pixel positioning using maximum likelihood method consists of the determination of the charge's interaction position by maximizing the likelihood function of its distribution. It presents the advantage that the

Cramer-Rao bound can be achieved. Thus, it is the method leading to best possible results. Though, it requires to know the likelihood function, which is not always the case.

These methods have been studied in more detail in the work of Lux [Lux, 2012]. Here, as an example, a barycentrical method will be presented, which was used by [Ghammraoui, 2012] to realize a 1D sub-pixel positioning in x-direction of a 4×4 detector by a factor of 4 to virtually obtain a 16×4 detector (Fig. I.26).

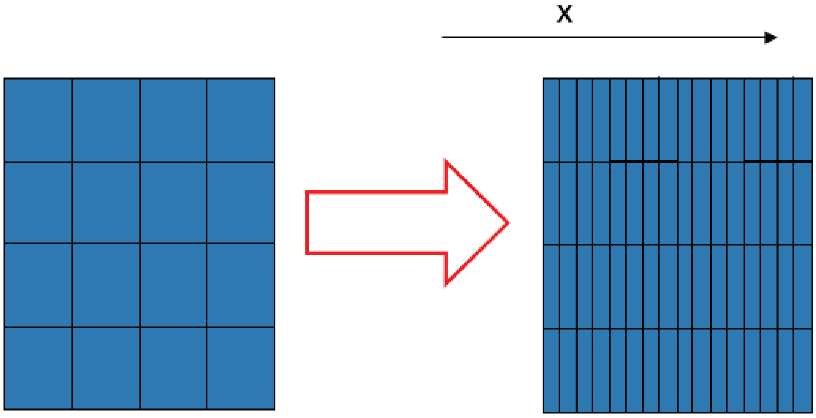

Figure I.26: Sub-pixel positioning of a factor 4 in x-direction [Ghammraoui, 2012].

This method uses the fact that the electronic cloud created by photon interaction in the detector, induces a charge not only on the main pixel (i.e. the collecting anode) but on each other anode. The induced charge is time depending and becomes zero except for the main pixel, when the electronic charge is collected. Sometimes the charge is collected by two neighboring anodes. This phenomenon is called charge sharing. In this case the maximum current will still be measured on the main pixel but another non negligible current will be present on a neighboring pixel. Figure I.27 shows an example of the evolution of the induced charge on different detector anodes.

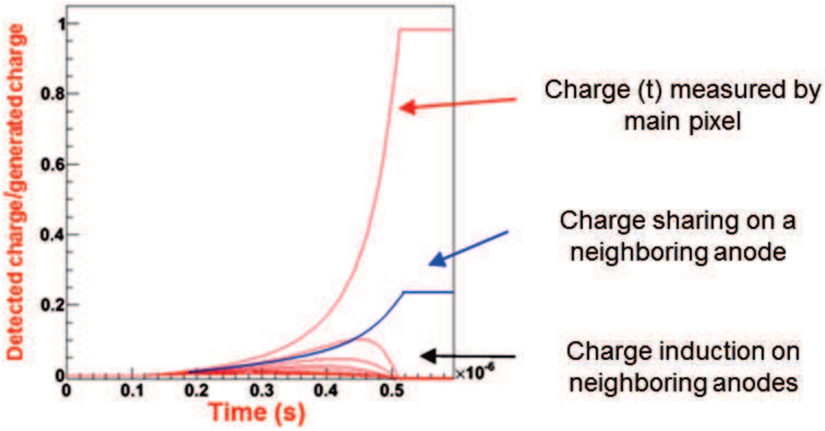

Figure I.27: Temporal evolution of charge measuring for the 16 pixels of the detector, after ionization near to the cathode (simulations realized by [Lux, 2012]).

The barycentrical method consists of the attribution of a weight to each pixel depending on the information collected on each pixel. Different types of information can be collected and exploited, such as the rise time and the charge. However, the measure has to be independent from interaction depth. As was explained in the previous section, the collected charge depends on the interaction depth. Therefore, instead of using the charge to weight different pixels, the difference Q between the maximum charge and the minimum charge during transitional regime is the same for each interaction depth as can be seen on figure I.28. Q is called excursion. To each pixel i a value Q_i of the excursion is attributed.

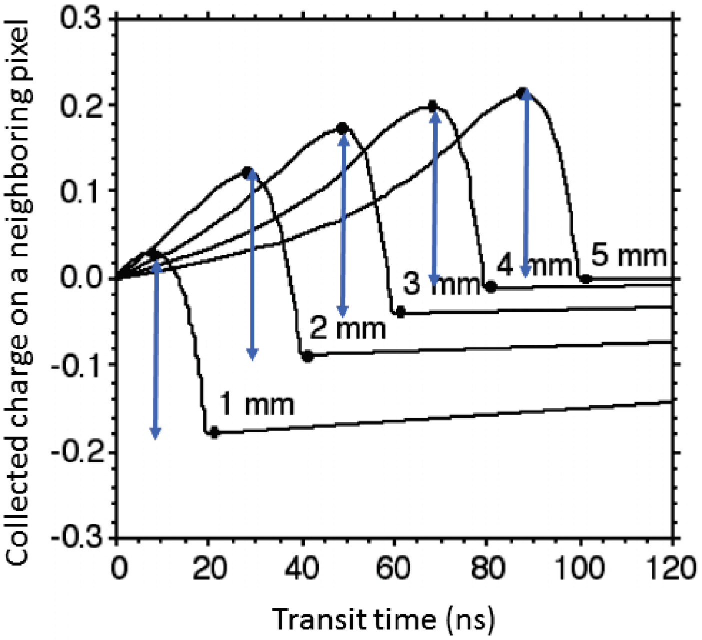

Figure I.28: Temporal evolution of the measured charge on one neighboring pixel for 5 different photons, which interacted at the same x, y-position but at different depths [Warburton, 1997]. Indicated mm-values correspond to the distances traveled by the electronic cloud until the anode.

The following step consists of the multiplication of the excursion values Q_i by weighting coefficients depending on their position with respect to the principal pixel. The barycentrical coordinate following x-axis B_x is calculated by:

$$B_x = \frac{\sum_{i=1}^{16} Q_i C_{1,i} C_{2,i}}{\sum_{i=1}^{16} Q_i C_{2,i}} \tag{I.1.20}$$

where $C_{1,i}$ is the positioning mask whose values correspond to the pixel index following x-axis and $C_{2,i}$ the weight applied to each pixel depending on its position with respect to the collecting pixel. Figure I.29 shows an example of the calculation of the barycentrical coordinate B_x. Its value depends on the position of interaction in x-direction. Weighting coefficients are fixed in a way that B_x of a pixel indexed 2 is confined between 1 (interaction at the left pixel edge) and 3 (interaction at the right pixel edge).

The advantage of sub-pixel positioning is that it can improve spatial resolution without degrading the spectral response by charge sharing (due to smaller anode size).

After reviewing the physical principles of X-ray diffraction and spectroscopic detectors, the

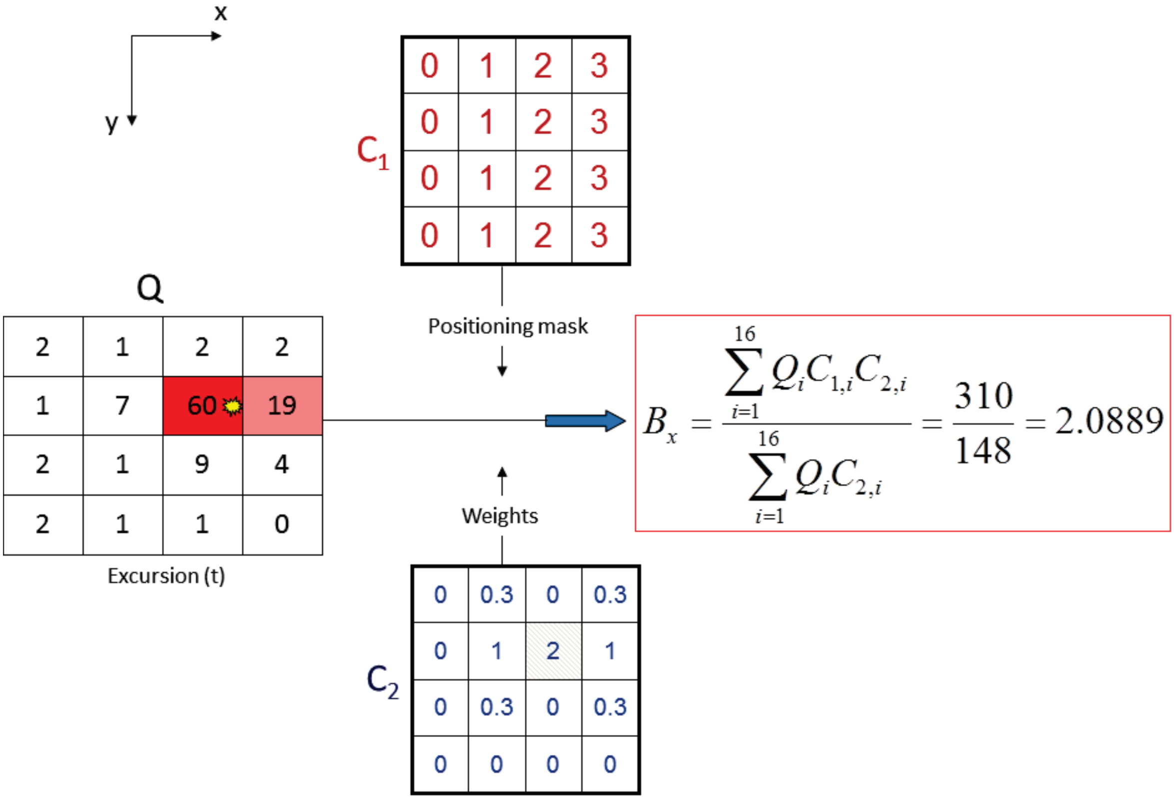

Figure I.29: Example of calculation of a barycentre B_x for a 4×4 detector [Ghammraoui, 2012].

next section will present some considerations about the materials we want to characterize with X-ray diffraction (biological tissues, illicit materials).

I.2 State of the art of material characterization using X-ray diffraction

Many studies have been realized to assess the potential of X-ray diffraction in different fields of application. These applications are very various such as detection of explosives in baggage ([Harding, 2009], [Jupp *et al.*, 2000], [Madden *et al.*, 2008]), liquid identification ([Harding *et al.*, 2010a], [Qu *et al.*, 2010], [Zhong *et al.*, 2010]), drug detection in parcels ([Cook *et al.*, 2009b], [Koutalonis *et al.*, 2009], [Pani *et al.*, 2009]), nondestructive testing [Garrity *et al.*, 2010] and separation of different biological soft tissues ([Evans *et al.*, 1991], [Kidane *et al.*, 1999], [Pani *et al.*, 2010]). However, this section will focus on characterization biological tissues and illicit materials during security scanning, which are the two applications considered in this work.

The first part is dedicated to the potential of X-ray diffraction to be used for classification of biological tissues, in cancerous and healthy tissue for example, which is still difficult with existing techniques. The different studies concern the measuring of tissue scattering signatures, the presentation of measuring methods as well as the proposition of combining different imaging techniques. The application, that will be focused on is breast tissue characterization as it is the mostly studied topic and as it is also the focus of the present work.

I.2.1 Biological tissue characterization

Several groups have measured molecular form factors of different biological tissues in order to investigate the use of X-ray diffraction to differentiate different tissue types in medical applications. [Peplow and Verghese, 1998] used monochromatic synchrotron radiation at different angles, i.e ADXRD, to measure molecular form factors of different animal tissues (pork fat, beef fat, pork muscle, beef muscle, pork kidney, beef kidney, pork liver, beef liver, pork heart and beef blood) and human breast tissue. Data were processed using Monte Carlo based corrections for air scattering, incoherent scattering and multiple scattering. It was found that most form factors of animal tissues are very similar to water, which is consistent with the composition of these tissues. Only adipose tissue form factors differ from water one and present a relatively sharp peak at lower momentum transfer values. Fat molecules are more regularly ordered over longer distances than water molecules. Human breast tissue measurements presented peaks corresponding to water peak and fat peak. These results were confirmed by [King *et al.*, 2011], who employed EDXRD to determine beef muscle, liver and kidney as well as pork fat. Hence, X-ray diffraction does not seem suitable to separate the different soft tissues but it can easily separate adipose tissues and soft tissues. [Kosanetzky *et al.*, 1987] also presents measurements of the molecular form factor of these tissues and he furthermore, investigated the ones of gray and white matter, tendon and bone. The pattern of dense bone shows very sharp peaks reflecting its polycrystalline structure. Tendon is similar to soft tissues but it has an additional peak at very low χ values. The shape of form factors of gray and white matter is very similar. Only their scattering intensity is different. White matter has a higher scattering amount, especially at low momentum transfer values. This can be explained by the fact, that white matter contains a great deal of fat as opposed to gray matter. The different form factors determined in this study can be observed in figure I.30.

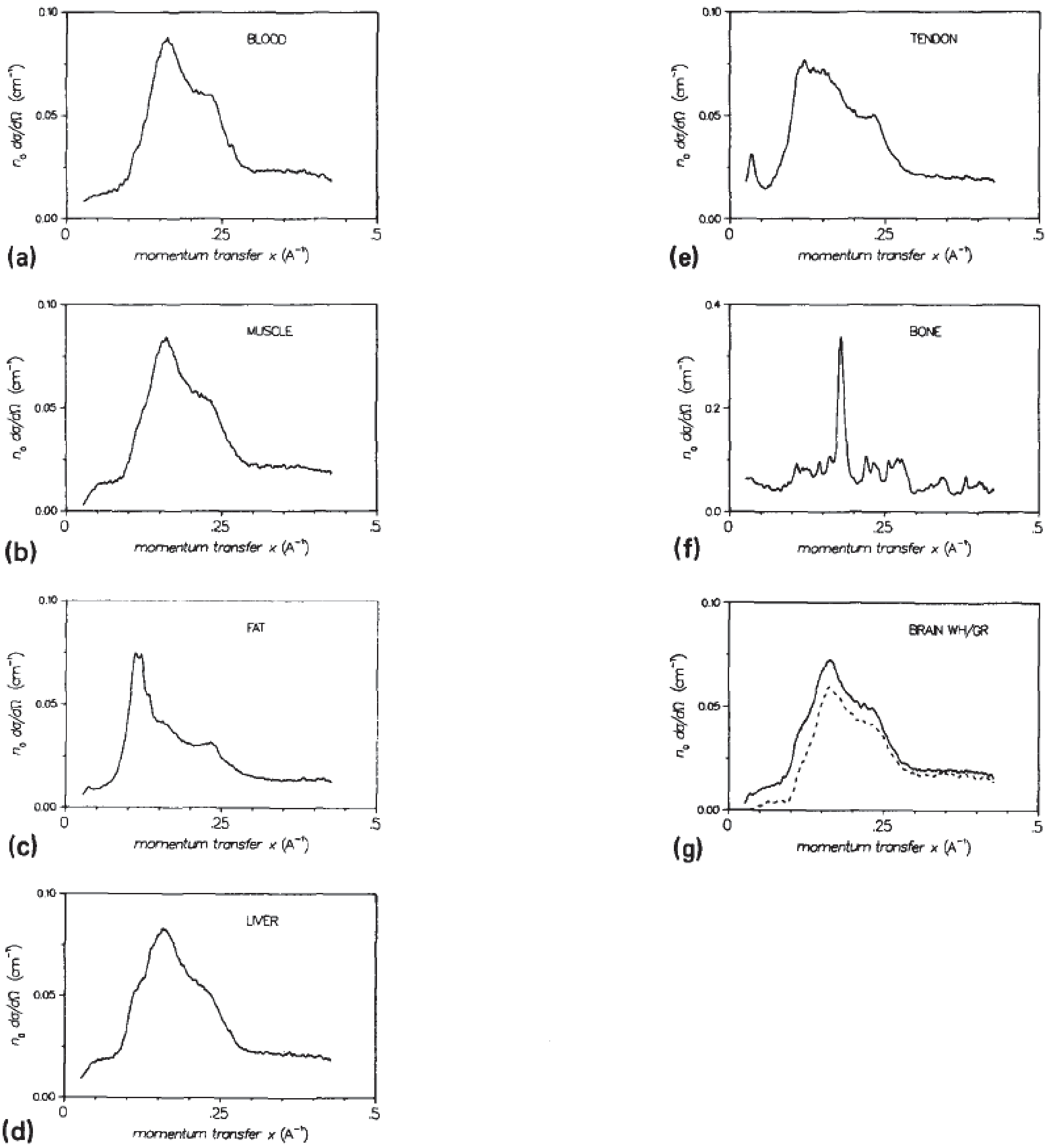

Figure I.30: Differential cross sections for biological materials: (a) blood, (b) muscle, (c) fat, (d) liver, (e) tendon, (f) dense bone, and (g) brain white/gray matter. [Kosanetzky *et al.*, 1987]

Figure I.31 shows a comparison of the form factors of different tissues obtained by [Peplow and Verghese, 1998], [King *et al.*, 2011] and [Kosanetzky *et al.*, 1987]. They are quite similar.

[Castro *et al.*, 2005] compared molecular form factors of healthy and cancerous uterus and kidney (Fig. I.32). In fact scattering signatures for healthy uterus and endometrial cancer as well as for healthy kidney and renal carcinoma are very similar. Each of them presents a peak at around 1.57 nm^{-1}. Peak heights relative to background are slightly different for healthy and cancerous uterus tissues (3.762$\pm$0.113 healthy and 3.713$\pm$0.111 cancerous). The difference in

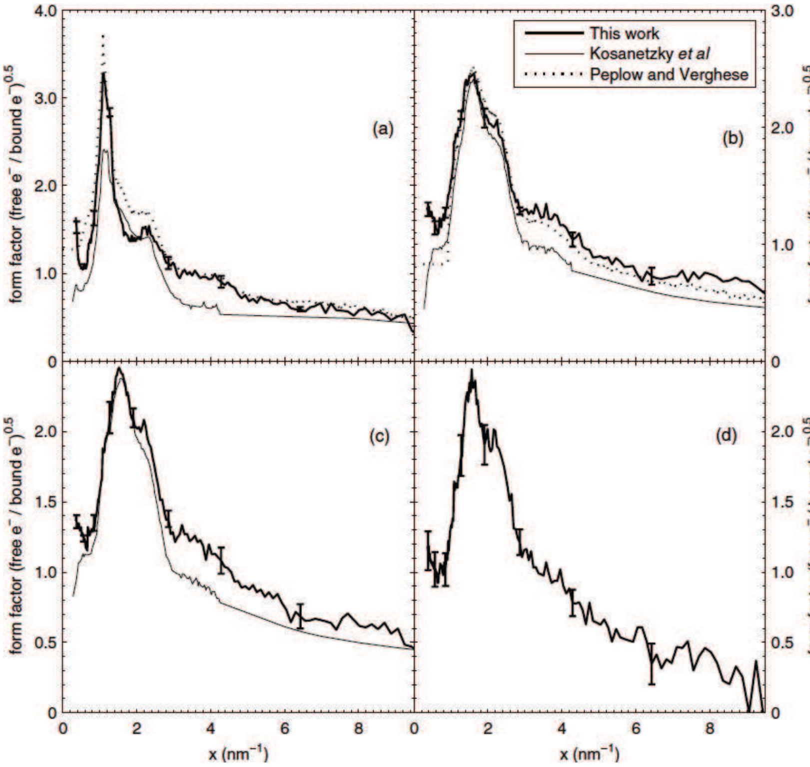

Figure I.31: Measured form factors of (a) fat, (b) muscle, (c) liver and (d) kidney. Comparison of the results obtained by [King *et al.*, 2011] to the ones found by [Peplow and Verghese, 1998] and [Kosanetzky *et al.*, 1987]. (Image taken from [King *et al.*, 2011].)

peak height is more apparent for kidney tissues, where the peak height relative to background of healthy tissue is about 4.038 ± 0.121 and 3.833 ± 0.115 for cancerous kidney tissue. In addition to uterus and kidney tissues, [Castro *et al.*, 2005] also compared scattering signatures of healthy and cancerous breast tissues. The first to publish X-ray patterns of a range of breast tissue types (adipose, fibroglandular, benign, carcinoma, fibrocystic and fibroadenoma) were Evans *et al* [Evans *et al.*, 1991] using ADXRD. It was found that signatures of adipose tissues, presenting a peak at $3.52°$, and cancerous tissues, peak at $5.38°$, are significantly different. Small differences were observed between fibrocystic tissues and fibroadenoma as well as between benign and cancerous tissues. This study has demonstrated the potential of X-ray diffraction to classify different breast tissue types.

The detection of small lesions using conventional mammography is difficult because of poor contrast. This is due to attenuation properties between healthy and diseased tissues, which are very similar. Hence, an alternative, more specific X-ray imaging technique is of great interest. That is why most of the studies concentrated on the determination of form factors of different breast tissues and especially the difference between healthy and cancerous breast tissue.

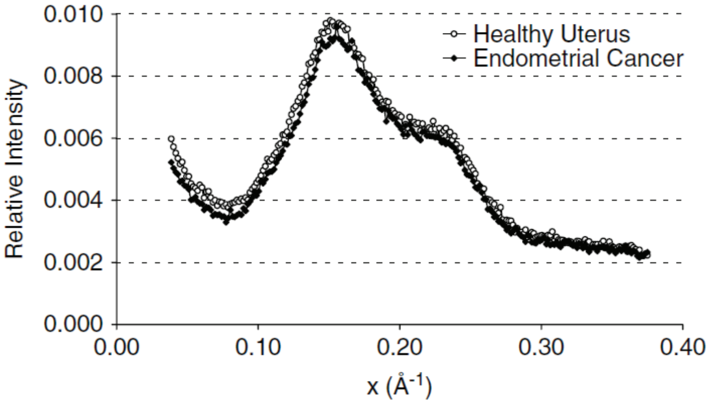

(a) *Experimental scattering signatures for healthy and cancerous uterus.*

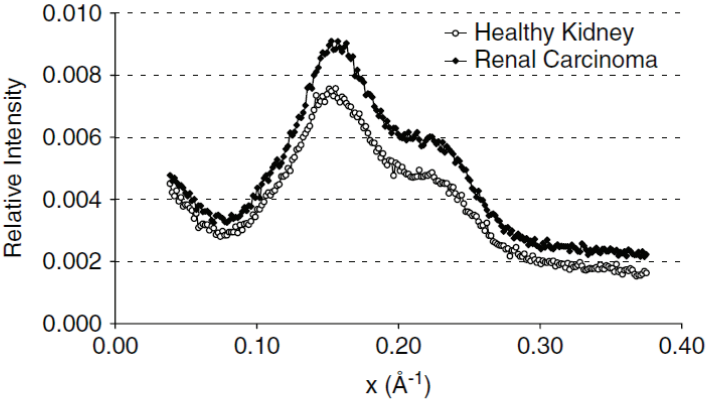

(b) *Experimental scattering signatures for healthy and cancerous kidney.*

Figure I.32: Experimental scattering signatures for healthy and cancerous tissues [Castro *et al.*, 2005].

Kidane *et al* [Kidane *et al.*, 1999], Poletti *et al* [Poletti *et al.*, 2002], Castro *et al* [Castro *et al.*, 2004], [Castro *et al.*, 2005] and Pani *et al* [Pani *et al.*, 2010] measured X-ray diffraction patterns for different breast tissue types in order to investigate the potential of X-ray diffraction signatures to be used to distinguish between healthy, benign and cancerous breast tissues. [Kidane *et al.*, 1999] and [Pani *et al.*, 2010] used EDXRD, whereas Poletti *et al* [Poletti *et al.*, 2002] and [Castro *et al.*, 2004], [Castro *et al.*, 2005] employed ADXRD. Different tissue classifications were used in theses studies. The breast samples in [Poletti *et al.*, 2002] were classified as glandular tissue, adipose tissue and cancerous tissue. Castro *et al* [Castro *et al.*, 2004], [Castro *et al.*, 2005] breast tissue samples were histologically classified as healthy (adipose and connective tissue) tissue and infiltrating duct carcinoma. Pani *et al* [Pani *et al.*, 2010] distinguished between adipose tissue, fibrosis, benign and cancerous tissue (poorly and well differentiated). Most studies only used a few samples. Kidane *et al* [Kidane *et al.*, 1999] tested a statistically significant number of samples (altogether 100) and differentiated a wider range of tissue types (adipose, fibrosis, fibroglandular, benign, fibrocystic change, fibroadenoma and carcinoma). The common result of the different studies was that healthy adipose tissue shows a sharp peak at low momentum transfer values around 1.1 nm^{-1} and carcinoma at higher momentum transfer values at around 1.6 nm^{-1}, which corresponds to the maximum of water molecular form factor (Fig. I.33).

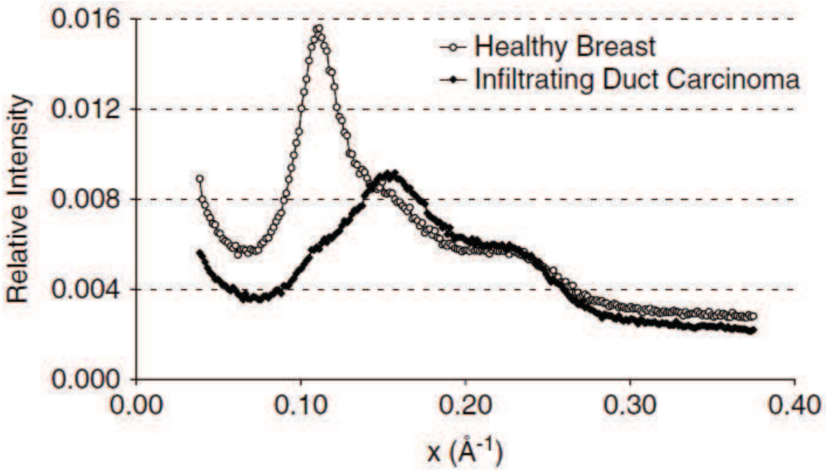

Figure I.33: Experimental scattering signatures for healthy adipose breast tissue and infiltrating duct carcinoma [Castro *et al.*, 2005].

In addition to X-diffraction pattern, some researchers also studied small-angle X-ray scattering (SAXS) properties of different breast tissues. These provide information about collagen structure, which was suggested as an important indicator of normal, healthy breast regions by [Lewis *et al.*, 2000]. Fernandez *et al* [Fernàndez *et al.*, 2002] studied the changes in collagen structure in cancerous tissues with SAXS by measuring the axial period of collagen fibrils of different breast tissue samples. Comparison of adipose tissue and invaded adipose tissue (Fig. I.34) SAXS pattern showed significant differences in intensity and peak presence between these tissue types. In a further study [Fernàndez *et al.*, 2005], suggested that combining SAXS and diffraction enhanced X-ray imaging, which uses transmission and phase information, to be a good method to obtain information about tumour growth and malignancy. In [Conceição *et al.*, 2010], they propose to combine SAXS and WAXS (wide angle X-ray scattering) technique, to classify breast tissues. WAXS allows to determine features at molecular level, corresponding to the same length range as conventional X-ray diffraction. SAXS provides information about changes at a supramolecular level such as collagen fibrils structure. However, these techniques are realized using synchrotron radiation, which does not seem feasible in clinical applications. Conventional X-ray diffraction and especially EDXRD seems to be more suitable for clinical routines.

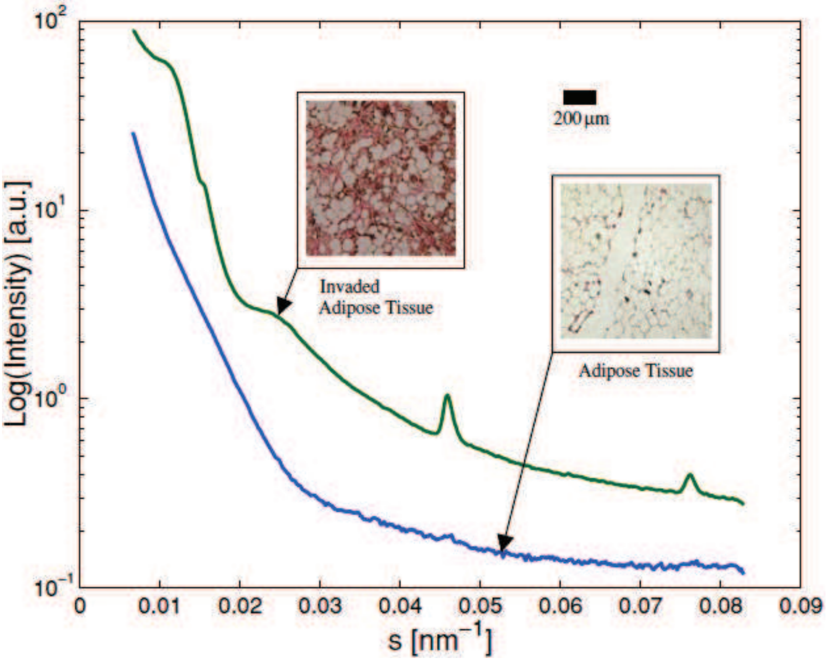

Figure I.34: Comparison of SAXS pattern and histological sections of healthy adipose tissue and adipose tissue invaded by carcinoma [Fernàndez *et al.*, 2002].

In another way LeClair *et al* [LeClair *et al.*, 2006] used a combination of EDXRD system and a semi-analytical model to extract differential linear scattering coefficients for breast tissues. Several teams used measured molecular form factors to update Monte Carlo code coherent scattering form factor tabulations in order to integrate molecular interference effects. Hence, [Tartari *et al.*, 2002] proposed an updating of form factor tabulations for coherent scattering of photons in tissues using the molecular form factorization proposed by [Narten and Levy, 1971]. [Ghammraoui and Badal, 2014] present upgraded versions of two open-source Monte

Carlo codes for the simulation of radiographic projections and computed tomography (CT), that have been adapted in order to be able to integrate the effect of molecular interference if wished. However, their update only concerns breast imaging applications.

These different studies have shown the potential of coherent X-ray scattering to separate healthy and cancerous breast tissue. Hence, researchers looked for an X-ray diffraction-based detection system for clinical use. Different imaging techniques, systems and data processing methods have been suggested in the literature. [Harding *et al.*, 1987] initially proposed the use of XRD imaging, as opposed to single-point measurements, using a tomographic approach. Their system was based on a multi-element Bismuth Germanate detector array in a quasi-hexagonal arrangement. Detector elements were arranged in a way that each detector group only detected photons scattered within a certain angular range. Data scanning was realized with a pencil beam and by rotating the sample and cross-sectional images were reconstructed using conventional CT reconstruction algorithms (first-generation CT geometry). Reconstruction could be realized at each scattering angle subtended by the detector elements and hence, images at different momentum transfer values presenting different contrasts could be obtained. The same group proposed another CT approach based on EDXRD, which does not require mathematical reconstruction [Harding *et al.*, 1990]. In fact, the object is scanned voxel by voxel, where a voxel is defined by the intersection of the primary beam with the angular acceptance of the scatter collimator (Fig. I.35). A sample slice acquisition can be obtained by scanning in two directions. Though, this technique seems time consuming. Moreover system sensitivity is limited by the use of only one scattering angle and the employed HPGe detector needs to be cooled.

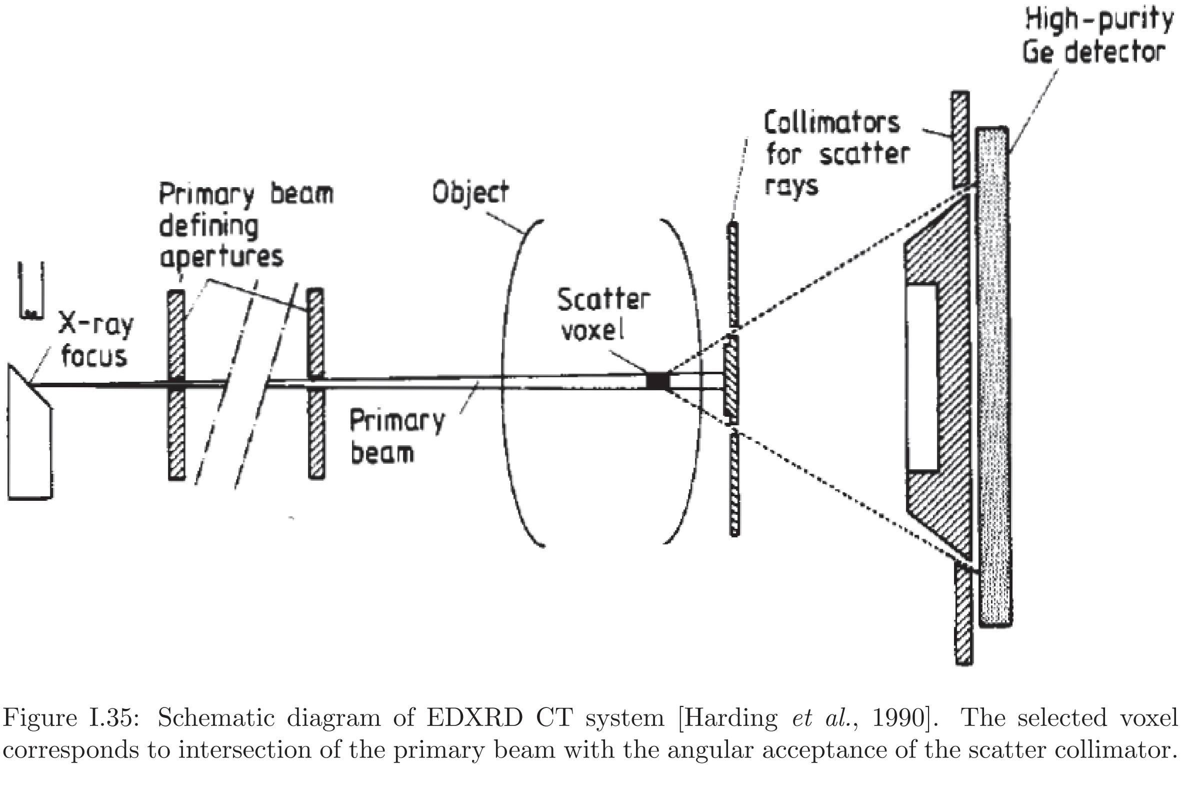

Figure I.35: Schematic diagram of EDXRD CT system [Harding *et al.*, 1990]. The selected voxel corresponds to intersection of the primary beam with the angular acceptance of the scatter collimator.

[Westmore *et al.*, 1997] have also suggested a first-generation CT geometry for scattering tomography, which employs several changes compared to [Harding *et al.*, 1987], in order to better respond to the requirements of coherent scattering CT. Scattered radiation was measured by a CsI XRII and the light from the output phosphor was coupled through a lens to a charge-coupled device (CCD). The data could be represented in two different ways: as a series of images showing coherent-scatter intensity at different scatter angles or as a set of material-specific images. [Griffiths *et al.*, 2008] and [Pani *et al.*, 2010] also proposed diffraction CT methods that are slightly different from the previously presented methods. The system of [Griffiths *et al.*, 2008] is based on ADXRD and uses synchrotron radiation and the detection is realized with a L3CCD camera. Data are reconstructed using an emission CT reconstruction algorithm. [Pani *et al.*, 2010] used EDXRDCT and the system is very similar to [Harding *et al.*, 1990]. The main difference to other papers lies in the use of X-ray diffraction CT for extraction of diffraction patterns over a range of momentum transfer values. This allows to compare diffraction patterns of different tissue types (Fig. I.36) but also to extract images at only one chosen momentum transfer value (Fig. I.37) as previous studies.

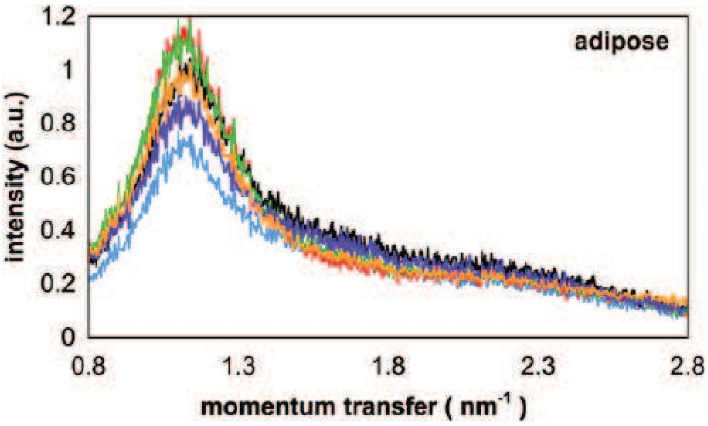

(a) *Adipose tissue*

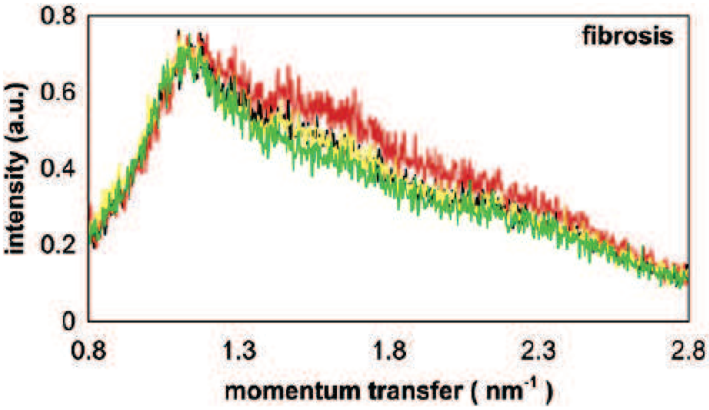

(b) *Fibrosis*

Figure I.36: Comparison of the diffraction patterns obtained for adipose tissue and fibrosis. Different colors correspond to diffraction patterns obtained from different samples with the same histological classification.

(a) *Reconstructed diffraction tomogram at 1.1 nm^{-1}.*

(b) *Reconstructed diffraction tomogram at 1.6 nm^{-1}.*

Figure I.37: Images of a breast tissue sample. The region marked "A" is adipose tissue and the region marked "B" is fibrosis. [Pani *et al.*, 2010]

[Maccabe *et al.*, 2013] propose a snapshot imaging technique called coded aperture X-ray scatter imaging (CAXSI) combining ADXRD with a coded aperture associated to a two-dimensional detector composed of energy-integrating pixels. This technique allows to acquire simultaneously the range and the identity of an object. In order to benefit from both approaches, ADXRD and EDXRD, a method called coded aperture coherent scatter spectral imaging (CACSSI) was suggested by [Greenberg *et al.*, 2013]. It uses an incident pencil beam, an energy-sensitive detector and a coded aperture between target object and the detector (Fig. I.38). With CACSSI quick measurement of location and molecular signature of the target object are possible. The use of a coded aperture requires deconvolution of the acquired spectra. Figure I.39 shows raw experimental data of a 10 mm thick sheet of high-density polyethylene (HDPE) and the full two-dimensional reconstruction of the object in χ-depth space. Estimated form factors obtained for different concentrations of methanol (MeOH) and water (H_2O can be seen in figure I.40). First, their reconstruction method did not take into account self-attenuation of the object, but recently they suggested the use of transmission computed tomography in order to integrate this information [Odinaka *et al.*, 2016]. [Lakshmanan *et al.*, 2016] presents a Monte Carlo evaluation of their system applied to breast cancer detection in terms of spatial resolution and classification. They determined a resolution of about 2.5 mm along the beam direction (z) and 0.75 mm in x and y directions corresponding to the beam width. First tests were realized on surgically excised breast tumor samples [Morris *et al.*, 2016]. Figure I.41 shows reconstruction results for two different pencil-beam raster scan locations with a high probability of presence of normal tissue (Fig. I.41.a) and cancerous tissue (Fig. I.41.b).

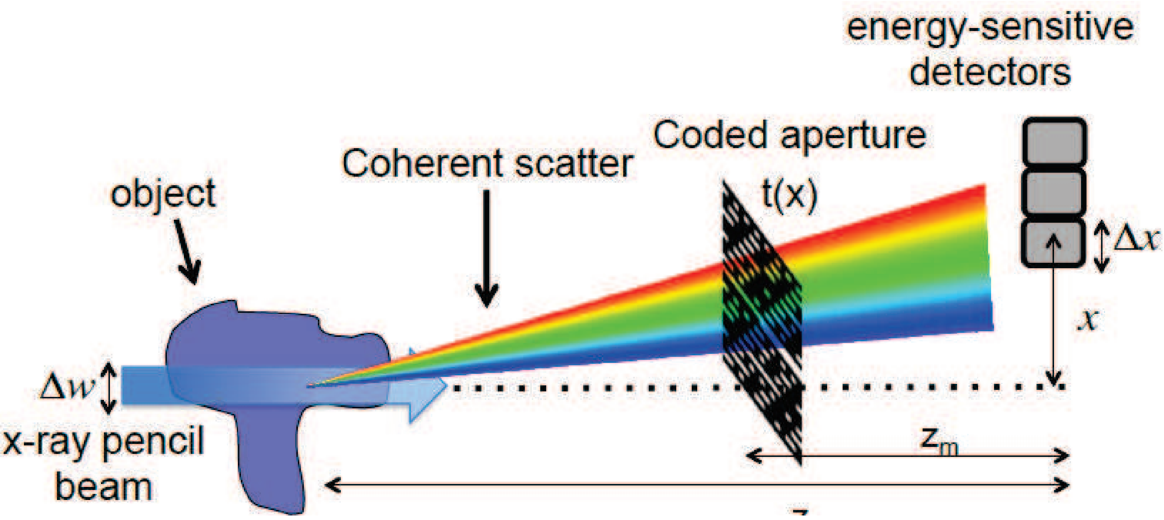

Figure I.38: Schematic diagram of CACSSI setup, including the X-ray source, collimators, coded aperture, object space, and detector [Greenberg *et al.*, 2013].

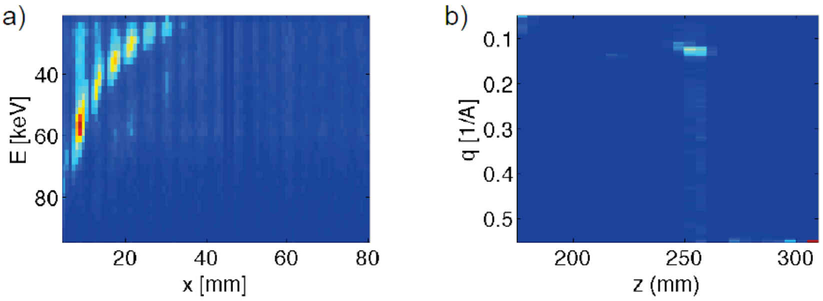

Figure I.39: Raw scatter data (a) and the full 2-dimensional reconstruction (b) of the object in q-z space for a 10 mm thick sheet of HDPE placed at z=252 mm [Greenberg *et al.*, 2013].

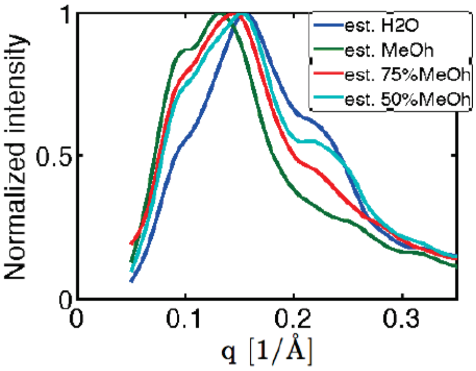

Figure I.40: Momentum transfer spectra for a 10 mm vial containing a mixture of MEOH and H_2O at various concentrations [Greenberg *et al.*, 2013].

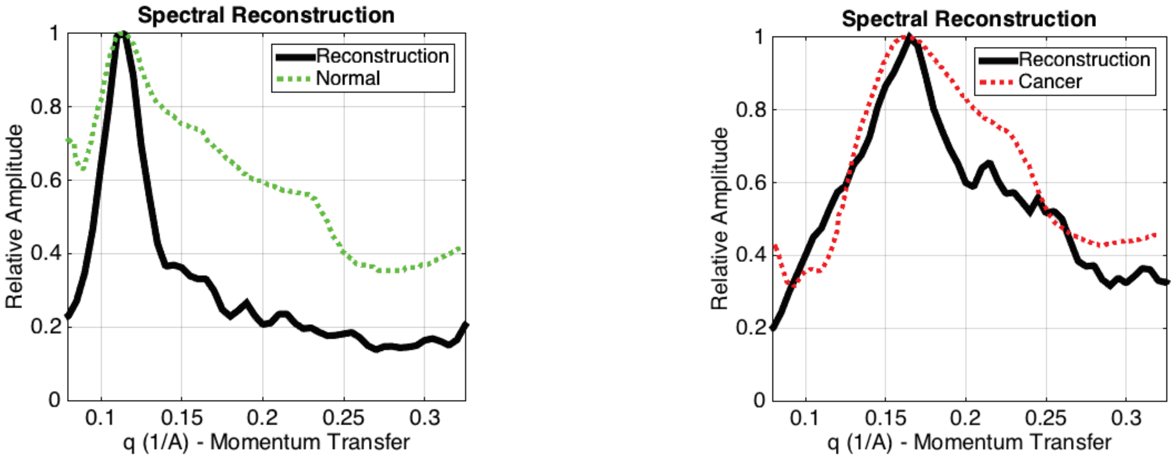

(a) *High probability of normal tissue along beam path.*

(b) *Region of high probability of cancerous tissue presence.*

Figure I.41: Spectral reconstruction from 1.5 mm-by-1.5 mm pencil-beam scans [Morris *et al.*, 2016].

An optimized EDXRD system for potential clinical application was proposed by Chaparian *et al.* In [Chaparian *et al.*, 2010], they present the optimized configuration and the different parameters, that were used to optimize the system. The system is made of a primary collimation defining a pencil beam, a rotational symmetric scatter collimatior consisting of two diaphragms of different diameters, and a HPGe detector (Fig. I.42). The optimized system parameters are shown in figure I.43. They validated their system in [Ali Chaparian, 2012] by comparing acquired diffraction patterns of biological tissues to results from previous studies. Bohndiek *et al* suggested in [Bohndiek *et al.*, 2008] the use of a CMOS active pixel sensor system, which could perform diffraction pattern recognition ”on-the-fly”. In [Bohndiek *et al.*, 2009], they tested multivariate data analysis on acquired data and concluded that their detector could provide a semi-automated, quantitative measurement system for analysis of breast biopsy samples. The use of EDXRD as a biopsy aid is also discussed in [Griffiths *et al.*, 2008].

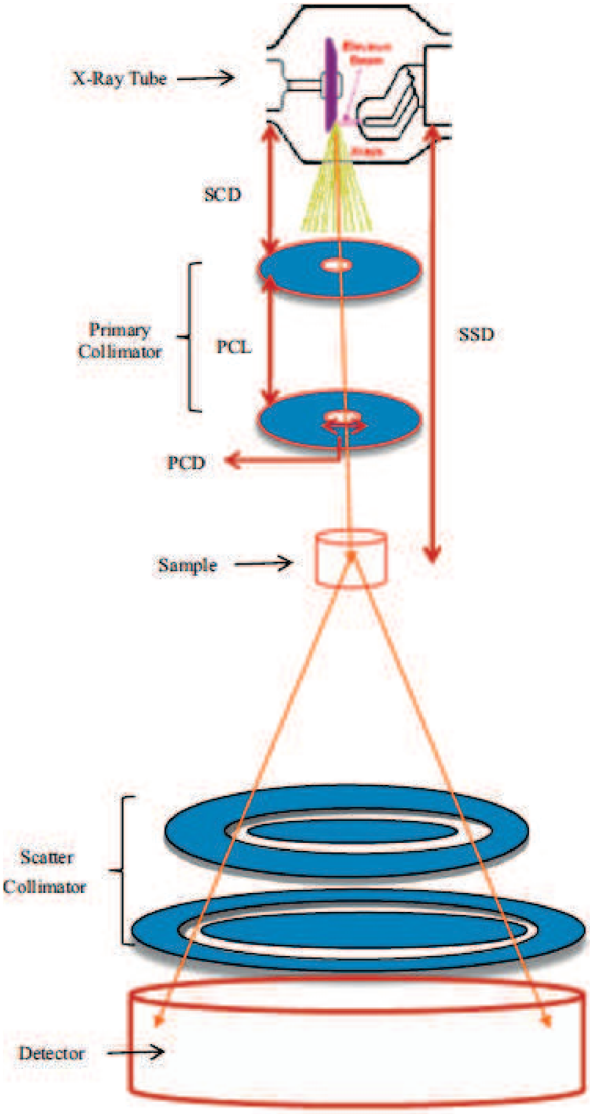

Figure I.42: Schematic view of the EDXRD system used in [Chaparian *et al.*, 2010].

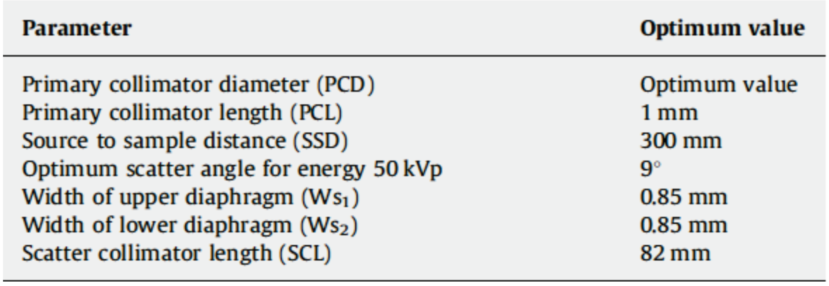

Parameter	Optimum value
Primary collimator diameter (PCD)	Optimum value
Primary collimator length (PCL)	1 mm
Source to sample distance (SSD)	300 mm
Optimum scatter angle for energy 50 kVp	9°
Width of upper diaphragm (Ws_1)	0.85 mm
Width of lower diaphragm (Ws_2)	0.85 mm
Scatter collimator length (SCL)	82 mm

Figure I.43: Optimum parameters determined by [Chaparian *et al.*, 2010] to obtain breast tissue diffraction pattern of 5 % momentum resolution and 10 and 2 mm for vertical and horizontal spatial resolution respectively.

XRD is not always proposed as an alone standing technique to characterize tissues but associated to other techniques. [Pani *et al.*, 2007] suggest to do diffraction imaging simultaneously with transmission imaging to increase contrast and provide tissue discrimination. Figure I.44 shows a comparison of a transmission image and a diffraction image of the same plexiglas phantom.

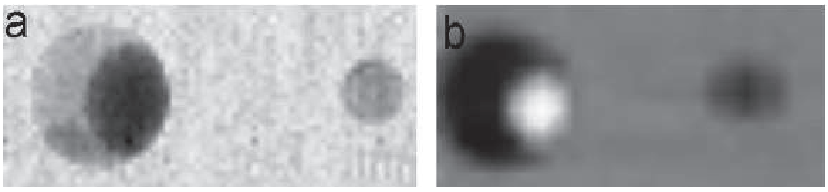

Figure I.44: Transmission (a) and diffraction (b) images of a plexiglass phantom 0.5 cm thick with holes 4 and 2 mm in diameter filled with water. An air bubble can be seen in the larger of the holes, whose contrast is opposite for the two imaging techniques. [Pani *et al.*, 2007]

The association of Compton and coherent scattering information to classify breast tissue was proposed by [Ryan and Farquharson, 2007] by the use of multivariate data analysis. Different models including different parameters for principal component analysis (PCA) were tested to separate normal and malignant tissues. The best model had a sensitivity of 54 % and a specificity of 100 %.

Geraki *et al* suggested to merge information provided by X-ray fluorescence (XRF) and EDXRD in [Geraki *et al.*, 2004] and [Farquharson and Geraki, 2004]. XRF is used to quantify trace elements in breast tissue samples whereas EDXRD is used to determine tissue composition. In [Farquharson and Geraki, 2004] the showed that combination of these two data types leads to a better mean prediction (Fig. I.45).

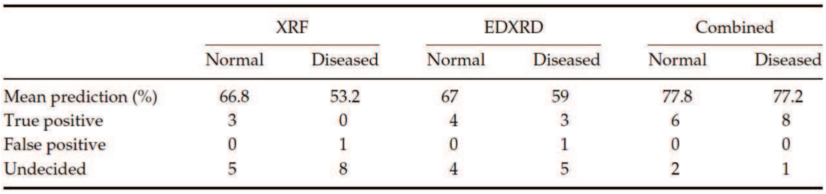

	XRF		EDXRD		Combined	
	Normal	Diseased	Normal	Diseased	Normal	Diseased
Mean prediction (%)	66.8	53.2	67	59	77.8	77.2
True positive	3	0	4	3	6	8
False positive	0	1	0	1	0	0
Undecided	5	8	4	5	2	1

Figure I.45: Mean predictions, true and false positives for each data group and tissue type using the classification technique.

I.2.2 Illicit materials characterization

Several research teams are interested in the use of X-ray diffraction to detect illicit materials such as explosives and drugs. The main actors in this application field are the University College London (R. Speller, R. Luggar, S. Pani...), Chinese Academy of Sciences (L. Li, F. Zhang, B. Sun...) Morpho Detection company (G. Harding *et al.*), INSA LVA-CNDRI (laboratoire vibration acoustique et contrôle non destructif par rayonnements ionisants) of Lyon (P. Duvauchelle *et al.*), University College of Southampton and L-3 Communications Security and Detection Systems (R.W. Madden *et al.*).

Different classes of explosives can be distinguished: plastic or organic explosives used in industry and military; liquid amorphous and gel explosives and home-made explosives (HMEs). The first class presents XRD pattern with sharp well known peaks at low momentum transfer values. Figure I.46 shows examples of acquired EDXRD spectra of pure explosives constituents and military and industrial explosives [Strecker *et al.*, 1993]. Recipes for HMEs are widely available and their ingredients are relatively easy to obtain. Their dangerousness is variable and ranges from "weed killer and sugar" to highly-explosive triacetone triperoxide (TATP) [Harding, 2009]. A representative XRD spectrum of HMEs can be seen in figure I.47.

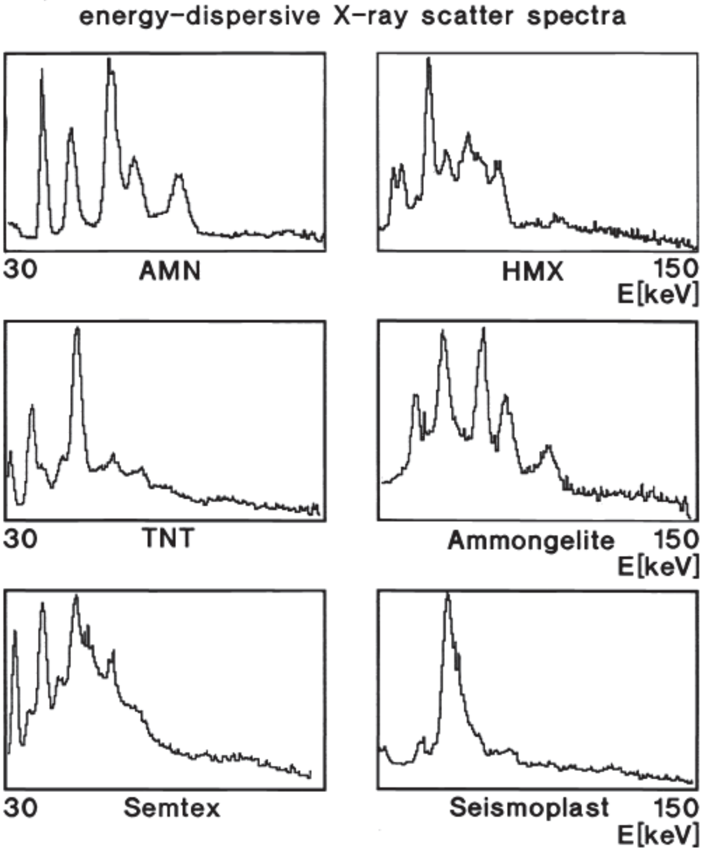

Figure I.46: Measured EDXRD spectra of pure explosives constituents: AMN (Ammonium-Nitrate (NH_4NO_3)), HMX (Octogen); and of military and industrial explosives: TNT, Ammongelite, Semtex and Seismoplast [Strecker *et al.*, 1993].

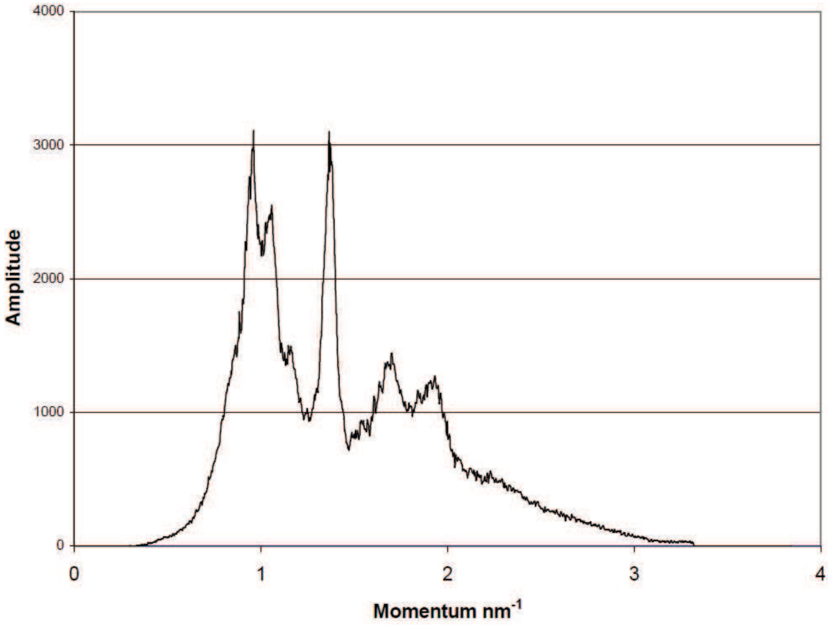

Figure I.47: XRD profile of representative HME [Harding, 2009].

[Luggar *et al.*, 1997] compared the XRD pattern of two explosives to diffraction profiles of typical suitcase contents (Fig. I.48). XRD spectra of typical suitcase contents present only very few broad peaks and can be well distinguished from explosives. The only exception is sugar which produces more than three discrete diffraction peaks. A simple analysis to identify suspicious cases could be peak counting [Luggar *et al.*, 1997] or the definition of an adapted energy window (in EDXRD) [Strecker *et al.*, 1993] (see figure I.49).

The use of ADXRD to detect explosives in baggage was only proposed by three authors. In fact, ADXRD requires a monochromatic incident X-ray beam and the need of moving parts in order to acquire the whole diffraction spectrum, which makes ADXRD a very time consuming inspection method. Furthermore, moving parts are very bulky especially if parallelization of several diffractometers is considered. Hence, these systems are suggested at a second control level.

[Beevor *et al.*, 1995] proposed the ADXRD system, which can be seen in figure I.50.a, for non-invasive baggage inspection. The system is composed of two primary collimators separated by a monochromator whose bandwith is situated between 57.49 keV and 59.38 keV. Secondary collimation is made of 0.3 mm shimming steel strips slotted into a grooved aluminium casing and radially spaced by 0.5 degrees. Each shim is aligned with the nominal focal spot at the center of the volume element to be inspected. Each detector pixel (SIT camera + intensifier tube) measures diffraction intensity at the scattering angle fixed by the corresponding shim. Figure I.50.b shows acquired diffraction spectra of different explosives: Semtex, PETN and RDX. Their diffraction signatures are well differentiated.

[Jupp *et al.*, 2000] presented a prototype of an ADXRD based luggage inspection system similar to the previous one. However, they suggest the use of a spectroscopic detector allowing to select photons in the required energy range. Thus, many of the restrictions imposed by the use of the filter pair to define the energy window can be removed.

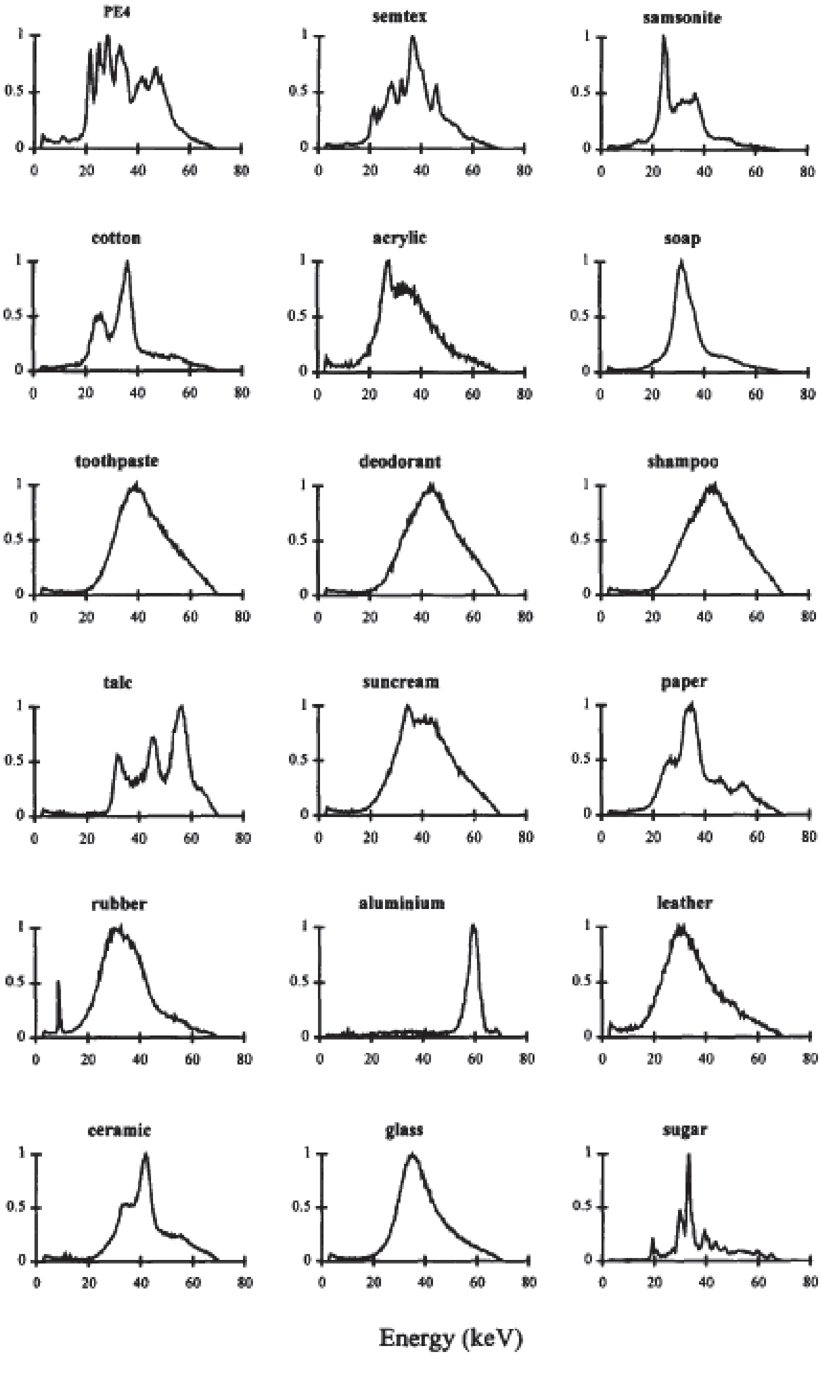

Figure I.48: Diffraction profiles of two explosives and typical baggage contents [Luggar *et al.*, 1997].

As the majority of suspect materials within suitcases are polycrystalline, [Dicken *et al.*, 2010] considered the use of powder diffraction method to detect explosives. Their system is represented in figure I.51. It comprises a fine-focus X-ray tube with a molybdenum target and 40 kV accelerating voltage, a scintillator detector located on an arm that rotates about a central point with constant radius. A global rotation of the inspection volume is introduced in order to separate different materials.

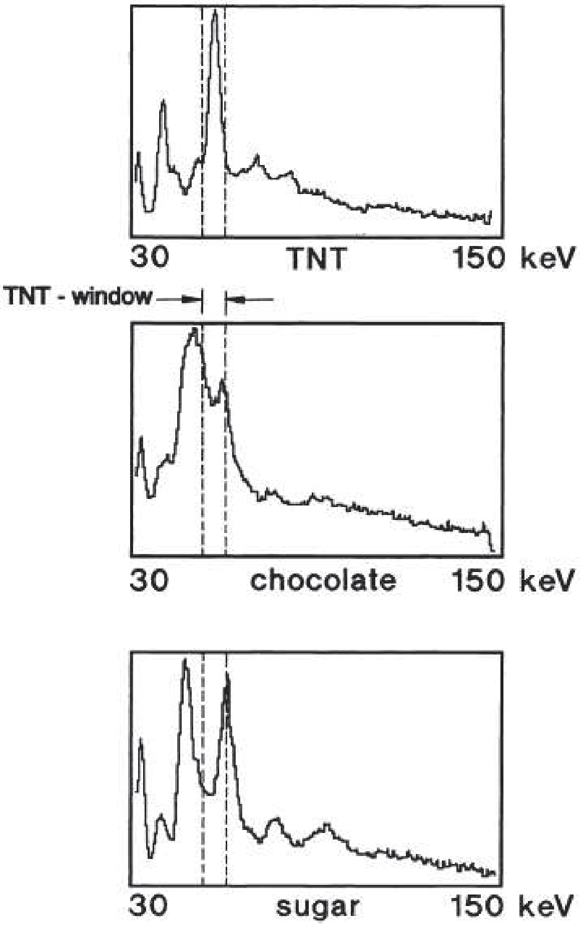

Figure I.49: Comparison of X-ray scatter spectra of TNT, chocolate and sugar [Strecker *et al.*, 1993].

As already mentioned, ADXRD detection methods are very time consuming and bulky. EDXRD allows the acquisition of a whole diffraction spectrum in one step and is less bulky. Emergence of well solved room temperature spectroscopic detectors resolved the problem of the cooling needed by germanium detectors, and many workers were interested in the use of EDXRD for explosive detection in baggage.

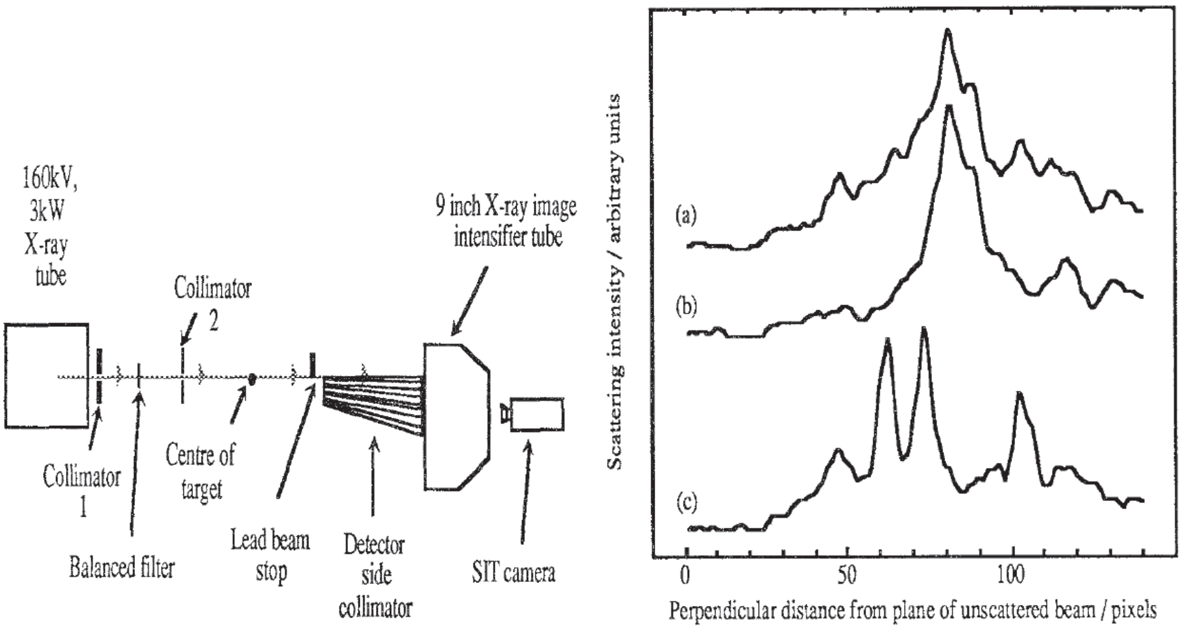

(a) *ADXRD apparatus.* (b) *Scattering profiles.*

Figure I.50: Schematic representation of the ADXRD apparatus used by [Beevor *et al.*, 1995] and measured diffraction spectra of Semtex (a), PETN (b) and RDX (c) (at about 60 keV).

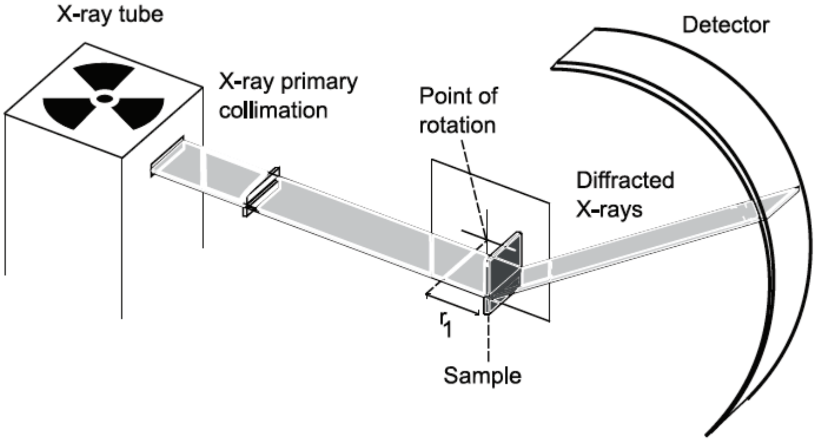

Figure I.51: The geometry of the X-ray diffractometer when the sample is displaced from the point of rotation by distance r_1 [Dicken *et al.*, 2010].

Recently, [Dicken *et al.*, 2015] proposed an alternate to the powder diffraction system in [Dicken *et al.*, 2010], which uses EDXRD but based on an ADXRD system architecture. This geometry is called focal construct technology (FCT) and employs an annular beam of monochromatic radiation and translating detector. The authors suggest the use of a polychromatic incident source and a stationary energy-sensitive "point" detector. Figure I.52.a shows an illustration of their system. In the case of a (poly)crystalline sample, polychromatic Debye rings can be observed. Polychromatic Debye rings of different *d*-spacings (spacing between the atomic planes) are superimposed upon each other but at the center of each composite pattern is a high intensity focal spot (Bragg maxima), which may be sampled by the energy resolving point detector to produce an intensity against energy/wavelength plot. Figure I.52.b corresponds to the discretized representation of a continuum of polychromatic Debye rings. Examples of determined scattering spectra for different acquisition times can be seen in figure I.53.

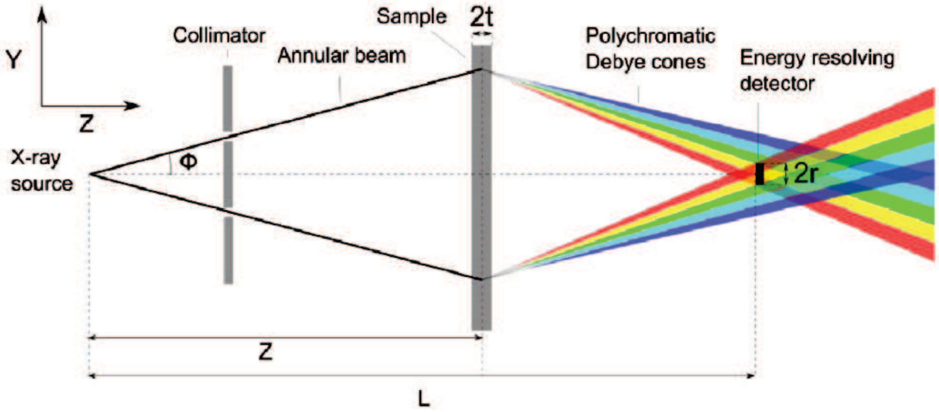

(a) *Schematic showing an annular beam incident normally upon an extended polycrystalline sample.*

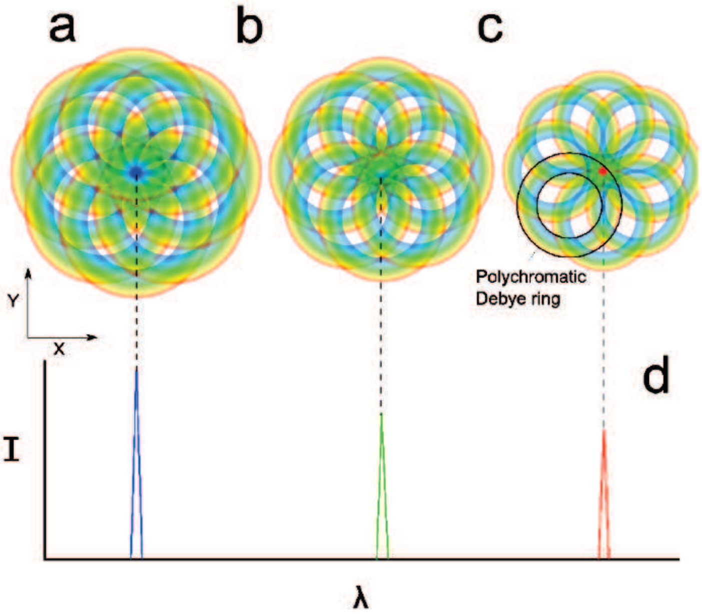

(b) *Polychromatic Debye rings: small (a), intermediary (b), and large (c) d-spacings.*

Figure I.52: Experimental setup for EDXRD with annular beam and discretized representation of a continuum of polychromatic Debye rings produced by FCT [Dicken *et al.*, 2015].

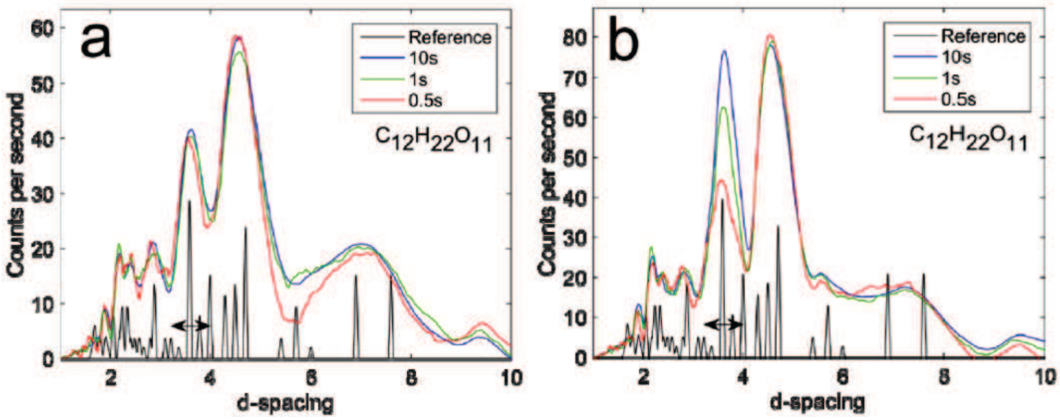

Figure I.53: X-ray diffraction pattern from small (a), and large (b) grained sucrose for 10, 1 and 0.5 second integration times respectively [Dicken *et al.*, 2015]. The *d*-spacings are given in.

In [Luggar *et al.*, 1997] an optimized geometry of an EDXRD system with a HPGe detector for the identification of sheet explosive in passenger baggage is presented. Different scattering angles (Fig. I.54), kinds of collimations as well as different tube potentials were tested and the impact of noise due to low measuring time on peak detection was also evaluated. It was shown that the best separation between explosives and typical suitcase contents is obtained with scattering angles between 4 and 5°, where a series of well resolved peaks can be observed. In this case, energies of observed peaks are higher than 30 keV, where attenuation of peak intensities is less important. It was found that the spectral shape is consistent with increasing noise. This is important because of the required short acquisition time. In further work [Luggar *et al.*, 1998], multivariate analysis (MVA) was applied to statistically poor EDXRD spectra to check whether rapid detection of explosive materials in the presence of overlying media was possible. It was feasible to detect sheet explosives within a briefcase with spectra containing only a several hundred counts.

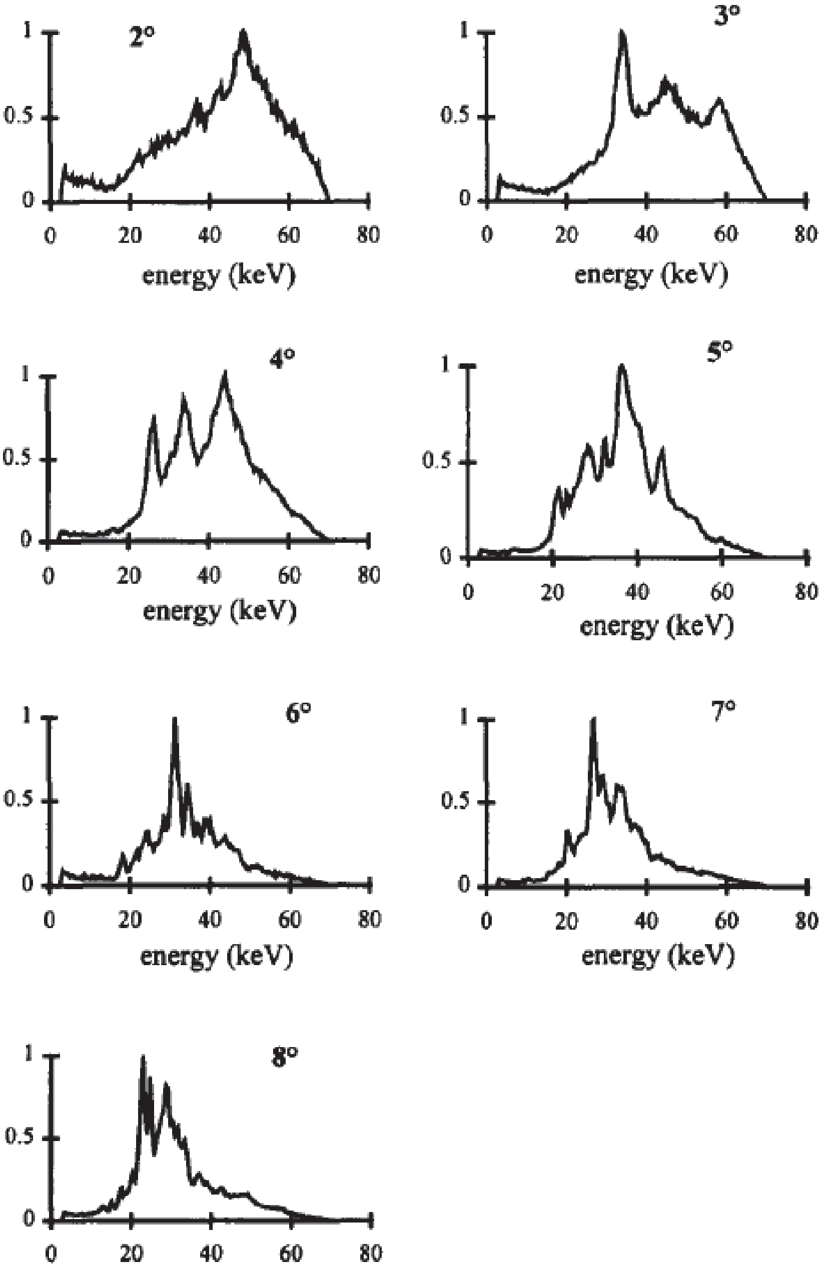

Figure I.54: Semtex diffraction profiles at scattering angles 2-8° [Luggar *et al.*, 1997].

The impact of the scattering angle on detection of several substances was also studied in [Li *et al.*, 2010] and [Sun *et al.*, 2010]. In [Li *et al.*, 2010] the optimum detection angles were determined to be 8° for methamphetamine, sugar and salt, and 6° for TNT with an incident X-ray spectrum with 75 keV maximum energy. The authors of [Sun *et al.*, 2010] compared TNT diffraction pattern acquired at different scattering angles (Fig. I.55.a) with a 60 kVp incident spectrum. They also tested different incident X-ray sources (Mo, W and Cu anode, Fig. I.55.b).

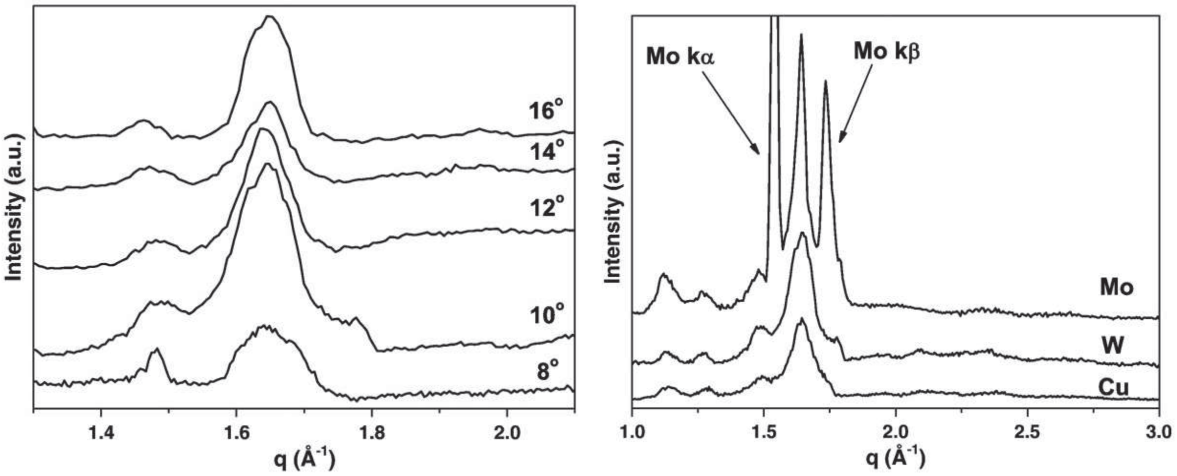

(a) *Pattern detected at different scattering angles with incident 60 kVp W spectrum.*

(b) *Pattern detected at 10° using different incident spectra.*

Figure I.55: Measured TNT spectra for different scattering angles and with different incident spectra [Sun *et al.*, 2010].

A complete detection system for airline security was developed by [Madden *et al.*, 2008]. Its performance has been demonstrated in tests with concealed explosives at the Transportation Security Laboratory and airline passenger baggage at Orlando International Airport. This system works in complement with CT explosive detection systems in order to significantly reduce the false alarm rate, which avoids manual bag check. The volume to be inspected is defined with analyzing algorithm using CT data. The incident X-ray source can move in two dimensions in the horizontal plane below the bag tunnel and is positioned directly below an individual object targeting a small volume within the object. A HPGe detector is fixed on a complementary two-dimensional transport system above the bag tunnel. A collimation system allows to limit the inspected volume to a diamond-shaped volume, about 50 mm in height by 25 mm in length by 1.5 mm in width (Fig I.56). This collimation system also permits to choose between two scattering angles which can be chosen depending on attenuation of objects within the inspected bags. The higher attenuation is, the higher has to be the photon energy to analyze the object. Transmitted radiation is also measured to realize a correction for attenuation. Neural network approach [Zhang, 2000] was considered to classify the data into explosives and non-explosives. However, a very large library would be required to adequately represent most objects and if a new class of explosives appears, it cannot be included without retraining the network. Hence, they opted for a combination of wavelet decomposition [Chui, 1992] and support vector machines (SVM) [Fradkin and Muchnik, 2006] to separate the samples into explosives and non-explosives.

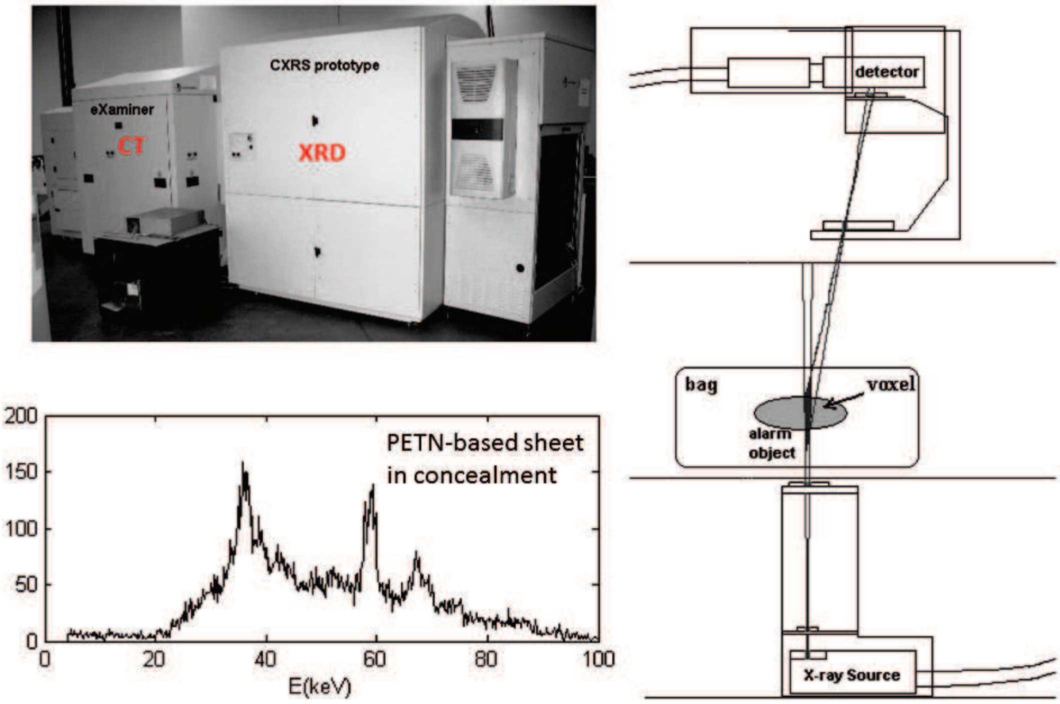

Figure I.56: XRD system for baggage inspection conceived by L-3 Communications Security and Detection Systems and an example of an acquired diffraction spectrum [Madden *et al.*, 2008].

Morpho detection appears to be one of the most important industrial actors in the use of X-ray diffraction for luggage inspection. At the present time, they offer two different EDXRD devices security control. XRD 3500 [Harding *et al.*, 2012] working with germanium detector is used as a second control level for luggage if the conventional control apparatus has detected a potential threat. Their second devices works with $CdZnTe$ detector and is dedicated to cabin baggage control at first control level. They have been working on the use of EDXRD in luggage control since several years and their system has known four generations. Each generation aimed to allow XRD-based baggage control in a shorter acquisition time.

First generation: Single-point tomographic XRD

The first generation system has been developed in order to gain acquisition time compared to existing ADXRD measuring techniques. Figure I.57 shows a schematic representation of the first generation system: a polychromatic incident pencil beam irradiates a given region of the object. An energy resolving detector (HPGe) is positioned at an angle θ with respect to the incident beam. This detector is equipped with a collimator so that it only sees radiation scattered from a localized volume element of the object. Thus, XRD yields direct tomographic information without the need to reconstruct from projections. An attenuation correction is carried out thanks to a transmission detector placed on the beam line. A raster scan is realized by moving the object. This first generation permits to measure one point in 1 s. It is a compact system and a fast result can be obtained with small samples. However, the scan of a larger object would be too long.

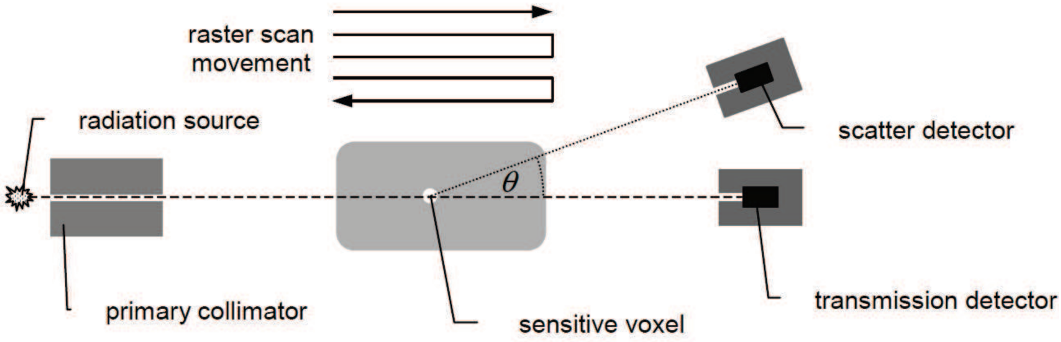

Figure I.57: Schematic representation of ”single-point” tomographic energy dispersive XRD imager [Harding, 2009].

Second generation: Line-parallel XDI
The second generation system is an improvement of the first model to further decrease the required scan time. The single scatter detector is replaced by an array of many detector elements. Thus, XRD profiles from a multiplicity of object voxels along the primary beam path can be acquired simultaneously. A two-dimensional raster scan movement is no longer necessary to record a 2D image. As can be seen in figure I.58 a linear translation movement is sufficient. It is possible to analyze 100 voxels per second.

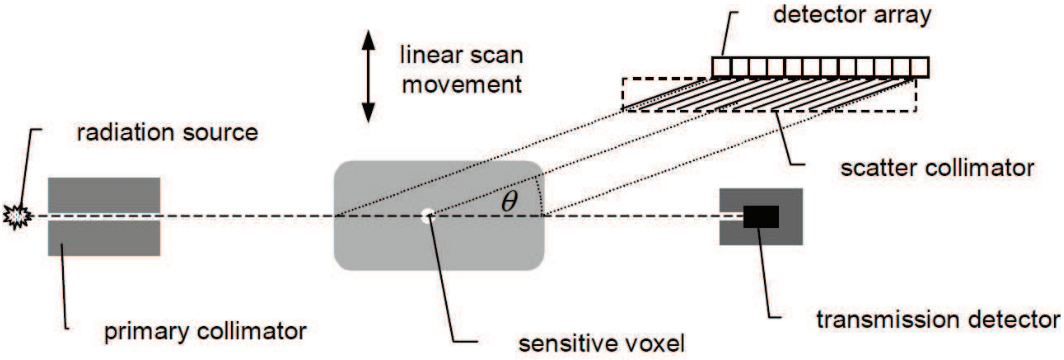

Figure I.58: Schematic representation of ”line-parallel” tomographic energy dispersive XRD imager [Harding, 2009].

Third generation: Area-parallel XDI
The third generation allows the simultaneous analysis of the local diffraction properties of a 2D array of voxels without the need of mechanical movements. Figure I.59 shows an example of a third generation XDI arrangement. Here, voxels lying on a planar 2D surface of the sample are simultaneously analyzed by a 2D pixellated, spectroscopic detector. A well-collimated fan beam in x,y-plane illuminates a slice of the object and the transmitted beam arrives on the detector on the central line. The detection surface is indexed by two variables: ϕ for columns and h for lines. Between the detector and the sample is placed a secondary collimation, which ensures that a given detector column (constant ϕ) only ”sees” object voxels lying on a narrow strip of angular width $\delta\phi$ around ϕ (equivalent to the second generation). It has to be noted that each detector pixel intercepts the same scattering angle θ. Thus, a 2D information $I(h, \phi)$ is measured at once. Three geometrical configurations of

the third generation XDI have been proposed: the direct fan-beam, the parallel (waterfall) beam and the inverse fan-beam, which are illustrated in figure I.60. It was shown that the inverse fan-beam configuration is the best [Harding *et al.*, 2010b].

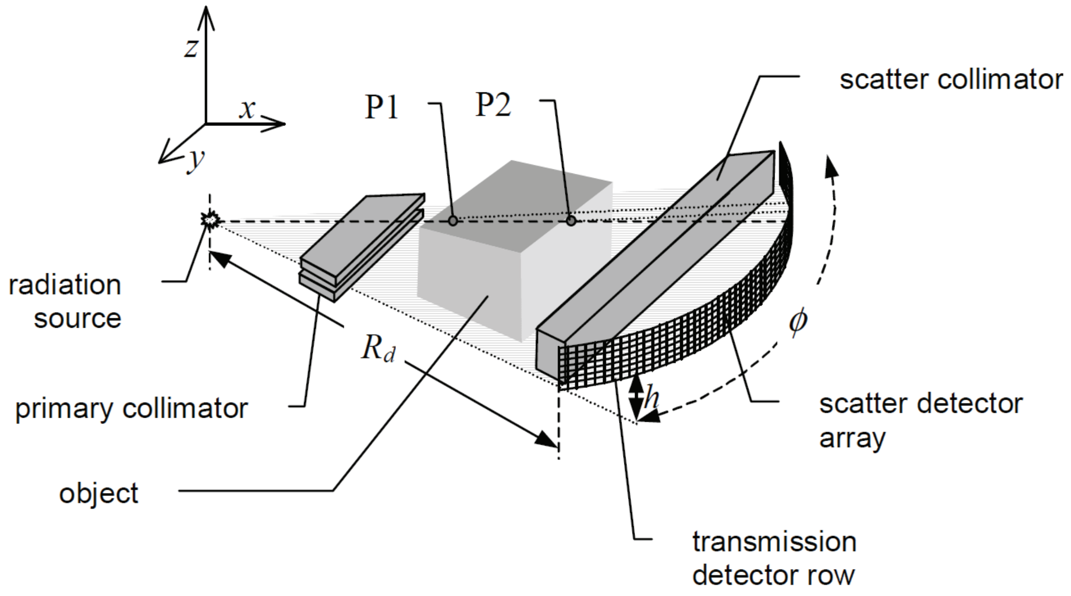

Figure I.59: Schematic representation of third generation, direct fan-beam XDI [Harding, 2009].

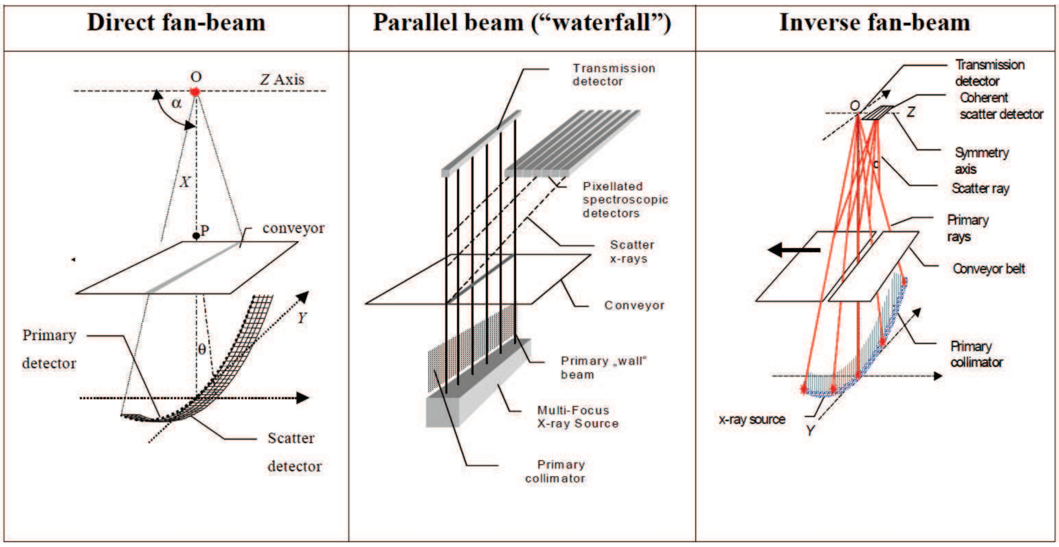

Figure I.60: Illustration of three alternative area-parallel geometries [Harding, 2009].

Fourth generation: Volume-parallel XDI

The developments of the third generation can be combined to obtain the fourth generation by the use of the so-called "parallel multi-direct fan-beam" as shown in figure I.61. This requires the use of a multi-focus X-ray source (MFXS), which is linearly segmented in z-axis direction. The aim is to reduce translatory motion needed to cover the whole 3D volume. However, due to increase in X-ray tube power loading, it was concluded that it made more sens to emphasize third generation rather than invest in development of the fourth generation [Harding, 2009].

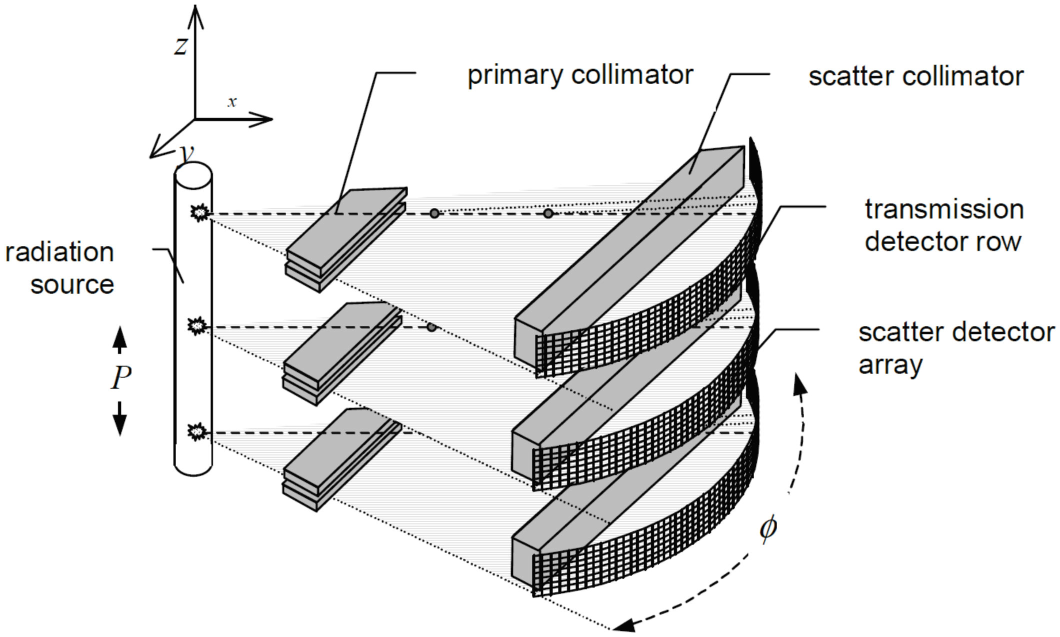

Figure I.61: Example of fourth generation XDI configuration: parallel multi-direct fan-beam XDI system [Harding, 2009].

[Peterzol *et al.*, 2011] have developed a simulation tool, which exploits kinematic theory of diffraction. They carried out a modeling-based optimization study for a portable EDXRD system to characterize dangerous/illicit objects inside objects. A scattering angle of 2.75° and an X-ray tube voltage $\leq$ 160 kVp were determined to be optimal. The same research team [Crespy *et al.*, 2010] proposed a detection method for explosives based on the procedure developed by Hanawalt [Langford and Louer, 1996] in 1936 to recognize an unknown substance from its diffraction spectrum. It consists in the determination of peak position in measured EDXRD spectrum and to compare them to a library. Here, the library only contains explosives. If at least one peak matches a peak of the data base, the maximum amount of explosive in the sample is calculated. The authors showed that explosives present their first peak between 1 and 1.4 nm^{-1}. However, sugar and graphite also verify this condition. Thus, the use of the two principal peaks (second peak between 1.2 and 1.6 nm^{-1}) was suggested, which allowed to reduce false alarm. Figure I.62 shows the classification results based on the position of the two main peaks.

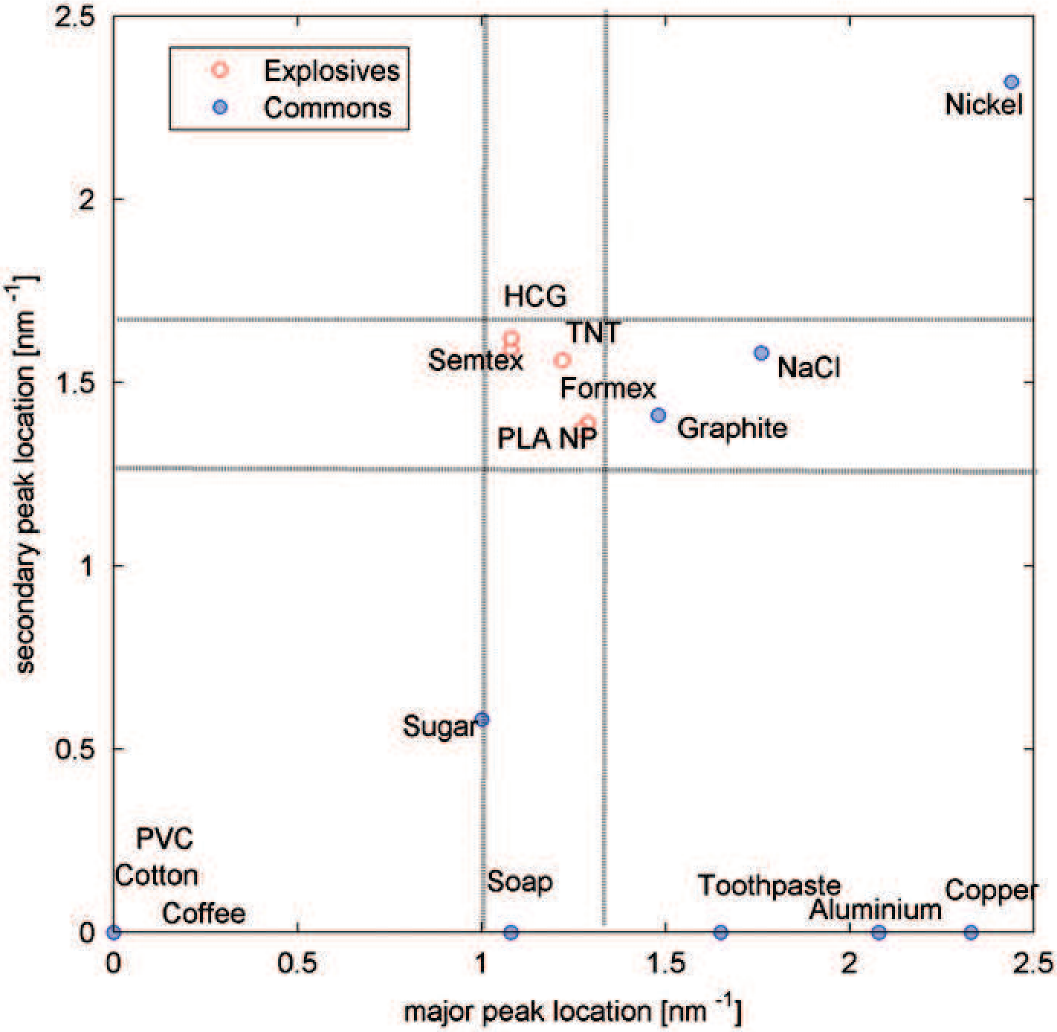

Figure I.62: Two main peaks location for spectra acquired with Ge detector [Crespy *et al.*, 2010].

The combination of ADXRD and EDXRD was proposed by [Malden and Speller, 2000] and [O'Flynn *et al.*, 2013]. Both articles aim the use of the benefits of both approaches and an increase in the measured flux, i.e. an increase in system sensitivity.

A schematic representation of a single detector system employed in [Malden and Speller, 2000] is shown in figure I.63. Acquired 2D data correspond to EDXRD spectra at different scattering angles. In order to extract scattering signatures of explosives, a measured image of a suitcase without explosives is subtracted from the image of suitcase with explosives (Fig I.64).

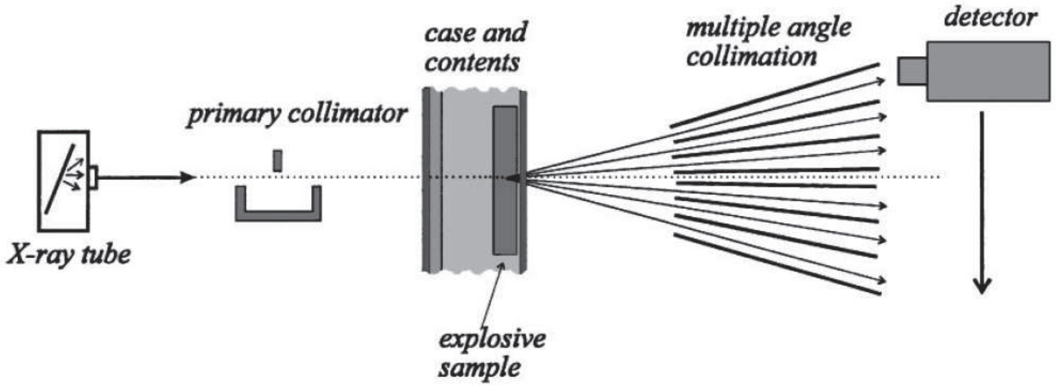

Figure I.63: Combination of ADXRD and EDXRD [Malden and Speller, 2000].

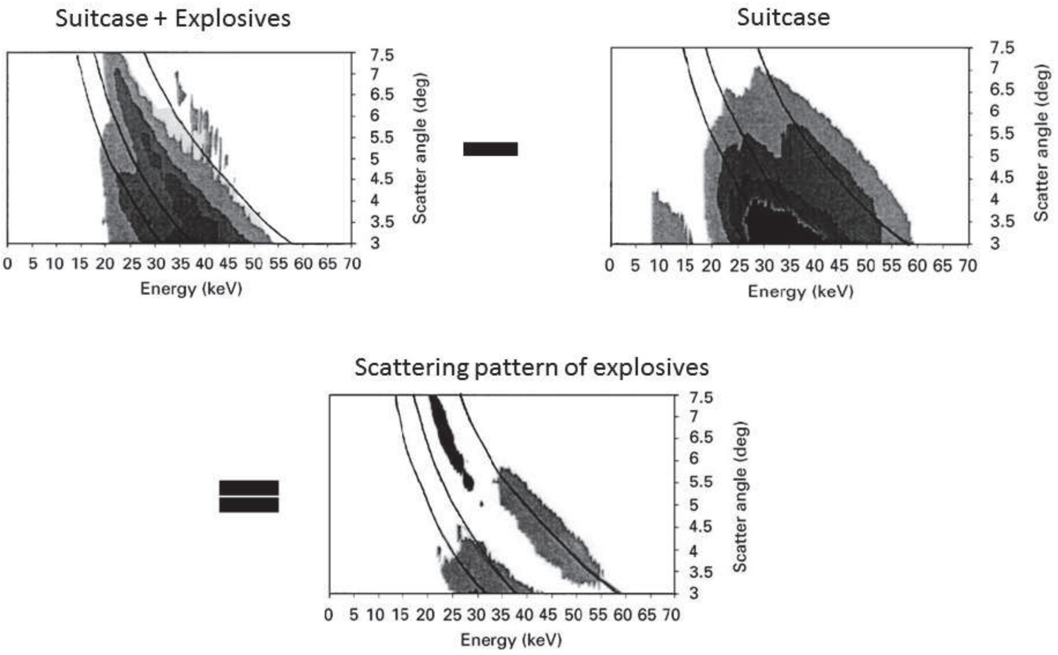

Figure I.64: An example of the subtraction of two energy-angle diagrams to find the areas characteristic of the explosives [Malden and Speller, 2000].

[O'Flynn *et al.*, 2013] used a pixelated energy-resolving $CdTe$ detector to simultaneously acquire EDXRD spectra at different scattering angles. Afterwards, they recombined the spectra at different scattering angles in the momentum transfer space. Figure I.65 shows an illustration of the principle of data recombining. For classification of the sample as explosive or not, principal component analysis and discriminant analysis were suggested (Fig. I.66).

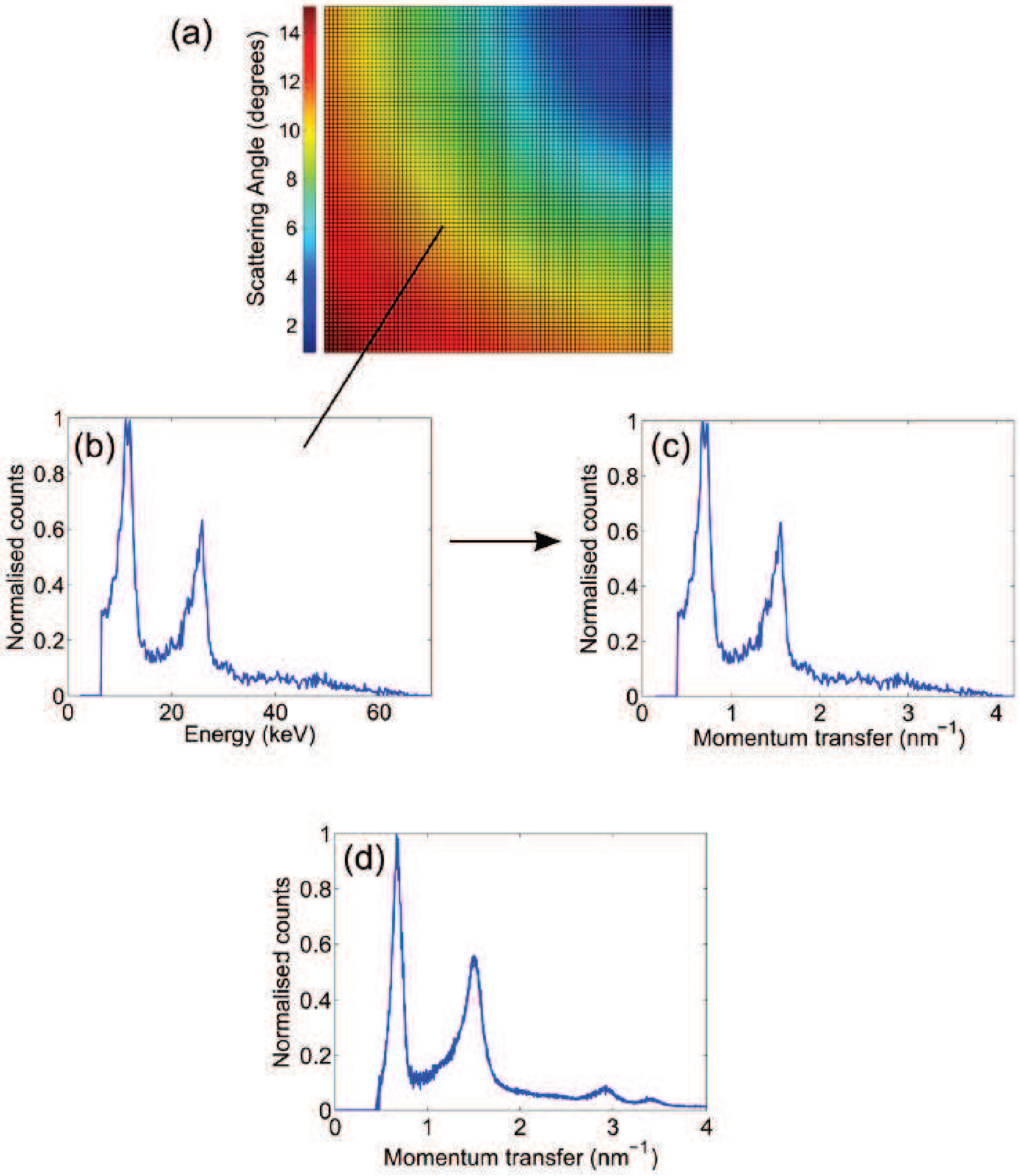

Figure I.65: Illustration of the data processing of combined ADXRD/EDXRD data: (a) a pixel map showing the scattering angle for each pixel based on an incident X-ray beam located off the top-right hand corner. (b) A typical energy spectrum measured by one pixel for caffeine sample. (c) Conversion into momentum transfer spectrum. (d) Summation of the spectra from all pixels gives an overall momentum transfer spectrum for the acquisition [O'Flynn *et al.*, 2013].

EDXRD-based detection of narcotics in air passenger luggage have been suggested by [Harding, 2009]. Extensive trials of narcotic detection have been carried out with good success, i.e. high detection rate with low false alarm rate. The use of EDXRD for illicit drug detection in parcels was also considered by [Cook *et al.*, 2007]. Figure I.67 shows examples of diffraction pattern of pure illicit drug samples. It can be seen that each drug presents characteristic pattern. [Cook *et al.*, 2007] demonstrated the feasibility of using an

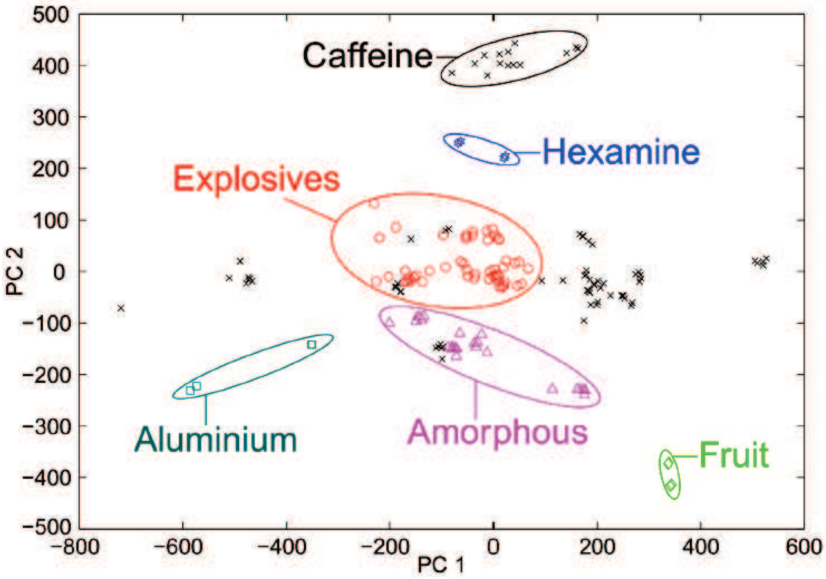

Figure I.66: Scores plot showing the first two principal components for time normalized XRD data. [O'Flynn *et al.*, 2013].

EDXRD system associated to multivariate analysis for detection and identification of illicit drugs. In fact, shapes and position of diffraction peaks in measured spectra are characteristic of the scattering substance and energy of used X-rays is sufficiently high to penetrate parcels containing other attenuating substances. [Pani *et al.*, 2009] developed a simulation program, which models the response of an EDXRD system. A schematic representation of the modeled diffractometer can be seen in figure I.68.a. Experimental and simulated spectra were in good agreement (Fig. I.68.b). Using this problem, they evaluated the impact of sample thickness (Fig. I.68.c), detector energy resolution (Fig. I.68.d) and scattering angle on the shape of diffraction pattern. Sample thickness was identified as the main factor affecting detected EDXRD spectra, whereas detector spectral resolution only showed little impact. Hence, it is possible to employ less resolving room-temperature detectors such as $CdZnTe$. In [Cook *et al.*, 2009a], the simulation software PANINI (Profile ANalyzer In Narcotic Investigation) to predict diffraction profiles has been evaluated and then used to test different system geometries, detectors, X-ray sources and counting statistics in order to determine an optimized system with the aid of MVA. The most promising systems were realized and tested thanks to an adaptable EDXRD system. [Cook *et al.*, 2009b] employed MVA on simulated and experimental EDXRD data to detect the presence of a drug and to determine its concentration. Different statistics were applied to assess the detection limits of the models and the associated sensitivity and specificity were calculated for different thresholds. MVA was proved to be effective to detect the presence of drugs and to measure its content.

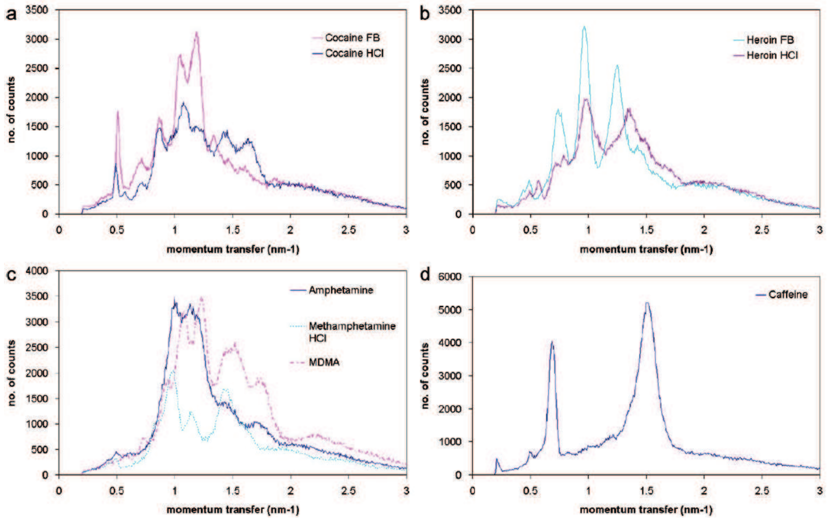

Figure I.67: Diffraction profiles of pure illicit drug samples and caffeine measured at 7° [Cook *et al.*, 2007].

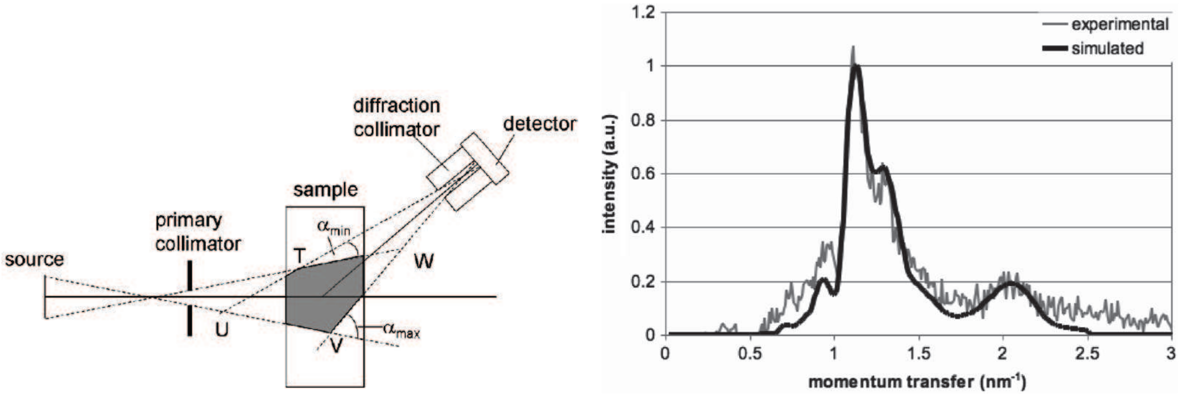

(a) *Modeled EDXRD diffractometer.*

(b) *Experimental vs. simulated data at 7°.*

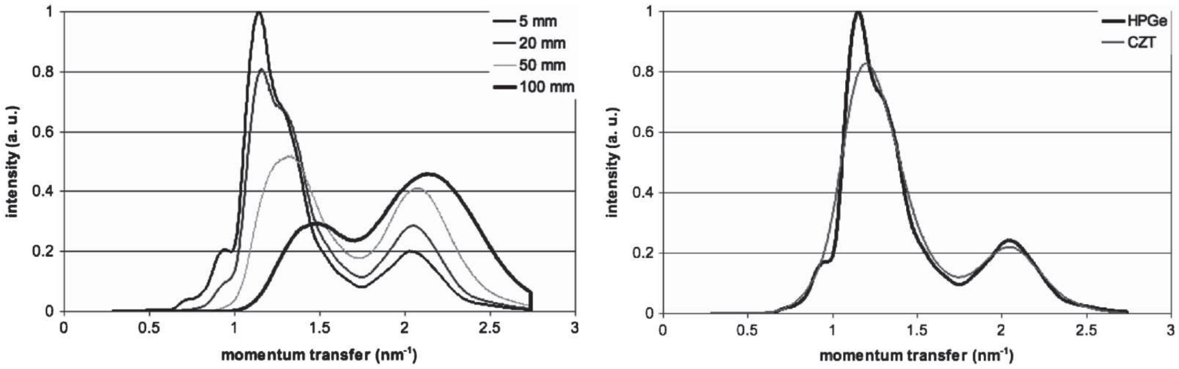

(c) *Effect of sample thickness on diffraction pattern at 6°.*

(d) *Effect of detector energy resolution on diffraction pattern at 6°.*

Figure I.68: Modeled EDXRD diffractometer and simulated Zirtec spectra with different parameters [Pani *et al.*, 2009].

As drugs are often transported by humans in their digestive system, [Zhang *et al.*, 2010a] investigated the use of EDXRD to detect heroin hidden in human body. They tested different scattering angles and acquisition times and they concluded that EDXRD could be a suitable technique for this issue. In their following work, they suggested different analyzing methods of EDXRD spectra to detect drugs covered by skin such as the use of coherence function [Zhang *et al.*, 2010b], [Yu *et al.*, 2010], singular value decomposition (SVD) [Zhang *et al.*, 2010c] and principal component analysis [Li *et al.*, 2011]. Figure I.69 shows the results of the SVD to separate heroin, skin and heroin covered by skin. In fact, The separability of heroin, skin and heroin covered by skin with EDXRD was found to be good.

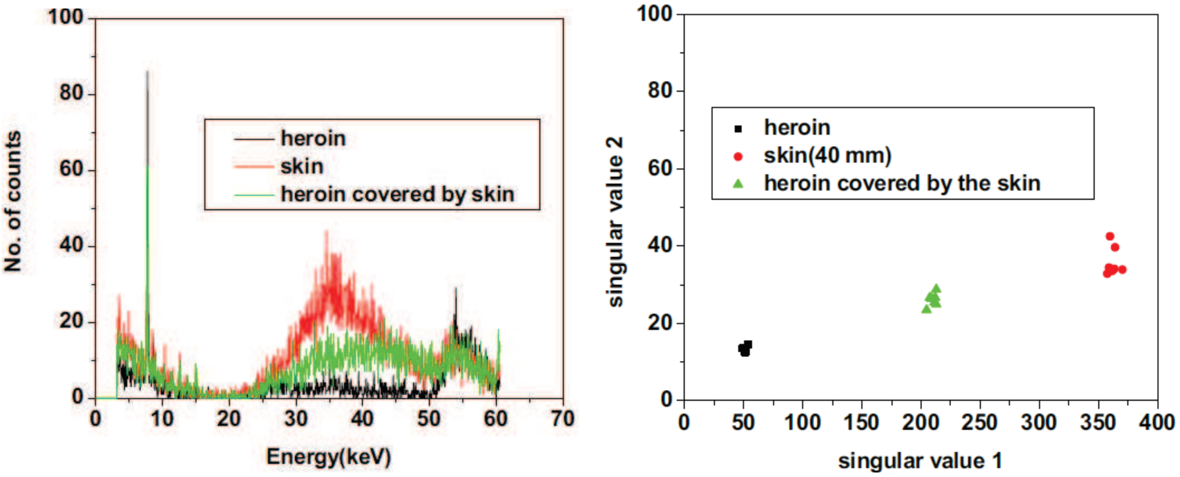

(a) *EDXRD spectra.* (b) *Plot of singular value 1 against singular value 2.*

Figure I.69: EDXRD spectra of pure heroin, skin and heroin covered by skin and results of SVD analysis [Zhang *et al.*, 2010c].

The problem of liquid identification using XRD was addressed by [Harding and Delfs, 2007], [Harding *et al.*, 2010a], [Zhang *et al.*, 2011] and [Zhong *et al.*, 2010]. [Harding *et al.*, 2010a] showed that amorphous materials such as liquids also presented characteristic scattering signatures. [Zhong *et al.*, 2010] made a proof of principle study, where they investigated three liquid systems of primary alcohols, ketones compounds and acids. It was found that each specific liquid material had a unique EDXRD profile (Fig I.70). [Zhang *et al.*, 2011] applied SVD on EDXRD spectra in order to identify liquid precursor chemicals. The method classified correctly the tested liquid precursor chemicals and it can be expected to be suitable to classify further liquid precursor chemicals.

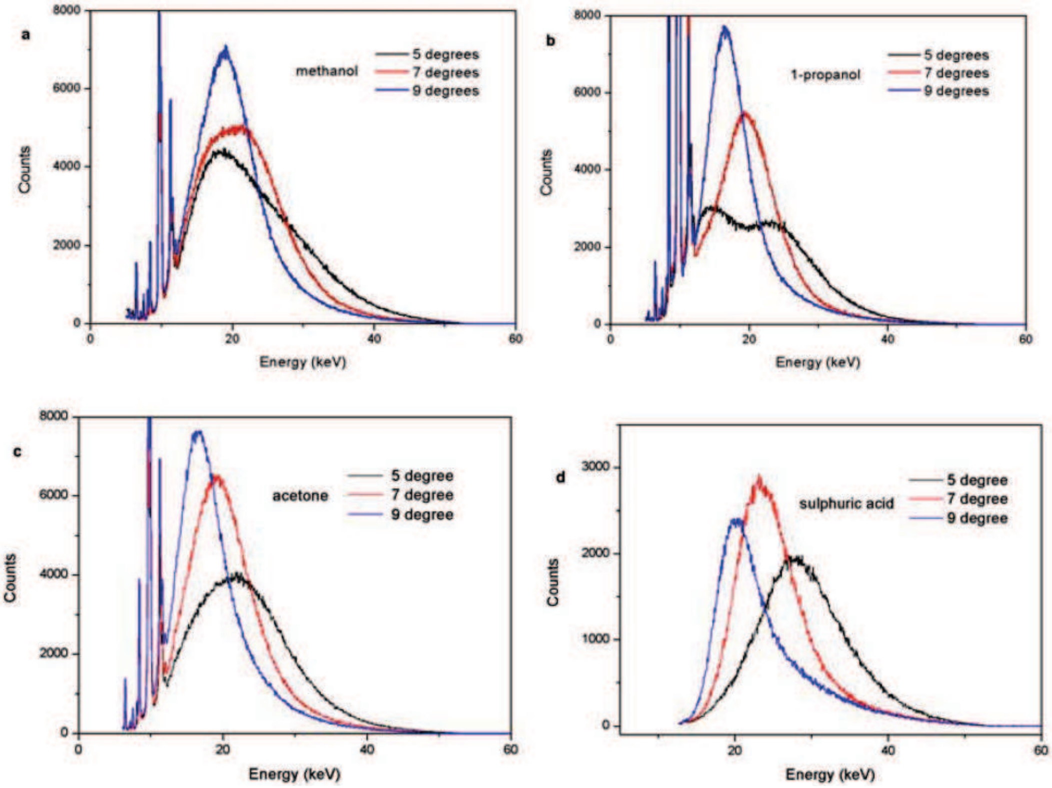

Figure I.70: Scattering spectra of different liquids from the three liquid systems at scattering angles of 5°, 7° and 9° [Zhong *et al.*, 2010].

In the last few years Duke University proposed different system architectures for X-ray scatter imaging using coded apertures. One of their intended applications of their systems is detection of explosives. In [MacCabe *et al.*, 2012], they present an imaging system, which uses an incident pencil beam and a coded aperture as secondary collimation, which is associated to an irradiance detector (Fig. I.71). This technique allowed them to determine the along-beam positions and momentum transfer profiles of two crystalline powders ($NaCl$ and Al). Figure I.72 shows reconstructed scattering profiles if both samples are in the beam. Different beam geometries have been tested such as fan beam [Maccabe *et al.*, 2013]. In further work, the use of a structured illumination was evaluated. The aim was to improve the source and detector efficiency for XRD imaging. In [Greenberg *et al.*, 2014] the object is illuminated by a spatially structured X-ray beam. During acquisition, the object moves relative the the X-ray source. The scatter signal is measured by a single, energy-resolving detector pixel. Measured raw data, which corresponds to a set of modulated curves in energy-time space, are used to estimate the coherent scattering form factor at each object voxel. This principle is illustrated in figure I.73. Overall scan time could be reduced by 1-2 orders of magnitude. In another communication [Pang *et al.*, 2014], the use of a pair of complementary coded apertures is proposed. One coded aperture is placed on the detector side in order to introduce a multiplexed measurement. The second coded aperture is positioned on source side and ensures a selective illumination of the object. This should decouple the ambiguity due to the increased parallelization for 4D imaging (one momentum transfer dimension and three spatial dimensions). Here, an energy-sensitive detector array is used. Figure I.74 shows a schematic representation of the system that was employed. The coherent form factor resolution with this system is mainly affected by detector energy resolution, which is different compared to "classical" EDXRD systems, where resolution is mainly limited by angular resolution of the secondary collimation.

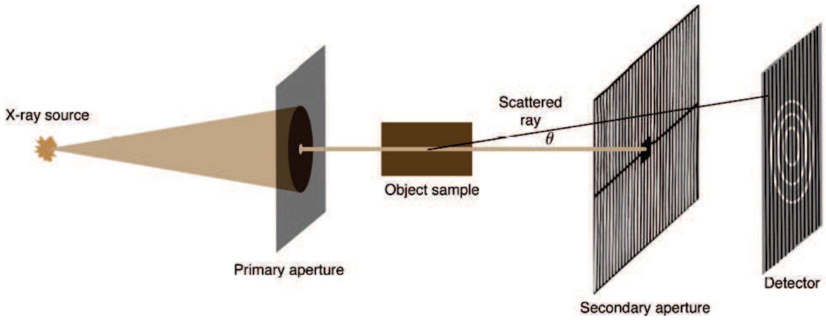

Figure I.71: Basic pencil beam coded aperture X-ray tomography system [MacCabe *et al.*, 2012].

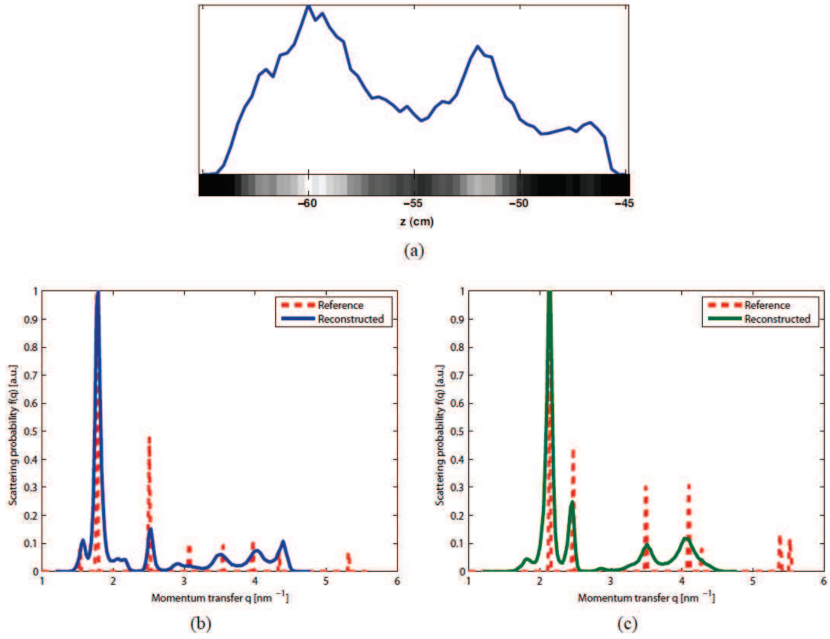

(a)

(b)

(c)

Figure I.72: Reconstruction results with $NaCl$ and Al sample in the beam. (a) Spatial scattering profile with both samples in the beam. (b) Momentum transfer profile for $NaCl$ at z=-59.3 cm. (c) Momentum transfer profile for Al at z=-52 cm [MacCabe *et al.*, 2012].

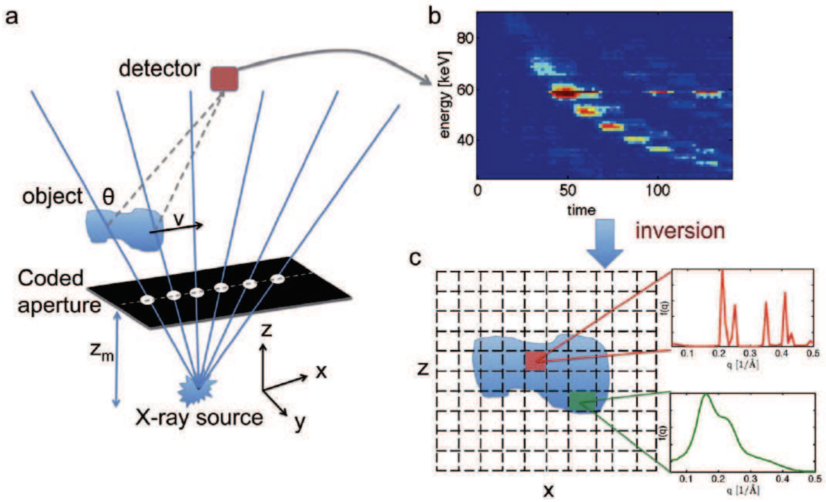

Figure I.73: Schematic representation of the imaging system proposed by [Greenberg *et al.*, 2014]. (a) The object is illuminated by a structured fan beam and the scatter signal is measured by a single, spectroscopic detector pixel. (b) Raw data consists of a set of modulated curves in energy-time space. (c) Estimated coherent scatter form factor at every object voxel.

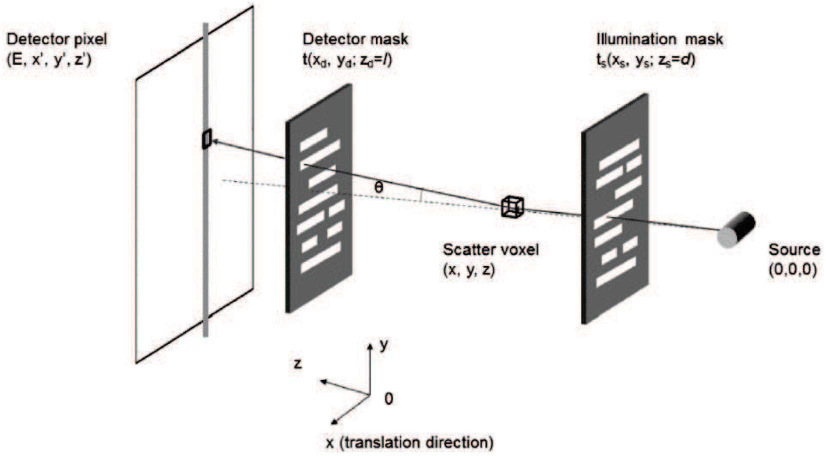

Figure I.74: Geometric setup for the coded aperture X-ray coherent scatter imaging system [Pang *et al.*, 2014].

I.3 System approach considered in this work

The present work is focused on the measurement of X-ray diffraction intensity as a function of incident photon energy as this technique is particularly suited for the targeted applications. In fact, this technique allows the use of a conventional X-ray tube, the acquisition of the whole spectrum at the same time and parallelized architectures to inspect an entire object in a reasonable time. Initially, only EDXRD should have been considered. However, very early during this work it turned out that a multi-angle EDXRD could be useful. Hence, in the following EDXRD or a combination of EDXRD and ADXRD will be used. In both cases, the use of a spectroscopic detector is required. Angular discrimination is realized thanks to spatial resolution of the detector. The laboratory, where this PhD work was realized, has developed different *CdTe* and *CdZnTe* spectroscopic detectors with good performance as well as the adequate signal processing. Hence, optimization process in this work will mainly concern the collimation system to select measured diffraction angle and improvement of the measured XRD data by reconstruction.

I.4 Conclusion

This chapter introduced the physical principles of X-ray diffraction. After a short explication of the different interactions of X-rays in matter, X-ray diffraction was explained in more detail. Crystalline matter leads to discrete XRD pattern with material characteristic Bragg peaks, whereas XRD signatures of amorphous matter correspond to continuous functions presenting one or more broad maxima material characteristic as well. Both Bragg peaks and broad maxima reflect distances between molecules within the inspected matter. XRD signal can be measured in two ways: angular dispersive XRD (fixed energy and varying scattering angle) and energy dispersive XRD (fixed scattering angle and varying energy). EDXRD systems are faster and less bulky than ADXRD systems. Hence, they seem more suitable for medical and industrial applications. However they require the use of spectroscopic detectors, which initially needed cooling system, e.g. HPGe detector. The emergence room-temperature spectroscopic detectors with satisfying resolution (interaction depth effect correction and sub-pixel positioning) such as *CdTe* and *CdZnTe*, made of EDXRD a promising technique for material characterization in different fields of application. The present work will concentrate on two chosen applications: breast cancer detection and detection of illicit materials in luggage.

The potential of XRD to classify biological tissues has been shown in several studies. Most studies concentrated on classification of different breast tissue types. This imaging technique seems to have a high potential to identify healthy and cancerous breast tissue and to present a higher contrast between these tissues than conventional mammography. Different methods to determine scattering signatures of breast tissues and to take them into account in Monte Carlo simulations have been proposed. Propositions of X-ray diffraction imaging systems suitable for clinical application have been made as well.

Detection of illicit materials such as explosives and drugs has been considered by numerous scientists. Different types of explosives, drugs and liquids all have characteristic distinguishable XRD pattern, which is why XRD seems to be a promising technology for security scanning at the airport. Most studies propose EDXRD for this purpose because of its higher acquisition speed and more compact acquisition systems. Different system geometries and analyzing methods have been presented. A leading actor in this application field is Morpho Detection. They dispose of two commercialized EDXRD systems for security check at the airport. The main limiting factor of this technique is still the long required scan time and blurring of the spectra by the acquisition system.

In the following, this work will present methods to characterize and optimize an XRD imaging systems for XRD-based mammography and detection of illicit materials in hand baggage. Methods to restore material proper diffraction signatures without system blurring will be introduced and tested on different scattering data. The aim is to obtain as much material characteristic information as possible from X-ray diffraction data. System characterization tools and restoring techniques will be used to propose a completely dimensioned XRD system for virtual breast biopsy and reflections concerning an alternative system for luggage control. Especially, the combination of EDXRD and ADXRD will be considered.

Chapter II

Characterization of an X-ray diffraction system

In the previous chapter the physical principles of X-ray diffraction and the different measuring techniques have been presented. The state of the art of the two applications of XRD, on which this work is focused on, was presented as well. To resume, the purpose of this work is to optimize XRD technique for the two selected applications: breast tissue characterization and illicit materials detection. This will make sure that as little information as possible is lost during acquisition, and hence, allow to retrieve a maximum of material proper information from these measurements.
To be able to optimize a system it is first of all necessary to model the different system components and the measured X-ray diffraction pattern. The first part of this chapter will present the modelization and the impact on system performance of the different system components as well as a complete model of an acquired XRD spectrum.

Optimization also requires a mean to quantify system performance, the so-called figures of merit (FOM). A FOM is a numerical quantity based on one or more characteristics of a system, device or method that represents a measure of efficiency or effectiveness. It allows to compare the performance of different possible technical solutions. The second part of this chapter presents the different figures of merit that were employed during this work to optimize, qualify and compare different systems. System optimization was mainly realized by detective quantum efficiency (DQE) calculations, which are object and task independent, whereas comparison of different systems was performed by the use of more object specific and task oriented figures of merit such as contrast to noise ratio (CNR) and receiver operating characteristic (ROC) curves.

First, concept of DQE calculations is introduced and their realization in EDXRD imaging is explained. The second section of this chapter is dedicated to criteria, which quantify the ability of a chosen imaging system to separate two materials. The more basic one is the CNR, which is described first. Afterwards the concept of ROC curves, which is a more complex and complete criteria, is introduced. During this work an analytical approach of ROC curve calculations has been developed and will be presented as well. Finally, the performance of a basic EDXRD system in terms of sensitivity and resolution is given using DQE calculations. The impact of the scattering angle and of different geometrical parameters are discussed in the corresponding section.

II.1 Modeling of an energy dispersive X-ray diffraction system

II.1.1 Incident X-ray source

X-rays can be obtained in different ways, e.g. synchrotron and X-ray tube. In this PhD work, only spectra from X-ray tubes have been considered, as this seems the most suitable way for the considered applications. An X-ray tube is a vacuum tube that produces X-rays and contains two principal elements (Fig. II.1):

1. Cathode: provides a source of electrons.
2. Anode: acts as the target for electrons and releases X-rays.

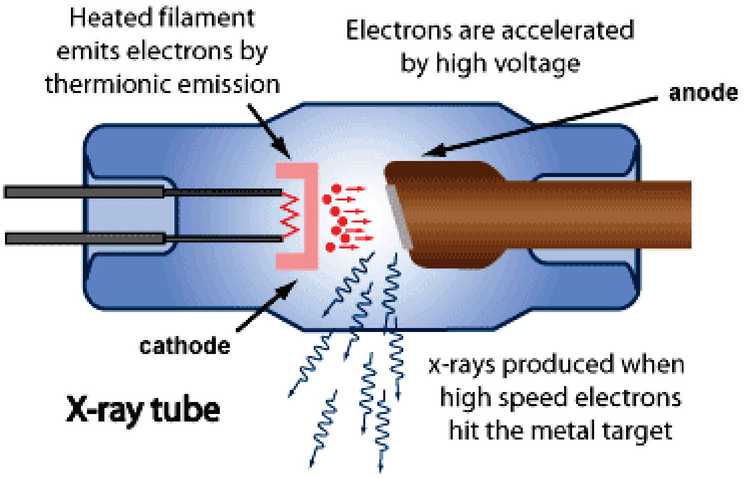

Figure II.1: Schematic view of an X-ray tube [ARPANSA, 2013].

The cathode, most often a tungsten filament, is heated electrically and emits electrons. These electrons are accelerated using a high voltage power source (in the range of 20 to 220 kV), which is connected across cathode and anode. They hit the anode material, usually tungsten, molybdenum or copper, and interact electrons, ions and nuclei within the anode material. This interaction leads to a sudden deceleration of incident electrons and causes emission of X-rays known as ”braking radiation” (bremsstrahlung). If the electrons have sufficiently high energy, they can expel an electron out of the atomic shell of the bombarded atom. The vacancy is filled by electrons from higher state. Their loss of energy is transformed in X-ray radiation with precise energies, determined by electron energy levels. This kind of X-rays is called ”characteristic X-rays” and is specific to the anode material. Thus, the incident X-ray spectrum is the combination of a smooth, continuous part due to bremsstrahlung and spikes, characteristic for the X-ray source. Figure II.2 shows a typical incident X-ray spectrum, which has been filtered to suppress photons with lower energy than 20 keV. The shape of the incident spectrum will affect the system sensitivity at different energies.

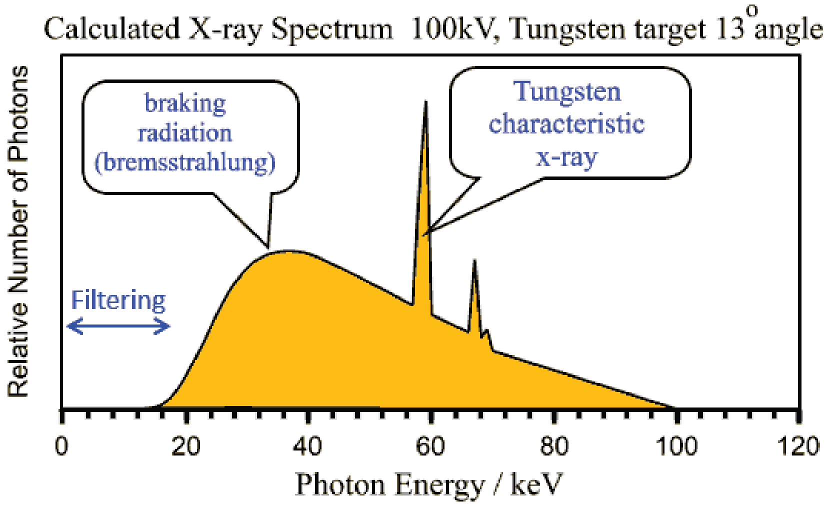

Figure II.2: Example of a typical X-ray spectrum provided by an X-ray tube [ARPANSA, 2013].

II.1.2 Collimation

A collimator is a device that is used to narrow a beam of particles or waves. It allows to reduce the spatial cross section of the beam or to select a specific beam direction.
An X-ray diffraction system comprises two types of collimation: the primary and the secondary collimation (see Fig. I.19, Fig. I.20).

The primary collimation is situated between the X-ray source and the sample. It allows to narrow the beam cross section and to chose the object area to be inspected.
The secondary collimation is located between the sample and the detector. It allows to select the scattering angle(s) Θ, at which diffraction spectra are measured. However, angular aperture of the collimation system is not infinitely small, and therefore detected photons can have a scattering angle within $\theta \in [\Theta - \Delta\theta, \Theta + \Delta\theta]$, where Θ corresponds to the nominal diffraction angle at which the detector has been placed (Fig. II.3). This angular incertainty could be described as a distribution $\Delta\theta$ around the nominal diffraction angle Θ. Angular resolution $\Delta\Theta$ induces a direct effect on energy resolution.

The relationship between energy and scattering angle is given by Bragg's law:

$$E = \frac{hc}{2d \sin\frac{\theta}{2}} \tag{II.1.1}$$

The derivative of E with respect to θ is given by:

$$\frac{dE}{d\theta} = \frac{hc}{2d} \cdot \frac{-1}{\left(\sin\frac{\theta}{2}\right)^2} \cdot \cos\frac{\theta}{2} \cdot \frac{1}{2} \tag{II.1.2}$$

By replacing $hc/2d\sin\frac{\theta}{2}$ with E, energy resolution ΔE_c due to angular resolution can be expressed as:

$$\Delta E_c = \frac{E}{2} \cot\left(\frac{\Theta}{2}\right) \Delta\Theta \tag{II.1.3}$$

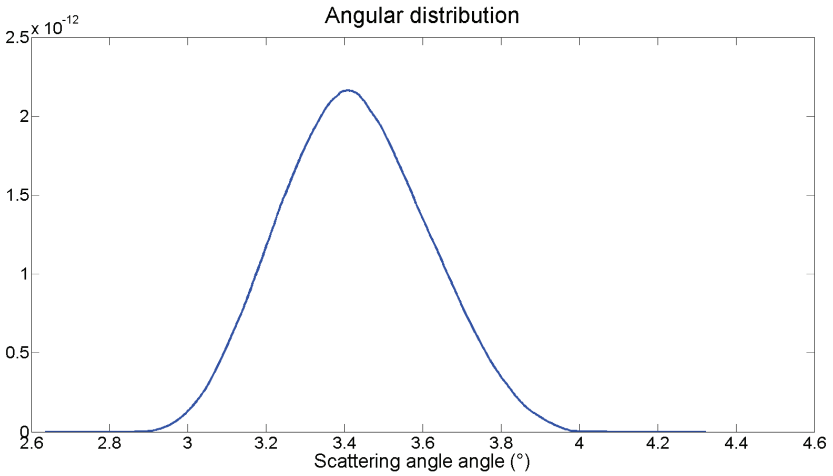

Figure II.3: Example of angular distribution for a nominal scattering angle $\Theta = 3.4°$.

By narrowing the aperture to approach Dirac delta function, it is possible to obtain a very high angular resolution. However, the sensitivity will be very low because of the small photon number that can cross the system. Conversely, sensitivity can be improved by increasing the aperture but resolution will be deteriorated. Furthermore, the inspected volume is defined by the primary and secondary collimation. Therefore, spatial resolution in the sample depends also on the employed collimation system. It is necessary to optimize the collimation to achieve an acceptable compromise between resolution and sensitivity.

II.1.3 Interaction inside the sample

As explained in chapter I, X-rays interact with the matter they penetrate. This interaction can take place without loss of energy (coherent scattering leading to diffraction signal) and with energy deposit (photoelectric effect, Compton effect). In this subsection, we discuss absorption and coherent scattering.

II.1.3.1 Absorption

Interaction with loss of energy results in an attenuation of incident X-rays. Their attenuation follows an exponential law (Fig. II.4):

$$N(L, E) = N_0(E) \cdot \exp\left(-\mu(E) L\right) \ , \tag{II.1.4}$$

where $N(L, E)$ corresponds to the remaining number of photons at energy E after crossing thickness L of matter. $N_0(E)$ is the initial number of photons at energy E, and $\mu(E)$ (in cm^{-1}) the energy depending linear absorption coefficient. The absorption coefficient depends furthermore on the atomic number Z of the matter, and density ρ.

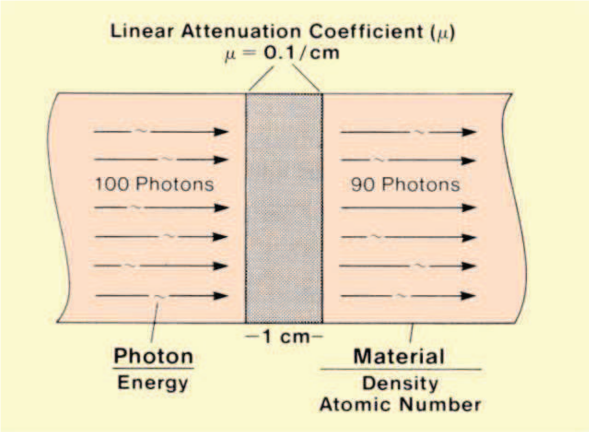

Figure II.4: Attenuation of a photon beam after crossing matter [Sprawls, 1995].

Sample attenuation reduces the detected signal, and since it is energy dependent, it also changes the energy distribution of detected photons (e.g. beam hardening).

II.1.3.2 Coherent scattering

Coherent scattering or diffraction signature F of a given material is modeled by:

$$F(\chi) = \frac{d\sigma_{Th}}{d\Omega} f^2(\chi)\, s(\chi)\, n \tag{II.1.5}$$

where n is the number of molecules per unit of volume. F corresponds to Bragg peaks in the case of crystalline matter I.1.2.2 and to a continuous function in the case of amorphous matter I.1.2.3.

II.1.4 Detector

Detector energy resolution is limited. In fact, the detected amplitudes for an monochromatic incident photon beam will not be the same for each photon. In consequence, the detected spectrum will not correspond to a Dirac delta function at the given energy but to a peak with the maximum at this energy and a certain width around this energy. Thus, an incident photon of the energy E_i is detected with an energy E_{det} estimated from the detected amplitude A. Some of the factors degrading energy resolution such as interaction depth (Sec. I.1.3.4) and charge sharing, effect due to splitting of electronical signal induction on two electrodes by one electron, can be corrected by adapted electronics. However, detector energy resolution will still not be perfect because of electronic noise. Electronic noise is due to the quantified nature of charge and follows a Gaussian distribution. Figure II.5 shows an example of a typical detector response matrix. It can be seen that most photons are detected around E_i but that there is a certain probability to be detected at significantly lower energy. This probability is due to charge sharing and fluorescence peaks of detector. In fact, incident X-rays may excite detector material, which emits radiation at a material characteristic energy to return in an unexcited state. An example of acquired source spectra of ^{241}Am and ^{57}Co can be seen in figure II.6. The principal peaks correspond to radioactive emission peak of the two sources (59.5 keV for ^{241}Am and 122 keV for ^{57}Co) widened by the detector's energy resolution. The small peak of ^{57}Co at about 136 keV also corresponds to an emission peak. The flat low energy tail that can be seen, especially in the case of ^{57}Co, is due to charge sharing. The small peaks around 23 and 27 keV are caused by detector material (Cd and Te) fluorescence.

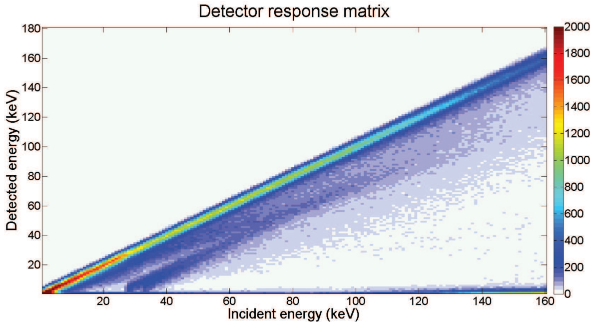

Figure II.5: Example of a detector matrix response. It can be seen that a photon with a given incident energy E_i has a certain probability to be detected at an energy E_d different from its real energy. This is mostly due to interaction depth and charge sharing.

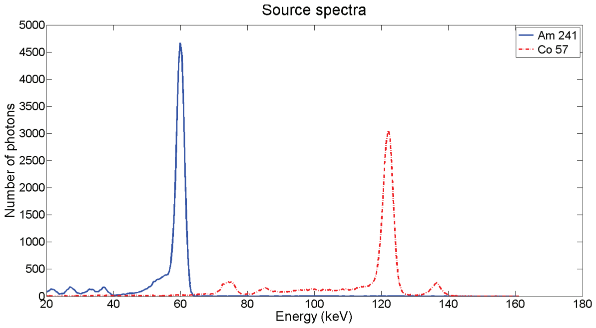

Figure II.6: Example of acquired source spectra: in blue ^{241}Am (main peak at 59.5 keV) and in red ^{57}Co (main peaks at 122 keV and 136 keV). The principal peaks correspond to radioactive emission of the two sources, whereas the small peaks around 23 and 27 keV correspond to the fluorescence peaks of the detector material. The flat low energy tail is due to charge sharing.

II.1.5 Photon noise

Photon noise, also known as Poisson noise, is a basic form of uncertainty, which is associated with the measurement of light. It is inherent to the quantized nature of light. Individually detected photons can be treated as independent events that follow a random temporal distribution, i.e. in two different time intervals of the same length the number of detected photons is variable. Consequently, photon counting is a typical Poisson process [Hasinoff, 2014], and the number N of detected photons is described by the discrete probability distribution as:

$$P(N=k)=\frac{e^{-\lambda}\lambda^k}{k!} \tag{II.1.6}$$

where λ is the mean number of expected photons. Poisson distributions have the property

that their variance is equal to their expectation $E[N] = Var[N] = \lambda$ and their standard deviation grows with the square root of the signal. The signal to noise ratio (SNR) is defined by $SNR = \sqrt{\lambda}$. Thus, photon noise is signal dependent and relatively weaker at higher signal levels, whereas its absolute value grows with growing signal.
For a very high number of detected photons, photon noise is often modeled as a Gaussian distribution, which can be justified by the central limit theorem. However, diffraction imaging is a photon-limited process and the number of detected photons in one energy channel is very small, e.g. 700 photons detected on 130 energy channels, i.e. about 5 photons per channel.

II.1.6 Global model

To finish this section, a global model of an EDXRD system will be presented. Following the previous section, a measured X-ray diffraction spectrum m transformed by the different elements of an EDXRD system, can be described by the following expression where the global system response $\mathcal{R}$ is factorized in separate terms:

$$\begin{aligned} m(A) &= \sum_{\chi} \mathcal{R}(A,\chi) \cdot F(\chi) \\ &= \sum_{E_i,\chi} R_d(A,E_i)\, S_{inc}(E_i)\, At(E_i)\, R_c(\chi/E_i) \cdot F(\chi) \end{aligned} \tag{II.1.7}$$

where

R_d is the spectroscopic detector response, which regroups the probability distributions for all incident photon energies.

S_{inc} the incident X-ray spectrum

At the attenuation within the sample. By using the small angle approximation $\cos\Theta \approx 1$, it is given by $\exp\left(-\mu\left(E\right)L\right)$ (see equation II.1.4). It can be determined by the use of a spectroscopic detector in transmission direction ($\Theta = 0°$).

R_c accounts for the angular distribution as well as for variation of the inspected volume with the angular aperture. The angular collimation distribution $R_c(\theta)$ is rewritten as $R_c(\chi/E_i)$ using the aforementioned relationship (Eq. I.1.19) between E_i, χ and θ.

F the diffraction pattern, specific for the sample material. If the inspected object is a crystal, F will correspond to Bragg peaks (each corresponding to a specific inter-planar spacing). In the case of an amorphous sample, F corresponds to the molecular form factor.

Figure II.7 shows the difference between the theoretical salt spectrum $F(\chi)$ (a), with crystalline structure, and a simulated salt spectrum $m(A)$ (b) using the presented model. The theoretical signature corresponds to Dirac peaks and depends on momentum transfer, whereas the simulated measure has broadened peaks and is represented as a function of measured energy.

The choice of the scattering angle combined with the energy range of the incident X-ray spectrum determines the range of observable χ during a measurement. In some cases,

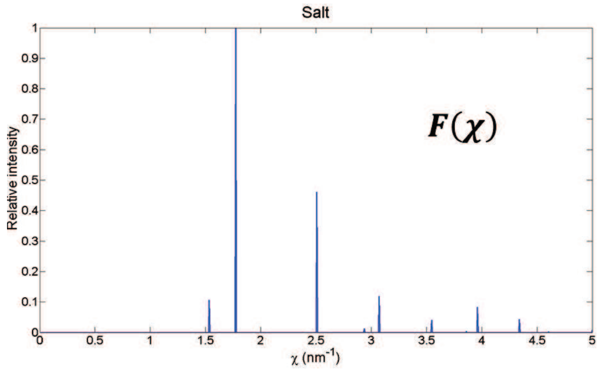

(a) *Theoretical salt diffraction spectrum*

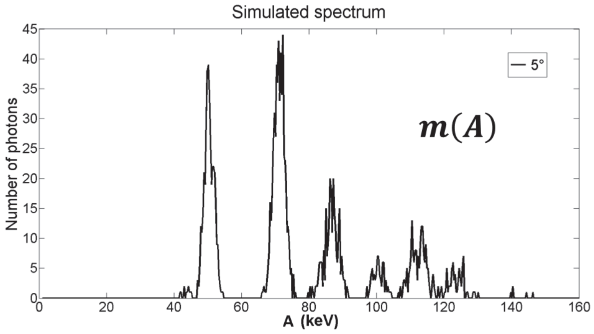

(b) *Simulated salt spectrum at 5°*

Figure II.7: Comparison between theoretical salt spectrum and simulated ”experimental” spectrum.

accessing a larger range of χ by combining EDXRD acquisitions at different diffraction angles in one reconstructed spectrum might also be of interest. Therefore, the mono-angle model has been extended to the multi-angle case.

The multi-angle direct model is very similar to the mono-angle one. It is supposed that diffraction spectra at different nominal diffraction angles Θ are acquired. Then the model can be written as:

$$m(A,\Theta) = \sum_{\chi} \mathcal{R}(A,\Theta,\chi) \cdot F(\chi) \tag{II.1.8}$$

where $m(A,\Theta)$ is the measured spectrum at the scattering angle Θ and $\mathcal{R}(A,\Theta,\chi)$ the system response at Θ.

The combination of EDXRD and ADXRD has been suggested by [O’Flynn *et al.*, 2013] to enhance the resolution.

Figure II.8 shows an example of a multi-angle salt spectrum between 2 and 5°. Several curved lines can be observed, which correspond to salt diffraction peaks. It can be seen that their detection energy depends on the scattering angle. This is due to the fact that these peaks correspond to a fixed value of momentum transfer, which depends on scattering angle and photon energy. Intensity maxima, which can be observed around 59 keV and 67 keV correspond to the effect of the source’s characteristic rays.

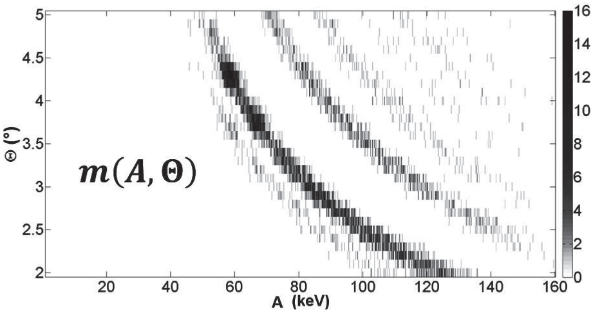

Figure II.8: Example of a multi-angle salt spectrum for scattering angles from 2 to 5° (0.1° step). Curved lines correspond to the different salt peaks and the intensity maxima around 59 keV and 67 keV are due to the source's characteristic rays. The line at 5° is the same as in figure II.7.b

II.2 Figures of merit to characterize an X-ray diffraction system

Knowing the model of an XRD system (Eq. II.1.7), different figures of merit (FOM) can be calculated to assess system performance. The following section will describe the FOMs employed in this work. First of all, the detective quantum efficiency (DQE), which is independent from inspected sample, is presented. Afterwards two sample depending FOMs (contrast to noise ratio (CNR) and receiver operating characteristic (ROC) curves) are introduced.

II.2.1 Detective quantum efficiency

In the literature, numerous figures of merit exist to describe performances of an imaging system ([Barrett, 1990], [Barrett *et al.*, 1995], [Pineda and Barrett, 2004]), e.g. sensitivity, resolution and signal to noise ratio (SNR). Detective quantum efficiency combines the effect of the signal (related to image contrast) and noise performance of an imaging system.
The concept was proposed by Albert Rose ([Rose, 1946], [Rose, 1953]) to describe performance of optical detectors such as television cameras or photoconductive devices and was known as useful quantum efficiency or equivalent quantum efficiency. Later, the DQE was introduced to medical imaging community by Shaw [Shaw, 1963]. In the first time, it was used to describe performance of X-ray film-screen systems. With the introduction of digital radiographic imaging systems, DQE was continued to be regarded as a convenient and reasonably accurate metric of system performance. Nowadays, it is widely used in X-ray transmission and sometimes in γ-Imaging. As it is not yet used for X-ray diffraction imaging, our proposition can be considered as new for the community.

II.2.1.1 Definition

The DQE describes how efficiently a system translates incident photons into a useful signal (relative to noise) within an image. It is generally expressed in the spatial frequency domain ν_x. Thus, the DQE of an ideal imaging system is equal to one at all spatial frequencies, meaning that all the incident radiation is absorbed and converted into image information. In practice, an imaging system loses efficiency on the high spatial frequencies, corresponding to object details. The DQE for a real linear system and under the assumption of wide-sense stationary processes can be written as [Cunningham and Shaw, 1999]:

$$DQE\left(\nu_x\right) = \frac{NEQ\left(\nu_x\right)}{\bar{q}} = \bar{q} \cdot \frac{S^2 \cdot \mathrm{MTF}^2\left(\nu_x\right)}{NPS_{out}\left(\nu_x\right)} \tag{II.2.1}$$

where NEQ corresponds to the noise equivalent quanta, $\bar{q}$ is the average number of input quanta, S the scaling factor (sensitivity) linking $\bar{q}$ to the average number of output quanta $\bar{d}$, MTF the modulus of the modulation transfer function and NPS_{out} the output noise power spectrum or Wiener spectrum. In fact, the DQE is the ratio of the worth of an image to its cost in terms of numbers of Poisson-distributed input quanta.

In the special case for which photon noise is the only significant source of noise, the DQE can be interpreted as the squared-SNR transfer relationship described as:

$$DQE\left(\nu_x\right) = \frac{SNR^2_{out}\left(\bar{q}, \nu_x\right)}{SNR^2_{in}\left(\bar{q}, \nu_x\right)} \tag{II.2.2}$$

where the input signal to noise ratio $SNR^2_{in}\left(\bar{q}, \nu_x\right) = \bar{q}^2/NPS_{in}\left(\nu_x\right) = \bar{q}$ (for Poisson noise) and the output signal to noise ratio $SNR^2_{out}\left(\bar{q}, \nu_x\right) = \bar{q}^2 \cdot \; S^2 \cdot \mathrm{MTF}^2\left(\nu_x\right)/NPS_{out}\left(\nu_x\right)$.

As $\bar{d} = S \cdot \bar{q}$ and $\bar{d}^2/NPS_{out}\left(\nu_x\right) = \bar{d}$ (for photon noise) equation (II.2.1) can be simplified to:

$$DQE\left(\nu_x\right) = S \cdot \mathrm{MTF}^2\left(\nu_x\right) \tag{II.2.3}$$

II.2.1.2 Detective quantum efficiency in EDXRD imaging

In EDXRD, the main noise source is photon noise but there are some differences compared to conventional X-ray imaging systems that have to be taken into account in DQE calculations. The object to be imaged is in fact, in the k-space space, i.e. in the momentum transfer space (expressed in nm^{-1}), which indicates sample characteristic spatial frequencies. Thus, the frequency variable to be used is not ν_x but ν_χ. Furthermore, the processes are not stationary and the system performance depends on momentum transfer. Thus, Wigner-Ville distribution has to be used instead of Fourier transform, and DQE in EDXRD imaging is expressed as a function of momentum transfer χ and its associated frequency ν_χ [Marticke *et al.*, 2014] as:

$$DQE\left(\chi, \nu_\chi\right) = \sum_{\{A, \theta / \frac{A}{hc} \sin\frac{\theta}{2} = \chi\}} S(A, \Theta) \cdot \mathrm{MTF}^2(A, \Theta, \nu_\chi) \tag{II.2.4}$$

The system sensitivity S is given by $S\left(E_d, \Theta\right) = \sum_\chi \mathcal{R}(E_d, \Theta, \chi)$ and the MTF by the normalized Fourier transform of the response function (in χ-direction): $\mathrm{MTF}\left(E_d, \Theta, \nu_\chi\right) = \mathscr{F}\left\{\mathcal{R}(E_d, \Theta, \chi)/S\left(E_d, \Theta\right)\right\}$.

In fact, the DQE corresponds to the Wigner-Ville distribution of the the system response matrix normalized by system sensitivity. Thus, if the system response is known, it will be possible to directly calculate the DQE for the given EDXRD system. Here, the DQE expression corresponds to a matrix depending on χ and ν_χ due to the non-stationarity of EDXRD process. For easier interpretation and comparison of different acquisition systems, two different types of graphs can be extracted from DQE matrix: The system sensitivity and the global resolution. As can be seen from equation II.2.4, the DQE at zero frequency corresponds to the sensitivity (MTF is equal to one at zero frequency). Each line of the DQE corresponds to the system resolution of a given couple E_d and Θ, which defines one value of χ. By summing over all χ values, the global system resolution curve can be obtained.

To estimate the global system resolution from this curve, the DQE has to be normalized by the global system sensitivity (DQE at zero frequency). The resolution R can be approximated by:

$$\frac{1}{R} \approx \int_{-\infty}^{+\infty} \frac{DQE\,(\nu)}{DQE\,(0)} d\nu = 2 \int_{0}^{+\infty} \mathrm{MTF}^2(\nu) d\nu \tag{II.2.5}$$

Note that this definition is consistent with the full width at half maximum (FWHM) for a rectangular gate-shaped point spread function[1].

II.2.1.2.1 Link with Fisher information

Now we will present these definitions in a more signal processing context, where Fisher information is widely used. The Fisher information is a measure of the amount of information that an observable random variable X carries about a parameter of interest p. It considers local variations (low noise level or very close objects) as the DQE but on the contrary to the DQE, it depends on the object.

Fisher information is defined as the second moment of the score function, i.e. the log-likelihood function L. If there are N parameters so that p is a N×1 vector $p = [p_1, p_2, \ldots, p_N]^T$, then the Fisher information takes the form of an $N \times N$ matrix, the Fisher information matrix, with elements:

$$(I\,(p))_{ij} = E\left[\frac{\partial L\,(X,p)}{\partial p_i} \cdot \frac{\partial L\,(X,p)}{\partial p_j}\right] = -E\left[\frac{\partial^2 L\,(X,p)}{\partial p_i \partial p_j}\right] \tag{II.2.6}$$

In EDXRD imaging, the log-likelihood function $L\,(\mathbf{F})$ is expressed by:

$$L\,(\mathbf{F}) = \sum_{j=1}^{M} \left(- \sum_{k=1}^{N} R_{jk} F_k + m_j \log \left(\sum_{k=1}^{N} R_{jk} F_k \right) - \log\,(m_j!) \right) \tag{II.2.7}$$

The first derivative of the log-likelihood function is given by:

$$\frac{\partial L\,(\mathbf{F})}{\partial F_k} = \sum_{j=1}^{M} \left(-R_{jk} + m_j \frac{R_{jk}}{\sum_{k'=1}^{N} R_{jk'} F_{k'}} \right) \tag{II.2.8}$$

---

[1] N.B.: For a gate-shaped PSF of width R, we have $\int \mathrm{sinc}^2\, \phi \nu R dr = \frac{1}{R}$

Hence, the second derivative is equal to:

$$\frac{\partial^2 L(\mathbf{F})}{\partial F_k \partial F_l} = \sum_{j=1}^{M} m_j \frac{R_{jk} R_{jl}}{\left(\sum_{k'=1}^{N} R_{jk'} F_{k'}\right)^2} \tag{II.2.9}$$

Therefore, the kl component of Fisher information matrix (I) can be expressed as:

$$I_{kl} = E\left[\sum_{j=1}^{M} m_j \frac{R_{jk} R_{jl}}{\left(\sum_{k'=N}^{M} R_{jk'} F_{k'}\right)^2}\right] = \sum_{j=1}^{M} E\left[m_j\right] \frac{R_{jk} R_{jl}}{\left(\sum_{k'=N}^{M} R_{jk'} F_{k'}\right)^2} \tag{II.2.10}$$

Since m_j follows a Poisson law of parameter $\sum_{k'=1}^{N} R_{jk'} F_{k'}$, $E\left[m_j\right] = \sum_{k'=1}^{N} R_{jk'} F_{k'}$, the previous expression simplifies to:

$$I_{kl} = \sum_{j=1}^{M} \frac{R_{jk} R_{jl}}{\sum_{k'=1}^{N} R_{jk'} F_{k'}} \tag{II.2.11}$$

If we consider a homogeneous object $\mathbf{F} = \mathbf{1}$ (i.e. an object where each χ value is equiprobable) then equation II.2.11 becomes:

$$I_{kl} = \sum_{j=1}^{M} \frac{R_{jk} R_{jl}}{\sum_{k'=1}^{N} R_{jk'}} \tag{II.2.12}$$

This hypothesis allowed us to suppress the object dependence of Fisher information. However, it corresponds to a matrix depending on χ_k and χ_l. Using a change of variables to $\bar{\chi}_{kl} = \frac{\chi_k + \chi_l}{2}$ and $\Delta\chi_{kl} = \chi_k - \chi_l$, equation II.2.12 can be written as:

$$I_{kl} = \sum_{j=1}^{M} \frac{\Gamma_{R_j}\left(\bar{\chi}_{kl}, \Delta\chi_{kl}\right)}{S_j\left(\bar{\chi}_{kl}\right)} \tag{II.2.13}$$

where $\Gamma_{\Re} = R\left(\bar{\chi}_{kl} - \frac{\Delta\chi_{kl}}{2}\right) \cdot R\left(\bar{\chi}_{kl} + \frac{\Delta\chi_{kl}}{2}\right)$ is the local autocorrelation of the system response matrix and S the system sensitivity. In fact, this change of variables is part of the calculation of the Wigner-Ville distribution.

The MTF is given by:

$$MTF_j\left(\bar{\chi}_{kl}, \nu_{\chi_{kl}}\right) = \left(\mathscr{F}_{\Delta\chi_{kl}}\left\{\frac{\Gamma_{R_j}\left(\bar{\chi}_{kl}, \Delta\chi_{kl}\right)}{S_j\left(\bar{\chi}_{kl}\right)}\right\}\right)^{\frac{1}{2}} \tag{II.2.14}$$

The Fourier transform of Fisher information can therefore be expressed as:

$$\mathscr{I}\left(\bar{\chi}_{kl}, \nu_{\chi_{kl}}\right) = \sum_{j=1}^{M} S_j\left(\bar{\chi}_{kl}\right) \cdot MTF_j^2\left(\bar{\chi}_{kl}, \nu_{\chi_{kl}}\right) \tag{II.2.15}$$

We can see that this expression corresponds to the DQE (Eq. II.2.4). Thus, to conclude, the DQE corresponds to the information captured by the system under the hypothesis of a homogeneous object and low noise level, i.e. a small variation inside a uniform background.

II.2.2 Material separability

In the previous part of this chapter, a figure of merit, detective quantum efficiency, which can be used to assess the system performance in terms of resolution and sensitivity independently from considered materials/objects, was presented. However, it does not indicate whether a chosen diffraction imaging system is able to separate or not two materials. Therefore, the following section will introduce two figures of merit that allow to quantify separation power of an imaging system: the contrast to noise ratio and the receiver operation characteristic. On the contrary to the previously introduced figures of merit (DQE, Fisher information) and the contrast to noise ratio, the receiver operation characteristic is not limited to local variations (low noise and very close objects)

II.2.2.1 Contrast to noise ratio

The first one, called contrast to noise ratio (CNR) can be expressed as:

$$CNR = \left\| \frac{\Delta M}{\sigma} \right\| \tag{II.2.16}$$

where $\Delta M = M_A - M_B$ corresponds to the average difference of the signal intensities for signal producing structures A and B and σ corresponds to the standard deviation of the noise.
Diffraction measurements follow a Poisson law with parameter λ. As already mentioned in section II.1.5, photon noise is often modeled by a Gaussian distribution with parameters $\mu = \sigma = \lambda$. This approximation will be used in order to calculate CNR for diffraction systems. Let A and B be two materials having different diffraction signatures, which are normalized to one in order to correspond to probability distributions. Their mean signal intensities are M_A and M_B (Fig. II.9). Under the previous hypothesis, their standard deviations are equal to $\sqrt{M_A}$ and $\sqrt{M_B}$. It is assumed that the different measuring channels are independent and the standard deviation of $M_A - M_B$ on channel i is given by:

$$\sigma_i^2 = M_{A,i} + M_{B,i} \tag{II.2.17}$$

The squared CNR can therefore be written as:

$$CNR^2 = \sum_i \frac{(M_{A,i} - M_{B,i})^2}{(M_{A,i} + M_{B,i})} \tag{II.2.18}$$

The squared CNR (Eq. II.2.18) can be written in matrix format:

$$CNR^2 = \Delta^t g \Delta \tag{II.2.19}$$

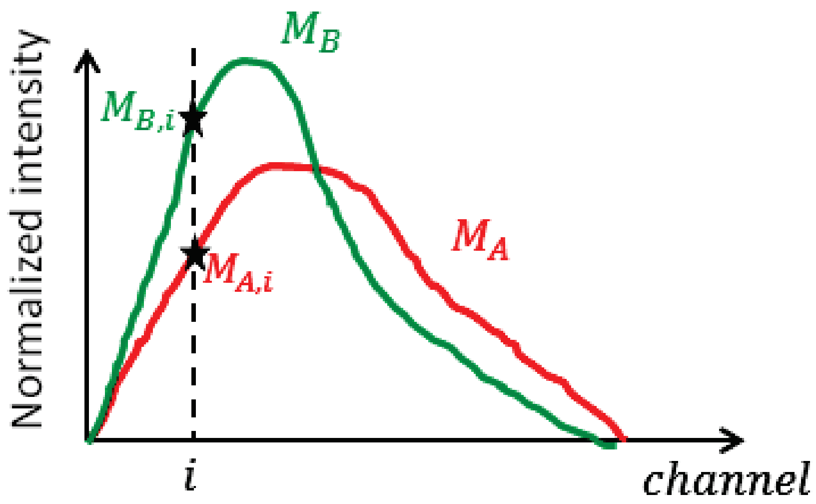

Figure II.9: Two different normalized diffraction signatures with mean values M_A and M_B. Each measuring channel i follows a Poisson law of parameter $M_{A,i}$ or $M_{B,i}$.

where $\Delta = M_A - M_B$ and g a diagonal matrix with entries $\frac{1}{M_{A,i}+M_B} = \frac{1}{\sigma_i^2}$. As A and B are considered to be Gaussian, g corresponds to the Fisher information matrix of the mean of A and B. In fact, the so defined CNR corresponds to the Mahalanobis distance of the two distributions A and B per photon (since the diffraction signatures are normalized to one) with Fisher information metric $\frac{1}{\sigma_A^2+\sigma_B^2}$. In this special case of a diagonal matrix, this distance is equal to the normalized Euclidean distance. Figure II.10 illustrates this in the case of one and two channels.

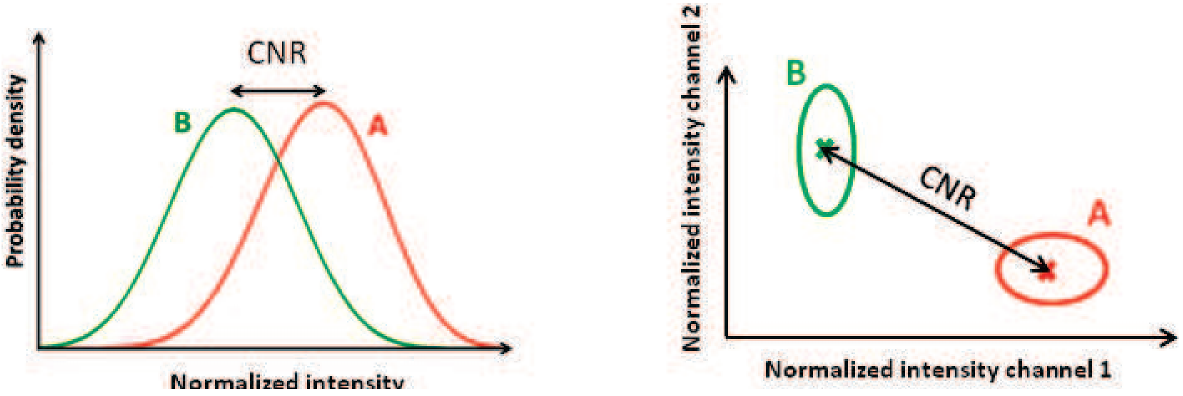

Figure II.10: Illustration of the interpretation of CNR in the case of one or two measuring channels.

Hence, the inverse of the CNR corresponds to the number of photons, which is necessary to have a distance of one standard deviation between the two distributions. In the present work the CNR will primarily be used to calculate the required photon number to obtain a given separation (most often 3σ) between two diffraction patterns. It is also possible to establish a link between CNR and DQE which is explained in appendix A.

II.2.2.2 Receiver operating characteristic (ROC) curves

We show that the CNR measures the separation power of an imaging system. But it does not indicate whether the detection rate will be high and whether there will be or not false positives. However, these two criteria are important in most applications. In medical applications, it is important to detect a pathology in most cases because this can be a question of life or death. It is also important to not find a pathology, if there is none (false positive) because this false alarm might lead to unnecessary surgery and induces a great deal of unnecessary mental stress to patients. In security applications detection rate must be high otherwise this might cost human lives and the number of false positives has to be as low as possible because each false alarm costs a great deal of time and money. The ROC curves allow to take into account these two criteria.

The receiver operating characteristic was developed during Second World War in order to assess the precision of discrimination between signal and noise during radar and sonar detection. Since, ROC analysis has been applied in many domains and especially, in the development of diagnostic tests in medicine [Lusted, 1971], [van Erkel and Pattynama, 1998].

II.2.2.2.1 Definition and objectives

If a binary decision has to be taken between a material A and B, there are four different outcomes.

1. A is chosen and the sample is A: true positive (TP)
2. A is chosen but the sample is B: false positive (FP) or false alarm
3. B is chosen and the sample is B: true negative (TN)
4. B is chosen and the sample is A, false negative (FN)

The sensitivity of a binary decision test is given by:

$$\text{Sensitivity} = \frac{TP}{TP + FN} \tag{II.2.20}$$

It corresponds to the detection rate.

The specificity measures the capacity of a test to identify non critical cases. It corresponds to the false positive rate and is expressed as:

$$\text{Specificity} = \frac{TN}{TN + FP} \tag{II.2.21}$$

The decision whether the sample is part of the class A or B is taken by defining a decision variable λ known as observer. If the value of λ is above a certain threshold λ_t, the test is positive otherwise the outcome is negative. Figure II.11 shows an illustration of this principle.

A receiver operating characteristic (ROC) curve is a representation of the true positive rate as a function of the false negative rate. It is obtained by moving the threshold (Fig. II.12).

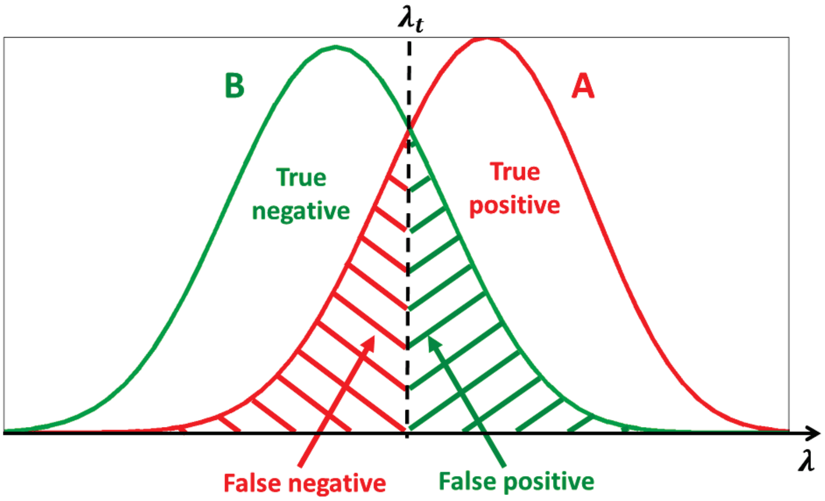

Figure II.11: The threshold position λ_t fixes the number of true and false negative and the number of true and false positive.

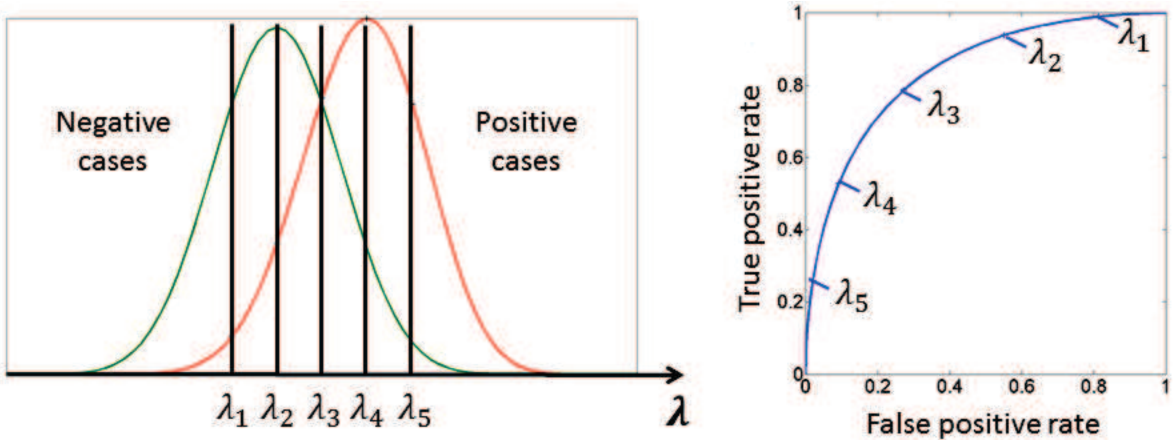

Figure II.12: By varying the threshold λ_t the proportion of false positive and true positive changes. A ROC curve corresponds to the graphical representation of the true positive rate as a function of false negative rate. Each point of the curve corresponds to a different threshold.

Figure II.13 shows examples of ROC curves of different systems/tests between an ideal system (case **A**) and a perfect random process (case **D**).

A corresponds to the ROC curve of an ideal test because it has a detection of 100% with zero false positives. **D** is called the chance line. A test that corresponds to this ROC curve is useless since it is not better than coin flipping.

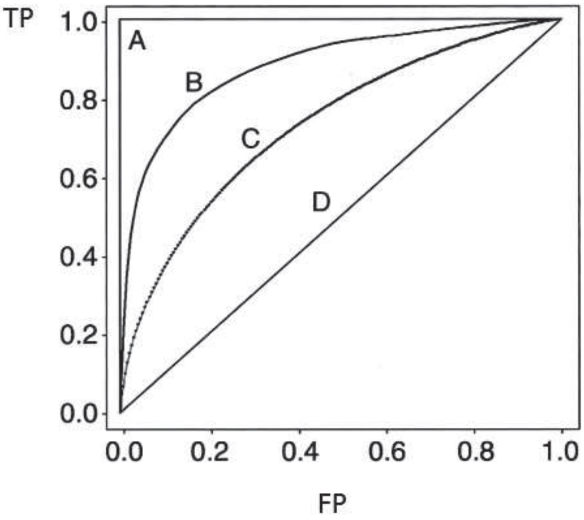

Figure II.13: Examples of different ROC curves. **A** corresponds to an ideal system and **D** to the chance line, i.e. test not better than coin flipping. The higher area under these curves the better is the corresponding system performance.

A criterion to compare two different systems using ROC curves is the area under the curve (AUC). Since both the TP rate and the FP rate range from 0 to 1, the area under the ROC curve also ranges from 0 to 1 (ideal test). The ROC curves shown in figure II.13 are symmetric about the negative diagonal. In this case, higher values of AUC indicate higher TP fractions for any given FP fraction. Systems with higher AUC are then preferable. Though, ROC curves need not to be symmetric as can be seen in figure II.14. The AUC of the two ROC curves in figure II.14 are the same. Here, AUC is not adequate to chose between two systems.

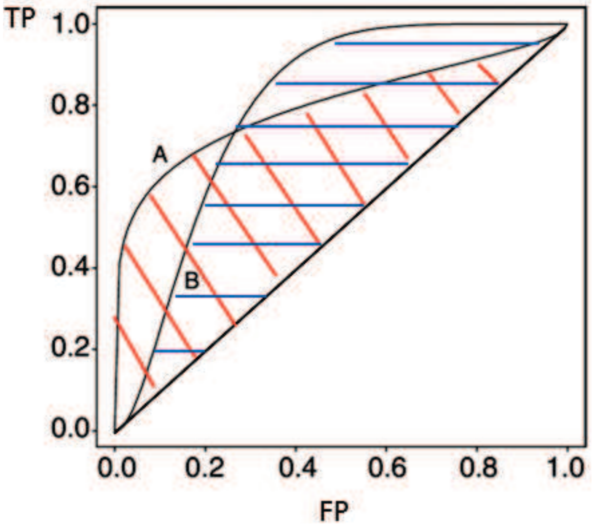

Figure II.14: Example of ROC curves, which are not symmetric to the negative diagonal and which have the same area under the curve (red shaded is equal to blue shaded area). Here, the area criterion is not adequate to choose between these two systems.

If Gaussian approximation is made as in the previous section, a link between the CNR and AUC can be established. Under the assumption that the test statistic is normally distributed under both hypothesis, the AUC can be derived from the signal to noise ratio (SNR) through the following relationship [Barrett and Myers, 2004]:

$$AUC = \frac{1}{2} + \frac{1}{2}\,\mathrm{erf}\left(\frac{SNR_\lambda}{2}\right) \tag{II.2.22}$$

where

$$(SNR_\lambda)^2 = \sum_i \frac{(M_{A,i} - M_{B,i})^2}{\frac{1}{2}\sigma^2_{A,i} + \frac{1}{2}\sigma^2_{B,i}} = 2 \cdot \sum_i \frac{(M_{A,i} - M_{B,i})^2}{\sigma^2_{A,i} + \sigma^2_{B,i}} \tag{II.2.23}$$

By comparison with equation II.2.18 we recognize that $(SNR_\lambda)^2 = 2 \cdot CNR^2$. It has to be noticed that M_A and M_B are not normalized as in section II.2.2.1.

II.2.2.2.2 Analytical receiver operating characteristic curves calculations

As explained previously, in order to obtain a ROC curve, it is necessary to decide whether a set of observations **x** belongs to the probability distribution of class A or B (We will only say **A** and **B** to designate the probability distributions of the two classes A and B.). The means by which the decision is taken, or the strategy, is called observer or decision-maker. During longtime, the observer in medical imaging to detect a lesion for instance, were exclusively physicians. Nowadays, a great deal of research efforts are done to develop computer algorithms to carry out this task and to help the physicians to formulate a diagnosis (computer aided diagnosis). The most known observer is the so called ideal observer or Bayesian observer. It uses all statistical information (in the image as well as any prior information) available concerning the task in order to maximize task performance [Barrett and Myers, 2004] as measured by Bayesian risk or some other related measure of performance. Unlike human observers, the ideal observer does not add any noise or uncertainty in the decision-making process. Decision errors are only due to variability in object classes and noise in the measurement system. Hence, the performance of the Bayesian observer provides an upper bound on the performance of any observer. To be able to use it, it is necessary to know the distributions **A** and **B**, which might not always be the case.

The ideal observer is defined as the ratio between the likelihood function of the measured data x under each of the hypothesis, H_A and H_B:

$$\Lambda(\mathbf{x}) = \frac{P(\mathbf{x}|\mathbf{A})}{P(\mathbf{x}|\mathbf{B})} \tag{II.2.24}$$

Λ corresponds to the test statistic (its outcome depends on the form of the probability distributions **A** and **B**) and is known as likelihood ratio. In many cases it is more convenient to consider the logarithm of the likelihood ratio:

$$\lambda\left(\mathbf{x}\right)=\ln\left(\Lambda\left(\mathbf{x}\right)\right)=\ln\left[\frac{P\left(\mathbf{x}|\mathbf{A}\right)}{P\left(\mathbf{x}|\mathbf{B}\right)}\right]\underset{\mathbf{B}}{\overset{\mathbf{A}}{\gtrless}}\lambda_t \tag{II.2.25}$$

The decision, which hypothesis to choose, is taken by comparing the likelihood ratio to a threshold λ_t. If $\lambda\left(x\right)$ is higher than λ_t, x belongs to **A** otherwise to **B**. Each point of a ROC curve corresponds to a different threshold.
Typically, ROC curves are obtained by realizing an appropriate number of observations of both distributions **A** and **B** and for each observation the probability of detecting **A** or **B** is calculated for different thresholds. This technique requires a high number of observations of laws $P\left(\mathbf{x}|\mathbf{A}\right)$ and $P\left(\mathbf{x}|\mathbf{B}\right)$ to draw a complete ROC curve.

In this section an alternative analytical method [Marticke *et al.*, 2015b] based on information geometry [Amari, 2010] is suggested.
Let A and B be the two materials to be separated using EDXRD (as for CNR calculations). Both of them follow a Poisson law with parameters A_i and B_i for channel i ($1 \leq i \leq k$, $k \in \mathbb{N}$). We will use the Fisher metric, which is natural in probability density space. Thus, their likelihood ratio is expressed as:

$$\Lambda\left(\mathbf{x}\right)=\prod_{i=1}^{k}\frac{A_i^{x_i}}{B_i^{x_i}}\,e^{-A_i+B_i} \tag{II.2.26}$$

The logarithm of Λ is given by:

$$\lambda\left(\mathbf{x}\right)=\sum_{i=1}^{k}x_i\ln\left(A_i/B_i\right)-A_i+B_i \tag{II.2.27}$$

with $\sum_{i=1}^{k}A_i=\sum_{i=1}^{k}B_i$. Differentiation of λ with respect to x_i leads to:

$$\nabla_{x_i}\lambda\left(\mathbf{x}\right)=\nabla_{x_i}\ln\left(\Lambda\left(x\right)\right)=\ln\left(A_i/B_i\right) \tag{II.2.28}$$

Hence, λ is linear in $\mathbf{x}$ and the gradient is constant in the whole space. It can be established that in the present case (independent Poisson laws for each channel), if $x_i = A_i$, then:

$$\lambda\left(\mathbf{x}=\mathbf{A}\right)=D_{KL}\left(\mathbf{A}||\mathbf{B}\right) \tag{II.2.29}$$

It is known that in the space of probability distributions the general expression of a geodesic Γ between two distributions P and Q is given by [Dabak, 1992], [Dabak and Johnson, 2002]

$$\Gamma : t\in[0;1]\mapsto P^tQ^{1-t} \tag{II.2.30}$$

In the case of Poisson laws **B** and **A** equation II.2.30 becomes:

$$\Gamma : t\in[0;1]\mapsto \mathbf{A}^t\mathbf{B}^{1-t} \tag{II.2.31}$$

This corresponds to the geodesic relying **B** (starting point) to **A**. The points $\mathbf{x}_0$ being part of this curve correspond to the shortest path between **A** and **B**. In order to study the separability of **A** and **B** over the whole space, we will decompose **A** and **B** in their components on the geodesic and their components in the orthogonal direction. Information geometry in the sense of Fisher information theory will be used to approximate the probability distribution of a measuring point **x** of the space knowing **A** (and in the same way for **B**) by:

$$P\left(\mathbf{x}|\mathbf{A}\right) \propto e^{-D(\mathbf{x}||\mathbf{A})} \tag{II.2.32}$$

where $D\left(\mathbf{x}||\mathbf{A}\right) = \sum_{i=1}^{k} x_i \ln\left(\frac{x_i}{A_i}\right) - x_i + A_i$ (generalized Kullback-Leibler divergence) and with **x** having the same support as **A**. This approximation corresponds to a generalization of Sanov's theorem [Csiszár and Shields, 2004]. In Sanov's theorem, the probability is bounded as follows:

$$\binom{n+|N|-1}{|N|-1}^{-1} e^{-nD(\mathbf{x}||\mathbf{A})} \leq P\left(\mathbf{x}|\mathbf{A}\right) \leq \binom{n+|N|-1}{|N|-1} e^{-nD(\mathbf{x}||\mathbf{A})} \tag{II.2.33}$$

where n is the number of photons and $|N|$ the number of possible outcomes (number of channels).

Use of the Kullback-Leibler (KL) divergence implies several advantages. On the one hand, it allows to respect the variation of information quantity if the number of channels varies. On the other hand, it permits an easy decomposition of the probability distribution on the geodesic and the iso-Λ (lines with the same value of Λ in the space of probability distributions) by the following relation:

$$\begin{aligned} &D\left(\mathbf{x}||\mathbf{x}_0\left(t\right)\right) + D\left(\mathbf{x}_0\left(t\right)||\mathbf{A}\right) = \\ &D\left(\mathbf{x}||\mathbf{A}\right) + \sum_{i=1}^{k}\left[x_i - x_{0,i}\left(t\right)\right] \cdot \ln\left(A_i/x_{0,i}\left(t\right)\right) \end{aligned} \tag{II.2.34}$$

It is considered that **x** is part of a curve, which is parallel to the geodesic relying **B** and **A** and parameterized in the same way. $\mathbf{x}_0$ is the orthogonal projection (in the sense of Fisher information metric) of **x** on the geodesic between **B** and **A**, i.e. it is the probability distribution, which is the closest to the observation **x** and part of the geodesic Γ. Hence, the points **x** and $\mathbf{x}_0$ are part of the same iso-Λ. A replacement of $x_{0,i}\left(t\right)$ by $A_i^t B_i^{1-t}$ (Eq. II.2.31) transforms equation II.2.34 to:

$$\begin{aligned} &D\left(\mathbf{x}||\mathbf{x}_0\left(t\right)\right) + D\left(\mathbf{x}_0\left(t\right)||\mathbf{A}\right) = \\ &D\left(\mathbf{x}||\mathbf{A}\right) + \sum_{i=1}^{k}\left[x_i - x_{0,i}\left(t\right)\right]\left(1-t\right) \cdot \ln\left(A_i/B_i\right) \end{aligned} \tag{II.2.35}$$

The gradient $\ln\left(A_i/B_i\right)$ is orthogonal to the iso-Λ of which **x** and $\mathbf{x}_0$ are part of. This implies that the last part of equation II.2.35 is equal to zero. Thus, equation II.2.35 corresponds to the generalized Pythagorean theorem [Csiszár and Shields, 2004]. Consequently, each probability density can be decomposed in two terms:

$$P(\mathbf{x}|\mathbf{A}) \propto e^{-D(\mathbf{x}||\mathbf{x}_0(t))} e^{-D(\mathbf{x}_0(t)||\mathbf{A})} \tag{II.2.36}$$

The second term is constant for each $\mathbf{x}$ being part of the same iso-Λ (same t value) and the first term depends on the divergence value between the geodesic and the considered parallel curve to which $\mathbf{x}$ belongs to. Figure II.15 gives an illustration of these considerations for the case of two channels. Summation over all existing parallel curves in the space leads to calculation of the probability for one iso-Λ. It can be concluded that it is sufficient to only consider the points $\mathbf{x}_0$ of the geodesic between $\mathbf{B}$ and $\mathbf{A}$ by normalizing as follows:

$$P(\mathbf{x}(t)|\mathbf{A}) = \frac{e^{-D(\mathbf{x}_0(t)||\mathbf{A})}}{\int_t e^{-D(\mathbf{x}_0(t)||\mathbf{A})} dt} \tag{II.2.37}$$

Hence, to draw a ROC curve the distributions $P(\mathbf{x}(t)|\mathbf{A})$ and $P(\mathbf{x}(t)|\mathbf{B})$ and the corresponding λ, have to be only calculated for the points $\mathbf{x}_0(t)$ being part of the geodesic. Afterwards, the probability of true positives and false positives have to be calculated for different thresholds λ_t. These probabilities correspond to the hatched areas on figure II.11. In practice, this means to calculate the cumulative distribution functions as a function of λ and to plot $F_{\mathbf{B}}$ as a function of $F_{\mathbf{A}}$.
To conclude, the steps to analytically obtain a ROC curve can be summarized as follows:

1. Normalize the molecular form factors of the two materials A and B to be separated in order to obtain the detection probability for each detection channel
2. Multiply distributions by the number of photons to be considered (photon noise)
3. Calculate observations $\mathbf{x}_0$ belonging to the geodesic line: $x_{0,i}(t) = A_i^t B_i^{1-t}$
4. Calculate the probability density functions $P(\mathbf{x}(t)|\mathbf{A})$ and $P(\mathbf{x}(t)|\mathbf{B})$ using the suggested approximation
5. Determine the cumulative distribution functions $F_{\mathbf{A}}(\mathbf{x}(t))$ and $F_{\mathbf{B}}(\mathbf{x}(t))$
6. Plot $F_{\mathbf{B}}(\mathbf{x}(t))$ as a function of $F_{\mathbf{A}}(\mathbf{x}(t))$, which corresponds to the ROC curve

It has to be noticed that Sanov's approximation is valid only in the case of a high number of photons. However, this approximation is less rough than Gaussian approximation, and for considered distributions of amorphous diffraction pattern, e.g. carcinoma and fibroglandular tissue (Fig. II.16), the convergence is fast enough. It was verified by generating a set of observations (at 5, 20 and 100 photons) of $\mathbf{A}$ (carcinoma) and $\mathbf{B}$ (fibroglandular tissue using Monte-Carlo (MC) method. Afterwards, using these simulations, the probability distributions of $\mathbf{A}$ and $\mathbf{B}$ have been calculated as a function of λ. Figure II.17.a shows these probability distributions as a function of λ at 20 photons superimposed to the distributions obtained using the proposed approximation. These distributions are already very close. Comparison of ROC curves at 5, 20 and 100 photons confirms that the difference becomes negligible at 20 photons (Fig. II.17.b).

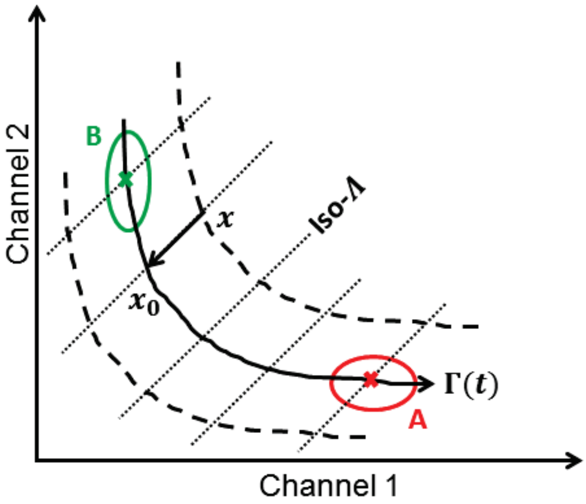

Figure II.15: Example of a geodesic and the corresponding iso-Λ for two channels.

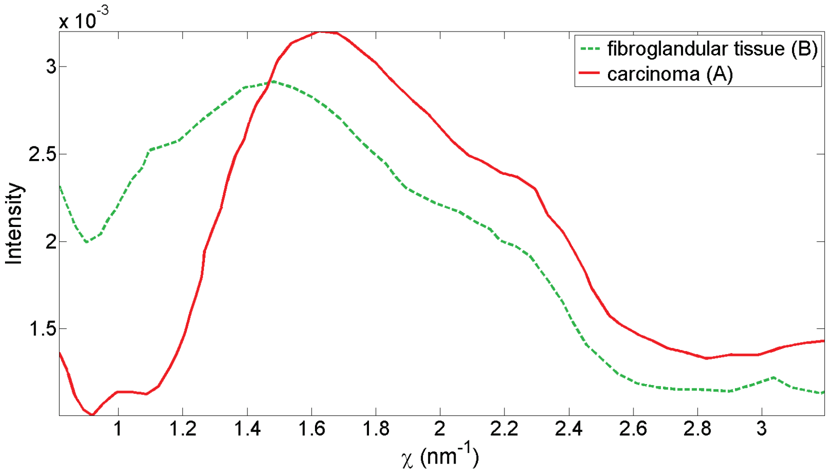

Figure II.16: Diffraction pattern of fibroglandular tissue and carcinoma [Kidane *et al.*, 1999].

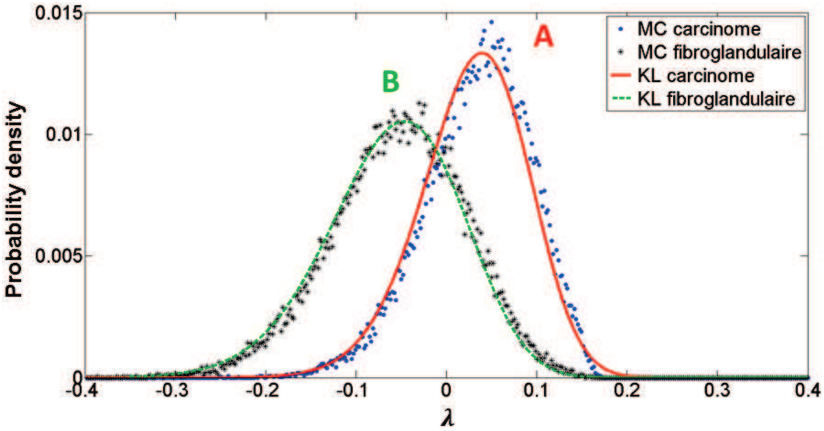

(a) *Probability distributions as a function of λ.*

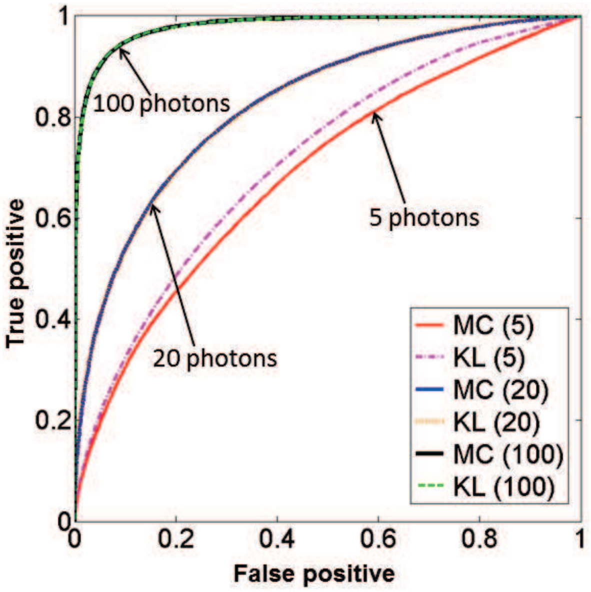

(b) *ROC curves.*

Figure II.17: Comparaison of the results obtained using Monte-Carlo (MC) simulation and with the proposed method (KL).

II.3 Performance of a basic EDXRD system

One of the most important factors to optimize in EDXRD is the scattering angle. Combined with the incident X-ray spectrum, it will decide of the range of momentum transfer that will be accessible during measurement. Another important element to optimize is the collimation system, which plays an important role in resolution and sensitivity of the whole imaging system.

II.3.1 Impact of the scattering angle: mono- versus multi-angle system

In order to understand the importance of the choice of the scattering angle for a given EDXRD system, the DQE results for different scattering angles and for a multi-angle system are compared in this section. The reference system that was chosen corresponds to one of the experimental configurations that can be used in our laboratory. Figure II.18 shows a schematic representation of the system with dimension indications. The primary collimation corresponds to a double slit as well as the secondary collimation and the incident spectrum is a normal X-ray tube (with tungsten anode) spectrum with 160 kV voltage (Fig. II.19). The simulated detector pixel is based on MINIGAMI probe, a spectroscopic CZT detector with a pixel size of $2.5 \times 2.5\ mm^2$. However, the detector response was taken to be Gaussian with σ distributed linearly between 1 and 2 as a function of energy (0-160 keV) in order to have $\sigma \approx 1.4$ keV at 59 keV[2]. This means that energy resolution follows a Gaussian law and that the low energy tail and the fluorescence peaks explained in section II.1.4 are neglected. However, the width of the Gaussian detector response, which was calibrated experimentally, already gives a good indication of the impact of the spectral resolution of the detector on measured diffraction pattern. Figure II.20 shows the detector response that was used.

For absorption 4 cm of salt were considered.

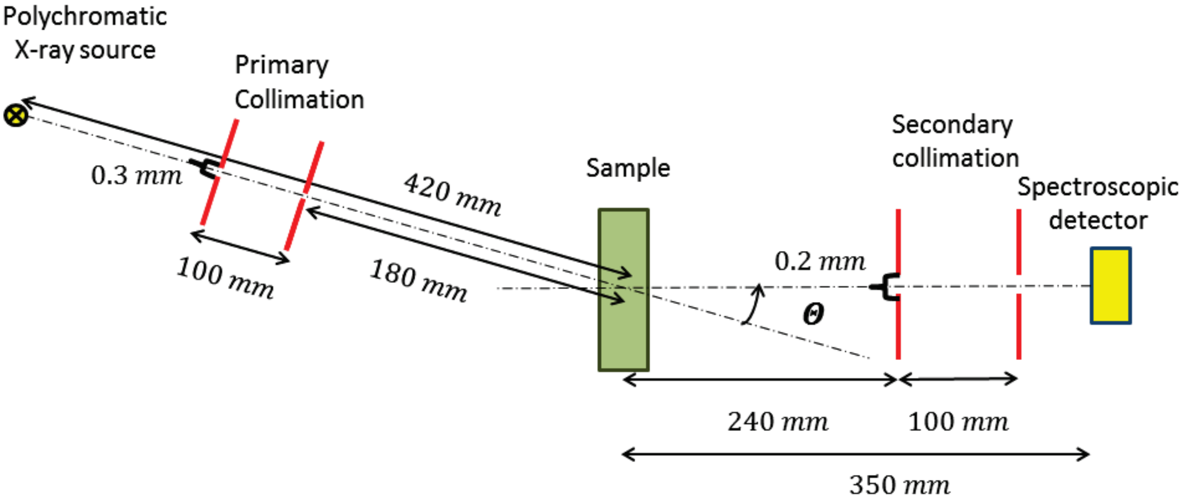

Figure II.18: Schematic representation of the system configuration, that was used to mono- and multi-angle DQE and also to simulate mono- and multi-angle spectra.

---

[2] Resolution measured for MINIGAMI probe using a radioactive source.

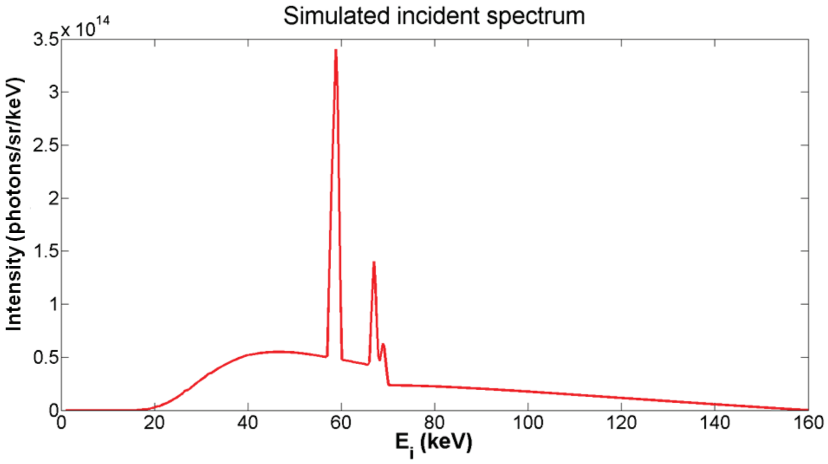

Figure II.19: Simulated incident tungsten spectrum (10 s at 11.25 mA) used for simulations of EDXRD spectra.

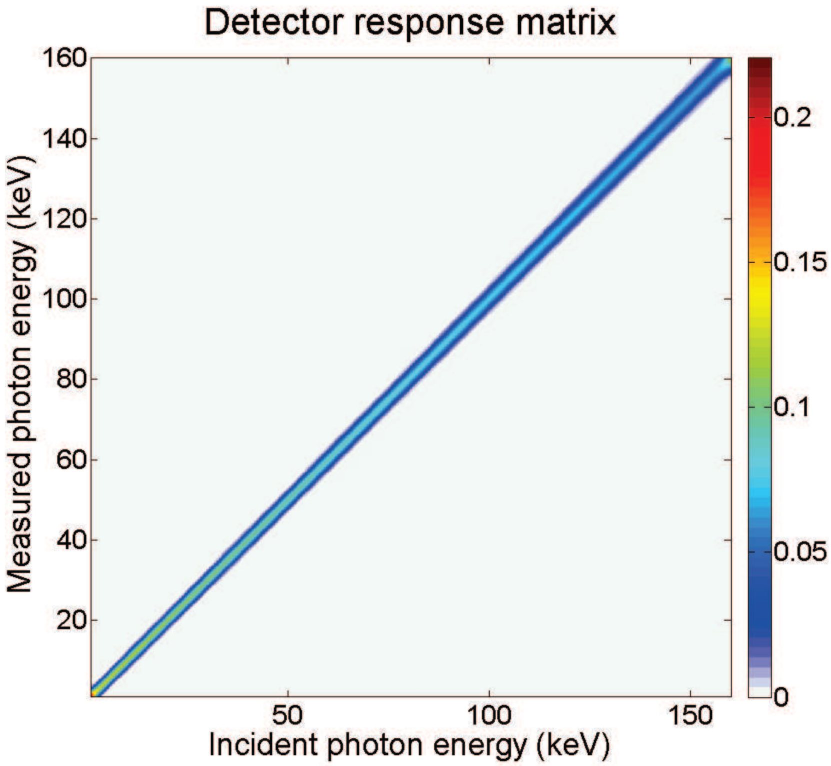

Figure II.20: Gaussian detector response that was employed for spectrum simulation, DQE calculations and reconstruction. σ-values are distributed linearly between 1 and 2 as a function of energy (0-160 keV) in order to have $\sigma \approx 1.4$ keV at 59 keV.

DQE (Eq. II.2.4) was calculated for two different mono-angle systems at 2° and 5° and for a multi-angle system with angles between 2° and 5° with step of 0.1°, i.e. 31 different scattering angles. The sensitivity curves (DQE at zero frequency) of the different systems can be seen in figure II.21.

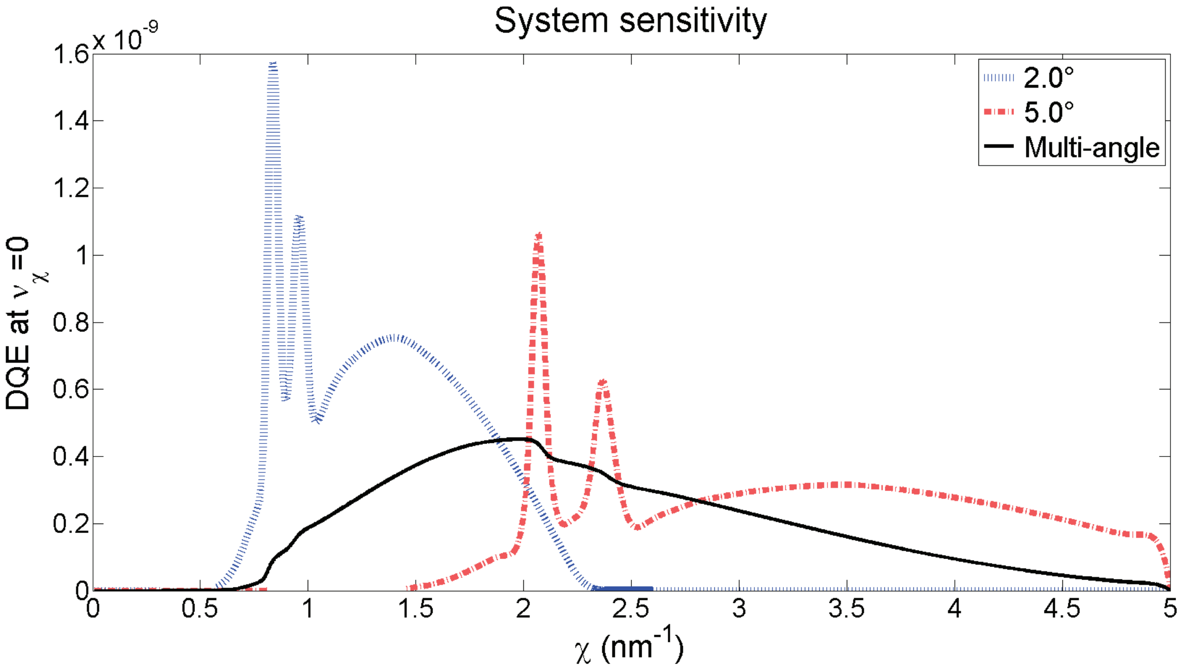

Figure II.21: Comparison of sensitivity curves from different systems: 2° (blue dotted line), 5° (red dashed line) and multi-angle (black solid line). The multi-angle system covers a larger range of χ, and the adverse effect (hypersensitivity) due to the characteristic rays of the incident source is smoothed. The resolution of the multi-angle system corresponds to an average resolution of the corresponding mono-angle systems.

The multi-angle configuration allows to cover a χ-range from 0.7 to 5.0 nm^{-1}, which is significantly larger than for the mono-angle systems, which cover 0.5 to 2.4 nm^{-1} at 2° and 1.5 to 5 nm^{-1} at 5°. It has to be noticed that the mono-angle system at 5° covers in reality χ-values higher than 5 nm^{-1} (up to around 5.8 nm^{-1}), which have been cut as values of interest were limited to 5 nm^{-1}. Furthermore, it can be seen that the adverse effect of the characteristic rays of the incident X-ray source is remarkably smoothed in the multi-angle case. The characteristic rays can be clearly observed in the mono-angle case and they lead to a kind of hypersensitivity at some momentum transfer values, e.g. 2.1 and 2.4 nm^{-1} for the 5° system. Hence, multi-angle acquisitions ensure a sensitivity that is almost uniform over the range of χ they cover.

Figure II.22 shows the global resolution curves of the three systems, which are compared. It can be noticed that the multi-angle configuration permits to maintain a similar resolution curve compared to mono-angle systems. Comparison of the resolution curves of the two mono-angle systems shows that the choice of the scattering angle slightly impacts the system resolution. Increasing scattering angle decreases intensity of the global resolution curve. Furthermore, it can be seen that the total sensitivity (summed DQE at zero frequency) is almost the same for each system even though it is slightly underestimated at 5° because of the missing part of χ-values over 5 nm^{-1}.

Only the distribution of this sensitivity is significantly different for the three systems. This explains, why the system at 5° has a lower resolution curve. It has almost the same global system sensitivity as the 2° system but the range of covered χ-values is significantly larger.

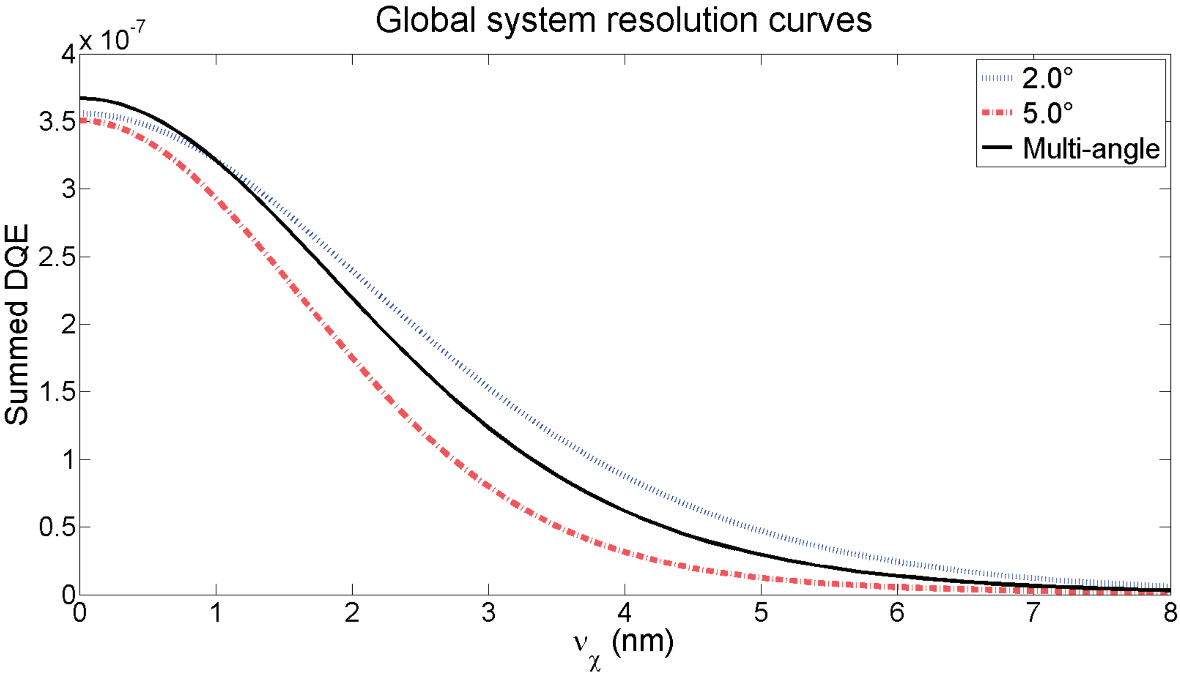

Figure II.22: Comparison of the global resolution curves from different systems: 2° (blue dotted line), 5° (red dashed line) and multi-angle (black solid line). The resolution curve of the multi-angle system corresponds to an average resolution of the corresponding mono-angle systems.

These simple examples show that the choice of the scattering angle is essential for the momentum transfer values that can be measured. Momentum transfer is linked to the characteristic distances in the sample, i.e. spacing between atomic planes in crystalline samples and the mean distance between molecules in amorphous samples. Thus, the choice of scattering angle impacts the range of sample characteristic distances, that can be observed. Moreover, the combination of EDXRD and ADXRD allows to enlarge the accessible χ-range and to smooth the sensitivity profile.

II.3.2 Geometrical parameters

As shown in the previous section, the scattering angle influences mainly the distribution of the total sensitivity over the different χ values but does not remarkably changes its integral value. The system resolution will only be slightly influenced by diffraction angle choice, if the detector surface, e.g. a pixel, is the same for each angle. The following study will assess the influence of other system parameters on resolution and sensitivity. Figure II.23 shows the different parameters that will be varied (in red): the distance between detector and sample center D_D, the distance between the X-ray source and the sample center, and the angular apertures of the primary and secondary collimation $\Delta\theta_S$ and $\Delta\theta_D$.

The system is similar to the previous system presented in figure II.18 with still one detector pixel (same spectral response as in the previous section) and double slit collimation but with varying distances and angular apertures. The scattering angle was fixed at 3° and the absorption corresponds to a 6 cm thick salt sample. In order to reduce the number of varying parameters, the first studies were realized on a symmetric system, i.e. $D_S = D_D = D$, $\Delta\theta_S = \Delta\theta_D = \Delta\theta$ and the pixel size is about 1 mm, which is the same as the source's foyer size.

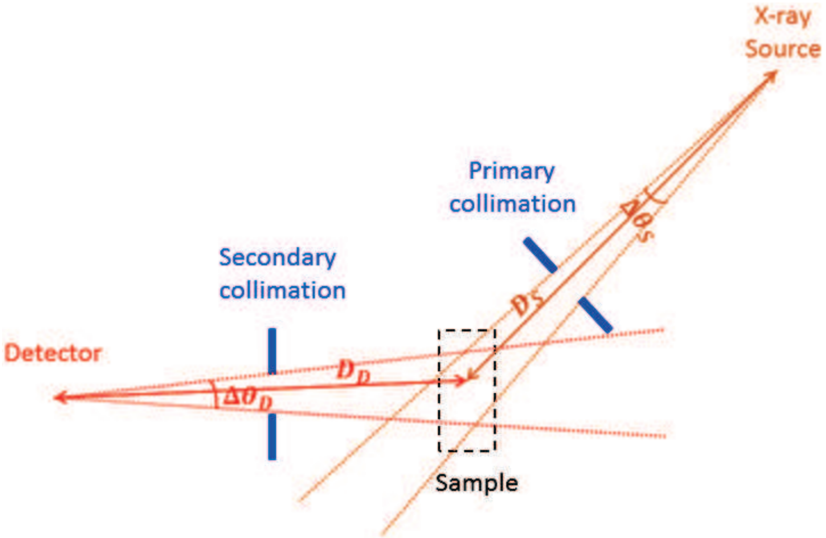

Figure II.23: Schematic view of the different geometrical parameters, which were varied to assess their impact on system performance.

Figure II.24 shows the sensitivity profiles for the described symmetric system for D between 200 mm and 450 mm. The angular aperture was fixed at 0.2°.

The accessible χ-range is the same for each D, which could be expected since it is determined by the combination of θ and the energy range of the incident X-ray spectrum. Sensitivity[3] diminishes with increasing distance D. This can be explained by the fact that the solid angle of the detector and the source decrease with increasing D. Indeed, the detector surface and the source surface remain the same for each different D.

The inspected volume[4] increases with increasing distance D (Fig. II.25). However, the sample is almost entirely covered by the inspected volume at the smallest distance. Hence, sensitivity is not increased by higher inspected volume.

---

[3] The characteristic rays are less pronounced as in the previous section. This is due to the higher sample thickness, 6 cm instead of 4 cm, which increases the sample absorption.

[4] Intersection of the cone "seen" by the source and the cone inspected by the detector.

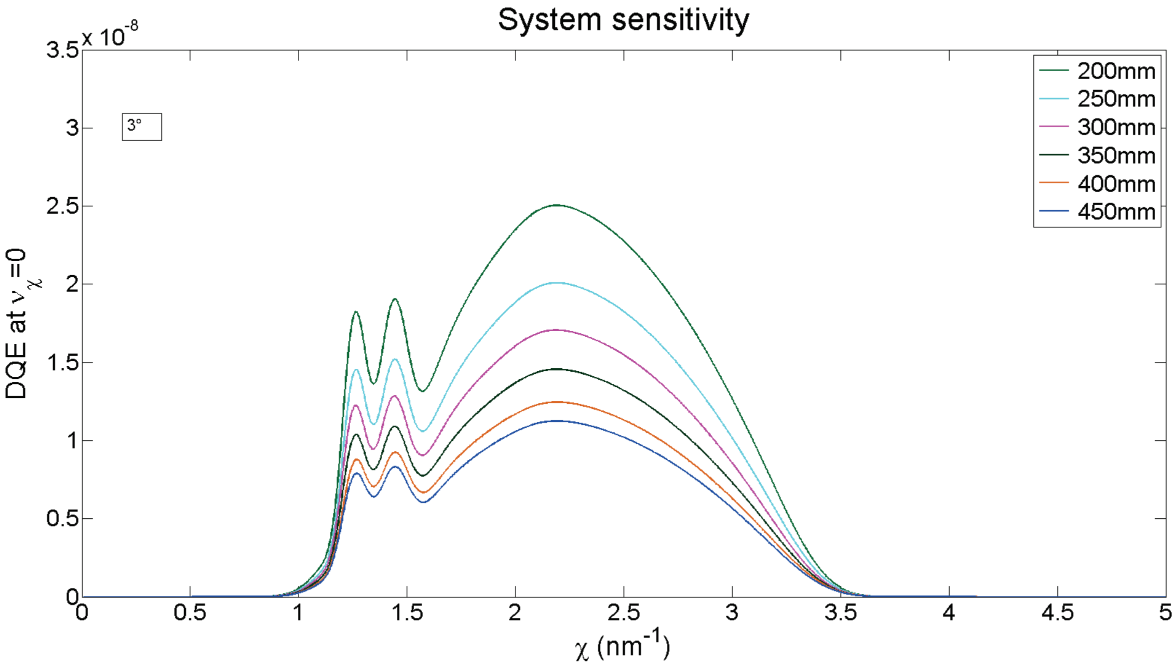

Figure II.24: Sensitivity curves obtained for different distances D (and constant angular aperture $\Delta = 0.2°$) of a symmetric system. The closer the detector and the source are the the more the sensitivity increases.

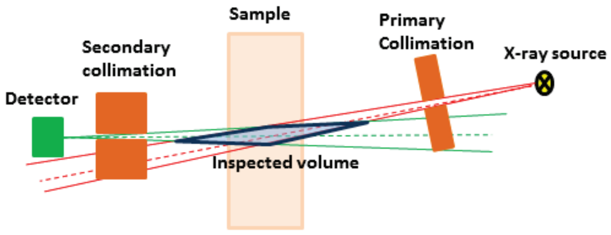

(a) *Small distance D.*

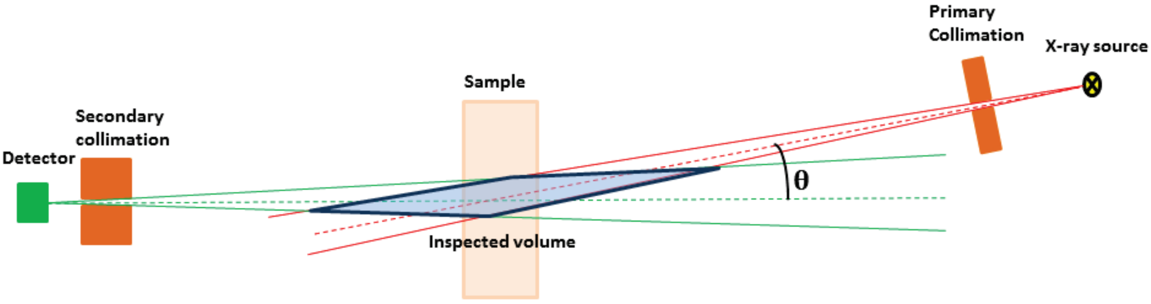

(b) *High distance D.*

Figure II.25: Illustration of the inspected volume, which corresponds to the intersection of the cone "seen" by the source and the cone inspected by the detector. It increases with increasing distance D.

The global system resolution curves for different D can be observed in figure II.26. The decreasing system sensitivity with increasing D induces a decrease of intensity of global resolution curves. Hence, the system will resolve less details with increasing distance D.

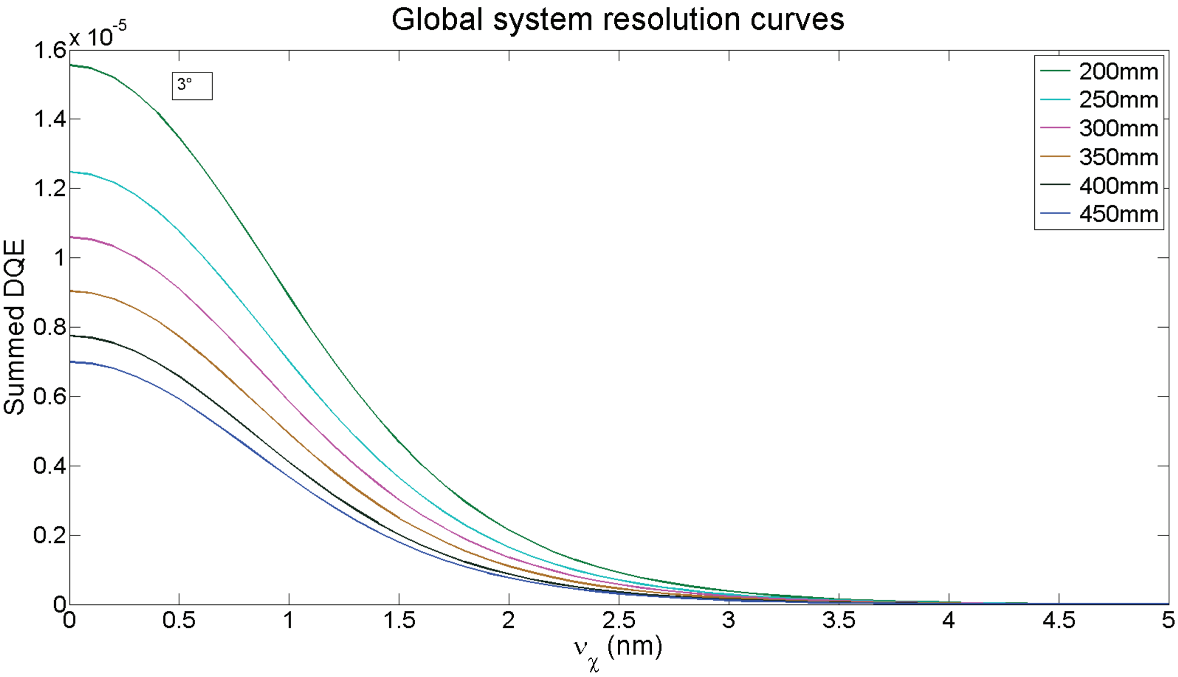

Figure II.26: Comparaison of the resolution of symmetric systems with different distances D (and constant angular aperture $\Delta = 0.2°$). It can be seen that the resolution curve decreases if D increases. This is due to decreasing system sensitivity.

Sensitivity profile and resolution curves for different angular apertures are represented on figure II.27 and II.28. Here, D is constant at 450 mm.

As can be seen in figure II.27, the smaller the angular aperture the lower are the sensitivity values. This can be explained by the fact, that a small angular aperture is very selective and only permits to a very small number of photons to cross the collimation slit. The wider the aperture, the higher are the inspected volume and the number of photons from different directions, "accepted" by the collimation. For low χ values, the loss of sensitivity is dominant and the resolution is better for increasing $\Delta\theta$. However, resolution curves cross at higher χ values, as can be seen on the zoom of figure II.28, and momentum transfer resolution gets better with small angular apertures.

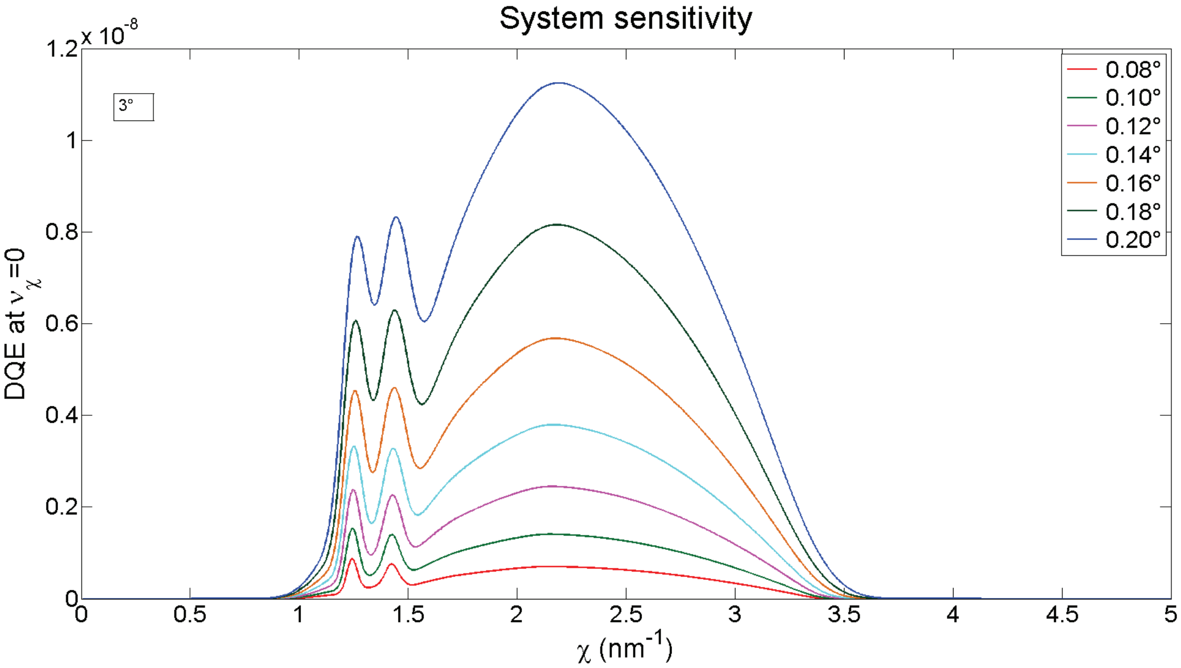

Figure II.27: Sensitivity curves obtained for different distances angular apertures (and constant distance $D = 450mm$) of a symmetric system. Sensitivity increases with increasing angular aperture.

This first study of the influence of geometric system parameters showed that sensitivity depends strongly on angular aperture and the distance between sample and source, and sample and detector. Resolution seems to be less affected by these parameters. Hence, the well known compromise between sensitivity and resolution is not clearly visible in this study, especially in the case of varying distance. This might be due to the fact, that the distance between detector/source and collimation slits was always the same with varying distance D in order to keep the same angular aperture for each distance. As χ-resolution depends on angular and energy resolution, it will not change if both of them remain the same. If the collimation position relative to the object and collimation slits were kept the same while the detector/source moves, there should be an impact on resolution as in this case, angular aperture changes.

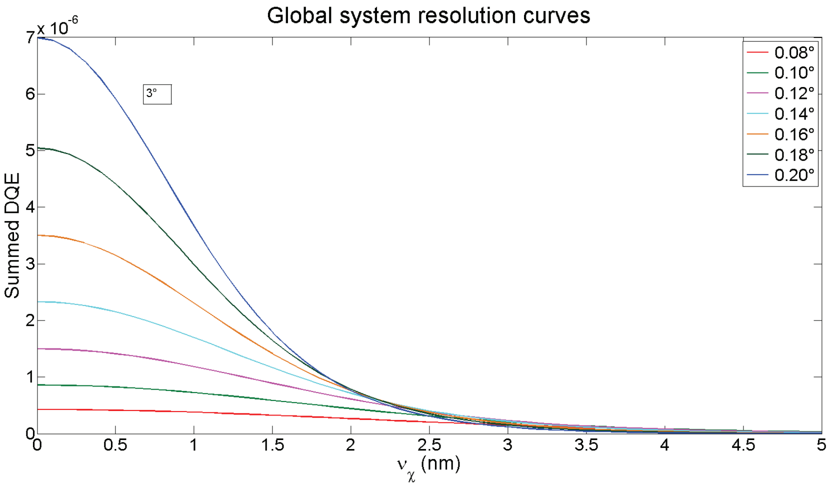

(a) *Resolution curves for different tested angular apertures.*

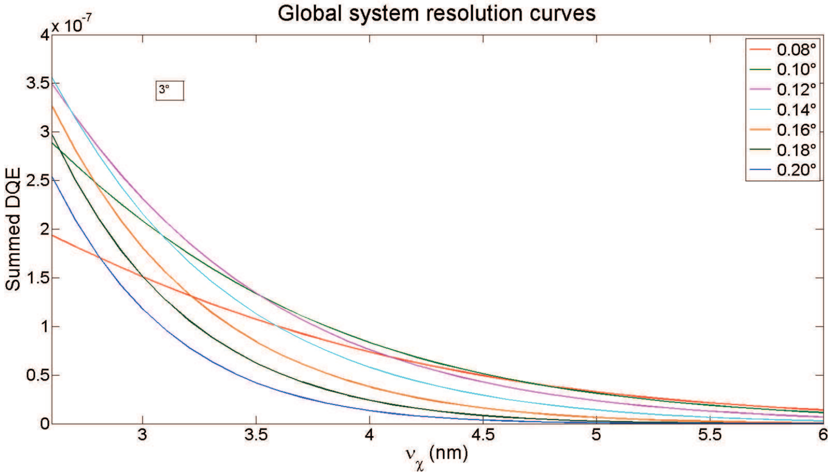

(b) *Zoom of the upper figure (from 2.5 to 6 nm).*

Figure II.28: Comparaison of the resolution of symmetric systems with angular apertures (and constant distance $D = 450mm$). The resolution curves cross and their order is inverted from a certain χ value.

Simulations for asymmetric systems were realized as well. Figure II.29 shows that the variation of D_S does not impact neither system sensitivity nor system resolution. This seems normal since DQE is normalized by the number of incident photons. In fact, even if more photons were incident on the sample thanks to changes in system parameters, the performances per incident photon are unchanged. Hence, all changes in sensitivity and resolution, that were observed previously were due to the variation of D_D and $\Delta\theta_D$, which was confirmed by calculations of asymmetric system DQE shown in figure II.30. It can be seen that the variation of system sensitivity (Fig. II.30.a) and the variation of system resolution (Fig. II.30.b) with $\Delta\theta_D$ are the same as for the symmetric system.

The previous study of the performance of a simple XRD system allowed us to get a feeling on how different system parameters might influence on the global performance. However, it is not possible to optimize the system parameters independently of a specified application. The

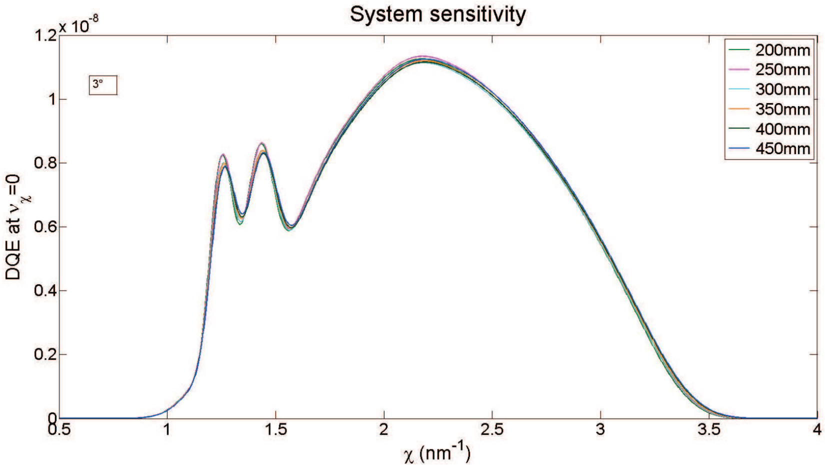

(a) *Sensitivity curves of an asymmetric system for different distances source-sample.*

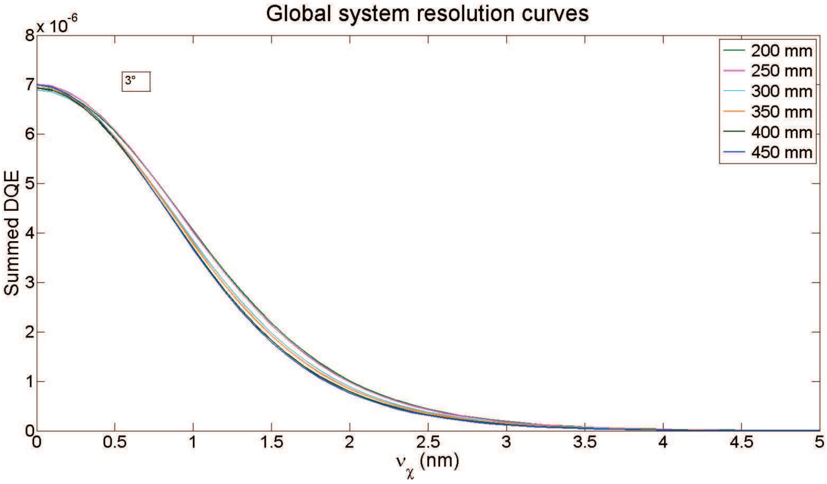

(b) *System resolution of an asymmetric system for different distances source-sample.*

Figure II.29: DQE comparison of an asymmetric system for different distances D_S (Angular apertures are about 0.2° and $D_D = 450mm$). It can be seen that the variation of source parameters has no effective impact on the system performances, which is due to the fact that calculated DQE are normalized by the number of incident photons.

incident spectrum will not necessarily be the same. In medical applications, the sample to be inspected correspond to tissues with little absorption power and small thickness. Hence, high energy photons do not seem necessary. Choice of the incident spectrum for medical applications will be discussed in chapter IV. In the case of luggage inspection, the samples are thicker and may contain materials with high X-ray absorption power. The incident spectrum has to be chosen to be suitable to detect sufficient X-ray diffraction signal (Chap. V). Moreover, the distance between the sample and the source/detector depends on the application. A baggage is much thicker than a breast and a baggage tunnel is larger than the holder for breast imaging. Finally, the exposition time might be limited by maximum

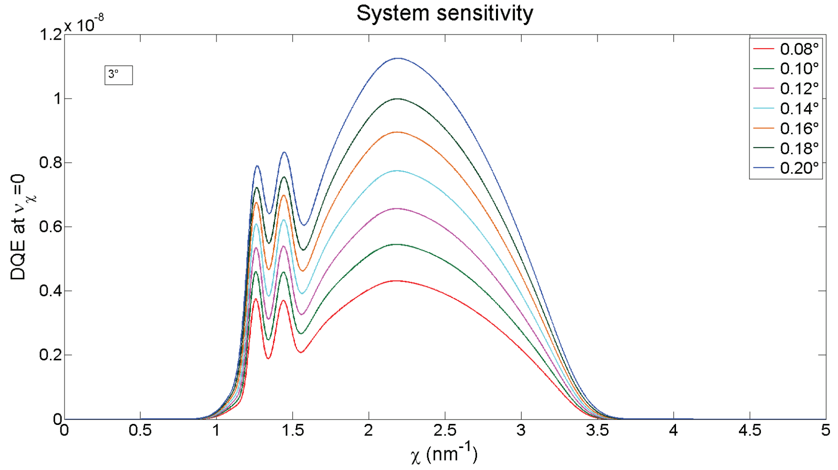

(a) *Sensitivity curves of an asymmetric system for different angular apertures of the secondary collimation.*

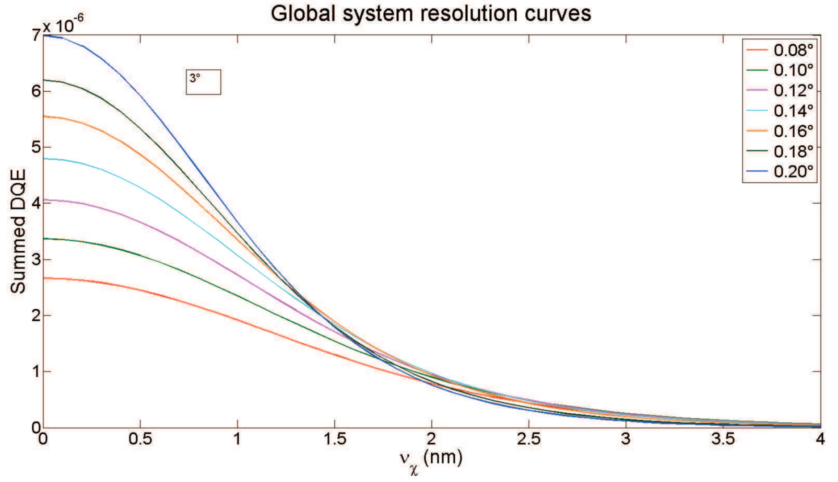

(b) *System resolution of an asymmetric system for different angular apertures of the secondary collimation.*

Figure II.30: DQE comparison of an asymmetric system for different angular apertures $\Delta\theta_D$ (Distances are about 450 mm and $\Delta\theta_S = 0.2°$). The same observations as for the symmetric system can be made.

dose to be delivered (medical application) or by time constraints (security check). The χ-range to be targeted might also be different. Therefore, it is necessary to optimize the system separately for each application by respecting the different constraints.

II.4 Conclusion

This second chapter was dedicated to the presentation of different figures of merit that can be used to assess the performances of an X-ray diffraction imaging system.

The first part of this chapter presented the different components of an EDXRD diffraction system and their modeling. This lead to the proposition of a global model of an acquired

EDXRD spectrum for the mono-angle case as well expansion to multi-angle acquisition. The model is formulated in a way that the material characteristic form factor F simply has to be multiplied by the global system response $\mathcal{R}$. Knowing $\mathcal{R}$ is primordial to be able to characterize a system using FOM. In addition to the model of a classical mono-angle EDXRD system an expansion to a multi-angle model of an EDXRD system combining EDXRD information at different scattering angles, was proposed. This allows to simulate multi-angle spectra and to assess performances of such a multi-angle EDXRD system.

The second part of this chapter was dedicated to the different figures of merit used in the present work.

First, detective quantum efficiency (DQE) was introduced. This figure of merit allows to quantify system performance independently from the imaged object. It combines sensitivity, resolution and SNR of an imaging system. The DQE can be calculated by using the system response matrix. Generally, DQE is used in X-ray transmission imaging. Here, we explained how to use it in X-ray diffraction imaging. As diffraction imaging is a non stationary process, the DQE in EDXRD imaging is a function of momentum transfer χ and its associated frequency variable ν_χ. By summing over all χ values, it is possible to access to global system resolution. DQE at zero frequency corresponds to the system sensitivity.

Afterwards, figures of merit allowing to assess material separation power of an EDXRD system were presented: contrast to noise ratio (CNR) and receiver operating characteristic (ROC) curve.

CNR is a very basic criterion, which indicates the degree of separability of two different materials using a given imaging system. In the present case, it corresponds to the quadratic distance per photon of two distributions A and B. Its inverse gives the number of photons, that is needed to have a distance of one standard deviation between A and B.

ROC curves do not only quantify the separation of two materials but they also take into account criteria such as detection rate and false positive rate, which involve human lives and high cost. A ROC curve corresponds to a graphical representation of true positive rate as a function of false positive rate. If ROC curves of different systems to compare are all symmetric to the negative diagonal, the system with the highest value of the area under the curve should be chosen. If this is not the case, a detection rate can be fixed and the system with the lowest corresponding false positive rate is the most performing one.

In general, ROC curves are obtained by generating different observations of the two probability distributions corresponding to A and to B and by calculating, for varying threshold λ_t of the statistical observer, the probability to detect A or B for each observation. However, this chapter proposed a new method of calculating ROC curves analytically. This method is based on information geometry. Inspired by Sanov's theorem it was proposed to approximate the probability distributions, with the help of the generalized Kullback-Leibler divergence. It was shown that using this approximation it is sufficient to only consider the points $\mathbf{x}_0$ being part of the geodesic relying $\mathbf{B}$ to $\mathbf{A}$ to cover the whole space and to construct the corresponding ROC curve.

The last part of this chapter presented the DQE results on a simple EDXRD system, which can be found in our laboratory.

First of all the importance of the choice of the scattering angle and the use of a multi-angle system were discussed. DQE curves showed that the scattering angle strongly influences the χ-range that will be accessible by the system and also the global system sensitivity. The comparison between mono- and multi-angle system showed that multi-angle acquisitions not only allow to increase global system sensitivity as shown previously [O'Flynn *et al.*, 2013] but also to enlarge the system sensitivity to a wider range of momentum transfer values. It also smooths the adverse effect of the characteristic rays of the incident X-ray spectrum. These advantages will be used in chapter IV concerning XRD-based mammography to keep the delivered dose as low as possible.

The influence of distance between sample and detector, and sample and source as well as the impact of angular aperture of primary and secondary collimation were also studied. In fact, DQE changes were all induced by parameter variation on detector side because DQE calculations were realized by normalizing by the number of incident photons. If the angular aperture is enlarged the sensitivity is increased but resolution is decreased from a certain χ value on. An increase of the distance leads to a decrease of sensitivity and only to a slight decrease in resolution. In fact, the well known compromise between sensitivity and resolution cannot be observed in this case because the angular aperture is always adjusted to remain the same for each distance and momentum transfer resolution is mainly impacted by angular resolution. Resolution would probably have shown more variations if collimation did not move with detector/source and kept the same slit size.

This study has helped to understand the influence of different basic parameters, and it showed that it is not possible to optimize system parameters independently from the targeted application as the constraints will not be the same for different applications.

Chapter IV and chapter V will present the different constraints for XRD-based mammography and security scan using XRD as well as system characterization and optimization using the the FOM introduced in this chapter.

The following chapter is dedicated to the reconstruction of material characteristic information (Bragg peaks or molecular form factor) from EDXRD spectra.This requires the knowledge of the system performance and especially the global model of an acquired XRD spectrum introduced in this chapter.

Chapter III

Reconstruction of X-ray diffraction pattern

In the case of an ideal diffraction system, i.e. in the case of a flat X-ray spectrum, collimators with an infinite angular resolution and a detector not adding neither noise nor blurring to the data, the detected diffraction spectrum of a pure crystalline powder sample would only contain a few Bragg peaks, characteristic of the sample material. However, such a system does not exist. In practice, an X-ray spectrum is not flat, angular resolution of the collimation system and detector resolution are finite.

In order to improve material characterization, it is interesting to reconstruct or deconvolve the original diffraction pattern. Furthermore, reconstruction or deconvolution allows combining information from EDXRD-spectra at different scattering angles. Deconvolution of measured XRD data (without multiplexing) using a complete model of EDXRD acquisition chain (collimation resolution, absorption, etc.) was proposed in only one article [Soulez *et al.*, 2011].

In EDXRD, the aim of reconstruction is to estimate the theoretical or reference diffraction pattern F from measured data. Assuming linearity, at a given measurement $\mathbf{m}$, the convolution product of F with the system response is observed. Supposing that the system response $\mathcal{R}$ (Eq. II.1.7) is known, this corresponds to a typical inverse problem, which can be solved in different manners.

Reconstruction of EDXRD data is an ill-posed problem [Hadamard, 1902]. The system response is a rectangular matrix and its rank is lower than the dimension of the object to be reconstructed. Hence, uniqueness of solution is not guaranteed. In the case of continuous models, a discretization and quantization are necessary to obtain a numerical solution. This loss of information may lead to numerical instabilities of the reconstruction algorithms. Actually, some small errors in initial data may induce very high errors in reconstructed data. For example, experimental data present ”errors” due to noise, which is not taken into account by the model. Thus, if a solution of this inverse problem exists, it is conceivable that there might be many other solutions. It is necessary to chose the ”right” one. To that end, some additional prior information or constraints (such as positivity) must be introduced, to obtain a so-called regularized solution.

There are two principal types of deconvolution algorithms[1]

1. Deterministic methods using regularization constraints
2. Statistical methods

The first one consists of a class of technical solutions, which modify an ill-posed problem into a well-posed problem, by approximation. Thus, a physically acceptable and sufficiently stable approximate solution can be obtained. Seminal work for these regularization techniques were proposed by Tikhonov [Tikhonov and Arsenin, 1977], [Groetsch, 1984]. These methods are based on minimization of a functional, which includes different constraints. A review of several of these methods, among which the Tikhonov-Miller regularization procedure, the Van Cittert algorithm of deconvolution and the Gold deconvolution algorithm can be found in [Morhac and Matousek, 2009]. Applications of these latter approaches in the framework of crystalline diffraction were developed in Rajaona's Master Thesis [Rajaona, 2012]. It was shown that these methods were not appropriate to EDXRD spectrum reconstruction: in most cases spectrum positivity was not ensured, the number of reconstructed diffraction peaks was incorrect and their relative peak intensities were not respected.
Therefore, statistical methods were preferred in the present work, as they allow to take photon noise into account, which is the most important problem in the previous deconvolution techniques. Moreover, it is also possible to consider other a priori such as the nature of the spectrum to reconstruct, i.e. discrete peaks (crystalline materials) or continuous spectrum (amorphous materials), by introduction of penalty terms for instance. There are many different statistical reconstruction algorithms. Most of them are based on the maximization of probability terms. Most popular approaches include maximum likelihood methods (see e.g. [Shepp and Vardi, 1982]) and maximum a posteriori approaches, that rely on introducing prior distributions in a Bayesian framework (see e.g. [Giovannelli *et al.*, 1994], [Morhac and Matousek, 2009]). Another important class of deconvolution methods are information theoretic approaches. They consist in picking among all possible distributions, compatible with the data and constraints, the one with the highest entropy [Ables, 1974], [Meng and Ramsden, 2000]. Finally, an important class of methods called maximum likelihood expectation maximization (MLEM) were also proposed. These methods involve a set of intermediate complete unobserved data (say x), which could easily lead to estimate the true (unconvolved) data. As these data are not observed, it was proposed by [A. P. Dempster, 1977] to maximize the marginalized likelihood , that is to find the true data that maximize the expectation of the likelihood. Therefore, it is called MLEM.

As this method was shown to perform very well on crystalline diffraction spectrum reconstruction [Rajaona, 2012], the present work will focus on this algorithm.

In the following chapter, MLEM algorithm as well as a criteria to assess reconstruction result will be described. MLEM reconstruction is tested on simulated and experimental EDXRD data of crystalline and amorphous samples. As reconstructed XRD signatures of amorphous materials is not satisfying different regularization methods are proposed and tested on the same data.

---

[1] This separation is commonly used but both could be categorized as statistical methods. In fact, deterministic methods using regularization constraints could also be considered as statistical methods with non explicit hypothesis.

III.1 Maximum Likelihood Expectation Maximization (MLEM) for X-ray diffraction

The MLEM algorithm was initially developed within the framework of reconstruction of images in emission tomography [Shepp and Vardi, 1982], [Vardi *et al.*, 1985], [Lange and Carson, 1984]. Nowadays, this algorithm is employed in numerous tomographic reconstruction problems and often associated to regularization techniques. It is based on the iterative maximization of the log-likelihood function.

III.1.1 Algorithm

Suppose that the measurement $\boldsymbol{\mathcal{M}}$ (expected measurement), following the model described in the previous chapter (Sec. II.1.6), can be written as:

$$\boldsymbol{\mathcal{M}} = \mathcal{R} \cdot \mathbf{F} \tag{III.1.1}$$

$\boldsymbol{\mathcal{M}} \in \mathbb{R}^M$, $\mathbf{F} \in \mathbb{R}^N$ is the theoretical spectrum to be reconstructed and $\mathcal{R} \in \mathbb{R}^{M \times N}$ the system matrix. M corresponds to the number of measured energy bins and N to the number of bins chosen for discretization of $\mathbf{F}$ ($\mathbf{F} = [F_1 ... F_N]$. It is assumed that the number of photons associated to the momentum transfer bin "k" follows a Poisson law of parameter F_k, defined as:

$$F_k = \int_{\mathbb{R}} F(\chi)\, b_i(\chi)\, d\chi \tag{III.1.2}$$

with $F(\chi)$ the continuous spectrum and b_k the binning operator (box function, for example). Furthermore, it is assumed that the F_k are independent variables. As a result of independence, the number of photons received in channel "j", noted m_j follows a Poisson law of parameter $\sum_{k=1}^{N} R_{jk} F_k = \mathcal{M}_j$. Thus, assuming that all measurement energy channels are independent, it comes:

$$\begin{aligned} P_{\boldsymbol{\mathcal{M}}}(\mathbf{m}) &= \prod_{j=1}^{M} P_{\mathcal{M}_j}(m_j) \\ &= \prod_{j=1}^{M} e^{-\mathcal{M}_j} \frac{\mathcal{M}_j^{m_j}}{m_j!} \end{aligned} \tag{III.1.3}$$

The likelihood function of $\mathbf{F}$ (XRD pattern to be reconstructed), knowing observed measurements $\mathbf{m}$, with the constraint of $F_k \geq 0$, is given by:

$$P(\mathbf{m} \mid \mathbf{F}) = \prod_{j=1}^{M} e^{-\sum_{k=1}^{N} R_{jk} F_k} \frac{\left(\sum_{k=1}^{N} R_{jk} F_k\right)^{m_j}}{m_j!} \tag{III.1.4}$$

Maximum likelihood approach consists in maximization of $P(\mathbf{m} \mid \mathbf{F})$ versus $\mathbf{F}$. For practical reasons, it is often the log-likelihood function $\log [P(\mathbf{m} \mid \mathbf{F})] = L(\mathbf{F})$ that is maximized:

$$L(\mathbf{F}) = \sum_{j=1}^{M} \left(-\sum_{k=1}^{N} R_{jk} F_k + m_j \log \left(\sum_{k=1}^{N} R_{jk} F_k \right) - \log (m_j!) \right) \tag{III.1.5}$$

In order to maximize $L(\mathbf{F})$, it is necessary to solve $\frac{\partial L(\mathbf{F})}{\partial F_k} = 0$, $\forall F_k \leq \{F_1 ... F_N\}$:

$$\begin{aligned} \frac{\partial L(\mathbf{F})}{\partial F_k} &= \sum_{j=1}^{M} \left(-R_{jk} + m_j \frac{R_{jk}}{\sum_{k'=1}^{N} R_{jk'} F_{k'}} \right) \\ &= 0 \end{aligned} \tag{III.1.6}$$

The calculation of the Hessian $H_{ij} = \frac{\partial^2 L(\mathbf{F})}{\partial F_i \partial F_j}$ allows to verify that this extremum corresponds to a maximum.

The resolution of equation III.1.6 leads to the research of a solution for a set of coupled equations non-linear in $F_{k'}$. This difficulty is intrinsically linked to the nature of the log-likelihood function of the Poisson process. In order to resolve this problem in MLEM framework, we introduce a set of complete unobserved data $\mathbf{x}$ permitting to estimate $\mathbf{F}$ directly:

$$x_{jk} = R_{jk} F_k \ ; \ \mathcal{M}_j = \sum_k x_{jk} \tag{III.1.7}$$

As the system response matrix $\mathcal{R}$ is supposed to be known, $\mathbf{F}$ can be estimated easily using $\mathbf{x}$.

The number of photons in each bin F_k are random variables following a Poisson law. Hence, x_{jk} correspond to independent Poisson random variables with parameter $R_{jk} F_k$. In fact, x_{jk} is considered to be a number of non observed photons, which are emitted in frequency bin F_k and detected in the measurement bin $\mathcal{M}_j$. Its log-likelihood function can be expressed as:

$$\begin{aligned} L(\mathbf{x} \mid \mathbf{F}^n, \mathbf{m}) &= \log \prod_j \prod_k P(x_{jk} \mid \mathbf{F}^n, \mathbf{m}) \\ &= \log \prod_j \prod_k e^{R_{jk} F_k^n} \frac{(R_{jk} F_k^n)^{x_{jk}}}{x_{jk}!} \\ &= \sum_j \sum_k [x_{jk} \log (R_{jk} F_k^n) - R_{jk} F_k^n - \log (x_{jk}!)] \end{aligned} \tag{III.1.8}$$

The principle of the expectation maximization algorithm proposed by [A. P. Dempster, 1977] consists in the marginalization of $L(\mathbf{x} \mid \mathbf{F}^n, \mathbf{m})$ with respect to non observed data $\mathbf{x}$, and to recalculate a new value $\mathbf{F}^{n+1}$ of the estimate $\hat{\mathbf{F}}$, which maximizes the marginalized likelihood-function. The expectation of the log-likelihood function with respect to $\mathbf{x}$ is calculated as:

$$E_{\mathbf{x}}\left[L\left(\mathbf{x} \mid \mathbf{F}^n, \mathbf{m}\right)\right] = \sum_j \sum_k E\left[x_{jk} \mid \mathbf{F}^n, \mathbf{m}\right] \log\left(R_{jk} F_k^n\right) - R_{jk} F_k^n + C^{'}\left(\mathbf{F}\right) \tag{III.1.9}$$

where $C^{'}\left(\mathbf{F}\right)$ does not depend on $\mathbf{F}^n$ and hence, not on $\hat{\mathbf{F}}$.

We have to calculate $E\left[x_{jk} \mid \mathbf{F}^n, \mathbf{m}\right]$. The probability distribution of x_{jk} knowing $\mathbf{m}$ is given by:

$$\begin{aligned} P\left(x_{jk} = q \mid m_j = m, \mathbf{F}\right) &= \frac{P\left(x_{jk} = q; m_j = m, \mathbf{F}\right)}{P\left(m_j = m, \mathbf{F}\right)} \\ &= e^{-R_{jk}F_k} \frac{\left(R_{jk}F_k\right)^q}{q!} \cdot e^{-\sum_{l \neq k} R_{jl}F_l} \frac{\left(\sum_{l \neq k} R_{jl}F_l\right)^{m-q}}{(m-q)!} \\ &\cdot \frac{m!}{e^{-\sum_l R_{jl}F_l}\left(\sum_l R_{jl}F_l\right)^m} \\ &= \frac{m!}{q!\,(m-q)!} \cdot \frac{\left(R_{jk}F_k\right)^q}{\left(\sum_l R_{jl}F_l\right)^q} \cdot \frac{\left(\sum_{l \neq k} R_{jl}F_l\right)^{m-q}}{\left(\sum_l R_{jl}F_l\right)^{m-q}} \end{aligned} \tag{III.1.10}$$

A binomial distribution with parameters $\left(m, p = \frac{R_{jk}F_k}{\sum_l R_{jl}F_l}\right)$. Expectation value of a binomial distribution is well known to be equal to mp. Thus, $E\left[x_{jk} \mid \mathbf{F}^n, \mathbf{m}\right]$ becomes:

$$E\left[x_{jk} \mid \mathbf{F}^n, \mathbf{m}\right] = \frac{m_j R_{jk} F_k^n}{\sum_l R_{jl} F_l^n} \tag{III.1.11}$$

This allows to determine the expectation of the log-likelihood function:

$$E_{\mathbf{x}}\left[L\left(\mathbf{x} \mid \mathbf{F}^n, \mathbf{m}\right)\right] = \sum_j \sum_k \frac{m_j R_{jk} F_k^n}{\sum_l R_{jl} F_l^n} \log\left(R_{jk} F_k^n\right) - R_{jk} F_k^n + C^{'}\left(\mathbf{F}\right) \tag{III.1.12}$$

This is called the E-step (expectation step). To finish, a new value for estimate $\hat{\mathbf{F}}$ maximizing this expectation by maintaining the values obtained with $R_{jk}F_k$, has to be determined (M-step). Therefore, the partial derivative of expectation with respect to F_k has to be calculated and the value of F_k^n leading to this derivative to be equal to zero:

$$\frac{\partial E_{\mathbf{x}}\left[L\left(\mathbf{x} \mid \mathbf{F}^n, \mathbf{m}\right)\right]}{\partial F_k} = \sum_j \frac{m_j R_{jk} F_k^n}{\sum_l R_{jl} F_l^n} \cdot \frac{R_{jk}}{R_{jk} F_k} - R_{jk} \Bigg|_{F_k^{n+1}} = 0 \tag{III.1.13}$$

which is equivalent to:

$$\frac{1}{F_k^{n+1}} \sum_j \left(\frac{m_j R_{jk} F_k^n}{\sum_l R_{jl} F_l^n}\right) - \sum_j R_{jk} = 0 \tag{III.1.14}$$

This leads to the following iterative solution in MLEM framework [Shepp and Vardi, 1982]:

$$F_k^{n+1} = F_k^n \frac{1}{\sum_{j=1}^{M} R_{jk}} \sum_{j=1}^{M} \left(\frac{m_j R_{jk}}{\sum_{l=1}^{N} R_{jl} F_l^n} \right) \tag{III.1.15}$$

The choice of F_k^0 as a positive valued function, ensures the non-negativity of the final results. It can be seen that numerical instabilities might occur in the case where $R_{jk} \sim 0$.

This iterative algorithm can be decomposed in different steps, which are represented in a schematic view in figure III.1.

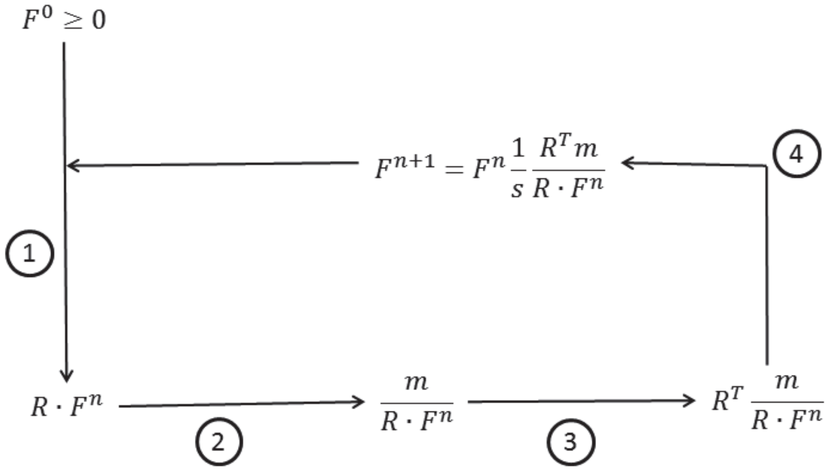

Figure III.1: Schematic representation of MLEM algorithm: 1. Projection of current estimate, 2. Calculation of measure to projection ratio, 3. Back projection to obtain "relative error image", 4. Updating of the estimate after normalizing by system sensitivity $S = \sum_{j=1}^{M} R_{jk}$.

It has to be noticed that the development of this MLEM algorithm was realized under two important assumptions:

- Photon emissions in bin "k" follow a Poisson process with mean F_k (quantity to be estimated) and are independent
- Measurements m_j correspond to realizations of a Poisson random process with parameter $\mathcal{M}_j$ and they are independent.

Hence, this deconvolution algorithm seems adapted for reconstruction of crystalline spectra, where there are only a few discrete diffraction peaks. In this case, the assumption of independence between the different energy/momentum transfer bins is satisfied. However, in the case of continuous amorphous spectra neighboring bins are not independent of each other and reconstructed spectra might not be correct.

If two independent measurements $\mathbf{m}_1$ and $\mathbf{m}_2$ at scattering angles Θ_1 and Θ_2 are realized, and the system model is assumed to be linear, it will be possible to write:

$$\begin{bmatrix} \boldsymbol{\mathcal{M}}_1 \\ \boldsymbol{\mathcal{M}}_2 \end{bmatrix} = \begin{bmatrix} \mathcal{R}_1 \\ \mathcal{R}_2 \end{bmatrix} \cdot \mathbf{F} \tag{III.1.16}$$

where $\boldsymbol{\mathcal{M}}_1$ and $\boldsymbol{\mathcal{M}}_2$ are column vectors with Poisson parameters of $\mathbf{m}_1$ and $\mathbf{m}_2$ of lengths M_1 and M_2. $\mathcal{R}_1$ and $\mathcal{R}_2$ are the system response matrices at scattering angles Θ_1 and Θ_2. If both measurements are independent, the iterative MLEM solution will be given by:

$$F_k^{n+1} = F_k^n \frac{1}{\sum_{j=1}^{M_1+M_2} R_{jk}} \sum_{j=1}^{M_1+M_2} \left(\frac{m_j R_{jk}}{\sum_{l=1}^{N} R_{jl} F_l^n} \right) \tag{III.1.17}$$

This formula will be easy to generalize to A angles, if the measurements are independent. It was used in its generalized form for multi-angle reconstructions.

III.1.2 Criterion of reconstruction performance: relative error

In order to assess quantitatively a reconstruction result, it is required to define a performance criterion. A very basic criterion, which can be easily employed is the relative error. In this work, it is defined as the mean of the relative error of each momentum transfer bin:

$$E_{rel} = \frac{1}{Nb_\chi} \sum_\chi \frac{|\hat{F}(\chi) - F_{th}(\chi)|}{F_{th}(\chi)} \tag{III.1.18}$$

where $\hat{F}$ is the estimated spectrum, F_{th} the theoretical spectrum and Nb_χ the number of χ values over which is summed. It is important to take only into account χ values at which the system is sensitive. In fact, this definition corresponds to a mean relative error over the χ sensitivity range. Asymptotically, equation III.1.18 becomes the estimation of an error weighted by the expected variance[2] for each channel. If the number of photons in each channel is high enough to approximate the Poisson law by a normal distribution (Sec. II.2.2.1), this error will correspond to the total Fisher information.

However, this definition is only suitable for amorphous signatures as they are continuous.
In the case of crystalline signatures, the relative error was calculated for each reconstructed peak position:

$$E_{rel,pos} = \frac{|\hat{\chi} - \chi_{th}|}{\chi_{th}} \tag{III.1.19}$$

where $\hat{\chi}$ is the estimated peak position and χ_{th} the theoretical peak position.

Relative error of the relative peak amplitudes was calculated for each peak as well:

$$E_{rel,amp} = \frac{|\hat{A}_{rel}(\chi) - A_{th,rel}(\chi_{th})|}{A_{th,rel}(\chi_{th})} \tag{III.1.20}$$

In fact, absolute peak height is less important than the relative height between the different peaks. That is why crystalline diffraction pattern were normalized by the maximum amplitude, i.e. the main peak's amplitude is equal to one.

---

[2] The variance of a Poisson process with parameter F_i is equal to F_i.

III.1.3 Reconstructed crystalline signatures

In order to validate the MLEM reconstruction algorithm, it was first tested on simulated and experimental crystalline EDXRD spectra.

III.1.3.1 Simulated spectra

The simulated acquisition system is the same as presented in section II.3.1[3] and the tested materials are salt and TNT of 4 cm in thickness. The salt signature has a few widely spaced Bragg peaks and its lowest χ-value is around 1.5 nm^{-1}. TNT has more peaks the main ones being in the range of 0.5 to 1.5 nm^{-1}. Thus, the signatures (Fig. III.2) of these materials are quite different and it is interesting to compare their reconstruction results as well as the influence of the chosen scattering angle.

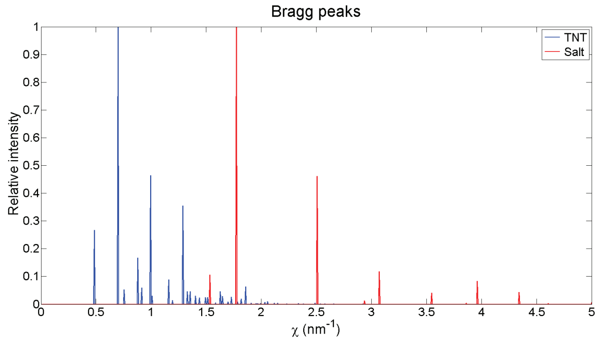

Figure III.2: Theoretical Bragg peaks of salt (red) and TNT (blue).

Salt and TNT spectra were simulated for 2° and 5° in the mono-angle case and for multi-angle reconstruction salt and TNT spectra were simulated between 2° and 5° at 0.1° step. Momentum transfer bins were about $\Delta\chi = 0.01$ nm^{-1} and energy bins about $\Delta E = \frac{160}{512} \approx 0.31$. The number of detected photons per spectrum is about 10^4 for TNT and 10^3 for salt. Multi-angle simulations were realized so that the overall number of incident photons at the surface are the same as in mono-angle configuration. Therefore, the number of photons at a given Θ is much smaller in the multi-angle than in the mono-angle case (Fig. III.3, the grey intensity corresponds to the number of photons in multi-angle spectra). To reconstruct the different material signatures, the MLEM algorithm without a priori was employed. The number of iterations was fixed to 80. The most important criterion for reconstructed Bragg peaks is their position, and it did not change significantly at higher iteration numbers. Hence, it was not necessary to increase reconstruction time by increasing the number of iterations.

The simulated salt spectra are represented in figure III.3. The total number of detected photons is about 3500 at 2° (Fig. III.3.a) and 1500 at 5° (Fig. III.3.b). In the multi-angle spectrum (Fig. III.3.c) the number of detected photons is about 4000, which is higher than in mono-angle spectra even though the number of incident photons was the same for each spectrum. The number of detected photons at one angle in the multi-angle spectrum is much smaller than in mono-angle case. However, the shape of the spectrum lines at 2° and 5° are the same as their mono-angle counterpart, and the proportion of detected photons at a given angle remains the same. Thus, the ratio between the number of detected photons in

---

[3] N.B.: The detector response is taken to be Gaussian, i.e. low-energy tail is neglected.

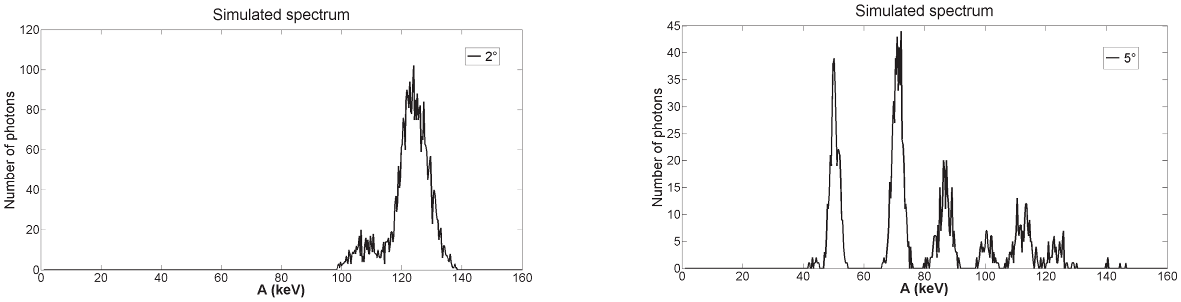

(a) *Mono-angle 2°: 3500 detected photons.* (b) *Mono-angle 5°: 1500 detected photons.*

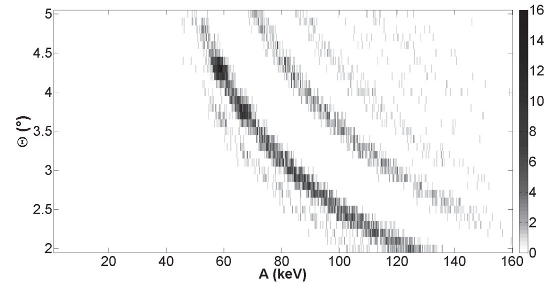

(c) *Multi-angle: 4000 detected photons.*

Figure III.3: Examples of noisy simulated salt spectra: mono-angle spectra at 2° and 5° (a,b) and multi-angle spectrum (c) between 2° and 5° with a step of 0.1°.

2° mono-angle spectrum and 5° mono-angle spectrum $3500/1500 \approx 2.33$ is the same as the ratio between the number of photons detected at 2° and 5° in the multi-angle spectrum, i.e. 118/51. At energies about 59 and 67 keV a high photon density can be observed in the multi-angle spectrum. These energies correspond to characteristic rays of the incident tungsten X-ray spectrum. Hence, the number of photons emitted at these energies is much higher than at other energies and leads to higher diffraction signal at some angles (when combination of scattering angle and energy corresponds to a Bragg peak).

The reconstructed signatures were superimposed to the theoretical salt Bragg peaks F (dashed lines) and are presented in figure III.4. They were obtained by averaging reconstructions of 100 simulated noisy spectra. The relative intensities of reconstructed signatures as well as of theoretical signatures were normalized in a way that the highest peak has an amplitude of one.

Reconstructed salt Bragg peaks do not correspond to the theoretical Dirac delta shape, used to simulate noisy EDXRD spectra, but present a certain width (Fig. III.4). As the system response for simulated spectra is exactly known, this effect is due to photon noise and possibly to the number of iterations (peaks become thinner with each iteration), which was limited to 80. Though, their positions are well reconstructed if the peaks are in the χ-range of system sensitivity (see section II.3.1). At a scattering angle of 2°, only the two first diffraction peaks of salt can be reconstructed. Acquisitions at 5° allow reconstruction of the remaining salt peaks at higher χ values. However, the peak at 1.5 nm^{-1} is not well reconstructed (it appears to be split in two peaks) since it is not in the sensitivity range of the 5°-system (see section II.3.1). In multi-angle reconstruction, it is possible to reconstruct each diffraction peak of salt with a

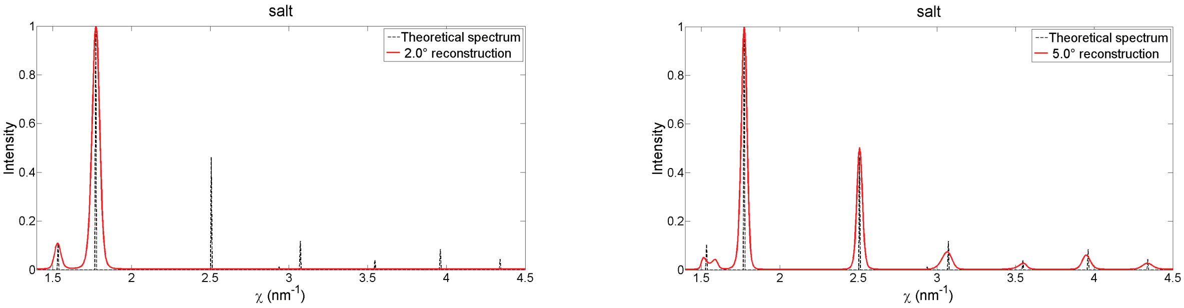

(a) *Averaged reconstruction from simulated salt spectra at 2°.*

(b) *Averaged reconstruction from simulated salt spectra at 5°.*

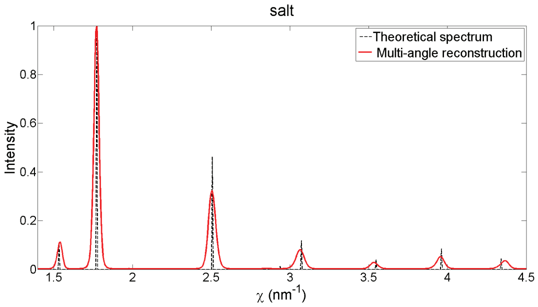

(c) *Averaged multi-angle reconstruction from simulated salt spectra.*

Figure III.4: Reconstructed salt peaks (red) for mono-angle systems at 2° (a) and 5° (b) and for multi-angle system (c) superimposed to theoretical peaks (dashed lines). Average was calculated over reconstructed signatures from 100 different simulated noisy spectra.

correct position thanks to the larger sensitivity range. Table III.1 represents the relative error (Eq. III.1.19) of the position of each reconstructed salt peak. Each restored peak position has been determined with an error less than 1 %. Reconstructed relative peak intensities present higher relative errors (Eq. III.1.20) up to almost 42 % for 5° (Tab. III.2). However, the main peak was correctly "identified" as main peak with relative intensity equal to one.

Theoretical peak position (nm^{-1})	2°	5°	Multi-angle
1.53	0	**X**	0.65
1.77	0	0	0
2.51	**X**	0	0.40
3.07	**X**	0.33	0.33
3.55	**X**	0	0.56
3.96	**X**	0.25	0
4.34	**X**	0	0.69

Table III.1: Relative errors(in %) for peak position of the different restored salt peaks using simulated salt spectra. **X** means that the peak was not reconstructed at the considered angle.

Theoretical relative peak amplitude	2°	5°	Multi-angle
0.11	0	**X**	0
1	0	0	0
0.46	**X**	8.69	30.43
0.12	**X**	41.67	33.33
0.04	**X**	25	25
0.08	**X**	25	37.5
0.04	**X**	25	0

Table III.2: Relative errors(in %) for relative amplitude of the different restored salt peaks using simulated salt spectra. **X** means that the peak was not reconstructed at the considered angle.

Fig. III.5 shows the simulated TNT spectra. Characteristic rays of the incident X-ray spectrum are again clearly visible in multi-angle spectrum (Fig. III.5.c). The number of detected photons is about $7.5 \cdot 10^4$ for 2° mono-angle simulation (Fig. III.5.a) and about $1.1 \cdot 10^4$ for 5° (Fig. III.5.b). Here, the multi-angle spectrum contains about $4.0 \cdot 10^4$, which lies between detected photon numbers of the mono-angle systems. In fact, the system at 2° seems to be ideal for TNT detection, as it covers the whole χ-range that is important to characterize TNT (see sensitivity of 2° system in section II.3.1), and sensitivity is concentrated on this momentum transfer region of interest. The system at 5° does not cover the whole *chi*-range of interest, and sensitivity is distributed over a larger range of momentum transfer values. Hence, it is less sensitive at a given χ-value. Multi-angle system comprises the "ideal" angle but also numerous less adapted angles.

TNT spectra are less noisy (smoother) than the salt spectra, which is due to significantly higher incident photon number and in consequence, higher detected photon numbers.

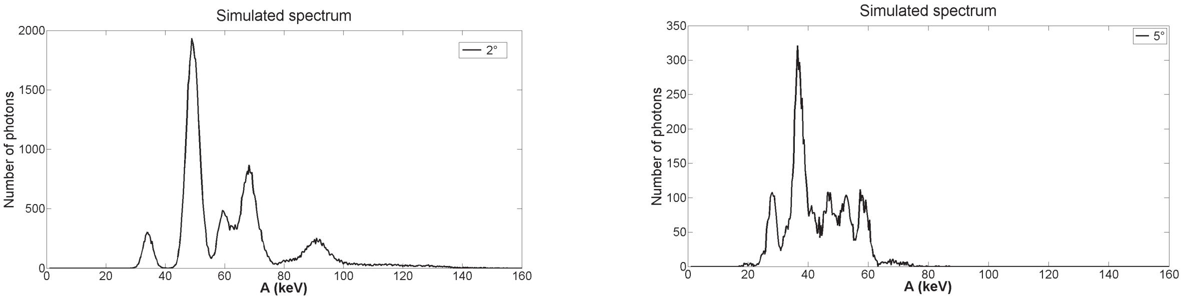

(a) *Mono-angle 2°:* $7.5 \cdot 10^4$ *detected photons.* (b) *Mono-angle 5°:* $1.1 \cdot 10^4$ *detected photons.*

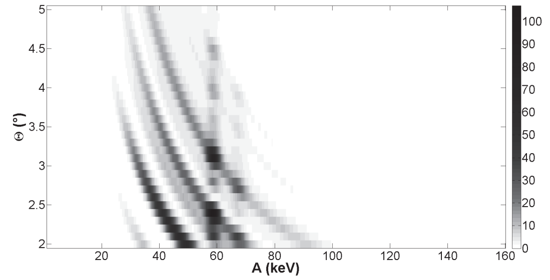

(c) *Multi-angle:* $4.0 \cdot 10^4$ *detected photons.*

Figure III.5: Examples of noisy simulated TNT spectra: mono-angle spectra at 2° and 5° (a,b) and multi-angle spectrum (c) between 2° and 5° with a step of 0.1°.

Figure III.6 shows the corresponding TNT reconstruction results. At 2°, the first two peaks (at 0.5 nm^{-1} and 0.7 nm^{-1}) are very well reconstructed in position (see table III.3, relative errors of 0 %). Peaks at χ values higher than 0.7 nm^{-1} and with relative amplitudes higher than 0.1 are less well reconstructed but the relative error of their peak position remains small around 1 %. If their relative intensity is lower than 0.1, they are badly or not at all reconstructed (continuous corrugated line). This is due to limited system resolution (peaks too close to each other to be resolved separately) and to diffraction intensity, which is too low compared to diffraction intensity of main peaks (only a small number of atomic planes associated to these χ-values). At 5°, neither the first expected peak (at 0.5 nm^{-1}), nor the main peak (at 0.7 nm^{-1}) were reconstructed. The peak that could be taken for the principal peak, which was slightly shifted, corresponds to a boundary effect. If there was no normalization to one of the highest peak, its amplitude would be very high (it increased with each iteration). In fact, the 5° system is not sensitive to these χ-values. The intensity of the next peak at 0.88 nm^{-1} is much lower than at 2° because it is still at a χ value with very poor system sensitivity at 5°. This is also confirmed by relative errors of relative peak intensity (Tab. III.4), which are high in both cases (most of them higher than 30 %) but significantly higher for reconstructed peaks at 5° (60 % and more).

Multi-angle reconstruction gives access to the same peaks as 2° mono-angle reconstruction. However, multi-angle reconstruction improves the precision of the restored peak position. Almost each reconstructed peak position is correct and leads to a relative error equal to zero (Tab. III.3). In general, relative errors of peak position remain around 1 % or less. The comparison of the relative errors of relative amplitudes of reconstructed peaks in table III.4 shows that multi-angle reconstruction allows to better estimate relative peak intensities than mono-angle systems.

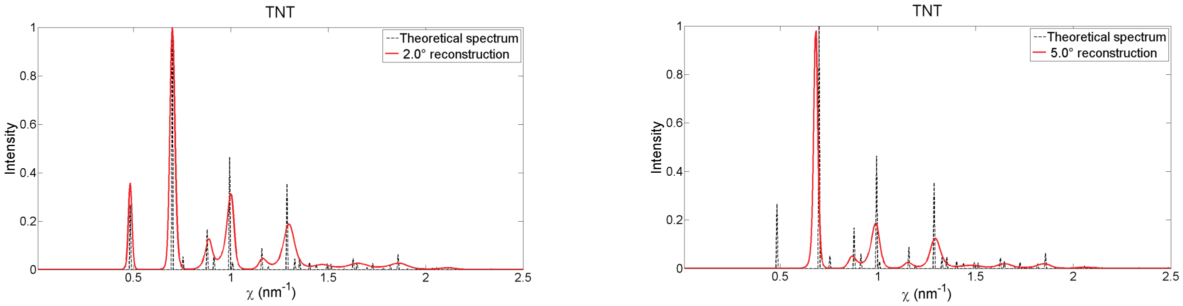

(a) *Averaged reconstruction from simulated TNT spectra at 2°.*

(b) *Averaged reconstruction from simulated salt spectra at 5°.*

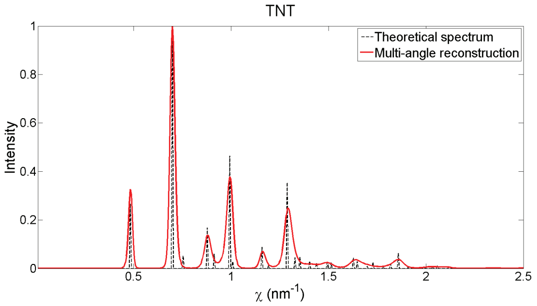

(c) *Averaged multi-angle reconstruction from simulated salt spectra.*

Figure III.6: Reconstructed TNT peaks (red) for mono-angle systems at 2° (a) and 5° (b) and for multi-angle system (c) superimposed to theoretical peaks (dashed lines). Average was calculated over reconstructed signatures from 100 different simulated noisy spectra.

Theoretical Peak position (nm^{-1})	2°	5°	Multi-angle
0.48	0	**X**	0
0.70	0	**X**	0
0.88	1.14	1.14	0
0.99	1.01	0	0
1.16	0	0.86	0
1.29	0.78	0	0
1.63	1.23	1.23	0.61
1.86	0	0.54	0

Table III.3: Relative errors (in %) for peak positions of the different reconstructed TNT peaks. **X** means that the peak was not reconstructed at the considered angle.

Theoretical relative peak amplitude	2°	5°	Multi-angle
0.27	33.33	**X**	22.22
1	0	**X**	0
0.17	23.53	70.59	17.65
0.46	32.61	58.69	17.39
0.09	44.44	66.67	11.11
0.36	47.22	63.89	30.56
0.05	40	60	20
0.06	50	66.67	33.33

Table III.4: Relative errors (in %) for relative amplitudes of the different reconstructed TNT peaks. **X** means that the peak was not reconstructed at the considered angle.

To conclude, in the case of TNT, multi-angle reconstruction has lower interest than in the case of salt since the needed χ-range is well covered at 2°. Though, multi-angle reconstruction improves the precision of the restored peak position and also the reconstructed relative amplitude. It might be interesting to add some lower scattering angles but it is difficult to acquire at lower angles because separation of photons coming from the transmitted beam ($\Theta = 0^\circ$) becomes more and more complicate with decreasing scattering angle. This example shows that it is important to adapt the energy-range and the scattering angle to the material to be imaged.

III.1.3.2 Experimental spectra

The previously simulated salt spectra were also acquired experimentally in the laboratory by arranging the same system geometry. For real data, the salt was contained in a plastic recipient and the sample thickness was only about 3.3 cm instead of 4 cm. Momentum transfer bin was about 0.01 nm^{-1} and energy bin about 0.47 keV. Mono-angle and multi-angle acquisitions were realized by adapting the acquisition time in order to have the same number of incident photons in mono-angle and multi-angle acquisitions (310 s for mono-angle spectra and 10 s per angle for multi-angle spectrum). Diffraction spectra were measured using MINIGAMI probe, a 4×4 pixel CdZnTe detector with 2.5 × 2.5 mm^2 pixel size and good energy resolution of about 3.1 % at 122 keV. Its flux acceptance is around 10^6 counts/s [Verger *et al.*, 2007], [Montemont *et al.*, 2012], [Montemont *et al.*, 2003]. Energies below 20 keV cannot be detected. Only one pixel was irradiated during measurements.

The attenuated incident spectrum was measured by an energy resolving transmission detector[4]. The number of photons in the final diffraction spectra is about the same order of magnitude as in the salt simulations. Since, the spectra were acquired with a real system, the detector response, which partly distorts the spectrum, corresponds to a real response with a limited spectral resolution (the same as in simulations, i.e. MINIGAMI probe), but it also

---

[4] A CdTe detector of 800 × 800 μm^2 for high flux applications (up to $2 \cdot 10^7$ counts/s). Its energy resolution is about 5.5 % at 122 keV) [Brambilla *et al.*, 2009]. In fact, this is a prototype elaborate as part of the development of the detector ME100 from Multix.

presents the low-energy tail (Sec. I.1.3.4) caused by charge sharing and varying interaction depth.. However, for reconstruction the simple Gaussian detector response (sec. II.3.1) from simulations was used. The number of iterations of MLEM algorithm was fixed to 100 because convergence was slower than with simulated data. In fact, in the case of experimental spectra it cannot be expected to reconstruct theoretical Dirac Bragg peaks (except at 0 K) because of thermal oscillations of crystals. Hence, the distance between atomic planes oscillates, and reconstructed Bragg peaks present a certain width, that is not only due to number of iterations. Reconstruction results are **not averaged** since there was **only one measured spectrum** for each angle.
Figure III.7 shows the experimental mono- and multi-angle salt spectra, which are similar to the simulated ones (Fig. III.3) but less noisy due to higher detected photon number. As in simulations, the number of detected photons in the multi-angle spectrum (7500 detected photons) is significantly higher than at 2° (5100 detected photons) and at 5° (4700 detected photons). The spectrum at 5° presents an extra peak around 59 keV. This corresponds to a peak due to background scattering amplified by the source's characteristic rays (hypersensitivity). Possible sources of background scattering are scattering of surrounding air, scattering of the plastic recipient and impurities in the salt. Another difference compared to simulated spectra can be noticed especially for the spectrum at 2°. There is a non negligible number of photons detected at energies lower than 100 keV, which is not the case for simulated data at 2°. This is due to the low-energy tail part of the detector response.

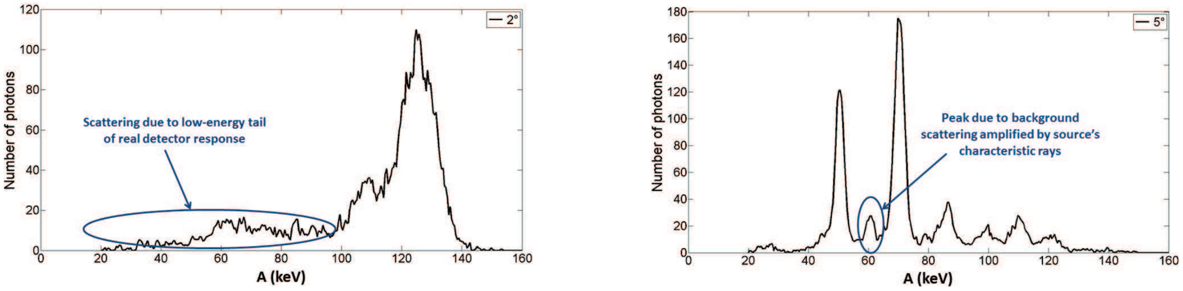

(a) *Measured mono-angle salt spectrum at 2°: 5100 detected photons.*

(b) *Measured mono-angle salt spectrum at 5°: 4700 detected photons.*

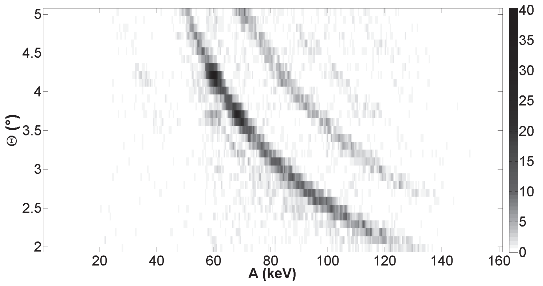

(c) *Measured multi-angle salt spectrum : 7500 detected photons.*

Figure III.7: Measured salt spectra that were used to test reconstruction methods.

Relative errors of the reconstructed relative peak amplitude are given in table III.6. As for simulations, relative errors on reconstructed relative peak intensities are much higher (up to 100 %) than for reconstructed peak positions. Multi-angle reconstruction allows to decrease the relative error except for the peak at 3.55 nm^{-1}, where it is increased from 25 % at 5° to 50 %. The peak at 2.51 nm^{-1} with 100 % relative error on relative peak amplitude at 5°, only presents around 9 % relative error for multi-angle reconstruction.

As in section III.1.3.1 for simulated data, an EDXRD system at 2° allows to measure and reconstruct the first two salt peaks (Fig. III.8) with less resolution than in simulated experiment. At 5°, the first peak is not reconstructed (same as in simulations), which was to be expected, as the system sensitivity is very low at this χ-value. However, the last peak is not reconstructed either. In fact, the detected intensity was too close to background scattering level and treated as noise during reconstruction process. Furthermore, an additional reconstructed peak can be observed. It corresponds to the peak due to hypersensitivity around 59 keV because of the characteristic rays of incident X-ray spectrum (see section II.3.1). Peak positions of the small peaks (relative intensity below 0.1) at higher momentum transfer values are not exact. They are shifted to smaller χ-values. This can be explained by inaccuracies in the system response used for reconstruction, e.g. the detector response (Gaussian approximation) and the angular resolution, which were obtained by simulation, as well as by impurities in the salt (this was not pure $NaCl$ but marine salt containing additional minerals). Though, relative errors of peak positions remain small (Tab. III.5). Most of them are below 1 %, and the highest relative error of peak position is still below 3 %. Multi-angle reconstruction allows to restore almost all salt peaks [Marticke *et al.*, 2014] but again with a shift in position to lower χ-values, and with missing peak at 4.3 nm^{-1}. The smoothed sensitivity of multi-angle systems (Sec. II.3.1) avoids the detection of background peaks due to the source's characteristic rays.

Theoretical Peak position (nm^{-1})	2°	5°	Multi-angle
1.53	0.65	**X**	0.65
1.77	0.56	0.56	0
2.51	**X**	0.8	0.8
3.07	**X**	0.65	0.65
3.55	**X**	1.13	0.85
3.96	**X**	1.77	2.78
4.34	**X**	**X**	**X**

Table III.5: Relative errors for peak positions of the different restored salt peaks using measured salt spectra. **X** means that the peak with not reconstructed at the considered angle.

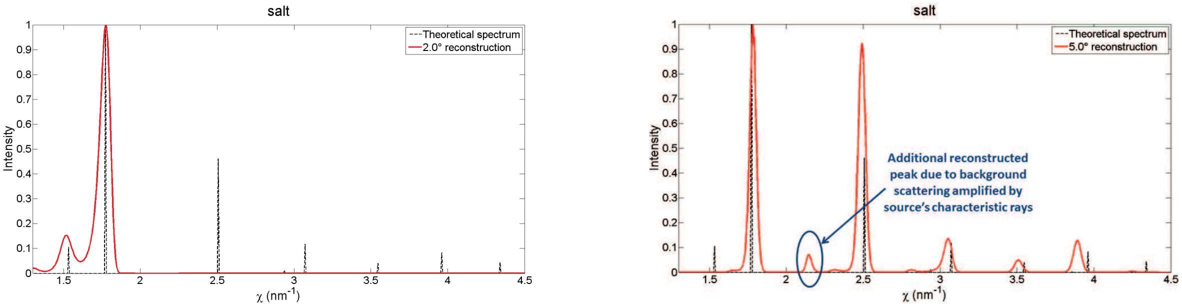

Additional reconstructed peak due to background scattering amplified by source's characteristic rays

(a) *Reconstructed salt peaks from experimental data at 2°.*

(b) *Reconstructed salt peaks from experimental data at 5°.*

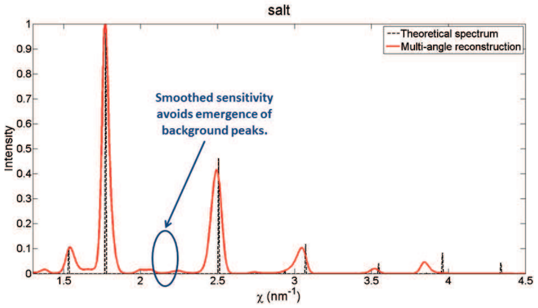

Smoothed sensitivity avoids emergence of background peaks.

(c) *Reconstructed salt peaks from experimental multi-angle data data.*

Figure III.8: Reconstructed salt peaks (red) for mono-angle systems at 2° (a) and 5° (b) and for multi-angle system (c) superimposed to theoretical peaks (dashed lines).

Theoretical relative peak amplitude	2°	5°	Multi-angle
0.11	36.36	**X**	0
1	0	0	0
0.46	**X**	100	8.69
0.12	**X**	16.67	16.67
0.04	**X**	25	50
0.08	**X**	62.5	37.5
0.04	**X**	**X**	**X**

Table III.6: Relative errors for relative amplitude of the different restored salt peaks using measured salt spectra. **X** means that the peak with not reconstructed at the considered angle.

These experimental results confirm the utility of the combination of EDXRD and ADXRD. It permits with the same incident photon statistic to get a higher number of detected photons than mono-angle systems. By the use of an energy- and spatial-resolving detector the acquisition time could be the same as in mono-angle case or even shorter if the number of detected photons is reduced to the number obtained with one scattering angle. It was confirmed that material signatures can be reconstructed in a larger χ-range as it was suggested by simulated data. Finally, the smoothed sensitivity profile of the multi-angle system helps to avoid background scattering peaks induced by the source's characteristic rays in mono-angle systems.

III.1.4 Reconstructed amorphous signatures

MLEM algorithm, tested on simulated crystalline spectra by [Rajaona, 2012], was validated on experimental data. In addition to this, MLEM-based multi-angle reconstruction was proposed. So far, MLEM algorithm has not yet been used to restore amorphous XRD signatures, which are continuous. Therefore some EXDRD spectra of different amorphous materials were simulated and experimentally acquired.

III.1.4.1 Simulated spectra

In the following, reconstruction results of simulated spectra of water and pork fat will be presented. These two amorphous materials were chosen because water and fat diffraction signatures play an important role in mammography application of EDXRD (Chap. IV).
Simulations are realized with $\theta = 3°$, the sample thickness is about 4 cm. Momentum transfer bins and energy bins were of the same size as in section III.1.3.1. The simulated system is represented in figure III.9 as well as its angular distribution, corresponding to sensitivity of the system to different scattering angles. System sensitivity is situated between 0.6 and 3.3 nm^{-1}. Spectra were simulated for only one detector pixel (yellow pixel in figure III.9) The number of photons in the simulated pork fat diffraction spectrum is about 700. This corresponds to a realistic photon number for targeted applications, which can be acquired within some seconds. Water spectrum was simulated with around 10^4 detected photons to have the same order of magnitude as in the experimental spectrum (Sec. III.1.4.2). Furthermore, this high difference in detected photon numbers allows at the same time to evaluate the impact of detected photon number, i.e. noise level, on reconstruction results. Relative noise (ration between noise and signal) in the case of Poisson noise is given by $\sqrt{N}/N = 1/\sqrt{N}$, where N is the number of photons. It can be considered for each measuring bin (N corresponds to the photon number in one channel.) or for the whole spectrum (N corresponds to the number of detected photons in the spectrum). Here, global relative noise will be considered.

As for crystalline spectra, 100 noisy spectra were simulated. The reconstruction results correspond to an average of reconstructed XRD pattern (after 100 iterations) of 100 simulated noisy spectra.

Figure III.10 shows examples of the simulated spectra. Global relative noise in the pork fat spectrum is about $1/\sqrt{700} \approx 0.04$ whereas global relative noise in simulated water spectrum is about $1/\sqrt{1.4 \cdot 10^4} \approx 0.009$. As expected, the pork fat spectrum is noisier than the water spectrum because. The two peaks in the water spectrum do not correspond to high scattering power at these energies but they are due to the characteristic rays of the incident X-ray source. In the pork fat spectrum only the peak around 59 keV can be clearly identified.

Figure III.11 shows the reconstructed molecular form factors (see section I.1.2.3) from simulated spectra in red, which are superimposed to the form factors given in the literature [Peplow and Verghese, 1998]. The water signature is very close to the one used to simulate

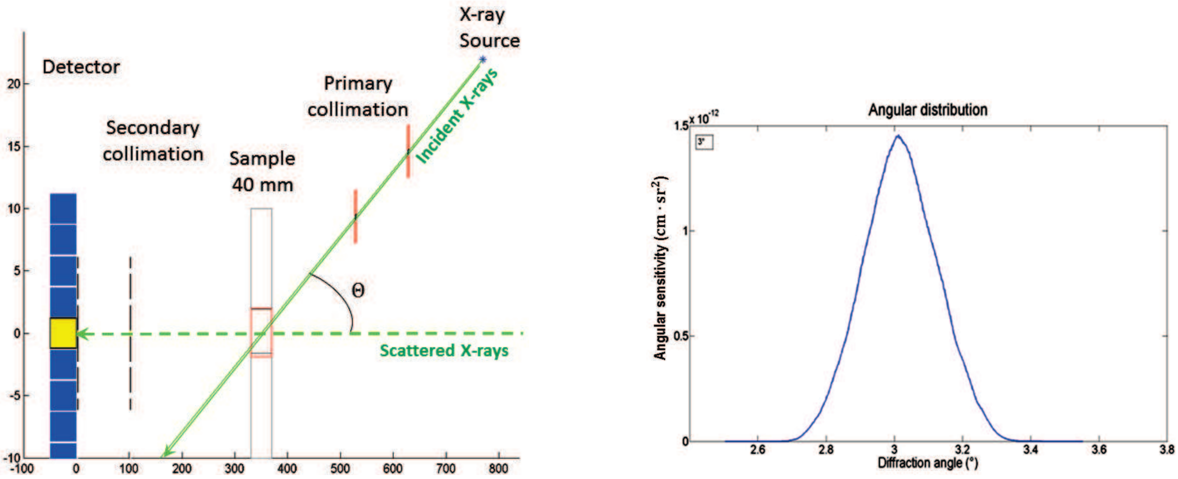

(a) *Schematic view of the system configuration. The scale is in mm in both directions.*

(b) *Angular distribution.*

Figure III.9: Schematic view of the system used to simulate amorphous spectra and the corresponding angular distribution. In fact, the angular distribution indicates to which scattering angles the considered system is sensitive. Signal was only considered on the yellow pixel.

the spectra. It only presents some weak oscillations and the relative error is only about 2.06 % (Eq. III.1.18, Tab. III.7). However, its standard deviation (light dotted lines) is relatively high (at the reconstructed main peak 0.17 ± 0.03). The reconstructed pork fat signature presents more oscillations than the reconstructed water spectrum and the principal maximum is not exactly at the expected χ-value. Its standard deviation is more important (0.3 ± 0.14 at the reconstructed maximum) than for water and the relative error [5] is about 13.65 %. Hence, higher relative noise in the spectrum to be restored seems to induce more noise in the reconstructed material signatures. Though, this is only one example, and further studies should be carried out to understand the impact of noise level on reconstruction results.

Despite the oscillations, the reconstruction results of simulated spectra using MLEM without a priori remain satisfying, as both tissue types could be separated using these reconstruction results.

III.1.4.2 Experimental spectrum

The experimental water spectrum was acquired at 3.4° and the scheme of the system configuration is represented in figure III.12.a. This system is sensitive to momentum transfer values between 0.7 and 3.7 nm^{-1}. Here again, the signal on only one pixel (yellow) was considered. The attenuated incident spectrum was measured by the same transmission detector as the salt spectrum in section III.1.3.2, and the detector response used for the reconstruction is the same as well. As only one water spectrum was measured, there is no average of reconstructed (100 iterations) experimental water spectra.

---

[5] Relative error is only calculated over the χ-range covered by system sensitivity: 0.6 to 3.3 nm^{-1}. Nb_χ was equal to 270.

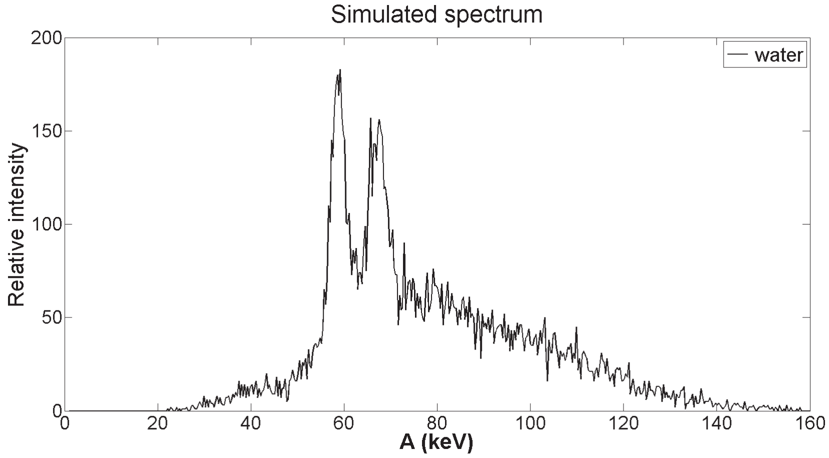

(a) *Simulated water spectrum at* 3°*:* $1.4 \cdot 10^4$ *detected photons.*

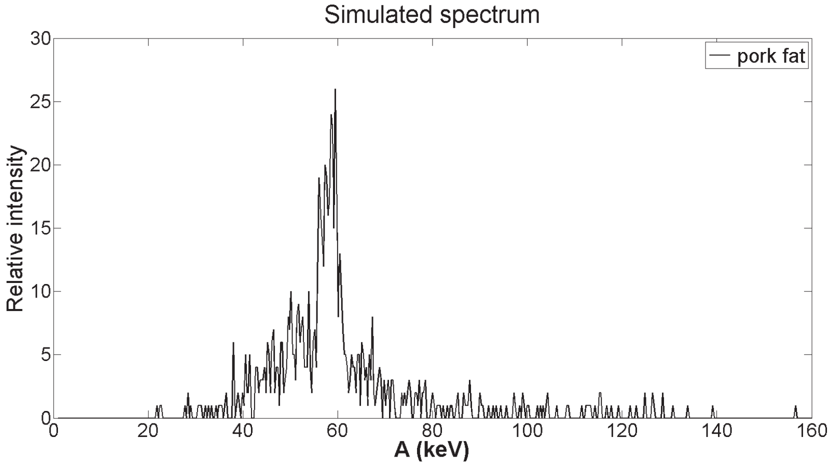

(b) *Simulated pork fat spectrum at* 3°*: 700 detected photons.*

Figure III.10: Simulated amorphous spectra. The characteristic rays of incident tungsten spectrum are clearly visible in the water spectrum. The pork fat spectrum only presents the peak at 59 keV.

The main difference between simulated and real acquisition system is the position of the secondary collimation, which is in contact with the detector for simulations, whereas it was situated at about 120 mm from the detector during experiments. By comparing figures III.9.a and III.12.a, it can be seen that the second range of slits is in contact (in fact, it is almost not visible on the scheme) with the detector in the first case, whereas it is not (well visible on the scheme) in the second case. Hence, system sensitivity and angular resolution are not exactly the same for the two systems. Sensitivity is higher for experimental set-up because the entire pixel can be illuminated whereas in simulations only a part (as big as the collimation slit) was illuminated. Angular resolution (Fig. III.12.b) is decreased because the range of detected angles is slightly increased.

The measured water spectrum is represented in figure III.13 and its shape is very similar to the simulated spectrum. Characteristic peaks of the incident source can be observed and there is almost no signal at energies higher than 140 keV. Its relative noise (about 0.004) is

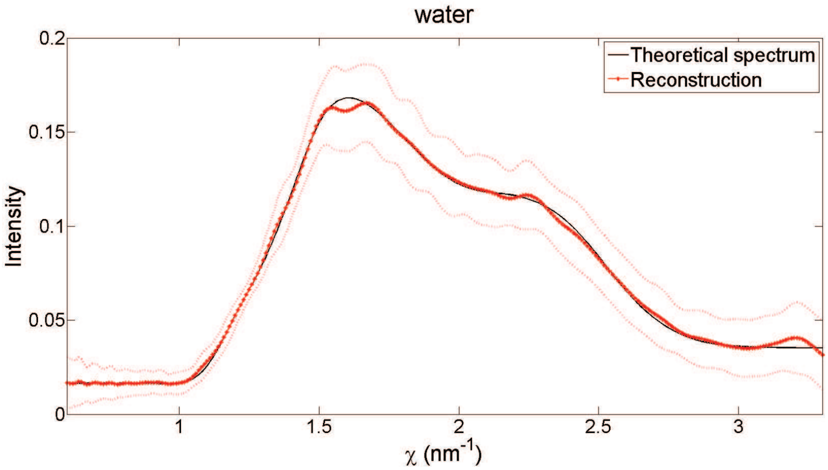

(a) *Averaged reconstruction of the simulated water spectrum at* 3°.

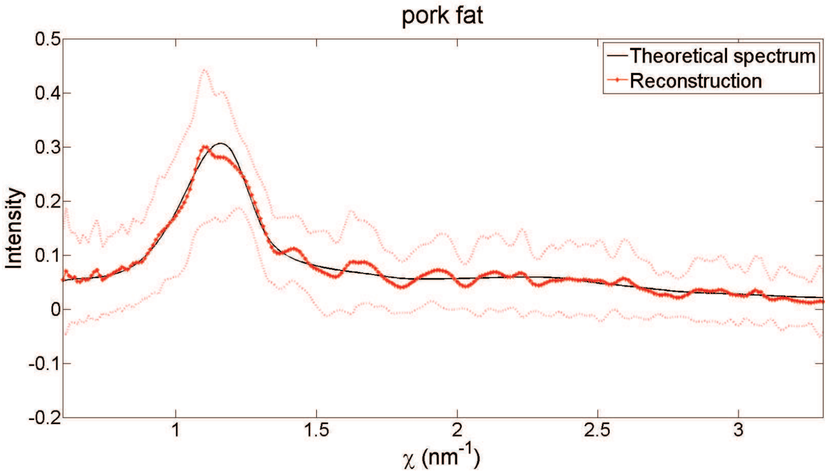

(b) *Averaged reconstruction of the simulated pork fat spectrum at* 3°.

Figure III.11: Averaged reconstructions (red) of simulated spectra using MLEM algorithm without a priori superimposed to the "theoretical" material signature (black). The light red lines correspond to the standard deviation. The reconstructions are oscillating especially for small photon statistics. Average was calculated over reconstructed signatures from 100 different simulated noisy spectra.

lower because the photon number is about six times higher than in the simulated spectrum.

The reconstruction result of the experimental water spectrum seen in figure III.14, presents strong oscillations. The structure of the water signature cannot be recognized. The relative error calculated from normalized reconstructed and "theoretical" molecular form factors is about 86.33 %.

As briefly mentioned in section III.1, amorphous spectra do not satisfy the condition of independence of momentum transfer bins and energy bins. Amorphous scattering signatures are continuous and the value in a given bin is not independent from values in the neighboring channels. The presented MLEM algorithm is based on the assumption of independent momentum transfer and energy bins. In fact, MLEM algorithm without a priori, assuming independence of the measuring bins, corresponds to reconstruction on a base of Dirac

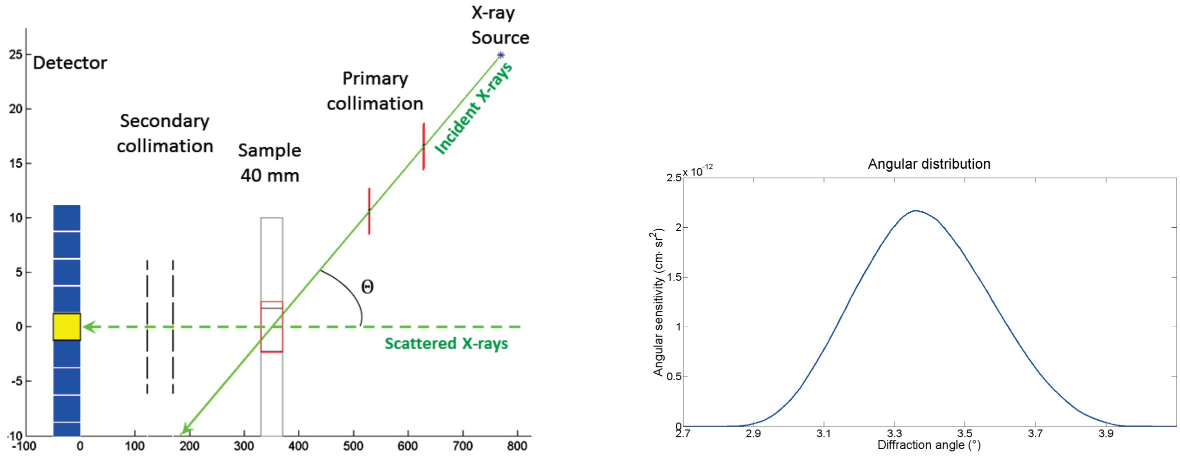

(a) *Schematic view of the system configuration. The scale is in mm in both directions.*

(b) *Angular distribution.*

Figure III.12: Schematic view of the system used to acquire water EDXRD spectrum and the corresponding angular distribution. In fact, the angular distribution indicates to which scattering angles the considered system is sensitive. Signal was only considered on the yellow pixel.

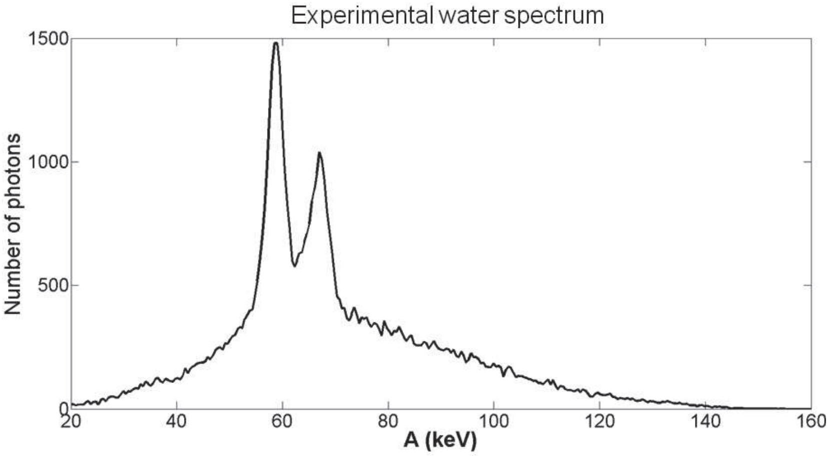

Figure III.13: Acquired water spectrum at 3.4°: $6.3 \cdot 10^4$ detected photons.

distribution. Reconstructed peak heights of neighboring bins are independent and hence, the reconstructed spectrum is not necessarily smooth. Therefore, reconstructed amorphous spectra using this algorithm are akin to present oscillations (Fig. III.11 and Fig. III.14).

The following section is dedicated to the proposition of regularization techniques allowing to smooth these oscillations in the reconstructed amorphous material signatures.

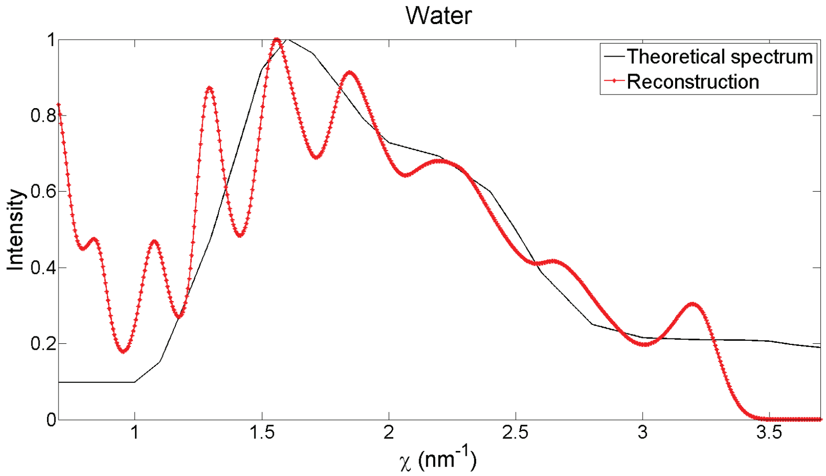

Figure III.14: Reconstruction (red) of the acquired water spectrum at 3.4° using MLEM algorithm superimposed to the ”theoretical” water molecular form factor. The reconstruction strongly oscillates and the water signature is not recognizable.

III.2 Regularization techniques for amorphous X-ray diffraction pattern reconstruction

As concluded in the previous section, MLEM algorithm without an a priori knowledge is not appropriate for deconvolution of continuous spectra due to non independence between the different energy and momentum transfer bins. In order to obtain smoother reconstruction results, two techniques are proposed. First, the idea to reconstruct the signal expansion on a given dictionary was considered. If the dictionary is chosen to be composed of ”smooth” components, then, this will allow to take into account the correlation between momentum transfer bins. Secondly, the introduction of a resolution kernel (similar to method of sieves in [Stute and Comtat, 2013]) has been tested. This solution permits to account for limited system resolution. Hence, apparition of oscillations, corresponding to details smaller than the system resolution, are avoided.

III.2.1 Use of a dictionary

III.2.1.1 Principle

The use of a dictionary in the MLEM algorithm, allows to introduce a prior on the shape of the signature to reconstruct. Reconstruction using a dictionary means that reconstructed spectra correspond to the projection of the original spectra on the dictionary, that was employed. The model of equation III.1.1 used during deconvolution has to be slightly modified.

Let $\mathcal{A} \in \mathbb{R}^{N \times L}$ be defined as:

$$\mathcal{A} = \mathcal{R} \cdot \mathcal{B} \tag{III.2.1}$$

where $\mathcal{B} \in \mathbb{R}^{M \times L}$ is the dictionary. Then, the model used for reconstruction can be written as:

$$\boldsymbol{\mathcal{M}} = \mathcal{A} \cdot \mathbf{c} \tag{III.2.2}$$

with $\mathbf{c} \in \mathbb{R}^L$ the projection coefficients on the elements of the base of the spectrum to be restored. Deconvolution is realized with MLEM algorithm using this model.

Using this modified model, equation III.1.17 becomes:

$$c_l^{n+1} = c_l^n \frac{1}{\sum_{j=1}^N A_{jl}} \sum_{j=1}^N \left(\frac{m_j A_{jl}}{\sum_{l'=1}^L A_{jl'} c_{l'}^n} \right) \tag{III.2.3}$$

In order to obtain the researched spectrum, it is necessary to reproject the reconstructed data. Hence, the reconstructed signature is given by:

$$\mathbf{F} = \mathcal{B} \cdot \mathbf{c} \tag{III.2.4}$$

The dictionary may consist of "theoretical" (measured reference spectra) diffraction spectra of different amorphous materials or of purely mathematical continuous functions. In the following paragraphs these two types of dictionaries will be explained.

III.2.1.1.1 Amorphous dictionary

In the case of a dictionary composed of reference spectra of amorphous materials, i.e. molecular form factors, the reconstruction process corresponds to a decomposition of the measured spectrum on the elements of the dictionary. Thus, this technique can also be used to classify the measured spectrum (E.g. an acquired spectrum of breast tissue and a dictionary composed of healthy breast tissue and cancerous breast tissue. If the projection coefficient of cancerous tissue is significantly higher than the one of healthy tissue, the inspected sample will be classified as cancerous.). An example of such a dictionary is represented in figure III.15. The first nine components of the dictionary are very similar. In fact, these are all materials containing a great deal of water. Thus, their molecular form factor is very similar to the one of water. It seems not necessary to include all these elements in the dictionary as the information is redundant (especially elements five to nine).

Though, it is difficult to create such a dictionary since there is no complete database of molecular form factors of amorphous materials. The only ones that are known (see sec. I.1.2.3) are measured and not exact. Differences in the spectra can be seen by comparing results of different articles. The water spectra in [Peplow and Verghese, 1998] and [King and Johns, 2002] are not exactly the same, they are slightly shifted (Fig. III.16). Another problem is that there are only very few (about twenty) molecular form factors that have been measured and it might be possible that the measured spectrum cannot be decomposed on the different elements of the dictionary. The quality of reconstruction will depend on the materials that are used in the dictionary. Therefore, it is interesting to consider a mathematical dictionary which will not depend on the prior knowledge of theoretical spectra of all amorphous materials.

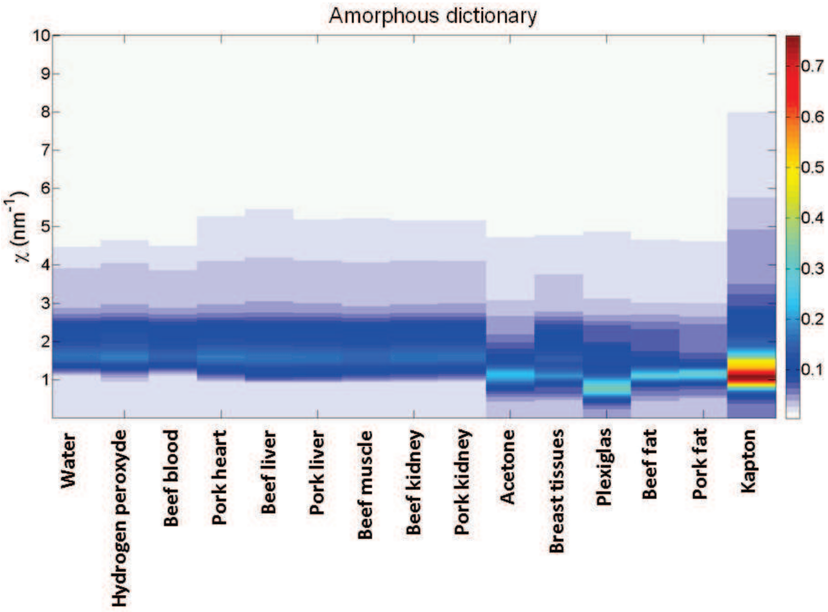

Figure III.15: Example of a dictionary using amorphous molecular form factors of different materials. The first nine elements of the dictionary are very similar. In fact, these materials all contain a great deal of water, and their XRD signatures are very similar to water signature.

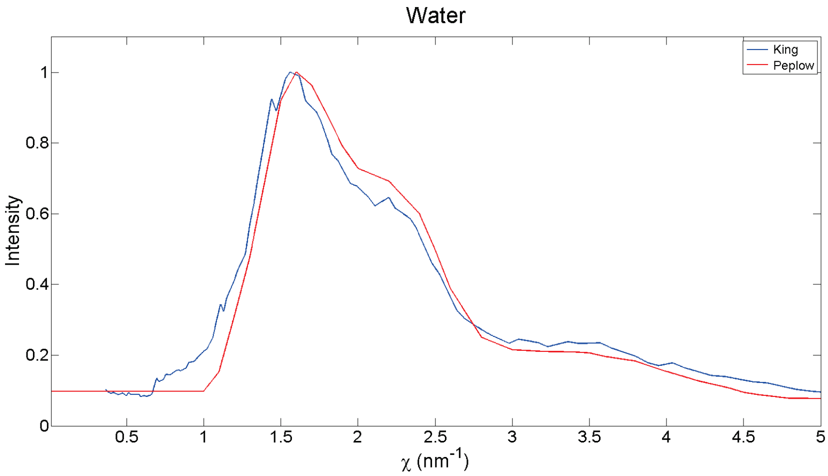

Figure III.16: Two determined water spectra. The blue one corresponds to the spectrum measured by [King and Johns, 2002] and the red one was measured by [Peplow and Verghese, 1998]. They are very similar but the principal maximum is slightly shifted.

III.2.1.1.2 Mathematical dictionary

A mathematical dictionary is composed of continuous mathematical functions instead of molecular form factors. The functions that have been tested are Lorentzian functions because the shape of amorphous spectra especially those of acetone and fat is similar to a Lorentzian distribution. A Lorentzian (or Cauchy) distribution is defined as:

$$\mathcal{L}(x) = \frac{\Gamma}{2\pi} \frac{1}{\left(\frac{1}{2}\Gamma\right)^2 + (x - x_0)^2} \tag{III.2.5}$$

with x_0 the center and Γ the full width at half maximum (FWHM). To construct the dictionary, it is necessary to set x_0 and Γ. x_0 corresponds to different values of χ and they are sampled between 0.01 and 10 nm^{-1} at a 0.1 nm^{-1} step. Γ values were estimated by fitting each theoretical amorphous spectrum by a linear combination of Lorentzian functions. Initial values of the x_0 and Γ, to be determined during interpolation, were set to one.

For water interpolations with different numbers of Lorentzian functions (one to five different Lorentzian functions) were tested. Figure III.17 shows the estimated Lorentzian parameters for water signature. The best reproduction of the shape of the water signature was obtained for interpolation with two Lorentzian functions. Hence, interpolation with two Lorentzian functions was realized for XRD pattern of the other amorphous materials. Examples of the estimated parameters are represented in figure III.18. All estimated parameter couples (x_0, Γ) are plotted in a graph (Fig. III.19). This allowed to estimate the most common FWHM. It is also possible to vary Γ as a function of x_0 but in this work Γ was kept the same for each x_0. Γ values of about 0.2 nm^{-1}, 0.3 nm^{-1} and 0.5 nm^{-1} seem suitable as several estimated Γ are close to these values. Figure III.20 shows an example of such a dictionary.

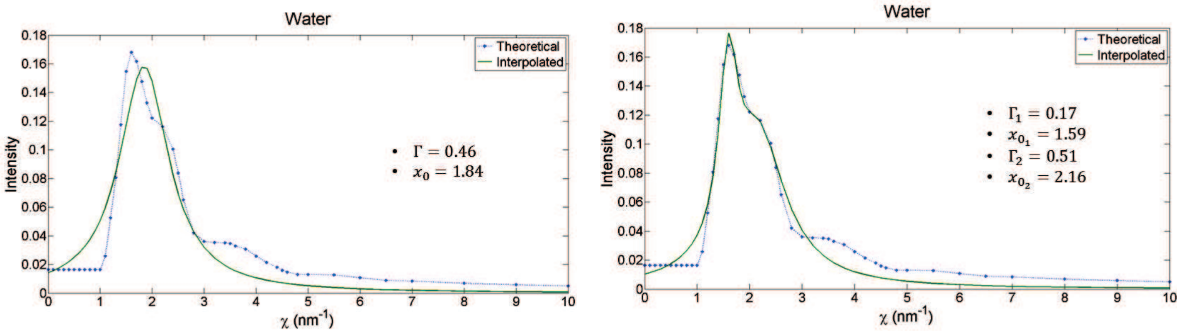

(a) *One Lorentzian function.* (b) *Two Lorentzian functions.*

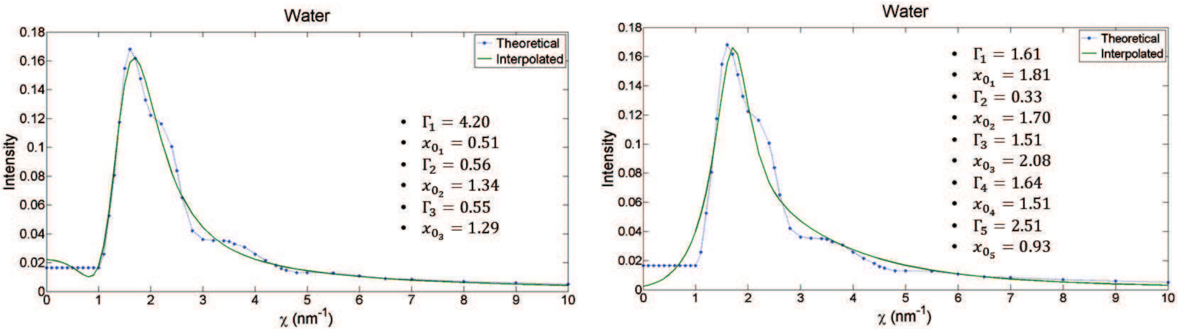

(c) *Three Lorentzian functions.* (d) *Five Lorentzian functions.*

Figure III.17: Interpolated water signatures (blue dotted lines) using linear combinations of different numbers of Lorentzian functions, and the associated estimated parameters. The green continuous line corresponds to the reference water diffraction pattern. Interpolation with two Lorentzian functions leads to best reproduction of water signature shape.

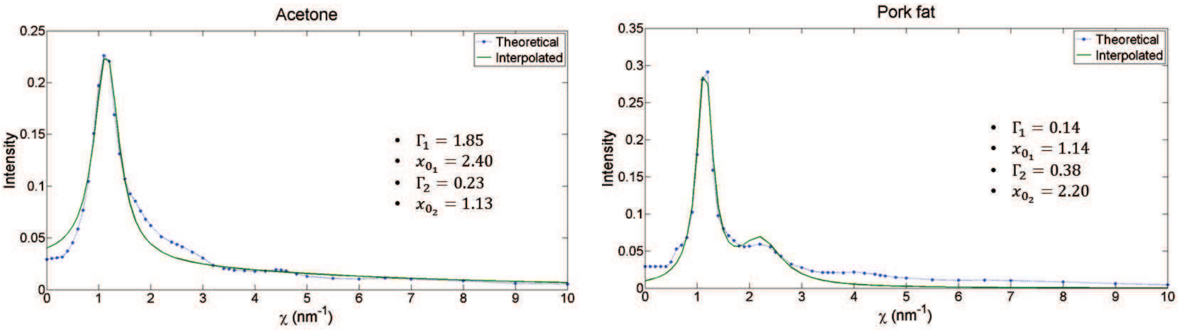

(a) *Acetone.* (b) *Pork fat.*

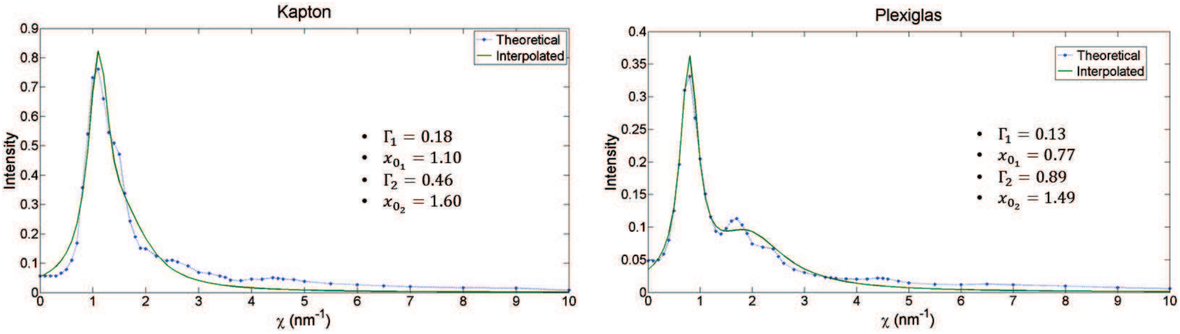

(c) *Kapton.* (d) *Plexiglas.*

Figure III.18: Interpolated signatures (blue dotted lines) of different materials using a linear combination of two Lorentzian functions, and the associated estimated parameters. The green continuous line corresponds to the reference water diffraction pattern.

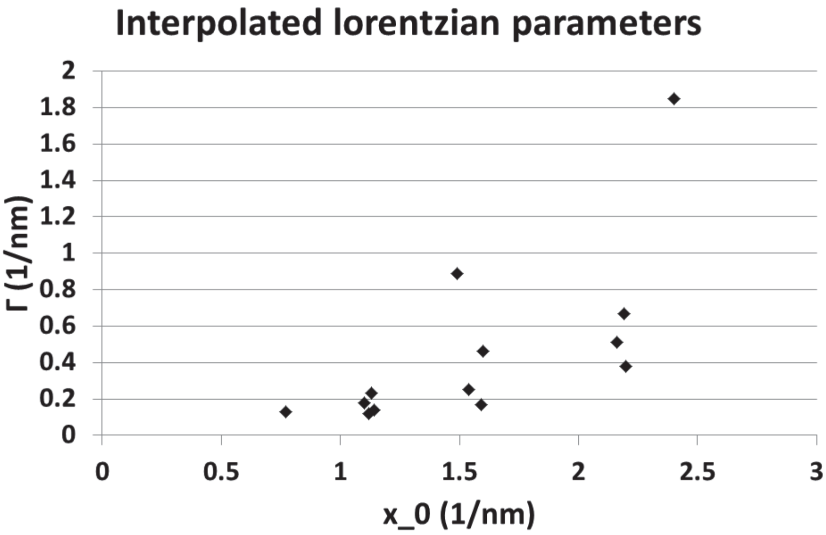

Figure III.19: Plot of estimated parameters for interpolation of amorphous XRD signatures using two Lorentzian functions.

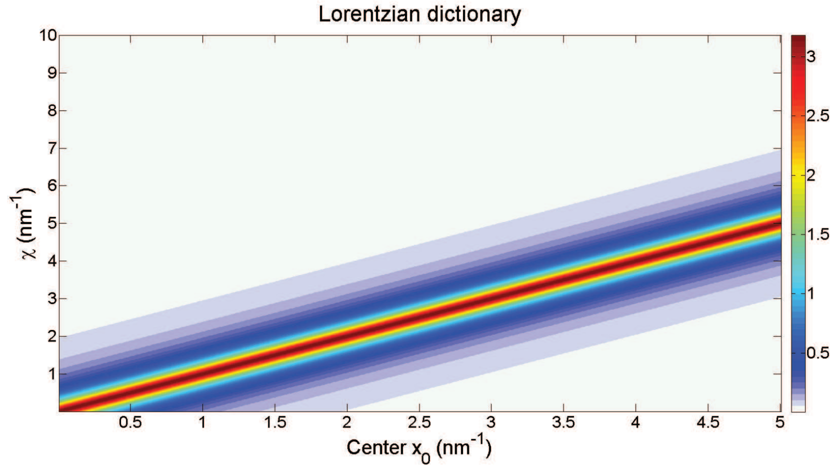

(a) *Lorentzian dictionary matrix.*

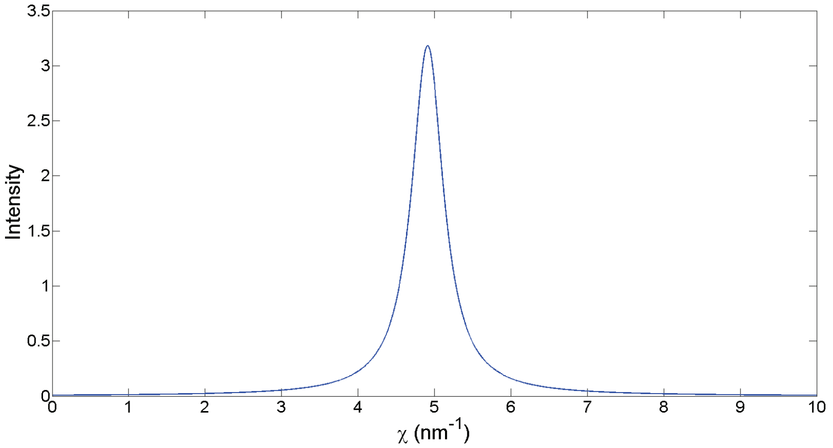

(b) *Profile for one x_0 value.*

Figure III.20: Example of a Lorentzian dictionary with $\Gamma = 0.2nm^{-1}$.

III.2.1.2 Reconstructed signatures using an amorphous dictionary

The use of an amorphous dictionary for reconstruction of amorphous XRD signatures was tested on the same spectra as previously (Sec. III.1.4). Reconstruction was always realized with a dictionary that did not contain the material to be reconstructed.

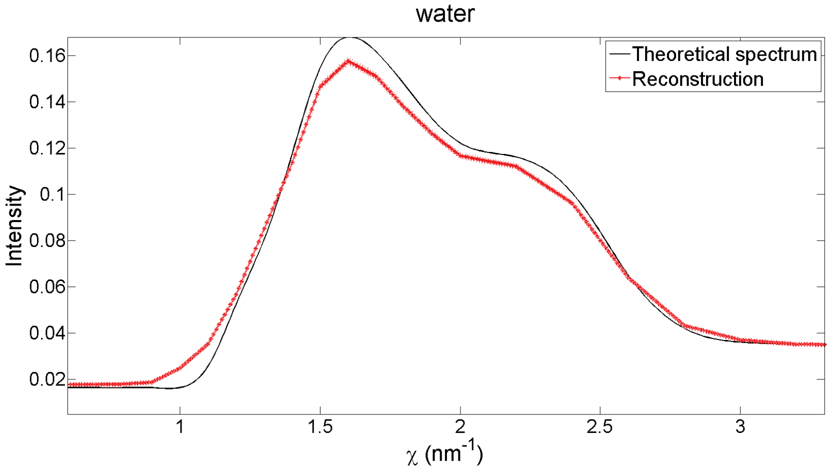

(a) *Averaged reconstruction of the simulated water spectrum at* 3°.

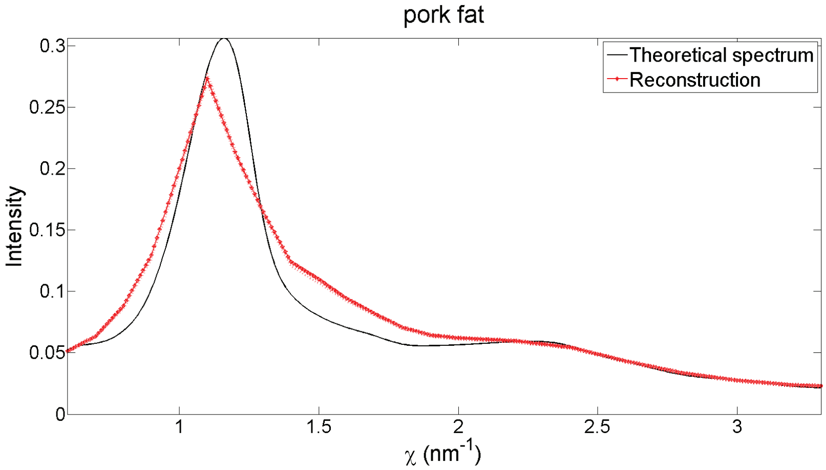

(b) *Averaged reconstruction of the simulated pork fat spectrum at* 3°.

Figure III.21: Averaged reconstructions (red) of simulated spectra using an amorphous dictionary superimposed to the "theoretical" material signature (black). The light red lines correspond to the standard deviation. The water signature is well reconstructed but the pork fat signature is shifted to lower momentum transfer values. In fact, this corresponds to the peak of beef fat (Fig. III.22). Hence, reconstruction results strongly depend on the elements that are part of the amorphous dictionary used to reconstruct.

Reconstructed water and pork fat signatures are represented in figure III.21 (average over reconstructions of 100 different noisy spectra after 100 iterations). Water signature was well reconstructed but as there is a loss of intensity for the main maximum, the relative error is about 7.46 % and thus, higher than with basic MLEM algorithm. Though, there is no oscillation at all and the standard deviation is so small that it is almost superimposed to the mean reconstructed form factor. Pork fat reconstruction is also very smooth and its standard deviation is also small. The relative error is slightly smaller than with MLEM method. However, the principal rebound is shifted to lower χ values. In fact, this could be due to the fact that the base contained beef fat, whose main peak is at lower momentum transfer values (Fig. III.22). This shows, that reconstruction results strongly depend on the elements that are part of the dictionary, which was to be expected.

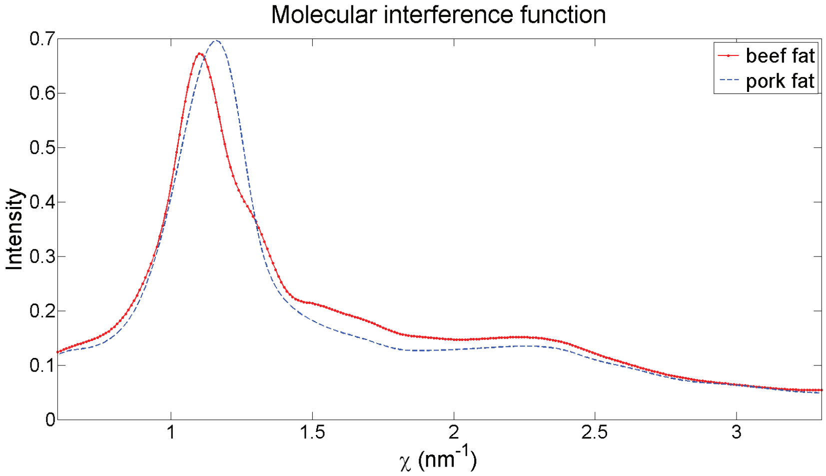

Figure III.22: Comparison between pork and beef fat molecular form factors.

The reconstruction result of the experimental spectrum is shown in figure III.23 (100 iterations). The characteristic shape of the water spectrum is well reconstructed without oscillations, and especially for χ values higher than 1.4 nm^{-1}, the reconstructed water signature is very close to the "theoretical" one. The relative error is about 60.84 %, which is smaller than with MLEM reconstruction but remains still high. However, the shape is much more recognizable than previously.

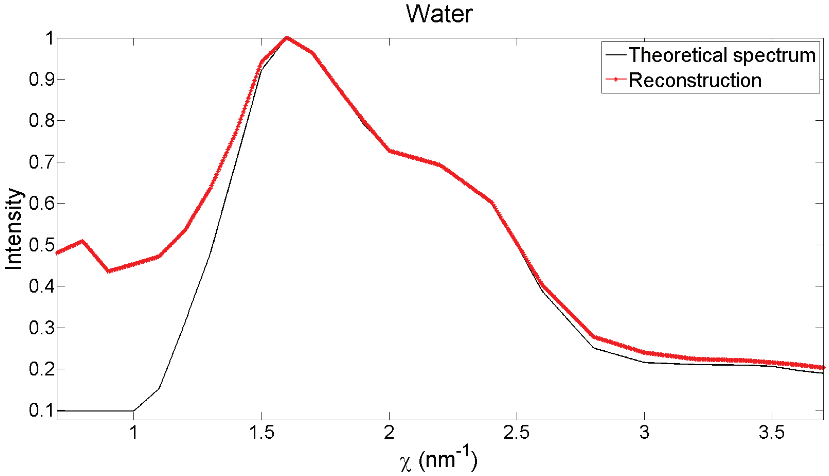

Figure III.23: Reconstruction of the water signature from experimental data at 3.4° using an amorphous dictionary. For χ values higher than 1.4 nm^{-1} water signature is well reconstructed. Relative error is mostly due to the reconstruction part at low momentum transfer values.

Many of the dictionary's elements are very similar to water signature. Thus, this method seems to be suitable if the material is similar to the dictionary elements, even for experimental data. It might even be used for material detection if the XRD signature to reconstruct is included in the dictionary. In fact, this is the case for application of XRD in mammography. There are only a limited number of tissue types and if each tissue type is part of the dictionary, the different tissues can be detected.

If the XRD pattern to be restored is not similar to the elements in the dictionary, the reconstruction result might be deformed. That is why the possibility of a more ”neutral” mathematical dictionary was considered.

III.2.1.3 Reconstructed signatures using a Lorentzian base

Different types of Lorentzian dictionaries have been tested. The simplest one is the one that is represented in figure III.20 with one unique Γ for all χ ($\Gamma = 0.2nm^{-1}$). A base with $\Gamma = 0.1nm^{-1}$ was also tested. This type of dictionary will be referred to as two-dimensional as it is stored in a 2D matrix (one dimension for χ-values and one dimension for x_0 values). A three-dimensional dictionary is stored in a 3D matrix (one dimension for χ-values, one dimension for x_0 values associated to one value of Γ and one dimension for x_0 values associated to a second value of Γ). In the first case, a linear combination of Lorentzian functions with the same Γ value and different x_0 values is determined during reconstruction. In the second case, a linear combination of Lorentzian functions with two possible Γ values at each value of x_0 is used to reconstruct the amorphous XRD pattern.

More complex and higher dimensional bases were tried:

- Three dimensional dictionary: Two Γ values were assigned to each momentum transfer value ($\Gamma = 0.2nm^{-1}$ and $\Gamma = 0.5nm^{-1}$)
- Four dimensional dictionary: Three Γ values were assigned to each momentum transfer value ($\Gamma = 0.1nm^{-1}$, $\Gamma = 0.3nm^{-1}$ and $\Gamma = 0.5nm^{-1}$)
- Five dimensional dictionary: Four Γ values were assigned to each momentum transfer value ($\Gamma = 0.1nm^{-1}$, $\Gamma = 0.2nm^{-1}$, $\Gamma = 0.3nm^{-1}$ and $\Gamma = 0.5nm^{-1}$)

Only the best reconstruction results (in terms of relative error) are represented, which are obtained with two-dimensional dictionary with $\Gamma = 0.1nm^{-1}$ for each of the three spectra to reconstruct. The other results are summarized in table III.7 at the end of the chapter, which gives the relative error for each reconstruction. If the dictionary was too high dimensional, the results deteriorated. Only one relatively narrow peak similar to a Lorentzian curve was reconstructed. Figure III.24 shows the restored water and pork fat signatures from simulated spectra (average over reconstructions of 100 different noisy spectra after 100 iterations) and figure III.25 water signature (after 100 iterations) from experimental data. Restored signatures from simulated spectra do not present oscillations and are very close to the one that was used to simulate spectra, and the relative errors are very small: 3.18 % for pork fat and 2.3 % for water. Standard deviation of reconstructions is very low for water (at estimated maximum: 0.17 ± 0.007) and noticeable higher for pork fat (at estimated peak: 0.27 ± 0.02). However, since the shape of the standard deviation is the same as the signature’s shape, this is still acceptable (under 10 %).

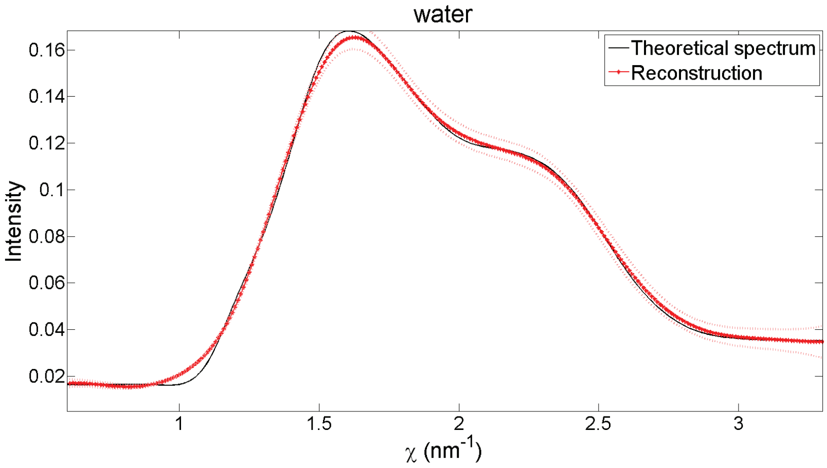

(a) *Averaged reconstruction of the simulated water spectrum at 3°.*

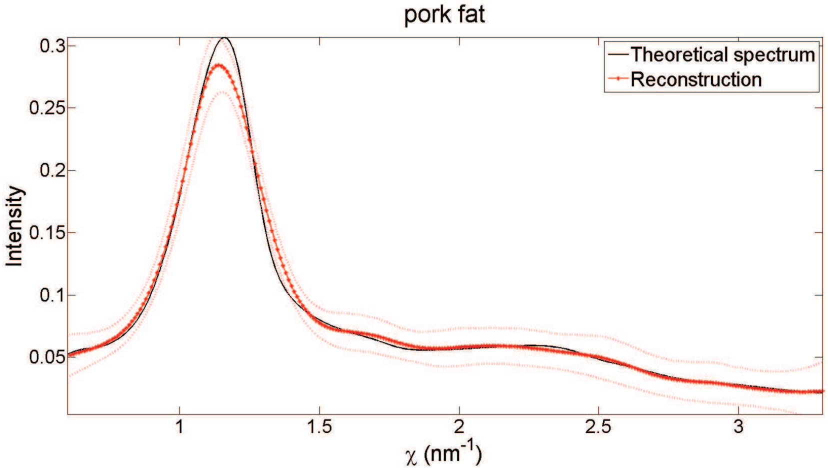

(b) *Averaged reconstruction of the simulated pork fat spectrum at 3°.*

Figure III.24: Averaged reconstructions (red) of simulated spectra using a Lorentzian base with $\Gamma = 0.1nm^{-1}$ superimposed to the "theoretical" material signature (black). The light red lines correspond to the standard deviation. The molecular form factors are well reconstructed. However, there is a loss of the reconstructed intensity.

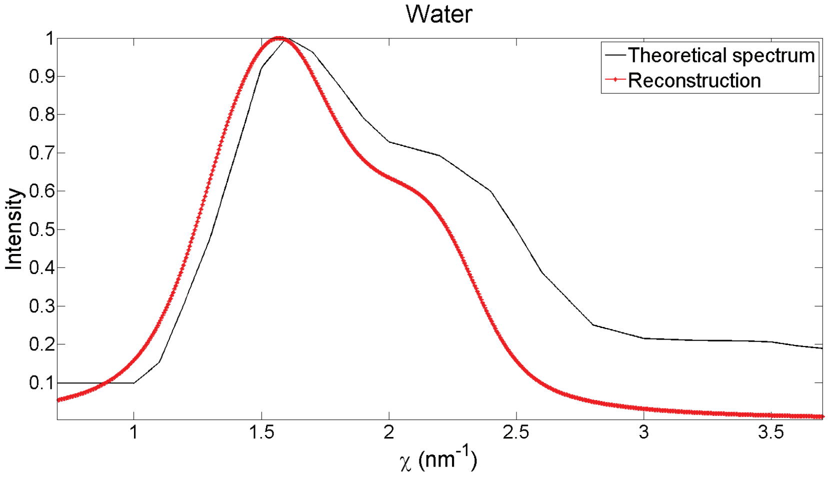

Figure III.25: Reconstructed water signature (red) from experimental data at 3.4° employing a Lorentzian base. The shape of the signature is well restored but there is a shift between the reconstructed form factor and the one given by [Peplow and Verghese, 1998] (black).

The reconstructed molecular form factor using the measured water spectrum is very smooth and its shape is very similar to the water signature given in literature ([Peplow and Verghese, 1998]). The relative error is about 50.74 %, which is still high but smaller than in the case of an amorphous base. However, the reconstructed signature seems to be shifted to lower χ values. Since the "theoretical" signature is also the result of experiments, there might also be some inaccuracies in peak positions. If the reconstructed form factor is superimposed with the one determined by [King and Johns, 2002], there is no shift anymore (Fig. III.26). One possible explanation for this difference might be different acquisition temperatures, which could lead to different mean distances between the molecules [Narten *et al.*, 1967] and thus, to slightly different diffraction maxima. Another explanation could be a difference in water purity between the two studies.

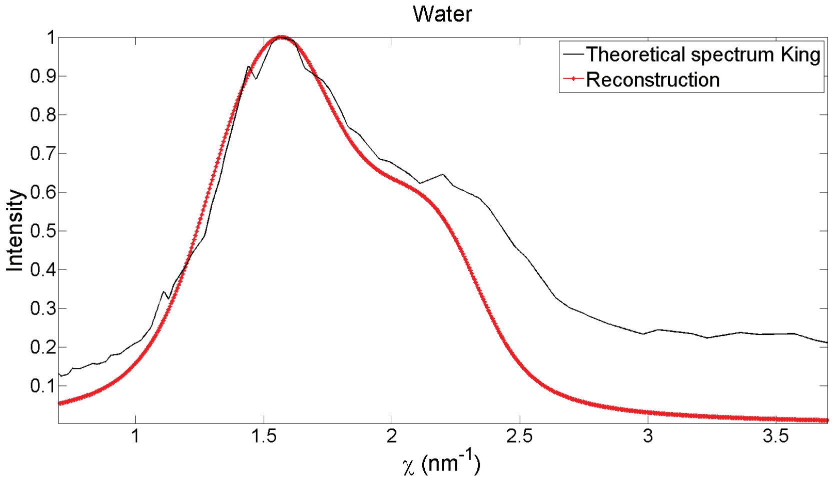

Figure III.26: Superposition of the reconstructed water form factor using the experimental spectrum at 3.4° by the Lorentzian base technique with the water signature give by [King and Johns, 2002] (black). There is no shift between them.

The use of a Lorentzian dictionary to reconstruct amorphous spectra seems to be a well adapted technique even though the relative error in the experimental case remains high. However, the choice of the Γ values is based on values estimated by interpolation of only a few amorphous materials, and it was chosen more or less arbitrary among these values. It might not be the same for any amorphous spectrum. That is why it would be interesting to use a technique, that could be parameterized by parameters of the acquisition system. This is the idea behind the use of a resolution kernel.

III.2.2 Reconstruction with a resolution kernel

III.2.2.1 Principle

This method consists in limiting the possible solutions to a subset in the space of all solutions, where components above a certain frequency cannot exist. In practice, each estimate $\mathbf{F}^{n+1}$ is filtered by a Gaussian (low-pass) filter before reiterating the algorithm (Fig. III.27). A Gaussian filter is a filter whose impulse response is a Gaussian function. Application of a Gaussian filter means that the initial signal is convolved with a Gaussian function. As its

Fourier transform is also a Gaussian function, application of a Gaussian filter induces the reduction of the signal's high-frequency components. This is why it is called a low-pass filter. Only low frequencies can pass. Oscillations in reconstructed amorphous XRD pattern correspond to high-frequency components. The use of the resolution kernel is meant to avoid their emergence.

Equation III.1.17 is modified by integration of the filtering step to:

$$F_k^{n+1} = F_k^{n'} \frac{1}{\sum_{j=1}^{N} R_{jk}} \sum_{j=1}^{N} \left(\frac{m_j R_{jk}}{\sum_{k'=1}^{M} R_{jk'} F_{k'}^{n'}} \right) \tag{III.2.6}$$

where

$$F_k^{n'} = \mathcal{K} \cdot F_k^n \tag{III.2.7}$$

with $\mathcal{K} \in \mathbb{R}^{N \times N}$ is the Gaussian kernel matrix

In order not to filter arbitrary frequencies, the kernel width is determined using the point spread function (PSF) of the system, which describes the response of the system to a point source or a point object. As the system response depends on the momentum transfer χ, the kernel's standard deviation varies with χ values. This procedure ensures that the reconstructed spectrum does not contain frequencies that cannot be resolved by the used system.

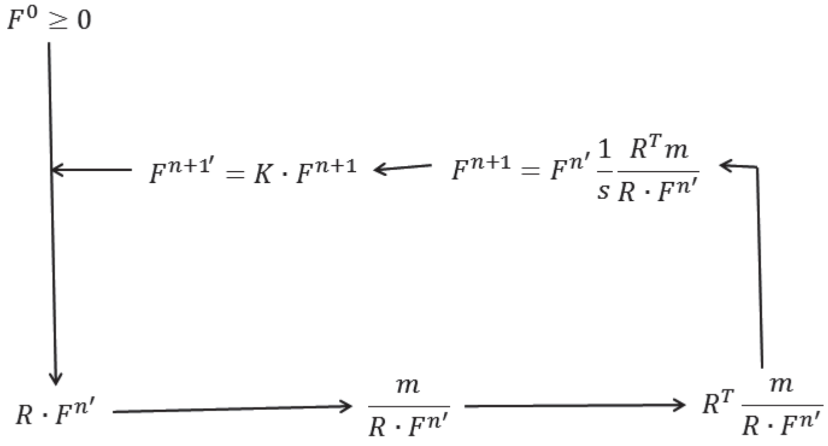

Figure III.27: Schematic representation of MLEM algorithm using a resolution kernel: Each estimate $\mathbf{f}^{n+1}$ is convoluted by the resolution kernel K before reiterating.

Figure III.28 shows an example of a resolution kernel.

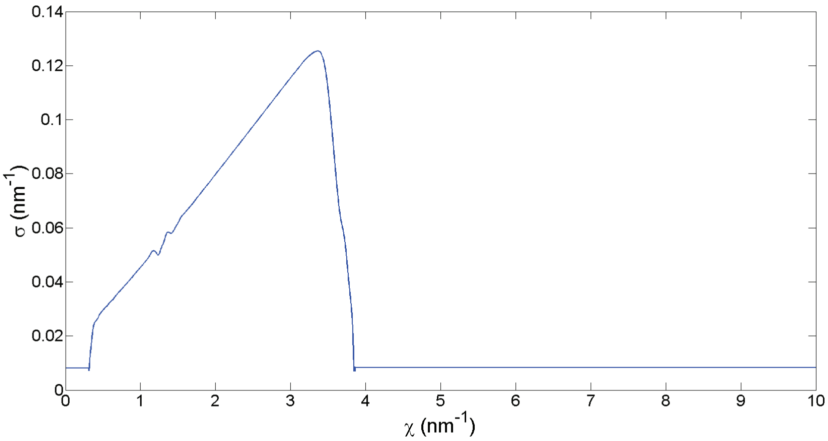

(a) *Kernel width as a function of* χ

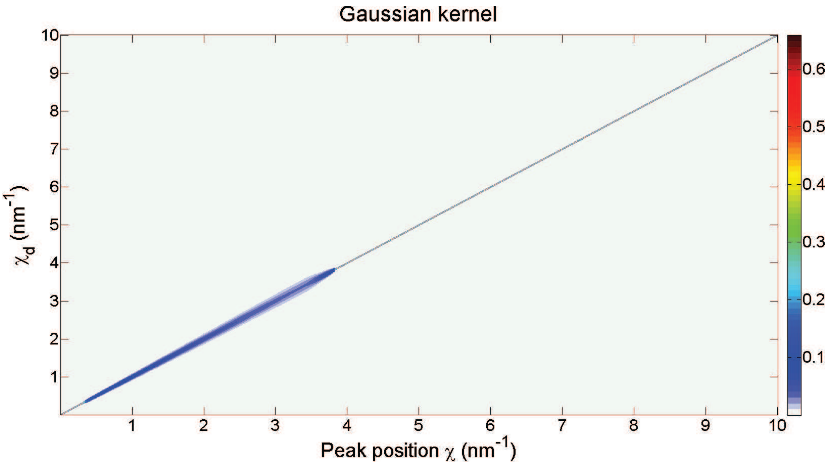

(b) *Gaussian kernel*

Figure III.28: Example of a Gaussian kernel with varying kernel width

III.2.2.2 Reconstructed signatures using a resolution kernel

The reconstruction results of simulated water and pork fat spectra (Fig. III.29) are satisfying and the relative error is very small, i.e. 3.97 % for pork fat and only 1.15 % for water (best water reconstruction result). However, the principal maximum presents a shift in both cases (to higher χ-values for water and to lower χ-values for pork fat), which is also visible in the standard deviation curves. This might be due to a problem of normalization of the resolution kernel, which leads to a loss of energy in the reconstructed data. Further investigations have to be realized in order to resolve this problem.

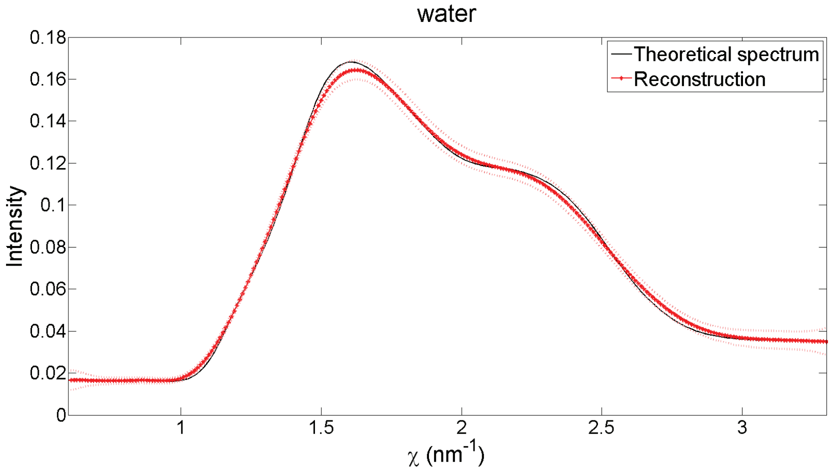

(a) *Averaged reconstruction of the simulated water spectrum at* 3°.

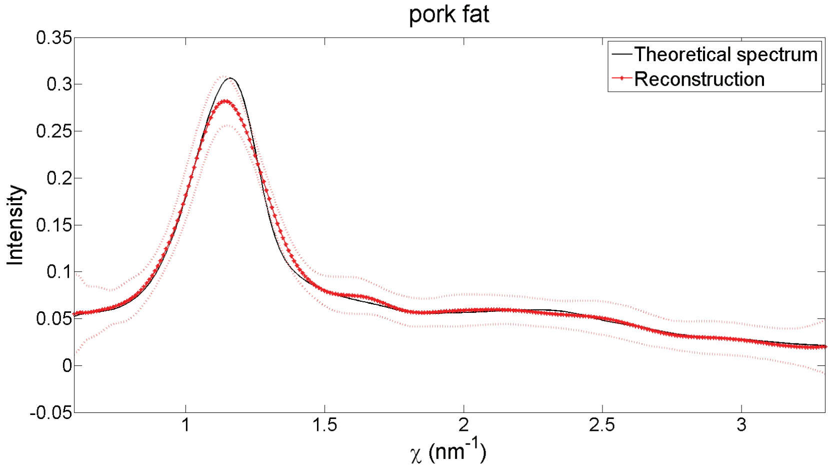

(b) *Averaged reconstruction of the simulated pork fat spectrum at* 3°.

Figure III.29: Averaged reconstructions (red) of simulated spectra using a variable Gaussian resolution kernel superimposed to the "theoretical" material signature (black). The light red lines correspond to the standard deviation. The reconstruction results are satisfying but there is a light loss of intensity and the main maxima are slightly shifted.

The reconstructed experimental spectrum (Fig. III.30 corresponds to the average of the reconstructions after 100 iterations of 100 different noisy spectra) is free of oscillations but it is very broad and does not present the characteristic shape of the water signature. The relative error is about 105.19 % (Tab. III.7), which is even higher than with MLEM algorithm without a priori. It seems that the width of the kernel used for reconstruction was not suitable (underestimated system resolution). In fact, the system response, that was used to estimate the PSF and thus, the kernel width, is based on the acquired attenuated incident spectrum, the simulated collimation response and a Gaussian detector response. It is possible that the simulated collimation response does not exactly match the response of the acquisition system (not exactly the same angle, not exactly the same angular aperture). Furthermore, the use of a Gaussian detector response is too simplistic. This is illustrated by figure III.31, which shows the experimental spectrum and the simulated spectrum that would be obtained (without noise) with the system response, used to reconstruct the measured data. The two spectra are very similar for energies higher than 57 keV but the simulated spectrum is clearly lower than the measured spectrum at low energies. This is due to the neglected low energy tail in the detector response and the simulated collimation response. A more realistic system response should be employed to reconstruct experimental data.

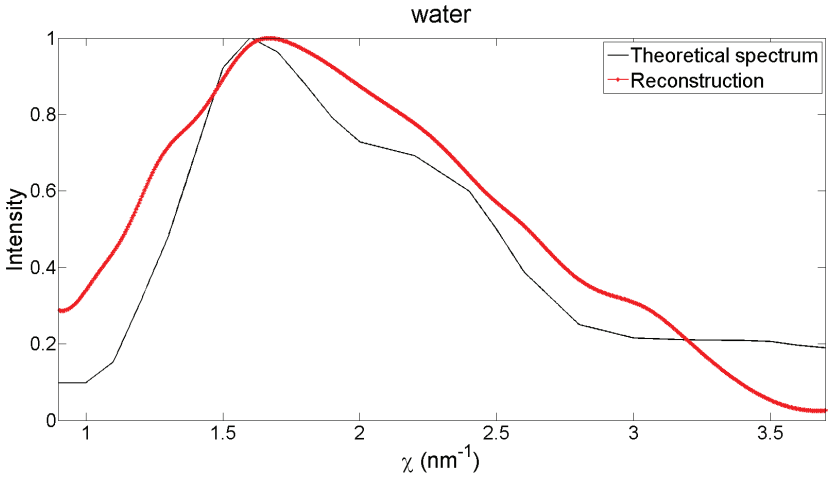

Figure III.30: Reconstructed experimental water spectrum (red) using a variable Gaussian resolution kernel superimposed to the theoretical water signature (black). It seems that the resolution kernel is too strong because the shape of the water signature is almost completely lost. This might be due to the system response matrix used for reconstruction that was not exact.

The use of a resolution kernel seems to be a good alternative to the use of a dictionary, to reconstruct amorphous spectra if the system response is well known (simulated spectra). However, the problem of the shift of the reconstructed signature is still present and should be resolved. If the system response is not exactly known (experimental data), the reconstruction result will not be satisfying. Hence, this technique seems not to be suitable for the moment. The different parts of the system response have to be better determined in order to obtain a more suitable resolution kernel.

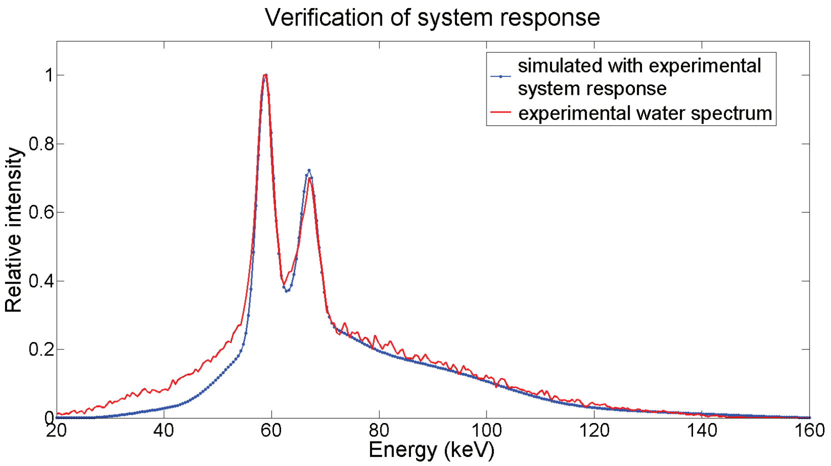

Figure III.31: Comparison between the acquired water spectrum and the one that would be obtained with the system response, which was used for reconstruction. It can be seen that the number of photons at low energies is underestimated because of neglecting the low energy tail in the detector response.

Method	pork fat	water	water (experimental)
MLEM	13.65	2.06	86.33
Amorphous base	10.75	7.46	60.84
2D Lorentzian ($\gamma = 0.2$)	8.54	10.79	93.44
2D Lorentzian ($\gamma = 0.1$)	3.18	2.3	50.74
3D Lorentzian	9.02	11.31	89.17
4D Lorentzian	4.32	4.7	101.64
5D Lorentzian	10.62	11.15	157.96
Resolution kernel	3.97	1.15	105.19

Table III.7: Summarizing table of relative errors (in %) obtained with the different reconstruction methods.

III.3 Conclusion

This chapter was dedicated to reconstruction of EDXRD spectra. The present work uses a maximum likelihood expectation maximization approach. MLEM algorithm ensures positive reconstruction results if positive initialization is introduced. It is based on the hypothesis of independence of the different energy/momentum transfer bins. This condition is satisfied for crystalline spectra that only present a few diffraction peaks, whereas it is less true for continuous amorphous spectra.

MLEM reconstruction algorithm was tested on simulated and experimentally acquired crystalline spectra (salt and TNT) and amorphous spectra (pork fat and water).

The reconstructed Bragg peaks using MLEM algorithm are satisfying for simulated and acquired data, as the peaks are at the right χ value (relative errors mostly around 1 % or less) even though they present a certain width. The comparison of mono-angle and multi-angle salt reconstructions confirmed that multi-angle systems allow to reconstruct over a larger range of χ and that the smoothed sensitivity avoids emergence of small background peaks due to hypersensitivity in mono-angle case. This is interesting especially for experimental data, where there might be background scattering from other materials such as the sample recipient. These reconstruction results also highlighted the importance to adapt the scattering angle to the material to be imaged. If the material is unknown or if it is a mixture of different materials, multi-angle acquisitions is interesting in order to cover a momentum transfer range that is sufficiently large.

MLEM algorithm without a priori is not well suited for amorphous spectra since the different measuring channels do not verify the independence hypothesis. The reconstructed spectra present oscillations, that are especially strong in the case of experimentally obtained spectra. In order to be able to reconstruct amorphous spectra using MLEM algorithm, it is necessary to use some regularization techniques.

Two regularization techniques have been discussed. One possibility is to reconstruct by using a dictionary, which can be composed of different theoretical spectra of amorphous materials or purely mathematical continuous functions. Reconstruction results with an amorphous dictionary strongly depend on the composition of the dictionary. Mathematical functions are more generic and it is possible to have a more complete dictionary with flexible peak positions and FWHM. Functions used in this work are Lorentzian distributions because the shape of amorphous spectra especially of acetone and fat spectra is similar to this kind of function.

The use of an amorphous dictionary leads to satisfying reconstructions if the elements in the dictionary are similar to the material to be reconstructed. Otherwise the reconstruction can be deformed or biased. This method presents the advantage that it can be used to detect/identify different materials. It will be used in chapter IV to identify the different tissue types in a breast phantom.

The best results for simulated and experimental amorphous data were obtained by using a Lorentzian base. However, the choice of Γ was based on only a few amorphous spectra, and its value might not be suitable for any amorphous material.

The second possibility of regularization is to use a resolution kernel during reconstruction. Kernel width was determined for each χ value using the system point spread function for each χ value. This method works well for simulated spectra since the system parameters are exactly known. Though, the reconstructed experimental water spectrum is not satisfying as system response used for reconstruction is too approximate. In future work a better estimation of the system response should be realized.

It would also be interesting to test other reconstruction method such as the space-alternating generalized expectation maximization (SAGE) method proposed by [Fessler and Hero, 1995] or Bayesian methods.

The following chapter concerns breast imaging using an XRD system. An optimized acquisition system will be proposed with the help of the different FOM introduced in chapter II and the outcomes of the DQE study of a simple system, especially multi-angle acquisition. A complete simulation study of the whole system associated to a breast phantom will be presented and amorphous base reconstruction method will be used to restore a scan slice of the breast phantom.

Chapter IV

X-ray diffraction based breast tissue classification

Classical mammography is based on the difference of absorption between normal breast tissue and cancerous tissue. However, in some cases the absorption is only slightly different, e.g. fibroglandular tissue and breast tumor, and this leads to numerous false diagnostics and unnecessary biopsies. Therefore, a more specific method, which could decrease the number of false positives, has to be developed. This work proposes the use of XRD as a second control level if conventional mammography outcome is unclear, because of too high breast density for instance. X-ray diffraction allows to access to the molecular structure of the different tissues and is more specific than X-ray absorption. Hence, it delivers additional information concerning the tissue to be identified. This chapter will first describe the different tissue types present in a breast and their imaging properties in transmission and XRD imaging in order to choose the case to be studied in XRD. The following section concerns system optimization for XRD based breast tissue classification. System constraints such as dimensions of the acquisition and the maximum dose to be delivered to the patient are described and an analytical method for DQE calculations of a collimation system are introduced. The study of the impact of different system parameters leads to an optimization strategy. Following this plan of action two optimized collimation configurations can be proposed. Their properties such as sensitivity and resolution are presented in the third section of this chapter. The last section is dedicated to a simulation study of the complete optimized XRD system associated to a breast phantom. After the description of the simulated system and the specific strategy to accelerate simulations of XRD spectra, reconstruction method and dose estimation method are clarified. Performances of the two proposed collimation systems are compared and the impact on tumor detectability of different parameters such as the incident spectrum and tumor position are studied. Finally, the use of slight multiplexing is evaluated.

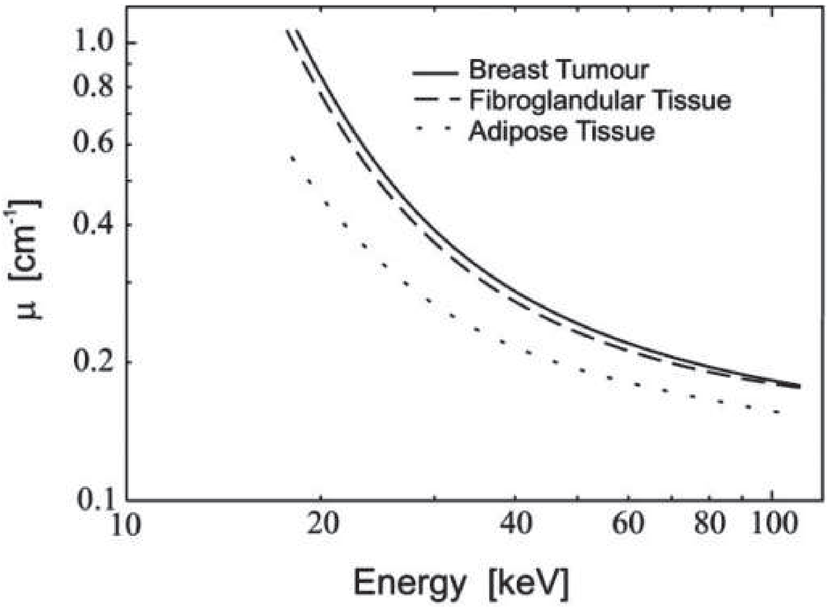

Figure IV.1: Linear X-ray attenuation coefficients of fat, fibroglandular tissue in the breast and breast tumors plotted versus X-ray energy. Absorption of fibroglandular tissue and cancerous tissue is very close. Hence, it is difficult to distinguish these two tissue types in classical mammography. (Image taken from [Johns and Yaffe, 1987].)

IV.1 Different breast tissue types

A normal breast is composed of three different component tissues: adipose tissue, glandular tissue and fibrous connective tissues. The fibrous connective tissue also known as stroma is a mixture of ligaments and scar tissues. Glandular tissue is a functional tissue type, which groups the lobules, essential for the milk production, and the ducts. Fibrous and glandular tissue are often summarized as fibroglandular tissues. The amount of glandular and fibrous tissue is dependent on the hormonal activity and fluctuates within the menstrual cycle. The postmenopausal breast for instance shows a reduction in the amount of glandular tissue, whereas the stroma increases. Other hormonal fluctuations might lead to a rise of fibroglandular tissue, which is called breast fibrosis. This leads to breast tissue, which is healthy but more dense than normal breast tissue. A-ray absorption of fibroglandular tissue and breast tumor are very similar (Fig. IV.1). Hence, if breast tissue is composed of a big part of fibroglandular tissue and only a little part of adipose tissue (case of breast fibrosis), the separation between cancerous tissue and healthy tissue will become more difficult in classical mammography. Figure IV.2 summarizes the different tissues types present in a breast.

Another difficulty is the presence of neoplasm, which corresponds to an abnormal mass of tissue. A neoplasm can correspond to a so called fibroadenoma, which is a benign tissue transformation, or to a carcinoma, which is a cancerous tumor. The attenuation of these two types of neoplasm is very similar. However, their shape is different. A fibroadenoma is well defined and sharply demarcated, whereas a carcinoma is ill-defined and has a stellate form. Hence, using the anatomical information from classical mammography or breast CT, it might be possible to distinguish between benign and malignant neoplasm. Therefore, their separation will not be treated in this work.

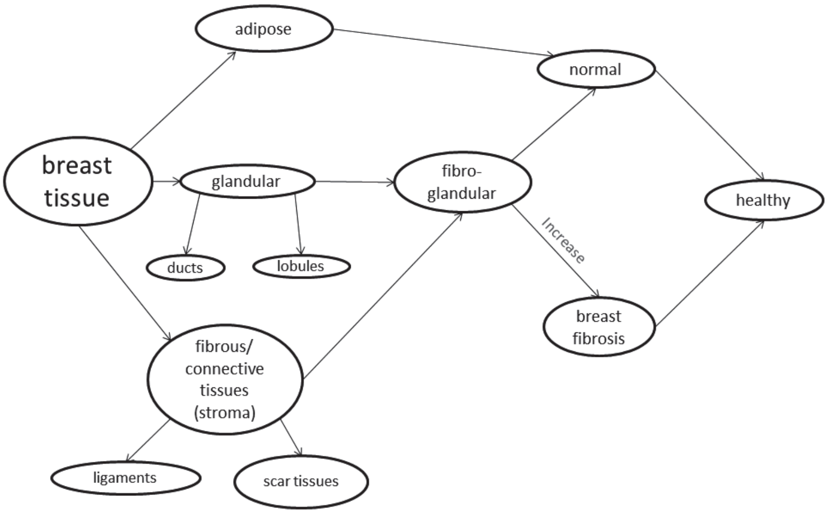

Figure IV.2: Schematic representation of the different breast tissue types.

IV.1.1 Breast tissue signatures in X-ray diffraction

Numerous teams have studied X-ray diffraction signatures of the different breast tissues. [Kidane *et al.*, 1999] for instance has acquired signatures of all possible breast tissue types. Figure IV.3 shows the scattering signatures obtained for adipose tissue, carcinoma, fibroadenoma, fibroglandular tissue and other benign disease tissue. Adipose tissue presents a sharp peak at about 1.1 nm^{-1}, which is close to the beef and pork fat peaks shown in section III.2.1.2. It is the only tissue to present a sharp demarcated peak. Diffraction intensity of the other tissue types is lower and only fibroglandular tissue presents a significant diffraction intensity at momentum transfer values of the fat peak. Diffraction pattern of pathological tissues have their maximum around the water "peak" (1.6 nm^{-1}) and are very close. It should not be hoped to separate these tissue types by X-ray diffraction. Figure IV.4 shows a comparison of normal breast tissue, fibroglandular tissue and pure carcinoma diffraction patterns. In fact, normal tissue is characterized by the presence of the adipose tissue maximum and lower but still existent diffraction intensity around the water peak. Fibroglandular tissue also diffracts around the fat peak but less than normal tissue and around water peak but more than normal tissue. They still contain adipocytes but a significantly smaller amount than normal tissue. Pure carcinoma diffraction signature is similar to water signature. It almost does not diffract around the fat. Cancerous cell agglomerations do not contain many adipocytes. Thus, the difference between cancerous tissues and healthy tissues can be made by the determination of the presence or absence of the fat "peak". This observation was also confirmed by [Pani *et al.*, 2010] (fat peak and fibrous peak) and [Conceição *et al.*, 2010] (fatty acid peak and water-like peak). In the following the signatures of fibroglandular tissue and carcinoma from [Kidane *et al.*, 1999] (Fig. IV.4) will be used because this seems to be one of the most difficult cases in classical mammography and it is possible to distinguish their scattering signatures. The data from [Kidane *et al.*, 1999] were chosen because results in this article correspond to a mean of several different breast samples and they indicate the variability of the different samples. Hence, there are some information about intraclass variability, which might be taken into account during optimization process.

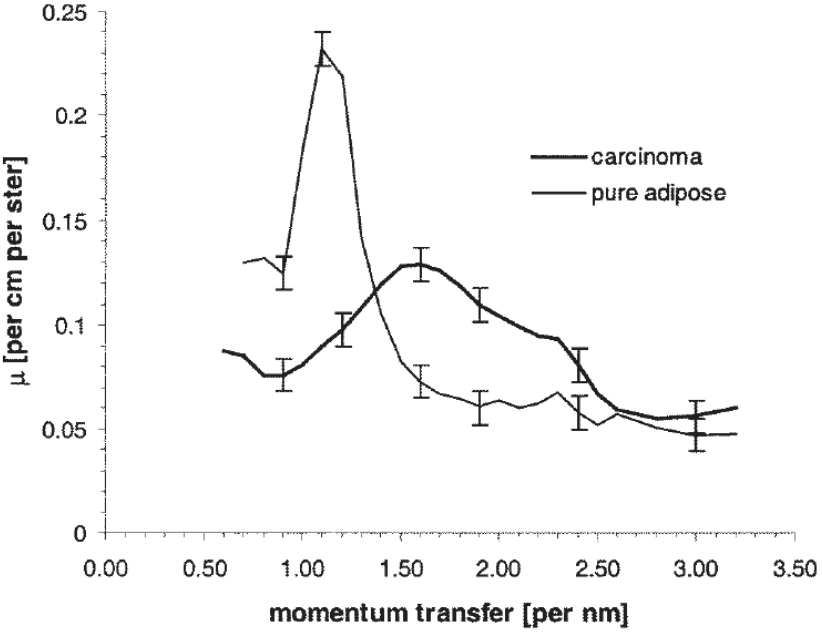

(a) *Comparison between adipose tissue and carcinoma.*

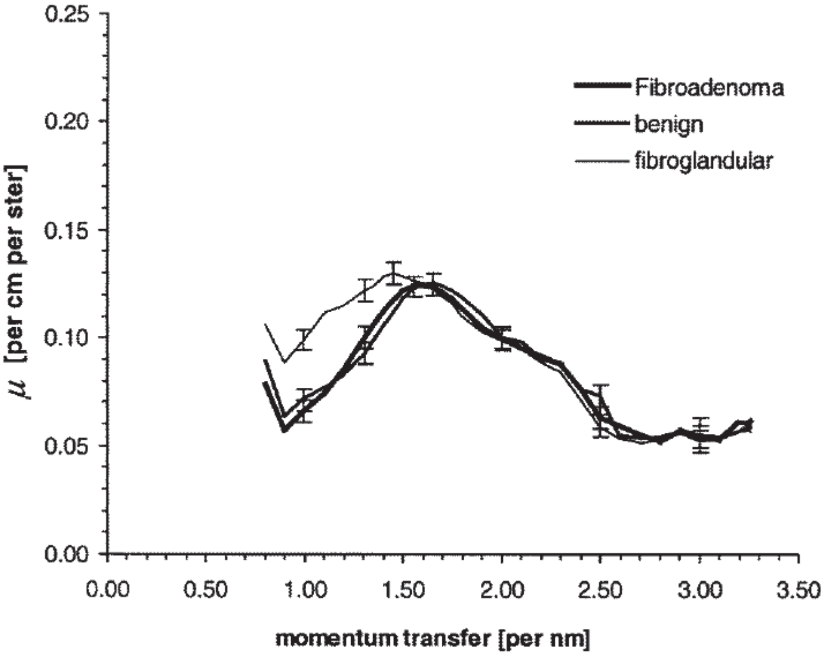

(b) *Comparison between fibroglandular tissue and different begnin pathological breast tissue.*

Figure IV.3: Measured scattering signatures of different breast tissue types. Only adipose and fibroglandular tissue present a significant scattering intensity at low momentum transfer values [Kidane *et al.*, 1999].

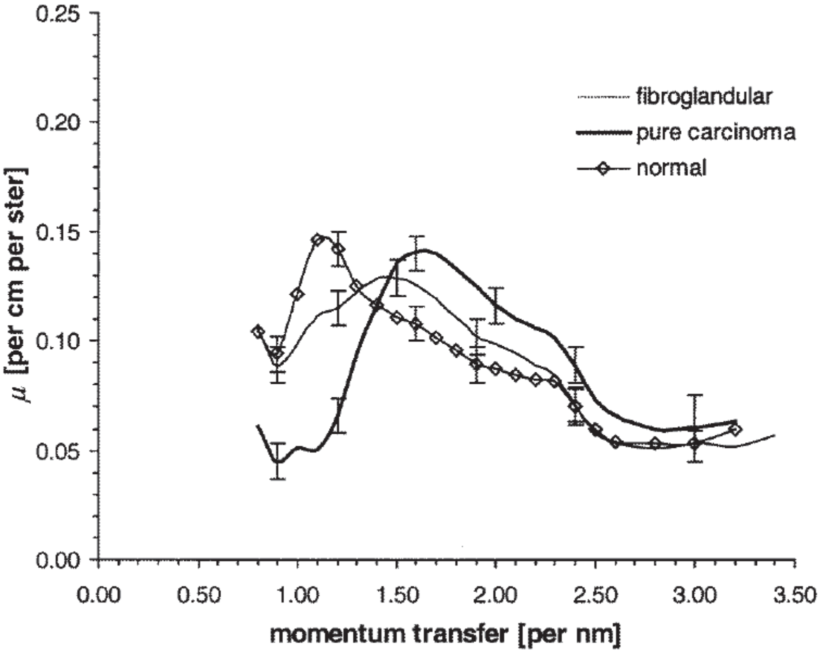

Figure IV.4: Comparison of the scatter signatures of pure carcinoma with normal breast tissue (50:50 fat/fibrous mixture) and fibroglandular tissue [Kidane *et al.*, 1999].

IV.1.2 Breast tissue separability with X-ray diffraction

In order to know whether fibroglandular tissue and carcinoma present a good separability in XRD, tissue separability was first studied on pure tissues and supposing an ideal acquisition system, i.e. no distortion of the reference diffraction pattern by the system. In the following, CNR calculation results and ROC curve results are presented.

IV.1.2.1 Contrast to noise ratio

Figure IV.5 shows the result of CNR calculations for fibroglandular tissue and pure carcinoma as a function of momentum transfer. It can be seen that is maximum is at 1.1 nm^{-1}, which corresponds to the fat peak present in healthy tissue and missing in cancerous tissue. Hence, it is important to be as sensitive as possible around this momentum transfer value. The summed CNR^2 is around 0.05. This indicates that the number of photons required to have a distance of one standard deviation between fibroglandular tissue distribution and carcinoma distribution is about 22. A distance of three standard deviations requires about 195 photons. These results indicate the minimum number of photons that will be necessary to well separate these tissues with an ideal system. For a real system, the required number of photons will increase.

IV.1.2.2 ROC curves

Another possibility to evaluate tissue separability and to take into account detection rate and false positive rate is ROC curve calculation.

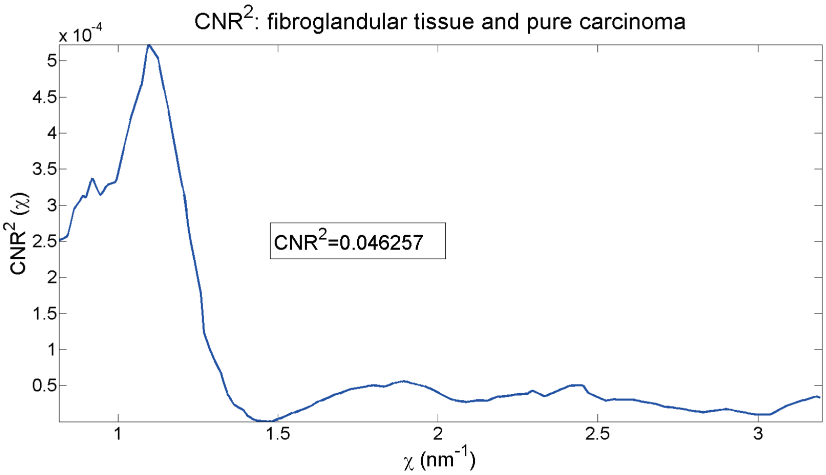

Figure IV.5: Calculated CNR between fibroglandular tissue and pure carcinoma for an ideal EDXRD imaging system.

Figure IV.6 shows examples of ROC curves for real data of conventional mammography, where tissue classification is realized by a computer, a human or a human assisted by a computer. These curves are similar and on the average a 90 % detection rate implies a 40 % false positive rate, which seems quite high.

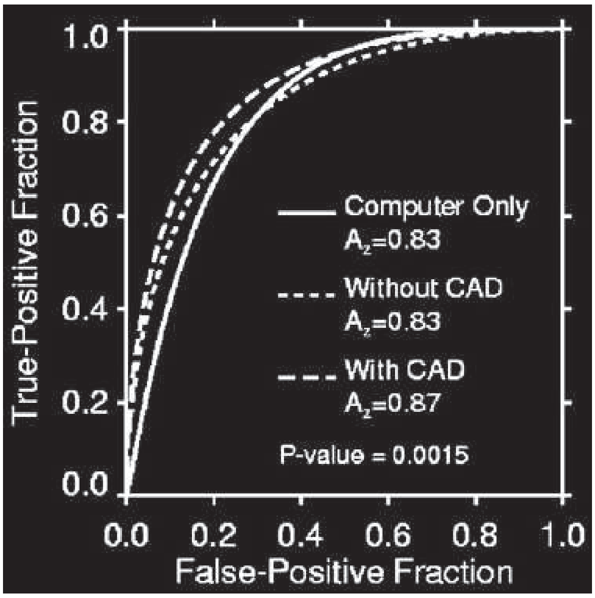

Figure IV.6: Example of ROC curve analysis for classical mammography with computer-assisted detection (CAD). A comparison of the ROC curves for computer only (no human analysis), without CAD (only human analysis), and with CAD (human and computer analysis) [Janet E. Joy *et al.*, 2005].

In figure IV.7 , ROC curves and the corresponding area under the curve (AUC) for separability of fibroglandular tissue and pure carcinoma with an ideal imaging system can be seen for different photon statistics (= number of detected photons) corresponding to 1σ, 2σ and 3σ

separation. To have a good separation of 2σ between the two tissue types and a smaller false positive rate at 90 % detection rate about 80 photons would be needed with an ideal system. However, this is far from sufficient to conclude that X-ray diffraction is more specific than conventional mammography. Further calculations, which take into account the system response, have to be realized. These calculations would indicate whether X-ray diffraction is a suitable technique for a second control level and they might also help to choose between different system configurations. Though, even then, one should be careful by comparing results to the here presented conventional mammography ROC curve as it was obtained with real data, whereas results in the present work are always for simulated data. These curves were mostly shown to give an idea of what is possible with current mammography systems.

In the following parts of this chapter, an XRD imaging system will be optimized and simulated in order to assess its tissue separation power.

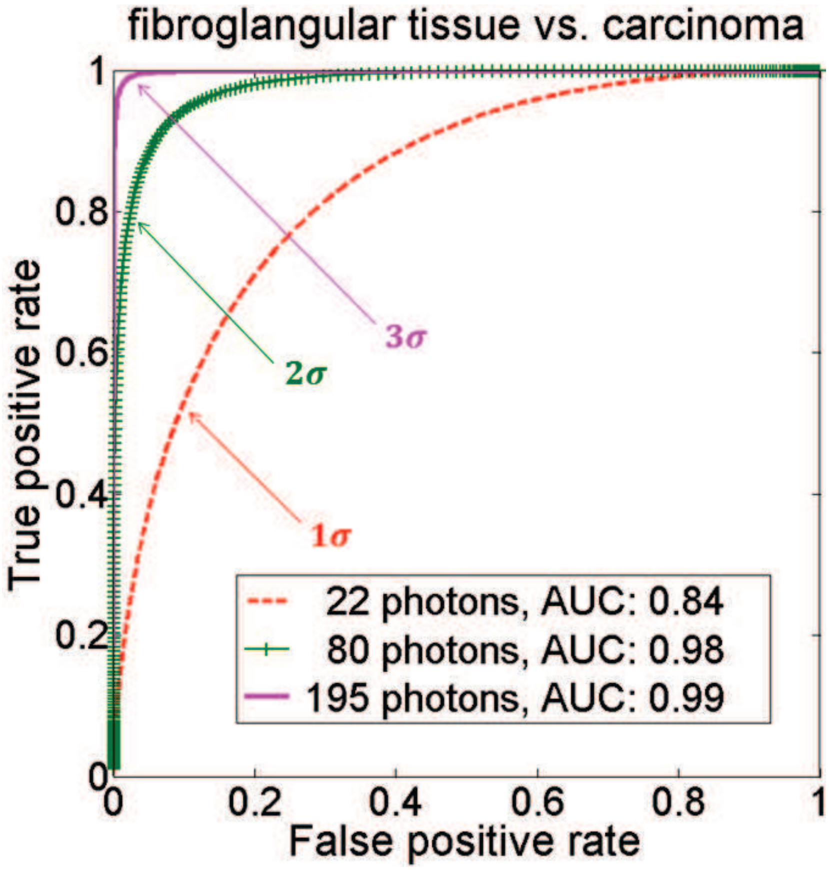

Figure IV.7: Calculated ROC curves and the corresponding area under the curve for separability of fibroglandular tissue and pure carcinoma using an ideal imaging system.

IV.2 Optimization of an X-ray diffraction system for breast imaging

This part of the chapter is dedicated to the optimization of an XRD system for breast imaging, and especially to the optimization of the secondary collimation system. First, the constraints to take into account during optimization process are explained. Then a new analytical method to calculate DQE of a collimation system will be presented. The influence of the different system parameters is evaluated, which leads to an optimization strategy in order to respect system constraints.

IV.2.1 System constraints

Different factors have to be taken into account for system optimization.

- **Object size**: The object size can be fixed. In classical mammography the breast is compressed and depending on the initial thickness, the imaged breast thickness will be between 2 and 8 cm. In XRD based breast imaging, this principle will be conserved and for the following study, the breast thickness is fixed to **5 cm**.
- **Maximum delivered radiation dose**: It is important to respect the maximum radiation dose that can be delivered during mammography. The dose corresponds to the energy that is absorbed per kilogram of tissue and its unity is Gray (1 Gy = 1 J/kg). Depending on the imaging technique (film or digital) the dose for classical mammography is **between 1 and 3 mGy**. The dose to be delivered depends on the number of photons that are necessary to separate carcinoma and fibroglandular tissue scattering signatures as well as on the energy of the incident X-ray photons. Energy deposit is mainly due to photoelectric interaction and Compton scattering. X-ray diffraction makes use of Rayleigh interaction. Hence, it is important to choose an incident energy range allowing the highest Rayleigh interaction rate that is possible and avoiding delivery of useless dose. In order to choose an adapted incident spectrum, a comparison of the linear attenuation coefficient of the different types of interaction was realized. Attenuation coefficients were taken for water since tissue absorption is very close to the absorption of water. Figure IV.8 shows these different attenuation coefficients and illustrates that for energies under 20 keV photoelectric absorption largely dominates. In fact, at these energies almost each photon would be absorbed by this process[1] and this would generate a dose deposit without information about diffraction signature. Hence, energy lower than 20 keV should be filtered to avoid this dose deposit. With increasing energy photoelectric and Rayleigh interaction cross section decreases, whereas Compton scattering remains constant. Therefore, it is not useful to allow photons with too high energies because Rayleigh cross section and thus diffraction signal would be very small. It might be appropriate to stop filter incident photons with energies higher than 100 keV. The average energy deposit in a 100x100x50 mm^3 water phantom was simulated in order to confirm conjectures emitted using attenuation coefficients. Figure IV.9 shows

  the mean energy deposit per photon as a function of photon energy and the energy deposit per as a function of the last interaction type[2] in 50 mm of a material whose chemical composition is close to average breast tissue (H: 9.82%, C: 33.15%, N: 3.41%,

---

[1] Energy around 20 keV is interesting in classical mammography because the absorption contrast is very high.

[2] The last interaction type before leaving the object is given in the graph. However, the energy deposit can be due to different interactions (multiple interactions).

O: 51.96%, P: 0.50%, S: 0.52%, K: 0.63% [Duck, 1990], percentages correspond to mass fractions) both obtained by Monte-Carlo simulations with PENELOPE [Salvat *et al.*, 2008]. Energy deposit increases very strongly until around 25 keV. There is a local minimum at 60 keV and afterwards, it continues to grow. By linking it to the energy deposit by interaction type, it can be seen that energy deposit at low energies is mainly due to photons interacting by photoelectric effect at last corresponding to an absorption. These photons do not contribute to signal but only to dose deposit. Energy deposit corresponding to other interactions only starts at about 20 keV. At around 50 keV, energy deposit by photons undergoing Rayleigh scattering as last interaction increases. As Rayleigh scattering is per definition without loss of energy, this means that these photons underwent Compton scattering before. Hence, the incident photon direction before coherent scattering cannot be known, which introduces blurring in diffraction information. Energy deposit by Compton scattering increases continuously with increasing energy, and hence dose deposit. This simulation confirms that an incident X-ray spectrum between 20 and 100 keV makes sens.

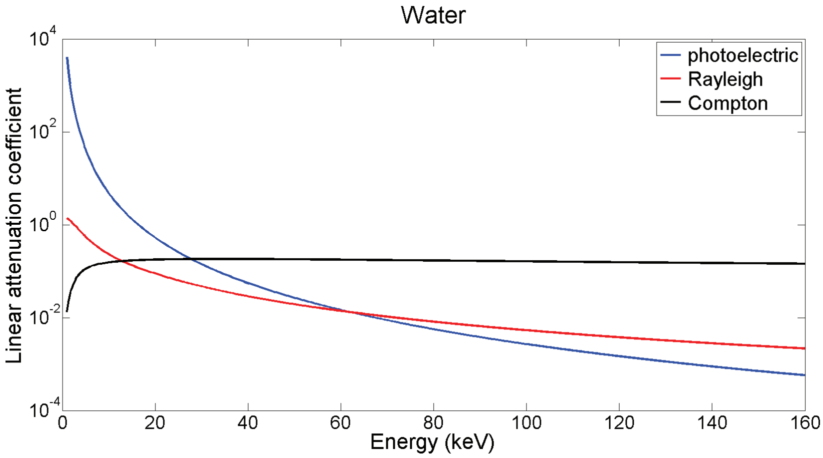

Figure IV.8: Comparison of the linear attenuation coefficients of water for different types of interaction.

- **Momentum transfer range and resolution**: Another important constraint to fix is the χ-range to be imaged and the momentum transfer resolution that is necessary to separate carcinoma and fibroglandular tissue. As explained before, the tissue signatures to be used will be the ones presented by [Kidane *et al.*, 1999]. Figure IV.10 shows the two considered signatures. A momentum transfer values between 1 nm^{-1} and 2.5 nm^{-1} seem to cover the most important range of χ. As explained in the previous section, in order to know whether the tissue is healthy, it is necessary to be able to measure separately signal at fat peak (1.1 nm^{-1}) and water peak (1.6 nm^{-1}) momentum transfer. To separate these peaks a resolution of at least 0.2 nm^{-1} is required, which corresponds to $\nu_\chi = 5$ nm.

- **Collimation type**: The idea is to use X-ray diffraction as a second level of control after classical mammography. Thus, the position (x,y) of the suspicious region is known from mammography imaging but not the depth. In order to minimize the dose to be

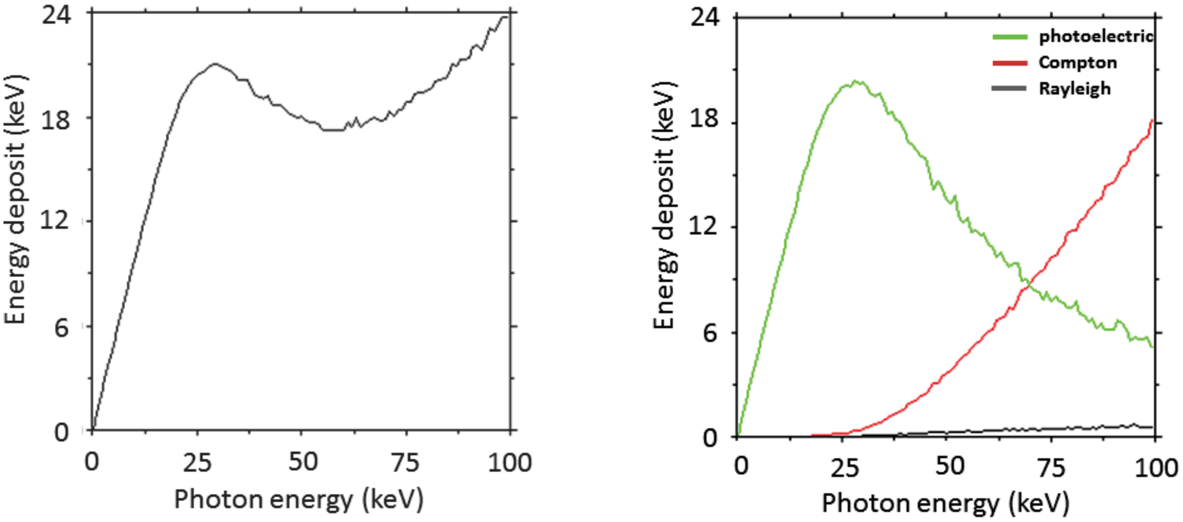

(a) *Energy deposit for all interaction types.*

(b) *Energy deposit as a function of the last interaction type: photoelectric (green),Compton (red), Rayleigh (black).*

Figure IV.9: Deposited energy per photon (multiple interactions included) in 50 mm of a material with average chemical composition of breast tissue as a function of interacting photon energy (generated with PENELOPE 2008 [Salvat *et al.*, 2008]).

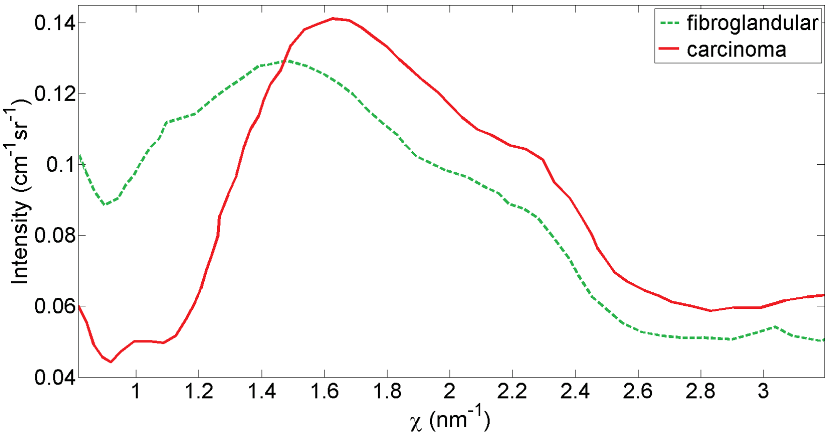

Figure IV.10: Diffraction signatures of fibroglandular tissue (light green dotted line) and pure carcinoma (red line) [Kidane *et al.*, 1999].

delivered a small pencil beam (about 1 mm^2) combined to a convergent collimation system seems to be appropriate. There are two possibilities:

1. Collimation system convergent in one point (monofocal) + mechanical depth scan.
2. Collimation system convergent on the z-axis over the whole sample thickness (multifocal).

Figure IV.11 shows a schematic representation of these two kinds of collimation systems.

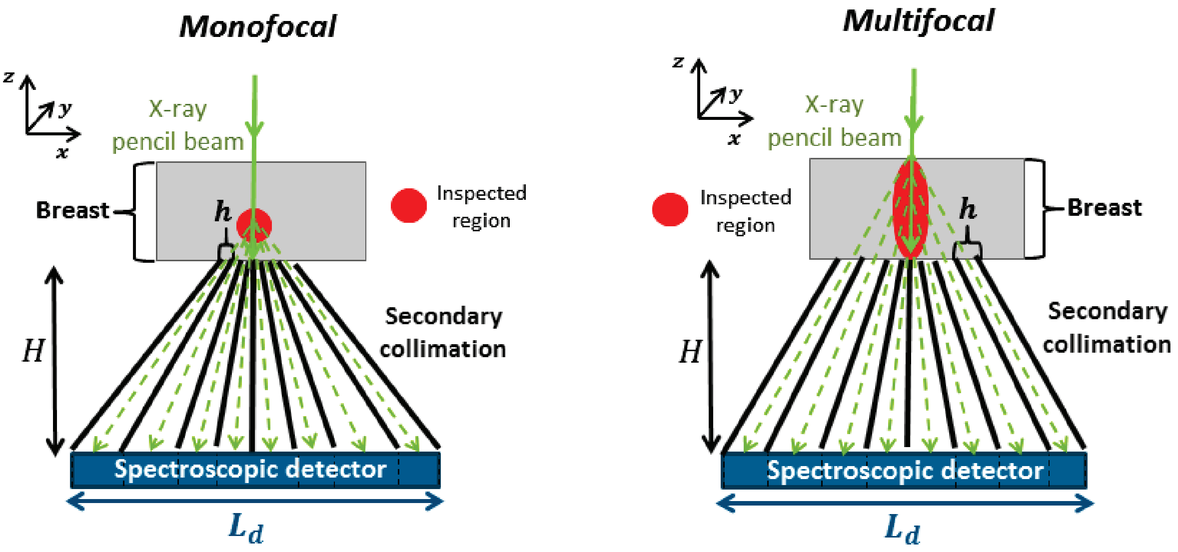

(a) *Monofocal system: Depth scan is necessary.*

(b) *Multifocal system: Depth scan is not necessary.*

Figure IV.11: Schematic view of the two possible convergent collimation systems. H corresponds to the collimation height, h to the hole size and L_d to the detector dimension.

These two different configurations will be evaluated in the next section.
The spatial resolution of the detector should not be worse than 1 mm but it is not the most critical system parameter.

IV.2.2 Analytical detective quantum efficiency calculations for a collimation system without multiplexing

Traditionally, DQE calculations are used to assess and optimize detector performance of an imaging system. However, assumed an ideal detector, it is possible to use this concept to optimize the collimation, the most important element to be optimized in EDXRD. It plays an important role in spatial and spectral resolution and defines, in combination with the incident X-ray spectrum, the χ range to be inspected.
This part will be about optimizing the secondary collimation. The primary collimation is assumed to be fixed in a way to obtain a very thin incident pencil beam.
In fact, the secondary collimation can be considered as an assembly of couples hole-pixel (Fig. IV.12). Hence, it is possible to determine the DQE for each hole-pixel pair of the collimation and to add them together afterwards to obtain the system DQE.

IV.2.2.1 Spatial resolution of a pair hole-pixel

As mentioned before, the incident beam is fixed to be a very thin pencil beam. Thus, it is assumed that diffraction signal is only emitted from the z-axis ($x = 0$) and the resolution to be determined is Δz, which will also determine the angular resolution $\Delta\theta$. Spatial resolution can be divided in two parts: resolution due to pixel size and resolution due to hole size. The

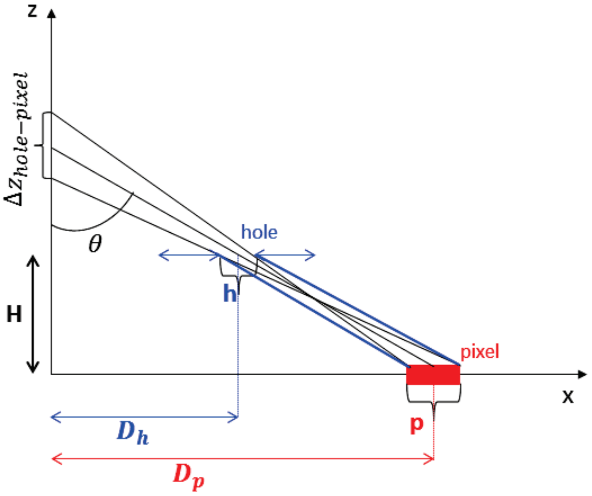

Figure IV.12: Schematic representation of the system parameters for one hole-pixel pair and the spatial resolution $\Delta z_{hole-pixel}$ of this pair.

pixel part corresponds to the projection of the pixel on z-axis by one point, e.g. the center, of the hole (Fig. IV.13.a). The resulting resolution on z-axis is given by:

$$\Delta z_p = \frac{HD_h p}{\left[(D_p - D_h)^2 - \left(\frac{p}{2}\right)^2\right]} \approx \frac{HD_h p}{(D_p - D_h)^2} \tag{IV.2.1}$$

The hole contribution corresponds to the part of the z-axis, that is seen by the center point of the pixel via the hole (Fig. IV.13.b) and can be calculated using:

$$\Delta z_h = \frac{HD_p h}{\left[(D_p - D_h)^2 - \left(\frac{h}{2}\right)^2\right]} \approx \frac{HD_p h}{(D_p - D_h)^2} \tag{IV.2.2}$$

The resolution of a hole-pixel pair can be represented as a kind of parallelogram (Fig. IV.14). In fact, each point of the pixel ”sees” a certain part Δz_h of the z-axis but the central z value is not the same. By summing in x-direction, a trapezoid is obtained, which corresponds to the resolution of this pair. Its height is proportional to the sensitivity. In fact, it corresponds to the point spread function (PSF) of the hole-pixel pair. The PSF can be calculated by the convolution of two rectangular functions of widths Δz_p and Δz_h:

$$\mathrm{PSF}_{hp} = \Pi_{\Delta z_p} * \Pi_{\Delta z_h} \tag{IV.2.3}$$

It is well known that the convolution in the direct space is transformed into a product in Fourier space. Furthermore, the Fourier transform of the PSF corresponds to the modulation transfer function (MTF) and is thus, given by:

$$\mathrm{MTF}_{hp}(\nu_z) = \mathscr{F}\left\{\Pi_{\Delta z_p}\right\} \cdot \mathscr{F}\left\{\Pi_{\Delta z_h}\right\} = \mathrm{sinc}\left(\pi\nu_z\Delta z_p\right)\mathrm{sinc}\left(\pi\nu_z\Delta z_h\right) \tag{IV.2.4}$$

$\mathscr{F}$ is the operator for the Fourier transform.

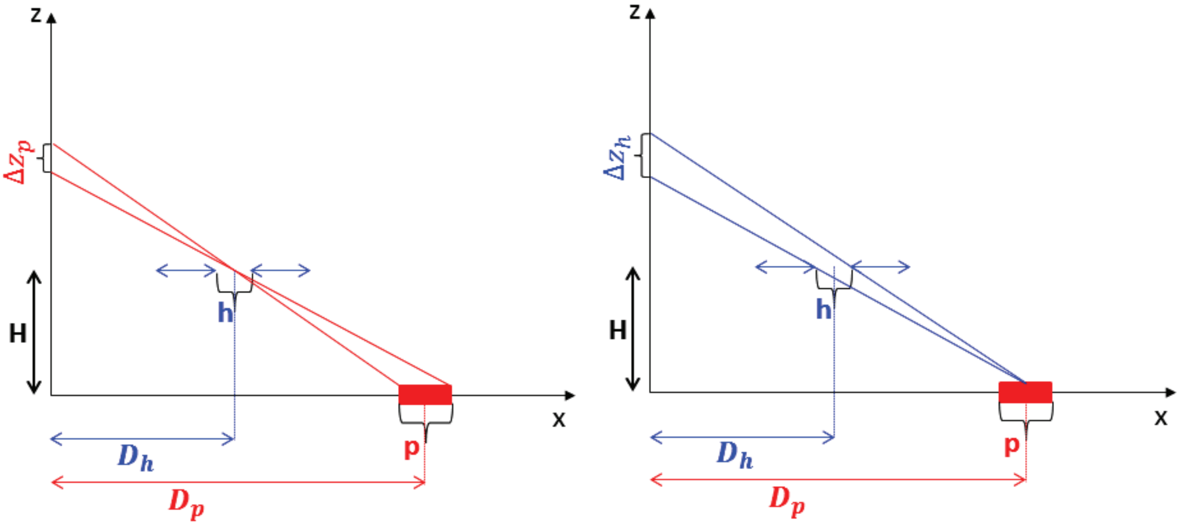

(a) *Resolution due to the pixel size: It corresponds to the projection of the pixel on the z-axis by the center of the hole.*

(b) *Resolution due to the hole size: It corresponds to the part of the z-axis, that is seen by the center point of the pixel via the hole.*

Figure IV.13: Schematic representation of the spatial resolution due to the pixel size and to the hole size.

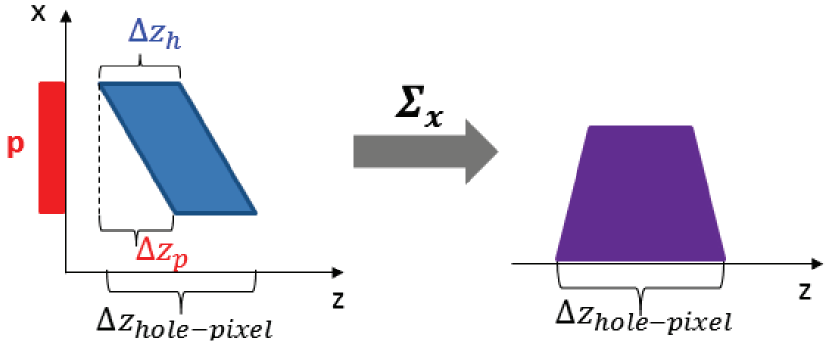

Figure IV.14: The spatial resolution of a hole-pixel pair can be represented as a kind of parallelogram. By summing in x-direction, a trapezoid is obtained, whose lower base corresponds to the spatial resolution of the hole-pixel pair.

By using equation II.2.3, the DQE of a hole-pixel pair can be deduced as:

$$DQE_{hp}\left(\nu_z\right) = S_{hp} \cdot \mathrm{sinc}^2\left(\pi\nu_z\Delta z_p\right)\mathrm{sinc}^2\left(\pi\nu_z\Delta z_h\right) \qquad \text{(IV.2.5)}$$

where S_{hp} corresponds to the sensitivity of one pair hole-pixel.

IV.2.2.2 System sensitivity of a pair hole-pixel

Sensitivity is calculated for one sample point (here, one z value) and corresponds to the ratio between useful detection surface and the surface that radiates from this point. Here, the useful surface corresponds to a small element of the detector pdx. p corresponds to the length of the detector element in y-direction and dx to the one in x-direction. In fact, the detector is considered to be a linear detector array of width (y-dimension) p positioned on the x-axis (y=0) or parallel to it (y fixed as a non-zero value). The radiating surface corresponds to a sphere with radius $R = \sqrt{x^2+y^2+z^2}$ (Fig. IV.15). A small fraction of sensitivity is therefore given by:

$$dS = \frac{pdx \cdot \cos\theta}{4\pi R^2} = \frac{pdx \cdot z}{4\pi \left(x^2+y^2+z^2\right)^{3/2}} \tag{IV.2.6}$$

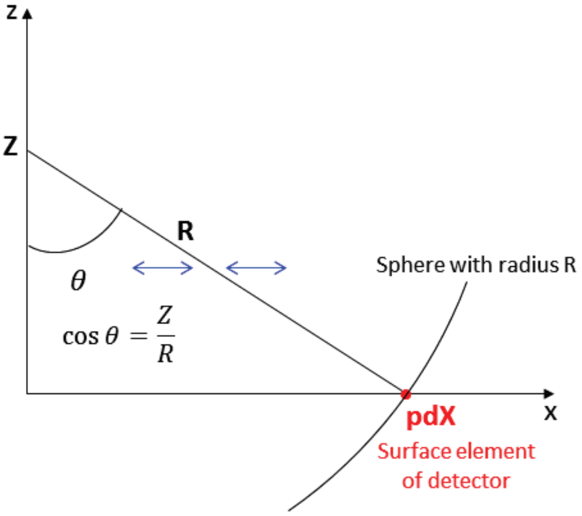

Figure IV.15: Schematic illustration of the sensitivity calculations.

The sensitivity of a pair hole-pixel can be obtained as follows:

$$S_{hp} = \int\limits_{z_{min}(P)}^{z_{max}(P)} \int\limits_{x_{min}(P,z)}^{x_{max}(P,z)} \frac{p \cdot z}{4\pi \left(x^2+z^2\right)^{3/2}} dx \tag{IV.2.7}$$

where x_{min} and x_{max} correspond respectively to the smallest and largest x position "seeing" z and being part of the pixel number P. It is important to only integrate over the z values, by which the considered pixel is irradiated (between $z_{min}(P)$ and $z_{max}(P)$), as the other z values do not contribute to the pixel sensitivity of the considered pixel.

The whole sensitivity for one z value is obtained by integration over all x, that can "see" this z via their associated hole:

$$S(z) = \sum_{pixels} \int\limits_{x_{min}(P,z)}^{x_{max}(P,z)} \frac{p \cdot z}{4\pi \left(x^2+y^2+z^2\right)^{3/2}} dx \tag{IV.2.8}$$

The sum over the different pixels is necessary because different pixels might detect signal from the same z position but not the whole pixel might "see" it.

IV.2.2.3 Spatial resolution and sensitivity of the entire collimation

After explaining how to determine spatial resolution and sensitivity of one hole-pixel pair, this section will show DQE and the sensitivity calculations for different collimation configurations without multiplexing. This means that each pixel receives photons passing through only one hole.

First of all, a simple linear detection array and one line of holes are considered. This corresponds to a 2D configuration and the collimation DQE is obtained by summing over all pixels:

$$DQE_a\left(\nu_z\right) = \sum_{pixels} DQE_{hp}\left(\nu_z\right) \tag{IV.2.9}$$

The sensitivity profile, i.e. sensitivity as a function of z values, in this case is given by equation IV.2.8.

The detective quantum efficiency of a fan-beam collimation (collimation in x-direction but not in y-direction) can be obtained by summing the DQE of the previous 2D case for different y-positions of the detector array. Holes correspond in fact to slits in y-direction.

$$DQE_{fb}\left(\nu_z\right) = \sum_{y} DQE_a\left(y, \nu_z\right) \tag{IV.2.10}$$

Sensitivity is calculated by summing equation IV.2.8 over the different y values that are considered.

Another possible collimation would be a conical collimation (collimation in x- and y-direction). Diffraction signal depends on the scattering angle θ and presents therefore a cylindrical symmetry. Thus, it seems useful to use cylindrical coordinates (Fig. IV.16). A detector surface element corresponds now to $rdrd\phi$ and sensitivity becomes:

$$S\left(z\right) = \sum_{pixels} \int_{r_{min}(P,z)}^{r_{max}(P,z)} \int_{0}^{2\pi} \frac{r \cdot z}{4\pi\left(r^2 + z^2\right)^{3/2}} d\phi dr \tag{IV.2.11}$$

The "pixels" correspond in this case to small annuli with width p, and D_p is the distance between the center and the middle of the annulus as shown in figure IV.17. The DQE can be calculated using equations IV.2.5 and IV.2.9.

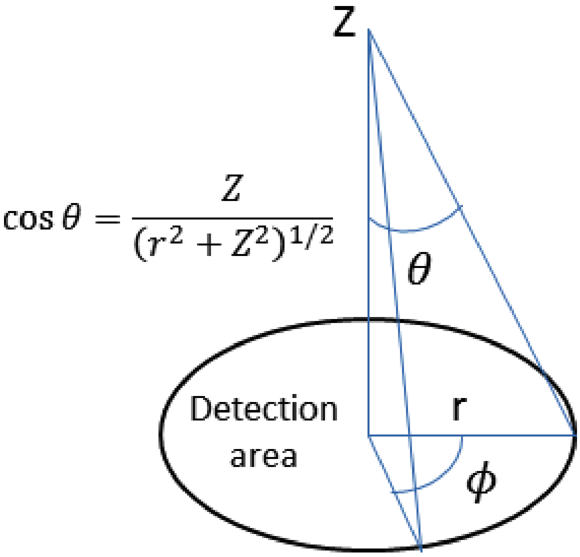

Figure IV.16: Illustration of the cylindrical geometry. θ corresponds to the scattering angle. Sensitivity has to be integrated from $\phi = 0$ to $\phi = 2\pi$.

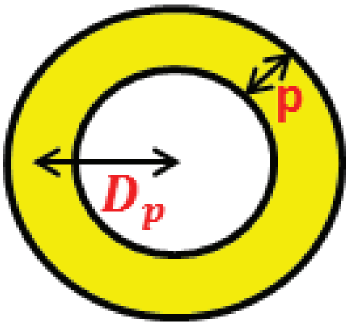

Figure IV.17: Illustration of a "pixel" in cylindrical coordinates.

IV.2.2.4 Angular resolution

In diffraction imaging, the angular resolution is at least as important as the spatial resolution since diffraction signal strongly depends on the scattering angle θ. Angular resolution can be deduced from spatial resolution. θ and z are related by (Fig IV.18):

$$\tan\theta = \frac{x}{z} \tag{IV.2.12}$$

The derivate with respect to z of θ is:

$$\frac{d\theta}{dz} = -\frac{x}{z^2}\cdot\frac{1}{1+\frac{x^2}{z^2}} = -\frac{1}{\sqrt{x^2+z^2}}\sin\theta \tag{IV.2.13}$$

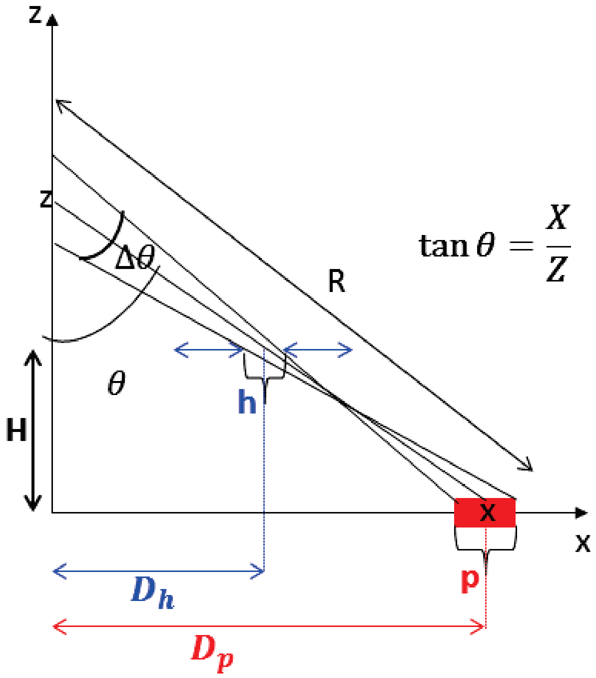

Figure IV.18: Illustration of angular resolution $\Delta\theta$ and the parameters that are used to determine it.

Hence, $\Delta\theta$ can be expressed as:

$$\Delta\theta = -\frac{1}{\sqrt{x^2+z^2}} \sin\theta \Delta z \tag{IV.2.14}$$

The angular resolution can also be separated in the contribution of the pixel and the hole. After some calculations and geometrical considerations, these two contributions can be written as:

$$\Delta\theta_p = -\cos^2\theta \cdot \frac{D_h p}{D_p H} \tag{IV.2.15}$$

and

$$\Delta\theta_h = -\cos^2\theta \cdot \frac{h}{H} \tag{IV.2.16}$$

Detective quantum efficiency can be calculated as previously:

$$DQE_{hp,\theta}\left(\nu_\theta\right) = S_{hp}\,\mathrm{sinc}^2\left(\pi\nu_\theta\Delta\theta_p\right)\mathrm{sinc}^2\left(\pi\nu_\theta\Delta\theta_h\right) \tag{IV.2.17}$$

IV.2.2.5 Momentum transfer resolution

In fact, diffraction does not only depend on scattering angle θ but also on energy, and the physical variable combining both of them corresponds to the momentum transfer χ

(Sec. I.1.2.4, equation I.1.19). The collimation only influences θ and therefore, in this section only the momentum transfer resolution due to angular resolution will be considered (degradation due to finite energy resolution of detector is not taken into account):

$$\frac{d\chi}{d\theta} = \frac{1}{2}\cos\frac{\theta}{2} \cdot \frac{E}{hc} \tag{IV.2.18}$$

where hc corresponds to the Planck constant multiplied by the velocity of light.

Thus, $\Delta\chi$ can be written as:

$$\Delta\chi_{p/h} = \cos\frac{\theta}{2} \cdot \frac{E}{2hc}\Delta\theta_{p/h} \tag{IV.2.19}$$

And the corresponding DQE can be deduced as:

$$DQE_{hp,\chi}\left(E, \nu_\chi\right) = S_{hp}\,\mathrm{sinc}^2\left(\pi\nu_\chi\Delta\chi_p\right)\mathrm{sinc}^2\left(\pi\nu_\chi\Delta\chi_h\right) \tag{IV.2.20}$$

This expression depends on the photon energy. However, if the incident spectrum was fixed, the mean momentum transfer resolution for the given spectrum can be calculated by integrating the DQE over the spectrum:

$$DQE_{hp,\chi}\left(\nu_\chi\right) = \int_{E_{min}}^{E_{max}} DQE_{hp,\chi}\left(E, \nu_\chi\right) \cdot S\left(E\right) dE \tag{IV.2.21}$$

where S is the normalized incident spectrum.

IV.2.3 Analytical collimation optimization

The analytical DQE calculation methods introduced in the previous section will be used to study the influence of the different system parameters on system performance. This allows to be able to know how to optimize them and to establish an optimization strategy.

IV.2.3.1 Influence of the different parameters

The present study was realized with a conical collimation (cylindrical geometry). In order to define the collimation, the detector was divided in as many parts as the number of holes (Fig. IV.19). The detector area of each part is the same, which means that the number of pixels (pixel annuli of thickness p) per part is not the same for each part (Fig. IV.20). Each detector part only receives signal via its attributed hole, i.e. no multiplexing. The following parameters were fixed by default:

- Minimum focal distance f_{min}: 25 mm
- Maximum focal distance f_{max}: 50 mm
- Number of holes Nb_h: 10
- Hole size h: 0.5 mm

- Pixel size p: 0.5 mm
- Collimation height H: 100 mm
- Detector dimension L_d: 100 mm

Figure IV.19 illustrates the different system parameters. Focal distances correspond to the z value (minus H) that is targeted by the middle of the detector part passing through the center of the hole. The minimum focal distance is chosen to be at least 25 mm because otherwise the hole position would be to close to z-axis and there is the risk to intercept transmitted (not diffracted) radiation. The sample is supposed to be 50 mm thick breast. It is considered to be in contact with the collimation. Hence, the sample is situated between $Z = H$ and $Z = H + 50$ mm. In the following paragraph, the impact of the different parameters will be studied by varying only one of the parameters at a time.

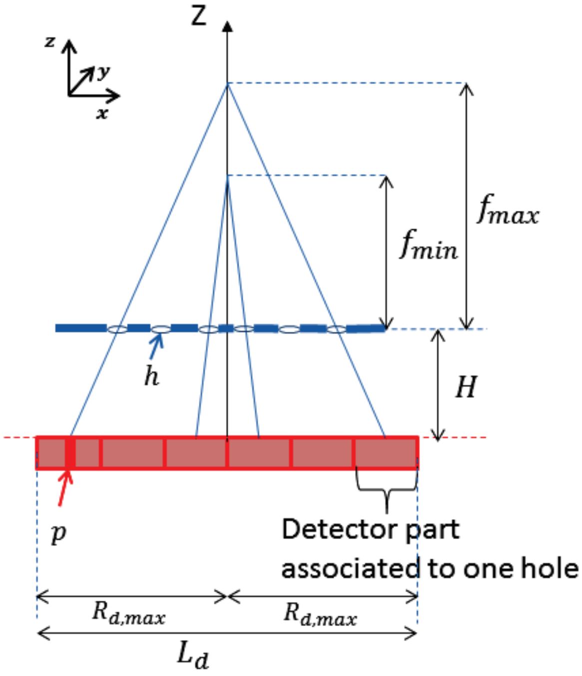

Figure IV.19: Illustration of the different system parameters to be optimized.

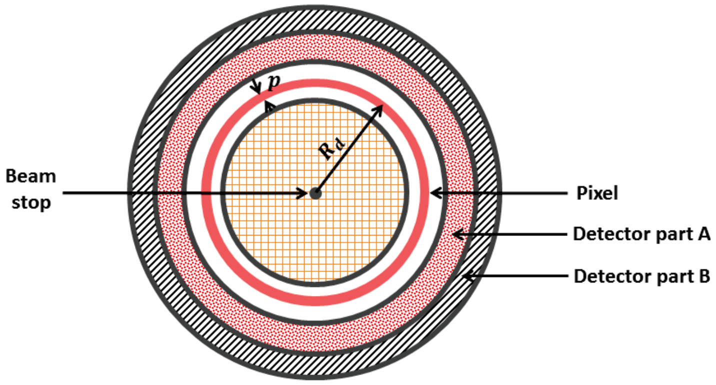

Figure IV.20: The detector is divided in as many parts as the number of collimation holes. Each part has the same surface (detection surface of detector part A = detection surface of detector part B, for instance) but not the same thickness. As pixels are defined as concentric annuli of thickness p with varying radius in the center R_d, the number of pixels is not the same for each detector part.

IV.2.3.1.1 Minimum focal distance f_{min}

As can be seen in figure IV.21, the fixed minimum focal distance influences the distribution of the global system sensitivity. The closer its value is to the maximum focal distance the more the sensitivity concentrated around one z value. In fact, by fixing f_{min} and f_{max}, it is decided whether the collimation system is mono- or multifocal. Thus, if f_{min} equals f_{max} this corresponds to a monofocal collimation. However, it can be observed that there is still some sensitivity left at low z values for $f_{min} = f_{max}$. That is due to the limited spatial resolution of the system, especially of the first hole (Fig. IV.26 for instance).

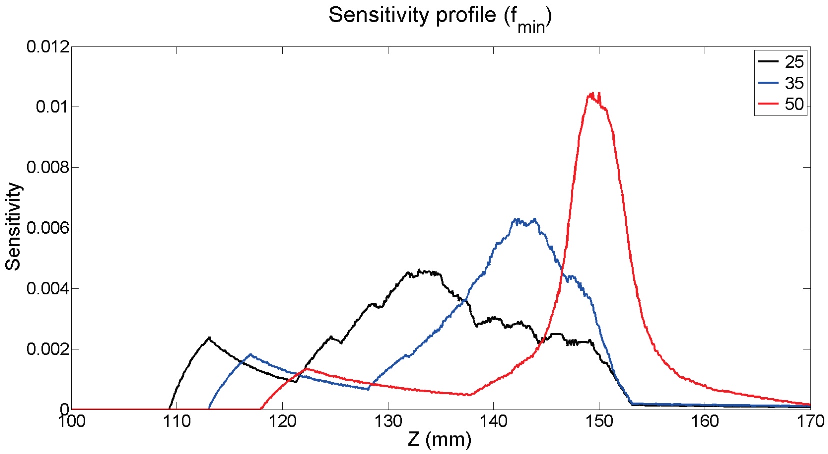

Figure IV.21: Sensitivity profile for different minimum focal distances.

IV.2.3.1.2 Number of holes Nb_h

The number of holes also impacts the sensitivity distribution (Fig. IV.22). With increasing number of holes the sensitivity profile becomes more smooth. For two holes the sensitivity region of each hole can be clearly identified, whereas at twenty holes this effect is much less significant. Global sensitivity is very slightly impacted. It increases with increasing hole number: 0.994 mm with two holes, 0.111 mm with 11 holes and 0.114 mm with 20 holes.

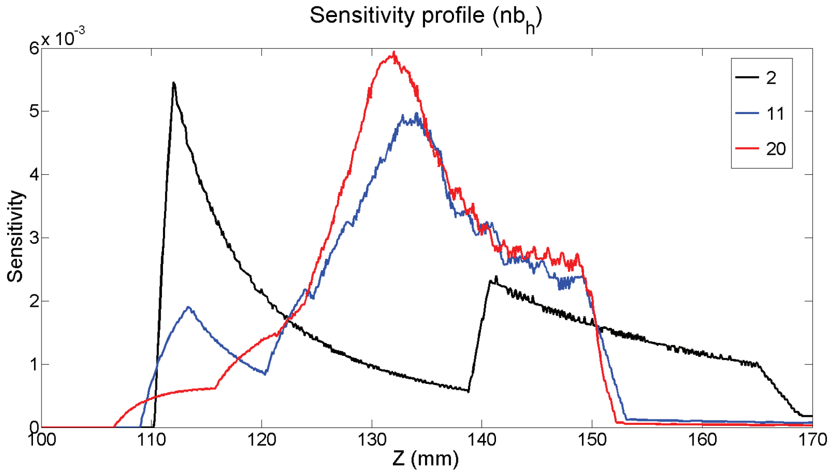

Figure IV.22: Sensitivity profile for different hole numbers.

IV.2.3.1.3 Hole size h

Figure IV.23 shows the spatial and angular resolution for varying hole size. This parameter influences the global system sensitivity (DQE at zero frequency), which increases with increasing hole size. The resolution also depends on h. If h is increased resolution is deteriorated. Momentum transfer resolution is not represented but it also decreases since it depends on angular resolution. Thus, here, the compromise between sensitivity and resolution is clearly visible.

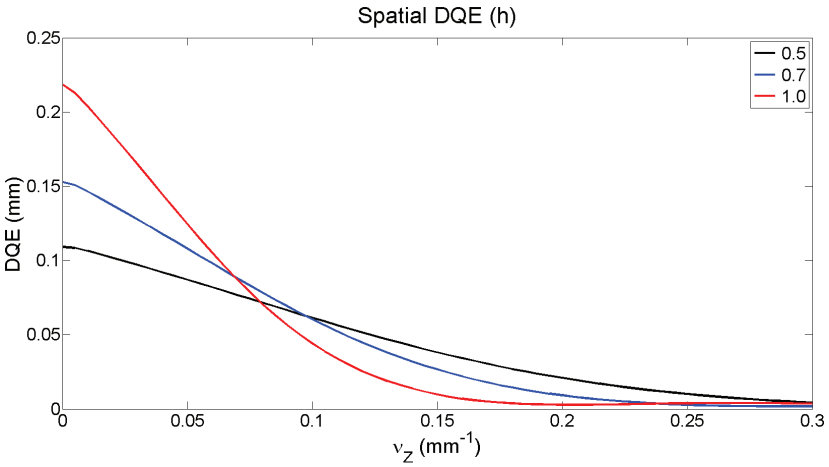

(a) *Spatial resolution.*

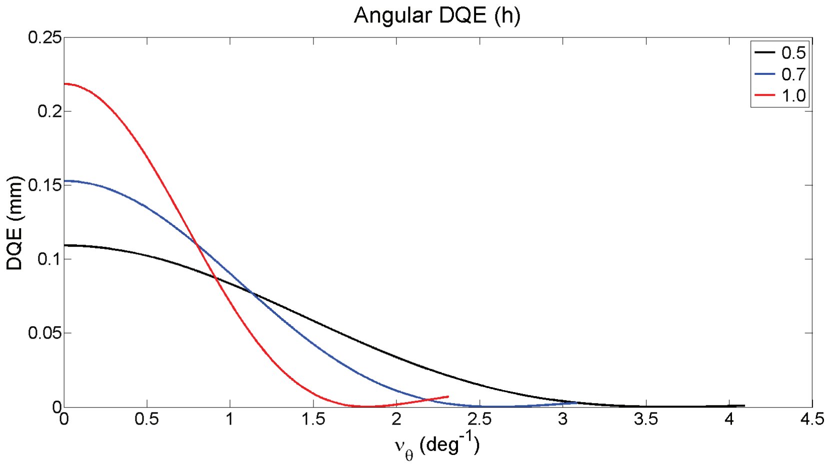

(b) *Angular resolution.*

Figure IV.23: Spatial and angular resolution for different hole sizes.

IV.2.3.1.4 Pixel size p

Pixel size has very low impact on the system sensitivity. It slightly impacts the system resolution (Fig. IV.24). If the pixel size increases the resolution decreases. However, it seems that hole size is dominant on system resolution and sensitivity in this collimation configuration.

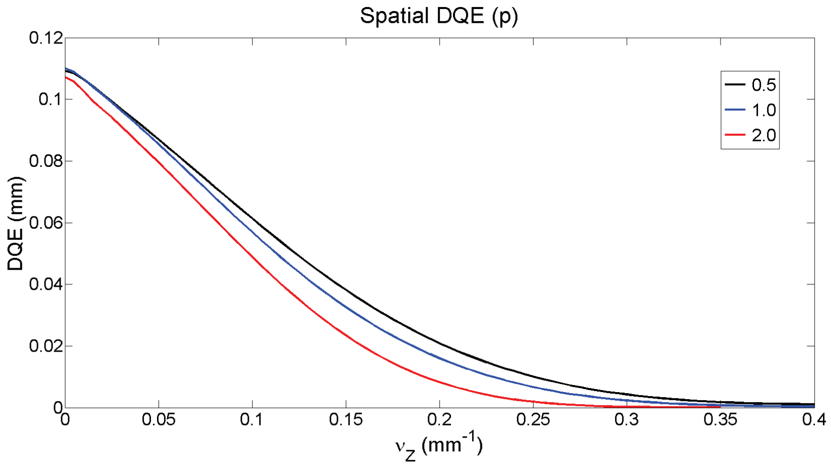

(a) *Spatial resolution.*

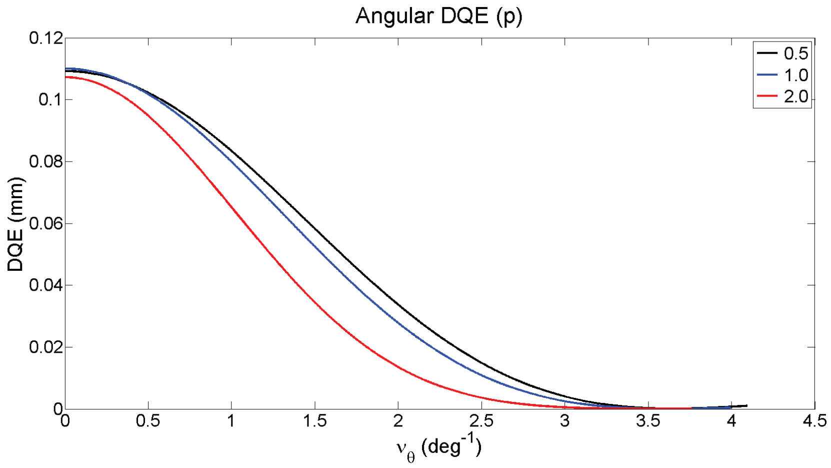

(b) *Angular resolution.*

Figure IV.24: Spatial and angular resolution for different pixel sizes.

IV.2.3.1.5 Collimation height H

If collimation height is increased, system sensitivity falls and resolution increases (Fig. IV.25). Hence, here again, a compromise between sensitivity and resolution has to be found. However, the most important impact of H is the scattering angle range that can be measured. The maximum scattering angle becomes smaller if H increases (Fig. IV.26). Hence, H will be chosen to access the right angles.

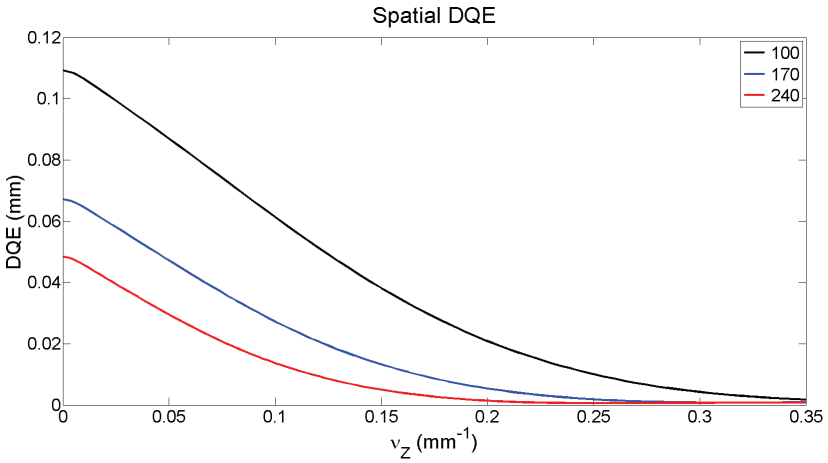

(a) *Spatial resolution.*

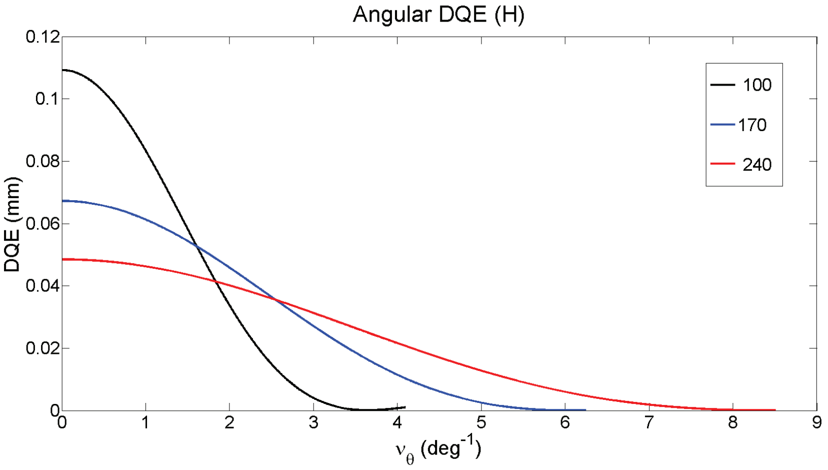

(b) *Angular resolution.*

Figure IV.25: Spatial and angular resolution for different collimation heights H.

IV.2.3.1.6 Detector dimension L_d

If the detector size is increased, the global system sensitivity will increase (Fig. IV.27) because the detection area becomes larger. Thanks to this sensitivity increase, the resolution is increased at the same time. If the collimation height is fixed, an increasing detector size will also allow to intercept higher scattering angles (Fig. IV.28). This factor as well as higher costs for larger detectors has to be taken into account when optimizing the system parameters.

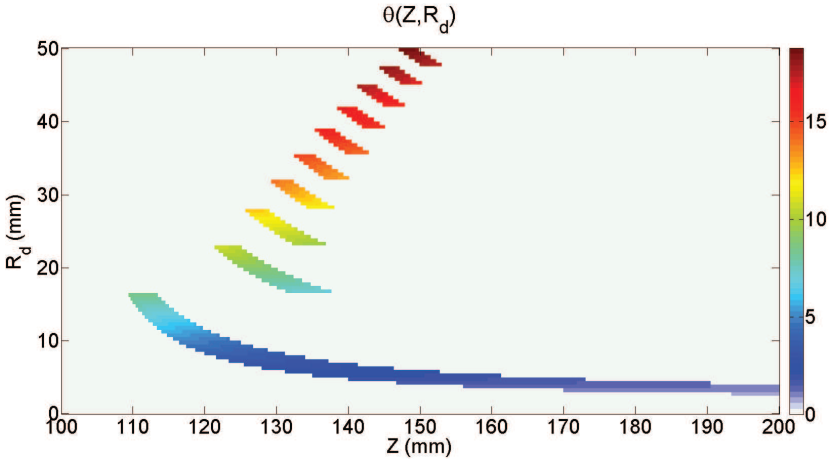

(a) $H = 100$ *mm*

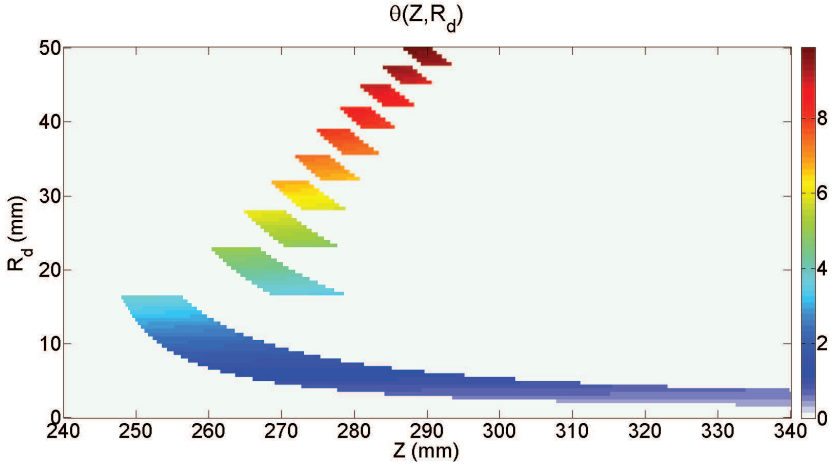

(b) $H = 240$ *mm*

Figure IV.26: Covered scattering angles θ for different collimation heights H.

IV.2.3.1.7 Incident photon energy

Figure IV.29 shows the influence of the incident photon energy on momentum transfer resolution. It can be seen that higher energies induce a lower momentum transfer resolution, which is another reason, for the incident X-ray spectrum not to be too high in energy.

In fact, χ resolution depends on angular resolution, spectral resolution of the detector and the energy of incident photons.
Table IV.1 summarizes the impact of the different system parameters.

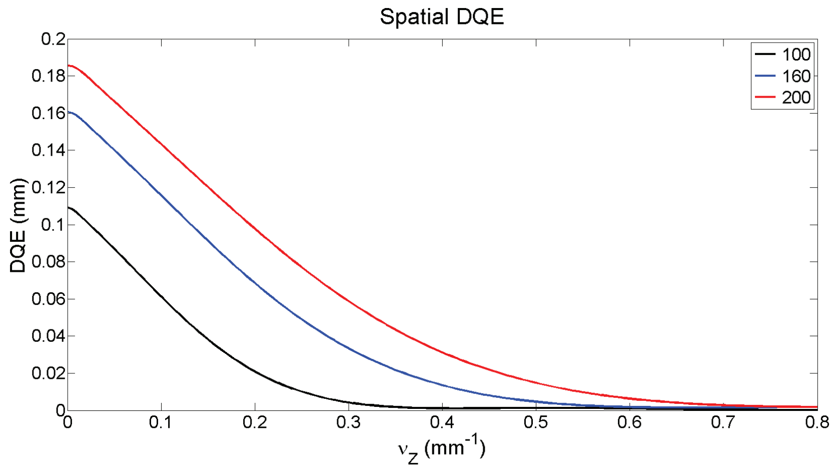

(a) *Spatial resolution.*

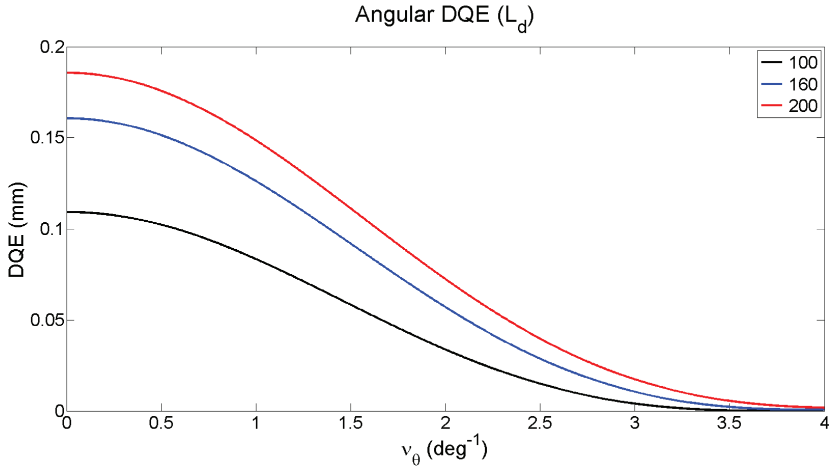

(b) *Angular resolution.*

Figure IV.27: Spatial and angular resolution for different detector dimensions L_d.

	Global sensitivity	Sensitivity distribution	Resolution	θ-range
f_{min}		*		
f_{max}		*		
Nb_h		*		
p			-	
h	+		-	
H	-		+	*
L_d	+			*

Table IV.1: Summary of the impact of the different system parameters. "+" means that the variable increases with increasing system parameter, "-" that it is falls with rising system parameter and "*" that the change cannot be expressed by an increase or a decrease.

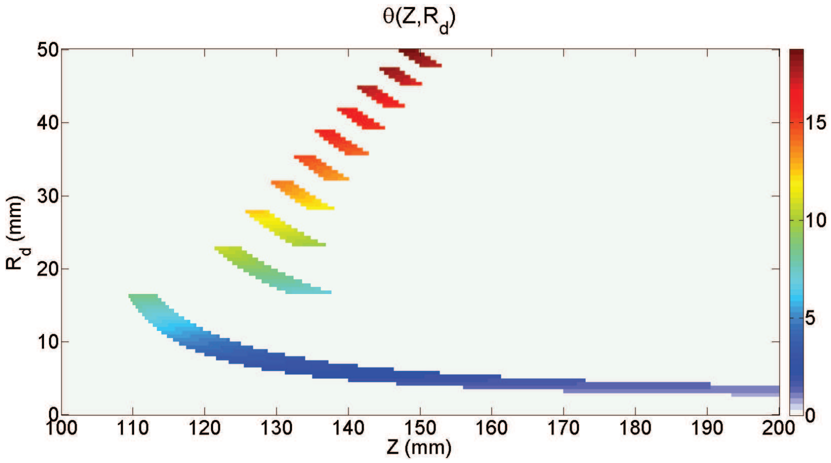

(a) L_d = *100 mm*

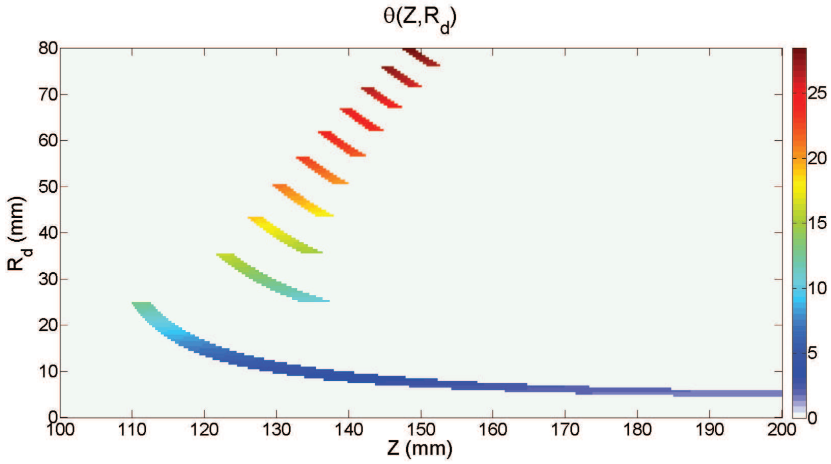

(b) L_d = *160 mm*

Figure IV.28: Covered scattering angles θ for different detector dimensions L_d.

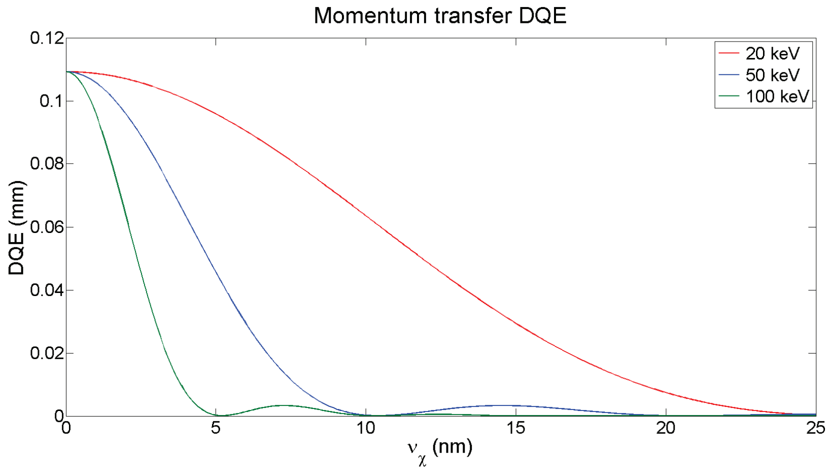

Figure IV.29: Influence of photon energy on momentum transfer resolution.

IV.2.3.2 Optimization strategy

As the impact of the different parameters on system performances is known, it is possible to establish an optimization strategy, which takes into account the different constraints explained in section IV.2.1. First of all, it is important to be able to measure the required χ-range to separate the two tissue types, i.e. between 1 and 2.5 nm^{-1}. The sensitivity to these χ values is determined by the energy range of the incident spectrum and the range of scattering angles that can be measured by the system. As the energy range is already fixed between 20 and 100 keV, this permits to determine the range of θ required to meet the momentum transfer requirements. In fact, this technique will lead to a different range of angles for each energy. It is not necessary to cover all momentum transfer values at each energy. Hence, the angular range might be restricted. However, it is important to be able to measure the whole χ-range at each Z position in the sample. With given detector dimension the angular range is fixed by the collimation height. Thus, collimation height has to be adjusted in order to cover the previously determined scattering angles. As collimation heights strongly impacts on system sensitivity, the hole size can be fixed afterwards in a way that sensitivity and momentum transfer resolution are sufficient. Even though the required χ resolution is about 0.2 nm^{-1} resolution due to collimation system should be higher as the spectral resolution of the detector is not taken into account yet. Figure IV.30 summarizes the described optimization strategy.

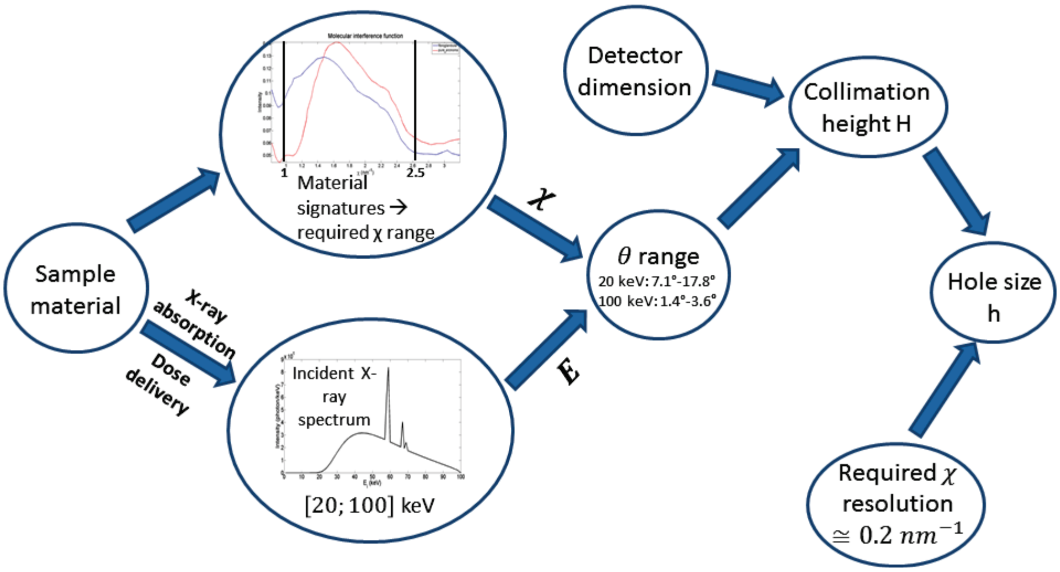

Figure IV.30: Schematic representation of the optimization process.

The previously described strategy was applied in order to optimize a multifocal and a monofocal collimation system by following the steps below:

1. Calculation of the angular range, which covers the required χ-range at 60 keV (middle of the fixed incident spectrum) $\Rightarrow$ 2.3° to 5.9°
2. Calculation of collimation height H so that the center of the first/inner hole aims 2.3°
3. Adjust h in order to obtain the best possible sensitivity by respecting resolution constraints

4. Adjust the number of holes in order to ensure sufficiently large collimation septa[3], to avoid "transparency" (photons are able to cross walls between holes) and to be able to manufacture the collimation system
5. Detector dimension may be adjusted to improve system sensitivity but angles should not become to high

Since pixel size had little impact, it was fixed at 1 mm.

IV.3 Optimized collimation systems

This section presents the performance in terms of sensitivity and resolution of a multifocal collimation and a monofocal collimation obtained by following the different steps explained at the end of the previous section.

Optimization strategy lead to the following parameters for the multifocal collimation:

- Pixel size $p = 1$ mm
- Minimum focal distance $f_{min} = 25$ mm
- Maximum focal distance $f_{max} = 50$ mm
- Collimation height $H = 230$ mm
- Hole size $h = 0.8$ mm
- Number of holes $Nb_h = 7$
- Detector dimension $L_d = 100$ mm

The parameters for the monofocal collimation are:

- Pixel size $p = 1$ mm
- Minimum focal distance $f_{min} = 50$ mm
- Maximum focal distance $f_{max} = 50$ mm
- Collimation height $H = 255$ mm
- Hole size $h = 0.8$ mm
- Number of holes $Nb_h = 4$
- Detector dimension $L_d = 120$ mm

---

[3] Separation walls between two holes

Focal distances associated to each hole between f_{min} (inner hole) and f_{max} (outer hole) follow a linear distribution. Knowing the different focal distances permits to determine the position of each hole. In order to obtain a performing collimation system, it is required to define the septa (= walls) which separate the different holes and avoid multiplexing. Calculations are explained in appendix B.

It has to be noted that the two configurations were optimized in order to obtain approximately the same global sensitivity (integrated sensitivity over all pixels and z values) and to cover almost the same angular range [Marticke *et al.*, 2015a]. Thus, the detector of the monofocal system is larger and this configuration will be more cost-intensive. In the following, it will first be explained how to determine the septa if the hole positions are known and afterwards, performances of these two configurations will be compared.

IV.3.1 Sensitivity

Figure IV.31 shows the sensitivity distribution of the two configurations. It can be seen that the spatial resolution of the first hole is very poor for both configurations, i.e. it covers many z-values. Maximum sensitivity is almost the same in both cases. By comparing the sensitivity profiles (Fig. IV.32), it can be observed that the monofocal system presents a maximum around 50 mm in the sample, which corresponds to the fixed focus. It is significantly higher than the one of the multifocal system, which confirms that sensitivity is actually more concentrated around the focus than for the multifocal collimation. However, focus is not perfect, since the distribution around 50 mm is rather large. This is due to the poor resolution of the first hole and to larger holes resulting from the sensitivity-resolution compromise.

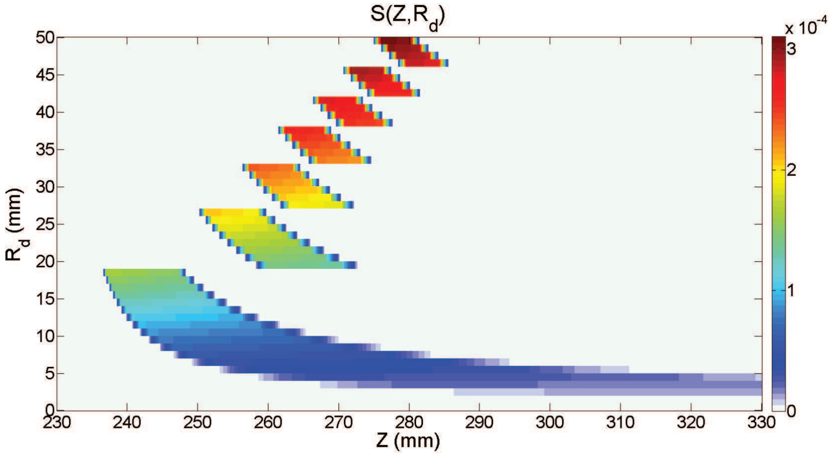

(a) *Multifocal*

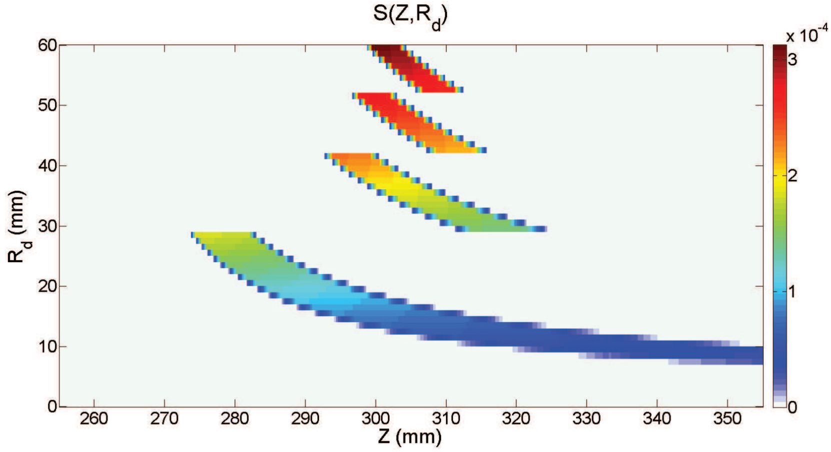

(b) *Monofocal*

Figure IV.31: Sensitivity distribution of multi- and monofocal optimized collimation system.

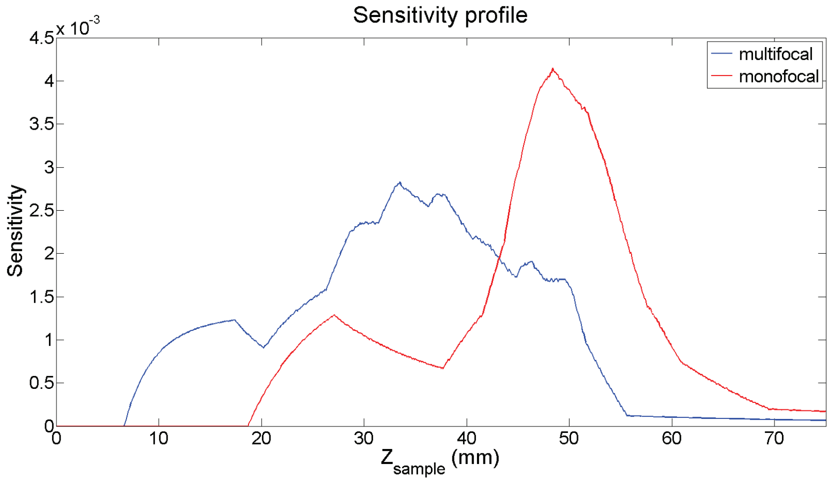

Figure IV.32: Sensitivity profile of optimized collimation systems as a function of the position in the sample Z_{sample}.

IV.3.2 Resolution

Comparison of the spatial resolution curves of the two collimations is shown in figure IV.33. This representation confirms that the global sensitivity (DQE at zero frequency [4]) is almost exactly the same for both configurations. Multifocal resolution[5] is about 9.6 mm and monofocal resolution about 8.7 mm. Thus, in both cases the spatial resolution is quite poor and might not be sufficient. It might be necessary to adjust the sensitivity-resolution compromise in order to improve the spatial resolution in the sample. Another possibility might be to not take into account the first hole if a better resolved image is wished but that would also imply a loss of sensitivity.

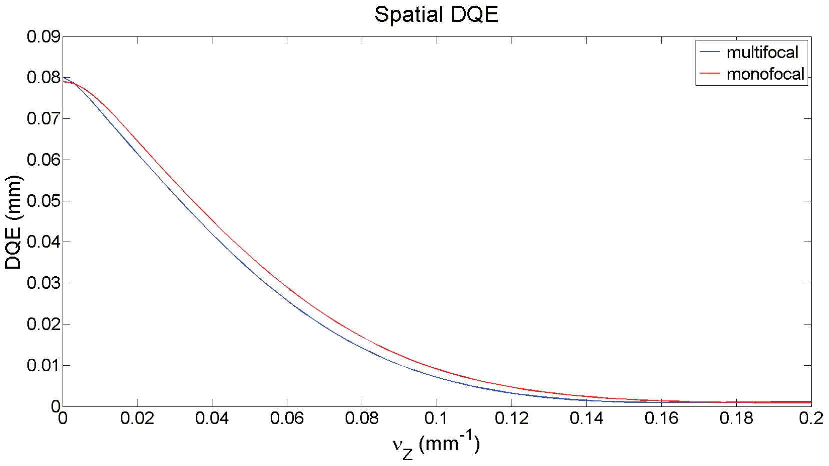

Figure IV.33: Comparison of the spatial resolution curves of the optimized collimation systems. About 9.6 mm for the multifocal system and 8.7 mm for monofocal system.

Figure IV.34 compares the angular resolution curves of the two optimized collimation systems. Angular resolution of the multifocal collimation is about 0.21° and the one of the monofocal system is about 0.19°, which is almost the same. Unlike spatial resolution, angular resolution is sufficient for our needs.

The resolution that is the most important in diffraction imaging is the momentum transfer resolution. Its resolution curves for an incident filtered tungsten spectrum (energies between 20 and 100 keV) are shown in figure IV.35. This leads to a mean (over the whole spectrum) momentum transfer resolution of about 0.07 nm^{-1} in the multifocal case and 0.06 nm^{-1} in the monofocal case. The required momentum transfer resolution is 0.2 nm^{-1}. Hence, this seems reasonable even if detector resolution is not taken into account yet. Momentum transfer resolutions for different energy values (20, 60 and 100 keV) are given in table IV.2. At 100 keV, χ-resolution is still 0.15 nm^{-1} for multiangle collimation and 0.13 nm^{-1}. If a mean energy resolution of 3 keV is considered, this corresponds to 5 % at 60 keV. This leads to a resolution of 0.1 nm^{-1} at 2 nm^{-1}. At 20 keV this resolution will be lower and 100 keV it will be higher, but in average the global momentum transfer resolution should not be worse than the required 0.2 nm^{-1}.

---

[4] If a sensitivity value without unity is needed, the DQE value at zero frequency just has to be divided by the sample thickness. Here, this leads to a global sensitivity of about $1.6 \cdot 10^{-3}$.

[5] Resolution is calculated as explained in section II.2.1.2.

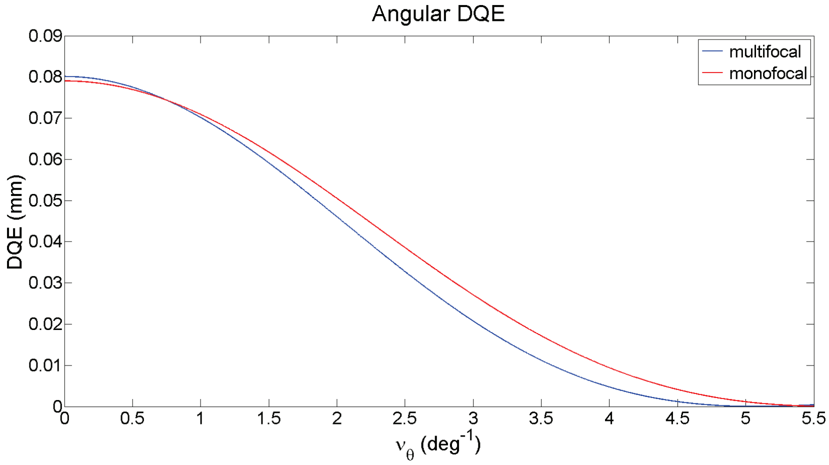

Figure IV.34: Comparison of the angular resolution of the optimized collimation systems. About 0.21° for the multifocal system and 0.19° for monofocal system.

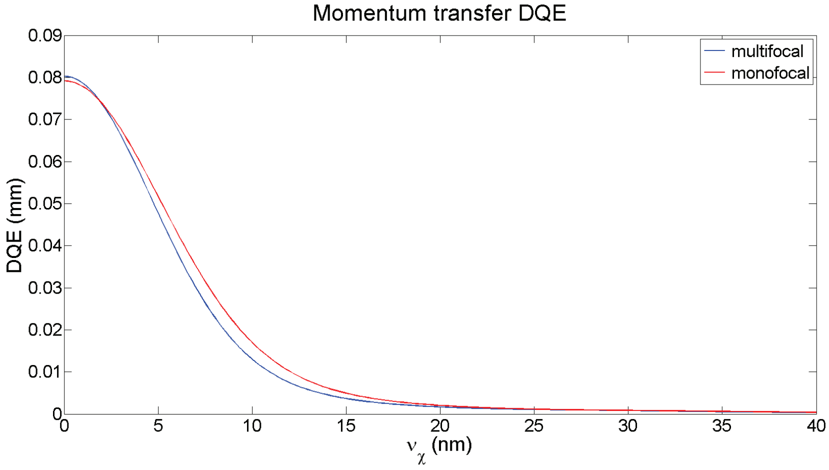

Figure IV.35: Comparison of the momentum transfer resolution (calculated for an energy of about 60 keV) of the optimized collimation systems.

Table IV.2 summarizes the different resolution results for the two collimation systems.

	Spatial (mm)	Angular (°)	χ at 20 keV (nm^{-1})	χ at 60 keV (nm^{-1})	χ at 100 keV (nm^{-1})
Multifocal	9.6	0.21	0.029	0.09	0.15
Monofocal	8.7	0.19	0.027	0.08	0.13

Table IV.2: Mean resolution results for the two collimation systems (without detector spectral response).

IV.3.3 Covered angles and momentum transfer values

Figure IV.36 shows the different angles that are covered by the system as a function of z and the detector position. It can be seen that the external holes cover higher angles and that the angular range is almost the same for both configurations. Figure IV.37 indicates the χ-range covered by each hole of both collimation systems. The region of interest corresponds to the required χ-range. It can be seen that χ-range is well covered except for the last hole, where low χ values are missing. Here, sensitivity is used for unsuitable χ-values. This might be a problem for the multifocal system if a tumour is situated at Z values covered by the last hole. For monofocal system this should not be a problem as each hole is focused on the same object point. To avoid the problem of the last hole, its associated scattering angles should be decreased. This can be realized by increasing collimation height or by decreasing detector dimension. Though, in both cases global sensitivity would be decreased.

A study of tissue separability with both systems should show whether both collimation are suitable to separate fibroglandular and cancerous tissues.

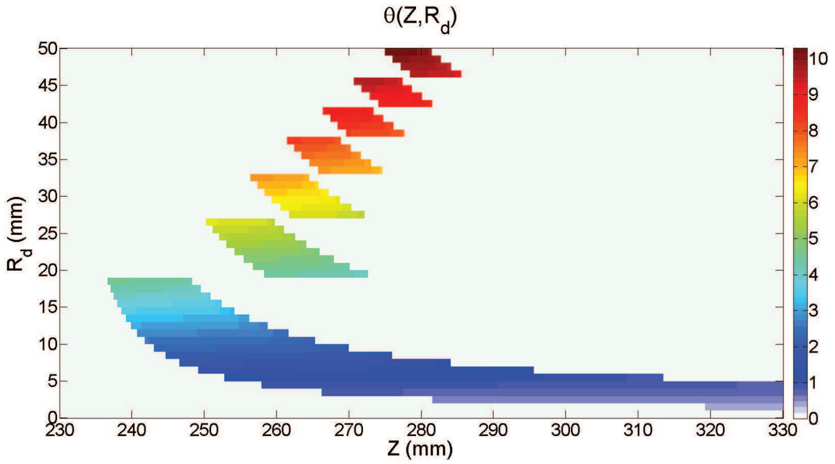

(a) *Multifocal*

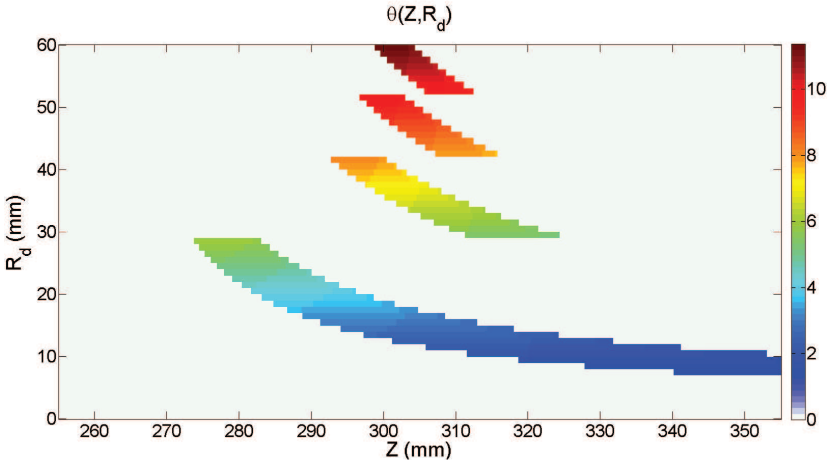

(b) *Monofocal*

Figure IV.36: Acessible angles by multi- and monofocal optimized collimation systems.

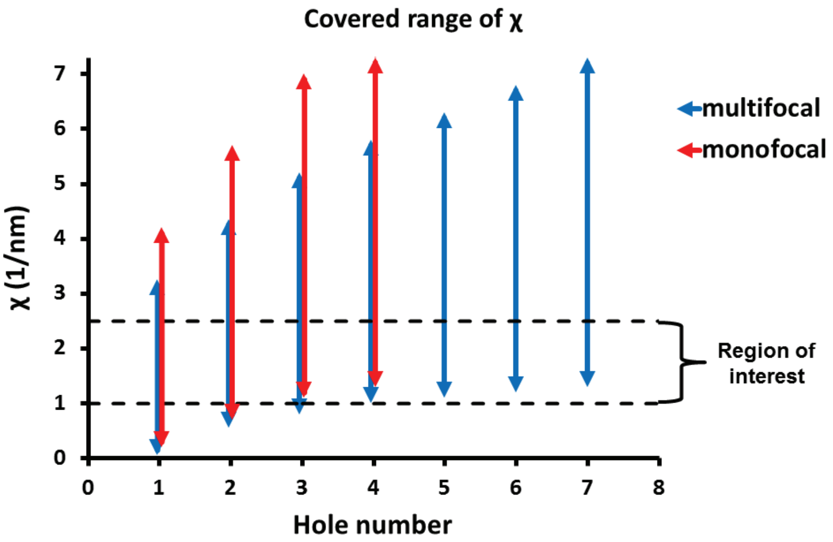

Figure IV.37: χ values covered by the optimized multi- and monofocal collimation systems. The region of interest corresponds to the χ-range that is necessary to separate cancerous and fibroglandular tissue scattering signatures.

In order to finalize this study, it was necessary to realize realistic simulations of the whole XRD system associated to a breast phantom, which take into account the incident X-ray spectrum, sample absorption and the detector response. The following section presents the different simulations and their results.

IV.4 Simulation study of the complete X-ray diffraction system associated to a breast phantom

The capacity of the two optimized collimation systems to distinguish between carcinoma and fibroglandular tissue was assessed using Monte-Carlo simulations of the whole XRD system and a realistic breast phantom. These simulations were performed with PENELOPE [Salvat *et al.*, 2008], by adapting cross-sections for coherent scattering to take intra- and intermolecular radiation interferences into account. Cross-sections used in PENELOPE for Rayleigh scattering only contain the Thomson cross-section and the coherent scatter form factor (Eq. I.1.8). We replaced these cross-sections by the diffraction signatures determined by [Kidane *et al.*, 1999] (Figure IV.10).

IV.4.1 Simulated XRD system

A schematic view of the whole XRD system that was simulated is given in figure IV.38. It can be noticed that the detector dimension L_d is equal to two times $R_{d,max}$. In fact, in the following, each result depending on the detector position will be given as a function of R_d, which corresponds to the radius of a circle with its center coinciding with the center of the detector. As diffraction symmetry is inherently cylindrical and as the collimation systems are both conical, measured information only depend on R_d-position on the detector and not on x- and y-position.

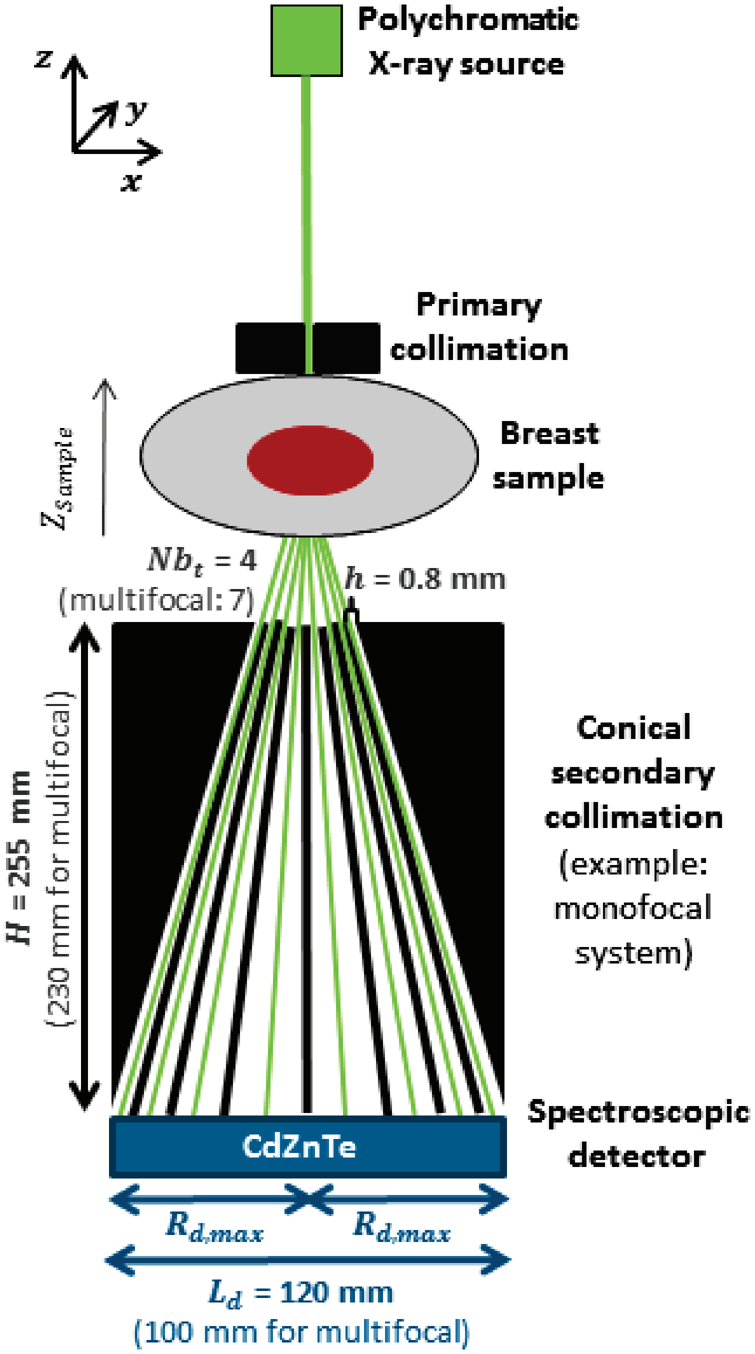

Figure IV.38: Schematic representation of the simulated XRD system.

IV.4.1.1 Incident X-ray beam

The incident X-ray source was simulated using SpekCalc [Poludniowski *et al.*, 2009]. The anode material was tungsten, and the anode angle was about 70°. A 0.2 mm copper filter was used to suppress photons below 20 keV as these photons would be almost entirely absorbed by photoelectric interaction (Figure IV.9) producing a dose deposit without generating any diffraction signal. The choice of a tungsten anode instead of a molybdenum as normally used in mammography can be justified by the fact that molybdenum presents low Bremsstrahlung intensity compared to its characteristic peaks. In EDXRD it is important to have a more continuous distribution of photons over the different energies of the incident spectrum. Hence, tungsten is a suitable choice.

To study the impact of the maximum spectrum energy on system performances, a range of tube voltages, between 40 kV and 150 kV, were tested (Fig IV.39).

The primary collimation system (in contact with the object to be imaged) was simulated in a perfect absorbing material to obtain a thin pencil beam with a diameter of 1 mm. This collimator was located at 175 mm from the X-ray source focus. The focus was also set to be 1 mm.

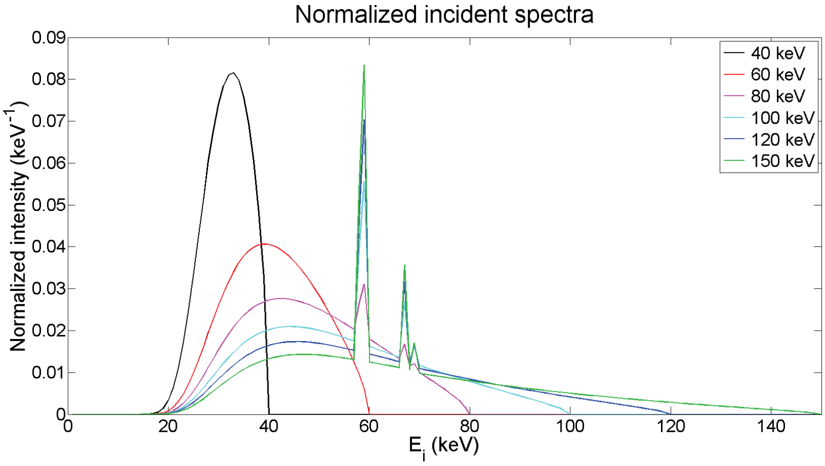

Figure IV.39: Simulated incident tungsten spectra (normalized to one) all filtered with 0.2 mm of copper.

IV.4.1.2 Secondary collimation

The previously described optimized collimation systems (mono- and multifocal) were simulated in order to assess their performances. As explained previously both collimations are conical, which is in line with the intrinsic symmetry of XRD. They are composed of hollow iron cones nested one inside the other. A beam-stop was placed in the center to stop signal coming from X-ray transmission.

Both systems require an x,y-scan to image the whole region identified as suspect by conventional mammography. However, most of the results are given for one point in x,y-plan (the center) over the whole depth. Hence, in the case of monofocal collimation a Z-scan with four scan positions (focus on Z_{Sample} = 15, 25, 35 and 45 mm) was simulated.

As can be seen in figure IV.32 the system sensitivity of multifocal configuration does not cover exactly the whole sample (from $Z_{Sample} = 0$ mm to $Z_{Sample} = 50$ mm). Instead it covers partly Z_{Sample} values that are not part of the sample. A gap of 10 mm was introduced between the secondary collimation system and the phantom. The corrected sensitivity distribution of the multifocal collimation is shown in figure IV.40.

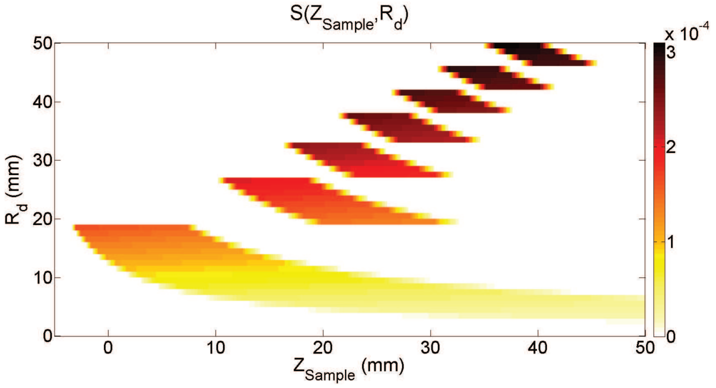

(a) *Sensitivity distribution.*

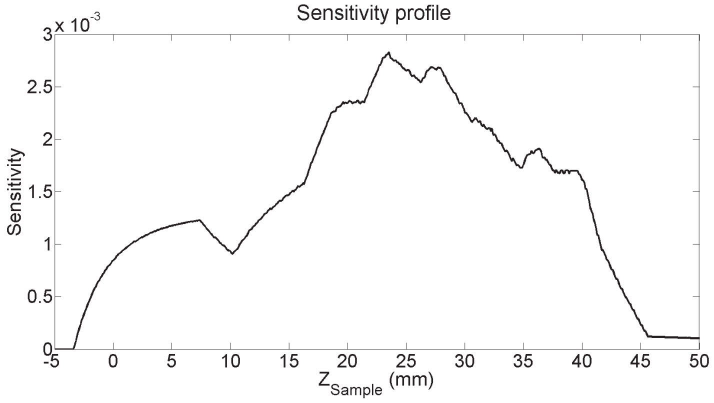

(b) *Sensitivity profile.*

Figure IV.40: Sensitivity distribution and sensitivity profile of the simulated multifocal X-ray diffraction system across the sample (sample starts at 0 and ends at 50 mm) after introduction of a gap of 10 mm between sample and secondary collimation.

IV.4.1.3 Detector

For this study, we considered a 5 mm thick 2D 10×10 cm^2 (or 12×12 cm^2 for monofocal collimation system) spectroscopic CdZnTe detector with 2.5 mm anode pitch.

In a previous study [Montemont *et al.*, 2014], it was shown that a spatial resolution of 0.4 mm can be achieved at 60 keV with this detector geometry using transient signal processing (sub-pixelization). Here, a relatively large, 1 mm, sub-pixel size was used for our system simulations. The associated ASIC (Application-Specific Integrated Circuit) model was IDeFX-HD [Michalowska *et al.*, 2010], which combines low noise and low power. In practice, the average energy resolution was about 2.5% at 122 keV.

Using these characteristics a detector response matrix (DRM) was obtained using Tasmania, a simulation environment developed in our laboratory. This detector response model combines an interaction model using PENELOPE [Salvat *et al.*, 2008] and the electric field and charge transport model described in [Montemont *et al.*, 2006]. Figure IV.41 shows the simulated DRM. Here, the low-energy (Sec. I.1.3.4) tail was taken into account.

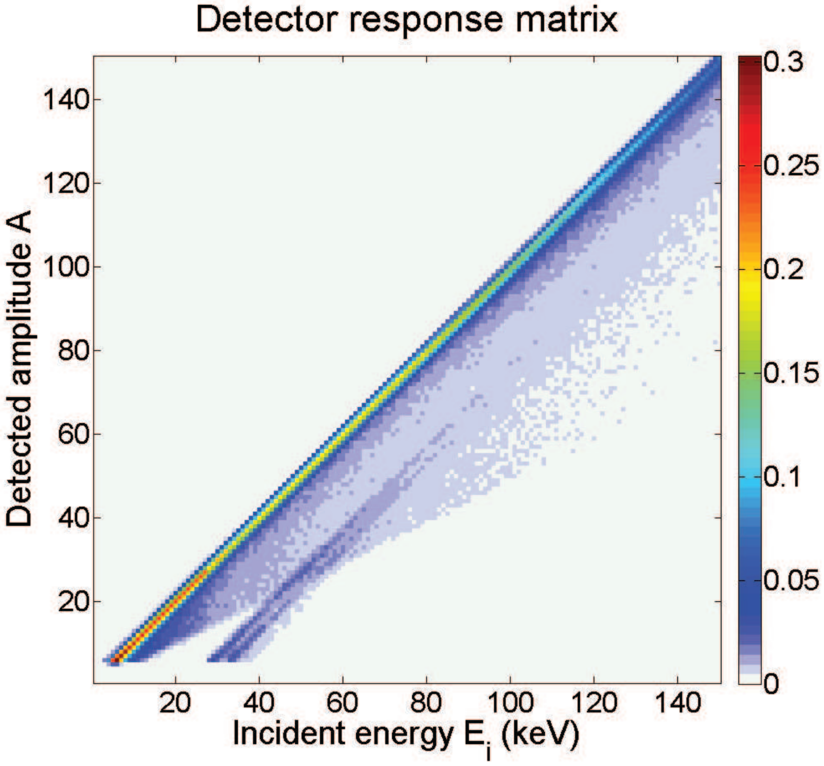

Figure IV.41: Simulated response matrix for 5 mm thick 2D 10×10 mm spectroscopic CdZnTe detector.

IV.4.2 Breast phantom

The simulated breast phantom is a 50 mm thick, and 150 mm diameter cylinder of adipose tissue containing an ellipsoid of fibroglandular tissue (diameter: 70 mm) corresponding to a region with altered composition. To assess the impact of the thickness of this fibroglandular tissue, this ellipsoid was simulated in a range of sizes: 20, 30 and 40 mm. This allowed us to verify whether high density breast tissue can be imaged with XRD. A small spherical nodule of carcinoma was located in the center of the phantom to simulate the presence of a tumor. The diameter of this nodule was about 4 mm, which corresponds to a very small tumor size at the limit of detection in scintimammography. A healthy breast phantom was simulated without nodule. Figure IV.42 shows a schematic representation of the phantom breast sample.

As system sensitivity of multifocal collimation is not the same over the whole sample thickness, it is important to study the impact of tumor position on its detectability using this collimation system. The tumor was always located in the fibroglandular mass as this location will result in doubtful mammography results. Therefore, tumor position variation study was realized with 40 mm fibroglandular thickness. Four tumor offset positions were tested: +20 mm,

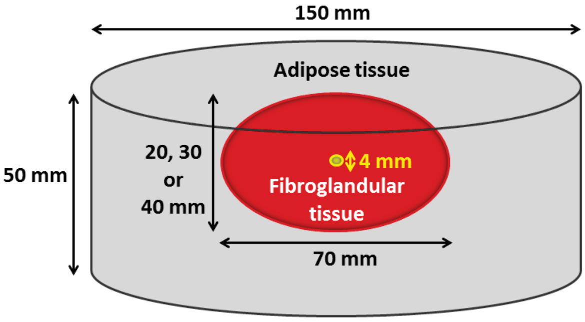

Figure IV.42: Simulated breast phantom presenting a pure carcinoma nodule (yellow sphere).

+10 mm, -10 mm and -20 mm. A positive tumor offset corresponds to a greater distance between tumor and detector, while a negative offset corresponds to a shorter distance.

IV.4.3 Realized simulations

To limit simulation time and variance, diffraction spectra were simulated in several steps. A description of the simulation method is given in appendix C. XRD spectra of the different phantoms were simulated for varying incident photon numbers and for different incident X-ray spectra (maximum energies between 40 and 150 keV). A scan in x-direction was simulated as well, in order to test the reconstruction of a phantom slice of the phantom's center (y=0). The scan step was chosen to be 1 mm. Simulation method of the scan slice is also described in appendix C.

IV.4.4 Reconstruction method

The reconstruction method to reconstruct the simulated scan slice corresponds to MLEM algorithm with the use of a dictionary as explained in section III.2.1. The dictionary is composed of amorphous reference signatures (fibroglandular tissue, carcinoma and adipose tissue). However, it has to be specified that the reference signatures were not the "theoretical" signatures. In fact, these signatures already include distortion by the collimation system and absorption (5 cm for each pure tissue type). Hence, the dictionary only has to be multiplied by the DRM to obtain the system matrix $\mathcal{A}^6$ as explained in section III.2.1. However, the fact that absorption is already included in the pure tissue signatures might lead to inaccuracy in reconstruction process. Absorption of fibroglandular tissue and carcinoma is very similar (that is why conventional mammography leads to unclear outcome) but absorption by adipose tissue is much higher. This technique was chosen as it was faster and easier to implement.
The aim of reconstruction is to process measurements, $m(A, R_d, x)$, to estimate the material coefficients of the mask, $t\,(Z, i, x)$, which can be represented in a color image, using material i as a single color channel.

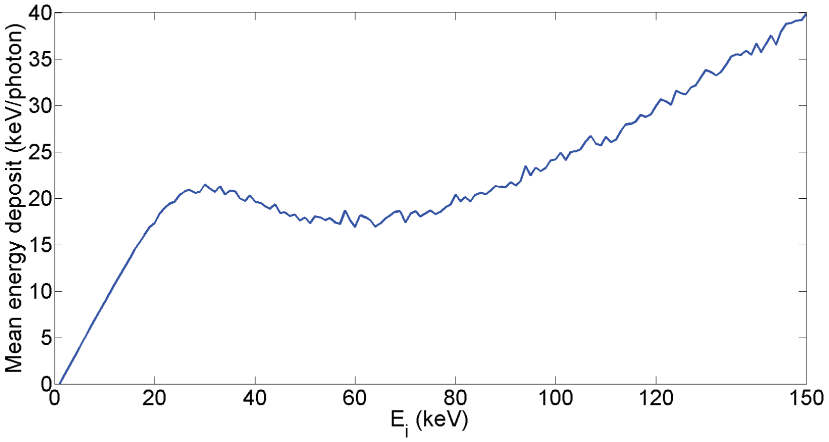

Figure IV.43: Mean energy deposit per photon (multiple interactions included) in 50 mm of a material with average chemical composition of breast tissue IV.2.1 as a function of incident photon energy.

IV.4.5 Dose estimation

Dose was estimated using the incident X-ray spectrum S_{inc}, the mean energy deposit E_{mean} per photon as a function of incident photon energy E_i (Fig. IV.43) and the calculated required incident photon number N_{ph} to obtain the desired separation between scattering spectra with and without carcinoma.
The mean total energy deposit D_E for a given incident spectrum can be calculated using:

$$D_E = \frac{\sum_{E_i} E_{mean}\left(E_i\right) \cdot S_{inc}\left(E_i\right)}{\sum_{E_i} S_{inc}\left(E_i\right)} \tag{IV.4.1}$$

The result is given in keV. For an incident spectrum with maximum energy of 100 keV the mean total energy deposit is about 18.88 keV. Knowing the required number of incident photons, the required mean dose can be calculated as follows:

$$D = \frac{D_E \cdot 1.6 \cdot 10^{-16} \cdot N_{ph}}{m_{irr}} \tag{IV.4.2}$$

where $1.6 \cdot 10^{-16}$ is the conversion factor to transform keV into joules (J) and m_{irr} corresponds to the directly irradiated mass. In the present case the irradiated mass is about $5 \cdot 10^{-5}$ kg (i.e. pencil beam surface $(10^{-6} m^2)$ × sample thickness $(50 \cdot 10^{-3} m)$ × sample density $(1 kg \cdot m^{-3})$).

IV.4.6 Results

The last part of this chapter presents the results of the different simulations. All results are given by taking into account the detector response except in section IV.4.6.1, where the impact of the detector response is studied. Results for the monofocal collimation are obtained by a global analysis taking into account the four scan positions.

---

[6] The explicit direct model used for reconstruction is given by equation C.2.1 in appendix C.

Figure IV.44 and figure IV.45 show two sample spectra as a function of the detected amplitude A and the detector position R_d (normalized by the number of incident photons) to be distinguished for monofocal and multifocal collimation respectively. The fibroglandular region was 30 mm thick and the incident spectrum had a maximum energy of 100 keV. For the monofocal collimation, the scan position focused on the center of the breast phantom, i.e. the tumor, is represented.

By summing the normalized spectra of multifocal collimation in both directions (A and R_d), the object depending global sensitivity can be determined, taking geometrical factors into account as well as the sample interaction cross-section. It corresponds to the ratio between the number of incident photons on the sample and the number of detected photons. This is not exactly the same quantity as defined in section IV.2.2, which is purely geometrical (which proportion of photons emitted isotropically at a given z can be detected by the system) and does not take into account interaction cross-section in the sample.

In this case, object depending global sensitivity was approximately $2 \cdot 10^{-3}$. Multiplication of this value by the number of incident photons gives the total number of photons detected. In the case of monofocal collimation a mean object depending sensitivity of the four scan positions was determined, which is also around $2 \cdot 10^{-3}$.

The CNR^2 per incident photon of the multifocal system is about $2 \cdot 10^{-6}$, which is very low, explaining why the differences between the two spectra (without tumor (Figure IV.45.a); with tumor (Figure IV.45.b)) are not directly visible by comparison of the two spectra. Mean CNR^2 of a Z-scan with the monofocal collimation configuration is even lower, only about $1.3 \cdot 10^{-6}$.

Figure IV.44.c and figure IV.45.c show the difference in absolute value between the spectra with and without tumor. From these figures, it becomes obvious that the difference to be detected is only in the order of a few percent (difference values between 10^{-8} and 10^{-7} compared to spectrum values of about 10^{-6}).

Hereafter, the photon number and associated dose are mostly given for a separation of 1σ, 2σ or 3σ between spectra with and without tumor. Figure IV.46 shows the ROC curves corresponding to these separations.

The degree of separation for 3σ corresponds to an almost perfect separation based on the associated ROC curve [Marticke *et al.*, 2015b]. The number of incident photons required to attain this separation will be around $7 \cdot 10^6$ for monofocal collimation system and $5 \cdot 10^6$ for the multifocal system. If a tube current of about 10 mA is fixed, a few cm^2 (region identified as suspicious during conventional mammography) could be scanned within some seconds, which is reasonable.

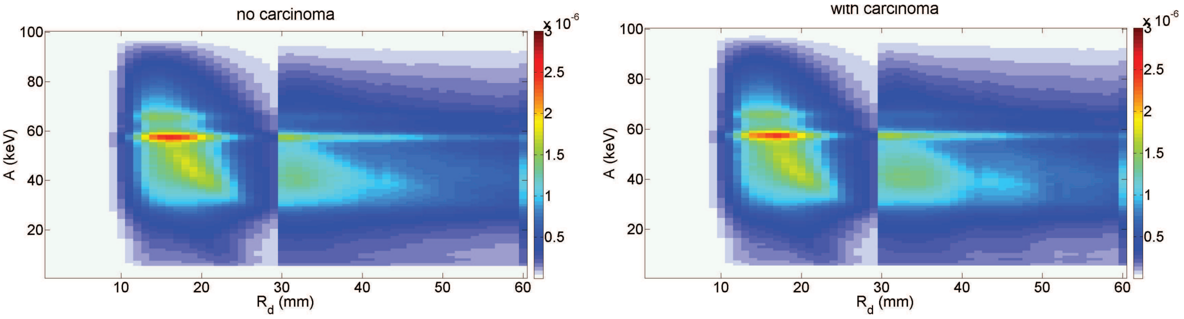

(a) *Spectrum without tumor.* (b) *Spectrum with tumor.*

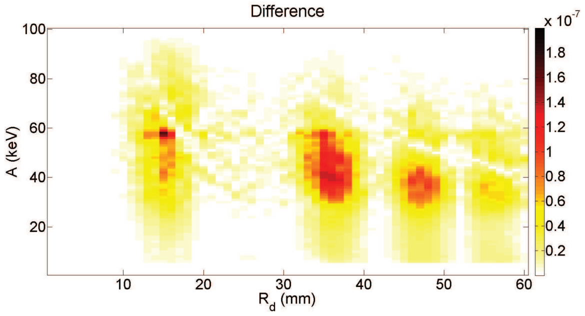

(c) *Absolute value of the difference.*

Figure IV.44: Example of simulated spectra (30 mm fibroglandular thickness, incident spectrum with 100 keV maximum energy) for monofocal collimation configuration (scan position with focus on the tumor), and the absolute value of their difference. The spectra are normalized by the number of incident photons. It can be noticed that the difference to be detected is very small compared to spectrum values.

IV.4.6.1 Impact of the detector response

First of all, the impact of the detector spectral resolution on the required number of photons was evaluated. Figure IV.47 represents the required incident photon number for different levels of separation between healthy breast tissue and carcinoma for the phantom with 30 mm fibroglandular tissue thickness and 100 kVp incident X-ray spectrum for both collimation systems. Deterioration of the XRD spectra due to the effect of DRM leads to an increase around 1.5 times of the number of required incident photons. It can be noticed that the multifocal system requires almost the same photon number with DRM as the monofocal system without DRM for the same separation.

The corresponding number of detected photons for 3σ separation is shown in figure IV.48. As the global system sensitivities are almost the same for both collimation systems, the required number of detected photons is higher for the monofocal collimation ($\approx 1.5 \cdot 10^4$) as well.

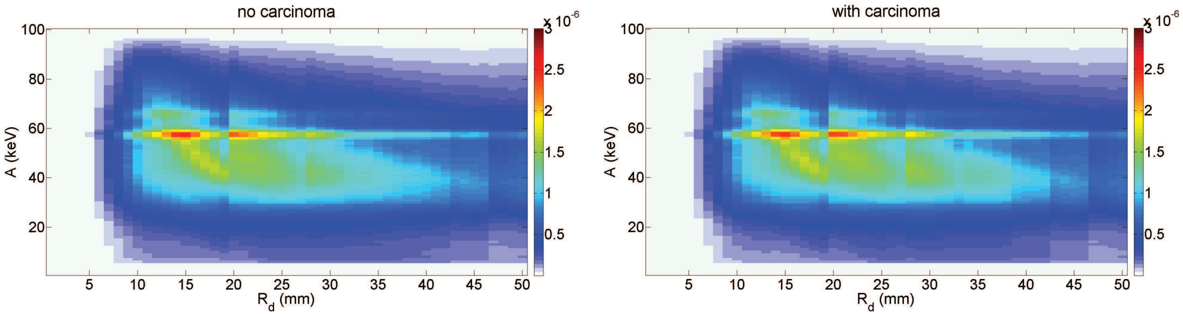

(a) *Spectrum without tumor.* (b) *Spectrum with tumor.*

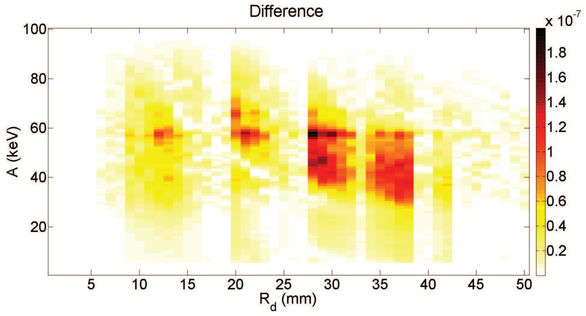

(c) *Absolute value of the difference.*

Figure IV.45: Example of simulated spectra (30 mm fibroglandular thickness, incident spectrum with 100 keV maximum energy) for multifocal collimation configuration, and the absolute value of their difference. The spectra are normalized by the number of incident photons. The difference to be detected is very small compared to spectrum values.

IV.4.6.2 Monofocal versus multifocal collimation system

ROC curves for different incident photons numbers were generated, using the analytical method presented in chapter II, in order to study the evolution of the discrimination power with increasing photon number for both collimation configurations. The simulated spectra were the same as in the previous section (30 mm fibroglandular tissue, 100 kVp incident spectrum).

As can be seen in figure IV.49, 1000 photons lead to a ROC curve corresponding to the chance line. Phantom with and without tumor cannot be discriminated. $1 \cdot 10^6$ incident photons seem to be at least necessary in order to achieve a correct separation between the different phantom types. Performance of the monofocal system at this photon number is similar to the system of conventional mammography mentioned in section IV.1.2.2. $1 \cdot 10^7$ incident photons lead to an almost perfect separation with the monofocal collimation system and to a perfect separation with the multifocal system[7].

This study confirms that the multifocal system is more powerful than the monofocal system at least with an 100 kVp incident spectrum. In the following, this will be checked for different incident spectra.

---

[7] The ROC curve was not represented as it coincides with the axis of the system of coordinates.

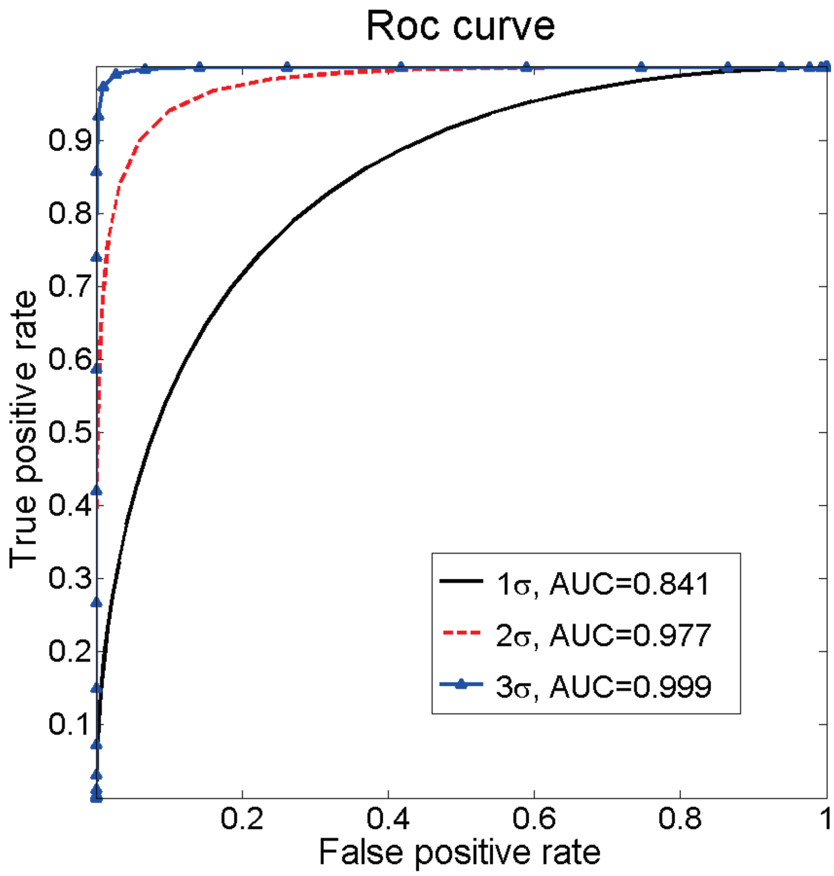

Figure IV.46: ROC curves corresponding to different separations between phantom with and without tumor.

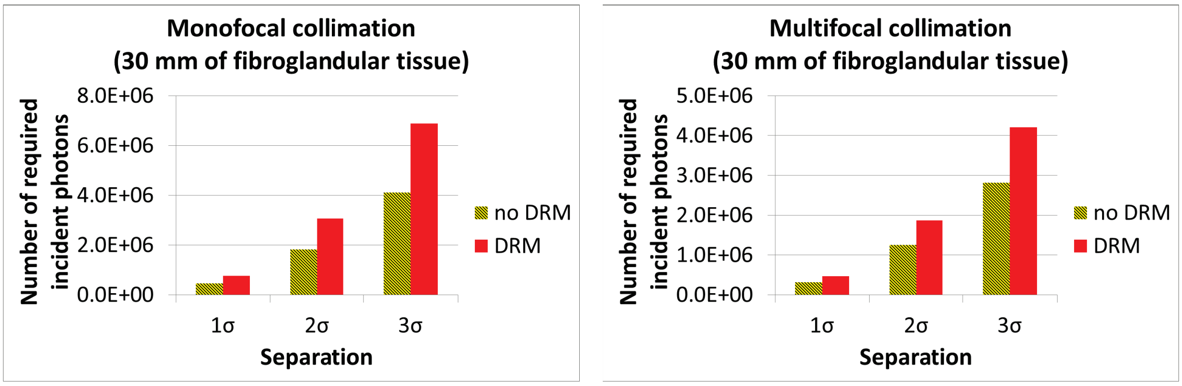

(a) *Monofocal collimation.* (b) *Multifocal collimation.*

Figure IV.47: Study of the effect of DRM: Required number of incident photons to obtain a separation of 1σ, 2σ and 3σ between phantom with and without tumor. The incident spectrum was the one with 100 keV maximum energy.

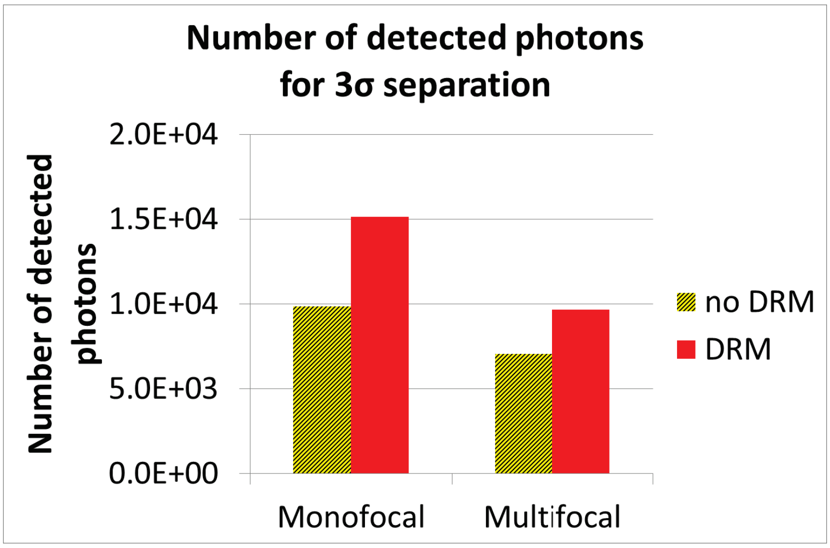

Figure IV.48: Number of detected photons required to have a 3σ separation with and without DRM for both collimation systems (same simulations as in figure IV.47).

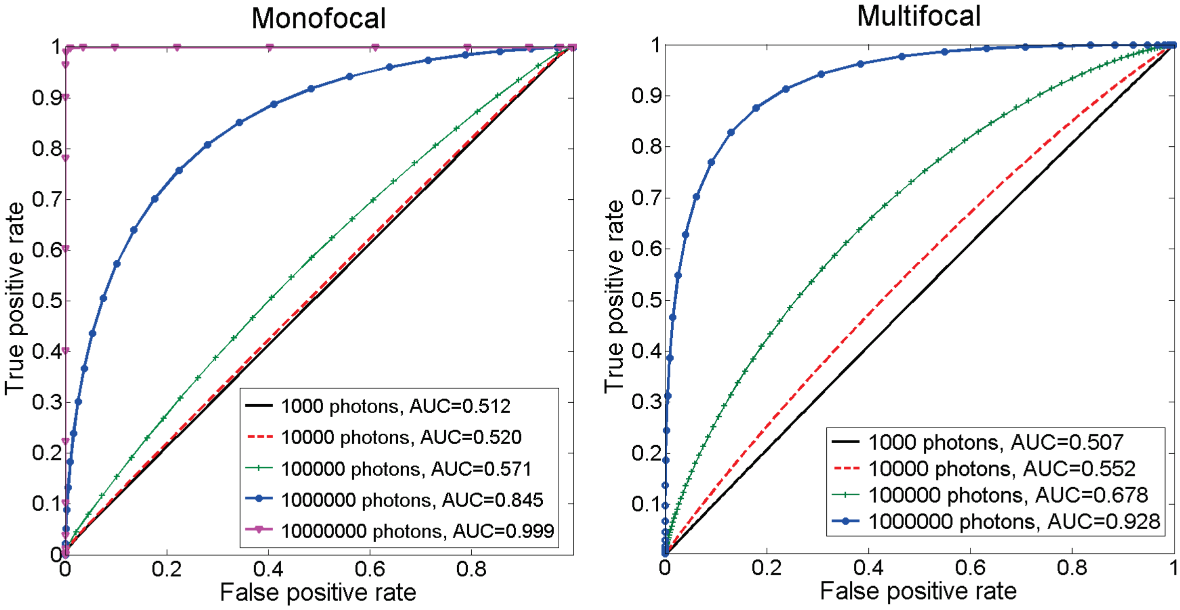

(a) *Monofocal collimation.*

(b) *Multifocal collimation.*

Figure IV.49: ROC curves and associated AUC corresponding to different incident photon numbers.

IV.4.6.3 Influence of different maximum energies

Figure IV.50.a shows the required photon number to detect a tumor situated at the center of the field of view for a phantom with 30 mm thick fibroglandular tissue section as a function of the maximum energy of the incident spectrum. The corresponding dose received by samples is represented in figure IV.50.b. For the multifocal collimation a minimum around $3.6 \cdot 10^6$ photons can be observed at 60 and 70 keV corresponding to a dose of about 0.21 mGy. For the monofocal system the minimum is situated at 50 keV maximum energy. These "optimum" energy values are only valid for the here presented systems. If the geometrical system were different, "optimum" incident spectra might change.

For spectra with lower maximum energy, the combination of photon energy and intercepted angles is less appropriate and absorption remains higher than coherent scattering. At higher energies, the probability of absorption and coherent scattering continue to decrease, whereas Compton scattering probability remains constant. Hence, the proportion of signal due to Compton scattering increases steadily with increasing photon energy, causing blurring of the spectrum and unnecessary radiation exposure. However, even though the received dose increases with higher maximum spectrum energy, the total dose still remains low and acceptable compared to conventional mammography, where delivered dose is between 1 and 3 mGy [Stines, 2007] or even higher [Hendrick, 2010].

It can be noticed that the monofocal scan always requires more photons, i.e. more dose, than the multifocal acquisition except for 40 keV maximum energy. Moreover both systems require an x,y-scan to image the region identified as suspect by mammography. Hence, the monofocal system requiring a scan in the z-direction as well, appears too complex for routine use in practice. This would require devices to be able to move in x-, y- and z-direction and scan time would significantly increased. Hence, the following results are only presented for the multifocal system.

IV.4.6.4 Impact of fibroglandular thickness for the multifocal collimation

The results for the required photon number and the corresponding dose for an incident spectrum with a maximum energy of 100 keV and different fibroglandular thicknesses are summarized in table IV.3. Fibroglandular thickness has a negligible impact on the number of photons required, thus averaging at about $4{\cdot}10^6$ for a corresponding dose of about 0.24 mGy. This dose is low compared to conventional mammography, where the dose delivered is at least between 1 and 3 mGy.

Hence, scattering signatures for cancerous tissues and fibroglandular tissues are sufficiently decorrelated to be distinguished even when the number of detected photons ($\approx$ 9000) is small. Furthermore, as the required dose does not significantly vary with fibroglandular tissue thickness, high density breast regions do not seem a problem in XRD, unlike in conventional mammography.

Fibroglandular thickness (mm)	Required incident photon number	Required dose (mGy)
20	$3.85{\cdot}10^6$	0.232
30	$4.20{\cdot}10^6$	0.253
40	$4.12{\cdot}10^6$	0.244

Table IV.3: Incident photon number and dose required to obtain a separation of 3σ for an incident spectrum with maximum energy of 100 keV.

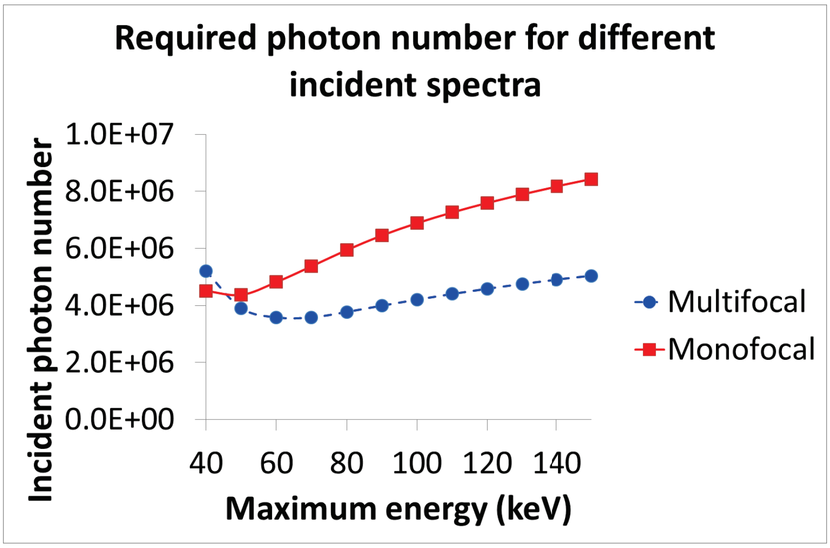

(a) *Required number of incident photons.*

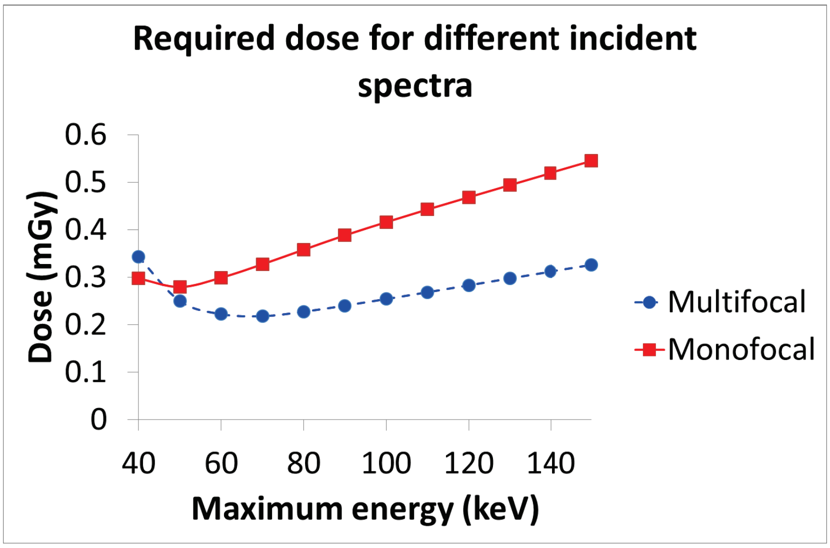

(b) *Required dose.*

Figure IV.50: Comparison of the required photon number and dose to attain 3σ separation between phantom with and without tumor for different incident spectra.

IV.4.6.5 Impact of tumor position for the multifocal collimation

Figure IV.51 shows the absolute values for the difference between phantoms with and without tumor for different tumor offsets in deptth. The segments on the graphs correspond to the different holes in the collimation system. If the tumor is located in the center (no offset), it can be "seen" by five holes. Indeed, these holes are sensitive to signal from the center (Figure IV.40.a). If a tumor offset is introduced, the difference will not be detected by the same holes, as the system has a variable sensitivity distribution. The first hole always detects part of the difference, as it is sensitive throughout the sample thickness. The difference was notably low for the +20 mm offset, where the tumor was positioned at $Z_{Sample} = 45$ mm. This position corresponds to a very low sensitivity region for the system configuration presented.

The received doses for different tumor offsets and maximum spectrum energies are presented in Figure IV.52. These data confirm that a tumor at +20 mm offset is more difficult to detect than tumor in other positions and requires an approximately 5-fold higher dose. However, the total dose received still remains below that with conventional mammography (1-3 mGy).

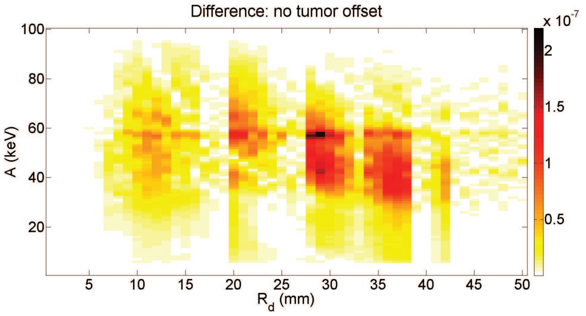

(a) *No tumor offset, i.e. tumor in the center (Z_{sample} = 25 mm).*

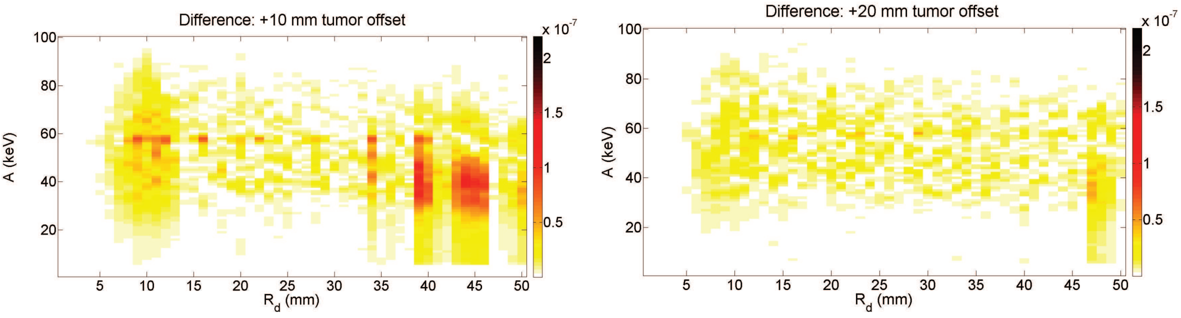

(b) *+10 mm tumor offset (Z_{sample} = 35 mm).* (c) *+20 mm tumor offset (Z_{sample} = 45 mm).*

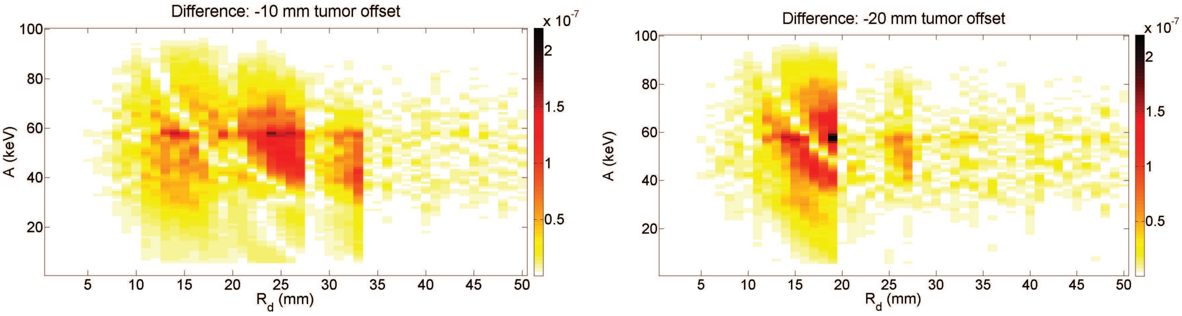

(d) *-10 mm tumor offset (Z_{sample} = 15 mm).* (e) *-20 mm tumor offset (Z_{sample} = 5 mm).*

Figure IV.51: Difference spectra (multifocal collimation) with and without tumor offsets. The difference was very low for an offset of +20 mm, which can be explained by lower sensitivity in this position (Figure IV.40).

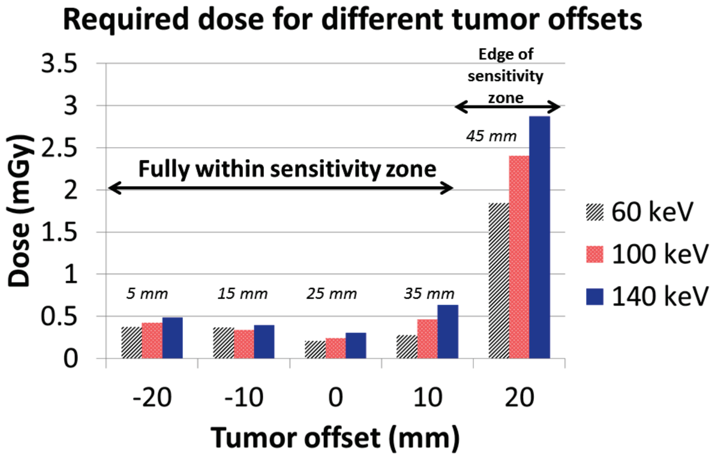

Figure IV.52: Dose required to distinguish (3σ separation) between spectra with and without carcinoma. Numbers above the bars indicate the position of the tumor within the sample (depth). All tumors were fully within the field of view, except for +20 mm, which explains the significantly higher dose required in this case.

IV.4.6.6 Reconstructed phantom slice for the multifocal collimation

Figure IV.53 shows an example of a simulated spectrum at $x = 0$ (corresponding to the phantom's center) for a phantom (30 mm fibroglandular tissue thickness, 100 kVp incident spectrum) with a tumor at its center. The number of incident photons was about $5 \cdot 10^6$, corresponding to approximately 10^4 detected photons. The number of photons per channel was very low, producing a relatively noisy spectrum. However, the number of incident photons is within the order of magnitude determined previously to obtain a 3 σ separation between phantoms with and without tumor.

Each scan slice was simulated using the same incident photon parameters, and the image of the breast was reconstructed (Figure IV.54). It should be noted that the field of view for the image was set smaller than the phantom height. Hence, only 5 mm of adipose tissue is visible on the upper and lower parts of the image, rather than 10 mm.

This reconstruction clearly shows that the tumor will only be found in the reconstructed image if it is actually in the simulated phantom slice (Figure IV.54.b and fig IV.54.d), and therefore no false positive results should be produced. Compared to reconstructions at 60 kVp, reconstructions at 100 kVp seem to have a better spatial resolution in the z-direction and present fewer edge artifacts at the limit between fibroglandular tissue and adipose tissue, especially at low depths within the sample. This difference is due to lack of information in the momentum transfer space at low depths. The first hole in the collimation system is sensitive to low depth values, but the corresponding scattering angles are also low. Thus, to cover the same momentum transfer range as for other holes, a higher energy value would be needed. It appears that the information obtained at 60 kVp is not sufficient to distinguish between fibroglandular and adipose tissue. Reconstruction artifacts (i.e. detection of carcinoma) in the upper corners of the images at 60 kVp were also caused by the lack of information at this energy level. As for low depths, these high depth values are only covered by the first hole with very low diffraction angles. The same observations are made for reconstructions based on XRD spectra without noise, which are shown in figure IV.55. The only difference is that reconstructed fibroglandular region is more homogeneous than in reconstructions using noisy signal. Hence, reconstruction defaults are due to the acquisition system (especially limited spatial resolution) and not to noise.

Because of these results, it appears that higher energies could be useful even though, for the system described here, detection of the small tumor was determined to be optimum (in terms of dose received) at 60 keV maximum energy. However, the optimal energy was determined based on the capacity to distinguish between presence and absence of a tumor, whereas here we require spatial information concerning each tissue type to reconstruct an image slice.

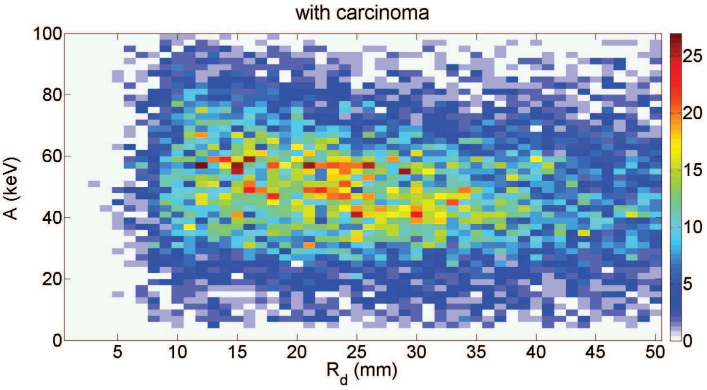

Figure IV.53: Example of spectrum with tumor used for image reconstruction at x = 0: 30 mm fibroglandular thickness, 100 keV maximum energy in the incident spectrum (100 kVp), $5 \cdot 10^6$ incident photons.

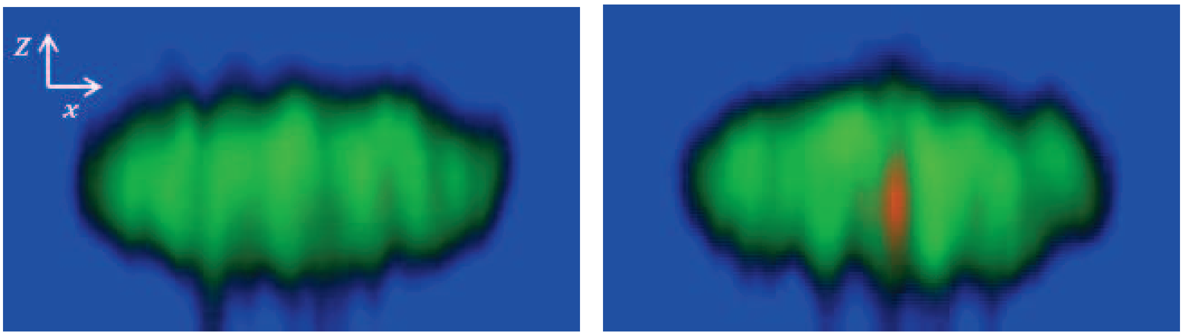

(a) *No tumor (100 kVp).* (b) *With tumor (100 kVp).*

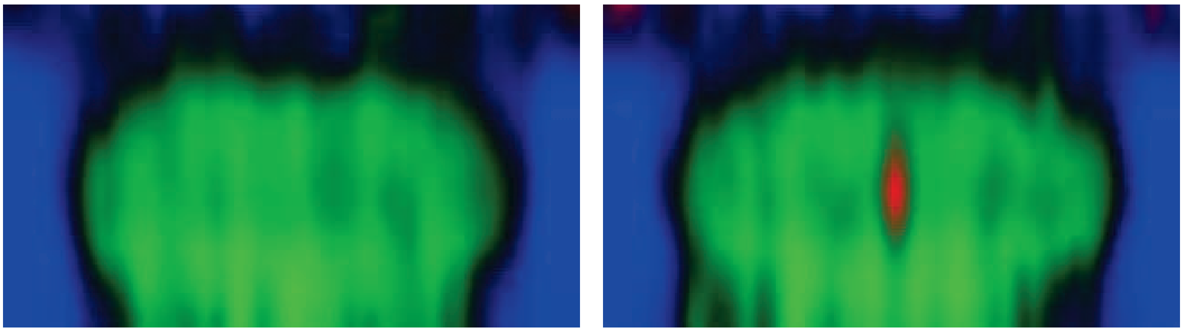

(c) *No tumor (60 kVp).* (d) *With tumor (60 kVp).*

Figure IV.54: Reconstructed images for XRD spectra acquired with an incident spectrum at 100 kVp or 60 kVp (blue = adipose tissue, green = fibroglandular tissue, red = carcinoma).

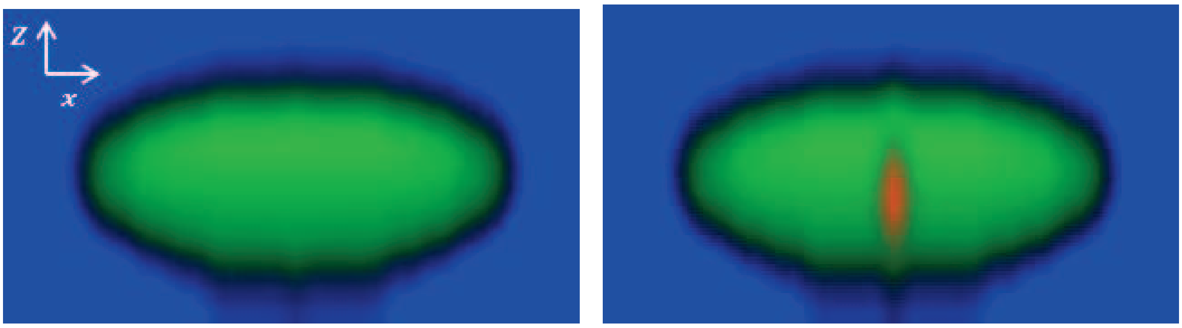

(a) *No tumor (100 kVp).* (b) *With tumor (100 kVp).*

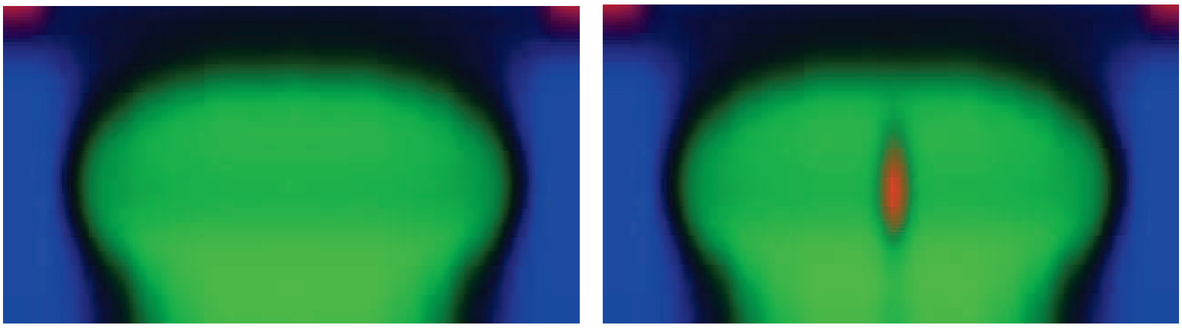

(c) *No tumor (60 kVp).* (d) *With tumor (60 kVp).*

Figure IV.55: Reconstructed images from XRD spectra without noise acquired with incident spectra at 100 kVp or 60 kVp (blue = adipose tissue, green = fibroglandular tissue, red = carcinoma).

IV.4.6.7 Impact of slight multiplexing

As the introduction of multiplexing in XRD imaging and especially the use of coded apertures [MacCabe *et al.*, 2012] is a discussed issue, a non exhaustive simulation study concerning the introduction of a limited multiplexing in the presented multifocal collimation system has been carried out.

An illustration of the meaning of limited multiplexing in this study is presented in figure IV.56. No multiplexing means that each part of the detector only receives signal from only one hole to which it is associated. In the case of limited multiplexing, a predefined percentage (at most 50 %) of the detector part intercepts photons coming from the associated hole as well as from the previous hole. In the example of figure IV.56, 50 % of the detector part receive signal from two holes. This is called 50 % multiplexing.

The technique of multiplexing allows to increase the number of detected photons by maintaining the same number of incident photons. In fact, it permits to improve the global system sensitivity. However, spatial information and hence, tissue information is mixed. Multiplexing will only be useful if the gain in sensitivity is higher than the loss of information, i.e. if the required dose for a given separation is smaller than without multiplexing.

The global system sensitivity[8] for different multiplexing percentages is represented in figure IV.57. As expected sensitivity increases with higher multiplexing percentages. At

---

[8] 100 kVp incident spectrum

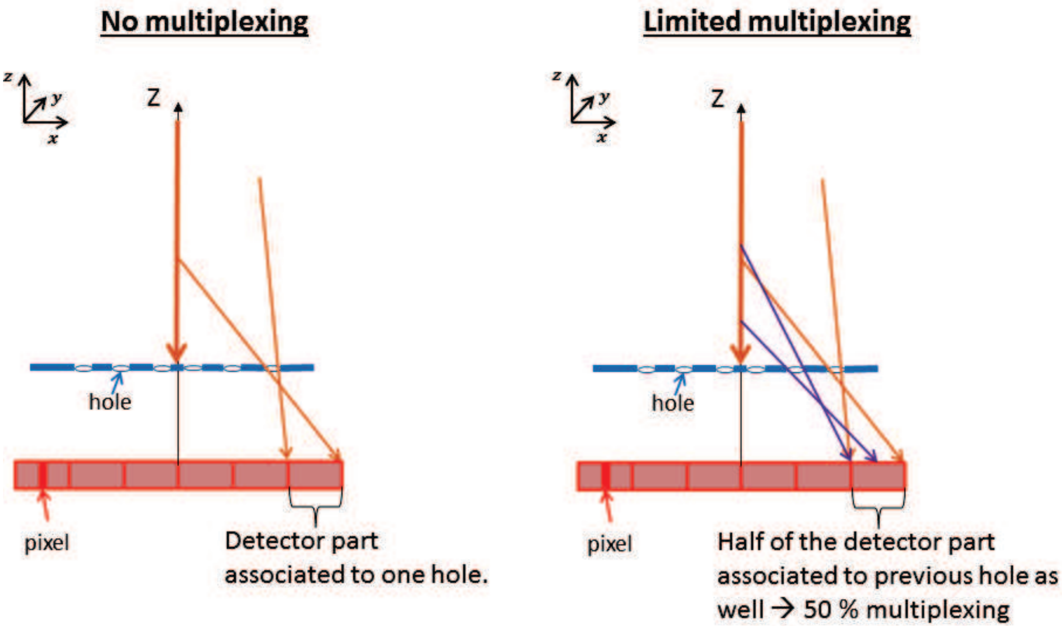

Figure IV.56: Illustration of the principle of limited multiplexing: A detector part does not only receive the signal from one hole but a predefined percentage of the detector part also receives signal coming from the previous hole. Here, 50 % of the detector part receive photons from two holes. This corresponds to 50 % multiplexing.

50 % multiplexing the sensitivity almost doubles. However, increased global sensitivity does not lead to a decrease of the required dose. On the contrary, the required dose even increases slightly, which means that decrease in resolution impacts more than the increase in sensitivity. Hence, for the present application with the presented system configuration multiplexing does not seem useful.

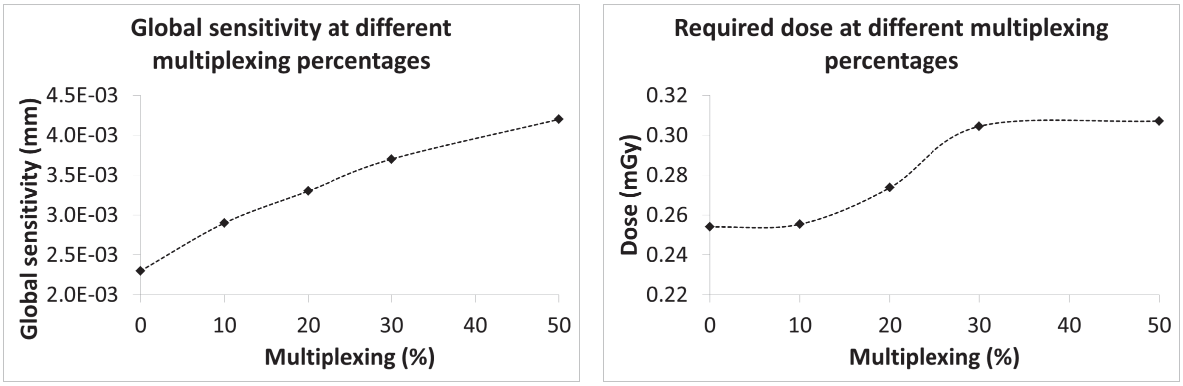

(a) *Object depending global system sensitivity.*

(b) *Required dose.*

Figure IV.57: Object depending global system sensitivity (for phantom with tumor) and required dose to have a separation of 3σ (for 100 kVp incident spectrum) for different multiplexing percentages. Both increase with increasing multiplexing percentage. Hence, the impact of resolution deterioration is more important than the one of sensitivity gain.

IV.5 Conclusion

This chapter was dedicated to the application of XRD to classify breast tissues. The idea is to use XRD as a second control level after conventional mammography if mammography outcome is doubtful.
A methodology of analytical DQE calculations to assess the performance of a collimation system was introduced, which allowed to study the influence of the different parameters on the system performance and to develop an optimization strategy. Following this plan of action two collimation systems have been proposed: one multifocal and one monofocal. Both systems have been tested in a simulation study of the complete XRD system associated to a breast phantom. The aim of this study was to assess the detectability of a small tumor of 4 mm in the phantom.

At first, the impact of the DRM on the separation power for both systems was assessed. The number of photons required to obtain a given separation is around 1.5 higher if the phantom spectra are blurred by the DRM. Comparison of ROC curves of monofocal and multifocal system for the same incident photon numbers has shown that the monofocal system is less performing, at least with a 100 kVp incident spectrum. Better performance of the multifocal collimation was confirmed by the study of the impact varying maximum spectrum energy on the required dose to achieve a 3σ separation. The maximum energy of the incident X-ray spectrum appears to be optimal at 60 keV for the multifocal system and at 50 keV for the monofocal system. These values are valid for the presented collimation systems but systems with different parameters might lead to another optimal incident spectrum.

As the monofocal collimation seems to be less performing and as it requires a depth-scan in addition to the x,y-scan, the rest of the study was only realized for the multifocal system.
Variation of the fibroglandular thickness did not affect the detectability of the tumor or the order of magnitude of the required dose. Hence, XRD should also be reliable for examination of breast with high density. The dose needed to achieve a 3σ separation is around 0.3 mGy if the tumor is situated in the center of the breast. This dose is very acceptable compared to conventional mammography (1-3 mGy). Even with the tumor situated at peripheral positions, the required dose to identify the tumor remains reasonable. Though, calculated required dose is based on given signatures of fibroglandular tissue and carcinoma. Variability of these signatures was not taken into account. There might be cases where the two scattering signatures are less separable, and the required dose is increased.

Reconstruction of a scan slice at different energies showed that it might be useful to apply higher energies in order to increase the amount of information supplied by the first hole in the collimation system, for which scattering angles are small. As extreme depth values are only covered by this hole, higher energies could provide access to the same χ-values as the other holes.
Even though spatial resolution of the presented XRD multifocal system is poor compared to other imaging techniques, it could be used to detect a small tumor.
Finally, the impact of limited multiplexing on the tumor detectability was assessed. In fact, global system sensitivity is increased as expected but required dose slightly increases as well. Thus, multiplexing does not seem advantageous for this application. However, it would be interesting to compare performance of the presented system with a system using a coded aperture as proposed by [Lakshmanan *et al.*, 2016].

This simulation study indicates that coherent scattering of X-rays can be used as a second control level in the case of unclear mammography result, and that this technique could help to reduce the number of unnecessary breast biopsies.

The sensitivity and specificity of the method were good even when the dose delivered was moderate. Scan-time also appears to be acceptable, with a tube current of about 10 mA, scan-time for a few cm^2 would be measured in seconds.

In future work, it will be necessary to manufacture the XRD system presented here so as to be able to make experimental measurements in order to confirm the simulation results. The impact of variability of tissue scattering signatures as well as varying breast thickness should also be studied.

Chapter V

Multiplexed collimation system in security check application

V.1 Security check with X-rays

At the present time, baggage control at the airport is mainly based on X-ray transmission imaging, i.e. on X-ray attenuation by matter. This imaging technique provides information about absorption properties of the different objects and their shape. Most systems are dual-energy systems, which acquire transmission images for two different energy windows. Depending on the manufacturer, dual-energy acquisition will be either realized by switching kV of the X-ray tube or by the use of a "sandwich" detector system, which consists of two scintillation layers one on top of the other [Carmi *et al.*, 2005]. The first layer permits the absorption of low energy photons, whereas the second layer absorbs the high energy photons. This system presents the advantage that the data is acquired simultaneously for the two energy windows. Two projection X-ray images are obtained. Assuming that the low-energy window represents "photoelectric plus Compton" attenuation and the high-energy window Compton only, photoelectric components can be isolated. Photoelectric absorption is more sensitive to the material type and allows a separation into inorganic and organic materials [Vogel, 2007]. High-energy Compton beam permits the determination of the effective density. Combination of these information allows identification of explosives. It is also possible to realize radiographic images of the object, where the different elements are colored according to three categories [Eilbert and Krug, 1993]: light elements ($Z < 10$), intermediary elements ($10 < Z < 20$) and heavy elements ($Z > 20$). Figure V.1 shows a comparison of a classical transmission image and a colored dual energy image. The color range indicates organic material corresponding to explosives. This method is limited by high positive rate in explosive detection, difficulties to detect explosives in sheet form (plastic explosives) and superimposed objects. Superimposed objects can be separated by CT scanners. However, severe problems of detection of explosives in sheet form remain and it is hard to differentiate between a fruit cake or cheese and plastic explosives, which have similar absorption coefficients [Zentai, 2008]. Figure V.2 shows linear attenuation coefficients of two explosives, water and acetone. They are all very similar. In 2004, it was estimated that the false alarm rate for CT systems certified by the Transportation and Security Administration was about 30 % [Harding, 2004]. Calculations of false alarm resolution in air passenger baggage inspection suggested that each percentage point reduction in the false alarm rate (without increasing false negative rate) would save about 25 million dollars for the US alone [Harding, 2009]. Multi-energy methods using spectroscopic detectors use attenuation information at a multitude of energies. They were initially proposed for luggage control by [Maitrejean *et al.*, 1998]. This measuring method combined to appropriate data processing [Beldjoudi *et al.*, 2012] allows improvement of false alarm rate. Though, multi-energy transmission methods still only use information provided by linear attenuation curves, which are very similar for explosives and other common organic materials as well as for liquid explosives and inoffensive liquids such as water. It is also possible that different mixtures of materials lead to the same X-ray attenuation. X-ray diffraction provides information on molecular structure of the inspected matter, which is much more discriminating than attenuation information. This work suggests the use of XRD for detection of illicit materials (explosives and drugs) in luggage at the airport. Morpho detection has already commercialized an EDXRD-based baggage control machine. This machine works at one fixed scattering angle. We would like to propose a system combining EDXRD and ADXRD, which allows to increase global system sensitivity and the covered χ-range (see Chap.II). Furthermore, benefits of increased sensitivity by multiplexing should be evaluated as well [MacCabe *et al.*, 2012]. This chapter will present a preliminary study concerning the different parameters and their impact on the performance of such a system. First, the materials to be identified during security check and the system constraints for this application will be presented. Afterwards, an analytical method of DQE calculations for a collimation system with limited multiplexing is introduced. The impact of the different system parameters on resolution and sensitivity is assessed. Finally, the impact of different multiplexing levels on a collimation system with given parameters, is studied. The influence of the attribution of the detector area to the different holes as well as the distribution of the focal distances of each collimation hole will be discussed as well.

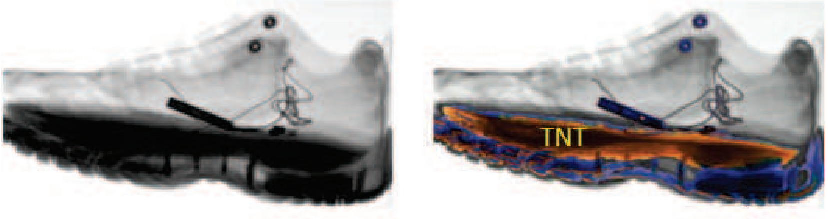

Figure V.1: Transmission (left) and dual energy imaging (right). The dual energy image allows to separate the TNT package from the sole [Vogel, 2007].

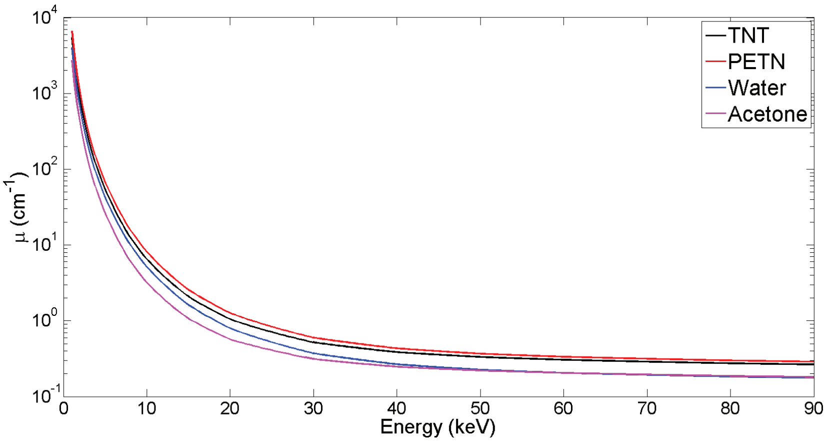

Figure V.2: Linear attenuation coefficients of TNT, PETN, water and acetone.

V.2 Materials to be detected during security check

Compared to mammography the situation of luggage control is more complex. In virtual breast biopsy only a limited number of tissue types can be encountered. Here, a high variety of materials can be found in a suitcase from clothes over cosmetics to food. They can be amorphous or crystalline. Figure V.3 shows XRD pattern of the four materials whose attenuation coefficients are represented in figure V.2. Their diffraction pattern are much more different than their attenuation curves.

Many of the materials to be detected during security screening are polycrystalline such as organic explosives and numerous drugs. Typically, explosives have large unit cells, which implies high d_{hkl}-values. Their main peaks are situated at $d_{hkl} > 0.3$ nm and hence at small momentum transfer values, where $\chi < 3.3\,\text{nm}^{-1}$. Most common materials with polycrystalline structure have smaller unit cells and hence, their diffraction peaks are found at higher χ-values. For example, figure V.4.a and b shows TNT Bragg peaks superimposed to salt and carbon Bragg peaks. In effect, salt and carbon characteristic peaks are at higher momentum transfer values than TNT peaks. Sugar is an important exception to this rule. It also has large unit cells and Bragg peaks are situated at low χ-values (Fig V.4.c). However, there are still sufficient characteristic Bragg peaks to separate sugar from TNT.

It has to be noted that many home-made explosives might be mixed with binders, which are often amorphous. This alters their diffraction pattern.

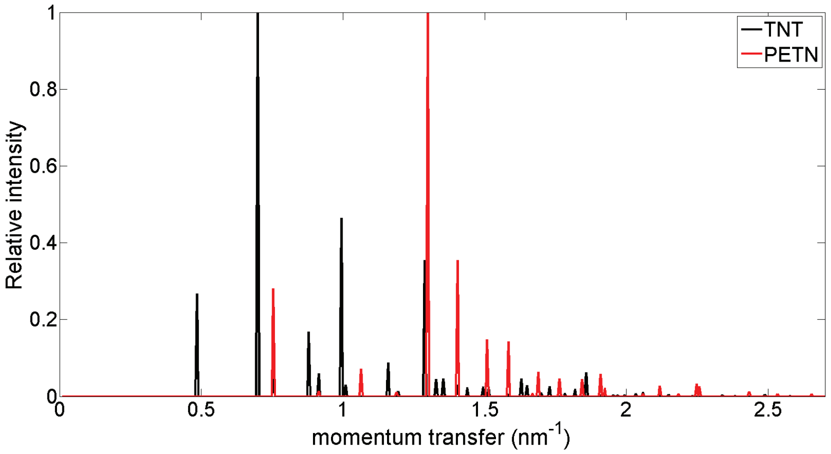

(a) *Polycrystalline explosives.*

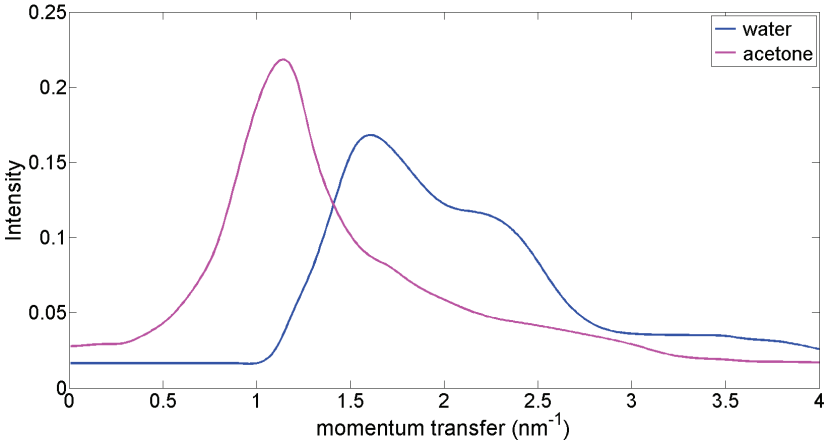

(b) *Liquids.*

Figure V.3: Scattering signatures of two explosives and two liquids.

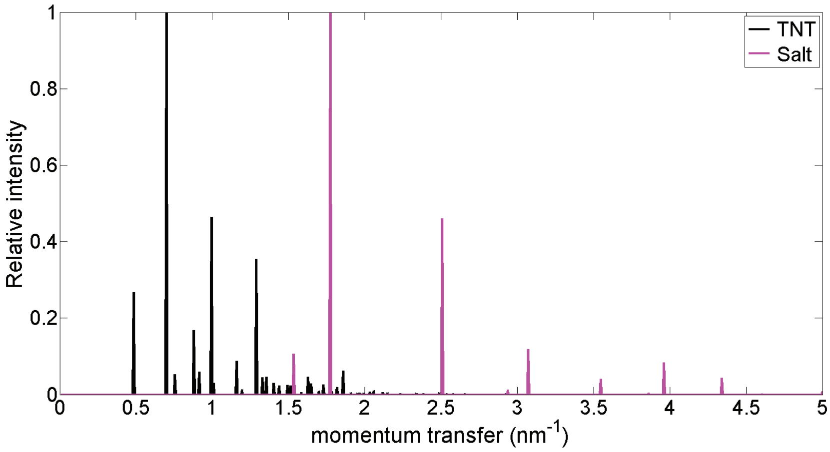

(a) *TNT and salt.*

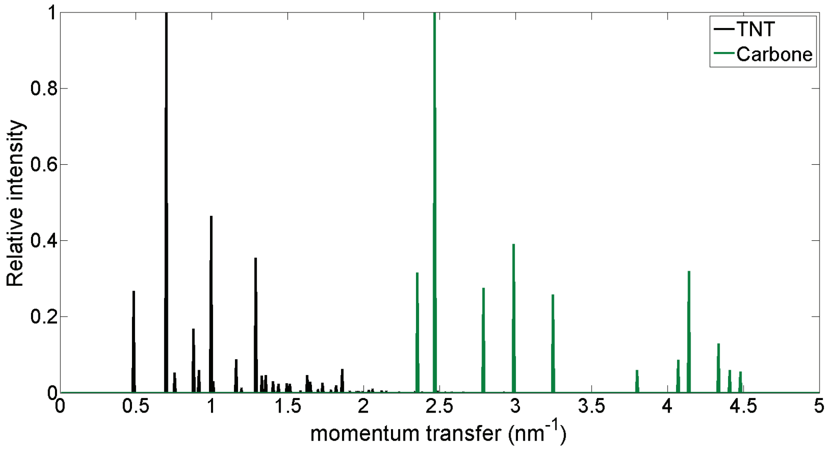

(b) *TNT and carbon.*

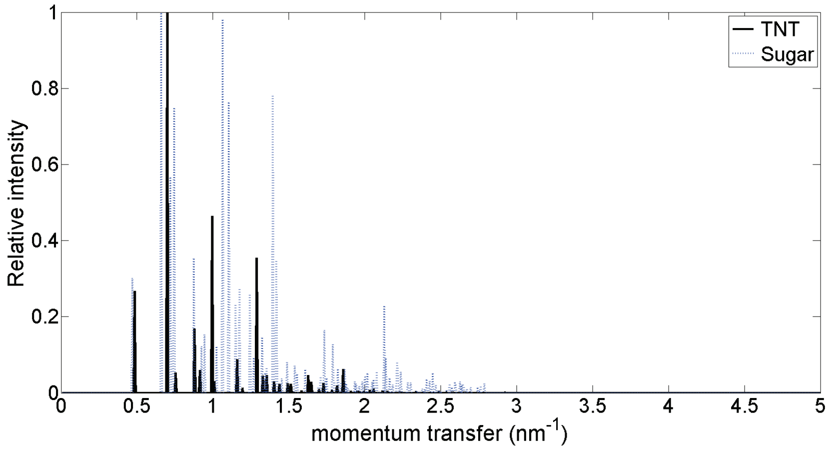

(c) *TNT and sugar.*

Figure V.4: Bragg peaks of common materials and TNT.

V.3 System constraints in security check application

Different factors have to be taken into account in order to propose a system for security check. First of all, the object size should be fixed. Depending on the kind of luggage (hold baggage or carry-on baggage) the size will no be the same. Here, a system for cabin luggage will be considered. Object size is fixed to **50 cm**, which corresponds to the maximum dimension of a hand baggage suitcase (otherwise it cannot pass the inspection tunnel). Hence, thickness of the inspected object is increased by a factor of ten compared to mammography. Furthermore, objects in luggage might be much more dense than breast tissue, which increases X-ray attenuation. Thus, incident photon energy has to be higher than in the previous application. [Harding *et al.*, 2009] suggests that adequate transmission through full-size suitcases in hold-baggage screening requires a tube potential of 150 keV to 200 keV to generate sufficient penetrating X-ray photons above 100 keV. Here, an incident X-ray spectrum produced by a tungsten anode at **150 kVp** tube potential will be considered.

As already pointed out, materials to be detected might be both crystalline and amorphous. Characteristic broad maxima of amorphous matter due to characteristic intra- and intermolecular distances are found at low χ-values between 0.5 and 3 nm^{-1}. Bragg peaks of explosives are also situated at low momentum transfer values. As it is not necessary to detect inoffensive crystalline objects, it might be sufficient to cover a χ-range between **0.5** and **3** $\mathbf{nm^{-1}}$ even though some peaks of harmless objects might not be covered. As the average energy of incident photons is higher as in virtual breast biopsy application, intercepted scattering angles should be smaller as previously. Photons scattered at high scattering angles (and transmitted) do not provide information useful to detect threat matter in baggage.

Required momentum transfer resolution is more difficult to define than in breast biopsy application as materials to be detected might be crystalline or amorphous. To be able to detect all Bragg peaks of TNT for instance a resolution of less than 0.1 nm^{-1} would be required. High resolution always implies loss in sensitivity. This would not be a problem for crystalline matter because their diffraction intensity is high. Though, amorphous matter does not diffract as much as crystalline matter and loss in sensitivity might prevent the identification of amorphous objects. It is not indispensable to measure each Bragg peak to identify crystalline matter. Detection of main peaks should be enough. Thus, a momentum transfer resolution between **0.1** and **0.2** $\mathbf{nm^{-1}}$ might be sufficient.

The limiting factor in security screening is not the delivered dose as in medical application but inspection time per piece of baggage and maximum tube power. Inspection time of an entire baggage should not be longer than **a few seconds**. Conveyor speed is around **0.1** $m \cdot s^{-1}$. Maximum X-ray tube power should be between **5** and **10 kW**. These two constraints will limit the number of photons to be received for each object point. This is another reason why the system should be as sensitive as possible, i.e. a number of scattered photons as high as possible should be detected and used for material identification.

We would like to propose an alternate XRD system for illicit material detection in hand baggage at first control level, which is more sensitive than existing systems. Therefore, photons at different scattering angles should be exploited. It is envisioned to use a similar system to the one proposed for virtual breast biopsy, i.e. a conical multifocal collimation system, allowing combination of EDXRD and ADXRD. To further increase system sensitivity this system is thought to introduce limited multiplexing. As a whole baggage piece has to be inspected in as less time as possible, the use of several modules of conical collimation plus detector juxtaposed one to another should be considered.

In the following, a preliminary study of one module with different multiplexing levels is presented. System parameters are not optimized though they have been chosen to be realistic (maximum luggage size, resolution, sensitivity, order of magnitude of parameters of existing systems). This study should help to develop an optimization strategy and to determine the best possible system parameters for the considered geometry. In order to be able to assess the performance of a multiplexed system, an analytical method to calculate the DQE of a collimation system with multiplexing will be presented in the next section.

V.4 Analytical DQE calculations for a collimation system with limited multiplexing

In the previous chapter a method to calculate analytically the DQE of a non-multiplexed secondary collimation system was presented. This chapter will present an equivalent method to calculate the detective quantum efficiency for a multiplexed secondary collimation system. The primary collimation is again assumed to be fixed in a way to obtain a very thin incident pencil beam.
Multiplexing will be limited to two holes, which means that a pixel "sees" two holes. Thus, the secondary collimation will be considered as an assembly of triplets of hole-hole-pixel (Fig. V.5). In fact, the secondary collimation can be considered as an assembly of couples hole-pixel (Fig. IV.12). To calculate the DQE of the collimation system, first, the DQE of each hole-hole-pixel triplet has to be determined. Afterwards, they will be added together to obtain the system DQE.

V.4.1 Spatial resolution of a triplet hole-hole-pixel

As previously (Sec. IV.2.2.1), it is assumed that diffraction signal is only emitted from the z-axis ($x = 0$). Spatial resolution can again be divided in two parts: resolution due to pixel size and resolution due to holes' size. Each part consists of the two contributions passing through the two considered holes.

V.4.1.1 Spatial resolution due to the holes' size

Figure V.6.a illustrates the contribution of the two holes to the resolution part due to the holes size. Each contribution corresponds to the part of the z-axis, that is seen by the center point of the pixel via each hole. Δz_{h_1} and Δz_{h_2} can be calculated using equation IV.2.2. The PSF of the hole contribution is given by the sum of two rectangular functions of widths Δz_{h_1} and Δz_{h_2} with a shift of $\Delta c = z_{c_2} - z_{c_1}$ between their centers. In a symmetrical coordinate plane, the situation can be represented as in figure V.6.b. It can be expressed as:

$$PSF_{hh} = \Pi_{\Delta z_{h_2}} * \delta_{-\frac{\Delta c}{2}} + \Pi_{\Delta z_{h_1}} * \delta_{+\frac{\Delta c}{2}} \tag{V.4.1}$$

The MTF due to the holes' size is obtained thanks to Fourier transform:

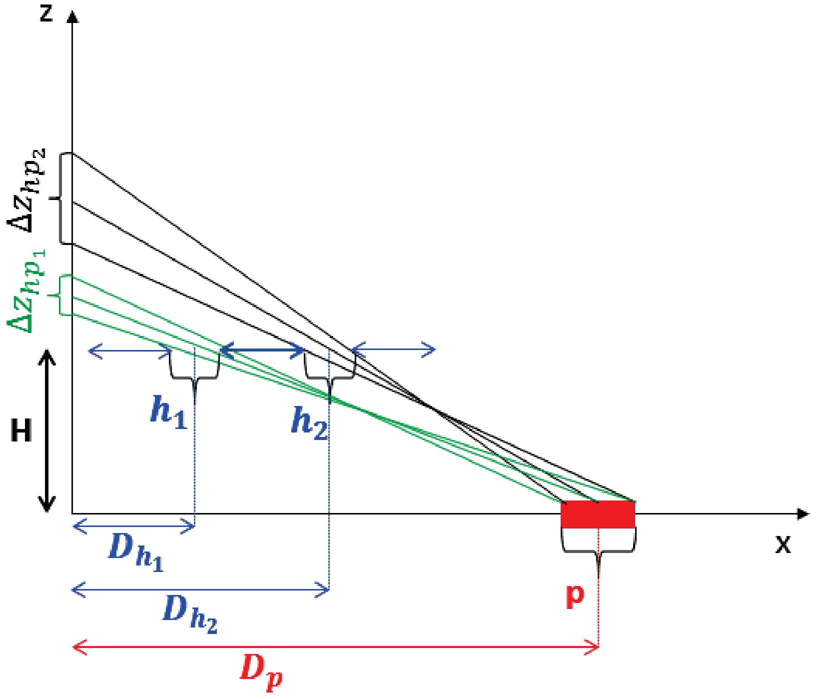

Figure V.5: Schematic representation of the system parameters for one hole-hole-pixel triplet and the spatial resolutions Δz_{hp_1} and Δz_{hp_2} associated to this triplet.

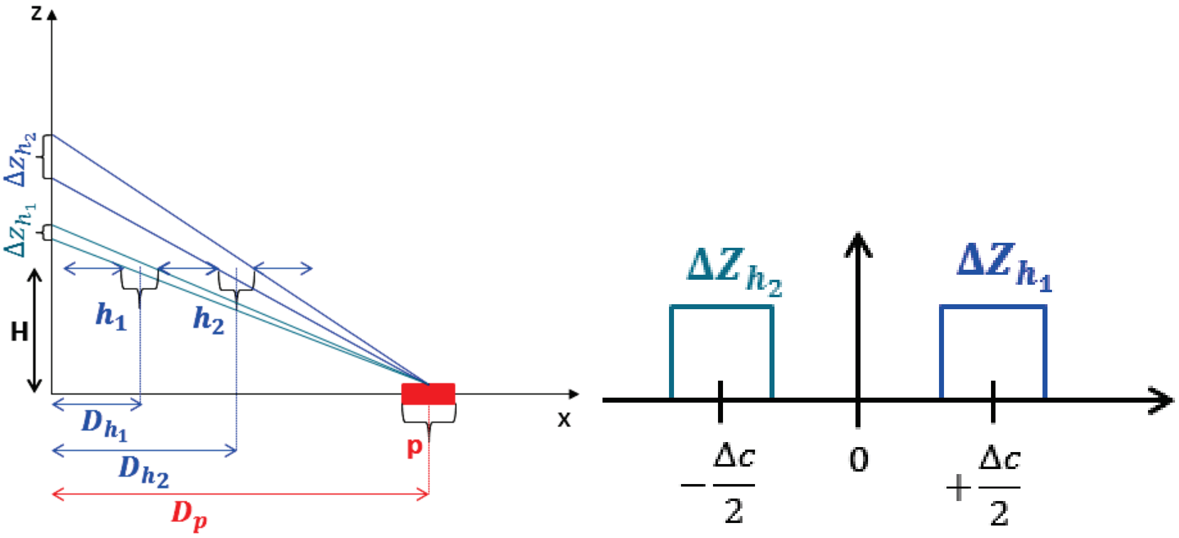

(a) *Spatial resolution due to the holes' size: It corresponds to the parts of the z-axis, that are seen by the center point of the pixel via the two holes.*

(b) *The PSF of a system with two holes is given by the sum of two rectangular functions of widths* Δz_{h_1} *and* Δz_{h_2} *with a shift of* $\Delta c = z_{c_2} - z_{c_1}$ *between their centers.*

Figure V.6: Illustration of spatial resolution due to the holes' size.

$$S_{hh} \cdot MTF_{hh}(\nu_z) = \Delta z_{h_2} sinc(\pi\nu_z\Delta z_{h_2}) \cdot e^{i2\pi\nu_z\frac{\Delta c}{2}} + \Delta z_{h_1} sinc(\pi\nu_z\Delta z_{h_1}) \cdot e^{-i2\pi\nu_z\frac{\Delta c}{2}} \quad \text{(V.4.2)}$$

where S_{hh} corresponds to the sensitivity due to hole size. For DQE calculations, the squared module of the MTF is needed. Knowing that $S_{hh}^2 = (\Delta z_{h_1} + \Delta z_{h_2})^2$ and using complex numbers for calculations, it can be found that:

$$\begin{aligned} |MTF_{hh}|^2 = &\frac{1}{(\Delta z_{h_1} + \Delta z_{h_2})^2 \pi^2 \nu_z^2} \cdot \{\sin^2(\pi\nu_z\Delta z_{h_2}) + \sin^2(\pi\nu_z\Delta z_{h_1}) \\ &+ 2\cos(2\pi\nu_z\Delta c)\sin(\pi\nu_z\Delta z_{h_1})\sin(\pi\nu_z\Delta z_{h_2})\} \end{aligned} \quad \text{(V.4.3)}$$

The last term corresponds to the interference term between the two holes.

V.4.1.2 Spatial resolution due to pixel size

Figure V.7 shows an illustration of the contribution of the two holes to the resolution part due to pixel size. Each contribution corresponds to the projection of the pixel on the z-axis by the center of one hole. Δz_{p_1} and Δz_{p_2} are given by equation IV.2.1.

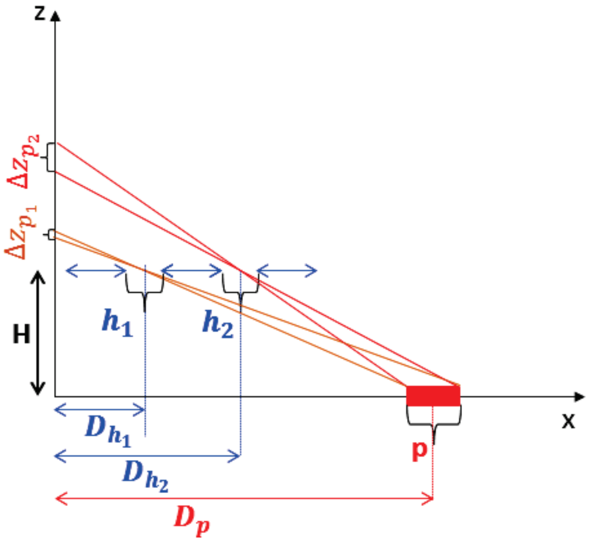

Figure V.7: Schematic representation of the spatial resolution due to the pixel size. It corresponds to the projection of the pixel on the z-axis by the center of each hole.

V.4.1.3 Spatial resolution of the hole-hole-pixel triplet

The PSF of a hole-hole-pixel triplet is given by:

$$PSF_{hhp} = \Pi_{\Delta z_{h_2}} * \delta_{-\frac{\Delta c}{2}} * \Pi_{\Delta z_{p_2}} + \Pi_{\Delta z_{h_1}} * \delta_{+\frac{\Delta c}{2}} * \Pi_{\Delta z_{p_1}} \quad \text{(V.4.4)}$$

However, in order to simplify calculations, it was assumed that it was possible to use a mean Δz_p:

$$\Delta z_p = \frac{\Delta z_{p_1} + \Delta z_{p_2}}{2} \tag{V.4.5}$$

Then equation V.4.4 can be rewritten as:

$$PSF_{hhp} = \left[\Pi_{\Delta z_{h_2}} * \delta_{-\frac{\Delta c}{2}} + \Pi_{\Delta z_{h_1}} * \delta_{+\frac{\Delta c}{2}}\right] * \Pi_{\Delta z_p} \tag{V.4.6}$$

The Fourier transform of PSF_{hhp} is equal to:

$$\begin{aligned}\mathscr{F}\left\{PSF_{hhp}\right\} = &\left[\Delta z_{h_2} sinc\left(\pi\nu_z \Delta z_{h_2}\right) \cdot e^{i2\pi\nu_z \frac{\Delta c}{2}} + \Delta z_{h_1} sinc\left(\pi\nu_z \Delta z_{h_1}\right) \cdot e^{-i2\pi\nu_z \frac{\Delta c}{2}}\right] \\ &\cdot sinc\left(\pi\nu_z \Delta z_p\right) \cdot \Delta z_p\end{aligned} \tag{V.4.7}$$

Using equation V.4.3 and normalizing by Δz_p^2, which corresponds to sensitivity due to pixel size, the module of the MTF of a hole-hole-pixel triplet is obtained:

$$\begin{aligned}\left|MTF_{hhp}\right|^2 = &\frac{sinc^2\left(\pi\nu_z \Delta z_p\right)}{\left(\Delta z_{h_1} + \Delta z_{h_2}\right)^2 \pi^2 \nu_z^2} \cdot \left\{\sin^2\left(\pi\nu_z \Delta z_{h_2}\right) + \sin^2\left(\pi\nu_z \Delta z_{h_1}\right)\right. \\ &\left.+ 2\cos\left(2\pi\nu_z \Delta c\right)\sin\left(\pi\nu_z \Delta z_{h_1}\right)\sin\left(\pi\nu_z \Delta z_{h_2}\right)\right\}\end{aligned} \tag{V.4.8}$$

The DQE of a hole-hole-pixel triplet can hence be deduced as:

$$DQE_{hhp}\left(\nu_z\right) = S_{hhp} \cdot \left|MTF_{hhp}\right|^2 \tag{V.4.9}$$

where S_{hhp} corresponds to the sensitivity of one pixel seeing two holes.

Figure V.8 shows an example of a calculated spatial DQE for 0 % and 30 % multiplexing. It can be seen that the DQE for 30 % multiplexing presents some rebounds. These rebounds are due to multiplexing and lead to higher sensitivity at some frequencies. In fact, these frequencies correspond to the ones in phase with the collimation system.

V.4.2 System sensitivity of a triplet hole-hole-pixel

System sensitivity contribution of the two holes is additive. Thus, it can be calculated separately for each hole in the same way as in section IV.2.2.2. The total sensitivity of one pixel seeing two holes is given by:

$$S_{hhp} = S_{h_1 p} + S_{h_2 p} \tag{V.4.10}$$

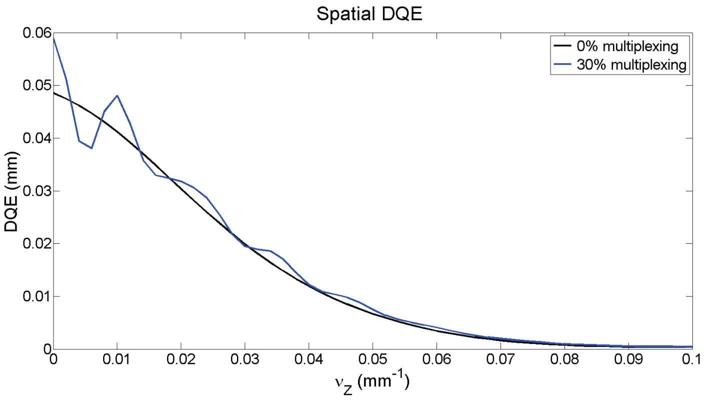

Figure V.8: Example of an analytically calculated spatial DQE curve for 0 % and 30 % multiplexing.

V.4.3 Angular resolution

Angular detective quantum efficiency can be determined as in section IV.2.2.4 using equations IV.2.15 and IV.2.16:

$$\begin{aligned} DQE_{hhp,\theta}(\nu_\theta) = S_{hhp} \cdot \frac{sinc^2(\pi\nu_\theta\Delta\theta_p)}{(\Delta\theta_{h_1}+\Delta\theta_{h_2})^2\pi^2\nu_\theta^2} \cdot \{&\sin^2(\pi\nu_\theta\Delta\theta_{h_2}) + \sin^2(\pi\nu_\theta\Delta\theta_{h_1}) \\ &+ 2\cos(2\pi\nu_\theta\Delta c_\theta)\sin(\pi\nu_\theta\Delta\theta_{h_1})\sin(\pi\nu_\theta\Delta\theta_{h_2})\} \end{aligned} \tag{V.4.11}$$

V.4.4 Momentum transfer resolution

Momentum transfer DQE is deduced in the same way as in section IV.2.2.5 using equation IV.2.19:

$$\begin{aligned} DQE_{hhp,\chi}(E,\nu_\chi) = S_{hhp} \cdot \frac{sinc^2(\pi\nu_\chi\Delta\chi_p)}{(\Delta\chi_{h_1}+\Delta\chi_{h_2})^2\pi^2\nu_\chi^2} \cdot \{&\sin^2(\pi\nu_\chi\Delta\chi_{h_2}) + \sin^2(\pi\nu_\chi\Delta\chi_{h_1}) \\ &+ 2\cos(2\pi\nu_\chi\Delta c_\chi)\sin(\pi\nu_\chi\Delta\chi_{h_1})\sin(\pi\nu_\chi\Delta\chi_{h_2})\} \end{aligned} \tag{V.4.12}$$

This expression depends on the photon energy. However, as the incident spectrum was fixed, the mean momentum transfer resolution for the given spectrum can be calculated by integrating the DQE over the spectrum:

$$DQE_{hhp,\chi}(\nu_\chi) = \int_{E_{min}}^{E_{max}} DQE_{hhp,\chi}(E,\nu_\chi) \cdot S(E)\,dE \tag{V.4.13}$$

where S is the normalized incident spectrum.

Figure V.9 shows an example of a DQE curve calculated for an incident photon energy of 150 keV and for an incident tungsten spectrum with maximum energy of 150 keV. By comparing these two curves, it can be noticed that the multiplexing effect (rebounds on the curve) is strongly smoothed by integration of the spectrum.

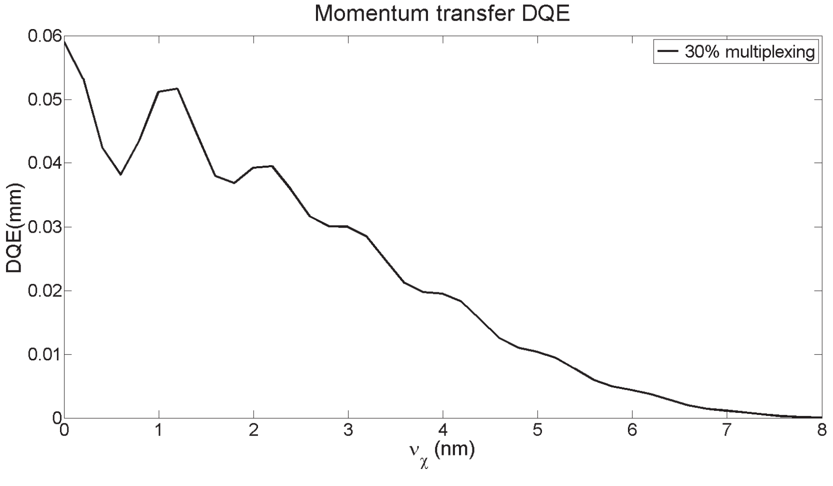

(a) *150 keV.*

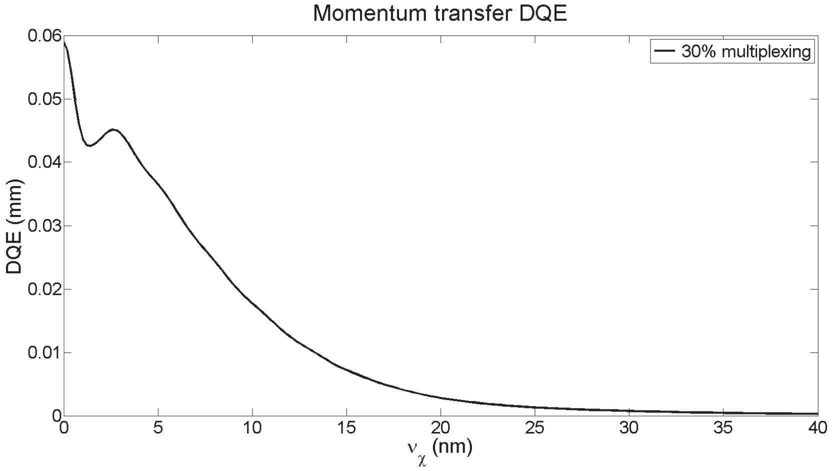

(b) *Integrated spectrum.*

Figure V.9: Momentum transfer DQE curves for 150 keV and with an integrated spectrum with maximum energy of 150 keV.

V.5 Influence of the different parameters

The analytical expressions for DQE calculations with multiplexing will be used to study the influence of the different system parameters on performance of a multiplexed collimation system.

The study was realized for a conical multifocal collimation with 50 % multiplexing as illustrated in figure IV.56 in section IV.4.6.7. In order to define the collimation, the detector was divided in as many parts as the number of holes as in section IV.2.3. The detector area of each part is the same, which means that the number of pixels (pixel annuli) per part is not the same for each part (Fig. IV.20). Each detector part receives signal from its "main hole" as in the non-multiplexed case and the half of the pixels of each part receive photons from a second more inner hole (Fig. IV.56).

The following parameters were fixed by default:

- Minimum focal distance f_{min}: 30 mm
- Maximum focal distance f_{max}: 500 mm
- Number of holes Nb_h: 10
- Hole size h: 0.5 mm
- Pixel size p: 0.5 mm
- Collimation height H: 250 mm
- Detector dimension L_d: 100 mm

These parameters were varied one by one in order to assess their impact on system performance.

V.5.1 Number of holes Nb_h

The number of holes impacts the sensitivity distribution (Fig. V.10). With increasing number of holes the sensitivity profile becomes more smooth. For five holes the sensitivity region of each hole can be clearly identified and sensitivity between two regions becomes almost zero. With increasing hole number the sensitivity between the different regions remains higher but regions are still well recognizable except for high Z_{sample} values. Global sensitivity, angular resolution and momentum transfer resolution do only change very little (Tab. V.1). Spatial resolution shows higher variation with hole number. The higher the hole number the lower is spatial resolution, which can be seen in table V.1 and on the DQE curves (Fig. V.11). Modulation due to multiplexing is more visible with increasing hole number. Hence, the more holes are present the more the system will be particularly sensitive at certain frequencies.

Nb_h	Global sensitivity	Spatial resolution (mm)	Angular resolution (°)	Momentum transfer resolution (nm^{-1})
5	0.062	17.96	0.16	0.067
10	0.066	20.40	0.17	0.071
15	0.068	21.67	0.18	0.072

Table V.1: Global sensitivity and mean resolution results for varying hole number.

V.5.2 Hole size h

Figure V.12 shows the spatial, the angular and momentum transfer resolution for varying hole size. This parameter influences the global system sensitivity (DQE at zero frequency), which increases with increasing hole size. The resolution also depends on h. If h is increased resolution is deteriorated (Tab. V.2). Depending on the frequencies to be resolved it can be interesting to use bigger holes in order to be more sensitive to lower frequencies.

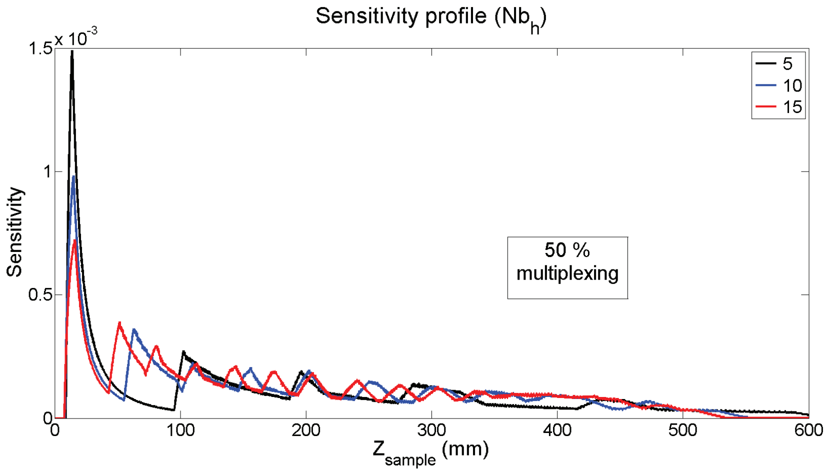

Figure V.10: Sensitivity profile for different hole numbers.

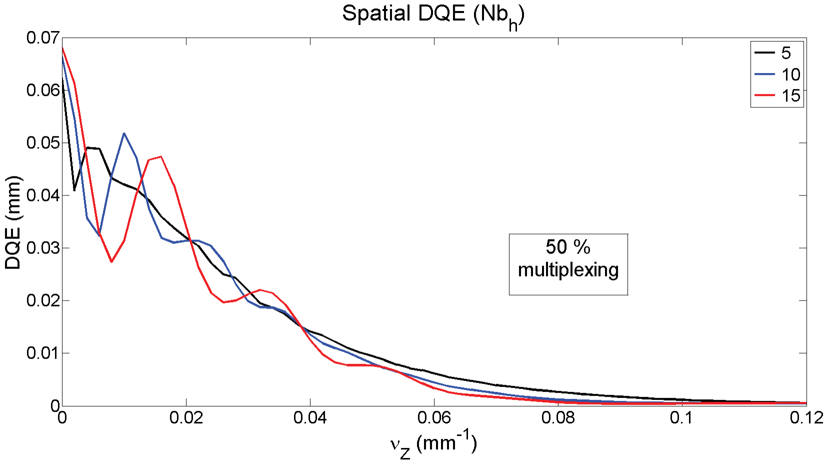

Figure V.11: Spatial DQE curves for different hole numbers.

V.5.3 Pixel size p

Table V.3 summarizes the global system sensitivity, the spatial, angular and momentum transfer resolution for two different pixel sizes. System sensitivity is only very slightly changed with increasing pixel size, which seems normal as the total detection area is still the same.

h (mm)	Global sensitivity	Spatial resolution (mm)	Angular resolution (°)	Momentum transfer resolution (nm^{-1})
0.5	0.066	20.41	0.17	0.071
0.7	0.093	27.23	0.24	0.096
1	0.133	37.16	0.33	0.131

Table V.2: Global sensitivity and mean resolution results for varying hole size.

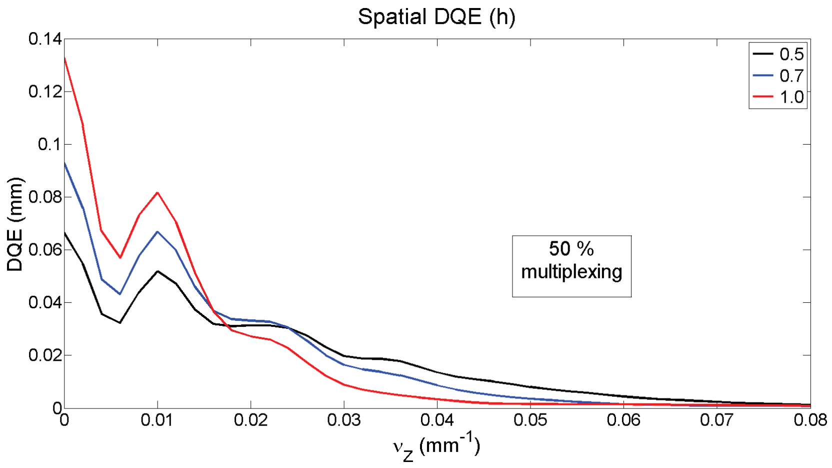

(a) *Spatial resolution.*

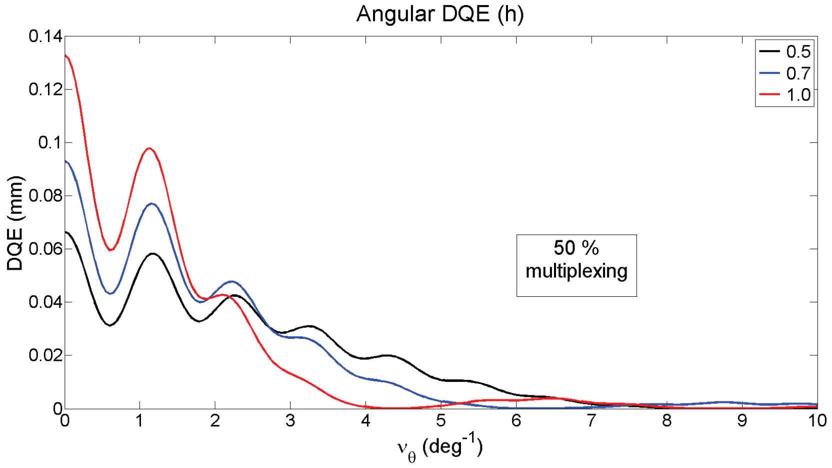

(b) *Angular resolution.*

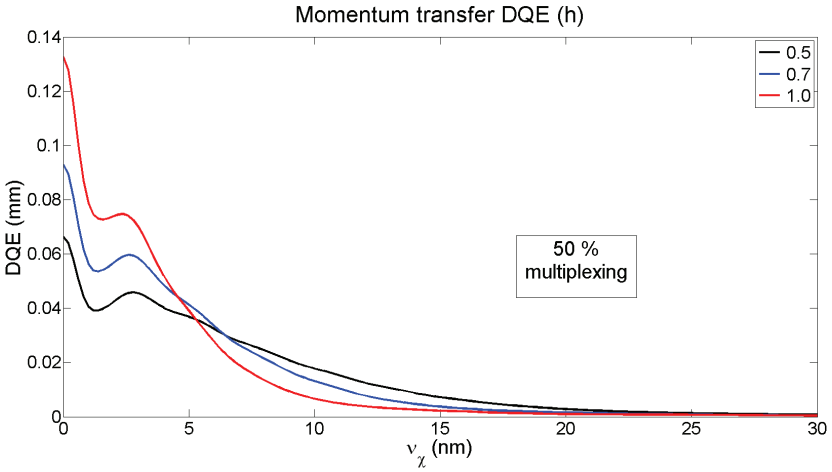

(c) *Momentum transfer resolution.*

Figure V.12: Spatial, angular and momentum transfer DQE curves for different hole sizes (h = 0.5, 0.7 or 1.0 mm).

However, pixel size impacts the system resolution, especially the spatial resolution, which decreases by 5 mm if pixel size is doubled. Figure V.13 shows the different DQE curves for the two tested pixel sizes, which also show the degradation of resolution. Probably the effect of resolution degradation is higher as in section IV.2.3.1 because of the multiplexing, which leads to more information mixing, and also because of the larger (ten times) field of view.

p (mm)	Global sensitivity	Spatial resolution (mm)	Angular resolution (°)	Momentum transfer resolution (nm^{-1})
0.5	0.066	20.41	0.17	0.071
1	0.069	25.07	0.21	0.085

Table V.3: Global sensitivity and mean resolution results for varying pixel size.

V.5.4 Collimation height H

If collimation height is increased system sensitivity and spatial resolution degrade (Tab. V.4, Fig. V.14 and Fig. V.15.a). Though, angular and momentum transfer resolution increase with increasing collimation height (Tab. V.4 and Fig. V.15.b and c). A compromise between sensitivity, minimum required spatial resolution and angular and momentum transfer resolution has to be found. Another important component to be taken into account are the scattering angles that can be measured, which strongly depend on collimation height. The higher H the smaller the scattering angles that are intercepted by the collimation system (Fig. V.16).

H (mm)	Global sensitivity	Spatial resolution (mm)	Angular resolution (°)	Momentum transfer resolution (nm^{-1})
100	0.162	16.39	0.46	0.184
250	0.066	20.41	0.17	0.071
500	0.033	26.75	0.08	0.035

Table V.4: Global sensitivity and mean resolution results for varying collimation height.

V.5.5 Detector dimension L_d

If the detector size is increased, the global system sensitivity will increase (Tab. V.5) because of higher detection area. Thanks to this sensitivity increase, the spatial resolution is improved as well as can be seen in table V.5 and figure V.17.a. However, angular and momentum transfer resolution do not change, which is also clearly visible on the corresponding DQE curves in figure V.17.b and c respectively. If the collimation height is fixed, an increasing detector size will also lead to higher intercepted scattering angles (Fig. V.18). A satisfying combination of collimation height and detector surface has to be found in order to cover the right scattering angles without having too high detector costs.

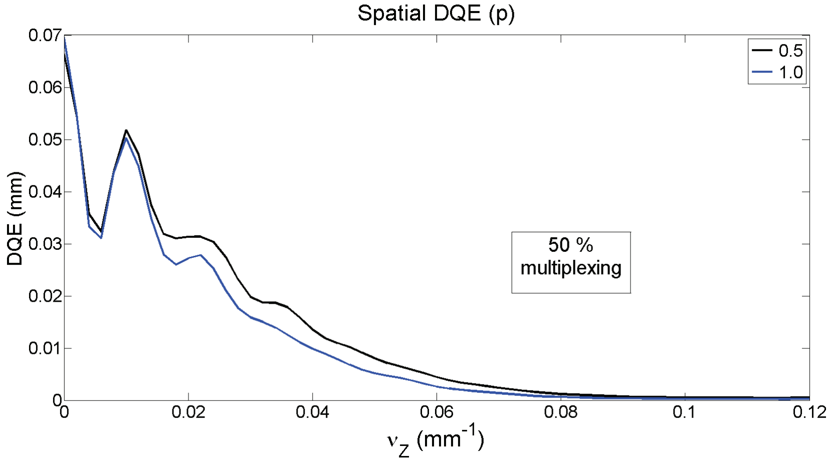

(a) *Spatial resolution.*

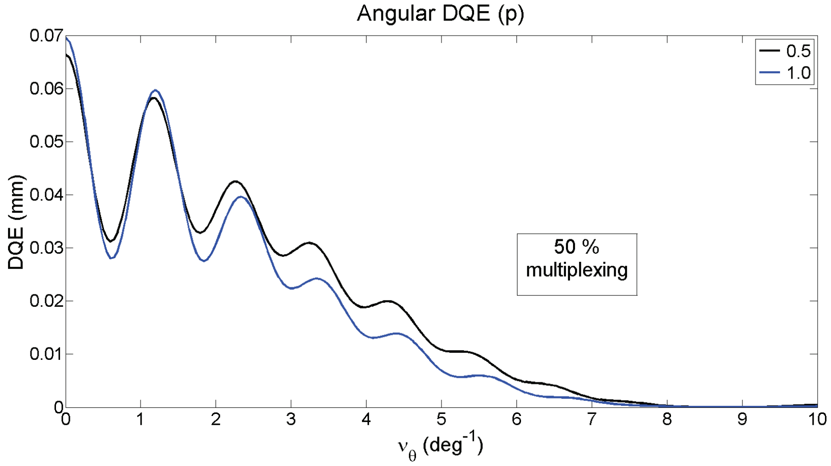

(b) *Angular resolution.*

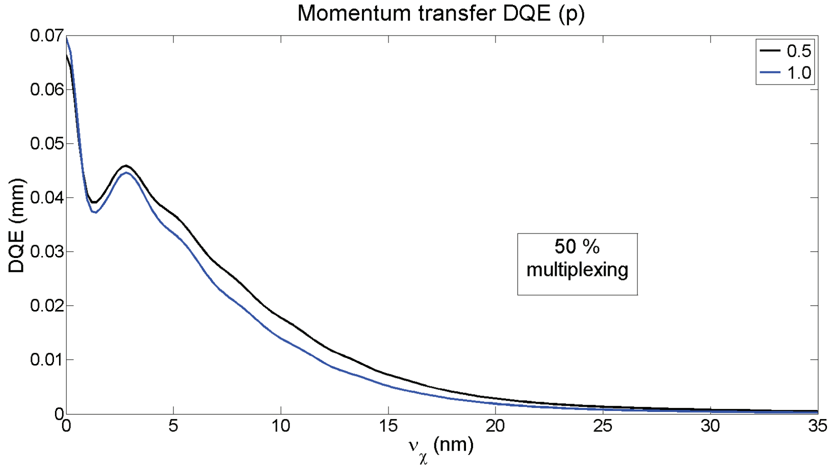

(c) *Momentum transfer resolution.*

Figure V.13: Spatial, angular and momentum transfer DQE curves for different pixel sizes ($p = 0.5$ or 1.0 mm).

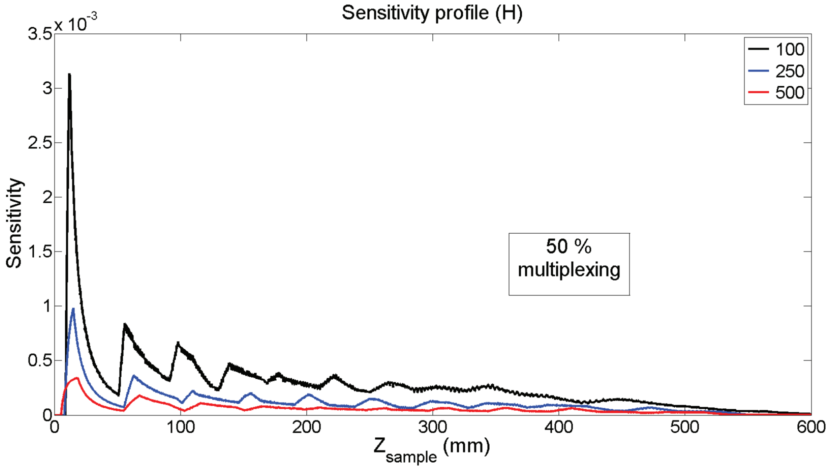

Figure V.14: Sensitivity profiles for different collimation heights H.

L_d (mm)	Global sensitivity	Spatial resolution (mm)	Angular resolution (°)	Momentum transfer resolution (nm^{-1})
50	0.035	41.97	0.18	0.074
100	0.066	20.41	0.17	0.071
150	0.099	14.19	0.17	0.071

Table V.5: Global sensitivity and mean resolution results for varying detector dimension.

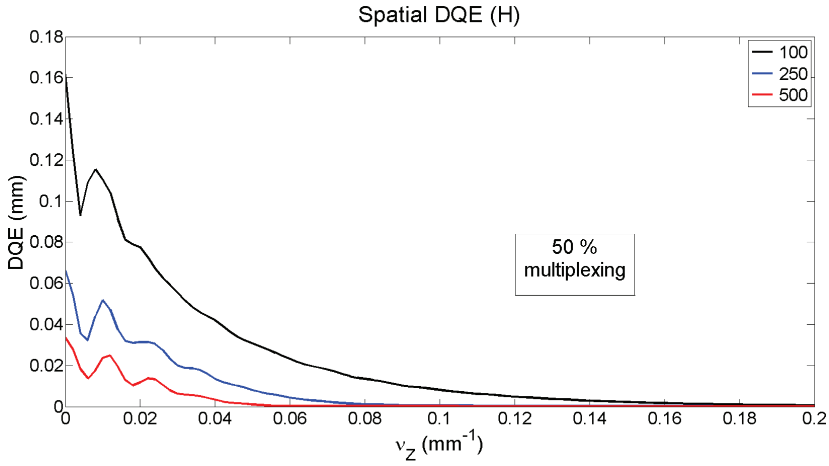

(a) *Spatial resolution.*

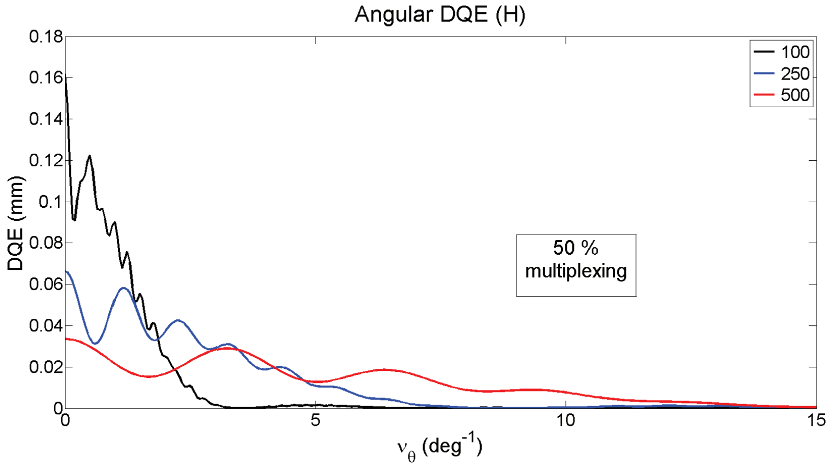

(b) *Angular resolution.*

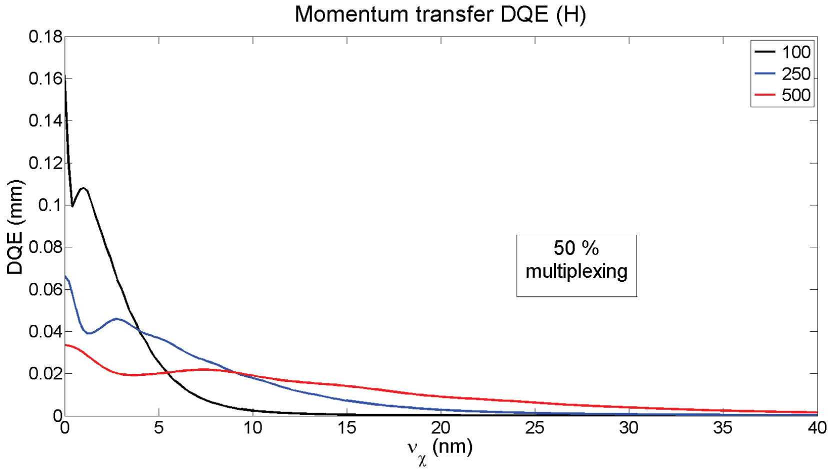

(c) *Momentum transfer resolution.*

Figure V.15: Spatial, angular and momentum transfer DQE curves for different collimation heights H ($H = 100$, 250 or 500 mm).

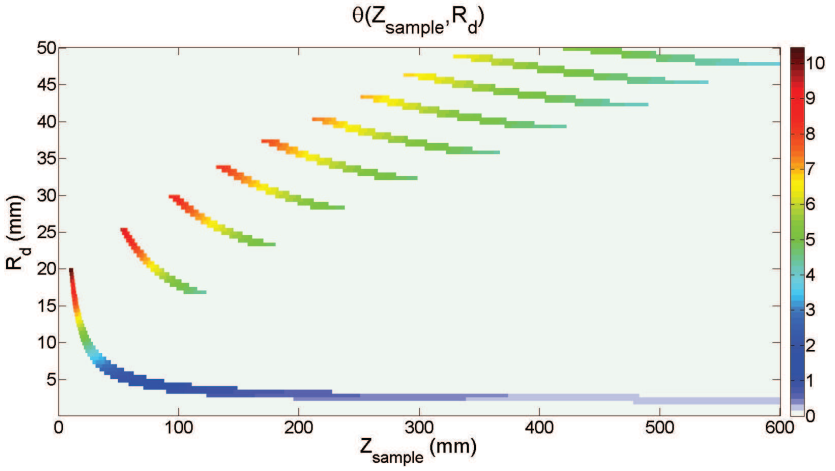

(a) *H = 100 mm*

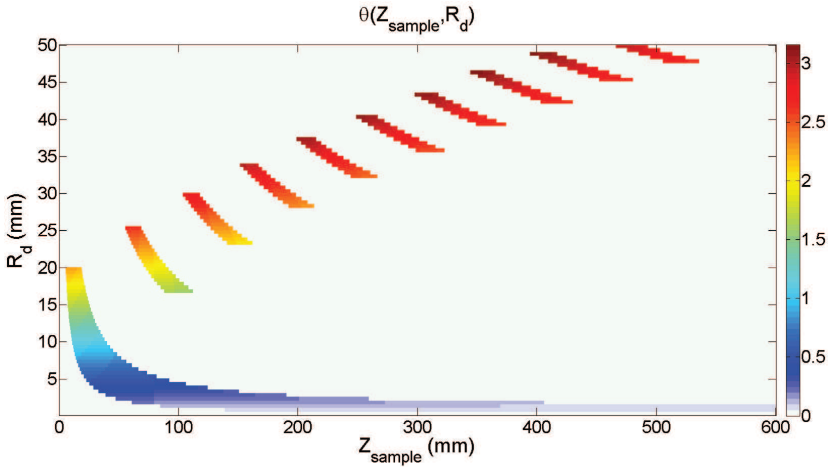

(b) *H = 500 mm*

Figure V.16: Covered scattering angles θ for different collimation heights H (50 % multiplexing).

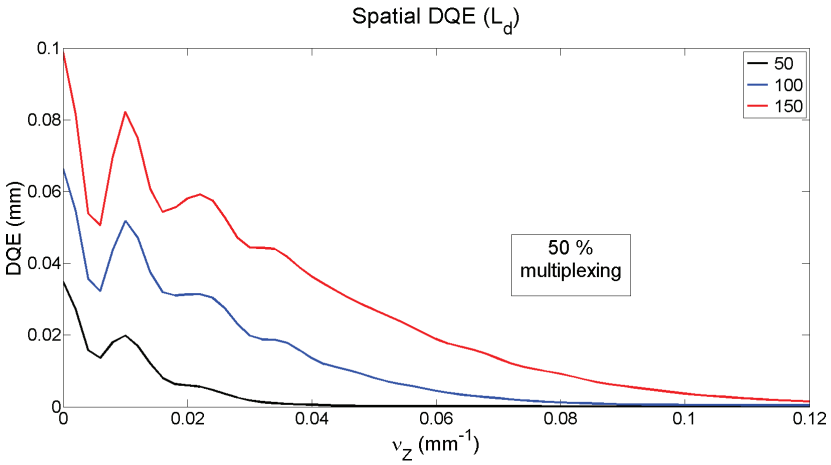

(a) *Spatial resolution.*

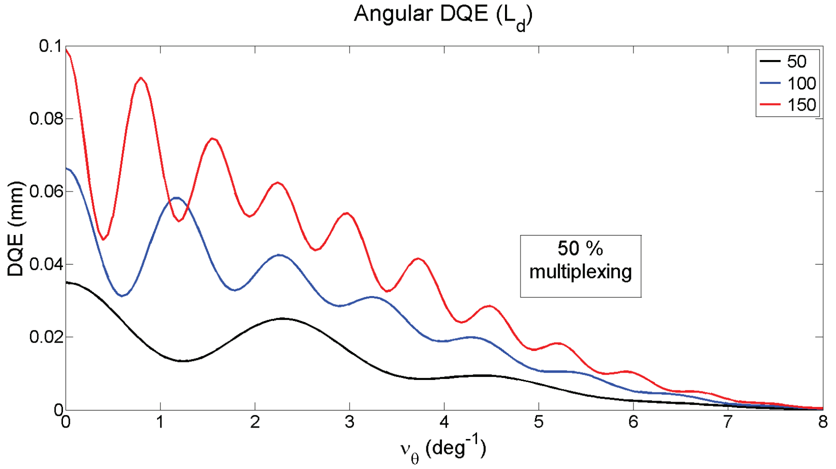

(b) *Angular resolution.*

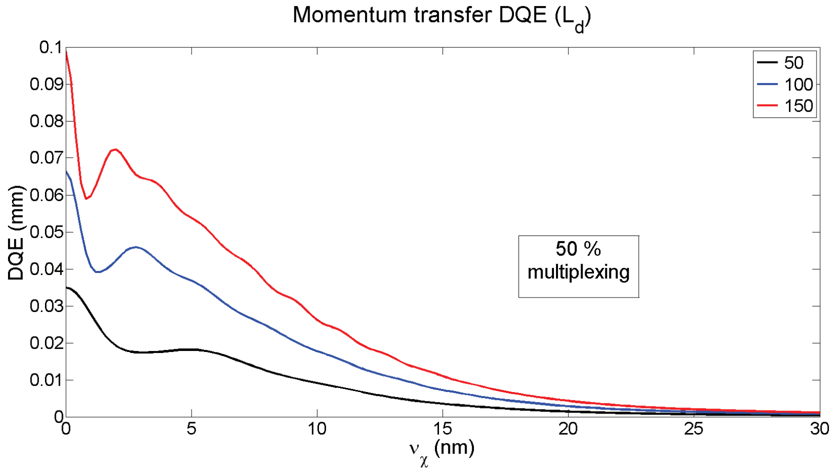

(c) *Momentum transfer resolution.*

Figure V.17: Spatial, angular and momentum transfer DQE curves for different detector dimensions L_d (L_d = 50, 100 or 150 mm).

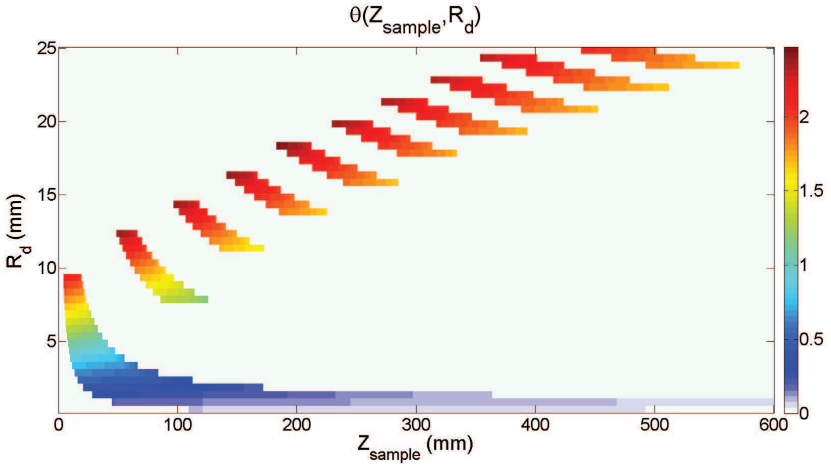

(a) L_d = *50 mm*

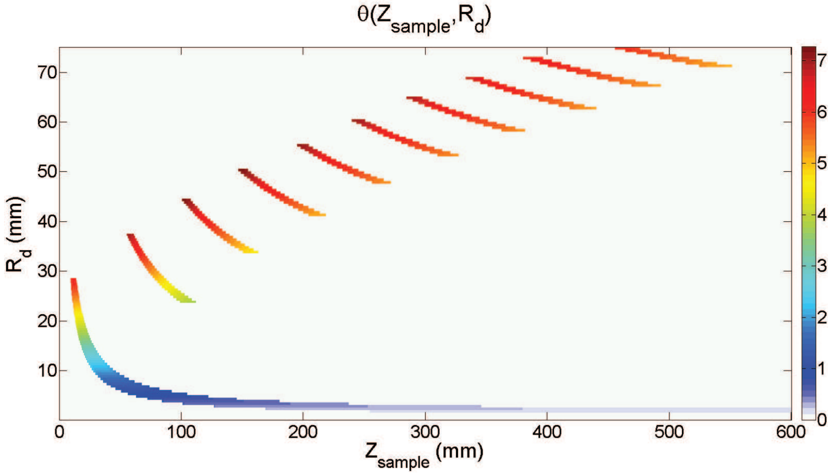

(b) L_d = *150 mm*

Figure V.18: Covered scattering angles θ for different detector dimensions L_d (50 % multiplexing).

V.6 Comparison of XRD systems with different multiplexing levels

The previous section studied the influence of the different system parameters on system performance for 50 % multiplexing and a given distribution of focal distances and a given repartition of the detector surface. Distribution of the focal distances (linear) and the repartition of the detector area (same detection area associated to each "main hole") were the same as for virtual breast biopsy in chapter IV. The impact of the different system parameters on system performance in the case of a multiplexed system is very similar to the one on a non-multiplexed system.

In the first part of this section the impact of multiplexing level on different system performances is analyzed. Afterwards, two other possible distributions of focal distances are evaluated. In fact, as the sample thickness is ten times higher than in mammography case, the linear distribution leads to a sensitivity profile which is very "toothed" and it would be beneficial to obtain a more smooth sensitivity distribution. At last, the repartition of the detector area is varied.

V.6.1 Considered system

The reference system, which is considered in this section, is the same as in the previous section:

- Minimum focal distance f_{min}: 30 mm
- Maximum focal distance f_{max}: 500 mm
- Number of holes Nb_h: 10
- Hole size h: 0.5 mm
- Pixel size p: 0.5 mm
- Collimation height H: 250 mm
- Detector dimension L_d: 100 mm

The secondary collimation is considered to be in contact with the object of 500 mm thickness. That is why the maximum focal distance is fixed at 500 mm. f_{min} is again fixed at a higher value than zero to avoid the signal coming from transmitted non-scattered photons. Distribution of focal distances between f_{min} and f_{max} is linear unless otherwise specified. Figure V.19 is a true to scale schematic representation of the system. It can be clearly seen that detector part thickness varies in order to have the same circular detection areas for each "main hole".

V.6.2 Impact of multiplexing level

The impact on sensitivity, resolution and covered angles and momentum transfer values of different multiplexing levels from zero to 100 % has been tested.

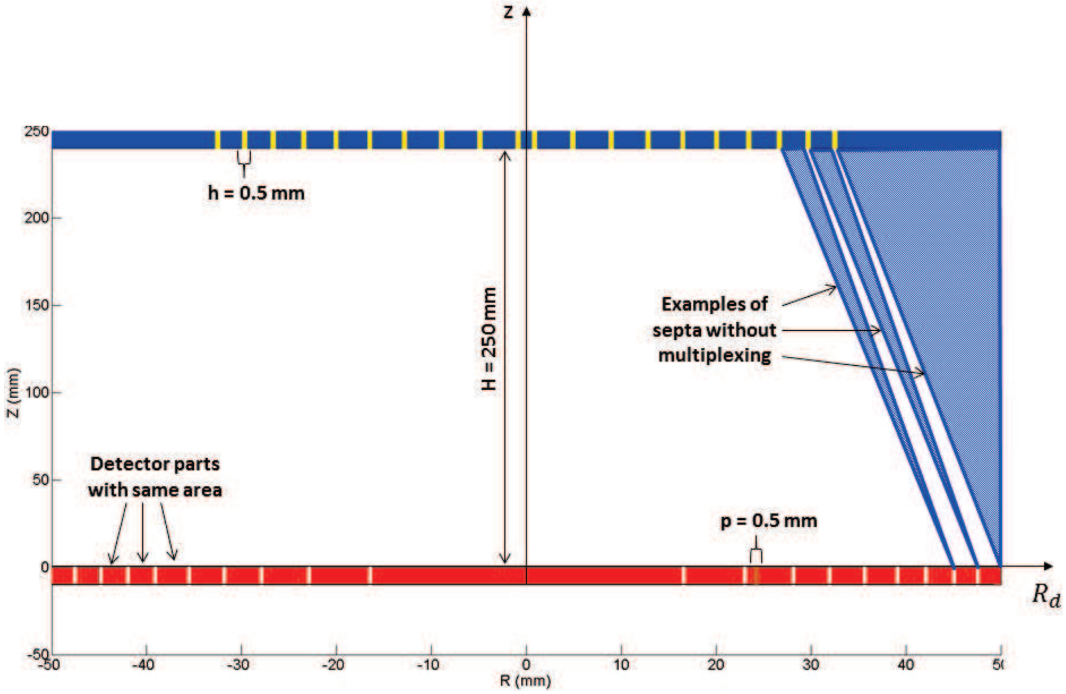

Figure V.19: Schematic representation of the reference system. It has to be noted that in reality there are septa between all holes (yellow). Here, only three septa have been drawn for the case without multiplexing as an example. Septa change for different multiplexing levels.

V.6.2.1 Sensitivity

Figure V.20 shows the sensitivity distribution of the considered system for different multiplexing percentages. For example, without multiplexing the detector region between 23 mm and 28 mm covers a z-range in the sample between around 110 mm and 160 mm. With multiplexing a second z-range at lower z-values is covered by several pixels of the same detector region. The higher the multiplexing percentage the more pixels of the considered detection region "see" two separate z-ranges in the sample, which leads to mixing of information. Sensitivity profiles for the same multiplexing levels are represented in figure V.21.a. Sensitivity is increased for each hole (corresponding to one "tooth" of the sensitivity curve) and maximum sensitivity of each hole is shifted to lower Z_{sample}-values. As can be seen in figure V.21.b, global system sensitivity increases steadily with increasing multiplexing percentage. At 100 % multiplexing, global sensitivity has almost doubled. This could be expected as each pixel of the detector (except for the pixels of the inner detector part) can receive signal from two holes.

V.6.2.2 Resolution

Spatial, angular and momentum transfer DQE curves for different multiplexing levels are shown in figure V.22.a, V.22.c and V.22.e. Oscillations in DQE curves due to multiplexing increase with increasing multiplexing especially for angular DQE. Here, the system is particularly sensitive to some angular frequencies. This should be due to hole distribution.

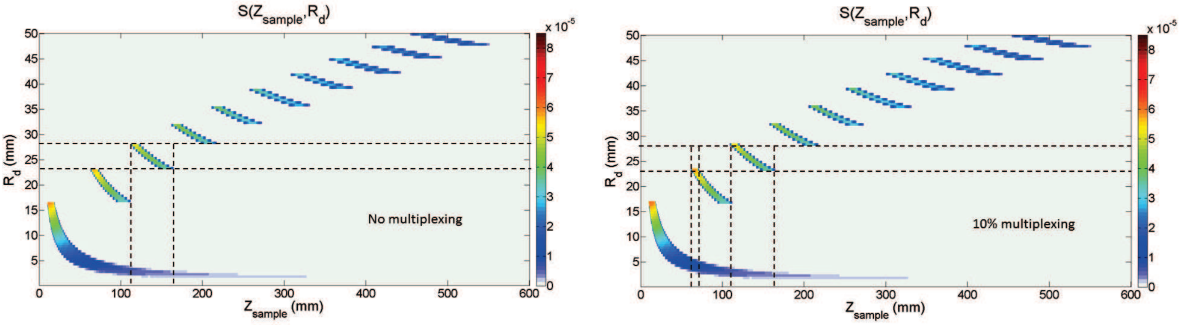

(a) *No multiplexing*

(b) *10 % multiplexing*

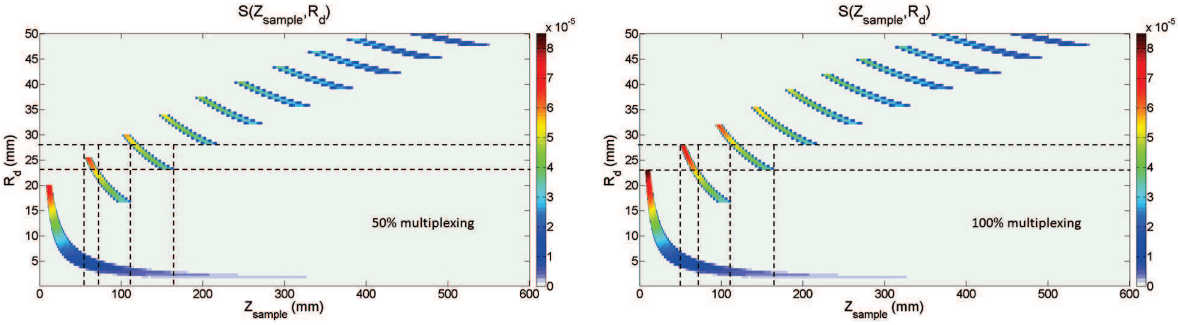

(c) *50 % multiplexing*

(d) *100 % multiplexing*

Figure V.20: Sensitivity distribution for different multiplexing percentages.

Integration of the shape of the incident X-ray spectrum smooths this effect. Thus, momentum transfer DQE only presents very few oscillations. Evolution of the different system resolutions can be seen in figure V.22.b, V.22.d and V.22.f. All kinds of resolution decrease with increasing multiplexing level, which was expected since multiplexing leads to mix of information. Spatial resolution is with around 20 mm lower than for the system optimized in the context of mammography. However, objects to be detected are bigger during security screening. A lower resolution might be acceptable. Average (integration over the incident X-ray spectrum) momentum transfer resolution on the contrary is good. Even with 100 % multiplexing χ resolution is better than 0.1 nm^{-1}.

V.6.2.3 Covered angles and momentum transfer values

Comparison of the covered scattering angles by the considered system at different multiplexing levels (Fig V.23) indicates that intercepted scattering angles by each hole increase if multiplexing is increased. Though, maximum θ is about 5.5° which is low compared with the intercepted angles of optimized systems in chapter IV. The corresponding covered χ-ranges (for an incident X-ray spectrum with 150 keV maximum energy) by each hole can be seen in figure V.24. Multiplexing leads globally to an increase in covered χ-values by each hole. The required χ-range is covered at any multiplexing level.

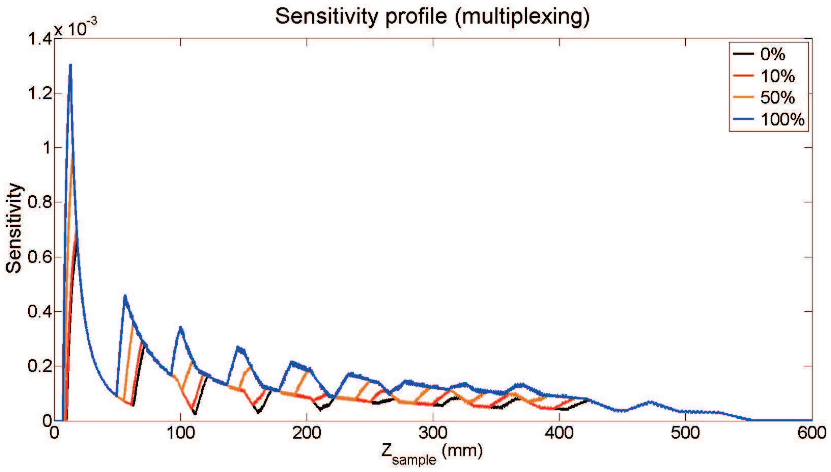

(a) *Sensitivity profile*

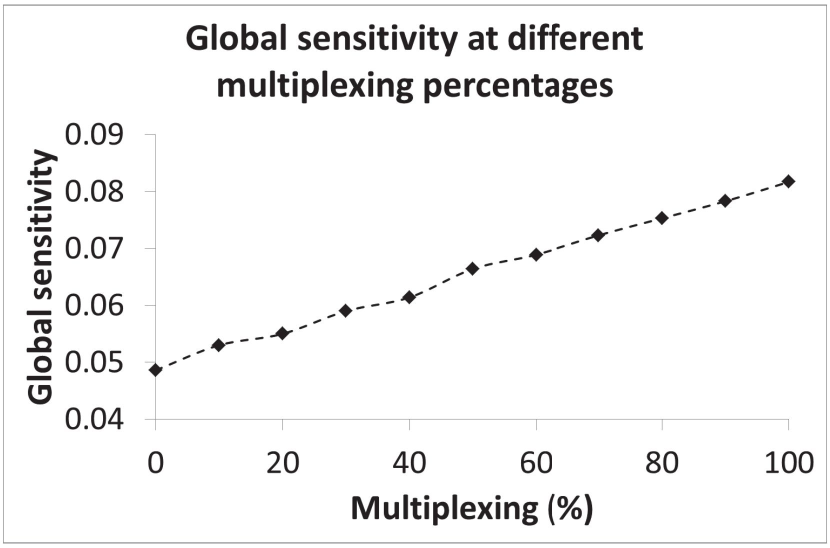

(b) *Global system sensitivity*

Figure V.21: Sensitivity profile and global system sensitivity for different multiplexing levels.

V.6.3 Impact of the distribution of focal distances

Sensitivity distribution along z-axis is very "toothed", which results in z-values to which the system is a lot less sensitive than to the rest (Fig. V.21). This should be avoided. In fact, sensitivity of the different holes is less overlapping than in for the biopsy case, which is mainly due to ten times higher sample size. One possibility to change sensitivity distribution along z-axis is to change the focal distances distribution between f_{min} and f_{max}. Two other possible distributions have been tested:

$$f\left(i\right) = f_{min} \cdot \sqrt{\left(\frac{R_{part}\left(i\right)}{R_{part}\left(i_{max}\right)}\right)^2 \cdot \left(\left(\frac{f_{max}}{f_{min}}\right)^2 - 1\right) + 1} \qquad \text{(V.6.1)}$$

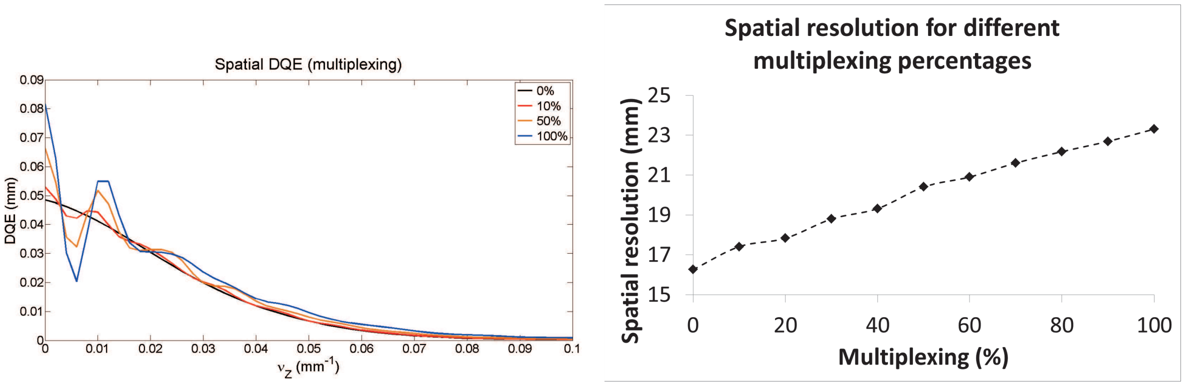

(a) *Spatial DQE curves.* (b) *Spatial resolution.*

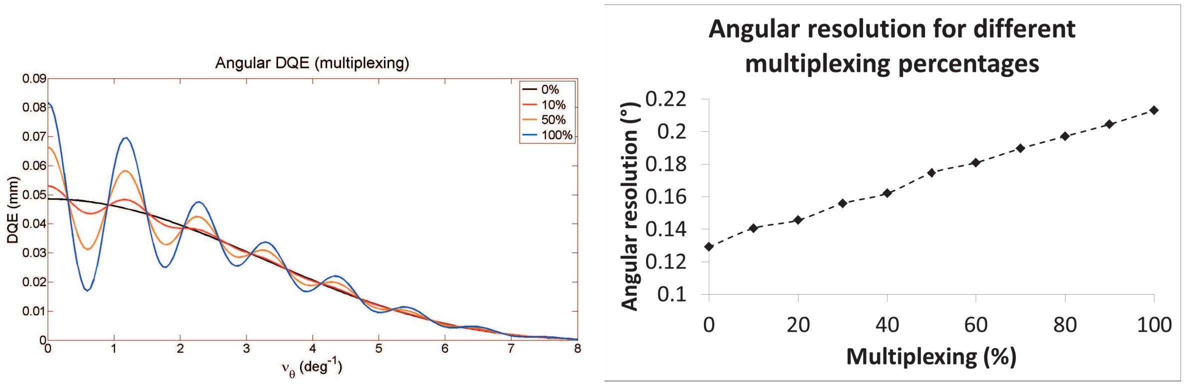

(c) *Angular DQE curves.* (d) *Angular resolution.*

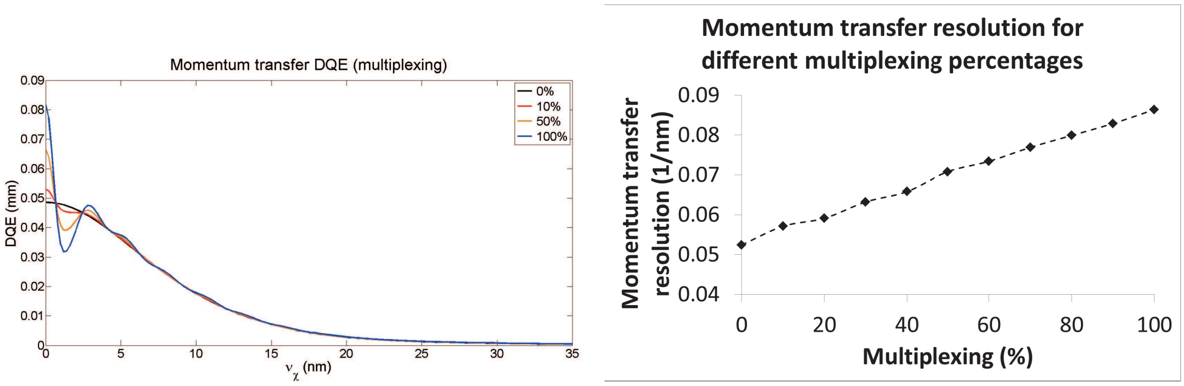

(e) *Momentum transfer DQE curves.* (f) *Momentum transfer resolution.*

Figure V.22: DQE curves and calculated resolution for different multiplexing levels.

where i corresponds to the number of the hole, i_{max} to the number of the last hole (here $i_{max} = 10$) and R_{part} to the radius corresponding to the center of the considered detector part (see figure V.25). This way to distribute the focal distances $f(i)$ is inspired by the work of [Benoit, 2013], where it was used for a multi-focal collimation in single photon emission computed tomography. In the following, this distribution will be referred to as *sqrt* focal distribution.

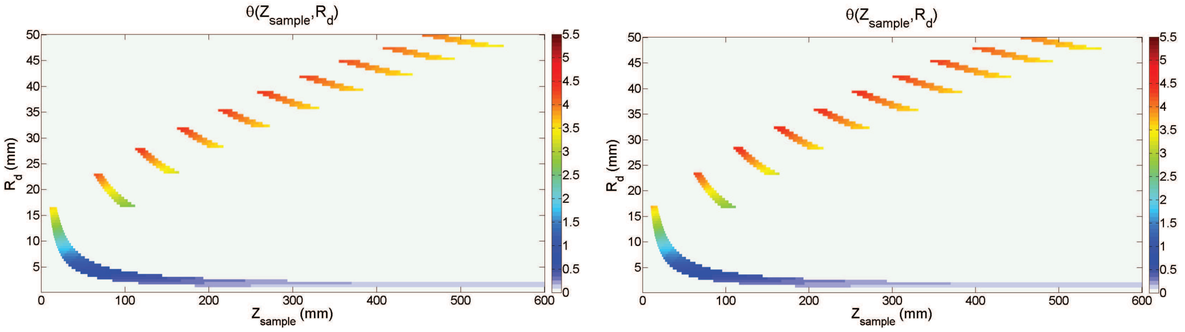

(a) *No multiplexing* (b) *10 % multiplexing*

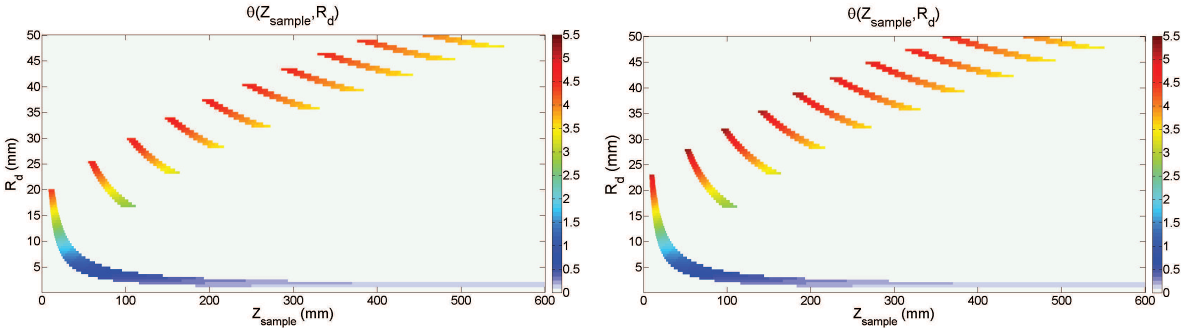

(c) *50 % multiplexing* (d) *100 % multiplexing*

Figure V.23: Distribution of intercepted scattering angles.

The second distribution of focal distances that was tested corresponds to an exponential distribution:

$$f\left(i\right) = f_{min} \cdot \exp\left(\left(i-1\right) \cdot \log\left(\frac{f_{max}}{f_{min}}\right) \cdot \frac{1}{Nb_h - 1}\right) \tag{V.6.2}$$

This focal distribution will be referred to as *exp*.

Figure V.26 shows the graphical representation of the three distributions of the focal distances (for f_{min} =30 mm and f_{max} =500 mm).

The impact on sensitivity distribution, resolution and covered angles and momentum transfer values will be tested in this section. Results will mostly be shown for 50 % multiplexing. Repartition of detector area remains the same, i.e. to each "main" hole the same detection area is attributed.

V.6.3.1 Sensitivity

Sensitivity distribution for the different focal distributions are represented in figure V.27 without multiplexing and for 50 % multiplexing. It can be noticed that overlapping of z-range for the different holes is much higher for *sqrt* than for the linear distribution even without multiplexing. This is not the case for *exp*, where there is no overlapping at all for high Z_{sample}-values even with 50 % multiplexing. There seem to be some z-values that are not covered at all

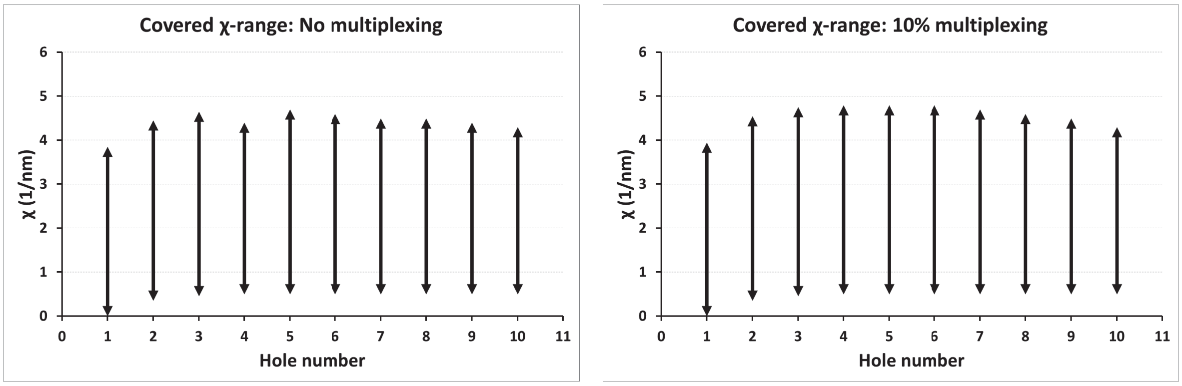

(a) *No multiplexing*

(b) *10 % multiplexing*

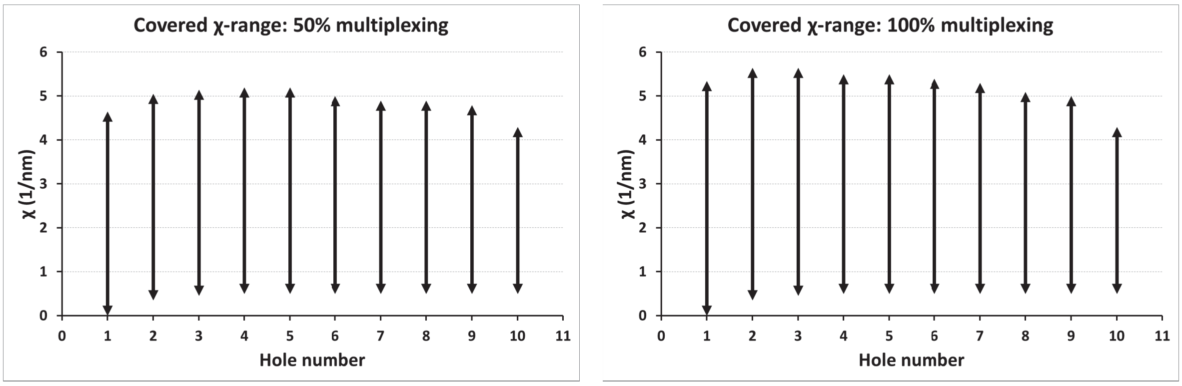

(c) *50 % multiplexing*

(d) *100 % multiplexing*

Figure V.24: Intercepted χ-ranges for different multiplexing levels.

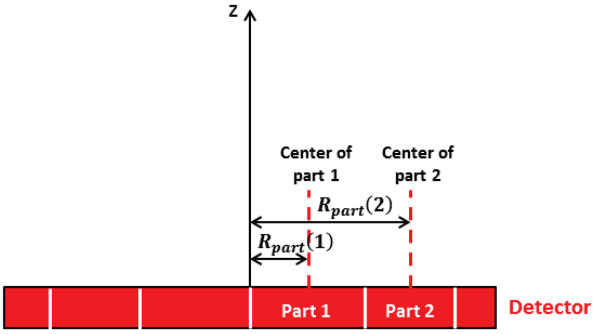

Figure V.25: Illustration of the meaning of R_{part} in the case of three detector parts.

with this focal distribution. This is even more visible with the sensitivity profile (Fig. V.28.a). There are lots of Z_{sample}-values that are not covered if *exp* focal distribution is used. On the contrary *sqrt* focal distribution leads to a relatively homogeneous sensitivity distribution. The only noticeable sensitivity decrease can be seen between the first and the second hole. However, sensitivity does not start at $Z_{sample} = 0$. A gap between secondary collimation and sample should be introduced, as done for virtual biopsy phantom simulations, in order to slightly shift sensitivity distribution. As regards global sensitivity, it is not impacted by

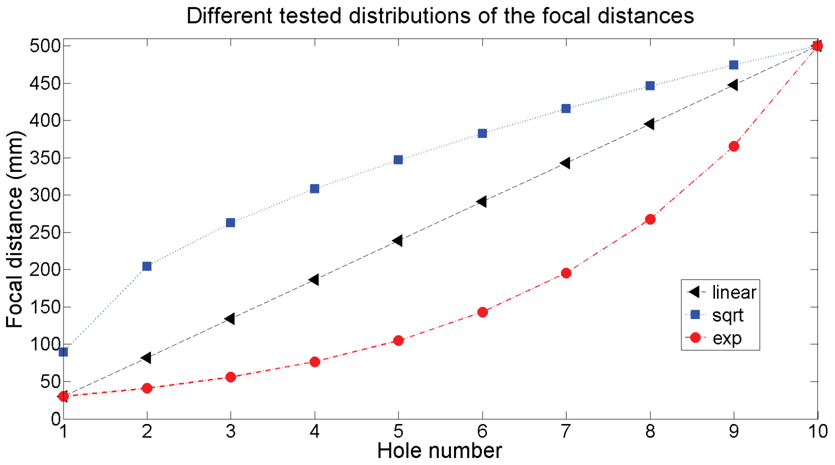

Figure V.26: Graphical representation of the tested focal distances distributions: focal distance as a function of the hole number (for f_{min} =30 mm and f_{max} =500 mm).

the different focal distributions (Fig. V.28.b) Since, *exp* focal distribution does not cover all Z_{sample}-values, it will not be considered anymore in the following sections.

V.6.3.2 Resolution

Figure V.29 shows the DQE curves for 50 % multiplexing and the resolution for varying multiplexing level for the different distributions of the focal distances. Angular and momentum transfer resolution are very little impacted. *sqrt* focal distribution slightly degrades angular and χ-resolution whereas *exp* focal distribution slightly increases them. Momentum transfer DQE curves are almost superimposed and angular DQE present a variation of oscillation frequency at low angular frequencies. The most important change can be observed for the spatial resolution, which is strongly decreased with *sqrt* focal distribution compared to linear focal distribution. Without multiplexing global resolution is about 16.5 mm for a the linear focal distribution and about 23.5 mm for the *sqrt* distribution. With increasing multiplexing percentage, this difference even increases. The degradation of spatial resolution is well highlighted by the DQE curves. The DQE curve for the linear distribution is situated over the curve for *sqrt* focal distribution for almost all spatial frequencies.

V.6.3.3 Covered angles and momentum transfer values

Variation of covered scattering angles by changing the focal distances distribution can be seen in figure V.30 for zero multiplexing and 50 % multiplexing. For *sqrt* distribution the covered scattering angles are only slightly lower than in the case of a linear distribution. The comparison of the covered χ-ranges for different multiplexing levels in figure V.31 shows that covered χ-ranges for each hole are still sufficient.

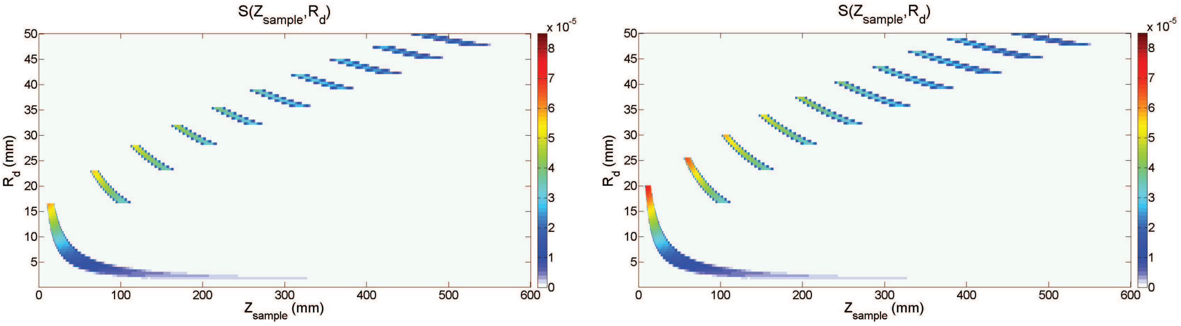

(a) *No multiplexing + linear focal distribution* (b) *50 % multiplexing + linear focal distribution*

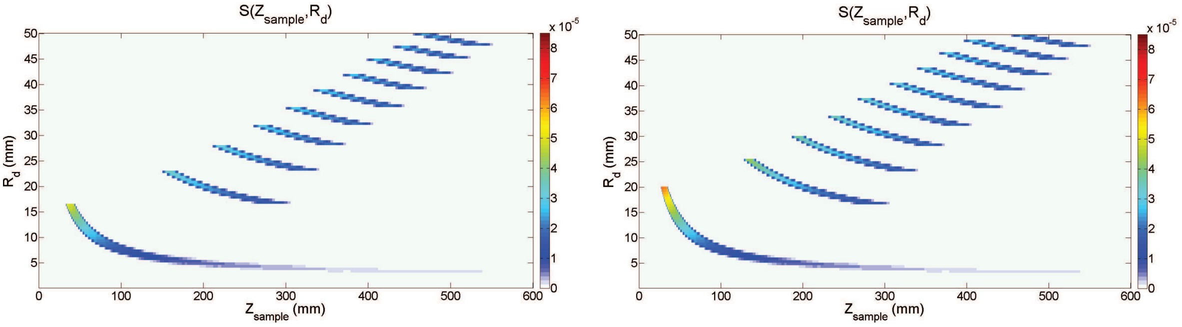

(c) *No multiplexing + sqrt focal distribution* (d) *50 % multiplexing + sqrt focal distribution*

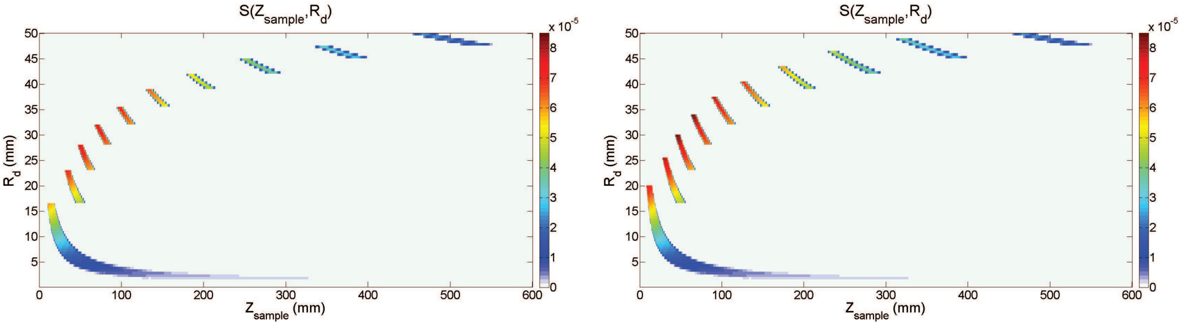

(e) *No multiplexing + exp focal distribution* (f) *50 % multiplexing + exp focal distribution*

Figure V.27: Sensitivity distribution for different focal distances distributions.

V.6.4 Impact of detector area repartition

Up to now each circular detector part associated to one hole was of the same surface, which means that the thickness of the different parts and hence, the number of circular "pixels" was not the same. In this section, the impact of a repartition with the same thickness for each detector part was evaluated. The two detector area repartitions will be referred as "same surface" (distribution used in the previous sections) and "same pixel number" repartition. The distribution of the focal distances is fixed to be linear.

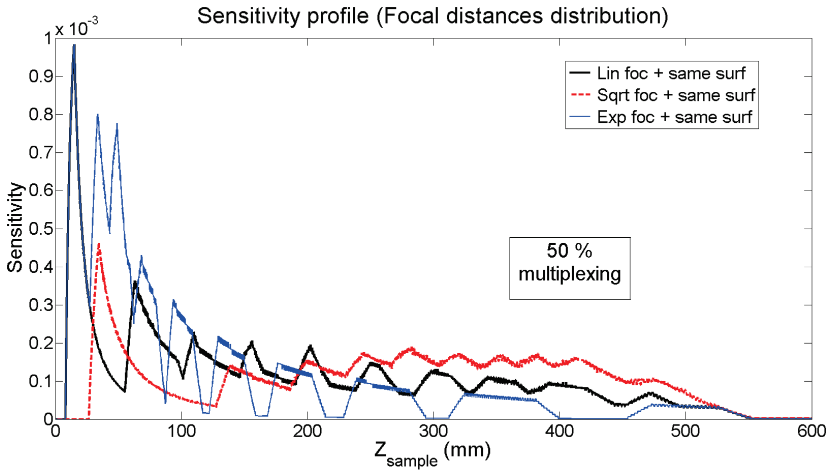

(a) *Sensitivity profile*

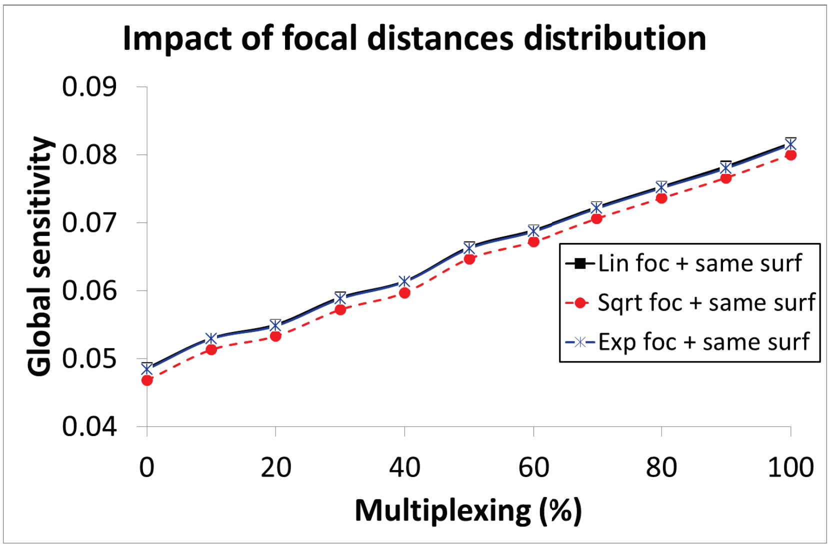

(b) *Global system sensitivity*

Figure V.28: Sensitivity profile and global system sensitivity for different distributions of the focal distances.

V.6.4.1 Sensitivity

By comparing sensitivity distributions for the two detector area repartitions (Fig. V.32), it can be noticed that overlapping of covered z-ranges by the different holes, is increased for the same pixel number repartition. However, maximum sensitivity value for each hole is smaller than with the same surface distribution, especially for the inner holes (small R_d). This seems normal as these parts "lost" detection area. Increased overlapping of z-ranges is reflected by a more homogeneous sensitivity profile (Fig V.33.a). The first hole lost a great deal of sensitivity, which is again due to decreased detector area attributed to this hole. Global sensitivity is the same for both detector area repartitions if there is no multiplexing (Fig. V.33.b). In fact, the total detection area remains the same. With increasing multiplexing level global sensitivity increase is higher for the same pixel number repartition. As multiplexing is determined in

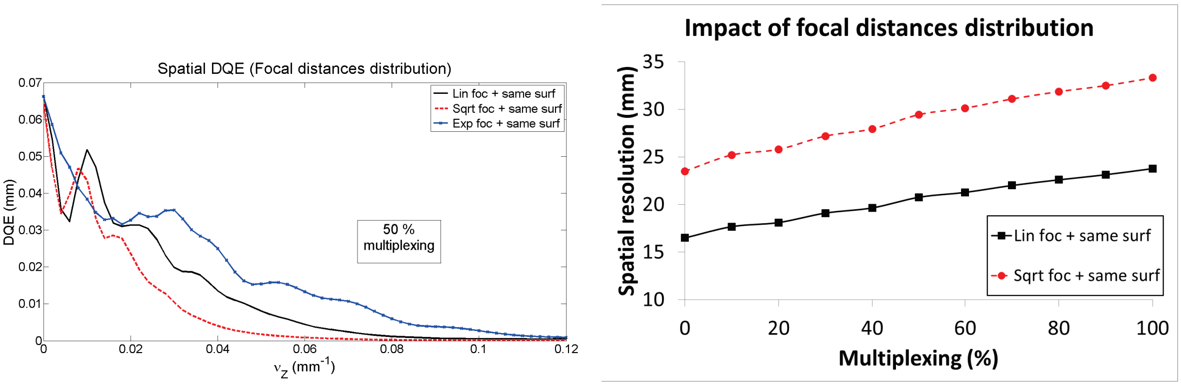

(a) *Spatial DQE curves.* (b) *Spatial resolution.*

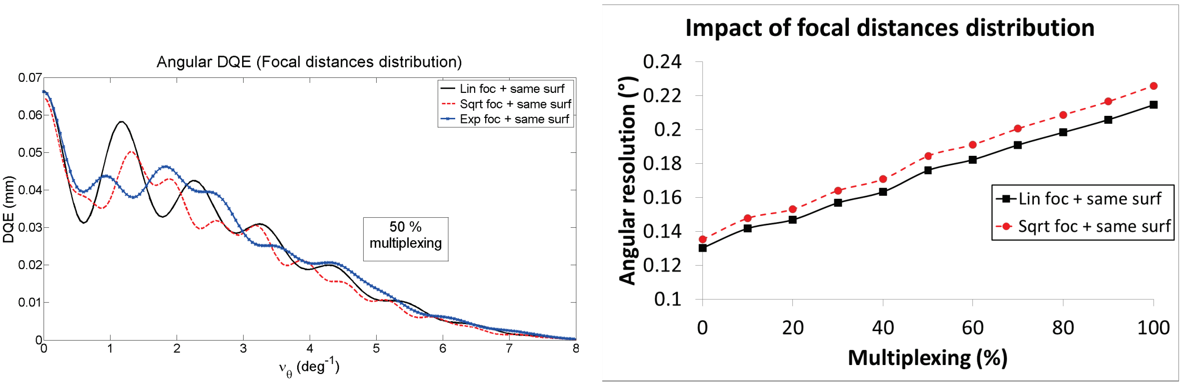

(c) *Angular DQE curves.* (d) *Angular resolution.*

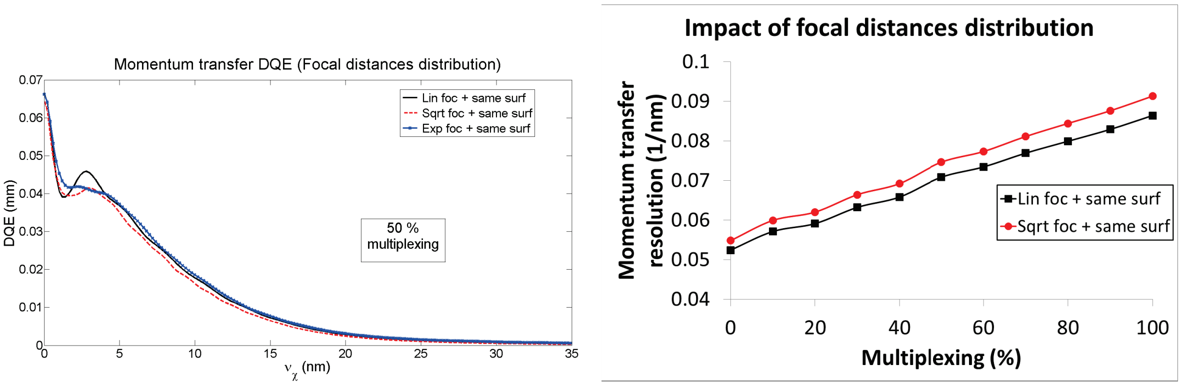

(e) *Momentum transfer DQE curves.* (f) *Momentum transfer resolution.*

Figure V.29: DQE curves and calculated resolution for different multiplexing levels and for different distributions of the focal distances.

percentages, detector surface receiving multiplexing signal is higher in case of same pixel number distribution.

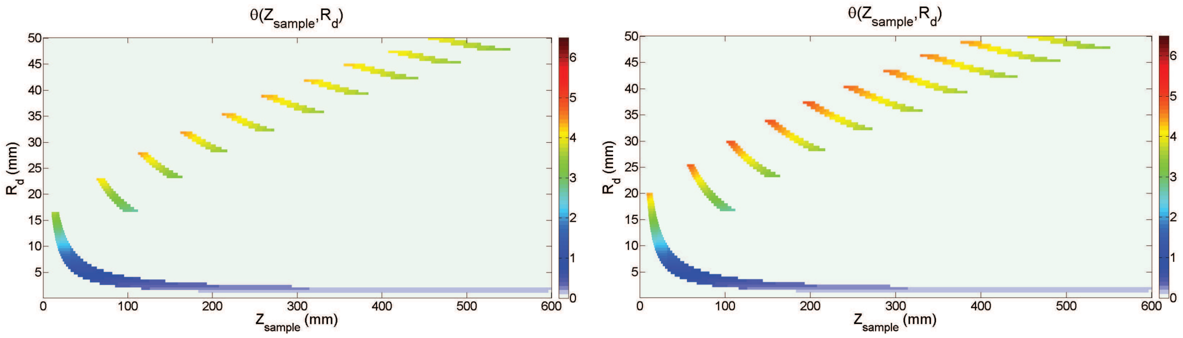

(a) *No multiplexing + linear focal distribution* (b) *50 % multiplexing + linear focal distribution*

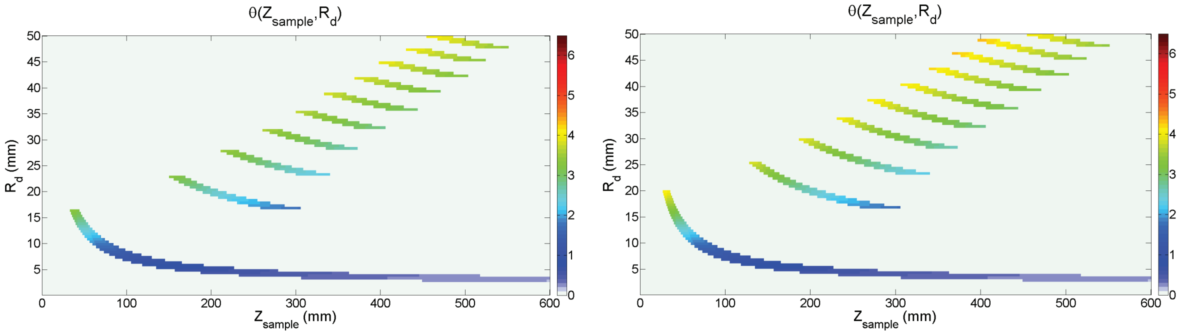

(c) *No multiplexing + sqrt focal distribution* (d) *50 % multiplexing + sqrt focal distribution*

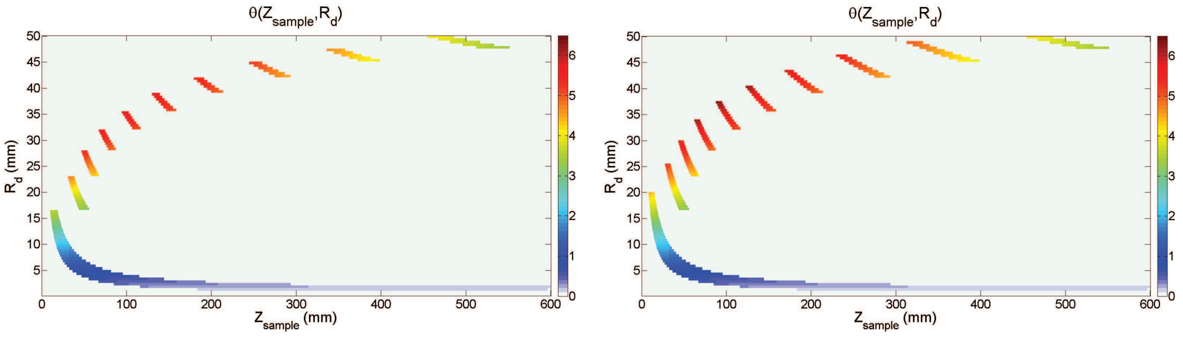

(e) *No multiplexing + exp focal distribution* (f) *50 % multiplexing + exp focal distribution*

Figure V.30: Distribution of intercepted scattering angles for different focal distances distributions.

V.6.4.2 Resolution

Change of detector area repartition has little influence on the angular and momentum transfer resolution. Momentum transfer DQE curves with 50 % multiplexing for both detector area repartitions are almost superimposed and angular DQE curves are very close as well. Angular and χ-resolution are the same in both cases without multiplexing. With increasing multiplexing level, they decrease slightly faster if same pixel number detector area repartition is used. Impact on spatial resolution is much more important. Without multiplexing the loss of spatial resolution is about 10 mm compared with same surface repartition. The loss will become even higher, if the system is multiplexed.

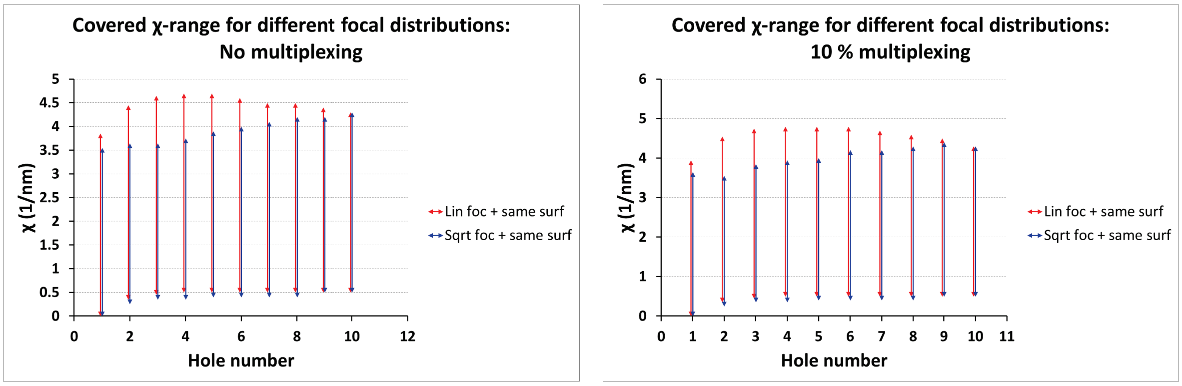

(a) *No multiplexing* (b) *10 % multiplexing*

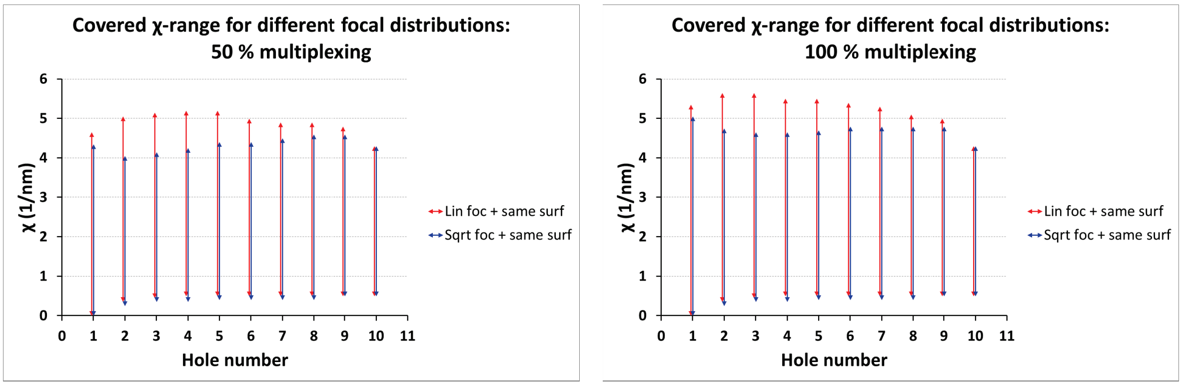

(c) *50 % multiplexing* (d) *100 % multiplexing*

Figure V.31: Intercepted χ-ranges at different multiplexing levels for different focal distances distributions.

V.6.4.3 Covered angles and momentum transfer values

As can be seen in figure V.35 intercepted scattering angles are globally lower for the same pixel number detector repartition. Hence, covered χ-values are also lower. Especially for the first three holes the accessible χ-range is very small (Fig. V.36). If there is no multiplexing the required χ-range is not entirely covered. Even with 100 % multiplexing, the first hole is not sensitive to χ-values higher than 2.5 nm^{-1}.

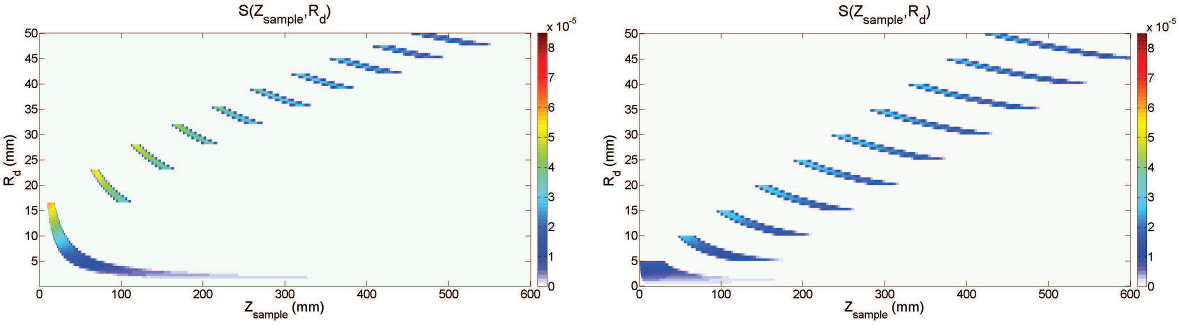

(a) *No multiplexing + same surface* (b) *No multiplexing + same pixel number*

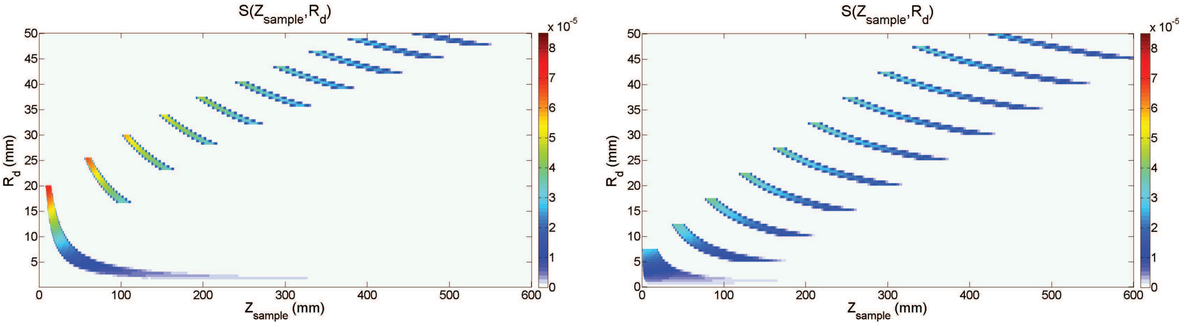

(c) *50 % multiplexing + same surface* (d) *50 % multiplexing + same pixel number*

Figure V.32: Sensitivity distribution for different detector surface repartitions.

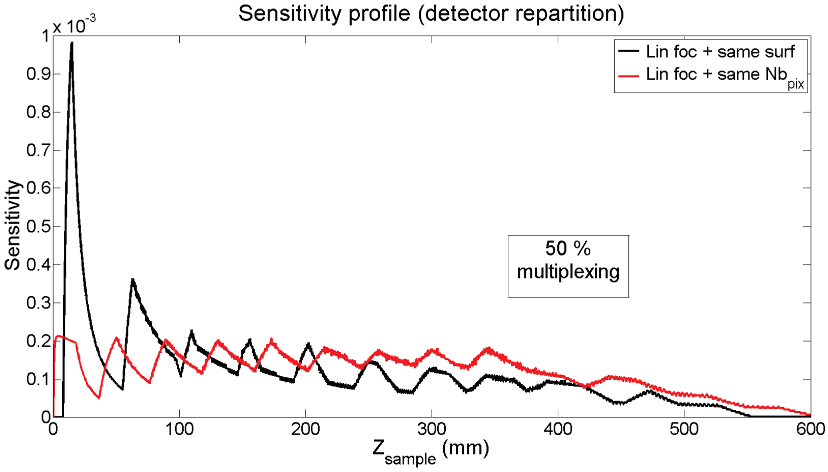

(a) *Sensitivity profile*

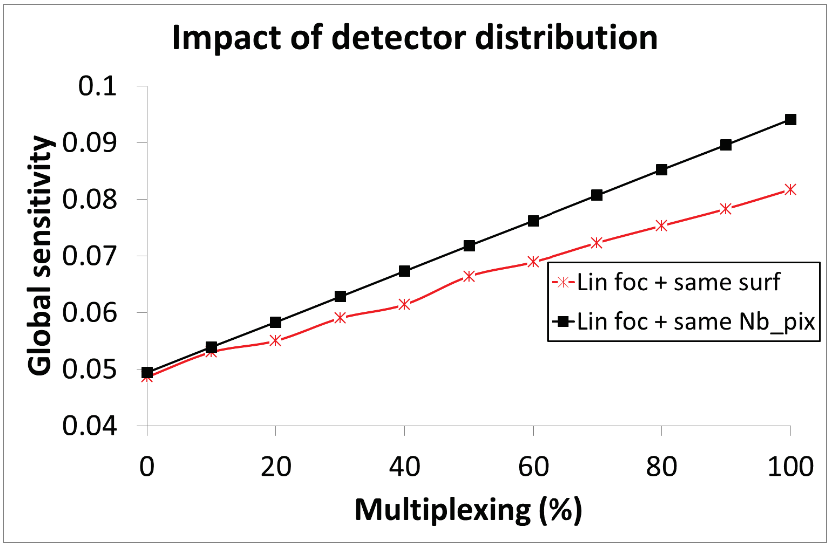

(b) *Global system sensitivity*

Figure V.33: Sensitivity profile and global system sensitivity for different repartitions of the detector surface.

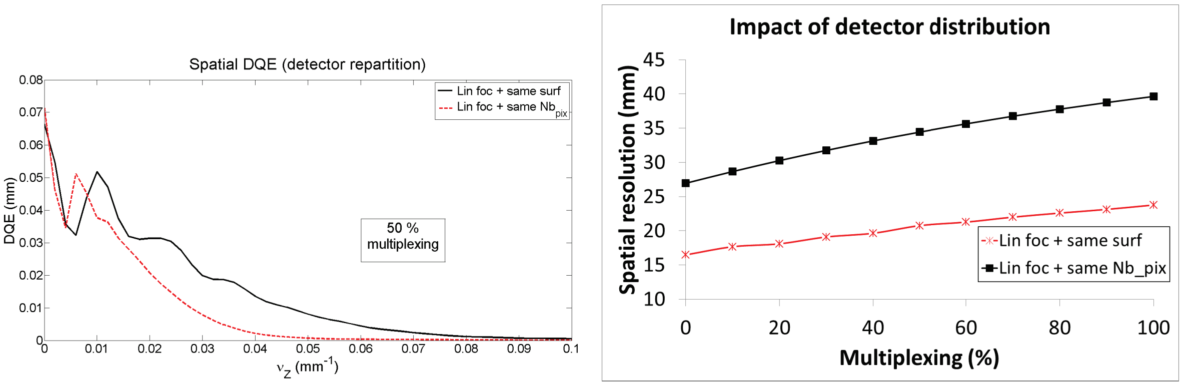

(a) *Spatial DQE curves.* (b) *Spatial resolution.*

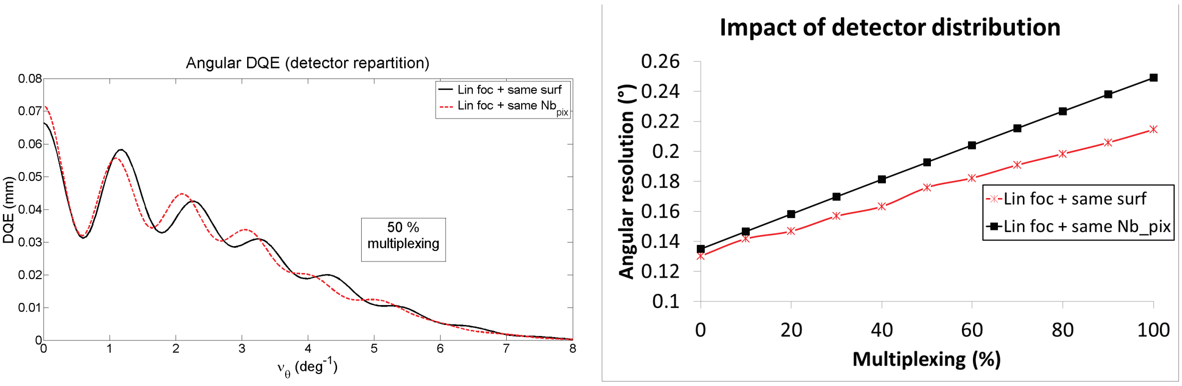

(c) *Angular DQE curves.* (d) *Angular resolution.*

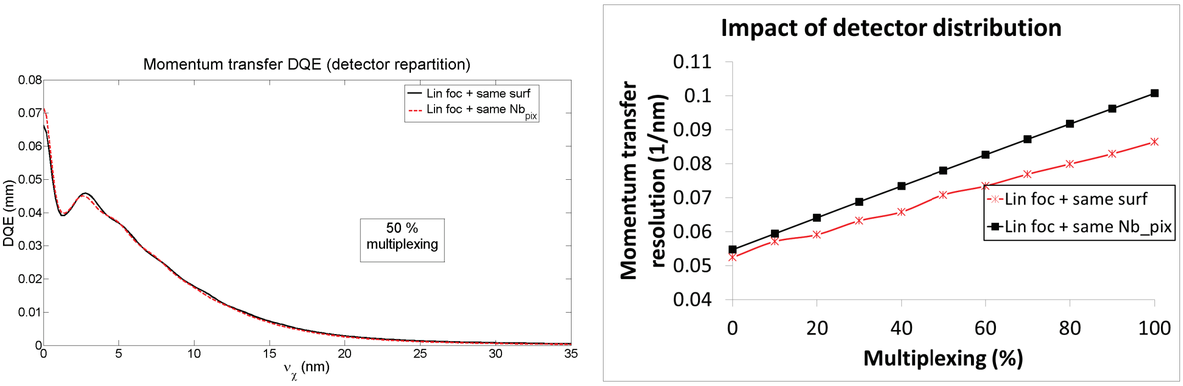

(e) *Momentum transfer DQE curves.* (f) *Momentum transfer resolution.*

Figure V.34: DQE curves and calculated resolution for different multiplexing levels and for different repartitions of the detector surface.

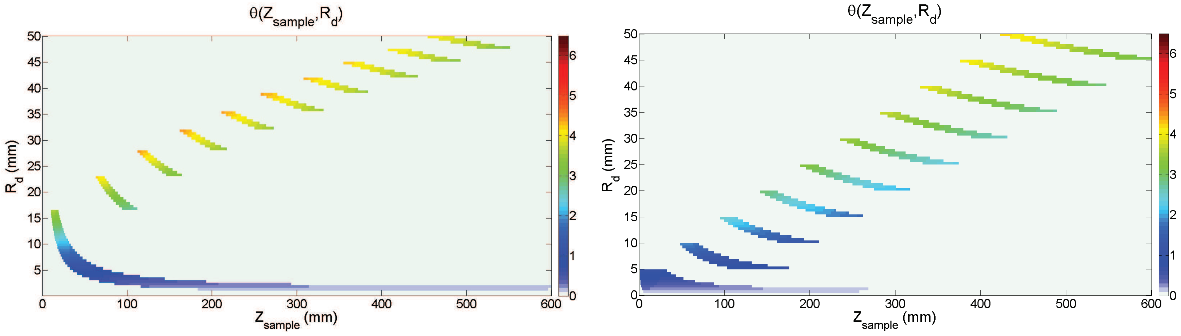

(a) *No multiplexing + same surface* (b) *No multiplexing + same pixel number*

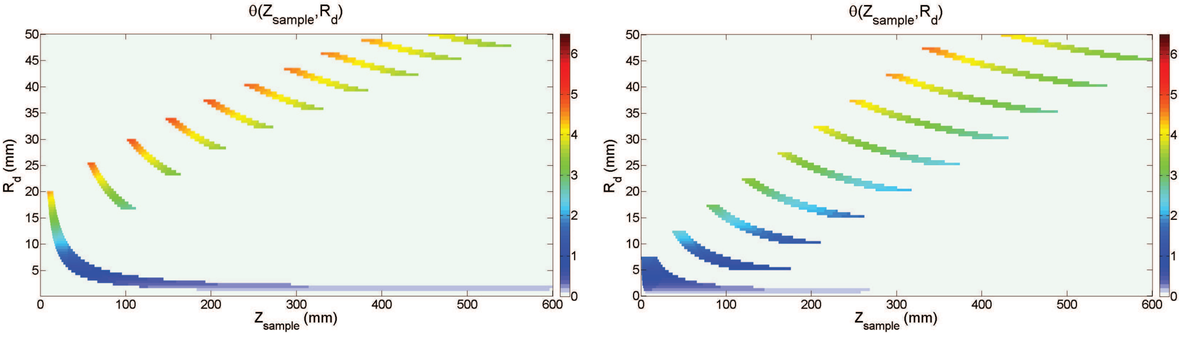

(c) *50 % multiplexing + same surface* (d) *50 % multiplexing + same pixel number*

Figure V.35: Distribution of interscepted scattering angles for different detector surface repartitions.

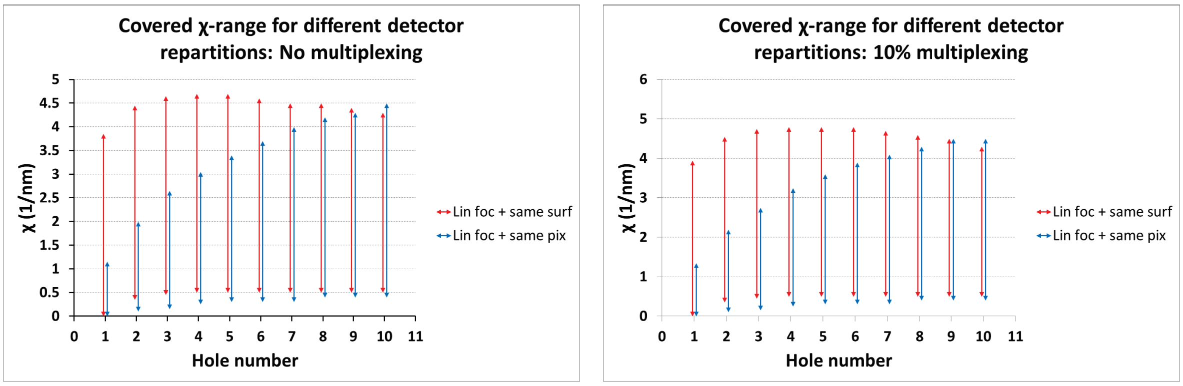

(a) *No multiplexing* (b) *10 % multiplexing*

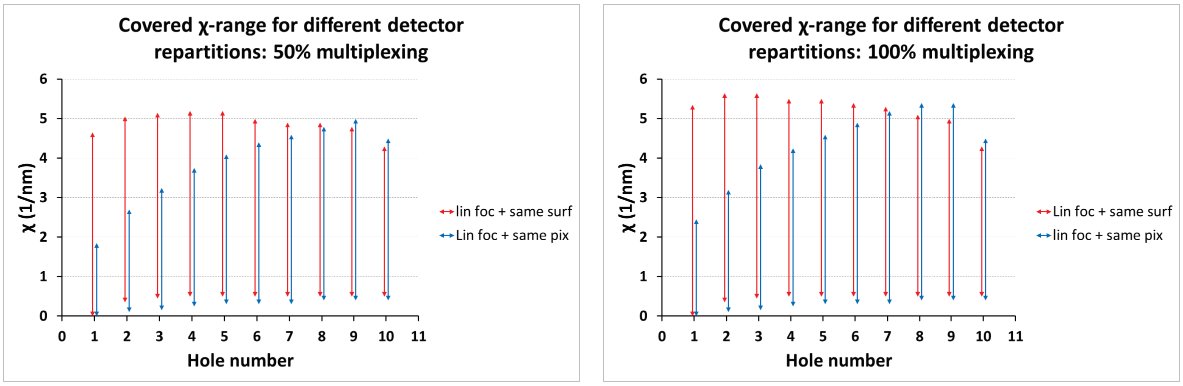

(c) *50 % multiplexing* (d) *100 % multiplexing*

Figure V.36: Intercepted χ-ranges at different multiplexing levels for different detector repartitions.

V.7 Conclusion

This chapter was dedicated to the application of XRD in security screening of hand baggage at the airport. The idea is to use an XRD-imaging machine for carry-on luggage control at the first control level. Such a system already exists. However, its sensitivity is still limited, and in consequence, scan time is relatively long. We would like to propose a more sensitive system to be able to further decrease necessary scan time. Therefore, we suggest to combine EDXRD and ADXRD allowing to increase system sensitivity χ-range and limited multiplexing to improve system sensitivity without too much loss of resolution. A tool to assess system performances was developed, which permits to optimize the different system parameters. A preliminary study of the impact of different parameters using this tool, was carried out.

First, the different materials to be detected during security check were presented. In contrast to virtual breast biopsy, where the tissues to be identified were all amorphous, the materials to be identified might be amorphous or crystalline. Thus, the system has to be resolving enough to separate the main peaks of polycrystalline explosives and drugs, and sensitive enough to detect the less diffracting amorphous illicit materials. System momentum transfer resolution should be between 0.1 and 0.2 nm^{-1}.

In order to be able to assess system performances of a collimation system with limited multiplexing, an analytical DQE calculation method was developed similar to the one presented in chapter IV. It was shown that the impact of the different system parameters is globally the same as without multiplexing. A reference conical multifocal collimation system was studied. Multiplexing increases the global system sensitivity but degrades system resolution. Average momentum transfer resolution remains good. Authorized multiplexing level will thus depend on the minimum spatial resolution that is required. As the objects to be detected exceed the size of the ones to be identified in XRD-based breast imaging, the spatial resolution may be lower.

Sensitivity profile of the reference system is very "toothed". The *sqrt* focal distances distribution or the change of the detector area repartition to a same pixel number distribution help to distribute system sensitivity more uniformly but with severe loss of spatial resolution. It is always a trade-off between sensitivity and resolution.

The present preliminary study should help to develop a strategy for collimation system optimization for this application. After optimization, the system should be simulated with a phantom of a typical filled suitcase with and without illicit material. Separability of legal and illicit amorphous materials can be assessed as previously using CNR and ROC calculations. In the case of polycrystalline, it should be verified whether approximations made during analytical ROC calculations are valid for polycristalline distributions. If required, the technique should be adapted to this kind of distributions. System performances (false alarm rate, scan speed) should be compared to existing EDXRD systems.

Conclusion and outlook

The purpose of this work was to optimize an energy dispersive X-ray diffraction (EDXRD) system, using a room temperature pixellated semiconductor detector, for one or two chosen applications. It was decided to first propose an optimized imaging system for diffraction based virtual biopsy and to think of an alternate XRD system for carry-on luggage screening afterwards. Optimization included two aspects: Acquisition system considerations to be able to acquire as much information as possible and data processing to extract as much information as possible by using an inverse problem approach. Hence, the work to be realized can be decomposed into three principal tasks: understanding of EDXRD imaging principles and the existing X-ray diffraction methods to characterize biological tissues and illicit materials (Chap. I), studying and testing reconstruction methods (Chap. III) and characterization of XRD systems in order to propose optimized system architectures for the chosen applications (Chap. II, IV, V).

Bibliography studies in chapter I have shown that numerous authors have investigated the separability of several biological tissues and that classification of breast tissue in healthy and cancerous seems to be a promising field of application of X-ray diffraction. All studies have found that there are two important momentum transfer peaks to distinguish healthy breast tissue from carcinoma: The adipose peak at 1.1 nm^{-1} (missing in cancerous tissue) and the water peak at 1.6 nm^{-1} (existing in both tissue types). Some imaging techniques to obtain diffraction CT and the use of an active pixel sensor system were proposed. One optimized EDXRD system for clinical applications was presented as well. However, the aspect of tissue separability and required dose was not treated. Some scientists suggested the association of XRD to other imaging technique and to combine the different information by multivariate data analysis.

State of the art studies of the use of XRD to detect illicit materials have shown that several workers have been interested in this question. Different kinds of illicit materials could be detected: explosives and drugs, which can be polycrystalline or amorphous. Explosive detection at the airport is the main issue as false alarm resolution is very expensive and a more reliable control system is needed. Different system architectures using EDXRD have been proposed. Morpho detection commercialized two EDXRD systems for baggage control: one to resolve false alarm for hold baggage and one for hand baggage control at first control level. Drug detection was suggested in different cases: luggage control at the airport, control of parcels and the detection of drugs hidden under human skin. As there is also a serious problem with liquid explosive detection in luggage, some workers were also interested in liquid identification using XRD. Different methods of analyzing XRD data do detect illicit materials were suggested. Most of them are based on singular value decomposition, principal component analysis or multivariate analysis. These methods are in general applied to acquired non reconstructed diffraction spectra except for the case, where a coded aperture was employed and reconstruction was indispensable.

The second chapter concerned the characterization of an X-ray diffraction system. First, the different system components deteriorating spectrum quality were explained and a mathematical model of an EDXRD imaging system was proposed. An extension to a multi-angle model corresponding to the combination of EDXRD and ADXRD was presented as well. Then, tools for system characterization and optimization were introduced. Resolution and sensitivity could be determined by detective quantum efficiency (DQE) calculations, which is a figure of merit only depending on system properties and not on sample properties. In EDXRD, DQE calculations can be realized by the use of a simulated system response. Unlike DQE calculations in X-ray transmission imaging, DQE calculations in EDXRD are based on non stationary processes. Hence, the calculated DQE does not only depend on frequency. Object-dependent criteria were proposed as well: contrast to noise ratio and receiver operating characteristic (ROC) curves. They give information about the separability of two materials acquired by a given imaging system. Classically ROC curves are constructed by testing numerous different realizations (simulated or measured) using different thresholds. In this dissertation an analytical method of ROC curve construction based on information geometry has been proposed. First, DQE calculations were realized for a basic EDXRD system, in order to evaluate the use of a multi-angle EDXRD system and to understand the influence of the different system parameters. It was shown that a multi-angle system allows to enlarge the momentum transfer sensitivity range. Furthermore, it permits to smooth the adverse effect of the source's characteristic rays in the detected spectra. Studying of the impact of different geometrical system parameters revealed that system parameters cannot be optimized independently from a given application.

The third chapter was dedicated to restoration of material characteristic XRD signatures from simulated and experimentally acquired spectra. In the present work a maximum likelihood expectation maximization (MLEM) approach was chosen for reconstruction. The algorithm without a priori was described in detail. It was tested on simulated data and experimental spectra provided by a basic EDXRD system. MLEM algorithm worked well in the case of crystalline spectra (TNT and salt) and it was confirmed that a multi-angle approach allows primarily to enlarge the covered momentum transfer range and hence, the number of restored diffraction peaks. For reconstruction of amorphous scattering signatures MLEM algorithm did not work well. Reconstructed spectra presented numerous oscillations. Hence, the algorithm had to be adapted for amorphous spectrum reconstruction by the use of regularization techniques (base, resolution kernel). Regularization techniques were also validated on simulated and experimental data (water and pork fat). These methods worked very well for simulated data, were the system response is exactly known. In the case of experimentally acquired spectra, these methods allowed to smooth the reconstructed material signature. However, the relative error remained at least about 50 %, which is probably due to the fact that the employed system response does not exactly correspond to the real system response. The best result was obtained with a Lorentzian base.

In future work, reconstruction method for amorphous should be revised as reconstructed amorphous signatures from experimental spectra were not satisfying. The system response and especially the detector response, on which is based the resolution kernel, should be improved to be closer to reality. It might also be interesting to test other reconstruction methods such as the space-alternating generalized expectation maximization (SAGE) method proposed by [Fessler and Hero, 1995] or Bayesian methods. The best would be to develop a reconstruction method, that is suitable for crystalline and amorphous XRD signatures, as both can be found in a typical suitcase.

Breast tissue characterization based on X-ray diffraction to resolve unclear outcome of conventional mammography is discussed in chapter IV. An analytical DQE calculation method to characterize a collimation system without multiplexing have been developed. Studying the impact of different system parameters using this method allowed to establish an optimization strategy. Two optimized convergent collimation systems, whose performances are very similar but one of them is multifocal and the second one is monofocal, have been proposed. Tissue separation power of both collimation systems was assessed in a simulation study of the complete XRD system associated to a breast phantom. It was found that the monofocal system is less performing. Variation of breast density indicated that XRD technique should also be reliable for examination of breast with high density. To conclude, XRD-based breast imaging appears to be a good way to reduce the number of invasive breast biopsies. Its sensitivity and specificity were good even when the dose delivered was moderate, and scan-time also should be acceptable.

As a next step, it will be necessary to confirm these simulation results with experimental measurements. A multifocal collimation system whose dimensions are very close to those suggested in this work has been manufactured and the first calibration measurements are in progress as part of the PhD thesis work of Damien Barbes [Barbes, 2016]. Though, for easier manufacturing the collimation was chosen to be composed of sheets and hence, scattered photons are collimated only in one direction. It would also be interesting to compare the proposed system to other possible systems, for example the system using a coded aperture proposed by [Lakshmanan *et al.*, 2016].
The impact of variability of tissue scattering signatures as well as varying breast thickness should also be studied.

The last chapter of this work presents a preliminary study concerning the use of a multifocal multiplexed collimation system for security screening of hand baggage at the airport. To this issue, an analytical method to calculate DQE curves for a collimation system with limited multiplexing have been developed. The study of the impact of the different system parameters on system performance, has shown that their influence on resolution and sensitivity is similar to the case without multiplexing. The higher the multiplexing level was the higher was system sensitivity and the lower were spatial, angular and momentum transfer resolution. A compromise between system sensitivity and needed resolution to detect illicit materials has to be found. By changing the distribution of focal distances and the repartition of the detector area, we tried to improve sensitivity distribution over the sample thickness. Here again, a trade-off between resolution and sensitivity distribution has to be found.

In order to be able to propose an alternative system for security screening, the preliminary study presented in this work should be used to develop an optimization strategy. Analytical DQE analysis can be used to determine an optimized system configuration. Afterwards a simulation study similar to the one presented for virtual breast biopsy should be realized. Here, the most important criteria would be required scan time with given X-ray tube power. It might be necessary to adapt the ROC calculation method as employed approximations might not be valid for crystalline signatures. Comparison with existing systems as the one developed by Harding *et al* should be carried out as well.

Resumé de la thèse en français

L'imagerie basée sur la diffraction des rayons X est une technique non-invasive puissante pour l'identification et caractérisation de matériaux différents. Comparée aux techniques traditionnelles utilisant la transmission des rayons X, elle permet d'extraire des informations beaucoup plus caractéristiques pour le matériau inspecté, comme les positions des pics de Bragg pour des matériaux cristallins et le facteur de forme moléculaire pour les matériaux amorphes. Le potentiel de cette méthode a été reconnu par de nombreuses équipes de recherche, et de nombreuses applications comme l'inspection de bagage, le contrôle non-destructif, la détection de drogue et la caractérisation de tissus biologiques ont été proposées. Cependant, cette méthode est limitée par le faible nombre de photons diffractés qui résulte en une faible sensibilité de cette technique. L'objectif de ce travail de thèse est d'optimiser toute la chaîne de caractérisation basé sur la diffraction de rayons X pour deux applications choisies, afin de surmonter cette limitation par la faible sensibilité. L'optimisation comprend deux aspects : l'optimisation du système d'acquisition et du traitement des données. La dernière concerne particulièrement la correction des spectres de diffraction dégradés par le processus d'acquisition.

Cette thèse est composée de cinq chapitres. Le premier chapitre explique les principes physiques de la diffraction et présente l'état de l'art de la caractérisation de tissus biologiques et de la détection de matériaux illicites en utilisation la diffraction X. Le phénomène de diffraction est dû à l'interférence de rayons X diffusé de façon cohérente sous un angle θ. On parle aussi de diffusion Rayleigh. La section efficace de la diffraction est donnée par.

$$\frac{d\sigma}{d\Omega} = \frac{d\sigma_{Th}}{d\Omega} \sum_{i=1}^{N_{atom}} f^2\left(\chi, Z_i\right) n_i V s_i\left(\chi\right)$$

Où $\frac{d\sigma_{Th}}{d\Omega}$ est la section efficace de Thomson correspondant à la diffusion élastique d'un photon sur un électron libre. f^2 est appelé le facteur de diffusion atomique ou facteur de forme de l'atome, il correspond à la transformée de Fourier de la densité électronique. n_i donne le nombre par unité de volume de l'atome "i" et N_{atom} le nombre d'atomes différents présents dans le volume d'inspection V. Z_i correspond au numéro atomique de l'atome "i" et $\chi = \frac{E}{hc} \cdot \sin\left(\frac{\theta}{2}\right)$ une variable proportionnelle au transfert de quantité de mouvement, qui sera référée comme transfert de quantité de mouvement. Sa valeur est donnée en nm^{-1}. La fonction s_i prend en compte l'interférence intra- et intermoléculaire et sa forme dépend de la structure moléculaire du matériau inspecté. Pour les matériaux cristallins, elle correspond à des pics discrets dont la position dépend des distances interréticulaires d_{hkl} des plans atomiques et qui est donnée par la loi de Bragg :

$$2d_{hkl}\sin\left(\frac{\theta}{2}\right) = n\lambda$$

Avec n un entier et λ la longueur d'onde de l'onde diffractée. Le transfert de quantité de mouvement est ici égale à $\chi = \frac{1}{2d_{hkl}}$.

Dans le cas de matériaux amorphes, s_i correspond à une fonction continue oscillant autour de un et convergeant vers un. Elle est appelée fonction d'interférence moléculaire. Ses maxima reflètent les distances intra- et intermoléculaires préférentielles du matériau de l'échantillon.

Il existe deux manières de mesurer un signal de diffraction : 1. Par dispersion angulaire (Angular Dispersive X-Ray Diffraction) et 2. par dispersion en énergie (Energy Dispersive X-Ray Diffraction). En ADXRD, un faisceau incident monochromatique est utilisé et le spectre est mesuré en fonction de l'angle de diffraction θ. C'est la méthode classique utilisée en cristallographie. Elle permet d'obtenir une haute résolution de pics de diffraction. Cependant, une source de rayons X monochromatique de haute intensité est difficile à obtenir et si on souhaite mesure le spectre entier en une seule prise une haute résolution spatiale du détecteur est requise. En EDXRD, le spectre est mesuré en fonction de l'énergie à un angle de diffraction fixe. L'emploi d'un détecteur spectrométrique permet l'utilisation d'une source à rayons X polychromatique. Comme la résolution du spectre de diffraction est donnée dans ce cas par la combinaison de la résolution angulaire de la collimation et de la résolution en énergie du détecteur, elle sera moins bonne qu'en ADXRD. Cependant, la méthode par dispersion d'énergie semble particulièrement adaptée au type d'applications visées car elle permet l'utilisation d'un tube à rayons X conventionnel, l'acquisition du spectre entier en une fois et des architectures parallélisées pour l'inspection d'un objet entier en un temps raisonnable. C'est la raison pour laquelle, ce sera la méthode préférée dans ce travail.

L'étude bibliographique de la caractérisation de tissus biologiques en utilisant la diffraction X montre que les signatures de diffraction d'une variété de tissus ont été déterminées. Notamment, la différence entre tissus cancéreux et tissus sains a été analysée. Il s'est avéré que les résultats les plus prometteurs sont obtenus dans la distinction entre tissus mammaires cancéreux et sains. Plusieurs équipes de chercheurs ont montré que les tissus mammaires sains présentent un maximum de diffraction autour de 1,1 nm^{-1} (pic de graisse) alors que les tissus cancéreux ont un maximum de diffraction vers 1,6 nm^{-1} (pic de l'eau). A cause du potentiel de la diffraction X dans la distinction entre tissus mammaires cancéreux et sains, une des applications choisies pour cette thèse est la détection du cancer du sein. La deuxième application visée dans ce travail est la détection de matériaux illicites dans les bagages à main à l'aéroport. Il a été montré que les différents explosifs et drogues ont des signatures de diffraction distinctes et que l'on est capable de les distinguer des matériaux communs dans une valise. En particulier, des liquides inoffensifs, comme l'eau, présentent des signatures distinctes de celle d'explosifs liquides ce qui rend cette technique très intéressante pour le contrôle de bagage à l'aéroport. Morpho Detection a développé une machine de détection d'explosifs basée sur l'EDXRD pour cette application, qui est commercialisée. Une augmentation en sensibilité reste toujours souhaitable. Afin d'augmenter la sensibilité du système d'acquisition, nous proposons dans ce travail une approche multi-angle en EDXRD qui a été évoquée par O'Flynn et al. pour une meilleure sensibilité. L'objectif est de proposer une architecture de système optimisée pour chaque application.

L'optimisation d'un système de mesure nécessite la modélisation du système ainsi que des moyens de caractérisation et de comparaison de différents systèmes d'acquisition. Dans le chapitre 2, un modèle d'un système de mesure en dispersion d'énergie est présenté ainsi que des facteurs de mérite permettant la caractérisation et la comparaison des systèmes d'acquisition. Un système d'EDXRD de base est composé d'une source de rayons X polychromatique, d'une collimation primaire, d'un échantillon, d'une collimation secondaire pour le choix de l'angle de diffraction et d'un détecteur spectrométrique. Le modèle prend en compte ces différentes composantes du système et des phénomènes physiques impactant sur la forme du spectre de diffraction détecté : La forme de la source de rayons X incidents, la résolution angulaire due aux deux collimations, l'absorption dans l'objet inspecté, la diffusion cohérente dans l'objet et la spectrale du détecteur. Selon ce modèle, une mesure de diffraction m à un angle nominatif Θ et une amplitude détectée A est donnée par:

$$m\left(A,\Theta\right)=\sum_{\chi}\mathcal{R}(A,\Theta,\chi)\cdot F(\chi)=\sum_{E_i,\chi}R_d(A,E_i)\;S_{inc}(E_i)\;At(E_i)\;R_c(\chi/E_i,\Theta)\cdot F(\chi)$$

Où

$\mathcal{R}$ est la réponse de système globale.

R_d est la réponse du détecteur spéctrométrique, regroupant les distributions de probabilité pour chaque énergie incidente E_i des photons.

S_{inc} correspond au spectre incident.

At est l'atténuation dans l'échantillon. Ici, l'approximation $\cos\Theta\approx 1$ pour des angles petits est utilisée. L'atténuation est donc donnée par $\exp\left(-\mu\left(E\right)L\right)$. Elle peut être déterminée par une mesure dans la direction de transmission ($\Theta=0°$) avec un détecteur spectrométrique.

R_c prend en compte la distribution angulaire et la variation du volume d'inspection.

F est la signature de diffraction du matériau inspecté égale à $F\left(\chi\right)=\frac{d\sigma_{Th}}{d\Omega}f^2\left(\chi\right)s\left(\chi\right)n$.

Ce modèle nous permettra de calculer la valeur de différents facteurs de mérite : L'efficacité de détection quantique (Detective Quantum Efficiency), le rapport contraste sur bruit (Contrast to Noise Ratio) et les courbes de caractéristiques opérationnelles de réception (Receiver Operating Characteristic). La DQE est un facteur de mérite permettant de décrire les performances d'un système d'imagerie en termes de sensibilité et résolution indépendamment de l'objet imagé. Elle est beaucoup utilisée en imagerie de transmission X (radiographie par exemple) et parfois aussi en imagerie γ. Jusqu'à présent, elle n'a pas été employée pour qualifier des systèmes de diffraction X. En général, son application se limite à la qualification du détecteur. Dans cette thèse, nous avons adapté les calculs de DQE à la diffraction X et nous avons élargi le concept afin de pouvoir qualifier tout le système de détection.

Sous l'hypothèse d'un système linéaire, de processus stationnaires et de bruit photonique (bruit de Poisson), la DQE est donnée par :

$$DQE\left(\nu_\chi\right)=S\cdot\mathrm{MTF}^2\left(\nu_x\right)$$

Avec S la sensibilité du système, MTF le module de la fonction de transfert de modulation et ν_χ la fréquence spatiale selon la direction des x. En EDXRD, on peut considérer un système linéaire et le bruit est bien photonique. Par contre, les processus ne sont pas stationnaires. La DQE en EDXRD dépendra donc de deux variables comme par exemple le transfert de quantité de mouvement χ et sa variable fréquentielle associée ν_χ:

$$DQE\left(\chi,\nu_\chi\right)=\sum_{\{E_d,\theta/\frac{E_d}{hc}\sin\frac{\theta}{2}=\chi\}} S(E_d,\Theta)\cdot \mathrm{MTF}^2(E_d,\Theta,\nu_\chi)$$

La sensibilité du système S est donnée par $S\left(E_d,\Theta\right)=\sum\limits_{\chi}\mathcal{R}(E_d,\Theta,\chi)$ et la MTF par la transformée de Fourier de la réponse du système $\mathrm{MTF}\left(E_d,\Theta,\nu_\chi\right)=\mathscr{F}\left\{\mathcal{R}(E_d,\Theta,\chi)/S\left(E_d,\Theta\right)\right\}$. Ici, l'exemple du transfert de quantité de mouvement a été choisi mais il est aussi possible de calculer une DQE angulaire ou spatiale en EDXRD. Connaissant la réponse du système, il est donc possible de calculer la DQE. A partir de ces calculs, la sensibilité du système peut être déterminée (DQE à la fréquence zéro sommée selon χ) ainsi que la résolution globale du système:

$$\frac{1}{R}\approx\int_{-\infty}^{+\infty}\frac{DQE\left(\nu\right)}{DQE\left(0\right)}d\nu=2\int_{0}^{+\infty}\mathrm{MTF}^2(\nu)d\nu$$

Cependant, la DQE ne donne pas d'information sur la séparabilité de matériaux différents en diffraction X. Pour cela, le CNR a été utilisé. Il donne la séparabilité de deux matériaux A et B pour un système d'imagerie et un nombre de photons donnés. Si on approxime le bruit de Poisson par un bruit gaussien, il est donné par :

$$CNR^2=\sum_i\frac{\left(M_{A,i}-M_{B,i}\right)^2}{\left(M_{A,i}+M_{B,i}\right)}$$

Avec $M_{A/B,i}$ l'espérance des signaux de diffraction du matériau A/B au canal de mesure "i" normalisé par le nombre de photons. Le CNR défini de cette manière correspond à la distance de Mahalanobis entre les distributions des matériaux A et B. Un CNR^2 égal à un correspond à une séparation de 1σ entre les deux distributions. L'inverse du CNR^2 donne le nombre de photons nécessaire pour obtenir une séparation de 1σ entre A et B. Le CNR sera donc utilisé pour calculer le nombre de photons requis pour la séparation souhaitée entre les distributions A et B. Le troisième facteur de mérite, les courbes ROC, donne une information sur le taux de détection pour un taux de fausses positives donné ce qui est une notion très importante aussi bien dans le domaine médical que dans le contrôle de bagage. Une courbe ROC correspond a la représentation graphique de la fraction de vrais positifs en fonction de la fraction de faux positifs. Classiquement, une courbe ROC est obtenue à partir de nombreuses observations (simulations ou mesures) des deux lois de probabilité de A et de B à séparer (e.g. tissus cancéreux et sains) qui sont ensuite attribuées à une des deux classes. Cette méthode, par intégration Monte-Carlo, nécessite un nombre élevé d'observations. Dans ce travail de thèse, une nouvelle méthode alternative analytique est proposée en se basant sur la géométrie d'information. En s'inspirant du théorème de Sanov et en utilisant le théorème de Pythagore généralisé, nous proposons d'approximer les distributions de probabilités de A et de B relatives à la mesure x, par :

$$P\left(\mathbf{x}\left(t\right)|\mathbf{A}\right)=\frac{e^{-D(\mathbf{x}_0(t)||\mathbf{A})}}{\int_t e^{-D(\mathbf{x}_0(t)||\mathbf{A})}dt}$$

Avec $D\left(\mathbf{x}||\mathbf{A}\right)=\sum_{i=1}^{k}x_i\ln\left(\frac{x_i}{A_i}\right)-x_i+A_i$ (divergence de Kullback-Leibler généralisée), x_0 la projection orthogonale au sens de la métrique de Fisher de x sur la géodésique entre B et A, c'est-à-dire la loi la plus proche de l'observation x qui se trouve sur cette géodésique, et t le paramètre de la géodésique. Nous avons montré qu'avec cette approximation, il est suffisant de ne considérer que les points x_0 de la géodésique liant les distributions A et B pour couvrir tout l'espace des mesures et de tracer la courbe ROC correspondante. Il suffit donc de connaître les distributions "théoriques" de A et B pour tracer la courbe ROC recherchée. Il faut noter que l'approximation de Sanov n'est en général valable que lorsque le nombre d'événements est élevé. Cependant, pour les distributions considérées (matériaux amorphes), la convergence est assez rapide. Nous l'avons vérifié par comparaison avec des résultats obtenus par simulations de Monte-Carlo.

Dans la dernière partie du chapitre 2, les performances d'un système d'EDXRD basique ont été étudiées par le biais de calculs de DQE. La comparaison de systèmes mono-angles (2° et 5°) avec un système multi-angle (entre 2° et 5° à un pas de 0,1°) a montré que des acquisitions EDXRD multi-angle permettent d'augmenter la plage de χ accessible et de supprimer l'hypersensibilité a certains valeurs de χ due aux raies caractéristiques de la source de rayons X utilisée. Une petite étude de l'impact de paramètres géométriques, comme l'ouverture angulaire des collimations ou la distance entre échantillon et source ou détecteur, a été réalisée. Elle a permis de conclure qu'il était impossible d'optimiser un système indépendamment de son application.

Le troisième chapitre de cette thèse est dédié à la reconstruction de signatures de diffraction. On souhaite estimer la signature de diffraction F à partir d'une mesure m connaissant la matrice de réponse du système $\mathcal{R}$ liant les deux par le modèle décrit auparavant dans le chapitre 2. L'algorithme proposé s'inscrit dans le cadre du maximum de vraisemblance. Il s'agit d'un algorithme MLEM (Maximum Likelihood Expectation Maximization) prenant en compte le modèle du bruit photonique. L'estimée F_k^{n+1} de F au canal "k" à la n+1ième itération est donnée par :

$$F_k^{n+1}=F_k^n\frac{1}{\sum_{j=1}^{N}R_{jk}}\sum_{j=1}^{N}\left(\frac{m_jR_{jk}}{\sum_{l=1}^{M}R_{jl}F_l^n}\right)$$

Une initialisation positive assure des résultats finaux positifs. Il peut être noté que des problèmes d'instabilité numérique peuvent se présenter lorsque R_{jk} est proche de zéro. Cet algorithme est valable sous deux hypothèses :

- Les émissions de photons dans le canal "k" suivent une loi de Poisson avec espérance F_k (quantité à être estimée) et sont indépendants.
- Les mesures m_j correspondent à des réalisations du processus de Poisson de paramètre λ_j et sont indépendants.

L'hypothèse d'indépendance est bien vérifiée dans le cas de spectres de diffraction de matériaux cristallins ne présentent que quelques pics. Si la signature à reconstruire provient d'un échantillon amorphe, ne semble pas être satisfaite ce qui mène à des erreurs de reconstruction.

Afin de pouvoir évaluer la qualité des résultats de reconstruction, l'erreur relative par rapport au spectre théorique est calculée. Dans le cas des amorphes, cette erreur est déterminé sur tout le spectre, alors que dans le cas des cristallins une erreur relative sur la position des pics et une erreur relative sur l'amplitude relative est déterminée.

La méthode de reconstruction est d'abord validée sur des spectres cristallins simulés afin de connaître précisément la matrice de réponse du système. Des spectres mono-angles (2° et 5°) et multi-angle (entre 2° et 5° à un pas de 0,1°) de 4 cm de sel et de 4 cm de TNT ont été simulés en utilisant le modèle. La comparaison des spectres mono- et multi-angles montre que le nombre de photons détectés est plus important pour une acquisition multi-angle. Cette technique permet donc, en effet, d'augmenter la sensibilité du système. En reconstruction mono-angle, il n'a pas été possible de restaurer tous les pics du sel car la plage de transfert de quantité de mouvement accessible n'était pas assez large. La reconstruction multi-angle a permis de reconstruire presque tous les pics de sel. L'erreur relative sur la position des pics reconstruits est faible (0,7% au maximum) alors que l'erreur relative sur l'amplitude relative est bien plus importante (42% au maximum). Dans le cas du TNT, la reconstruction multi-angle a également permis d'améliorer les résultats de reconstruction en réduisant l'erreur relative sur la position et notamment sur l'amplitude relative restaurée.

Afin de valider l'algorithme de reconstruction sur des données expérimentales, les mêmes spectres de sel ont aussi été acquis expérimentalement. Ces spectres présentent quelques différences par rapport aux spectres simulés. Le nombre de photons détectés à basse énergie est plus important ce qui est dû au modèle simplifié de la réponse du détecteur en simulation. De plus, un pic supplémentaire est apparu dans le spectre à 5° qui correspond au bruit de fond amplifié par les raies caractéristiques de la source. Après reconstruction, ce pic est toujours présent à 5° mais il ne l'est pas en multi-angle grâce à la sensibilité du système plus lisse, déjà observé auparavant avec les calculs de DQE. Les résultats de reconstruction sont similaires à ceux obtenus avec des spectres simulés. Un test de reconstruction sur des spectres amorphes simulés (eau et graisse de porc à 3°) et expérimental (eau à 3,4°) a montré que le manque d'indépendance entre les différents canaux de mesure mène à des oscillations dans le spectre reconstruit. C'est la raison pour laquelle différentes méthodes de régularisation ont été envisagées : L'utilisation d'un dictionnaire amorphe ou mathématique dans l'algorithme de reconstruction et l'utilisation d'un noyau de résolution. Dans le cas d'un dictionnaire amorphe, les éléments du dictionnaire sont des signatures de diffraction de référence de différents matériaux amorphes. Cette méthode a l'avantage qu'il sera en même temps possible d'identifier le matériau inspecté s'il fait partie de la base. Cependant, il n'existe que peu de signatures d'amorphes connues et les résultats sont fortement dépendant des éléments du dictionnaire. C'est pour cela, que l'option d'un dictionnaire mathématique contenant des distributions mathématiques (lorentziennes ou gaussiennes) a aussi été testée. L'utilisation d'un noyau de résolution consiste en une étape de filtrage par un filtre gaussien de l'estimée après chaque itération. La largeur du filtre peut être adaptée au système utilisé en utilisant la fonction d'étalement du point (Point Spread Function) du système.

Ces différentes méthodes ont été employées pour la reconstruction des différents spectres amorphes. Pour le spectre de graisse de porc simulé, toutes les méthodes ont amélioré l'erreur relative de la signature reconstruite mais le meilleur résultat (erreur relative de 3,18%) est obtenu avec un dictionnaire mathématique de lorentziennes. Dans le cas du spectre d'eau simulé, ces méthodes n'ont pas toujours apporté une amélioration. Le meilleur résultat correspond à celui avec le noyau de résolution (erreur relative de 1,15%). Les résultats de reconstruction du spectre d'eau expérimental ne sont en aucun cas très satisfaisants. La meilleure erreur relative obtenue est toujours égale à 50,75%. Ceci est probablement dû à un manque de précision dans la réponse du système utilisée (réponse des collimations simulée, réponse du détecteur simplifiée, absorption estimée à partir de mesures en transmission).

La classification de tissus mammaires à l'aide de la diffraction de rayons X est traité au chapitre 5. Dans le cadre de cette thèse, nous nous sommes concentrés sur la distinction entre tissus fibroglandulaires denses mais sains et tissus cancéreux. En effet, il s'agit du cas le plus difficile en mammographie classique qui mène souvent à des résultats douteux nécessitant une biopsie. Nous proposons d'utiliser la diffraction X en deuxième niveau de contrôle après la mammographie conventionnelle. L'objectif de cette partie est d'optimiser un système de diffraction X à cette fin et d'étudier si cet examen serait possible avec une dose délivrée raisonnable (ne pas dépasser les 1 à 3 mGy délivrés en mammographie conventionnelle). Afin de pouvoir imaginer et dimensionner un tel système, différentes contraintes ont été fixées. Le sein est comprimé comme en mammographie classique et pour l'étude une épaisseur de 5 cm est considérée. Pour limiter la dose délivrée au patient, le spectre incident est filtré de manière à éliminer tous les photons en dessous de 20 keV qui seraient quasiment entièrement absorbés. Une limite supérieure de 100 keV est suggérée car à hautes énergies la part de photons diffusés de manière incohérent devient trop importante par rapport à la part de photons diffusés sans perte d'énergie. La gamme de valeurs de χ à couvrir est entre 1 nm^{-1} et 2,5 nm^{-1} et la résolution en χ requise est autour de 0,2 nm^{-1} (il faut pouvoir séparer le pic de graisse autour de 1,1 nm^{-1} et le pic de l'eau autour de 1,6 nm^{-1}). Comme la position dans le plan (x,y) de la région douteuse est connu de la mammographie, le système de diffraction doit pouvoir viser cet endroit. La position en profondeur n'étant pas connu, il faut imager toute l'épaisseur du sein. A cette fin, une architecture de système composée d'un faisceau pinceau incident très fin (autour de 1 mm^2), d'une collimation secondaire convergente et d'un détecteur spectrométrique est proposée. Deux types de collimations convergentes sont considérés :

- Une collimation convergente en un point (monofocal) + scan mécanique en profondeur
- Une collimation convergente en (x,y) sur toute l'épaisseur du sein

Dans les deux cas, un scan sur une petite surface en (x,y) est requis. Comme les systèmes de collimation sont coniques, il s'agit automatiquement de systèmes d'EDXRD multi-angles.

Afin de pouvoir dimensionner les paramètres du système, et notamment de la collimation secondaire, pour la détection du cancer du sein, il faut pouvoir évaluer les performances du système en fonction des paramètres. Pour cela, des calculs analytiques de DQE pour la collimation secondaire ont été développés courant cette thèse. Ces calculs sont basés sur le fait qu'une collimation peut être considérée comme un ensemble de couples pixel-trou. Pour chaque couple, il est possible de calculer sa résolution et donc sa MTF$_{hp}$ ainsi que sa sensibilité S_{hp}, ce qui mène à la $DQE_{hp}(\nu) = S_{hp} \cdot \mathrm{MTF}_{hp}^2(\nu)$. Dans le cas d'un système sans multiplexage, c'est-à-dire chaque pixel ne reçoit du signal qu'à travers un seul trou, une DQE globale peut être calculée en sommant sur les contributions des couples pixel-trou :

$$DQE_{coll}\left(\nu\right) = \sum_{pixels} DQE_{hp}\left(\nu\right)$$

Ces calculs de DQE, ont été établis en spatial dans le sens de l'épaisseur du sein (axe des z), en angulaire et en transfert de quantité de mouvement.

Plusieurs types de collimation comme une ligne de trous, une collimation en éventail ou conique peuvent être considérés. Dans ce travail, la collimation conique a été retenue car elle permet de respecter la symétrie intrinsèque ce la diffraction et de profiter ainsi, d'un maximum de sensibilité.

Une étude de l'impact des différents paramètres du système sur la sensibilité globale, la distribution de sensibilité, la résolution et la plage angulaire accessible a permis d'établir une stratégie pour l'optimisation de la collimation secondaire. Connaissant la plage de χ requise et plage en énergie du spectre incident (fixée pour limiter la dose inutile), la plage angulaire peut être déterminée. La hauteur de la collimation est fixée de manière à bien couvrir cette plage angulaire et la taille des trous de collimation est réglée afin d'avoir la meilleure sensibilité possible tout en respectant la résolution en χ requise (0,2 nm^{-1}). Cette stratégie a donné lieu à deux systèmes de collimation optimisés : un monofocal et un multifocal. Leurs performances en termes de sensibilité (8%) et de résolution (entre 9 et 10 mm dans la direction de la profondeur de l'échantillon, autour de 0,2° en résolution angulaire et entre 0,03 et 0,15 nm^{-1} en χ) sont très similaires. Seule la distribution de la sensibilité change. Les angles couverts se situent entre 0 et 10°. La résolution en profondeur semble faible mais pour un système de diffraction, elle est tout à fait raisonnable sachant que de nombreux systèmes de diffraction n'offrent pas de résolution dans cette direction.

La dernière partie du chapitre 4 est dédiée à une étude de simulation pour évaluer la capacité des deux systèmes optimisés de détecter une petite tumeur de 4 mm de diamètre. Les deux systèmes ont été simulés en Monte-Carlo associés à un fantôme de sein composé de tissus adipeux et fibroglandulaire avec une petite tumeur au centre. Toutes les interactions dans l'objet, la collimation et le détecteur ont été prises en compte. La collimation est simulée en fer. Pour la simulation du détecteur, nous avons considéré un détecteur spectrométrique en CdZnTe de 5 mm d'épaisseur avec un pas de pixel de 2,5 mm (sous-pixels de 1 mm). Sa résolution moyenne en énergie était autour de 2,5% à 122 keV. L'impact de plusieurs paramètres sur la détection de la tumeur a été étudié : la réponse du détecteur, l'énergie maximale du spectre incident (de 40 à 150 keV), l'épaisseur de la couche fibroglandulaire (correspond à une densité plus ou moins élevée du sein) et la position de la tumeur. Dans chaque cas, le nombre de photons incidents nécessaire pour avoir une séparation de 3σ (séparation quasi parfaite en termes de courbes ROC) entre un fantôme avec et sans tumeur a été déterminée et ensuite, transformé en dose moyenne incidente requise. Du fait que le détecteur n'est pas parfait, le nombre de photon incident requis est augmenté d'un facteur 1,5. L'étude de l'impact de l'énergie maximale du spectre incident sur la dose nécessaire a montré que la dose requise pour la collimation monofocale est toujours au-dessus de celle pour la collimation multifocale sauf pour une énergie maximale de 40 keV. C'est pour cette raison que la suite de cette étude de simulation n'a été réalisée que pour la collimation multifocale.

La dose requise est faible (entre 0,2 et 0,3 mGy pour la collimation multifocale) pour chaque spectre incident testé. Cependant, un optimum semble être situé vers 60 keV. En ce qui concerne l'épaisseur variable de la couche fibroglandulaire, elle n'a que très peu d'impact sur la dose requise. La diffraction X semble être une méthode de détection adéquate même pour des seins denses qui posent de gros problèmes en mammographie classique. La variation de la position de la tumeur a montré que le système multifocal est capable de détecter la petite tumeur avec une faible dose (en dessous de 0,5 mGy) sur presque toute l'épaisseur du sein. Lorsque l'on se rapproche de la limite de la zone sensible, la dose requise augmente de manière très importante. Il faut donc veiller à bien positionner la collimation afin de couvrir toute l'épaisseur du sein.

Afin de tester la détection de tumeur dans une image, un scan dans la direction de l'axe des x du fantôme a été simulé. La reconstruction de cette tranche de fantôme est réalisée en utilisant l'algorithme MLEM présenté auparavant associé à un dictionnaire avec trois éléments (tissus adipeux, tissus fibroglandulaire et carcinome). Cette technique permet de situer les différents tissus dans l'image. La tumeur n'est reconstruite que lorsqu'elle se trouvait réellement dans le scan simulé. Cela indique qu'il ne devrait pas y avoir de fausse alarme. La tumeur reconstruite est étirée dans la direction de la profondeur ce qui reflète bien la résolution limitée du système.

Toute l'étude précédente a été réalisée avec un système de collimation n'autorisant pas le multiplexage. Cependant, quelques équipes s'intéressent à l'utilisation de systèmes multiplexés dans ce domaine d'application. Le multiplexage, c'est-à-dire la réception de photons par un pixel à travers plusieurs trous de collimation, permet d'augmenter la sensibilité globale du système mais dégrade par mélange d'information la résolution. Pour étudier l'intérêt du multiplexage dans le cas du type de système proposé pour la détection d'une petite tumeur dans le sein, nous avons simulé le système multifocal avec un multiplexage limité, i.e. chaque part de détecteur recoit de photons à travers son trou attribué et au maximum la moitié de la part du détecteur recoit du signal à travers le trou voisin. Le taux de multiplexage indique combien de pourcent de la part de détecteur "voient" un deuxième trou. Un taux de multiplexage de 50% signifie que la moitié de la part de détecteur recoit du rayonnement à travers deux trous. Plusieurs taux de multiplexage ont été testés. Plus il était élevé, plus la sensibilité du système était importante. Cependant, la dose requise augmentait en même temps. Le multiplexage semble donc sans intérêt dans ce cas précis.

Dans le dernier chapitre de cette thèse, nous nous sommes intéressés à l'intérêt que pourrait apporter une collimation multiplexée dans le cas du contrôle de bagage à mains. Les dimensions dans cette application sont très différentes. L'épaisseur d'une petite valise est autour de 50 cm et les objets recherchés sont également plus grands que dans le cas de l'imagerie du sein. Une perte de résolution spatiale serait probablement plus acceptable.

En contrôle de bagage les matériaux à détecter sont très variables. Ils peuvent être sous forme amorphe (liquide par exemple) mais aussi sous forme cristalline. Les pics de Bragg matériaux communs comme du sel ou du carbone, qui ont des structures cristallines relativement simples, peuvent être situés à des valeurs de transfert de quantité de mouvement au- dessus de 2,5 nm^{-1}. Cependant, les explosifs présentent des structures cristallines bien plus complexes et leurs pics de Bragg se trouvent à des valeurs de χ faibles. Les signatures de matériaux amorphes présentent toutes leur maximum à χ faibles. La plage de transfert de quantité de mouvement considérée peut donc être la même qu'en imagerie du sein (entre 1 et 2,5 nm^{-1}). Une résolution entre 0,1 et 0,2 nm^{-1} devrait être suffisante pour résoudre les pics principaux des matériaux cristallins et pour séparer les différents matériaux. Comme une valise est plus épaisse et plus dense qu'un sein, il faut considérer une tension du tube plus haute (entre 150 et 200 keV) pour avoir assez de photons au-dessus de 100 keV qui ne seront pas absorbés. Dans le cas du contrôle de bagage, le facteur limitant essentiel est le temps et donc, la tension du tube qui devrait être entre 5 et 10 keV. Un système le plus sensible possible pour intercepter un maximum de photons en peu de temps est donc d'un grand intérêt.

Nous souhaitons proposer un système (multifocal) similaire à celui en détection du cancer du sein pour le contrôle de bagage. Ce système a une bonne sensibilité grâce à son aspect multi-angle et conique. En ajoutant du multiplexage, nous souhaitons augmenter sa sensibilité d'avantage. Dans un système de contrôle final, il faudrait utiliser plusieurs de ces modules juxtaposés afin de pouvoir imager toute une valise sans devoir réaliser des scans coûteux en temps.

Dans cette thèse, une étude préliminaire concernant l'impact du taux de multiplexage sur les performances du système ainsi que l'impact sur la distribution de sensibilité de la distribution de la surface de détection et des distances focales associées aux différents trous de la collimation a été réalisée pour un système de référence avec des dimensions censées en contrôle de bagage. Pour cela, des calculs analytiques de DQE pour un système multiplexé ont été établis. Il faut noter que les contributions de DQE d'un pixel communicant avec deux trous ne peuvent pas être sommées. Il y a un terme d'interférence qui apparait. En ce qui concerne la sensibilité, les deux contributions peuvent être sommées pour former la sensibilité attribuée à un pixel. Grâce à cet outil, il sera possible d'optimiser les différents paramètres de système pour l'application du contrôle de bagage. L'étude préliminaire a bien confirmé que la sensibilité globale du système augmente de manière continue avec le taux de multiplexage. Des taux de multiplexage entre 0 et 100% ont été testés. En regardant la distribution de sensibilité dans l'objet et sur le détecteur il peut être clairement observé qu'une même zone de détecteur couvre plusieurs zones en profondeur dans l'objet avec un système multiplexé. Les différentes résolutions du système sont dégradées comme attendu mais la résolution critique semble être la résolution spatiale. La distribution des distances focales des différents trous de collimation change la distribution de sensibilité dans l'échantillon. En choisissant une distribution non linéaire entre la distance focale minimale et maximale, il est possible d'obtenir un profil de sensibilité plus homogène à travers tout l'échantillon. La distribution de la surface de détection a également un impact sur le profil de sensibilité dans la valise.

L'outil de calcul analytique de DQE et cette étude préliminaire devraient aider de développer une stratégie d'optimisation de système pour le contrôle de bagage et de dimensionner un tel système. Pour conclure, la diffraction des rayons X présente un grand potentiel dans la caractérisation et l'identification de matériaux grâce aux informations de structure moléculaire caractéristique du matériau inspecté, qu'elle fournit. Les études bibliographiques ont montré que de nombreuses applications comme la caractérisation de tissus biologiques, la détection de matériaux illicites et le contrôle non-destructif ont été envisagées. Ce travail de thèse se concentre sur la détection du cancer du sein et le contrôle de bagage à l'aéroport. Son objectif était d'optimiser la chaîne de caractérisation de matériaux en diffraction en termes de système d'acquisition et de traitement des données de diffraction.

Dans un premier temps, des outils de caractérisation de système en diffraction X ont été développés. Le concept de DQE a été élargi à la caractérisation de tout le système d'acquisition et adapté à la diffraction. Cet outil permet d'évaluer les performances du système d'acquisition indépendamment de son application. Une première étude des performances d'un système d'EDXRD a montré qu'une approche multi-angle est intéressante puisqu'elle permet d'augmenter la plage de transfert de quantité de mouvement accessible, de lisser la sensibilité en fonction de χ et d'augmenter le nombre de photons détectés, tout en gardant une bonne résolution. Pour déterminer le nombre de photons nécessaire pour obtenir une séparation fixée entre de matériaux A et B avec un système donné, des calculs de CNR ont été effectués. L'information sur le taux de détection et le taux de fausses alarmes est extraite de courbes ROC. Afin de faciliter la détermination des courbes ROC des systèmes différents, une méthode analytique a été développée courant cette thèse.

L'optimisation du traitement des données de diffraction s'est concentrée sur la reconstruction des signatures de diffraction à partir de spectres mesurés, dans ce travail. Un algorithme MLEM a été testé sur des spectres de diffraction simulés est mesurés. Les résultats obtenus avec des spectres cristallins sont très satisfaisant et l'intérêt d'une approche multi-angle a pu être confirmé. Pour la reconstruction de spectres de diffraction amorphes, cet algorithme ne semble pas être adapté car des hypothèses sous-jacentes d'indépendance ne sont pas valables. Des méthodes de régularisation (dictionnaire, noyau de résolution) ont alors été testées sur les mêmes données. Le meilleur résultat sur des données expérimentales est obtenu avec un dictionnaire mathématique de distributions lorentziennes. Cependant, l'erreur relative reste importante. Dans un futur travail, il serait intéressant de développer une méthode de reconstruction qui soit adaptée aussi bien aux spectres cristallins qu'aux spectres amorphes. Dans le contrôle de bagage, par exemple, on risque de trouver ces deux types de matériaux dans la même valise.

Deux systèmes de collimation optimisés (monofocal et multifocal) pour la détection du cancer du sein ont été déterminés à l'aide de calculs de DQE analytiques. Ces calculs ont été développés dans le cadre de cette thèse et permettent d'évaluer les performances d'un système de collimation en termes de sensibilité et résolution en fonction des différents paramètres du système. Le pouvoir de détection d'une petite tumeur de ces deux systèmes a été testé dans une étude de simulation réaliste du tout le système associé à un fantôme de sein. Il en résultait que le système monofocal nécessitant un scan en profondeur était moins performant que le système multifocal. Des variations de la densité du sein ont montré que la diffraction X est une méthode qui est aussi adaptée aux seins plus denses puisque la dose nécessaire à la détection de la tumeur restait faible. En deuxième niveau de contrôle, elle pourra aider à réduire le nombre de biopsies superflues. Dans une prochaine étape, il faudrait confirmer expérimentalement ces résultats prometteurs en simulation. Il faudrait aussi étudier l'impact de la variation de la signature de diffraction des différents tissus mammaires qui n'a pas été prise en compte jusqu'à présent.

A la fin de cette thèse, une étude préliminaire de l'intérêt d'utiliser un système de collimation multifocal et multiplexé en contrôle de bagage a été réalisée. Pour ce faire, des calculs analytiques de DQE avec multiplexage ont été établis. Grâce à cet outil et l'étude de l'impact des différents paramètres et du taux de multiplexage, il devrait être possible dans le futur travail de développer une stratégie d'optimisation et de déterminer les paramètres de système les plus adéquats. Ensuite, une étude similaire à celle en mammographie pourrait être réalisée. Il est aussi important de comparer ce système au système existant de Morpho Detection.

Appendix A

Link between CNR and DQE

In the case of very close objects A and B, it is possible to link CNR calculations in section II.2.2.1 to DQE calculations in section II.2.1.2.

If the objects A and B are very similar, i.e. $A = B + \delta$, then $M_A + M_B$ and $M_A - M_B$ can be approximated by:

$$M_A + M_B = \mathcal{R}\,(A + B) \approx 2\mathcal{R}B = 2\mathcal{R}\mathbb{1} \cdot N \tag{A.0.1}$$

and

$$M_A - M_B = \mathcal{R}\,(A - B) \approx \mathcal{R}\delta \tag{A.0.2}$$

where $\mathcal{R}$ is the system response matrix, $\mathbb{1}$ the identity matrix and N the number of events in each channel. The decomposition of B in $\mathbb{1} \cdot N$ corresponds to the assumption of a homogeneous object.

The squared CNR (Eq. II.2.18) can be written in matrix format and using previous approximations, it becomes:

$$CNR^2 = \frac{(\mathcal{R}\delta)^2}{2\mathcal{R}\mathbb{1} \cdot N} = \delta \frac{\mathcal{R}^t\mathcal{R}}{2N \cdot S}\delta \tag{A.0.3}$$

where $S = \mathcal{R}\mathbb{1}$ is the system sensitivity. We recognize the DQE $= \frac{\mathcal{R}^t\mathcal{R}}{S}$. In the case of similar objects, the CNR is obtained by projection of the DQE on their difference δ.

Appendix B

Determination of the septa using hole position

The previous optimization strategy allowed to determine the position of the different holes. However, in order to obtain a performing collimation system, it is necessary to define the septa which separate the different holes and avoid multiplexing.

For simulation a zero septa thickness was considered at detector level. Hence, septa points are situated at the separation between two detector parts associated to two different holes. Figure B.1 shows an illustration of the principle for the case of two holes. The septum's point is in I. The delimitation of the septum at sample level is given by R_{int} and R_{ext}:

$$\begin{aligned} R_{int} &= c_1 + \frac{h}{2} \\ R_{ext} &= c_2 - \frac{h}{2} \end{aligned} \tag{B.0.1}$$

In practice, a collimation with zero septum thickness is not achievable. Some tests showed that it wass possible to cut the collimation height to reasonable height T (at the half of H for instance) without having to much cross-talk. The inner and the outer delimitation T_{int} and T_{ext} of the septa at the lower bound of cut collimation (equivalent to R_{int} and R_{ext} at the upper bound) are given by:

$$\begin{aligned} T_{int} &= \left(c_1 + \frac{h}{2}\right) \cdot \left(1 - \frac{T}{H}\right) + \frac{I \cdot T}{H} \\ T_{int} &= \left(c_2 - \frac{h}{2}\right) \cdot \left(1 - \frac{T}{H}\right) + \frac{I \cdot T}{H} \end{aligned} \tag{B.0.2}$$

Another possibility would be to fix a minimum septum thickness at detector level (Fig. B.2). In this case, the septum limitations at detector level are calculated by:

$$\begin{aligned} I_{int} &= I - \frac{s}{2} \\ I_{ext} &= I + \frac{s}{2} \end{aligned} \tag{B.0.3}$$

Though, in this case a part of the detector would be covered by the collimation and not used to detect signal. This should be avoided as detector surface is expensive.

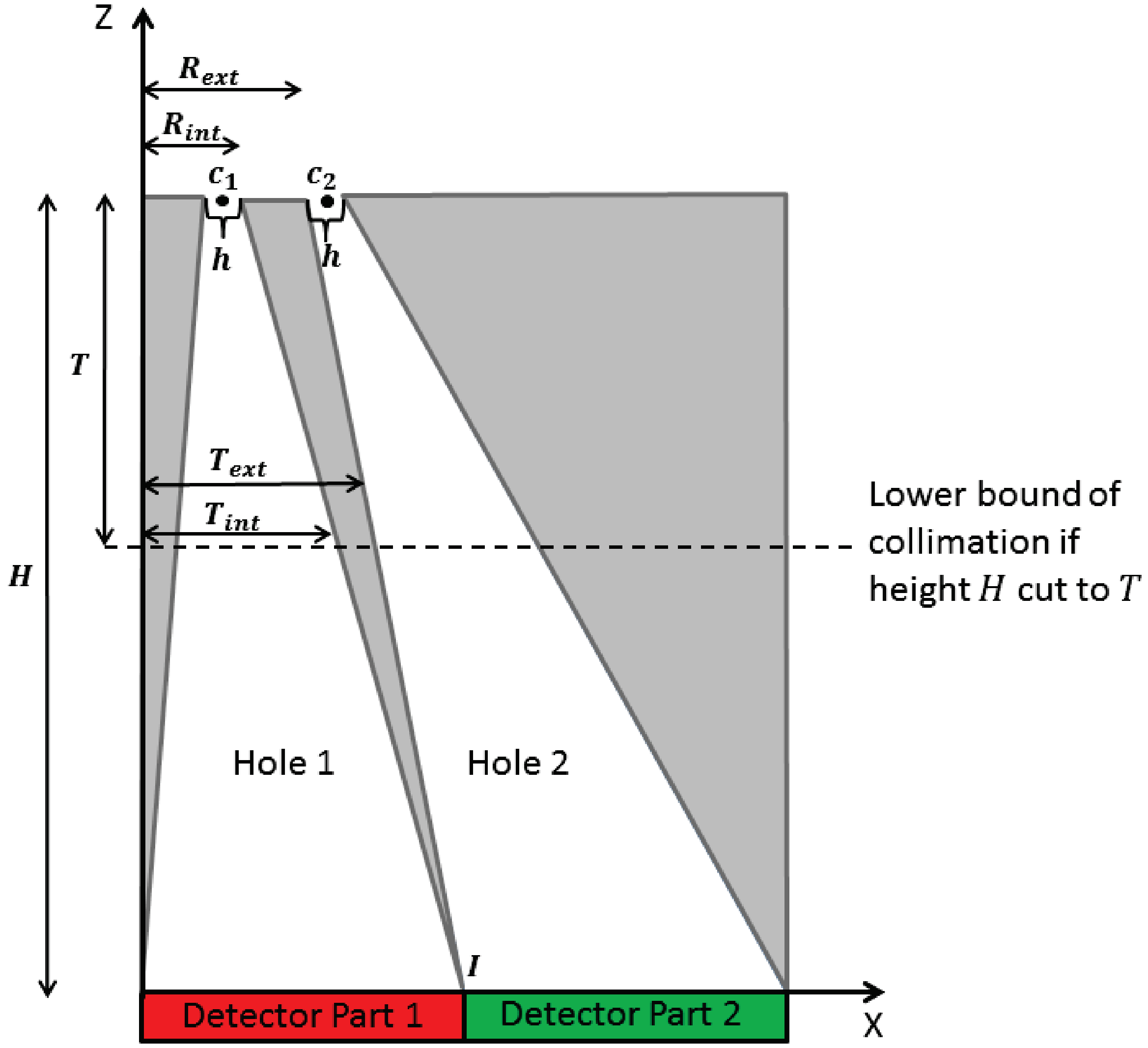

Figure B.1: Illustration of the calculation of a septum between two holes for the case of zero thickness at detector level and truncation T.

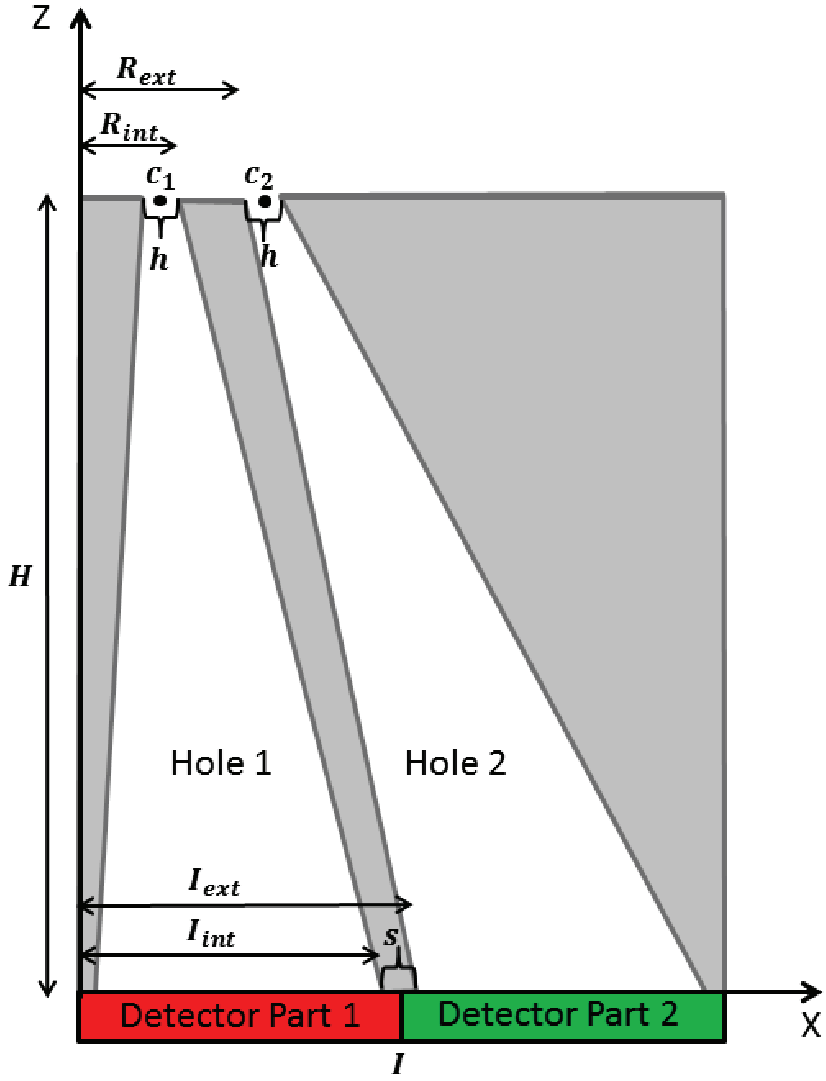

Figure B.2: Illustration of the calculation of a septum between two holes if a minimum thickness is fixed at detector level.

Appendix C

Simulation strategy and realized simulations

C.1 Simulation approach for XRD spectra

To limit simulation time and variance, diffraction spectra were simulated in several steps.
Firstly, three-dimensional XRD spectra with the number of detected photons, N_d, expressed as a function of E_i, E_d and R_d were simulated in a way to have a similar photon number in each detection channel. E_i corresponds to the incident photon energy and E_d to the photon energy incident on the detector after interacting with the collimation system and the sample. R_d is the position of the incident photon on the detector. These three-dimensional diffraction spectra do not take the detector response into account.

In practice, Monte-Carlo simulations without variance reduction were performed. Photons were launched at a given energy until a certain number of photons had been detected in the diffraction spectrum for this specific incident energy, or until the chosen limit of photons to launch was reached. This process was repeated for energies between 1 and 150 keV. For each incident energy, the number of photons launched, N_i, is listed. This makes up a non realistic relatively homogeneous incident spectrum, which depends on the sample. Figure C.1 shows an example of such an incident spectrum of launched photons for the breast phantom with 30 mm fibroglandular tissue and a carcinoma nodule in the center. It has a maximum (about 10^8 photons) at low energies. In fact, for photon energies below 20 keV photoelectric absorption is predominant whereas Rayleigh scattering is unlikely, and therefore the fixed maximum number of photons had to be launched at these energies. At medium energies, Rayleigh scattering probability is the highest relative to other interaction types (even though Compton scattering has higher probability) and therefore, less incident photons had to be launched to detect the wished diffraction signal. This explains the minimum at medium energies. At higher energies, Rayleigh scattering becomes more and more unlikely compared to Compton scattering. Hence, the spectrum of launched incident photons increases.

The total number of launched photons is about 10^{10} photons, whereas the number of detected photons ins only about 10^7 photons.

These simulations were used to calculate the probability that a photon with incident energy E_i would be incident on the detector at energy E_d and position R_d:

$$P\left(E_d, R_d | E_i\right) = \frac{N_d\left(E_i, E_d, R_d\right)}{N_i\left(E_i\right)} \tag{C.1.1}$$

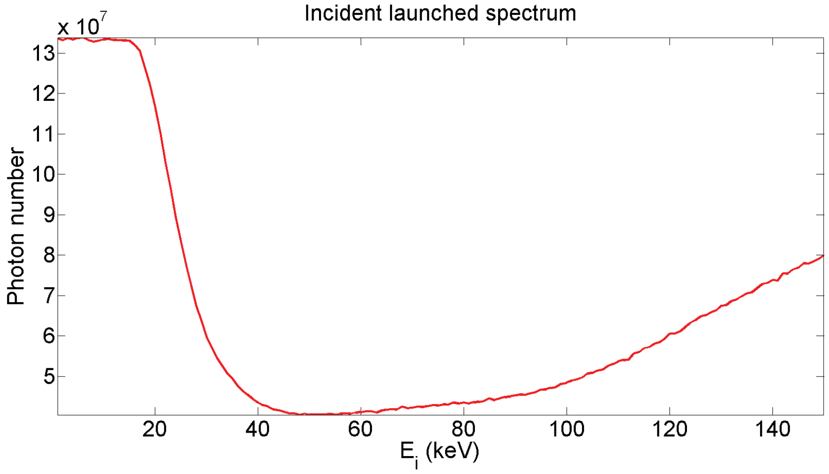

Figure C.1: Example of incident spectrum of launched photons.

Thus, we can take the shape of a realistic incident spectrum into account and calculate the probability of detection for a given incident spectrum:

$$P\left(E_d, R_d\right) = \int S\left(E_i\right) \cdot P\left(E_d, R_d | E_i\right) dE_i \tag{C.1.2}$$

where S corresponds to realistic incident X-ray spectrum which was normalized to unit.
The spectral detector resolution can be incorporated into the simulation by multiplying by the DRM corresponding to the probability $P\left(A|E_d\right)$ of detecting a given amplitude A knowing the incident photon energy E_d. In fact, the DRM acts like a low-pass filter and can be used to reduce variance in the final normalized diffraction spectrum:

$$P\left(A, R_d\right) = \int P\left(E_d, R_d\right) \cdot P\left(A|E_d\right) dE_d \tag{C.1.3}$$

In fact, this normalized XRD spectrum corresponds to the probability of detection per incident photon with amplitude A and at R_d.

A summary of the different simulation steps can be seen in figure C.2.

Different detected photon numbers can be taken into account by multiplying this normalized XRD spectrum by the desired number of photons.
This simulation technique in several steps allows to test any incident spectrum without the need to resimulate the whole system. Moreover, application of the DRM after simulation permits to filter the simulated spectra with a filter that has a physical sens and to avoid fortuitous separation between phantom with and without tumor. Otherwise without application of a filter the variance of simulated spectra would be too high (with a reasonable simulation time), which lead to strange results. For example, first, we found that the number of required photons to detect cancer decreased if a realistic detector response was take into account instead of considering an ideal detector. This was due to the fact that in this case, the variance of simulated spectra increased the difference between spectra with and without tumor. For determination of the required photon number, the knowledge of the "theoretical" spectrum obtained with our system without noise would be needed. Though, it is not known and has to be simulated (which implies always a remaining variance).

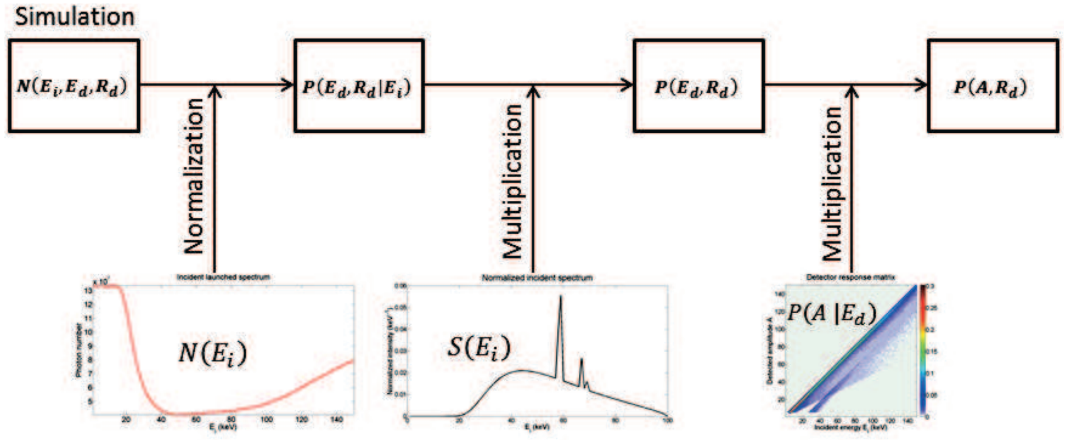

Figure C.2: Illustration of the different steps to simulate an XRD spectrum of the breast phantom.

C.2 Accelerated simulation of XRD scan slice

The simulation of a diffraction spectrum of the breast phantom for one x-position is quite long. An x-scan with 1 mm step would be very long. That is why an alternative simulation technique was employed to realize a scan slice of the phantom. This technique is based on the use of XRD spectra of 50 mm of pure tissues (adipose tissue, fibroglandular tissue and carcinoma) and multiplication of these pure tissue XRD spectra by a mask containing information about the spatial distribution of the different tissue types.
First normalized XRD of 50 mm of the three pure tissue types were simulated as described in the previous section (Eq. C.1.3). In fact, these spectra correspond to the system response of the three pure tissues. As for the simulation of the phantom, it is necessary to know the system response for different positions on the Z-axis, the number of photons was saved for each Z in the sample. Hence, the normalized pure tissue diffraction spectra correspond to the detection probability per incident photon $P\left(A, R_d, Z, i\right)$ with amplitude A, at R_d and coming from Z. These three spectra are gathered in one matrix, which will be called global response matrix $Rep\left(A, R_d, Z, i\right)$, where i corresponds to the index of the different tissues.

To generate a scan slice with a given incident photon number, the matrix $Resp$ is multiplied by this number. Then, it is multiplied by the phantom mask t defined by its coefficients in the basis $B = \{i, Z, x\}$, which are either equal to zero or to one as there is no tissue mixing in the considered breast phantoms. Hence, the simulated scan measure m is given by:

$$m\left(A, R_d, x\right) = \sum_{Z,i} Resp\left(A, R_d, Z, i\right) \cdot t\left(Z, i, x\right) \tag{C.2.1}$$

Figure C.3 shows the phantom mask and the pure tissue spectra for a given amplitude A. Multiplication of both of them leads to the measure m at the given amplitude.

Finally, Poisson noise is added in order to obtain a realistic spectrum.

Scans were simulated with and without tumor for 30 mm fibroglandular thickness and 60 keV and 100 keV incident spectra.

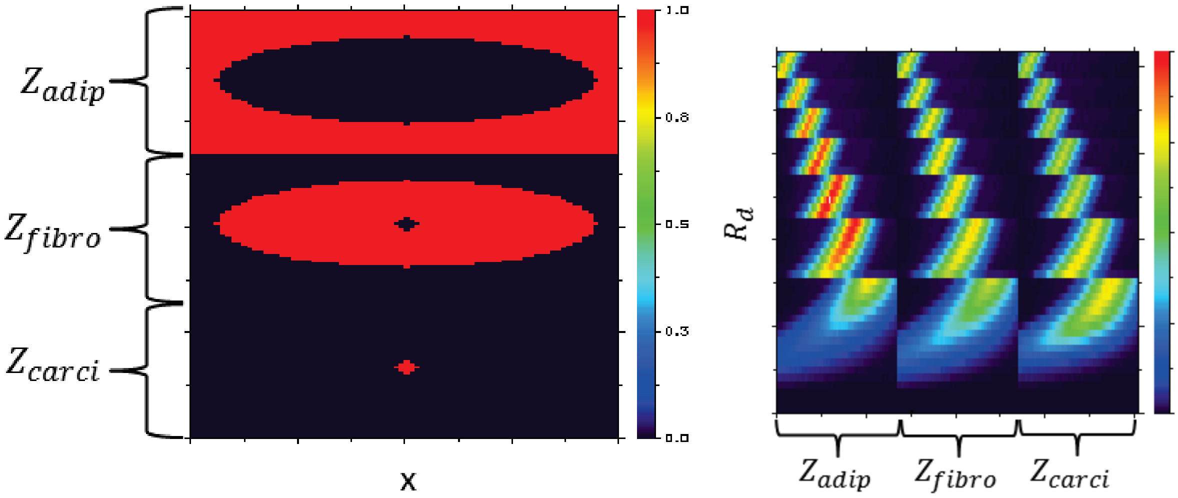

(a) *Phantom mask.*

(b) *Example of pure tissue spectra for a given amplitude* A.

Figure C.3: Illustration of the simulation strategy to simulate an x-scan slice.

List of personal work

This thesis work gave rise to the following publications:

Scientific article

F. Marticke, G. Montémont, C. Paulus, O. Michel, J. I. Mars and L. Verger (2016). *Simulation study of an X-ray diffraction system for breast tumor detection.* Submitted to "*Nuclear Instruments & Methods in Physics Research* ". (under revision)

Patent

F. Marticke, G. Montémont, C. Paulus. *Collimateur pour la spectrométrie de diffraction X, dispositif associé et son utilisation.* National reference FR 15 60443 (awaiting for approval).

Conferences

F. Marticke, C. Paulus, G. Montémont, O. Michel, J. I. Mars and L. Verger (2014). *Multi-angle reconstruction of energy dispersive X-ray diffraction spectra.* In *WHISPERS IEEE.*

F. Marticke, G. Montémont, C. Paulus, O. Michel, J. I. Mars and L. Verger (2015). *Calcul analytique de courbes COR en imagerie de diffraction X.* In *Gretsi* 2015, Lyon, 25ème édition.

F. Marticke, G. Montémont, C. Paulus, J. I. Mars, O. Michel and L. Verger (2015). *Energy dispersive X-ray diffraction system as a promising virtual biopsy.* In 2015 *IEEE Nuclear Science Symposium and Medical Imaging Conference* (NSS/MIC).

Bibliography

[A. P. Dempster, 1977] A. P. Dempster, N. M. Laird, D. B. R. (1977). Maximum likelihood from incomplete data via the em algorithm. *Journal of the Royal Statistical Society. Series B (Methodological)*, **39**:1–38.

[Ables, 1974] Ables, J. G. (1974). Maximum entropy spectral analysis. *Astronomy and Astrophysics Supplement*, **15**:383.

[Ali Chaparian, 2012] Ali Chaparian, M. A. O. (2012). Introducing an optimized method for obtaining x-ray diffraction patterns of biological tissues. *Iranian Journal of Medical Sciences*, **8**:9–17.

[Amari, 2010] Amari, S.-I. (2010). Information geometry in optimization, machine learning and statistical inference. *Front. Electr. Electron. Eng. China*, **5**:241–260.

[ARPANSA, 2013] ARPANSA (2013). Radiation protection - x-rays. www.arpansa.gov.au/radiationprotection/basics/xrays.cfm. Australian Radiation Protection and Nuclear Safety Agency (ARPANSA).

[Barbes, 2016] Barbes, D. (2016). *Nouveaux syst èmes d'imagerie médicale exploitant la diffraction X en dispersion d'énergie à l'aide de détecteurs spectrométriques CdZnTe.* PhD thesis, Université Grenoble Alpes.

[Barrett, 1990] Barrett, H. (1990). Objective assessment of image quality: effects of quantum noise and object variability. *Journal of the Optical Society of America. A, Optics and image science*, **7**:1266–1278.

[Barrett *et al.*, 1995] Barrett, H., Denny, J., Wagner, R., and Myers, K. (1995). Objective assessment of image quality. II. fisher information, fourier crosstalk, and figures of merit for task performance. *Journal of the Optical Society of America. A, Optics and image science*, **12**:834–852.

[Barrett and Myers, 2004] Barrett, H. H. and Myers, K. J. (2004). *Foundations of Image Science.* John Wiley & Sons, Inc., Hoboken, New Jersey.

[Beevor *et al.*, 1995] Beevor, S., Sander, J., Raitt, I., Burrows, J., and Mann, K. (1995). Non-invasive inspection of baggage using coherent x-ray scattering. In *Defence Research Agency, UK*, pages 301–305.

[Beldjoudi *et al.*, 2012] Beldjoudi, G., Rebuffel, V., Verger, L., Kaftandjian, V., and Rinkel, J. (2012). An optimised method for material identification using a photon counting detector. *Nuclear Instruments and Methods in Physics Research Section A: Accelerators, Spectrometers, Detectors and Associated Equipment*, **663**:26–36.

[Benoit, 2013] Benoit, D. (2013). *Design, reconstruction and evaluation of multi-focal collimation in single photon emission computed tomography for small-animal imaging.* PhD thesis, Université Paris Sud - Paris XI.

[Bohndiek *et al.*, 2008] Bohndiek, S. E., Cook, E. J., Arvanitis, C. D., Olivo, A., Royle, G. J., Clark, A. T., Prydderch, M. L., Turchetta, R., and Speller, R. D. (2008). A CMOS active pixel sensor system for laboratory- based x-ray diffraction studies of biological tissue. *Physics in Medicine and Biology*, **53**:655–672.

[Bohndiek *et al.*, 2009] Bohndiek, S. E., Royle, G. J., and Speller, R. D. (2009). An active pixel sensor x-ray diffraction (APXRD) system for breast cancer diagnosis. *Physics in Medicine and Biology*, **54**:3513–3527.

[Brambilla *et al.*, 2009] Brambilla, A., Boudou, C., Ouvrier-Buffet, P., Mougel, F., Gonon, G., Rinkel, J., and Verger, L. (2009). Spectrometric performances of cdte and cdznte semiconductor detector arrays at high x-ray flux. In *Nuclear Science Symposium Conference Record (NSS/MIC), 2009 IEEE.*

[Carmi *et al.*, 2005] Carmi, R., Naveh, G., and Altman, A. (2005). Material separation with dual-layer CT. In *IEEE Nuclear Science Symposium Conference Record, 2005.*

[Castro *et al.*, 2004] Castro, C. R. F., Barroso, R. C., Anjos, M. J., Lopes, R. T., and Braz, D. (2004). Coherent scattering characteristics of normal and pathological breast human tissues. *Radiation Physics and Chemistry*, **71**:649–651.

[Castro *et al.*, 2005] Castro, C. R. F., Barroso, R. C., and Lopes, R. T. (2005). Scattering signatures for some human tissues using synchrotron radiation. *X-Ray Spectrom.*, **34**:477–480.

[Chaparian *et al.*, 2009] Chaparian, A., Oghabian, M., and Changizi, V. (2009). Acquiring molecular interference functions of x-ray coherent scattering for breast tissues by combination of simulation and experimental methods. *Iranian Journal of Radiation Research*, **7(2)**:113–117.

[Chaparian *et al.*, 2010] Chaparian, A., Oghabian, M., Changizi, V., and Farquharson, M. (2010). The optimization of an energy-dispersive x-ray diffraction system for potential clinical application. *Applied Radiation and Isotopes*, **68**:2237–2245.

[Chui, 1992] Chui, C. K. (1992). *An Introduction to Wavelets.* Academic Press Professional, Inc.

[Conceição *et al.*, 2010] Conceição, A., Antoniassi, M., Poletti, M., and Caldas, L. (2010). Preliminary study of human breast tissue using synchrotron radiation combining WAXS and SAXS techniques. *Applied Radiation and Isotopes*, **68**:799–803.

[Cook *et al.*, 2007] Cook, E., Fong, R., Horrocks, J., Wilkinson, D., and Speller, R. (2007). Energy dispersive X-ray diffraction as a means to identify illicit materials: A preliminary optimisation study. *Applied Radiation and Isotopes*, **65**:959–967.

[Cook *et al.*, 2009a] Cook, E., Griffiths, J., Koutalonis, M., Gent, C., Pani, S., Horrocks, J., L., G., S., H., and Speller, R. (2009a). Illicit drug detection using energy dispersive x-ray diffraction. In *Proc. SPIE*, volume 7310.

[Cook *et al.*, 2009b] Cook, E., Pani, S., George, L., Hardwick, S., Horrocks, J., and Speller, R. (2009b). Multivariate data analysis for drug identification using energy-dispersive x-ray diffraction. *IEEE Transactions on Nuclear Science*, **56**:1459–1464.

[Cozzini *et al.*, 2010] Cozzini, C., Harding, G., and Edic, P. (2010). Energy dispersive x-ray diffraction spectral resolution considerations for security screening applications. In *IEEE in Nuclear Science Symposium Conference Record, Knoxville.*

[Crespy *et al.*, 2010] Crespy, C., Duvauchelle, P., Kaftandjian, V., Soulez, F., and Ponard, P. (2010). Energy dispersive X-ray diffraction to identify explosive substances: Spectra analysis procedure optimization. *Nuclear Instruments and Methods in Physics Research, Section A: Accelerators, Spectrometers, Detectors and Associated Equipment*, **623**:1050–1060.

[Csiszár and Shields, 2004] Csiszár, I. and Shields, P. (2004). *Information Theory and Statistics: A Tutorial.* now Publishers Inc.

[Cullity, 1956] Cullity, B. (1956). *Elements of X-Ray Diffraction.* Addison-Wesley 1956.

[Cunningham and Shaw, 1999] Cunningham, I. A. and Shaw, R. (1999). Signal-to-noise optimization of medical imaging systems. *Journal of the Optical Society of America A, Optics and Image Science*, **16**:621–632.

[Dabak, 1992] Dabak, A. G. (1992). *A geometry for detection theory.* PhD thesis, Rice University.

[Dabak and Johnson, 2002] Dabak, A. G. and Johnson, D. H. (2002). Relations between Kullback-Leibler distance and Fisher information. http://www.ece.rice.edu/ dhj/distance.pdf.

[Dicken *et al.*, 2015] Dicken, A., Evans, J., Rogers, K., Greenwood, C., Godber, S., Prokopiou, D., Stone, N., Clement, J., Lyburn, I., Martin, R., and Zioupos, P. (2015). Energy-dispersive X-ray diffraction using an annular beam. *Optics Express*, **23**:13443–13454.

[Dicken *et al.*, 2010] Dicken, A., Rogers, K., Evans, P., Rogers, J., and Chan, J. (2010). The separation of x-ray diffraction patterns for threat detection. *Applied Radiation and Isotopes*, **68**:439–443.

[Duck, 1990] Duck, F. A. (1990). *Physical Properties of Tissue: A Comprehensive Reference Book.* Academic Press.

[Eilbert and Krug, 1993] Eilbert, R. F. and Krug, K. D. (1993). Aspects of image recognition in Vivid Technologies' dual-energy x-ray system for explosives detection. In *Proc. SPIE 1824, Applications of Signal and Image Processing in Explosives Detection Systems.*

[Evans *et al.*, 1991] Evans, S. H., Bradley, D. A., Dance, D. R., Bateman, J. E., and Jones, C. H. (1991). Measurement of small-angle photon scattering for some breast tissues and tissue substitute materials. *Physics in Medicine and Biology*, **36**:7–18.

[Farquharson and Geraki, 2004] Farquharson, M. J. and Geraki, K. (2004). The use of combined trace element XRF and EDXRD data as a histopathology tool using a multivariate analysis approach in characterizing breast tissue. *X-Ray Spectrometry*, **33**:240–245.

[Fernàndez *et al.*, 2005] Fernàndez, M., Keyriläinen, J., Serimaa, R., Torkkeli, M., Karjalainen-Lindsberg, M.-L., Leidenius, M., von Smitten, K., Tenhunen, M., Fiedler, S., Bravin, A., Weiss, T. M., and Suortti, P. (2005). Human breast cancer in vitro: matching histo-pathology with small-angle x-ray scattering and diffraction enhanced x-ray imaging. *Phys Med Biol*, **50**:2991–3006.

[Fernàndez *et al.*, 2002] Fernàndez, M., Keyriläinen, J., Serimaa, R., Torkkeli, M., Karjalainen-Lindsberg, M.-L., Tenhunen, M., Thomlinson, W., Urban, V., and Suortti, P. (2002). Small-angle x-ray scattering studies of human breast tissue samples. *Physics in Medicine and Biology*, **47**:577–592.

[Fessler and Hero, 1995] Fessler, J. and Hero, A. (1995). Penalized maximum-likelihood image reconstruction using space-alternating generalized EM algorithms. *IEEE Transactions on Image Processing*, **4**:74–77.

[Fradkin and Muchnik, 2006] Fradkin, D. and Muchnik, I. (2006). Support vector machines for classification. *Discrete methods in epidemiology*, **70**:13–20.

[Garrity *et al.*, 2010] Garrity, D., De Rosa, A., Bradley, D., Jarman, S., Jenneson, P., and Vincent, S. (2010). Development of a prototype pipework scanning system based upon energy dispersive x-ray diffraction (EDXRD). *Nuclear Instruments and Methods in Physics Research, Section A: Accelerators, Spectrometers, Detectors and Associated Equipment*, **619**:287–290.

[Geraki *et al.*, 2004] Geraki, K., Farquharson, M., and Bradley, D. (2004). X-ray fluorescence and energy dispersive x-ray diffraction for the characterisation of breast tissue. *Radiation Physics and Chemistry*, **71**:969–970.

[Ghammraoui, 2012] Ghammraoui, B. (2012). *Etude d'un syst ème d'identification de matériaux par diffraction de rayons X à partir d'acquisitions spectrométriques multi pixels.* PhD thesis, L'Institut National des Sciences Appliquées de Lyon.

[Ghammraoui and Badal, 2014] Ghammraoui, B. and Badal, A. (2014). Monte carlo simulation of novel breast imaging modalities based on coherent x-ray scattering. *Phys. Med. Biol.*, **59**:3501.

[Giovannelli *et al.*, 1994] Giovannelli, J.-F., Idier, J., Querleux, B., Herment, A., and Demoment, G. (1994). Maximum likelihood and maximum a posteriori estimation of Gaussian spectra. Application to attenuation measurement and color Doppler velocimetry. In *Proceedings of International Ultrasonics Symposium.*

[Greenberg *et al.*, 2013] Greenberg, J., Krishnamurthy, K., and Brady, D. (2013). Snapshot molecular imaging using coded energy-sensitive detection. *Optics Express*, **21**:25480–25491.

[Greenberg *et al.*, 2014] Greenberg, J. A., Hassan, M., Krishnamurthy, K., and Brady, D. (2014). Structured illumination for tomographic X-ray diffraction imaging. *Analyst*, **139**:709–713.

[Griffiths *et al.*, 2008] Griffiths, J., Royle, G., Horrocks, J., Hanby, A., Pani, S., and Speller, R. (2008). Angular dispersive diffraction microCT of small breast tissue samples. *Radiation Physics and Chemistry*, **77**:373–380.

[Groetsch, 1984] Groetsch, C. W. (1984). *The Theory of Tikhonov Regularization for Fredholm Equations of the First Kind.* Pitman.

[Hadamard, 1902] Hadamard, J. (1902). Sur les problèmes aux dérivés partielles et leur signification physique. *Princeton University Bulletin*, **13**:49–52.

[Harding, 2004] Harding, G. (2004). X-ray scatter tomography for explosives detection. *Radiation Physics and Chemistry*, **71**:869–881.

[Harding, 2009] Harding, G. (2009). X-ray diffraction imaging-a multi-generational perspective. *Applied Radiation and Isotopes*, **67**:287–295.

[Harding and Delfs, 2007] Harding, G. and Delfs, J. (2007). Liquids identification with x-ray diffraction. In *Proceedings of SPIE - The International Society for Optical Engineering, vol. 6707.*

[Harding *et al.*, 2012] Harding, G., Fleckenstein, H., Kosciesza, D., Olesinski, S., Strecker, H., Theedt, T., and Zienert, G. (2012). X-ray diffraction imaging with the Multiple Inverse Fan Beam topology: Principles, performance and potential for security screening. *Applied Radiation and Isotopes*, **70**:1228–1237.

[Harding *et al.*, 2010a] Harding, G., Fleckenstein, H., Olesinski, S., and Zienert, G. (2010a). Liquid detection trial with x-ray diffraction. In *Proc. SPIE; California, USA.*

[Harding *et al.*, 1987] Harding, G., Kosanetzky, J., and Neitzel, U. (1987). X-ray diffraction computed tomography. *Medical Physics*, **14**:515–525.

[Harding *et al.*, 2010b] Harding, G., Kosciesza, D., Olesinski, S., and Strecker, H. (2010b). Experimental comparison of next-generation XDi topologies. In *Proc. of SPIE*, volume 7806.

[Harding *et al.*, 1990] Harding, G., Newton, M., and Kosanetzky, J. (1990). Energy-dispersive x-ray diffraction tomography. *Physics in Medicine and Biology*, **35**:33–41.

[Harding and Schreiber, 1999] Harding, G. and Schreiber, B. (1999). Coherent x-ray scatter imaging and its application in biomedical science and industry. *Radiation physics and chemistry*, **56**:229–245.

[Harding *et al.*, 2009] Harding, G., Strecker, H., Olesinski, S., and Frutschy, K. (2009). Radiation source considerations relevant to next-generation x-ray diffraction imaging for security screening applications. In *Proc. of SPIE*, volume 7450.

[Hasinoff, 2014] Hasinoff, S. W. (2014). *Computer Vision: A Reference Guide*, chapter Photon, Poisson noise, pages 608–610. Springer.

[Hendrick, 2010] Hendrick, R. E. (2010). Radiation doses and cancer risks from breast imaging studies. *Radiology*, **257**:246–253.

[Hubbell and Veigele, 1975] Hubbell, W. and Veigele, J. (1975). Atomic Form Factors, Incoherent Scattering Functions, and Photon Scattering Cross Sections. *J. Phys. Chem. Ref.*, **Data 4**:471–538.

[Iowa, 2014] Iowa, U. S. (2014). Solid state structure. www.nde-ed.org/EducationResources/CommunityCollege/Materials/Structure/solidstate.htm. NDT Resource Center.

[Janet E. Joy *et al.*, 2005] Janet E. Joy, E. E. P., Diana B. Petitti, Editors, C. o. N. A. t. E. D., Diagnosis of Breast Cancer, I. o. M., and Council, N. R. (2005). *Saving Women's Lives:: Strategies for Improving Breast Cancer Detection and Diagnosis*. National Academies Press.

[Johns and Yaffe, 1987] Johns, P. C. and Yaffe, M. J. (1987). X-ray characterisation of normal and neoplastic breast tissues. *Phys Med Biol*, **32**:675–695.

[Jupp *et al.*, 2000] Jupp, I., Durrant, P., Ramsden, D., Carter, T., Dermody, G., Pleasants, I., and Burrows, D. (2000). The non-invasive inspection of baggage using coherent x-ray scattering. *IEEE Transactions on Nuclear Science*, **47**:1987–1994.

[Kidane *et al.*, 1999] Kidane, G., Speller, R. D., Royle, G. J., and Hanby, A. M. (1999). X-ray scatter signatures for normal and neoplastic breast tissues. *Physics in Medicine and Biology*, **44**:1791–1802.

[King and Johns, 2002] King, B. and Johns, P. (2002). Measurement of coherent scattering form factors using an image plate. *Physics in Medicine and Biology*, **47**:163–175.

[King *et al.*, 2011] King, B., Landheer, K., and Johns, P. (2011). X-ray coherent scattering form factors of tissues, water and plastics using energy dispersion. *Physics in Medicine and Biology*, **56**:4377–4397.

[Kosanetzky *et al.*, 1987] Kosanetzky, J., Knoerr, B., Harding, G., and Neitzel, U. (1987). X-ray diffraction measurements of some plastic materials and body tissues. *Medical Physics*, **14**:526–532.

[Koutalonis *et al.*, 2009] Koutalonis, M., Cook, E., Griffiths, J., Horrocks, J., Gent, C., Pani, S., George, L., Hardwick, S., and Speller, R. (2009). Designing an in-field system for illicit drug detection using x-ray diffraction. In *IEEE Nuclear Science Symposium Conference Record (NSS/MIC)*, pages 862–867.

[Ladd and Palmer, 2013] Ladd, M. and Palmer, R. (2013). *Structure determination by X-ray crystallography: Analysis by X-rays and Neutrons*. Springer, 5th edition.

[Lakshmanan *et al.*, 2016] Lakshmanan, M. N., Morris, R. E., Greenberg, J. A., Samei, E., and Kapadia, A. J. (2016). Coded aperture coherent scatter imaging for breast cancer detection: a monte carlo evaluation. In *Proc. SPIE 9783, Medical Imaging 2016: Physics of Medical Imaging*.

[Lange and Carson, 1984] Lange, K. and Carson, R. (1984). Em reconstruction algorithms for emission and transmission tomography. *Journal of Computer Assisted Tomography*, **8**:306–316.

[Langford and Louer, 1996] Langford, J. I. and Louer, D. (1996). Powder diffraction. *Reports on Progress in Physics*, **59**:131.

[Lauriat, 2003] Lauriat, J.-P. (online since 2003). Cristallographie - diffraction. http://jean-pierre.lauriat.pagesperso-orange.fr.

[LeClair *et al.*, 2006] LeClair, R. J., Boileau, M. M., and Wang, Y. (2006). A semianalytic model to extract differential linear scattering coefficients of breast tissue from energy dispersive x-ray diffraction measurements. *Medical Physics*, **33**:959–967.

[Leo, 1994] Leo, W. R. (1994). *Techniques for Nuclear and Particle Physics Experiments*. Springer.

[Lewis *et al.*, 2000] Lewis, R. A., Rogers, K. D., Hall, C. J., Towns-Andrews, E., Slawson, S., Evans, A., Pinder, S. E., Ellis, I. O., Boggis, C. R. M., Hufton, A. P., and Dance, D. R. (2000). Breast cancer diagnosis using scattered x-rays. *Journal of Synchrotron Radiation*, **7**:348–352.

[Li *et al.*, 2010] Li, L., Li, M., Sun, B., Liu, J.-H., and Zhang, F. (2010). Confirm of the optimum detection angles of several substances using energy dispersive X-ray diffraction. In *Symposium on Security Detection and Information Processing*.

[Li *et al.*, 2011] Li, W., Yu, D., Zhang, F., Sun, B., Liu, J., Li, M., and Liu, J. (2011). Detection of heroin covered by skin by using robust principal components analysis. *Measurement: Journal of the International Measurement Confederation*, **44**:267–273.

[Luggar *et al.*, 1998] Luggar, R., Farquharson, M., Horrocks, J., and Lacey, R. (1998). Multivariate Analysis of Statistically Poor EDXRD Spectra for the Detection of Concealed Explosives. *X-Ray Spectrometry*, **27**:87–94.

[Luggar *et al.*, 1997] Luggar, R., Horrocks, J., Speller, R., and Lacey, R. (1997). Low angle x-ray scatter for explosives detection: A geometry optimization. *Applied Radiation and Isotopes*, **48**:215–224.

[Lusted, 1971] Lusted, L. B. (1971). Signal detectability and medical decision-making. *Science*, **171**:1217–1219.

[Lux, 2012] Lux, S. (2012). *Amélioration de la résolution spatiale de détecteurs à semi-conducteur, pour l'imagerie gamma et X, par l'exploitation de signaux transitoires*. PhD thesis, Université de Grenoble.

[Maccabe *et al.*, 2013] Maccabe, K., Holmgren, A., Tornai, M., and Brady, D. (2013). Snapshot 2d tomography via coded aperture x-ray scatter imaging. *Applied Optics*, **52**:4582–4589.

[MacCabe *et al.*, 2012] MacCabe, K., Krishnamurthy, K., Chawla, A., Marks, D., Samei, E., and Brady, D. (2012). Pencil beam coded aperture x-ray scatter imaging. *Opt. Express*, **20**:16310–16320.

[Madden *et al.*, 2008] Madden, R., Mahdavieh, J., Smith, R., and Subramanian, R. (2008). An explosives detection system for airline security using coherent x-ray scattering technology. In *Proc. of SPIE*.

[Maitrejean *et al.*, 1998] Maitrejean, S., Perion, D., and Sundermann, D. (1998). Multi-energy method: a new approach for measuring x-ray transmission as a function of energy with a Bremsstrahlung source and its application for heavy element identification. In *Proc. SPIE 3446, Hard X-Ray and Gamma-Ray Detector Physics and Applications*.

[Malden and Speller, 2000] Malden, C. and Speller, R. (2000). Cdznte array for the detection of explosives in baggage by energy-dispersive X-ray diffraction signatures at multiple scatter angles. *Nuclear Instruments and Methods in Physics Research, Section A: Accelerators, Spectrometers, Detectors and Associated Equipment*, **449**:408–415.

[Marticke *et al.*, 2015a] Marticke, F., Montémont, G., Paulus, C., Mars, J., Michel, O. J., and Verger, L. (2015a). Energy dispersive X-ray diffraction system as a promising virtual biopsy in mammography. In *2015 IEEE Nuclear Science Symposium and Medical Imaging Conference (NSS/MIC)*.

[Marticke *et al.*, 2015b] Marticke, F., Montémont, G., Paulus, C., Michel, O. J., Mars, J., and Verger, L. (2015b). Calcul analytique de courbes COR en imagerie de diffraction X. In *Gretsi 2015, Lyon, 25ème édition*.

[Marticke *et al.*, 2014] Marticke, F., Paulus, C., Montémont, G., Michel, O. J., Mars, J., and Verger, L. (2014). Multi angle reconstruction of energy dispersive X-ray diffraction spectra. In *WHISPERS IEEE*.

[Meng and Ramsden, 2000] Meng, L.-J. and Ramsden, D. (2000). An inter-comparison of three spectral-deconvolution algorithms for gamma-ray spectroscopy. *IEEE Transactions on Nuclear Science*, **47**:1329–1336.

[Michalowska *et al.*, 2010] Michalowska, A., Gevin, O., Lemaire, O., Lugiez, F., Baron, P., Grabas, H., Pinsard, F., Limousin, O., and Delagnes, E. (2010). IDeF-X HD: A low power multi-gain CMOS ASIC for the readout of Cd(Zn)Te detectors. In *2010 IEEE Nuclear Science Symposium Conference Record (NSS/MIC)*.

[Miller, 2014] Miller, C. (2014). Thomson and rayleigh scattering. www.astro.umd.edu/ miller/teaching/astr601/lecture13.pdf.

[Montemont *et al.*, 2006] Montemont, G., Gentet, M.-C., Monnet, O., Rustique, J., and Verger, L. (2006). Simulation and Design of Orthogonal Capacitive Strip CdZnTe Detectors. In *IEEE Nuclear Science Symposium Conference Record, 2006*.

[Montemont *et al.*, 2012] Montemont, G., Lux, S., Monnet, O., Stanchina, S., and Verger, L. (2012). Evaluation of a CZT gamma-ray detection module concept for SPECT. In *IEEE Nuclear Science Symposium and Medical Imaging Conference (NSS/MIC)*.

[Montemont *et al.*, 2014] Montemont, G., Lux, S., Monnet, O., Stanchina, S., and Verger, L. (2014). Studying Spatial Resolution of CZT Detectors Using Sub-Pixel Positioning for SPECT. *IEEE Transactions on Nuclear Science*, **61**:2559–2566.

[Montemont *et al.*, 2003] Montemont, G., Rostaing, J. P., and Verger, L. (2003). Experimental comparison of discrete and CMOS charge sensitive preamplifiers for CZT radiation detectors. *IEEE Transactions on Nuclear Science*, **50**:936–941.

[Morhac and Matousek, 2009] Morhac, M. and Matousek, V. (2009). Complete positive deconvolution of spectrometric data. *Digital Signal Processing*, **19**:372–392.

[Morris *et al.*, 2016] Morris, R. E., Albanese, K. E., Lakshmanan, M. N., McCall, S. J., Greenberg, J. A., and Kapadia, A. J. (2016). Validation of coded aperture coherent scatter spectral imaging for normal and neoplastic breast tissues via surgical pathology. In *Proc. SPIE 9783, Medical Imaging 2016: Physics of Medical Imaging*.

[Narten *et al.*, 1967] Narten, A. H., Danford, M. D., and Levy, H. A. (1967). X-ray diffraction study of liquid water in the temperature range 4-200 °c. *Discuss. Faraday Soc.*, **43**:97–107.

[Narten and Levy, 1971] Narten, A. H. and Levy, H. A. (1971). Liquid water: Molecular correlation functions from x-ray diffraction. *J. Chem. Phys.*, **55**:2263–2269.

[Odinaka *et al.*, 2016] Odinaka, I., Greenberg, J. A., Kaganovsky, Y., Holmgren, A., Hassan, M., Politte, D. G., O'Sullivan, J. A., Carin, L., and Brady, D. J. (2016). Coded aperture x-ray diffraction imaging with transmission computed tomography side-information. In *Proc. SPIE 9783, Medical Imaging 2016: Physics of Medical Imaging*.

[O'Flynn *et al.*, 2013] O'Flynn, D., Reid, C. B., Christodoulou, C., Wilson, M. D., Veale, M. C., Seller, P., Hills, D., Desai, H., Wong, B., and Speller, R. (2013). Explosive detection using pixellated x-ray diffraction (pixd). *JINST*, **8**:P03007.

[Pang *et al.*, 2014] Pang, S., Hassan, M., Greenberg, J., Holmgren, A., Krishnamurthy, K., and Brady, D. (2014). Complementary coded apertures for 4-dimensional x-ray coherent scatter imaging. *Optics Express*, **22**:22925.

[Pani *et al.*, 2009] Pani, S., Cook, E., Horrocks, J., George, L., Hardwick, S., and Speller, R. (2009). Modelling an energy-dispersive x-ray diffraction system for drug detection. *IEEE Transactions on Nuclear Science*, **56**:1238–1241.

[Pani *et al.*, 2010] Pani, S., Cook, E., Horrocks, J., Jones, J., and Speller, R. (2010). Characterization of breast tissue using energy-dispersive x-ray diffraction computed tomography. *Applied Radiation and Isotopes*, **68**:1980–1987.

[Pani *et al.*, 2007] Pani, S., Royle, G., Speller, R., Castoldi, A., Galimberti, A., and Guazzoni, C. (2007). Use of a novel controlled drift detector for diffraction enhanced breast imaging. *Nuclear Instruments and Methods in Physics Research Section A: Accelerators, Spectrometers, Detectors and Associated Equipment*, **573**:133–136.

[Pease *et al.*, 2013] Pease, C. S., Goode, A. R., McGraw, J. K., Baker, D., Jackson, J., and Gay, S. B. (2013). Atomic and molecular interactions. http://www.med-ed.virginia.edu/courses/rad/radbiol/01physics/phys-03-05.html. University of Virginia Health Sciences Center, Department of Radiology.

[Peplow and Verghese, 1998] Peplow, D. and Verghese, K. (1998). Measured molecular coherent scattering form factors of animal tissues, plastics and human breast tissue. *Physics in Medicine and Biology*, **43**:2431–2456.

[Peterzol *et al.*, 2011] Peterzol, A., Duvauchelle, P., Kaftandjian, V., and Ponard, P. (2011). Modeling-based optimization study for an EDXRD system in a portable configuration. *Nuclear Instruments and Methods in Physics Research, Section A: Accelerators, Spectrometers, Detectors and Associated Equipment*, **654**:450–463.

[Pineda and Barrett, 2004] Pineda, A. and Barrett, H. (2004). Figures of merit for detectors in digital radiography. i. flat background and deterministic blurring. *Medical Physics*, **31**:348–358.

[Poletti *et al.*, 2002] Poletti, M. E., Gonçalves, O. D., and Mazzaro, I. (2002). X-ray scattering from human breast tissues and breast-equivalent materials. *Phys. Med. Biol.*, **47**:47.

[Poletti *et al.*, 2004] Poletti, M. E., Gonçalves, O. D., and Mazzaro, I. (2004). Measurements of x-ray scatter signatures for some tissue-equivalent materials. *Nuclear Instruments and Methods in Physics Research Section B: Beam Interactions with Materials and Atoms*, **213**:595–598.

[Poludniowski *et al.*, 2009] Poludniowski, G., Landry, G., DeBlois, F., Evans, P. M., and Verhaegen, F. (2009). SpekCalc: a program to calculate photon spectra from tungsten anode x-ray tubes. *Phys. Med. Biol.*, **54**:N433.

[Qu *et al.*, 2010] Qu, D., Yu, D., Li, W., Zhang, Y., Sun, B., Zhong, Y., Li, M., and Liu, J. (2010). Identification of pure liquid precursor chemicals based on coherence function and fourier transform using energy dispersive x-ray diffraction scattering. In *Procedia Engineering*, volume 7, pages 158–164.

[Rajaona, 2012] Rajaona, H. (2012). *Méthodes d'inversion de spectres issus de détecteurs semi-conducteurs pour l'identification de matériaux en diffraction X.* PhD thesis, CEA-LETI LDET.

[Rose, 1946] Rose, A. (1946). A unified approach to the performance of photographic film, televison pick-up tubes, and the human eye. *J Soc Motion Pict Telev Eng*, **47**:273–294.

[Rose, 1953] Rose, A. (1953). Quantum and noise limitations of the visual process. *J. Opt. Soc. Am.*, **43**:715–716.

[Ryan and Farquharson, 2007] Ryan, E. and Farquharson, M. (2007). Breast tissue classification using x-ray scattering measurements and multivariate data analysis. *Physics in Medicine and Biology*, **52**:6679–6696.

[Salvat *et al.*, 2008] Salvat, F., Fernández-Varea, J. M., and Sempau, J. (2008). *PENELOPE-2008: A Code System for Monte Carlo Simulation of Electron and Photon Transport.* OECD.

[Seibert and Boone, 2005] Seibert, J. A. and Boone, J. M. (2005). X-ray imaging physics for nuclear medicine technologists. part 2: X-ray interactions and image formation. *J Nucl Med Technol*, **33**:3–18.

[Shaw, 1963] Shaw, R. (1963). The equivalent quantum efficiency of the photographic process. *J Photogr Sci*, **11**:199–204.

[Shepp and Vardi, 1982] Shepp, L. and Vardi, Y. (1982). Maximum likelihood reconstruction for emission tomography. *IEEE Transactions on Medical Imaging*, **1**:113–122.

[Soulez *et al.*, 2011] Soulez, F., Crespy, C., Kaftandjian, V., and Duvauchelle, P. (2011). Diffraction peaks restoration and extraction in energy dispersive x-ray diffraction. *Nuclear Instruments and Methods in Physics Research, Section A: Accelerators, Spectrometers, Detectors and Associated Equipment*, **654**:441–449.

[Speller, 2001] Speller, R. (2001). Radiation-based security. *Radiation Physics and Chemistry*, **61**:293–300.

[Sprawls, 1995] Sprawls, P. (1995). *Physical Principles of Medical Imaging, 2nd ed.* www.sprawls.org/ppmi2.

[Stines, 2007] Stines, J. (2007). Doses reçues par les patients lors des examens de dépistages et évaluation du rapport bénéfice/risque. In *Rencontres Nucléaire et santé.*

[Strecker *et al.*, 1993] Strecker, H., Harding, G., Bomsdorf, H., Kanzenbach, J., Linde, R., and Martens, G. (1993). Detection of explosives in airport baggage using coherent x-ray scatter. *Proceedings of SPIE - The International Society for Optical Engineering*, **2092**:399–410.

[Stute and Comtat, 2013] Stute, S. and Comtat, C. (2013). Practical considerations for image-based PSF and blobs reconstruction in PET. *Phys. Med. Biol.*, **58**:3849.

[Sun *et al.*, 2010] Sun, B., Li, M., Zhang, F., Zhong, Y., Kang, N., Lu, W., and Liu, J. (2010). The performance of a fast testing system for illicit materials detection based on energy-dispersive X-ray diffraction technique. *Microchemical Journal*, **95**:293–297.

[Tartari *et al.*, 2002] Tartari, A., Taibi, A., and Bonifazzi, C. (2002). Updating of form factor tabulations for coherent scattering of photons in tissues. *Physics in Medicine and Biology*, **47**:163–175.

[Tikhonov and Arsenin, 1977] Tikhonov, A. N. and Arsenin, V. Y. (1977). *Solutions of ill-posed problems.* V. H. Winston & Sons, Washington, D.C.: John Wiley & Sons, New York.

[van Erkel and Pattynama, 1998] van Erkel, A. R. and Pattynama, P. M. (1998). Receiver operating characteristic (ROC) analysis: basic principles and applications in radiology. *Eur J Radiol*, **27**:88–94.

[Vardi *et al.*, 1985] Vardi, Y., Shepp, L. A., and Kaufman, L. (1985). A statistical model for positron emission tomography. *Journal of the American Statistical Association*, **80**:8–20.

[Verger *et al.*, 2007] Verger, L., d'Aillon, E. G., Monnet, O., Montémont, G., and Pelliciari, B. (2007). New trends in γ-ray imaging using CdZnTe/CdTe at CEA-Leti. *Nucl. Instr. and Meth. A*, **571**:33–43.

[Verger *et al.*, 2004] Verger, L., Gentet, M., and Gerfault, L. (2004). Performance and perspectives of a cdznte-based gamma camera for medical imaging. *IEEE Transactions on Nuclear Science*, **51**:3111–3117.

[Vogel, 2007] Vogel, H. (2007). Search by X-rays applied technology. *European Journal of Radiology*, **63**:227–236.

[Warburton, 1997] Warburton, W. K. (1997). An approach to sub-pixel spatial resolution in room temperature x-ray detector arrays with good energy resolution. In *Symposium I Semiconductors for Room-Temperature Radiation II.*

[Westmore *et al.*, 1997] Westmore, M., Fenster, A., and Cunningham, I. (1997). Tomographic imaging of the angular-dependent coherent-scatter cross section. *Medical Physics*, **24**:3–10.

[Yu *et al.*, 2010] Yu, D., Li, M., Li, W., Zhang, F., Sun, B., and Liu, J. (2010). Energy dispersive X-ray diffraction research using coherence function. In *Symposium on Security Detection and Information Processing*, volume 7.

[Zentai, 2008] Zentai, G. (2008). X-ray imaging for homeland security. In *IEEE International Workshop on Imaging Systems and Techniques*, pages 1–6.

[Zhang *et al.*, 2010a] Zhang, F., Li, M., Li, W., Zhong, Y., and Liu, J. (2010a). Research and analysis of non-destructive detection of heroin hidden in human body. In *Symposium on Security Detection and Information Processing*, volume 7.

[Zhang *et al.*, 2010b] Zhang, F., Li, M., Qi, C.-X., Bai, S., Zhong, Y., Yu, D., and Liu, J.-H. (2010b). Identification of heroin covered by simulation skin using energy dispersive X-ray diffraction and Coherence Function. In *International Conference on Electrical and Control Engineering*.

[Zhang, 2000] Zhang, G. P. (2000). Neural networks for classification: A survey. *Trans. Sys. Man Cyber Part C*, **30**:451–462.

[Zhang *et al.*, 2010c] Zhang, Y., Li, M., Zhong, Y., Li, W., Sun, B., Yu, D., and Liu, J. (2010c). Analysis of skin influence in identification of heroin using singular value decomposition. In *Symposium on Security Detection and Information Processing*.

[Zhang *et al.*, 2011] Zhang, Y., Li, M.-Q., Zhong, Y., Li, W., Sun, B., Yu, D.-Y., and Liu, J.-H. (2011). Application of singular value decomposition for identification of liquid precursor chemicals using energy-dispersive x-ray scattering. *Instrumentation Science and Technology*, **39**:20–33.

[Zhong *et al.*, 2010] Zhong, Y., Sun, B., Yu, D., Li, W., Zhang, Y., Li, M., and Liu, J. (2010). Identification of liquid materials using energy dispersive x-ray scattering. In *Procedia Engineering*, volume 7, pages 135–142.

ABSTRACT

X-ray diffraction imaging is a powerful noninvasive technique to identify or characterize different materials. Compared to traditional techniques using X-ray transmission, it allows to extract more material characteristic information, such as the Bragg peak positions for crystalline materials as well as the molecular form factor for amorphous materials. The potential of this technique has been recognized by many researchers and numerous applications such as luggage inspection, nondestructive testing, drug detection and biological tissue characterization have been proposed.

The method of energy dispersive X-ray diffraction (EDXRD) is particularly suited for this type of applications as it allows the use of a conventional X-ray tube, the acquisition of the whole spectrum at the same time and parallelized architectures to inspect an entire object in a reasonable time. The purpose of the present work is to optimize the whole material characterization chain. Optimization comprises two aspects: optimization of the acquisition system and of data processing. The last one concerns especially the correction of diffraction pattern degraded by acquisition process. Reconstruction methods are proposed and validated on simulated and experimental spectra. System optimization is realized using figures of merit such as detective quantum efficiency (DQE), contrast to noise ratio (CNR) and receiver operating characteristic (ROC) curves.

The first chosen application is XRD based breast imaging which aims to distinguish cancerous tissues from healthy tissues. Two non-multiplexed collimation configurations combining EDXRD and ADXRD are proposed after optimization procedure. A simulation study of the whole system and a breast phantom was realized to determine the required dose to detect a 4 mm carcinoma nodule. The second application concerns detection of illicit materials during security check. The possible benefit of a multiplexed collimation system was examined.

Key words: X-ray imaging, inverse problem, system optimization, coherent scattering, breast cancer diagnosis, luggage inspection

RESUME

L’imagerie basée sur la diffraction des rayons X est une technique non-invasive puissante pour l’identification et caractérisation de matériaux différents. Comparée aux techniques traditionnelles utilisant la transmission des rayons X, elle permet d’extraire des informations beaucoup plus caractéristiques pour le matériau inspecté, comme les positions des pics de Bragg pour des matériaux cristallins et le facteur de forme moléculaire pour les matériaux amorphes. Le potentiel de cette méthode a été reconnu par de nombreuses équipes de recherche et de nombreuses applications comme l’inspection de bagage, le contrôle non-destructif, la détection de drogue et la caractérisation de tissus biologiques ont été proposées.

La méthode par dispersion d’énergie (EDXRD) est particulièrement adaptée à ce type d’application car elle permet l’utilisation d’un tube à rayons X conventionnel, l’acquisition du spectre entier en une fois et des architectures parallélisées pour l’inspection d’un objet entier en un temps raisonnable. L’objectif de ce travail est d’optimiser toute la chaîne de caractérisation. L’optimisation comprend deux aspects : l’optimisation du système d’acquisition et du traitement des données. La dernière concerne particulièrement la correction des spectres de diffraction dégradés par le processus d’acquisition. Des méthodes de reconstruction sont proposées et validées sur des spectres simulés et expérimentaux. L’optimisation du système est réalisée en utilisant des facteurs de mérite comme l’efficacité quantique de détection (DQE), le rapport contraste sur bruit (CNR) et les courbes de caractéristiques opérationnelles de réception (ROC).

La première application choisie, c’est l’imagerie du sein basée sur la diffraction qui a pour but de distinguer des tissus cancéreux des tissus sains. Deux configurations de collimation sans multiplexage combinant EDXRD et ADXRD sont proposées suite au processus d’optimisation. Une étude de simulation du système entier et d’un fantôme de sein a été réalisée afin de déterminer la dose requise pour la détection d’un petit carcinome de 4 mm. La deuxième application concerne la détection de matériaux illicites pendant le contrôle de sécurité. L’intérêt possible d’un système de collimation multiplexé a été étudié.

Mots clés: Imagerie par rayons X, problème inverse, optimisation de système, diffusion cohérente, diagnostic du cancer du sein, contrôle de bagage

CEA, LETI, Minatec Campus, F-38054 Grenoble, France
Univ. Grenoble-Alpes, Gipsa-Lab, F-38000 Grenoble, France